



University of Tehran

Print ISSN: 2322-2093

Online ISSN: 2423-6691

Volume 57, Number 1, June 2024

Civil Engineering Infrastructures Journal

CEIJ

Available online at
<http://ceij.ut.ac.ir/>

Civil Engineering Infrastructures Journal (CEIJ)

Semiannual Publication

Editor – in - Charge

Soltani, N., Professor
nsoltani@ut.ac.ir

Editor – in – Chief

Tabesh, M., Professor
mtabesh@ut.ac.ir

Executive Manager and Contact Person

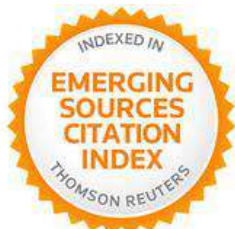
Akhtari, N.
cej@ut.ac.ir

Published by:

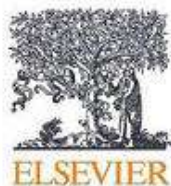


University of Tehran
College of Engineering

Indexed by:



Web of Science (ESCI)



Scopus

Civil Engineering Infrastructures
Journal (CEIJ)
College of Engineering
University of Tehran
P.O. Box: 11155-4563
Tehran, Iran.
Tel/ Fax: +98-21-88956097
Email: ceij@ut.ac.ir
Web Site: www.ceij.ir

Editorial Board

Askari, F., Associate Professor, International Institute of Earthquake Engineering and Seismology, Iran.

Aslani, F., Associate Professor, University of Western Australia, Australia.

Babazadeh, A., Associate Professor, University of Tehran, Iran.

Behnamfar, F., Associate Professor, Isfahan University of Technology, Iran.

EskandariGhadi, M., Professor, University of Tehran, Iran.

Fatahi, B., Associate Professor, University of Technology Sydney, Australia.

Gupta, R., Professor, Visvesvaraya National Institute of Technology, India.

Heravi, Gh.R., Professor, University of Tehran, Iran.

Kerachian, R., Professor, University of Tehran, Iran.

Mahmoudzadeh Kani, I., Professor, University of Tehran, Iran.

Mazza, F., Professor, University of Calabria, Italy.

Moghadas Nejad, F., Professor, Amirkabir University of Technology, Iran.

Moridpour, S., Associate Professor, RMIT University, Australia.

Motamed, R., Associate Professor, University of Nevada, USA.

Salehi Neyshabouri, A.A., Professor, Tarbiat Modarres University, Iran.

Nourani, V., Professor, University of Tabriz, Iran.

Ouhadi, V.R., Professor, Bu-Ali Sina University, Iran.

Shafei, B., Associate Professor, Iowa State University, USA.

Naderpajouh, N., Associate Professor, University of Sydney, Australia.

Shekarchizadeh, M., Professor, University of Tehran, Iran.

Shafieezadeh, A., Associate Professor, Ohio State University, USA.

Tanyimboh, T., Associate Professor, University of the Witwatersrand, South Africa.

Touran, A., Professor, Northeastern University, USA.

Towhata, I., Professor, University of Tokyo, Japan.

Zahraei, S.M., Professor, University of Tehran, Iran.

Advisory Board

Ahmadi, M.T., Professor, Tarbiat Modarres University, Iran.

Behnia, K., Associate Professor, University of Tehran, Iran.

Benekohal, R.F., Professor, University of Illinois, USA.

Gatmiri, B., Professor, University of Tehran, Iran.

Mobasher, B., Professor, Arizona State University, USA.

Motavali, M., Professor, Structural Engineering Research Laboratory, EMPA, Switzerland.

Rahimian, M., Professor, University of Tehran, Iran.

Saiidi, M., Professor, University of Nevada, Reno, USA.

Sorooshian, S., Professor, University of California, USA.

CONTENTS

Volume 57, Number 1, June 2024

Research Papers

- Compressive Strength and Microstructural Properties of Sustainable 1**
Concrete Containing Nanosilica, Alccofine and Metakaolin
Bhat, A.H., Naqash, J.A., Habib, T. and Islam, S.U.
- Damage Detection of Truss Bridges Using Wavelet Transform of Rotation Signal..... 17**
Ghafouri, H.R., Khajehdezfuly, A. and Saadat Poor, O.
- A Novel Method for Modal Analysis of Dam-Reservoir Systems 33**
Rezaiee-Pajand, M., Kazemiyani, M.S. and Mirjalili, Z.
- Comparison of the Mechanical Performance of Concrete Reinforced..... 61**
with Recycled Steel Fibers from Waste Tires and Hooked-End Steel
Fibers at Ambient and High Temperatures
Modarres, Y. and Ghalehnovi, M.
- Predicting the Fluctuation of Travel Time Reliability as a Result..... 85**
of Congestion Variations by Bagging-Based Regressors
Afandizadeh Zargari, Sh., Amoei Khorshidi, N., Mirzahosseini, H. and Shakoori, S.
- Effective Location of Shear Walls in High-Rise RCC Buildings..... 103**
Subjected to Lateral Loads
Shukla, K. and Nallasivam, K.
- Three-Dimensional Numerical Investigation of Tunnel Behavior 119**
Based on Different Constitutive Models and Associated Parametric
Analysis in Rock Medium
Chalajour, S. and Hataf, N.
- Optimization of Dynamic Compaction Procedure for Sandy Soils 145**
Bayat, M., Saadat, M. and Hojati, A.
- Pushover Analysis of Reinforced Concrete Moment-Resisting Frames to Account 157**
for the Variations of Axial Forces on the Moment Curvature Properties
Samadi, N., Aghayari, R. and Izadpanah, M.
- Upper Bound Solution for the Stability of Surcharged Soil Slope..... 175**
Using Nonlinear Failure Criterion
Aminpour, M.M. and Maleki, M.
- Determination of DBTT of Functionally Graded Steels Using Artificial Intelligence 189**
Anjali, K., Yesilyurt, S.N., Samui, P., Dalkilic, H.Y. and Katipoglu, O.M.
- Comparative Study of the Effects of Key Factors on Concrete-to-Concrete 205**
Bond Strength
Mack, V., Salehfard, R. and Habibnejad Korayem, A.



Compressive Strength and Microstructural Properties of Sustainable Concrete Containing Nanosilica, Alccofine and Metakaolin

Bhat, A. H.^{1*}, Naqash, J. A.², Habib, T.¹ and Islam, S. U.¹

¹ Ph.D. Candidate, Department of Civil Engineering, National Institute of Technology, Srinagar, India.

² Associate Professor, Department of Civil Engineering, National Institute of Technology, Srinagar, India.

© University of Tehran 2023

Received: 05 Sep. 2022;

Revised: 18 Jan. 2023;

Accepted: 27 Feb. 2023

ABSTRACT: Structural characteristics of concrete incorporating Colloidal Nanosilica (CNS), Metakaolin (MK) and Alccofine (AF) were comparatively studied using X-Ray Diffraction (XRD), Thermogravimetric Analysis (TGA), Field Emission Scanning Electron Microscope (FESEM), and Fourier Transform Infrared spectroscopy (FTIR). The plasticizer demand and compressive strength at 3,7,28 and 90 days of curing ages were also determined. The results indicated that the demand for plasticizer content increased with CNS and MK incorporation owing to their large surface area and rough surface texture, respectively. However, AF decreased the plasticizer demand due to glassy surface morphology. Also, the compressive strength increased with replacement ratio. The tetranary blended systems (M6) proved to be more advantageous compared to binary, ternary and normal OPC systems. FTIR, TGA, XRD and FESEM analysis were consistent with the results of compressive strength. The improvement in properties of concrete at early ages was attributed to filler and nucleation effect of CNS and AF. At later ages, CNS modified the CSH by increasing the length of silicate chains, AF and MK diminished the portlandite content by utilizing it in pozzolanic reaction and filling of pores partially or completely especially by secondary CSH gel, led to denser structure.

Keywords: Compressive Strength, FTIR, SEM, Sustainable Concrete, TGA/DSC, XRD.

1. Introduction

The quest for developing green concrete is increasing considerably during the present times as the demand from construction industry and environmental protection agencies increased. Considerable research has been carried out to study the use of mineral admixtures or Supplementary Cementing Materials (SCM) as partial replacement to cement. These mineral

admixtures are either produced from natural sources (Kaolinite, limestone, etc.) or are by-products or waste materials (Fly ash, Silica fume, Slag, etc.) from different industries. The engineering benefits by using these admixtures mainly resulted from their fine particle size and pozzolanic reactivity (Malhotra and Mehta, 2004).

Pozzolanic materials mainly silica fume, flyash, rice husk ash, slag etc have been used extensively in construction industry.

* Corresponding author E-mail: aabid_15phd2017@nitsri.net

The improvement in concrete properties due to the addition of slag as cement replacement has increased significantly and various specifications have been laid for manufacturing and use of slag cement in concrete mixtures (Bureau of Indian Standards, 2015). The mechanism responsible for improvement has been well documented (Özbay et al., 2016). The properties and microstructure development are critical to figure out the long-term performance typically in marine and acidic environmental conditions. The slow microstructure development at the early ages provides less resistance to adverse effects of surrounding environment. Alccofine (AF) or ultrafine slag is a new generation SCM having superior properties compared to normal slag, especially the strength gain at early ages. It is produced through a controlled granulation process resulting in an ultra-fine particle size and high reactivity. Compared to the normal slag, AF has produced concrete with better performance especially in terms of workability, segregation resistance, improvement in strength development and durability characteristics, owing to their large specific surface area of particles (Kavyateja et al., 2019; Shaat et al., 2020). Sharmila and Dhinakaran (2015) studied the effect of replacement of cement by 0-15% AF and reported that 10% AF produced concrete with superior hardened properties.

The metakaolin (MK) as SCM on the other hand has received considerable interest from researchers due to its higher pozzolanic characteristics (Abdelli et al., 2017; El-Diadamony et al., 2018). MK is produced from calcination of kaolin clay at 650-800 °C (Medri et al., 2020), substantially lower energy requirement for production compared to clinker (1400 °C). This means that the production energy and cost of MK are comparatively less than cement. Besides this, the difference with other SCMs is the MK is primary product and others are secondary or by-products. Therefore, MK can be manufactured in a

controlled process with desired characteristics. Wild et al. (1996) stated that MK is far superior than other pozzolans as it has the ability to accelerate the cement hydration, and specified that MK seems playing a catalytic effect on hydration reaction.

Various researchers have reported that MK increases the strength parameters at later ages (Ashok et al., 2021; Lima et al., 2023). Some studies even reported the increase of strength at early ages. The increase in strength at early age is believed to be as a result of pore filling effect of fine MK particles which occupy the space left between the cement grains (da Silva Andrade et al., 2018). However, the strength gain at later ages is as a result of pozzolanic reaction of MK with portlandite, which increases the hydrated aluminium silicates responsible for strength gain and improvement in durability properties like resistance to water and chloride ingress, sulphate and acid resistance etc. (Abdelmelek and Lubloy, 2021; Bhat and Naqash, 2022; Wang et al., 2018). Although some studies have reported the effects of introducing metakaolin as cement replacements (Al Menhosh et al., 2018; Sujjavanich et al., 2017; Zhan et al., 2020), however a systematic behaviour of MK was lacking.

Besides these continued efforts of replacing cement with mineral admixtures, various researchers (such as Hamed et al., 2019; Senff et al., 2012) anticipated that the quick advancement of nanotechnology might be effective for pushing concrete technology to next level in order to meet the desired qualities of concrete and its sustainability goals. For this, some studies have reported the impact of nano silica on performance of concrete and observed a considerable increase in strength and transport properties compared to normal concrete (Rong et al., 2020; Wang et al., 2018). The improvement of concrete performance is attributed to the filling effect and pozzolanic properties. However, it is also stated that due to its small size and high

specific surface area, it has enhanced the rate of cement hydration by acting as nucleating agent. Uddin et al. (2015) has studied the effect of nanosilica with silica fume and flyash in blended cement composites, and observed that strength, durability and microstructure were enhanced.

The focus of this paper is to develop a sustainable concrete matrix with enhanced characteristics than conventional concrete. This work studies the effect of replacing cement partially by AF, MK and CNS. Although the influence of binary additives on properties of concrete is studied. However, hardly any research is available in which the combined effect of CNS, MK and AF is thoroughly studied. Therefore, this is the motivation behind this study and it is highly reckoned that this will be useful for various stakeholders intending the usage of CNS, MK and AF in cement composites. This research studies binary, ternary and quaternary blended concrete composites of CNS, MK, AF and Portland cement. The effect of CNS (0-0.45%), MK (0-20%) and AF (0-20%) on workability and compressive strength are studied. Microstructural characterisation is carried out using various analytical tools such as X-Ray Diffraction (XRD), Thermogravimetric analysis (TGA), Field Emission Scanning Electron Microscope (FESEM), and Fourier Transform Infrared

Spectroscopy (FTIR) for supporting the experimental results.

2. Materials and Methods

2.1. Materials

Various materials used during this experimental work are as follows:

- Cement (OPC Grade 43), confirming to BIS: 8112 (2013) and ASTM type-I, supplied by Khyber Industries Pvt. Ltd.
- Nanosilica in colloidal form (30.58% solid content), manufactured and supplied by BEE CHEMS.
- AF, commercially manufactured and supplied by Counto Microfine Products Pvt. Ltd.
- MK was supplied by Kaomin Industries LLP.
- Good quality and well graded coarse aggregates of crushed boulders with maximum size of 20 mm and well graded river sand of maximum size of 4.75 mm were used during this experimental work. The specific gravity of coarse and fine aggregates determined experimentally were of 2.79 and 2.6, respectively. The gradation curves have been plotted and presented in Figure 1.
- Auramix-400, a poly-carboxylate ether-based plasticizer, was used as water reducing admixture, supplied by Fosroc Constructive Solutions.

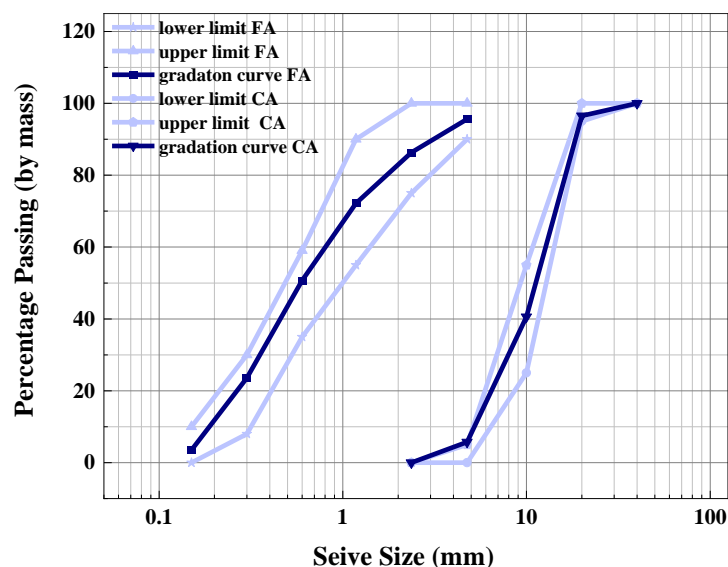


Table 1 shows the composition of Cement, CNS, MK and AF and Table 2 shows the characteristics and properties of cement used during this experimental work. It can be observed in Table 2 that CNS contains 99.5% silica, AF contains 35.5% of silica and 21.20% of alumina and MK

contains 52.52% of silica and 44.74% of alumina. The particle shape of MK, cement and AF were observed under FE-SEM and are presented in Figure 2. XRD analysis was carried out on MK, AF, cement and CNS to identify the crystalline phases Figure 3.

Table 1. Physical and chemical characteristics of Cement, MK, AF and CNS

| Chemical characteristics | Cement | MK | AF | CNS |
|--------------------------------------|---------|----------------|------------|-----------|
| SiO ₂ (%) | 19.44 | 52.54 | 35.51 | 99.55 |
| Al ₂ O ₃ (%) | 4.73 | 44.72 | 21.21 | <0.003 |
| Fe ₂ O ₃ (%) | 3.14 | 0.4 | - | <0.001 |
| CaO (%) | 62.3 | 0.14 | 32.3 | - |
| MgO (%) | 3.00 | 0.17 | 6.12 | - |
| SO ₃ (%) | 3.48 | 0.00 | 0.11 | - |
| Loss on ignition (%) | 2.16 | 0.48 | 0.68 | - |
| Physical characteristics | | | | |
| Form | Powder | Powder | Powder | Colloidal |
| Colour | Greyish | Pinkish white | Light grey | White |
| Size | - | 0.6-1.41 μ | 4-6 μ | 5-40 nm |
| Blaine fineness (m ² /kg) | 350 | 1670 | 1030 | - |
| Specific gravity | 3.14 | 2.61 | 2.87 | 1.22 |

Table 2. Properties and characteristics of Cement

| Specific gravity | Consistency | Setting time (min) | | Compressive strength (MPa) | |
|------------------|-------------|--------------------|-------|----------------------------|---------|
| | | Initial | Final | 7 days | 28 days |
| 3.14 | 29.55% | 119 | 225 | 35 | 46 |

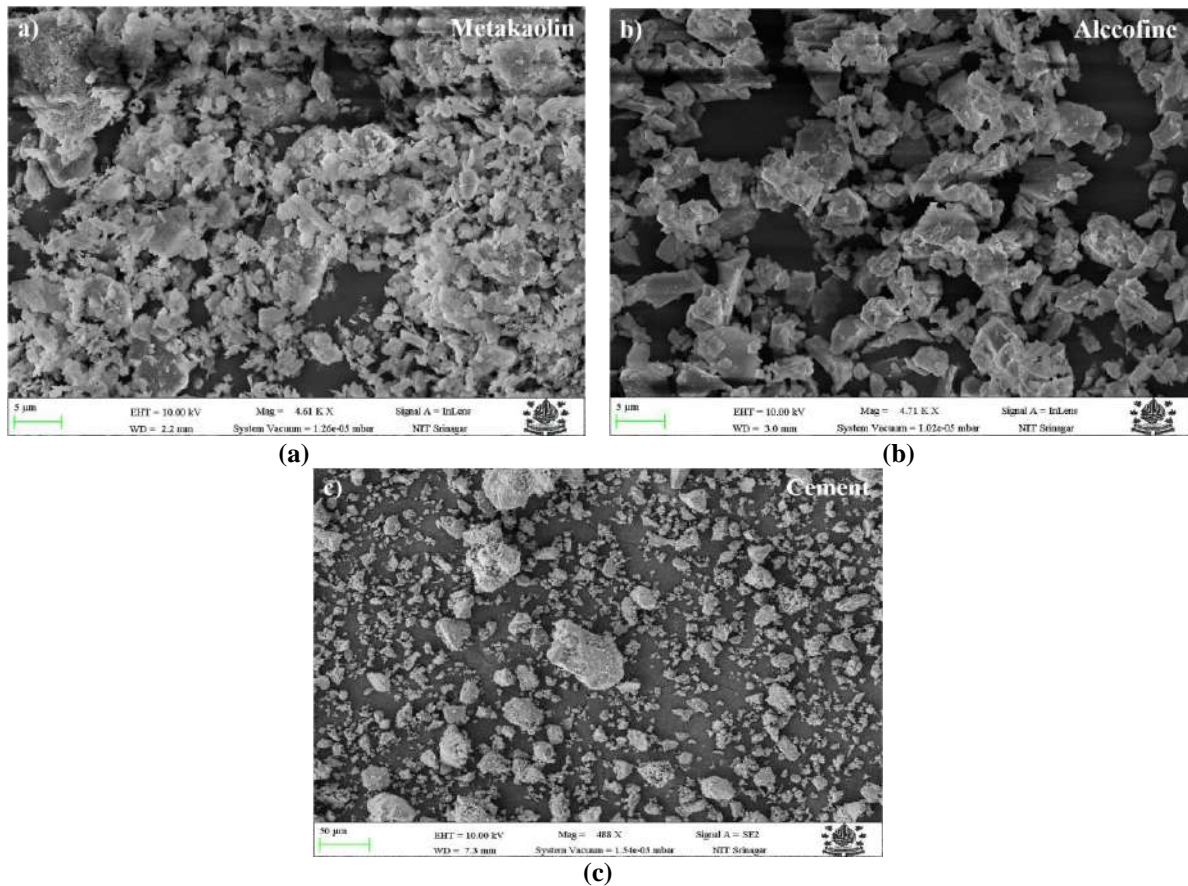


Fig. 2. FESEM of: a) MK; b) AF; and c) Cement

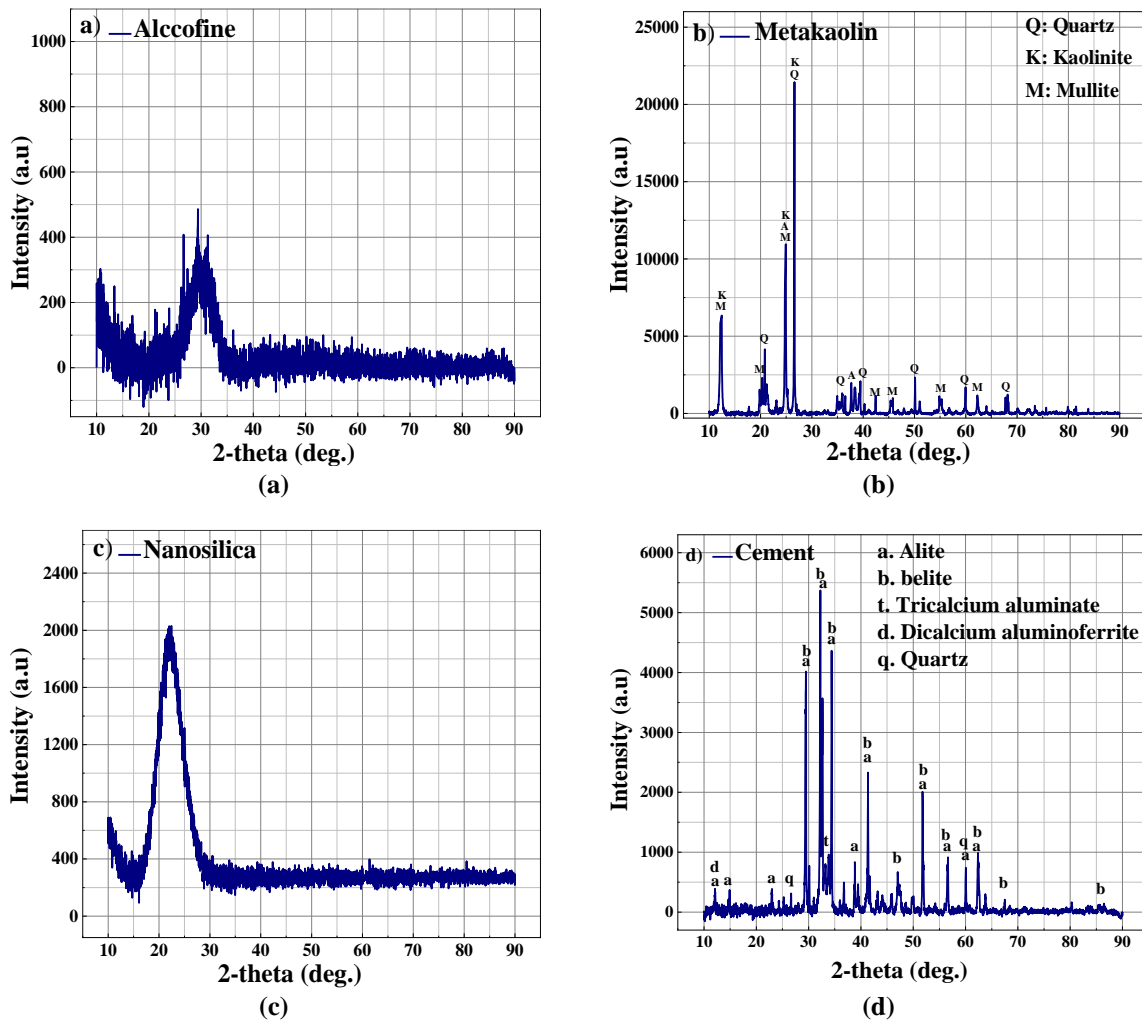


Fig. 3. XRD analysis of: a) AF; b) MK; c) CNS; and d) Cement

2.2. Mix Proportions

Trials for preparation of concrete mixtures of target strength 38 MPa for reference mixture at 28 days of curing age were carried out. The water to cement ratio was kept constant at 0.44. Nine different mixtures with varying replacement ratios of MK, AF and CNS were examined to study the influence on strength, workability and

microstructural characteristics of concrete mixtures. Table 3 lists the specifics of each of these mixes. The reference mix did not contain any mineral admixtures. Trials were also conducted for optimum dosages of plasticizer for achieving a target slump around 70 mm. The dosages were carefully selected in order to reduce the adverse effect of overdosing.

Table 3. Mix design

| Mix proportion | MK (%) | AF (%) | CNS (%) | Cement (kg) | MK (kg) | AF (kg) | CNS (kg) | FA (kg) | CA (kg) | Water (kg) | Plasticizer (gm) |
|----------------|--------|--------|---------|-------------|---------|---------|----------|---------|---------|------------|------------------|
| M0 | 0 | 0 | 0 | 350 | 0 | 0 | 0 | 747 | 1190 | 154 | 1989 |
| M1 | 0 | 0 | 0.45 | 348.425 | 0 | 0 | 1.575 | 747 | 1190 | 154 | 2623 |
| M2 | 0 | 20 | 0 | 280 | 0 | 70 | 0 | 747 | 1190 | 154 | 1523 |
| M3 | 20 | 0 | 0 | 280 | 70 | 0 | 0 | 747 | 1190 | 154 | 3443 |
| M4 | 0 | 20 | 0.45 | 278.425 | 0 | 70 | 1.575 | 747 | 1190 | 154 | 1858 |
| M5 | 5 | 15 | 0.45 | 278.425 | 17.5 | 52.5 | 1.575 | 747 | 1190 | 154 | 2203 |
| M6 | 10 | 10 | 0.45 | 278.425 | 35 | 35 | 1.575 | 747 | 1190 | 154 | 2871 |
| M7 | 15 | 05 | 0.45 | 278.425 | 52.5 | 17.5 | 1.575 | 747 | 1190 | 154 | 3557 |
| M8 | 20 | 0 | 0.45 | 278.425 | 70 | 0 | 1.575 | 747 | 1190 | 154 | 4247 |

2.3. Sample Preparation

All the concrete mixtures were prepared in a laboratory mixer of 100 litre capacity. Firstly, coarse aggregates, sand, cement, mineral admixtures were fed to a rotary mixer and dry mixed for 2 min. Subsequently half of water with CNS was added followed by plasticizer and remaining water. The mixing was continued for 5 min for obtaining a homogeneous mixture. The concrete batch was removed in a pan and tested for slump. The concrete was then poured into the suitable moulds and compacted with a vibrating table. The surface was finished using a chisel for smooth finish. After 24 hours, all of the specimens were de-moulded and cured in a pool of water (Figure 4) till the testing age.



Fig. 4. Curing of specimens in curing tank

2.4. Test Methods

Compression tests were performed on compression testing machine as per (BIS 516, 1959). The results were analysed statistically using ANOVA (Analysis of variance) and Duncan's homogeneity test with a confidence level of 5%. After completion of compression test at 28 days, the mortar pieces were collected, ground sieved through 45 μm sieve and were kept for XRD, TGA/DSC and FTIR analysis. XRD analysis was carried out on powdered concrete specimens by Rigaku Smart Lab Xray diffractometer under the standard conditions of $\text{Cu } \alpha = 1.54 \text{ \AA}$. The data was

obtained between 5° - 60° 2θ with step size of 0.02° and was processed and analysed by using PANalytical X'pert Highscore plus software. FTIR spectroscopy was carried out by using AIM-9000 spectrometer operating in the transmittance range of 4000 - 400 cm^{-1} . Thermal analysis (TGA/DSC) using Mettler-Toledo TGA/DSC+ GmbH was used to observe the weight loss and decomposition of hydration products particularly the consumption of portlandite with increase in temperature from 0 - $800 \text{ }^\circ\text{C}$. For FESEM small concrete chips were removed from the core of cubes and were used for FESEM observations using Zeiss Gemini-500. The specimens were polished, carbon coated and gold plated prior to FESEM analysis.

3. Results and Discussion

3.1. Plasticizer Demand

The workability of all concrete mixtures was evaluated by using slump test. The slump was kept fixed at around 70 mm and the dosages of Super Plasticizer (SP) were changed depending on the demand of added SCM's. Figure 5 shows the usage of plasticizer of all mixtures. As can be seen the demand of SP increased drastically with CNS and MK. However, the AF has increased the slump and hence less amount of SP was used. The effect of AF on workability can be attributed to the glassy surface morphology as was observed during FESEM analysis. Owing to this characteristic property, less water was used for surface wetting and therefore more water was available for assisting workability. This was also reported by Gopinathan and Anand (2018) and YB et al. (2021). However, the flaky and porous structure of MK (Khan et al., 2020) and the increased surface area of CNS have reduced the free water in matrix. In case of ternary and quaternary mixtures same effects were observed. The maximum and minimum SP demand was shown by M2 (20% MK and 0.45% CNS) and M8 (20% AF), respectively.

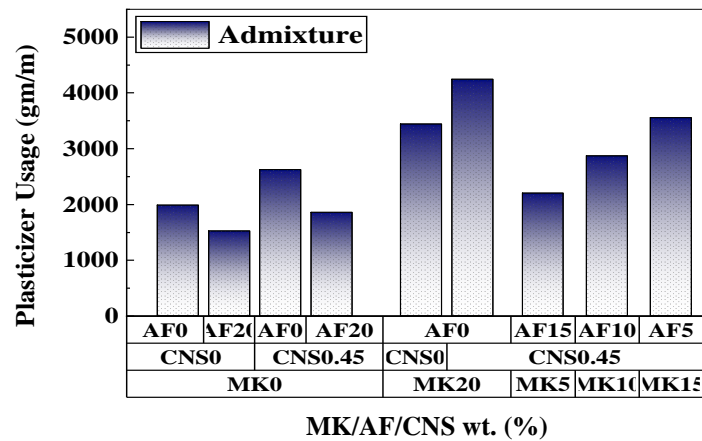


Fig. 5. Plasticizer demand of all concrete mixtures

3.2. Compressive Strength

Compressive Strength (CS) is said to be one of the main characteristics of concrete quality. Figure 6 illustrates the CS test results of normal and blended concrete systems containing 0-0.45% CNS, 0-20% AF and 0-20% MK. The results reveal that there is significant strength difference between normal and modified concrete mixtures. The ANOVA test was performed and different mixture combinations were considered as independent variables and CS as dependent variable. The results are displayed in Table 4. Duncan's Multiple Range Test (DMRT), a post hoc test for determination of critical comparison between means, was also performed. The results of DMRT and CS are shown in Table 5. It is observed that concrete compositions are significant in CS as the P-value (0.000146) is very less than confidence level (0.05).

Binary concrete mixtures containing 0.45% CNS and 20% AF had CS comparatively higher and very close to normal concrete at 28 days of curing age. However, in Duncan test, these mixtures (M₁ and M₂) were in the same homogeneous group as that of normal concrete. It was also observed that the early age strength was improved (Aleem et al., 2014; Flores et al., 2017; Hou et al., 2013) owing to nucleation (pore filling) and pozzolanic reactions, which reduced porosity and increased density of Interfacial Transition Zone (ITZ), and therefore increased strength development. This

behaviour resulted due to formation of more complicated and dense layer of hydrates that covered and firmly bound the fillers together (Salemi and Behfarnia, 2013). The ternary mixture (M₄) containing both CNS (0.45%) and AF (20%) had higher CS than binary mixtures and was between Groups 2 and 3 in the Duncan's test.

The binary mixture M₃ and ternary mixture M₈ had CS less than the normal concrete with M₃ in Group 1 and M₈ in between Groups 1 and 2. The quaternary mixtures had highest strength values, with M₇ between Groups 3 and 4, M₅ and M₆ in Group 4. In M₆ mixture, there was an increase in CS of 41.81% compared to normal concrete mixture. The strength difference between M₆ and M₃ was 53.17%, whereas the strength difference between M₃ and normal concrete mixture was -7.42%. Similarly, the strength difference between M₆ and M₄ was 22.26%, while the strength difference between M₄ and normal concrete was 15.98%. As a result of the above investigation, it is possible to conclude that the included SCM's have a synergistic impact, as was also reported by Bhat and Naqash (2022) and Sousa and Rêgo (2021). The increase in strength in modified concrete mixes can be attributed to addition of CNS in system which not only behaves as filler but also acted as activator for Pozzolanic reaction of MK and AF, and thereby densifying the microstructure and increased the strength development.

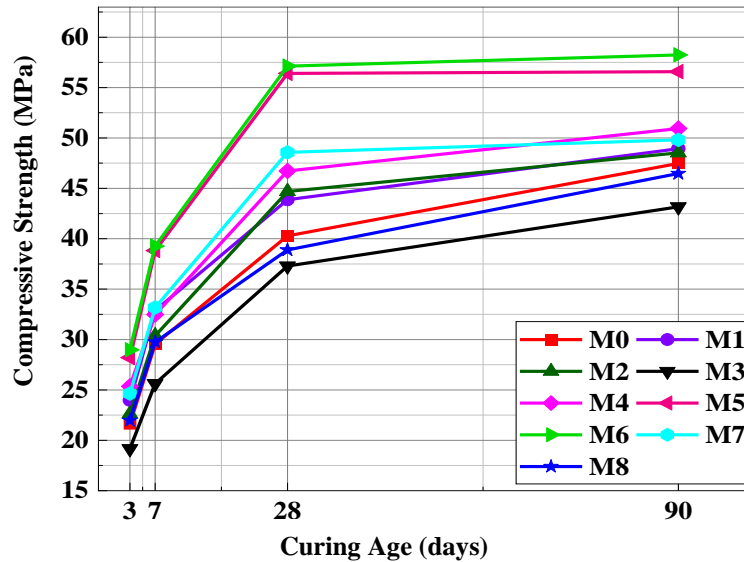


Fig. 6. Compressive strength of concrete with and without MK, AF and CNS

Table 4. Test results of ANOVA at 28 days

| Response variable | Input variable | Sum of squares | Mean sum of squares | F-value | p-value | Significance |
|-------------------|---------------------|----------------|---------------------|---------|----------|--------------|
| CS | Mixture composition | 1213.04 | 151.63 | 7.9 | 0.000146 | Yes |

Table 5. CS and Duncan homogeneous groups at 28 days

| Mixture | Compressive strength (MPa) | Standard deviation (MPa) | Groups | | | |
|---------|----------------------------|--------------------------|--------|---|---|---|
| | | | 1 | 2 | 3 | 4 |
| M3 | 37.29 | 5.92 | X | | | |
| M8 | 38.89 | 3.96 | X | X | | |
| M0 | 40.28 | 5.18 | X | X | X | |
| M1 | 43.87 | 4.93 | X | X | X | |
| M2 | 44.68 | 2.07 | X | X | X | |
| M4 | 46.72 | 5.63 | | X | X | |
| M7 | 48.57 | 5.68 | | | X | X |
| M5 | 56.4 | 0.81 | | | | X |
| M6 | 57.12 | 1.28 | | | | X |

3.3. Microstructural Characterization

3.3.1. X-Ray Diffraction

XRD patterns of M0, M1, M2, M3, M5 and M6 concrete mixes at 7 and 28 days of curing age are presented in Figures 7 and 8. The patterns of normal concrete indicates that Dicalcium and tricalcium silicates were observed and were still present inside the matrix at 28 days of age. However, the intensity of their peaks was less at 28 days compared to intensities at 7 days. The peaks of gypsum were not observed at 7 and 28 days of testing; which is evidence of tricalcium aluminate hydration during early days (Black et al., 2006). The peaks corresponding to the portlandite phase

increased with curing age which was obvious owing to hydration of silicates of clinker releasing CSH and portlandite. At 28 days of testing, peak intensity of calcium sulfoaluminate (ettringite) decreased which may be due to its transformation into a more stable calcium aluminate hydrate form, also reported by Barbhuiya et al. (2015). The quartz phase present in the aggregates was also presented (Bhat and Naqash, 2022). Besides, carbonates were detected and their intensity increased with age. The carbonates are mainly formed due to the reaction of atmospheric carbon dioxide with hydration products (Liu et al., 2019).

The XRD patterns of binary mixtures M1, M2, and M3 containing CNS, MK and

AF respectively as shown in Figure 7 indicate the presence of dicalcium, tricalcium silicate and portlandite peaks, however, their peak intensities were less than normal concrete. The additional peak of Hydrotalcite was observed in mixture containing AF (Blotevogel et al., 2020). The decrease in peaks corresponding to silicates of clinker were credited to the dilution effect of MK and AF and also the CNS increased the hydration rate by increasing the nucleation site for hydration reaction. The decrease of portlandite peak indicates its consumption in pozzolanic reaction.

Figure 8 shows XRD patterns of tetranary concrete mixtures (M5 and M6) containing cement, CNS, MK and AF at 7 and 28 days of curing. The patterns illustrate that the peak intensity of portlandite was less than binary and normal concrete due to pozzolanic reactions of CNS, MK and AF with portlandite. Furthermore, the peaks corresponding to carbonates and un-hydrated silicates decreased with hydration; indicating less carbonation of concrete with CNS, MK and AF. The quartz and cristobalite phases of fine aggregates were also observed. The formation of Hydrotalcite phase was observed, however, the peak intensity was lower than that of the binary mixture containing only Alccofine as the Supplementary Cementitious Material

(SCM).

3.3.2. TG/DSC Analysis

TG analysis was used to determine the quantity of portlandite content in all mixtures. Figures 9a and 9b show the TG, obtained TG and DTG curves, respectively. From DTG curves, the peaks between the temperature range of 25-300 °C are due to elimination of free water, dehydration of hydrates, etc. Decomposition of portlandite in all mixtures was observed in the temperature range of 395-530 °C and the corresponding weight loss at this temperature was calculated from TG curves. By using stoichiometry, the total content of portlandite decomposed in all mixtures was calculated and shown in Table 6. The portlandite index was calculated as the ratio between portlandite content of every mixture and normal concrete mix. Moreover, the peaks between 580-790 °C are from the decomposition of carbonates and the mass loss during this temperature range was significant (Reddy and Naqash, 2019).

From the results obtained (Table 6), it can be seen that, portlandite content decreased with the incorporation of SCM's in all concrete mixtures compared to reference mix and the maximum decrease was shown in M6. It was also observed that AF in M4 lead to decrease in portlandite more than MK in M3.

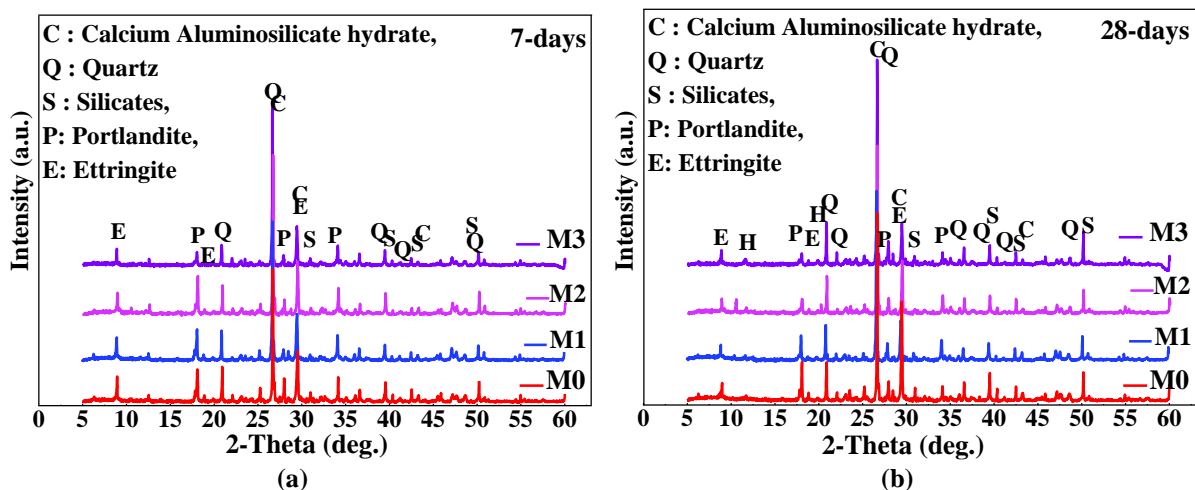


Fig. 7. XRD patterns of M0, M1, M2 and M3 at: a) 7 days; and b) 28 days

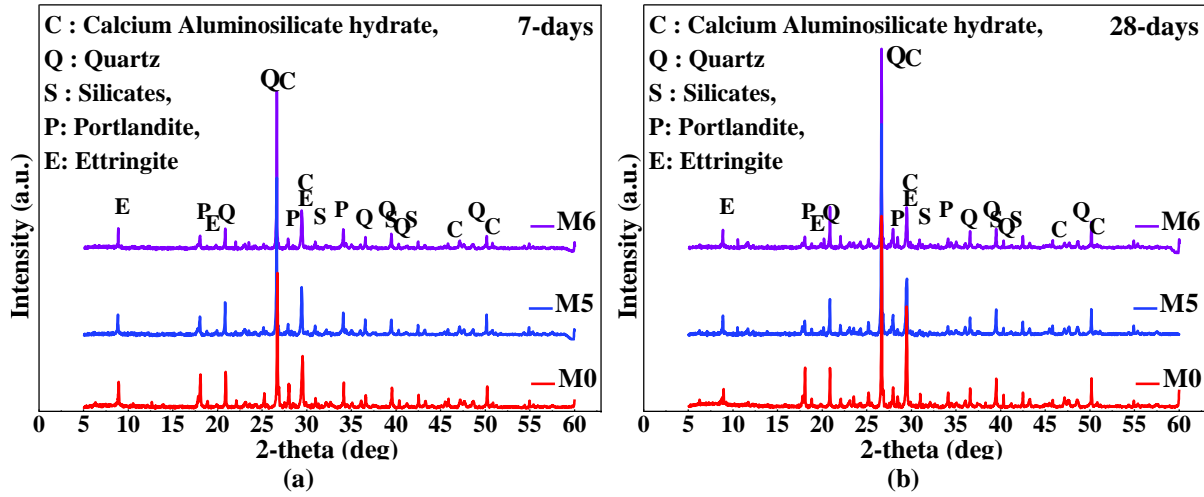


Fig. 8. XRD patterns of M6 at: a) 7 days; and b) 28 days

Table 6. Quantification of portlandite from TG analysis

| Mixture | Portlandite g/100 g of paste | Portlandite index |
|---------|------------------------------|-------------------|
| M0 | 18.67 | 1 |
| M1 | 17.23 | 0.922871 |
| M2 | 13.94 | 0.746652 |
| M3 | 14.27 | 0.764328 |
| M5 | 11.35 | 0.607927 |
| M6 | 10.08 | 0.539904 |

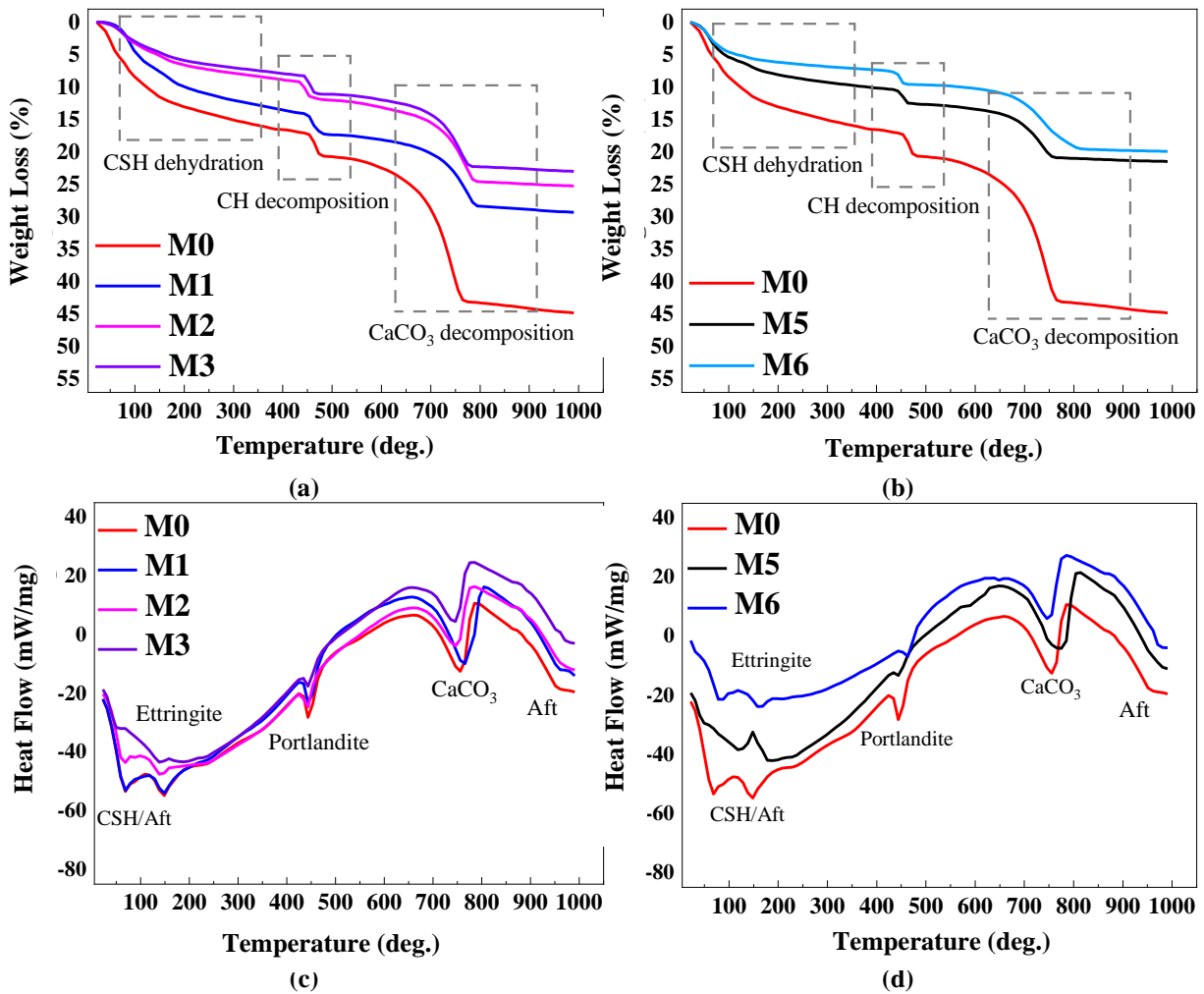


Fig. 9. Weight loss of: a) M0, M1, M2, M3; b) M0, M5, M6; and Heat flow of: c) M0, M1, M2, M3; and d) M0, M5, M6 at 90 days

3.3.3. FTIR Analysis

Infrared spectrum of all concrete mixtures obtained by FTIR spectroscopy are presented in Figure 10. The band observed in all mixtures at $3637\text{-}3643\text{ cm}^{-1}$ are associated to the functional O-H bonds of portlandite and the asymmetric stretching Si-O-Si bonds of CSH (Tobermorite) are observed at $975\text{-}959\text{ cm}^{-1}$. These are consistent with the study (Aleem et al., 2014). Comparing the mixtures, it is observed that normal concrete mixture has lowest transmittance at portlandite band and M6 has the highest transmittance value which indicates the lowest portlandite content (Guerrero Bustos et al., 2014; Ping et al., 1999). These observations can be attributed to the pozzolanic reactions of incorporated SCM's. Moreover, in case of

CSH band, the highest transmittance was observed in normal concrete and lowest in case of M6 mixture which indicates the possibility of higher CASH content compared to normal concrete. The bands at $1638\text{-}1647\text{ cm}^{-1}$ are of chemically bound water (H-O-H) of calcium silicate hydrates (Aleem et al., 2014). Stretching vibrations of S-O (SO_4^{2-}) at $1068\text{-}1084\text{ cm}^{-1}$ are the characteristic peaks of ettringite mono-sulfo-aluminate presence in mixtures. The intensity of which decreased with hydration and addition of SCM's. Besides, the strong bending and stretching vibrations of C-O bonds at $875\text{-}861\text{ cm}^{-1}$ and $1393\text{-}1416\text{ cm}^{-1}$ are of carbonates present, possibly coming with the aggregates or the absorption of atmospheric carbon dioxide during hydration.

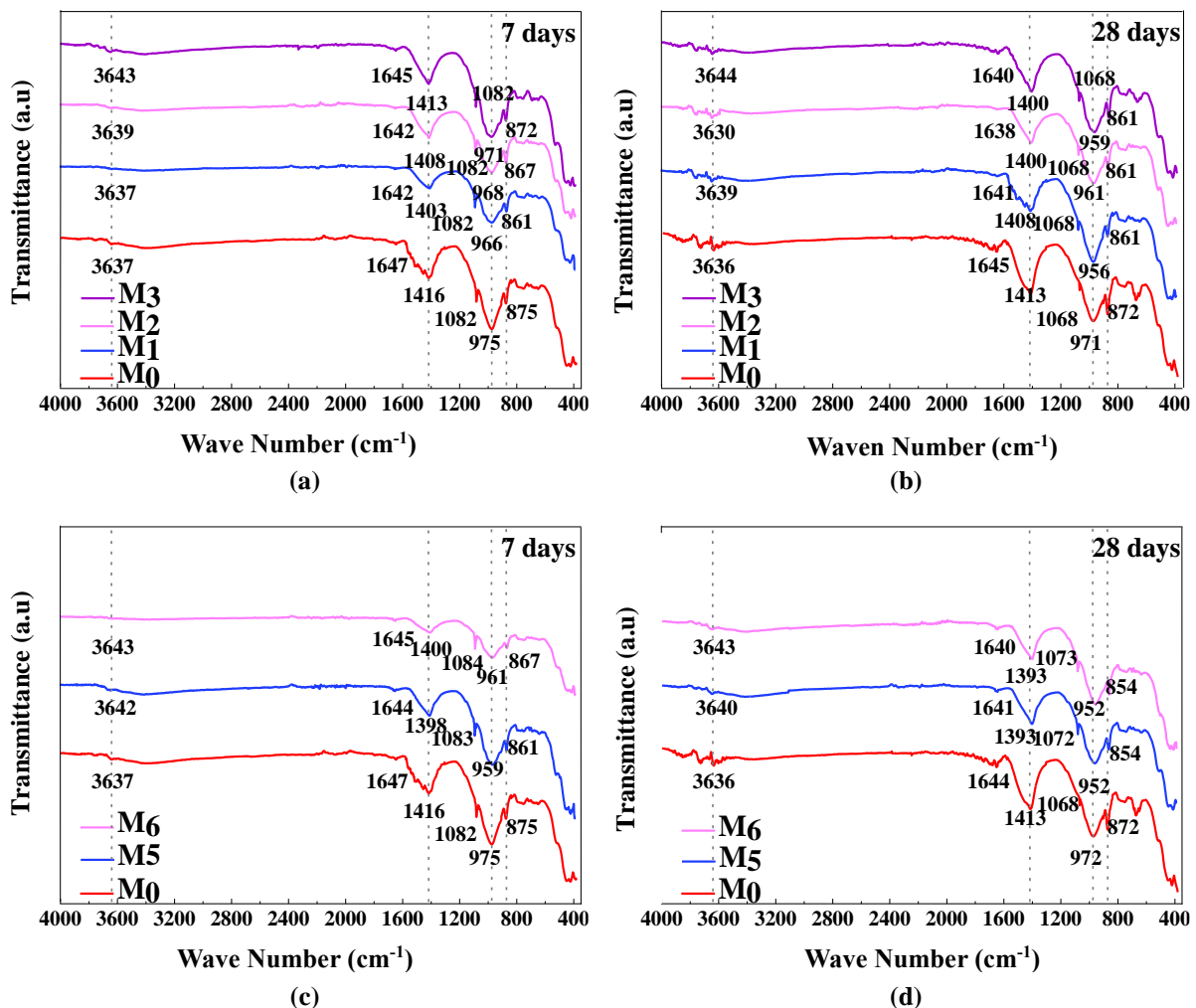


Fig. 10. FTIR spectrum of hardened concrete of M0, M1, M2, M3 at: a) 7 days; b) 28 days; and M0, M5, M6 at: c) 7 days; and d) 28 days

3.3.4. FESEM

The microstructure of concrete specimens M1, M2, M3, M4 and M6 were examined by FESEM and the effect at 28 days of curing age on ITZ morphology is presented in Figure 11. Specimens were taken out from the centre of concrete specimens. Figure 11a shows the micrograph of M1 concrete specimen. It illustrates the porous structure and also the hydrated products like CSH gel, portlandite crystals are clearly noticeable. Between the hydration compounds and other solids,

pores of variable sizes are clearly recognized. In contrast, the microstructure of M1, M2 and M3 (Figures 11b to 11d) are less porous, homogeneous and more uniform than M1. Therefore, it was expected that the compressive strength could be improved due to improved ITZ. Figures 11e and 11f show microstructure of M5 and M6 and it can be seen that the ITZ is more uniform, and compact compared to binary mixtures; which proves the synergistic properties of CNS, MK and AF.

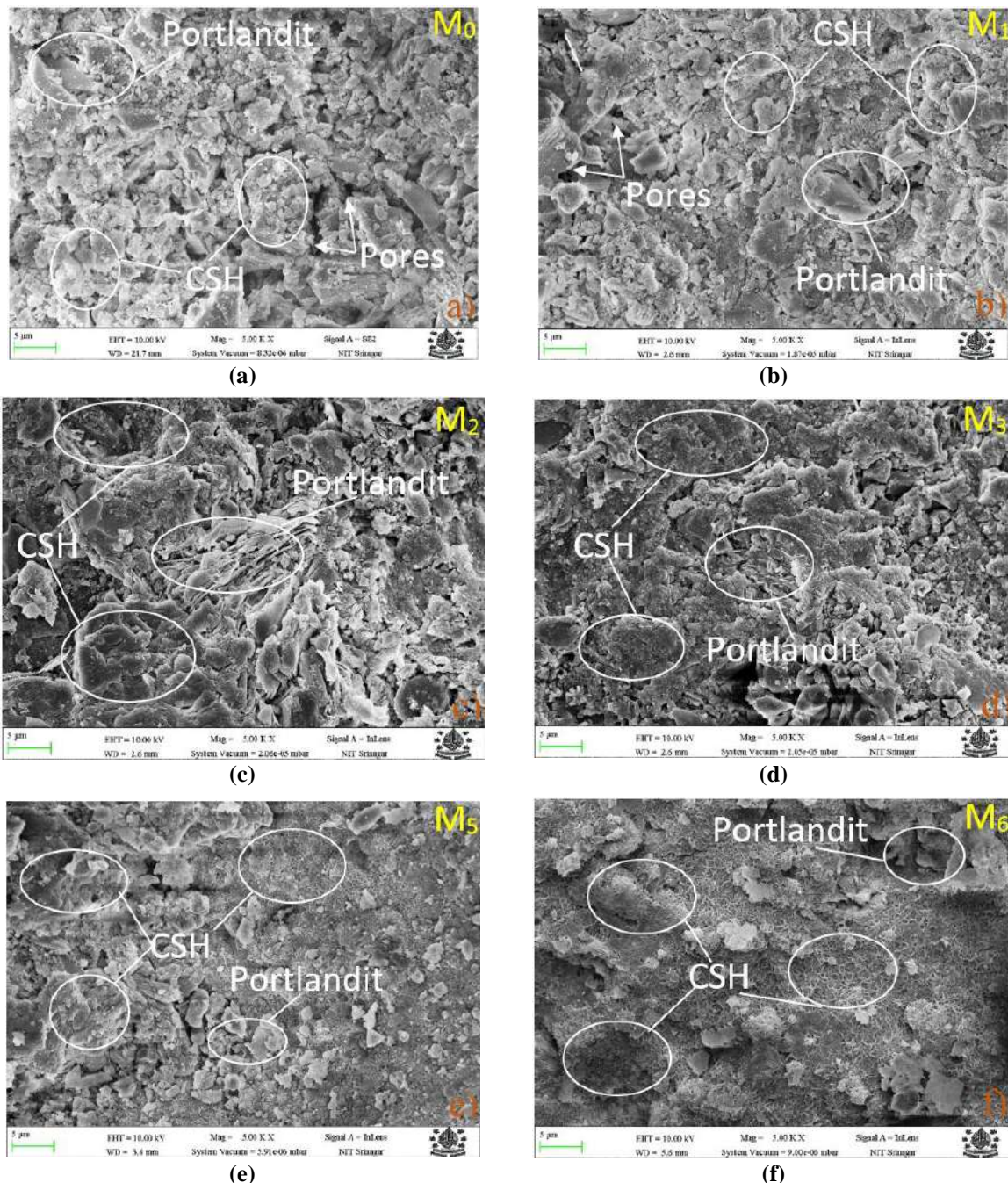


Fig. 11. FESEM images of hardened concrete microstructure at 28 days

3.4. Synergistic Approach of CNS, MK and AF

The CNS, MK and AF combination could improve the strength and microstructure as follows: the incorporation of small amount of CNS particles will accelerate and promote the cement hydration by providing additional sites. The hydration products will deposit on these nano sized particles and start growing to form conglomerates in which the CNS particle acts as nucleus. By this, the uniformly dispersion of nanoparticles will enhance microstructure by uniformly distributing conglomerates between the aggregates. Besides, silica nanoparticles will also prevent the growth of portlandite, Afm and Aft crystals; which are unfavourable for the strength of concrete. Also, the nanoparticles will fill the pores and therefore disrupts pore structure of concrete, which will reduce transport characteristics of concrete. However, in case of higher CNS content, the segregation of CNS particles creates weak zones and therefore reduce the strength. While, incorporation of MK and AF participate in pozzolanic reactions with the portlandite and increase the CSH gel content in matrix, therefore, the strength further increase compared to binary mixtures as was observed in compression test.

4. Conclusions

For CNS-MK-AF-Cement systems containing up to 20% MK and AF and 0-0.45% CNS, the following broad conclusions can be drawn:

- The demand for plasticizer content needed for keeping the consistency of mixtures with and without SCM's constant, increased with CNS and MK incorporation owing to their large surface area and rough surface texture respectively. However, AF decreased the plasticizer demand owing to glassy surface morphology.
- CNS and AF are complementary to MK: CNS and AF acts as filler and nucleating

sites for hydration reaction, thus improves early strength of concrete while MK improves later strength by pozzolanic reaction that refined the pore structure. The tetranary blended systems M6 proved to be more advantageous compared to binary, ternary and normal OPC system.

- CNS along with AF and MK proved as better system that modifies and presented a denser microstructure. CNS and AF at early ages, acted as filler and also provided the nucleating sites for precipitation of CSH gel, portlandite and other hydration products. At later ages, CNS modified the CSH by increasing the length of silicate chains (Kontoleontos et al., 2012), AF and MK diminishes the portlandite content by utilizing it in pozzolanic reaction and filling of pores partially or completely especially by secondary CSH gel, leading to denser structure.
- XRD analysis results showed reduction of peak intensities of portlandite with age as well as with replacement of CNS, AF and MK, confirming the utilization of portlandite in pozzolanic reaction and formation of secondary CSH gel, corroborating the results of FTIR and TGA/DSC analysis.

5. References

- Abdelli, K., Tahlaiti, M., Belarbi, R. and Nadjib, M. (2017). ScienceDirect ScienceDirect Influence of the pozzolanic reactivity of the Blast Furnace Slag Assessing the feasibility of using the and metakaolin on heat mortars temperature function for a long-term district heat", *Energy Procedia*, 139, 224-229, <https://doi.org/10.1016/j.egypro.2017.11.200>.
- Abdelmelek, N. and Lubloy, E. (2021). "Evaluation of the mechanical properties of high-strength cement paste at elevated temperatures using metakaolin", *Journal of Thermal Analysis and Calorimetry*, 145, 2891-2905, <https://doi.org/10.1007/s10973-020-09992-2>.
- Al Menhosh, A., Wang, Y., Wang, Y. and Augusthus-Nelson, L. (2018). "Long term durability properties of concrete modified with metakaolin and polymer admixture", *Construction and Building Materials*, 172, 41-51,

- <https://doi.org/10.1016/j.conbuildmat.2018.03.215>.
- Aleem, S.A.E., Heikal, M. and Morsi, W.M. (2014). "Hydration characteristic, thermal expansion and microstructure of cement containing nano-silica", *Construction and Building Materials*, 59, 151-160, <https://doi.org/10.1016/j.conbuildmat.2014.02.039>.
- Ashok, K., Kameswara Rao, B. and Sarath Chandra Kumar, B. (2021). "Experimental study on metakaolin & nano alumina based concrete", *IOP Conference Series: Materials Science and Engineering*, 1091, 012055, <https://doi.org/10.1088/1757-899x/1091/1/012055>.
- Barbhuiya, S., Chow, P.L. and Memon, S. (2015). "Microstructure, hydration and nanomechanical properties of concrete containing metakaolin", *Construction and Building Materials*, 95, 696-702, <https://doi.org/10.1016/j.conbuildmat.2015.07.101>.
- Bhat, A.H. and Naqash, J.A. (2022). "Experimental studies of sustainable concrete modified with colloidal nanosilica and metakaolin", *Journal of Building Pathology and Rehabilitation*, 7, 1-17, <https://doi.org/10.1007/s41024-021-00157-8>.
- BIS 516. (1959). *Method of tests for strength of concrete*, Bureau of Indian Standards; New Delhi, India.
- Black, L., Breen, C., Yarwood, J., Deng, C.S., Phipps, J. and Maitland, G. (2006). "Hydration of tricalcium aluminate (C3A) in the presence and absence of gypsum, Studied by Raman spectroscopy and X-ray diffraction", *Journal of Materials Chemistry*, 16, 1263-1272, <https://doi.org/10.1039/b509904h>.
- Blotevogel, S., Ehrenberg, A., Steger, L., Doussang, L., Kaknics, J., Patapy, C. and Cyr, M. (2020). "Ability of the R3 test to evaluate differences in early age reactivity of 16 industrial ground granulated blast furnace slags (GGBS)", *Cement and Concrete Research*, 130, 105998, <https://doi.org/10.1016/j.cemconres.2020.105998>.
- Bureau of Indian Standards. (2015). *Portland Slag Cement - Specification, IS 455*, Bureau of Indian Standards, New Delhi, India, 34.
- da Silva Andrade, D., da Silva Rêgo, J.H., Cesar Morais, P. and Frías Rojas, M. (2018). "Chemical and mechanical characterization of ternary cement pastes containing metakaolin and nanosilica", *Construction and Building Materials*, 159, 18-26, <https://doi.org/10.1016/j.conbuildmat.2017.10.101>.
- El-Diadamony, H., Amer, A.A., Sökkary, T.M. and El-Hoseny, S. (2018). "Hydration and characteristics of metakaolin pozzolanic cement pastes", *HBRC Journal*, 14, 150-158, <https://doi.org/10.1016/j.hbrcj.2015.05.005>.
- Flores, Y.C., Cordeiro, G.C., Toledo Filho, R.D. and Tavares, L.M. (2017). "Performance of Portland cement pastes containing nano-silica and different types of silica", *Construction and Building Materials*, 146, 524-530, <https://doi.org/10.1016/j.conbuildmat.2017.04.069>.
- Gopinathan, S. and Anand, K.B. (2018). "Properties of cement grout modified with ultra-fine slag" *Frontiers of Structural and Civil Engineering*, 12, 58-66, <https://doi.org/10.1007/s11709-017-0383-0>.
- Guerrero Bustos, A.M., Gaitero Redondo, J.J., Pérez Álvarez Quiñones, G. and Goni Elizalde, S. (2014). "Multi-scale analysis of cement pastes with nanosilica addition", *Advances in Cement Research*, 26, 271-80, <https://doi.org/10.1680/adcr.13.00023>.
- Hamed, N., El-Feky, M.S., Kohail, M., and Nasr, E.A.R. (2019). "Effect of nano-clay de-agglomeration on mechanical properties of concrete", *Construction and Building Materials*, 205, 245-256, <https://doi.org/10.1016/j.conbuildmat.2019.02.018>.
- Hou, P.K., Kawashima, S., Wang, K.J., Corr, D.J., Qian, J.S. and Shah, S.P. (2013). "Effects of colloidal nanosilica on rheological and mechanical properties of fly ash-cement mortar", *Cement and Concrete Composites*, 35, 12-22, <https://doi.org/10.1016/j.cemconcomp.2012.08.027>.
- Kavyateja, B.V., Guru Jawahar, J. and Sashidhar, C. (2019). Investigation on ternary blended self compacting concrete using fly ash and alccofine", *International Journal of Recent Technology and Engineering*, 7, 462-466.
- Khan, S.U., Ayub, T. and Shafiq, N. (2020). "Physical and mechanical properties of concrete with locally produced metakaolin and micro-silica as supplementary cementitious material", *Iranian Journal of Science and Technology - Transactions of Civil Engineering*, 44, 1199-1207, <https://doi.org/10.1007/s40996-020-00436-3>.
- Kontoleontos, F., Tsakiridis, P.E., Marinos, A., Kaloidas, V. and Katsioti, M. (2012). "Influence of colloidal nanosilica on ultrafine cement hydration: Physicochemical and microstructural characterization", *Construction and Building Materials*, 35, 347-360, <https://doi.org/10.1016/j.conbuildmat.2012.04.022>.
- Lima, N.B., Silva, D., Vilemen, P., Nascimento, H.C.B., Cruz, F., Santos, T.F.A., Oliveira, R., Póvoas, Y., Padron-Hernández, E. and Lima, N.B.D. (2023). "A chemical approach to the adhesion ability of cement-based mortars with metakaolin applied to solid substrates", *Journal*

- of *Building Engineering*, 65, 105643, <https://doi.org/10.1016/j.jobe.2022.105643>.
- Liu, W., Li, Y.Q., Tang, L.P. and Dong, Z.J. (2019). "XRD and ²⁹Si MAS NMR study on carbonated cement paste under accelerated carbonation using different concentration of CO₂", *Materials Today Communications*, 19, 464-470, <https://doi.org/10.1016/j.mtcomm.2019.05.007>.
- Mallhotra, V.M. and Mehta, P.K. (2004). *Pozzolanic and cementitious materials*, Amsterdam, The Netherlands: Gordon and Breach. <https://doi.org/10.1201/9781482296761>.
- Medri, V., Papa, E., Lizion, J. and Landi, E. (2020). "Metakaolin-based geopolymer beads: Production methods and characterization", *Journal of Cleaner Production*, 244, 118844, <https://doi.org/10.1016/j.jclepro.2019.118844>.
- Özbay, E., Erdemir, M. and Durmuş, H.I. (2016). "Utilization and efficiency of ground granulated blast furnace slag on concrete properties, A review", *Construction and Building Materials*, 105, 423-434, <https://doi.org/10.1016/j.conbuildmat.2015.12.153>.
- Ping, Y., Kirkpatrick, R.J., Brent, P., McMillan, P.F. and Cong, X. (1999). "Structure of calcium silicate hydrate (C-S-H): Near-, mid-, and far-infrared spectroscopy", *Journal of the American Ceramic Society*, 82, 742-748, <https://doi.org/10.1111/j.1151-2916.1999.tb01826.x>.
- Reddy, P.N. and Naqash, J.A. (2019). "Experimental study on TGA, XRD and SEM analysis of concrete with ultra-fine slag", *International Journal of Engineering, Transactions B: Applications*, 32, 679-684, <https://doi.org/10.5829/ije.2019.32.05b.09>.
- Rong, Z., Zhao, M. and Wang, Y. (2020). "Effects of modified nano-SiO₂ particles on properties of high-performance cement-based composites", *Materials*, 13, 1-12, <https://doi.org/10.3390/ma13030646>.
- Salemi, N. and Behfarnia K. (2013). "Effect of nano-particles on durability of fiber-reinforced concrete pavement", *Construction and Building Materials*, 48, 934-941, <https://doi.org/10.1016/j.conbuildmat.2013.07.037>.
- Senff, L., Hotza, D., Lucas, S., Ferreira, V.M. and Labrincha, J.A. (2012). "Effect of nano-SiO₂ and nano-TiO₂ addition on the rheological behavior and the hardened properties of cement mortars", *Materials Science & Engineering A*, 532, 354-361, <https://doi.org/10.1016/j.msea.2011.10.102>.
- Shaat, M., Fathy, A. and Wagih, A. (2020). "Correlation between grain boundary evolution and mechanical properties of ultrafine-grained metals", *Mechanics of Materials*, 143, 103321, <https://doi.org/10.1016/j.mechmat.2020.103321>.
- Shaikh, F.U.A. and Supit, S.W.M. (2015). "Chloride induced corrosion durability of high volume fly ash concretes containing nano particles", *Construction and Building Materials*, 99, 208-225, <https://doi.org/10.1016/j.conbuildmat.2015.09.030>.
- Sharmila, P. and Dhinakaran, G. (2015). "Strength and durability of ultra fine slag based high strength concrete", *Structural Engineering and Mechanics*, 55, 675-686, <https://doi.org/10.12989/sem.2015.55.3.675>.
- Sousa, M.I.C. and da Silva Rêgo, J.H. (2021). "Effect of nanosilica/metakaolin ratio on the calcium alumina silicate hydrate (C-A-S-H) formed in ternary cement pastes", *Journal of Building Engineering*, 38, 102226, <https://doi.org/10.1016/j.jobe.2021.102226>.
- Sujjavanich, S., Suwanvitaya, P., Chaysuwan, D. and Heness, G. (2017). "Synergistic effect of metakaolin and fly ash on properties of concrete", *Construction and Building Materials*, 155, 830-837, <https://doi.org/10.1016/j.conbuildmat.2017.08.072>.
- Wang, X.F., Huang, Y.J., Wu, G.Y., Fang, C., Li, D.W., Han, N.X. and Xing, F. (2018). "Effect of nano-SiO₂ on strength, shrinkage and cracking sensitivity of lightweight aggregate concrete", *Construction and Building Materials*, 175, 115-125, <https://doi.org/10.1016/j.conbuildmat.2018.04.113>.
- Wild, S., Khatib, J.M. and Jones, A. (1996). "Relative strength, pozzolanic activity and cement hydration in superplasticised metakaolin concrete", *Cement and Concrete Research*, 26, 1537-1544, [https://doi.org/10.1016/0008-8846\(96\)00148-2](https://doi.org/10.1016/0008-8846(96)00148-2).
- YB, R., Hossiney, N. and HT, D. (2021). "Properties of high strength concrete with reduced amount of Portland cement, A case study", *Cogent Engineering*, 8(1), 1938369, <https://doi.org/10.1080/23311916.2021.1938369>.
- Zhan, P., He, Z., Ma, Z., Liang, C. and Zhang, X. (2020). "Utilization of nano-metakaolin in concrete: A review", *Journal of Building Engineering*, 30, 101259, <https://doi.org/10.1016/j.jobe.2020.101259>.



This article is an open-access article distributed under the terms and conditions of the Creative Commons Attribution (CC-BY) license.



Damage Detection of Truss Bridges Using Wavelet Transform of Rotation Signal

Ghafouri, H.R.^{1*}, Khajehdezfuly, A.² and Saadat Poor, O.³

¹ Professor, Faculty of Civil Engineering and Architecture, Shahid Chamran University of Ahvaz, Ahvaz, Iran.

² Assistant Professor, Faculty of Civil Engineering and Architecture, Shahid Chamran University of Ahvaz, Ahvaz, Iran.

³ M.Sc. Student, Faculty of Civil Engineering and Architecture, Shahid Chamran University of Ahvaz, Ahvaz, Iran.

© University of Tehran 2023

Received: 27 Sep. 2022;

Revised: 02 Mar. 2023;

Accepted: 03 May 2023

ABSTRACT: Although some researchers indicated that the rotation response of the structure is a proper index to identify the damage location, Wavelet Transform (WT) of rotation response of the bridge is not yet used to detect the damage location in the previous studies. In this regard, a numerical model of a truss bridge was developed using finite element method. The static response of the model under one point-load and a six-axle locomotive was calculated. The response obtained from the model was compared with that of the literature to investigate the validity of the model developed in this study. The WT coefficients of horizontal, vertical and rotation responses of each member of the bridge were obtained based on the Gaus2 wavelet basis function. Several damage scenarios were considered for the bridge to investigate the effectiveness of WT of rotation response of the bridge to detect the damage location. The obtained results show that the WT of horizontal displacement is not a proper index to detect the damage in the bridge members. A Comparison between WT coefficients of vertical displacement and rotation for all members indicates that the rotation response is a proper index to identify the damage and loading locations. In some cases, while the damage causes a significant jump on the WT coefficients of rotations of the members, the WT coefficients of vertical displacement of these members are not influenced by the damage.

Keywords: Rotation Response, Structural Health Monitoring, Truss Bridge, Wavelet Transform.

1. Introduction

Structural health monitoring and damage detection are known as the most important areas in the repair and maintenance of the strategic structures such as bridge, tunnel and dam (Rezaifar and Doostmohammadi,

2016; Martinez et al., 2019; Moreu et al. 2017; Khajehdezfuly et al., 2023; Labibzadeh et al., 2019, 2022; Poorveis et al., 2023). In this regard, several methods have been developed in the literature to detect the damage location in these types of structures. The methods detect the damage

* Corresponding author E-mail: ghafouri_h@scu.ac.ir

location in the structures based on the different parameters such as natural frequencies, mode shapes or vibration responses of the structures (Sadeghi and Fathali, 2007; Tiboni et al., 2022; Rizzo and Enshaeian, 2022; Huang et al., 2020; Sadeghi and Hashemi Rezvani, 2013).

According to the literature, the Wavelet Transform (WT) is a useful approach to detect the damage location in the structures. For instance, Hou et al. (2013) detected the damage location by the wavelet transform of noisy response of the one degree of freedom structure. Some researchers applied Continuous Wavelet Transform (CWT) on the mode shapes of the beams to find the damage location (Miao et al., 2020; Janeliukstis et al., 2017). It should be noted that the bridge is usually subjected to the moving loads and the WT approach is implemented on the dynamic response of the bridge.

Moreover, it is not easy to measure the pseudo-static rotational responses under moving loads in practice. In fact, the time history of the response of the bridges and beams were usually measured in the previous studies. However, a review of the literature shows that the image processing approach is a practical method to measure the static and dynamic responses (deflection and rotation) of the beams and bridges under stationary and moving loads, respectively (Ma et al., 2021; Silva et al., 2012, 2014; Andreausa et al., 2017).

Accordingly, in several previous experimental studies, some researchers measured the static response of the damaged structure using the image processing approach in the laboratory and then adopted the WT approach to detect the damage location, respectively (Ma et al., 2021; Silva et al., 2012, 2014; Andreausa et al., 2017). For instance, Ovanesova and Suárez (2004) used WT of static and dynamic responses of the beams and frames to detect the damage. They indicated that the type of wavelet function has a significant effect on the results obtained from the WT.

Douka et al. (2003) applied CWT on the mode shapes of a cantilever beam to find the damage magnitude and its location. Several researchers detected the damage location on the plates and beams using CWT of plate response and mode shapes (Kumar and Singh, 2021; Khiem et al., 2021). Sun and Chang (2002) used WT technique in conjunction with neural network to identify the damage location in the structure.

There are many types of bridges around the world and numerous researchers have used WT and developed several wavelet-based approaches to detect the damage location in the bridge (Silik et al., 2021; Andrea et al., 2016; Kankanamge et al., 2020). For instance, Taha et al. (2004) detected damage location in the bridge using Discretized Wavelet Transform (DWT) approach in conjunction with neural network. Zhong and Oyadiji (2008) and Barone et al. (2008) simulated a bridge as simple beam under static loads and applied WT on the response of the beam in order to identify the crack location in the bridge.

Zhu and Law (2006) modeled a bridge under constant moving loads and used WT of noisy vertical displacement of the bridge mid-point to detect the location of the damage with high severity. The accuracy of their approach was significantly decreased when the load enters/leaves the bridge. Also, when the number of moving loads was increased, the results obtained from their approach had noisy content. Hester and Gonzalez (2011) improved the method developed by Zhu and Law (2006). They modeled a vehicle/bridge interaction model and used WT of vertical acceleration signal of bridge in order to detect the damage location in the bridge. In their work, the vehicle axles entering and leaving the bridge generated some high wavelet coefficients. In fact, their WT approach was not able to detect the damage near the supports.

Cantero and Basu (2014) identified the damage location in the bridge using WT of vertical acceleration of vehicle axles. Several studies have been conducted to find

the proper wavelet basis functions and scale factor in order to detect the damage location in the bridge (Serra and Lopez, 2017; Ghanbari Mardasi et al., 2018).

A brief review of the literature indicates that the WT approaches developed in the previous researches have several limitations. Firstly, most of WT approaches detect the damage with high severity. Secondly, as the number of vehicle axles loads increases, the accuracy of the results obtained from the WT approaches decreases. Thirdly, WT approaches are unable to identify the damage locations near the bridge supports. Although few researchers proved that the rotation response of the structure is a proper index to identify the damage location (Hester et al., 2020). WT of rotation response of the bridge is not used to detect the damage location in the previous studies. A review of the available studies shows that there is a need to assess the effectiveness of rotational response of structure on the damage detection using WT approach.

The rotational response of structure is divided into two main categories including pseudo-static and dynamic ones. This research is carried out to identify the damage location in the bridge using WT of pseudo-static rotation response. In this regard, a numerical model of truss bridge is developed using finite element method. The response of the model under different patterns of concentrated static load is obtained. Several damage scenarios are considered for the bridge to investigate the effectiveness of WT of rotation response of the bridge to identify the damage location.

2. Development of Damaged Bridge Numerical Model

In this study, both the excitation and structural response of the bridge are static. In other words, the static concentrated loads are applied to the bridge and then, the static response of the bridge components (including horizontal displacement, rotational deflection and vertical

displacement) are calculated through a static analysis. A review of the previous studies shows that the image processing approach is a practical method to measure the static responses (deflection and rotation) of the beams and bridges under the static loads (Ma et al., 2021; Silva et al., 2012, 2014; Andreausa et al., 2017). Accordingly, in several previous experimental studies, some researchers measured the static response of the damaged structures using image processing approach in the laboratory and then adopted the WT to detect the damage location (Ma et al., 2021; Silva et al., 2012, 2014; Andreausa et al., 2017).

The approach implemented in this study is same as the method proposed in Ma et al. (2021) and Andreausa et al. (2017). A truss bridge is modeled in this study using two-dimensional finite element method. A review of the previous studies shows that when all components of the lower chord of the truss bridge are subjected to the stationary or moving vertical external loads, the moment, shear and axial internal forces are induced in them and consequently, they are usually simulated using the frame elements (Kordi and Mahmoudi, 2022; Wan et al., 2022). As no vertical external force is applied to other members of the bridge truss, only axial force is induced in them and consequently, they usually are modeled using truss elements (Kordi and Mahmoudi, 2022; Wan et al., 2022). In this study to simplify the simulation process of the truss bridge, all members of the truss bridge are modeled using frame elements. It should be noted that, the internal shear and moment of all members of truss bridge except those of the lower chord are nearly zero because no vertical external force is applied to them.

A schematic view of the model is presented in Figure 1. Frame element is used to simulate the model (Figure 2) (Przemieniecki, 1985). Each frame element has two nodes and each node has three degrees of freedom in the local normal-tangential coordinate system (rotation about normal axis of plane (θ), displacement in

normal direction (u) and displacement in tangential direction (v).

The local (normal-tangential) and global coordinate systems of the frame element are shown in Figure 2. The equilibrium equation of the element e^{th} in the local coordinate system is presented in Eq. (1) (Przemieniecki, 1985).

$$\begin{Bmatrix} F_1 \\ V_1 \\ M_1 \\ F_2 \\ V_2 \\ M_2 \end{Bmatrix}_e = [K_e]_{6 \times 6} \begin{Bmatrix} u_1 \\ v_1 \\ \theta_1 \\ u_2 \\ v_2 \\ \theta_3 \end{Bmatrix}_e \quad (1)$$

where F_i , V_i , M_i , u_i , v_i and θ_i : are axial force, shear force, moment, displacement in tangential (axial) direction, displacement in normal displacement and, rotation about normal axis for i^{th} node of the e^{th} element, respectively. Also, $[K_e]_{6 \times 6}$ is the frame element stiffness matrix and presented in Eq. (2).

$$[K_e]_{6 \times 6} = \frac{1}{L} \begin{bmatrix} AE & 0 & 0 & -AE & 0 & 0 \\ 0 & \frac{12EI}{L^2} & \frac{6EI}{L} & 0 & -\frac{12EI}{L^2} & \frac{6EI}{L} \\ 0 & \frac{6EI}{L} & 4EI & 0 & -\frac{6EI}{L} & 2EI \\ -AE & 0 & 0 & AE & 0 & 0 \\ 0 & -\frac{12EI}{L^2} & -\frac{6EI}{L} & 0 & \frac{12EI}{L^2} & \frac{6EI}{L} \\ 0 & \frac{6EI}{L} & 2EI & 0 & -\frac{6EI}{L} & 4EI \end{bmatrix} \quad (2)$$

where A , E , I and L : denote cross-section area, modulus of elasticity, second moment of inertia and, length of the element, respectively.

The force and displacement vectors and, stiffness matrix of the element are converted from local coordinate system to global coordinate system using transformation matrix (Przemieniecki, 1985). The transformation matrix for each element is obtained from Eq. (3) in which, β : is the angle between axial element direction and horizontal direction.

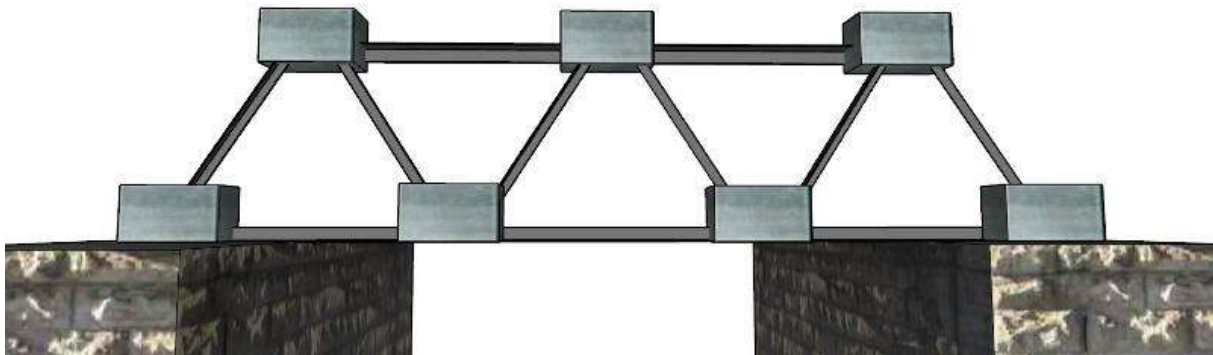


Fig. 1. Schematic view of truss bridge

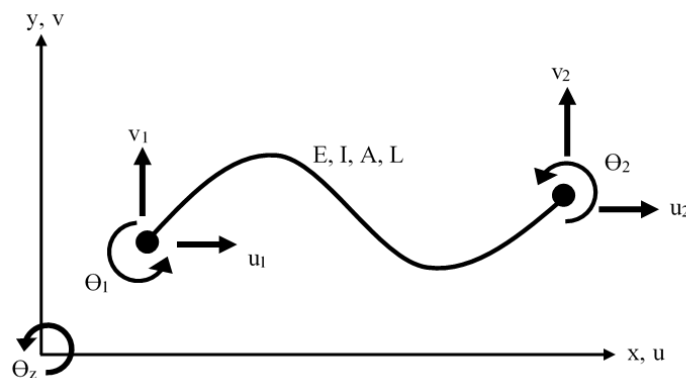


Fig. 2. Local and global coordinate system of frame element

$$[T] = \begin{bmatrix} \cos(\beta) & \sin(\beta) & 0 & 0 & 0 & 0 \\ -\sin(\beta) & \cos(\beta) & 0 & 0 & 0 & 0 \\ 0 & 0 & 1 & 0 & 0 & 0 \\ 0 & 0 & 0 & \cos(\beta) & \sin(\beta) & 0 \\ 0 & 0 & 0 & -\sin(\beta) & \cos(\beta) & 0 \\ 0 & 0 & 0 & 0 & 0 & 1 \end{bmatrix} \quad (3)$$

In order to consider the defect (or damage) at a special location of the bridge component (damaged component), a crack with depth of d_c is considered at that location (Figure 3). The flexural rigidity of the element at that location is decreased because of the crack (damaged element). The reduced flexural rigidity of the damaged element is obtained using Eq. (4) (Christides and Barr, 1999).

$$EI_c = \frac{EI}{1 + \frac{I}{I + I_c} e^{\left(\frac{-1.334|x-x_c|}{h}\right)}} \quad (4)$$

where EI_c : stands for flexural rigidity of the damaged element, EI : is flexural rigidity of undamaged element, I_c : is second moment inertia of the damaged element, h : is depth of cross-section, x_c : stands for damage location at the component and, x : is the length of the component. For a rectangular cross-section with depth h and width w , I_c is derived using Eq. (5), as follows:

$$I_d = \frac{1}{12} w(h - d_c)^3 \quad (5)$$

For instance, Figure 4 shows the effects of three crack depths located at $x_c/l = 0.2$ on the variation of flexural rigidity of a component with length of 1. As illustrated in this figure, the flexural rigidity of the component is reduced by the crack considered at $x_c/l = 0.2$ location. The reduction of flexural rigidity depends on the crack depth.

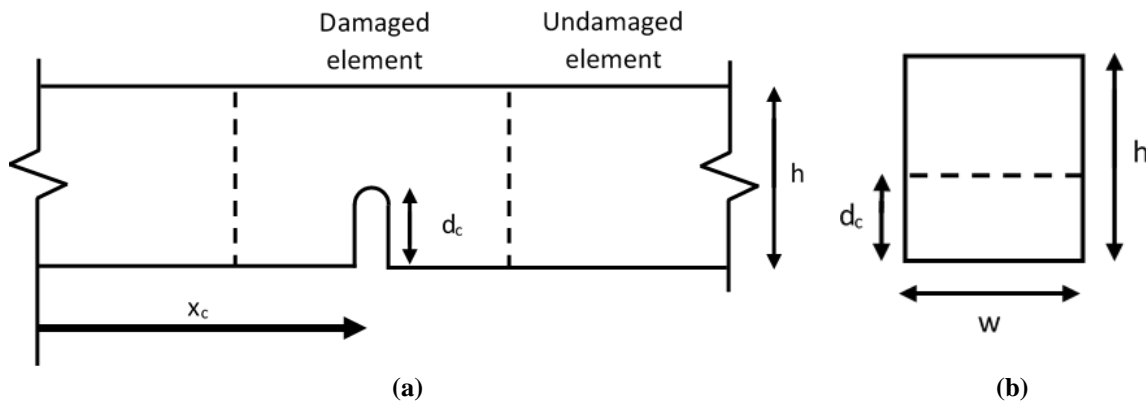


Fig. 3. Crack considered at the component: a) Longitudinal section; and b) Cross section

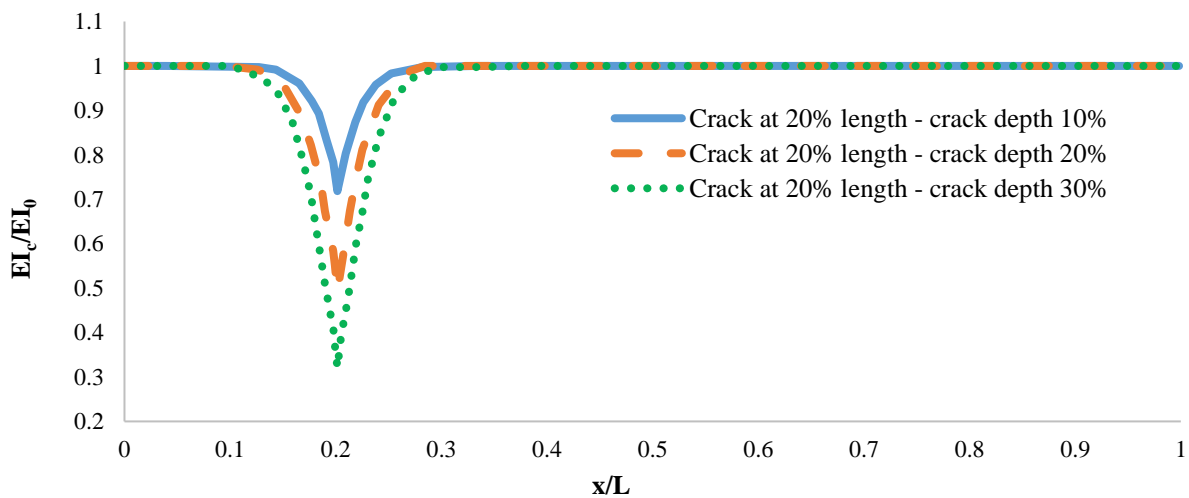


Fig. 4. Variation of flexural rigidity on the damaged component

The bridge is discretized by the frame elements. The force vectors and stiffness matrices of the elements in the global coordinate system are assembled to obtain the force vector ($\{F\}_T$) and stiffness matrix ($[K]_T$) of the model. The displacement vector ($\{\Delta\}_T$) of the model in global coordinate system is derived using Eq. (6).

$$\{\Delta\}_T = [K]_T^{-1}\{F\}_T \quad (6)$$

3. Validation of the Model

A comparison is made between the results obtained from the model developed in this study and those of presented in the literature in order to investigate the validation of the model. Mahato and Harish (2015) experimentally investigated the responses of the simply supported and cantilever beams under concentrated load. The bridge model is simplified to simulate the simply

supported and cantilever beams under concentrated load in order to make a comparison between the results obtained from the simplified model and those measured by Mahato and Harish (2015). The simply supported and cantilever beams simulated in this section are shown in Figure 5.

Mahato and Harish (2015) measured the maximum vertical displacement of the cantilever beam under different magnitudes of point load located at the mid-span and end-edge locations. Also, they investigate the maximum vertical displacement of the simply supported beam under mid-span concentrated load with different magnitudes. Figure 6 presents the results obtained from the simplified model developed in this study and those measured by Mahato and Harish (2015). As illustrated in Figure 6, the difference between the results is negligible.

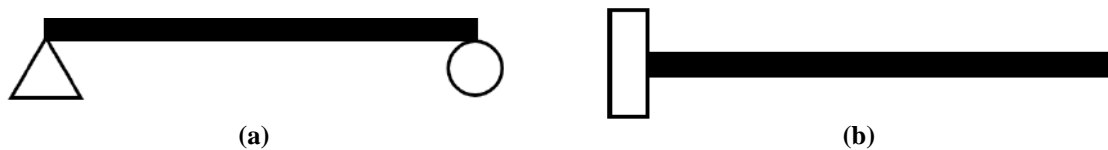


Fig. 5. Simplified beam model: a) Simply supported; and b) Cantilever

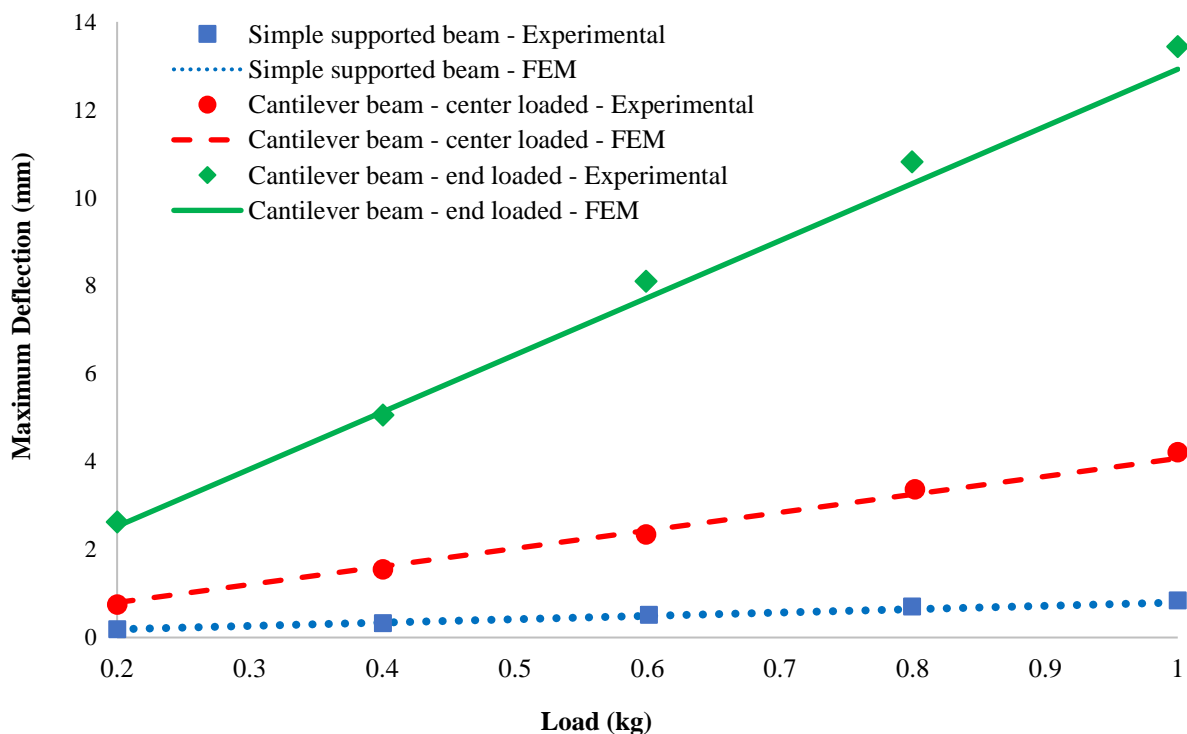


Fig. 6. Comparison between the results obtained from present study and previous study

4. Parametric Study

The effectiveness of wavelet transform of rotation signal of the bridge on the damage detection of truss bridge was investigated during the parametric study. In this regard, two scenarios were considered for the loading of the bridge. In the first scenario, one point-load was applied to the bridge. In the second scenario, a locomotive was stationed on the bridge. In a real condition, measurement noises are included in the identification results. However, the results obtained from the model developed in this study have no noise.

A review of the literature shows that in some cases, before implementation of WT on the responses of the damaged structure measured in the test, some filtration approaches were used to denoise the measured data (Ma et al., 2021). In this regard, a pre-filtration process was carried out for denoising the measured response of the structure. In this study, it was assumed that, the measured response of the bridge was denoised using a pre-filtration process and accordingly, the WT was implemented on the denoised data in all scenarios. The details are as follows.

4.1. Bridge under one Point-Load

The bridge presented in Figure 7 was simulated in this section. As illustrated in this figure, the truss bridge includes 11 members. The properties of bridge members are presented in Table 1. As

shown in Figure 7, a point load with magnitude of 500 N is applied on the mid-span of 6th member.

Table 1. Properties of bridge members

| Properties | Magnitude |
|--|------------------------|
| Young modulus (N/m ²) | 2×10^{11} |
| Second moment of inertia (m ⁴) | 8.33×10^{-10} |
| Length (m) | 1 |
| Height (m) | 0.01 |
| Width (m) | 0.01 |

According to Figure 7, three damages with different severities are considered at the different locations of members 4, 7 and 10. Three cracks with depths of 45, 35 and 25% were considered at members 4, 7 and 10, respectively. The location of the crack at member 4, 7 and 10 was $x_c/l = 0.8$, $x_c/l = 0.2$ and $x_c/l = 0.8$, respectively.

The bridge was modeled using 50 frame elements. The vertical, horizontal and rotation of each node were calculated. The undeformed and deformed shapes of the bridge are shown in Figure 8.

The wavelet coefficients of horizontal, vertical and rotation of each member of the bridge were calculated based on the Gaus2 wavelet basis function (Figures 9 and 10). As illustrated in Figures 9 and 10, wavelet coefficients of horizontal displacement of all members are not affected by the damages. In other words, the WT of horizontal displacement is not a proper index to detect the damage in the bridge members.

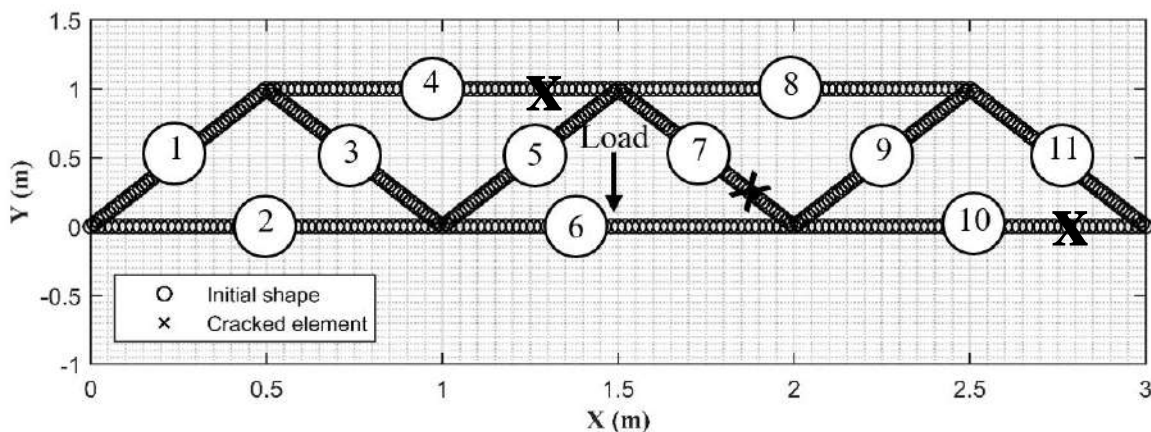


Fig. 7. The bridge model in the first scenario

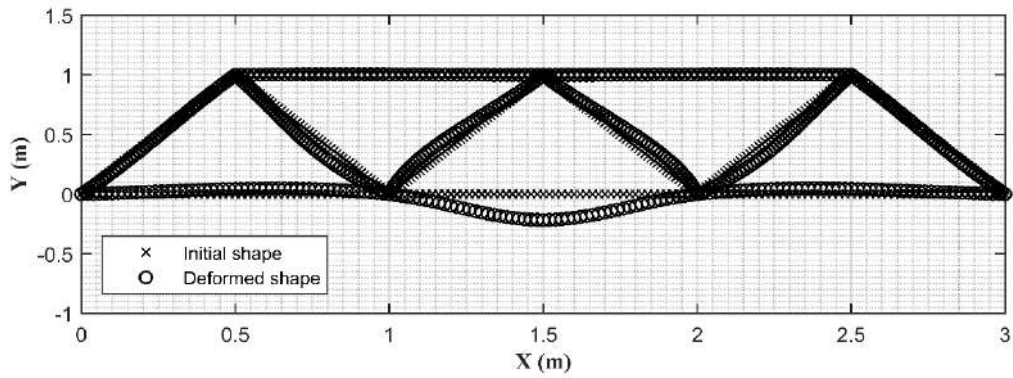


Fig. 8. Undeformed and deformed shapes of the bridge in the first scenario

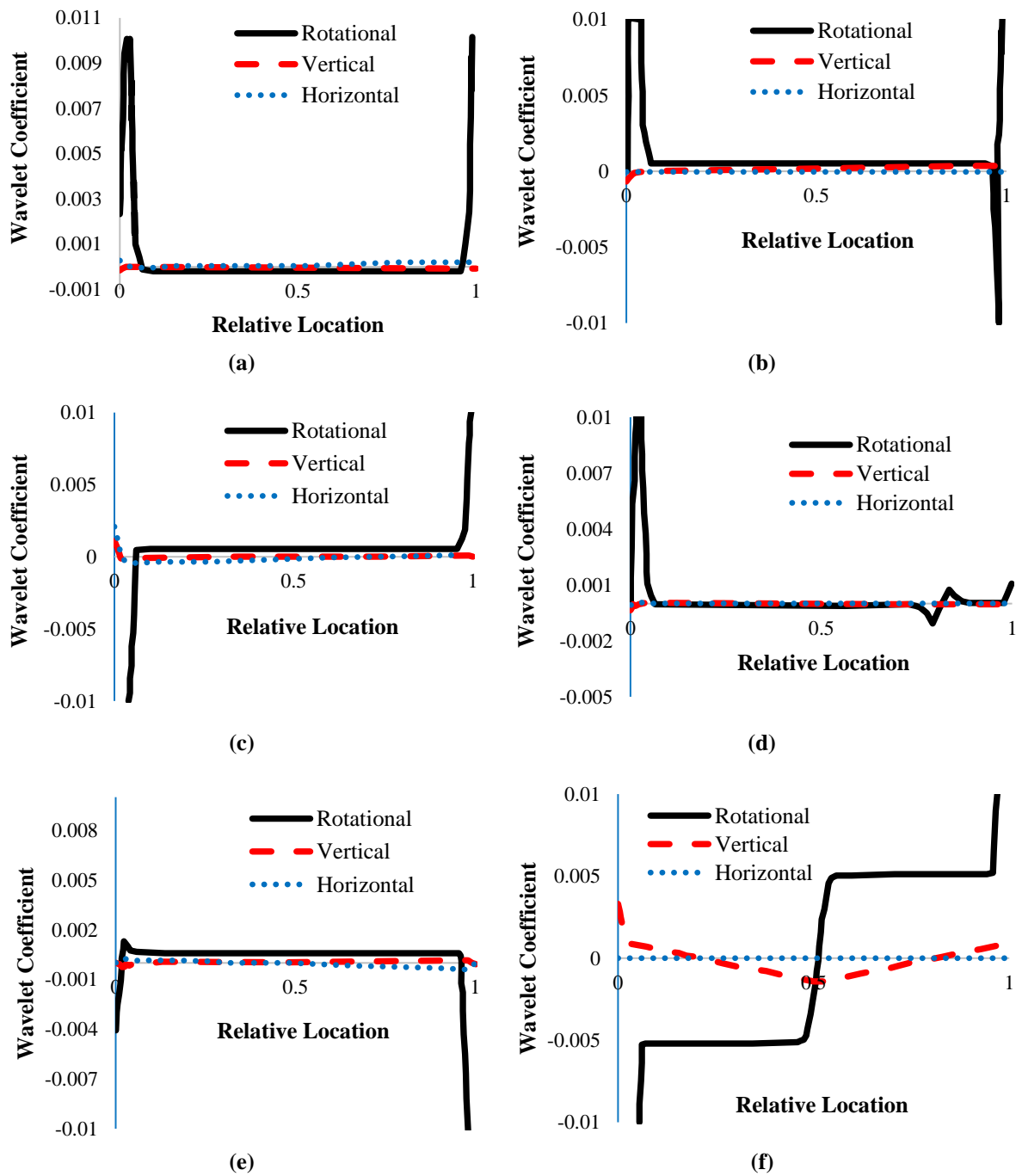


Fig. 9. Wavelet coefficients of members 1 to 6 for first scenario: a) Member 1; b) Member 2; c) Member 3; d) Member 4; e) Member 5; and f) Member 6

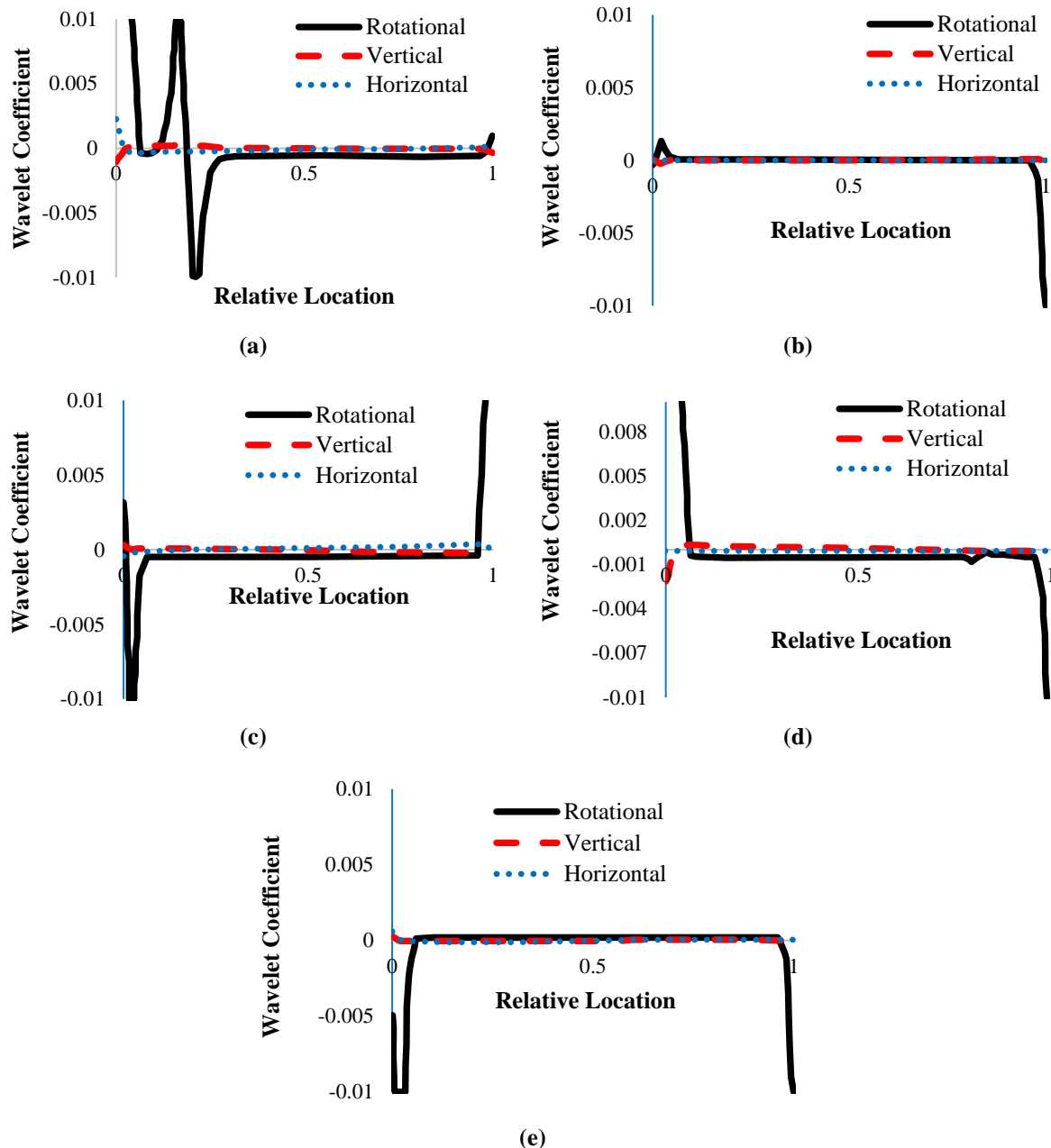


Fig. 10. Wavelet coefficients of members 7 to 11 for first scenario: a) Member 7; b) Member 8; c) Member 9; d) Member 10; and e) Member 11

A Comparison between WT coefficients of vertical displacement and rotation for all members shows that the rotation response is a proper index to identify the damage and loading locations. For instance, the damage location on the 4th and 10th members is illustrated as a jump in the WT coefficient of rotations of these members. However, the WT coefficients of vertical displacements of 4th and 10th members are constant over the members' length and the damage location is not detected. A significant jump is also seen in WT coefficient of rotation

response of Member 6. This jump corresponds to the loading location on the 6th member. Moreover, a significant variation is obvious in the WT coefficient of rotation response of the 7th member which corresponds to the damage location on Member 7. The WT coefficient of vertical displacement of Member 7 is not affected considerably by the damage on this member.

4.2. Bridge under one Locomotive

A six-axle locomotive was placed on the

bridge simulated in the previous section. As illustrated in Figure 11, six concentrated loads were applied to Members 2 and 6. The magnitude of each load is 100 N. As shown in Figure 11, three damages with different severity were considered on the 4, 6 and 8th members. Three cracks with depths of 30, 20 and 10% were considered at Members 4, 7 and 10, respectively. The location of the crack at Members 4, 6 and 8 was $x_c/l = 0.8$, $x_c/l = 0.7$ and $x_c/l = 0.5$, respectively.

The bridge was modeled using 50 refined frame elements. The vertical, horizontal and rotation of each node were calculated. The undeformed and deformed shapes of the bridge are shown in Figure 12.

The wavelet coefficients of horizontal, vertical and rotation of each member of the bridge were obtained based on the Gaus2 wavelet basis function (Figures 13 and 14). The trend of the results obtained in this section is same as those presented in the

previous section. As shown in these figures, wavelet coefficients of horizontal displacement of all members are not affected by the damages.

Assessment of the WT coefficients of vertical displacement and rotation for all members presented in Figures 13 and 14 prove that the rotation response is a proper index to detect the damage and loading locations. As shown in Figures 13 and 14, three concentrated point loads applied on the 2th and 6th members cause a step change in the WT coefficients of rotations of these members. However, the WT coefficients of vertical displacement of the 2th and 6th members are changed slightly by the concentrated point loads. While the damage causes a significant jump on the WT coefficients of rotations of the 4th, 6th and 8th members, the WT coefficients of vertical displacement of these members are not influenced by the damage.

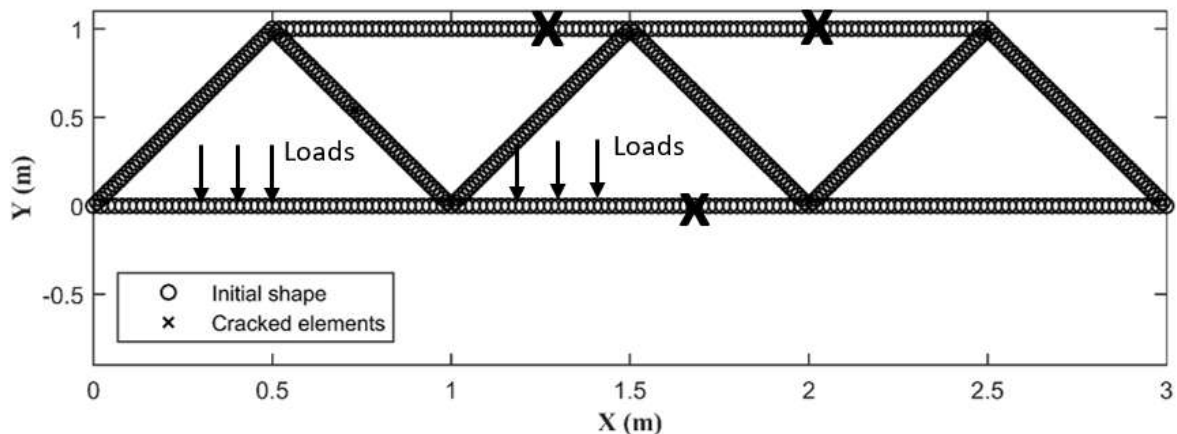


Fig. 11. The bridge model in the second scenario

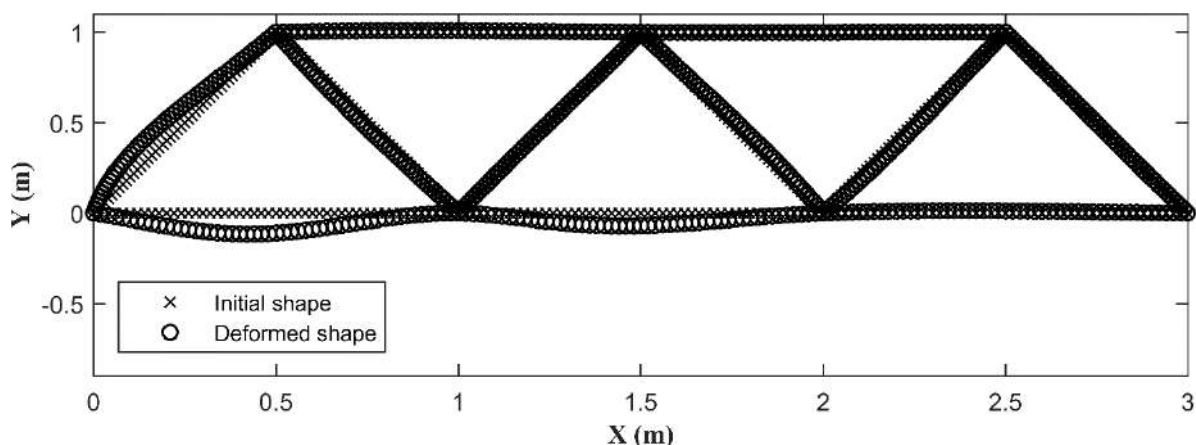


Fig. 12. Undeformed and deformed shapes of the bridge in the second scenario

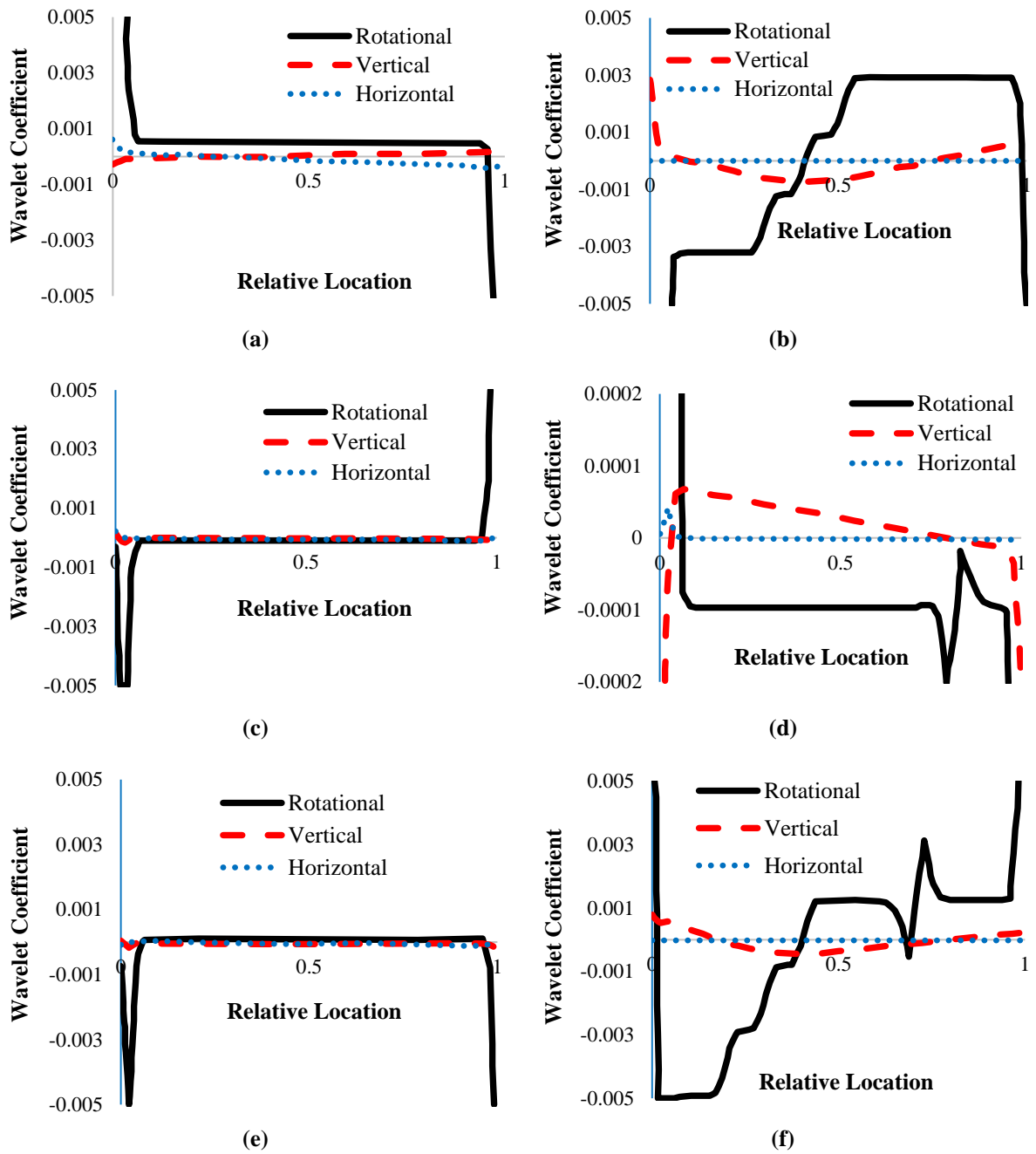
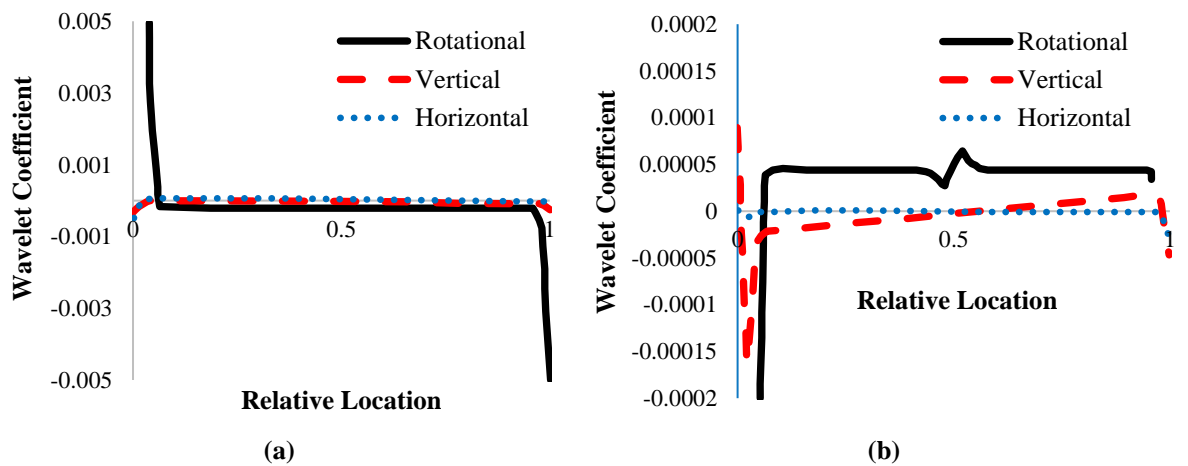


Fig. 13. Wavelet coefficients of Members 1 to 6 for the second scenario: a) Member 1; b) Member 2; c) Member 3; d) Member 4; e) Member 5; and f) Member 6



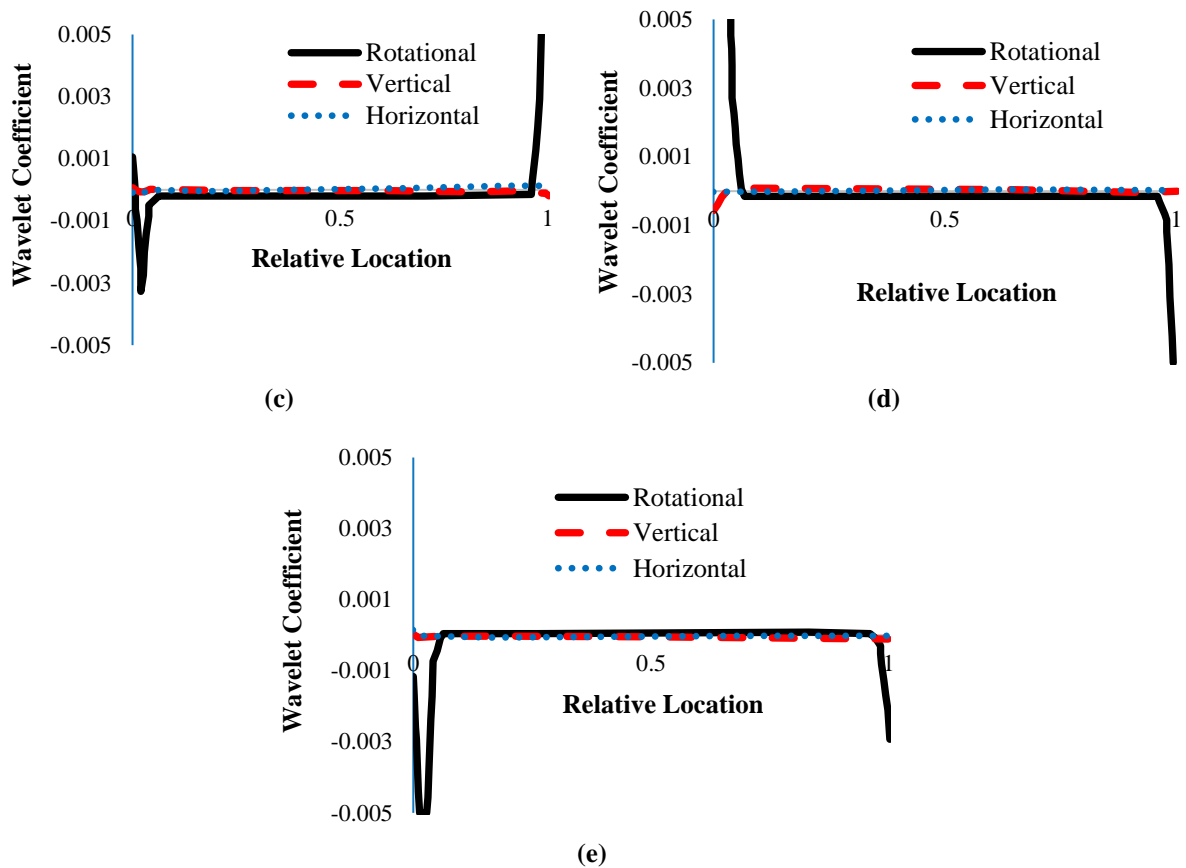


Fig. 14. Wavelet coefficients of Members 7 to 11 for the second scenario: a) Member 7; b) Member 8; c) Member 9; d) Member 10; and e) Member 11

5. Conclusions

A review of the literature indicated that the rotation response of the structure was a proper index to identify the damage location. On the other hand, the previous studies proved that the Wavelet Transform (WT) is a robust method to detect the damage location in the structure. However, WT of pseudo-static rotation response of the bridge was not used to detect the damage location in the literature. This study was carried out to eliminate this limitation. In this regard, a numerical model of a truss bridge was developed using finite element method. The members of the bridge were modeled using frame element. The static response of the model under one point-load and a six-axle locomotive was obtained. The responses obtained from the model was compared with those of open literature to investigate the validity of the responses. The WT coefficients of horizontal, vertical and rotation of each member of the bridge

were obtained based on the Gaus2 wavelet basis function. Several damage scenarios were considered for the bridge to investigate the effectiveness of WT of rotation response of the bridge to detect the damage location.

The results obtained from the study showed whereas the WT of horizontal displacement was not a proper index to detect the damage in the bridge members, a comparison between WT coefficients of vertical displacement and rotation for all members indicated that the rotation response can properly identify the damage and loading locations. In all cases (one- or three-point loads), while the damage causes a significant jump on the WT coefficients of rotations of the members, the WT coefficients of vertical displacement of these members are not influenced by the damage. The results indicated that the WT of pseudo-static rotation response is very effective approach to detect the damage location. In practice, image processing

approach was used to measure the pseudo-static rotation response of the structure and then, the WT approach was implemented on the the pseudo-static rotation response. The time history of rotation response of the structure was another type of rotation response (dynamic response) of the structure which usually measured in the tests. The outputs indicated the importance and necessity of investigation of the effectiveness of WT of time history of rotation response of the structure to identify the damage location.

It should be noted that the effect of noise measurement on the response of the structure was neglected in this study. Although this paper was the first one to show that the wavelet transformation of a rotational signal is a proper index to detect the damage location in the bridge, the measurement noises were neglected in the approach implemented in this study. The effect of noise measurement on the dynamic response of structure will be considered in the further study.

6. References

- Andrea, J., Kiremidjian, A., Liao, Y., Georgakis, C. and Rajagopal, R. (2016). "Structural health monitoring approach for detecting ice accretion on bridge cable using the Haar Wavelet Transform Sensors", In: *Sensors and Smart Structures Technologies for Civil, Mechanical, and Aerospace Systems 2016* (Vol. 9803, pp. 107-114), SPIE, <https://doi.org/10.1117/12.2219392>.
- Andreus, U., Baragatti, P., Casini, P. and Iacoviello, D. (2017). "Experimental damage evaluation of open and fatigue cracks of multi-cracked beams by using wavelet transform of static response via image analysis", *Structural Control Health Monitoring*, 24(4), 1-18, <https://doi.org/10.1002/stc.1902>.
- Barone, G., Marino, F. and Pirrotta, A. (2008). "Low stiffness variation in structural systems: identification and localization", *Structural Control and Health Monitoring*, 15(3), 450-470, <https://doi.org/10.1002/stc.246>.
- Cantero, D. and Basu, B. (2014). "Railway infrastructure damage detection using wavelet transformed acceleration response of traversing vehicle", *Structural Control and Health Monitoring*, 22(1), 62-70, <https://doi.org/10.1002/stc.1660>.
- Christides, S. and Barr, A.D.S. (1999). "One-dimensional theory of cracked Bernoulli-Euler beams", *International Journal of Mechanical Science*, 26(3), 639-638, [https://doi.org/10.1016/0020-7403\(84\)90017-1](https://doi.org/10.1016/0020-7403(84)90017-1).
- Douka, S., Loutridis, S. and Trochidis, A. (2003). "Crack identification in beams using wavelet analysis", *International Journal of Solids and Structures*, 40(13-14), 3557-3569, [https://doi.org/10.1016/S0020-7683\(03\)00147-1](https://doi.org/10.1016/S0020-7683(03)00147-1).
- Hester, D., Brownjohn, J., Huseynov, F., Obrien, E., Gonzalez, A. and Casero, M. (2020). "Identifying damage in a bridge by analysing rotation response to a moving load", *Structure and Infrastructure Engineering*, 16(7), 1050-1065, <https://doi.org/10.1080/15732479.2019.1680710>.
- Hester, D. and González, A. (2011). "A wavelet-based damage detection algorithm based on bridge acceleration response to a vehicle", *Journal of Mechanical Systems and Signal Processing*, 28(4), 145-146, <https://doi.org/10.1016/j.ymssp.2011.06.007>.
- Hou, Z., Noori, M. and Amand, R.S. (2000). "Wavelet-based approach for structural damage detection", *Journal of Engineering Mechanics*, 126(7), 677-683, [https://doi.org/10.1061/\(ASCE\)0733-9399\(2000\)126:7\(677\)](https://doi.org/10.1061/(ASCE)0733-9399(2000)126:7(677)).
- Huang, H.B., Yi, T.H., Li, H.N. and Liu, H. (2020). "Strain-based performance warning method for bridge main girders under variable operating conditions", *Journal of Bridge Engineering*, 25(3), 04020013, [https://doi.org/10.1061/\(ASCE\)BE.1943-5592.0001538](https://doi.org/10.1061/(ASCE)BE.1943-5592.0001538).
- Janeliukstis, R., Rucevskis, S., Wesolowski, M. and Chate, A. (2017). "Damage identification in beam structure based on thresholded variance of normalized wavelet scalogram", *3rd International Conference on Innovative Materials, Structures and Technologies (IMST 2017)*, Latvia, <https://doi.org/10.1088/1757-899X/251/1/012089>.
- Kankanamge, Y., Hu Y. and Shao, X. (2020). "Application of wavelet transform in structural health monitoring", *Earthquake Engineering and Engineering Vibration*, 19(2), 515-532, <https://doi.org/10.1007/s11803-020-0576-8>.
- Khajehdezfuly, A., Ehsanfard, F. and Labibzadeh, M. (2023). "Effect of fuse damper on cyclic performance of self-centring bridge pier", *Proceedings of the Institution of Civil Engineers-Bridge Engineering*, 176(03), 1-21, <https://doi.org/10.1680/jbren.22.00028>.
- Khiem, N.T., Lien, T.V. and Duc, N.T. (2021). "Crack identification in functionally graded material framed structures using stationary wavelet transform and neural network", *Journal*

- of Zhejiang University-SCIENCE A, 22(5), 657-671, <https://doi.org/10.1631/jzus.A2000402>.
- Kordi, A. and Mahmoudi, M. (2022). "Damage detection in truss bridges under moving load using time history response and members influence line curves", *Civil Engineering Infrastructures Journal*, 55(1), 183-194, <https://doi.org/10.22059/ceij.2021.314109.1723>.
- Kumar, R. and Singh, S.K. (2021). "Crack detection near the ends of a beam using wavelet transform and high-resolution beam deflection measurement", *European Journal of Mechanics - A/Solids*, 88(3), 13-25, <https://doi.org/10.1016/j.euromechsol.2021.104259>.
- Labibzadeh, M., Bostan Shirin, F. and Khajehdezfuly, A. (2022). "Improvement of performance of the RC beams using the longitudinal spiral reinforcements", *International Journal of Structural Integrity*, 13(06), 922-950, <https://doi.org/10.1108/IJSI-07-2022-0094>.
- Labibzadeh, M., Jamalpour, R, Jing, D.H. and Khajehdezfuly, A. (2019). "A numerical comparison between spiral transverse RC and CFST columns under loads of varying eccentricities", *Periodica Polytechnica Civil Engineering*, 63(04), 1171-1182, <https://doi.org/10.3311/PPci.14177>.
- Ma, Q., Solis, M. and Galvin, P. (2021), "Wavelet analysis of static deflections for multiple damage identification in beams", *Mechanical Systems and Signal Processing*, 147, 107103, <https://doi.org/10.1016/j.ymssp.2020.107103>.
- Mahato, B. and Harish, H.V. (2015). "Experimental verification of deflection of beam using theoretical and numerical approach", *International Journal of Advance Research in Engineering, Science & Technology*, 2(3), 2394-2444, <https://api.semanticscholar.org/CorpusID:73574711>.
- Martinez, D., Malekjafarian, A. and O'Brien, E. (2019). "Bridge health monitoring using deflection measurements under random traffic", *Structural Control Health Monitoring*, 27(9), 24-42, <https://doi.org/10.1002/stc.2593>.
- Miao, B., Wang, M., Yang, S., Luo, Y. and Yang, C. (2020). "An optimized damage identification method of beam using Wavelet and Neural Network", *Engineering*, 12(3), 748-76, <https://doi.org/10.4236/eng.2020.1210053>.
- Moreu, F., Kim, R.E., Spencer Jr, B.F. (2017). "Railroad bridge monitoring using wireless smart sensors", *Structural Control Health Monitoring*, 24(2), 34-51, <https://doi.org/10.1002/stc.1863>.
- Ovanosova, A.V. and Suarez, L.E. (2004). "Application of wavelet transforms to damage detection in frame structures", *Engineering Structures*, 26(5), 39-49, <https://doi.org/10.1016/j.engstruct.2003.08.009>.
- Poorveis, D., Khajehdezfuly, A. and Hosseini Dehdashti, S.A. (2023). "Development of a combined finite element/finite strip method to analysis the long-span box bridge having diaphragm", *Journal of Transportation Research*, 20(3), 127-148, <https://doi.org/10.22034/tri.2021.262969.2846>.
- Przemieniecki, J.S. (1985). *Theory of matrix structural analysis*, Dover Publications, New York, USA, <https://store.doverpublications.com/products/9780486649481>.
- Rezaifar, O. and Doostmohammadi, M.R. (2016). "Damage detection of axially loaded beam: A frequency-based method", *Civil Engineering Infrastructures Journal*, 49(1), 165-172, <https://doi.org/10.7508/ceij.2016.01.012>.
- Rizzo, P. and Enshaeian, A. (2022). "Challenges in bridge health monitoring: A review", *Sensors*, 21(13), 1-23, <https://doi.org/10.3390/s21134336>.
- Sadeghi, J. and Fathali, M. (2007). "Deterioration analysis of concrete bridges under inadmissible loads from the fatigue point of view", *Scientia Iranica*, 14(3), 185-192.
- Sadeghi, J. and Hashemi Rezvani, F. (2013). "Development of non-destructive method of detecting steel bars corrosion in bridge decks", *Structural Engineering and Mechanics: An International Journal*, 46(5), 615-627.
- Serra, R. and Lopez, R. (2017). "Damage detection methodology on beam-like structures based on combined modal wavelet transform strategy", *Journal of Mechanics and Industry*, 18(8), 1-18, <https://doi.org/10.1051/meca/2018007>.
- Silik, A., Noori, M., Altabey, W.A., Dang, J., Ghiasi, R. and Wu, Z. (2021). "Optimum wavelet selection for nonparametric analysis toward structural health monitoring for processing big data from sensor network: A comparative study", *Structural Health Monitoring*, 78(3), 1-17, <https://doi.org/10.1177/14759217211010261>.
- Silva, R.S.Y.C., Bezerra, L.M. and Pena, L.A.P. (2014). "Detecting open cracks insides beams using the BEM and wavelet transform", *Blucher Mechanical Engineering Proceedings*, 1(1), 1-9, <https://doi.org/10.5151/meceng-wccm2012-19292>.
- Silva, R.S.Y.C., Bezerra, L.M. and Brito, M.A.N. (2012), "Determination of damages in beams using wavelet transforms", *Proceedings of the World Congress on Engineering (WCE 2012)*, London, U.K, https://www.iaeng.org/publication/WCE2012/WCE2012_pp1211-1213.pdf.
- Sun, Z. and Chang, C.C. (2002), "Structural damage assessment based on wavelet packet transform", *Journal of Structural Engineering*, 128(10),

1354-1361,

[https://doi.org/10.1061/\(ASCE\)0733-9445\(2002\)128:10\(1354\)](https://doi.org/10.1061/(ASCE)0733-9445(2002)128:10(1354)).

- Taha, M.M.R., Nouredin, O. and El-Sheimy, A.N. (2004). "Introduction to the use of wavelet multiresolution analysis for intelligent structural health monitoring", *Canadian Journal of Civil Engineering*, 31(3), 719-731, <https://doi.org/10.1139/104-022>.
- Tiboni, M., Remino, C., Bussola, R. and Amici, C. (2022). "A review on vibration-based condition monitoring of rotating machinery", *Applied Sciences*, 972(12), 1-44, <https://doi.org/10.3390/app12030972>.
- Wan, P., Lei, X., Wu, W., Hu, Q., Wan, L. and Li, G. (2022). "Simulation analysis of coupled structural vibration of highway railway combined bridge induced by overlapping action of vehicle and train", *Geofluids*, 2022(1), 1986593, <https://doi.org/10.1155/2022/1986593>.
- Zhong, S. and Oyadiji, S.O. (2008). "Identification of cracks in beams with auxiliary mass spatial probing by stationary wavelet transform", *ASME Journal of Vibration and Acoustics*, 130(2), 1-18, <https://doi.org/10.1115/1.2891242>.
- Zhu, X.Q. and Law, S.S. (2006). "Wavelet-based crack identification of bridge beam from operational deflection time history", *International Journal of Solids and Structures*, 43(3), 2299-2317.



This article is an open-access article distributed under the terms and conditions of the Creative Commons Attribution (CC-BY) license.



A Novel Method for Modal Analysis of Dam-Reservoir Systems

Rezaiee-Pajand, M.^{1*}, Kazemiyan, M. S.² and Mirjalili, Z.³

¹ Professor, Department of Civil Engineering, Ferdowsi University of Mashhad, Mashhad, Iran.

² Assistant Professor, Department of Civil Engineering, Eqbal Lahoori Institute of Higher Education, Mashhad, Iran.

³ Ph.D. Candidate, Department of Civil Engineering, Ferdowsi University of Mashhad, Mashhad, Iran.

© University of Tehran 2023

Received: 05 Oct. 2022;

Revised: 03 Feb. 2023;

Accepted: 29 May 2023

ABSTRACT: For dynamic modal analysis of the gravity dams, it is required to solve the non-symmetric eigenvalue problem which is a time-consuming process. This paper aims to propose a new procedure for this purpose. In this novel method, there is no need to solve the non-symmetric coupled eigenproblem. Instead, two novel eigenvalue problems are formulated and solved. They are simultaneously applied for dynamic modal analysis of concrete gravity dams. They represent the cubic-symmetric forms of the respective non-symmetric Eigenvalue problem, and they are entitled “cubic ideal-coupled eigenproblems”. Moreover, it is proved that the decoupled and ideal-coupled schemes presented in the previous works can be considered as special cases of the current more general procedure. For solving the aforesaid cubic eigenproblems, the classical subspace algorithm is generalized. To assess the accuracy of the suggested technique, it is employed for the dynamic analysis of two well-known benchmark gravity dams in the frequency domain. The dam crest responses are calculated under upstream and vertical excitations for two different wave reflection coefficients. Then, the obtained results are compared with those of the decoupled and ideal-coupled approaches. Findings corroborate the fact that the authors' formulation is more accurate than the other two aforesaid tactics under all practical conditions.

Keywords: Concrete Gravity Dam, Coupled Method, Cubic Ideal-Coupled Method, Decoupled Method, Fluid-Structure Interaction, Ideal-Coupled Method.

1. Introduction

The dynamic behavior analysis of a concrete gravity dam-reservoir system can be effectively carried out using the Finite Element-(Finite Element-Hyper Element) technique, commonly abbreviated as FE-(FE-HE) (Aftabi Sani and Lotfi, 2010). In

other words, the dam is modeled with the help of solid finite elements, while the reservoir is divided into a near-field region and a far-field one. The former is near the dam and has an irregular shape, while the latter one is including rectangular strips extending to infinity. These two regions are modeled by the fluid finite element and the

* Corresponding author E-mail: mrpajand@yahoo.com

fluid hyper-elements, respectively (Aftabi Sani and Lotfi, 2010).

Generally, the dynamic analysis process can be performed in the time or frequency domain (Chandravanshi and Mukhopadhyay, 2017). For dam-reservoir systems, many nonlinear constitutive models have been developed for time domain analysis. On another note, the analysis can be conducted in the frequency domain either by the direct approach (Lotfi, 2005) or the modal one. In fluid-structure interaction problems, such as the dam-reservoir, various alternatives exist for conducting modal analysis (Lotfi, 2005). Some of them utilized the true coupled mode shapes of the system. Within these methodologies, a significant portion of the computational time is dedicated to solve the asymmetric Eigenvalue problem that governs the free vibration behavior of the dam-reservoir systems. To remedy this difficulty, various methods have been proposed for symmetrizing this problem (Rezaiee-Pajand et al., 2021). In general, the earlier ones used extra unknowns (in addition to the pressure) for the fluid domain to symmetrize the problem (Olson and Vandini, 1989). Moreover, they are not efficient, and some of them are not able to calculate the hydrostatic pressure (Everstine, 1981). In this condition, the “decoupled” (Samii and Lotfi, 2007) and “ideal-coupled” (Aftabi Sani and Lotfi, 2010) modal strategies have been proposed to defeat the deficiencies of the aforesaid methods. In the “decoupled” technique, the dam and reservoir Eigen-vectors are separately calculated. They are also applied in the solution procedure instead of the coupled Eigen-vectors. Similarly, the ideal-coupled method separately uses the Eigen-vectors of the dam and reservoir with modifications in comparison to the decoupled tactic. Based on the related literature, among various techniques symmetrizing the Eigen-problem solved in the dynamic analysis of the dam-reservoir systems, only these two methods use the Eigen-vectors of each domain for

developing a symmetric version of the originally non-symmetric coupled Eigen-problem.

They rely on the mode shapes of two symmetric Eigenvalue problems, which are relatively straightforward from a programming perspective. In a study conducted by Hariri-Ardebili and Mirzabozorg (2013), a direct time-domain approach was proposed for the dynamic stability analysis of the coupled dam-reservoir-foundation system in three-dimensional space. This approach takes into account the impact of the duration of ground motion on the system's dynamic structural stability. Gu et al. (2014) investigated the degradation and safety evaluation of a concrete gravity dam by employing a deterministic and a probabilistic method.

Chen et al. (2014) investigated the process of damage and rupture in concrete gravity dams subjected to strong ground motions. Afterward, Lokke and Chopra (2015) suggested a response spectrum analysis strategy estimating the peak response directly from the earthquake design spectrum. Mandal and Maity (2016) proposed a two-dimensional method considering both the fluid-structure and soil-structure interaction in finding the transient response of concrete gravity dams. In another research, Ansari and Agarwal (2017) proposed a new damage index for gravity dams. Furthermore, Guo et al. (2019) used the Lagrange multiplier method for including the dead loads of the arch dam in the dynamic analysis procedure. Moreover, Sotoudeh et al. (2019) conducted a seismic analysis of a system comprising a reservoir, gravity dam, and layered foundation, considering the effects of a vertically propagating earthquake. The methodology developed by Casas and Pavanello (2017) obtained optimal dynamic structural shape through parameter changing, in order to maximize the gap between two adjacent Eigenvalues and also avoid the resonance phenomena at a specific natural frequency interval in

coupled fluid-structure systems. Nariman et al. (2019) considered dam-reservoir-foundation interaction and used an extended finite element approach for damage detection of gravity dams. In a study by Liang et al. (2019) a probabilistic analysis was carried out to assess the seismic stability performance of a high arch dam. The analysis method incorporated considerations for contraction joints, boundaries of potential sliding rock masses, and the interaction between the dam and its foundation. Recently, Sotoudehnia et al. (2021) developed an iterative method for reducing the order of the coupled Eigenvalue problem related to fluid-structure interaction systems.

This paper aims to introduce a novel modal procedure for the mentioned issue, which is referred to as the cubic-ideal coupled approach. It is considered the enhancement of the “decoupled” and “ideal-coupled” modal techniques. This paper text is structured as follows. Section 2 provides a concise overview of the analysis approach. Then, the coupled, decoupled, and ideal-coupled Eigenproblems are reviewed in Section 3. Afterward, a new cubic-ideal coupled scheme is thoroughly introduced. Furthermore, it is proved that the decoupled and ideal-coupled techniques can be envisaged as special cases of authors' procedures. In Section 4, the cubic eigen vectors are employed for dynamic modal analysis. Section 5 deals with developing a new approach for solving the aforesaid Eigenvalue problem by generalizing the well-known subspace iteration algorithm. In Section 6, the dynamic responses of the triangle ideal dam and Pine Flat dam are achieved by using the special program developed by the authors. Finally, the discussion and conclusions are reported in Sections 7 and 8, respectively.

2. Analysis Method

The modal analysis technique is employed in this study (Chandravanshi and Mukhopadhyay, 2017). The FE-(FE-HE)

approach is employed to discretize both the dam and fluid domains. For simplicity, the formulation is initially explained without considering the far-field region of the reservoir. Then, the impacts of this region are added to the general case. Therefore, the coupled governing equation of the system takes on the following form (Rezaiee-Pajand et al., 2022) :

$$\begin{bmatrix} \mathbf{M} & \mathbf{0} \\ \mathbf{B} & \mathbf{G} \end{bmatrix} \begin{bmatrix} \ddot{\mathbf{r}} \\ \dot{\mathbf{p}} \end{bmatrix} + \begin{bmatrix} \mathbf{C} & \mathbf{0} \\ \mathbf{0} & \mathbf{L} \end{bmatrix} \begin{bmatrix} \dot{\mathbf{r}} \\ \dot{\mathbf{p}} \end{bmatrix} + \begin{bmatrix} \mathbf{K} & -\mathbf{B}^T \\ \mathbf{0} & \mathbf{H} \end{bmatrix} \begin{bmatrix} \mathbf{r} \\ \mathbf{p} \end{bmatrix} = \begin{bmatrix} -\mathbf{M}\mathbf{J}\mathbf{a}_g \\ -\mathbf{B}\mathbf{J}\mathbf{a}_g \end{bmatrix} \quad (1)$$

in which \mathbf{K} , \mathbf{M} , and \mathbf{C} : represent the stiffness, mass, and damping matrices of the dam body, respectively. Furthermore, \mathbf{H} , \mathbf{G} , and \mathbf{L} : correspond to the generalized stiffness, mass, and damping of the fluid domain. Moreover, \mathbf{B} : is the interaction matrix; it emerges in the finite element formulation as a result of vibrating the structure in contact with the water (Aftabi Sani and Lotfi, 2010). The provided matrix establishes a correlation between fluid pressure and structural acceleration. Furthermore, vectors \mathbf{r} and \mathbf{p} consist of undetermined nodal displacements and pressures, respectively. It should be added, \mathbf{J} is a matrix which each of its two rows are a 2×2 identity matrix. It is worthwhile to mention that each column of this matrix is related to a unit rigid body motion in the stream and vertical direction. Additionally, \mathbf{a}_g is the vector of ground accelerations. By performing the Fourier transform, the matrix Eq. (1) can be transformed into the following form.

$$\begin{bmatrix} -\omega^2\mathbf{M} + \mathbf{K}(1 + 2\beta_{d1}) & -\mathbf{B}^T \\ -\omega^2\mathbf{B} & -\omega^2\mathbf{G} + i\omega\mathbf{L} + \mathbf{H} \end{bmatrix} \begin{bmatrix} \mathbf{r} \\ \mathbf{p} \end{bmatrix} = \begin{bmatrix} -\mathbf{M}\mathbf{J}\mathbf{a}_g \\ -\mathbf{B}\mathbf{J}\mathbf{a}_g \end{bmatrix} \quad (2)$$

where i : represents the imaginary unit and ω : denotes the natural frequency of the system. It is important to note that the provided relation utilizes the hysteretic damping matrix, which takes on the following form (Aftabi Sani and Lotfi, 2010).

$$C = \frac{2\beta_d}{\omega} \mathbf{K} \quad (3)$$

where β_d : denotes the constant hysteretic factor associated with the dam body. It is important to highlight that Eq. (2) represents the coupled equation of a dam within a finite reservoir system in the frequency domain.

3. Free Vibration Analysis

It is evident that the Eigenvalue problem corresponding to Eq. (2) can be formulated as follows (Casas and Pavanello, 2017; Rezaiee-Pajand et al., 2023; Sotoudehnia et al., 2021).

$$\left(\omega^2 \begin{bmatrix} \mathbf{M} & \mathbf{0} \\ \mathbf{B} & \mathbf{G} \end{bmatrix} + \begin{bmatrix} -\mathbf{K} & \mathbf{B}^T \\ \mathbf{0} & -\mathbf{H} \end{bmatrix} \right) \begin{bmatrix} \mathbf{r} \\ \mathbf{p} \end{bmatrix} = \begin{bmatrix} \mathbf{0} \\ \mathbf{0} \end{bmatrix} \quad (4)$$

Obviously, this linear Eigenvalue problem is similar to the equation governing the free vibration of undamped systems. In contrast, it is not symmetric. To calculate the eigen pairs of the dam-reservoir system, solving this unsymmetrical linear Eigenvalue problem is necessary. Although it is preferred to solve the actual coupled equation of the dam-reservoir system, there are several more efficient alternatives, which will be presented in the following Sub-sections.

3.1. Coupled Eigenproblem

Through direct solution of the original eigenvalue problem (4), the actual coupled eigen pairs can be obtained. Usage of the achieved eigen vectors in modal analysis leads to more precise responses when contrasted with other available options. However, standard Eigen-solvers cannot be used to solve the mentioned equation due to their unsymmetrical nature. Based on the studies of other researchers, it has been found that methods for solving unsymmetrical Eigenvalue problems tend to be more time-consuming compared to symmetrical ones. From a programming perspective, they are also more intricate (Aftabi Sani and Lotfi, 2010; Felippa, 1985; Lotfi and Samii, 2012). It should be

reminded that the symmetric shapes of the aforesaid Eigenvalue problem can be achieved by introducing new variables. Nevertheless, these extra variables cause complexity in computer programming.

3.2. Decoupled Eigenproblem

A symmetrical form of the initial Eigenvalue problem (4) can be achieved by omitting the interaction matrix \mathbf{B} . It is referred to as the "decoupled" form and has the succeeding appearance (Lotfi, 2005):

$$\left(\omega^2 \begin{bmatrix} \mathbf{M} & \mathbf{0} \\ \mathbf{0} & \mathbf{G} \end{bmatrix} - \begin{bmatrix} \mathbf{K} & \mathbf{0} \\ \mathbf{0} & \mathbf{H} \end{bmatrix} \right) \begin{bmatrix} \mathbf{r} \\ \mathbf{p} \end{bmatrix} = \begin{bmatrix} \mathbf{0} \\ \mathbf{0} \end{bmatrix} \quad (5)$$

The symmetry of the decoupled Eigenvalue problem is quite apparent. This property allows for the utilization of standard Eigen-solvers to efficiently solve the problem. Note that; the eigen vectors obtained from these symmetric equations do not correspond to the actual mode shapes of the real system. Nonetheless, these modes can find application in a modal analysis strategy termed the "decoupled modal approach". It is worth mentioning that the decoupled eigen vectors can be regarded as the Ritz vectors. Therefore, it can be demonstrated that utilizing all of these modes leads to precise solutions. It is important to emphasize that the Eigenvalues obtained from the decoupled Eigenproblem represent the natural frequencies of the dam and reservoir individually (Aftabi Sani and Lotfi, 2010).

3.3. Ideal-Coupled Eigenproblem

Herein, the Eigenvalue problems associated with two ideal dam-reservoir systems are solved, rather than the actual coupled system. In the first ideal system, the fluid is considered incompressible, and in the second one, the dam is assumed to be massless. The Eigenvalues obtained from these idealized problems exhibit a higher degree of proximity to the natural frequencies of the real coupled dam-reservoir system, in contrast to the Eigenvalues derived from the decoupled approach. Additionally, the eigen vectors obtained from these computations are more

analogous to the actual mode shapes of the system. These vectors can be employed within a modal analysis approach referred to as the "ideal-coupled modal strategy" (Aftabi Sani and Lotfi, 2010). The first ideal Eigenproblem is presented in a simplified form as follows.

$$[\omega^2(\mathbf{M} + \mathbf{M}_a) - \mathbf{K}] \mathbf{r} = \mathbf{0} \quad (6)$$

where \mathbf{M}_a : represents the added mass matrix and can be obtained as below.

$$\mathbf{M}_a = \mathbf{B}^T \mathbf{H}^{-1} \mathbf{B} \quad (7)$$

Thus, by utilizing Eq. (8), it becomes possible to derive the pressure vector.

$$\mathbf{p} = \omega^2 \mathbf{H}^{-1} \mathbf{B} \mathbf{r} \quad (8)$$

It is obvious that the dimension of this Eigenproblem corresponds to the number of unknown nodal displacements. The formulation of the second ideal Eigenvalue problem is as follows.

$$[\omega^2(\mathbf{G} + \mathbf{G}_a) - \mathbf{H}] \mathbf{p} = \mathbf{0} \quad (9)$$

in which

$$\mathbf{G}_a = \mathbf{B} \mathbf{K}^{-1} \mathbf{B}^T \quad (10)$$

The displacement vector can be computed with the help of the next relation.

$$\mathbf{r} = \mathbf{K}^{-1} \mathbf{B}^T \mathbf{p} \quad (11)$$

Clearly, the dimensions of the second ideal Eigenvalue problem match the count of unknown nodal pressures in the fluid domain. The previously mentioned ideal Eigenproblems can be reformulated as Eq. (12).

$$\left(\omega^2 \begin{bmatrix} \mathbf{M} + \mathbf{M}_a & \mathbf{0} \\ \mathbf{0} & \mathbf{G} + \mathbf{G}_a \end{bmatrix} - \begin{bmatrix} \mathbf{K} & \mathbf{0} \\ \mathbf{0} & \mathbf{H} \end{bmatrix} \right) \begin{bmatrix} \mathbf{r} \\ \mathbf{p} \end{bmatrix} = \begin{bmatrix} \mathbf{0} \\ \mathbf{0} \end{bmatrix} \quad (12)$$

This Eigenproblem is a linear and symmetric one. As a result, the solution to this problem can be obtained through the application of commonly used standard methods. Obviously, eliminating \mathbf{M}_a and

\mathbf{G}_a from Eqs. (6-9) results in the decoupled Eigenvalue problem. Hence, the decoupled version of the actual Eigenproblem represents a specific instance of the ideal-coupled Eigenproblem. It is worthwhile to remark that the ideal-coupled approach is more accurate compared to the decoupled one (Aftabi Sani and Lotfi, 2010).

3.4. New Cubic Ideal-Coupled Eigenproblem

At this stage, a new symmetric form of the Eigenproblem (4) is introduced. It includes two different cubic Eigenvalue problems, which are separately discussed in this section. It is shown that both decoupled and ideal-coupled strategy can be envisaged as special cases of authors' formulation. Moreover, they are less accurate than the current method.

Using the lower partition equation of Eq. (4) and solving the pressure vector in terms of the displacement vector results in the subsequent relation.

$$\mathbf{p} = \omega^2 (\mathbf{H} - \omega^2 \mathbf{G})^{-1} \mathbf{B} \mathbf{r} \quad (13)$$

Obviously, $(\mathbf{H} - \omega^2 \mathbf{G})$ is the subtraction of two matrices, and it is required to be inverted for calculating the pressure vector. Recall that, Eq. (13) is the exact form of Eq. (8) which plays an important role in the ideal-coupled approach. It is worth mentioning that Eq. (8) can be obtained by removing \mathbf{G} from Eq. (13). By employing the second-order approximation of the Taylor series, this matrix inversion can be computed as follows (Bakhtiari-Nejad et al., 2005).

$$(\mathbf{H} - \omega^2 \mathbf{G})^{-1} \cong \mathbf{H}^{-1} + \omega^2 \mathbf{H}^{-1} \mathbf{G} \mathbf{H}^{-1} + \omega^4 \mathbf{H}^{-1} \mathbf{G} \mathbf{H}^{-1} \mathbf{G} \mathbf{H}^{-1} \quad (14)$$

Substituting this relation into Eq. (13) leads to the next result.

$$\mathbf{p} \cong \omega^2 (\mathbf{H}^{-1} + \omega^2 \mathbf{H}^{-1} \mathbf{G} \mathbf{H}^{-1} + \omega^4 \mathbf{H}^{-1} \mathbf{G} \mathbf{H}^{-1} \mathbf{G} \mathbf{H}^{-1}) \mathbf{B} \mathbf{r} \quad (15)$$

By inserting this equality into the upper partition of Eq. (4), the coming cubic Eigenvalue problem is achieved.

$$[\omega^6 \mathbf{QGH}^{-1} \mathbf{GQ}^T + \omega^4 \mathbf{QGQ}^T + \omega^2(\mathbf{M} + \mathbf{M}_a) - \mathbf{K}] \mathbf{r} = \mathbf{0} \quad (16)$$

in which

$$\mathbf{Q} = \mathbf{B}^T \mathbf{H}^{-1} \quad (17)$$

Certainly, the dimension of this cubic Eigenproblem is equivalent to the count of unknown nodal displacements in the system. Note that; eliminating the first two terms of Eq. (16) leads to Eq. (6). Accordingly, the first form of the ideal-coupled method is a special case of the first cubic ideal-coupled approach.

In what follows, the second cubic ideal Eigenproblem is established. To achieve this goal, the displacement vector is solved in terms of the pressure vector by utilizing the upper partition equation of Eq. (4). Consequently, the displacement vector can be computed as below.

$$\mathbf{r} = (\mathbf{K} - \omega^2 \mathbf{M})^{-1} \mathbf{B}^T \mathbf{p} \quad (18)$$

In fact, Eq. (11) is the approximate form of the last relation, in which \mathbf{M} is neglected. It should be added that Eq. (11) is one of the key formulas in the ideal-coupled technique. Similarly, $(\mathbf{K} - \omega^2 \mathbf{M})$ can be inverted with the help of the second-order approximation of the Taylor series. In this way, the succeeding relation can be written (Bakhtiari-Nejad et al., 2005).

$$(\mathbf{K} - \omega^2 \mathbf{M})^{-1} \cong \mathbf{K}^{-1} + \omega^2 \mathbf{K}^{-1} \mathbf{M} \mathbf{K}^{-1} + \omega^4 \mathbf{K}^{-1} \mathbf{M} \mathbf{K}^{-1} \mathbf{M} \mathbf{K}^{-1} \quad (19)$$

Substitution of the aforementioned equation into Eq. (18) yields the next equality.

$$\mathbf{r} \cong (\mathbf{K}^{-1} + \omega^2 \mathbf{K}^{-1} \mathbf{M} \mathbf{K}^{-1} + \omega^4 \mathbf{K}^{-1} \mathbf{M} \mathbf{K}^{-1} \mathbf{M} \mathbf{K}^{-1}) \mathbf{B}^T \mathbf{p} \quad (20)$$

Introducing this relationship into the lower partition of Eq. (4) leads to the next equation.

$$[\omega^6 \mathbf{S} \mathbf{M} \mathbf{K}^{-1} \mathbf{M} \mathbf{S}^T + \omega^4 \mathbf{S} \mathbf{M} \mathbf{S}^T + \omega^2(\mathbf{G} + \mathbf{G}_a) - \mathbf{H}] \mathbf{p} = \mathbf{0} \quad (21)$$

where

$$\mathbf{S} = \mathbf{B} \mathbf{K}^{-1} \quad (22)$$

It is clear that the dimension of this cubic Eigenproblem is equivalent to the count of unknown nodal displacements in the system. It is worthwhile to highlight that neglecting the first two terms of Eq. (21) leads to Eq. (9). Hence, the second form of the ideal-coupled scheme is a special case of the second cubic ideal-coupled approach. A $n \times n$ cubic Eigenproblem has Eigenvalues. According to the characteristics of the coefficient matrices, the Eigenvalues may be infinite or finite, and the finite values may be real or complex (Tisseur and Meerbergen, 2001). Obviously, real values are the approximate natural frequencies of the dam-reservoir system, and the other ones are fictitious. The aforesaid two cubic ideal-coupled Eigenvalue problems, i.e., Eqs. (16-21), can be expressed totally as the next shape.

$$\begin{aligned} & (\omega^6 \begin{bmatrix} \mathbf{QGH}^{-1} \mathbf{GQ}^T & \mathbf{0} \\ \mathbf{0} & \mathbf{S} \mathbf{M} \mathbf{K}^{-1} \mathbf{M} \mathbf{S}^T \end{bmatrix} \\ & + \omega^4 \begin{bmatrix} \mathbf{QGQ}^T & \mathbf{0} \\ \mathbf{0} & \mathbf{S} \mathbf{M} \mathbf{S}^T \end{bmatrix} \\ & + \omega^2 \begin{bmatrix} \mathbf{M} + \mathbf{M}_a & \mathbf{0} \\ \mathbf{0} & \mathbf{G} + \mathbf{G}_a \end{bmatrix} \\ & - \begin{bmatrix} \mathbf{K} & \mathbf{0} \\ \mathbf{0} & \mathbf{H} \end{bmatrix}) \begin{bmatrix} \mathbf{r} \\ \mathbf{p} \end{bmatrix} = \begin{bmatrix} \mathbf{0} \\ \mathbf{0} \end{bmatrix} \end{aligned} \quad (23)$$

By solving two separate cubic Eigenvalue problems, the solution of this combined symmetric Eigenproblem can be calculated. It is worthwhile to mention the current relationship can be changed into Eq. (12) by ignoring $\omega^4 \mathbf{Q} \mathbf{G} \mathbf{Q}^T$, $\omega^4 \mathbf{S} \mathbf{M} \mathbf{S}^T$, $\omega^6 \mathbf{Q} \mathbf{G} \mathbf{H}^{-1} \mathbf{G} \mathbf{Q}^T$ and $\omega^6 \mathbf{S} \mathbf{M} \mathbf{K}^{-1} \mathbf{M} \mathbf{S}^T$ terms.

4. Cubic Ideal-Coupled Modal Analysis

Herein, it is assumed that Eigenproblem (23) is solved, and the mode shapes are found. Consequently, the nodal displacements and pressures can be written as follows.

$$\begin{bmatrix} \mathbf{r} \\ \mathbf{p} \end{bmatrix} = \begin{bmatrix} \mathbf{X}_S & \mathbf{0} \\ \mathbf{0} & \mathbf{X}_F \end{bmatrix} \begin{bmatrix} \mathbf{Y}_S \\ \mathbf{Y}_F \end{bmatrix} \quad (24)$$

where \mathbf{X}_S and \mathbf{X}_F : are matrices, which include the eigen vectors of Eigenvalue problems (16) and (21), respectively. These vectors are regarded as the Ritz vectors stemming from the original coupled Eq. (2). They can be employed in combination to provide an approximate solution for the exact problem. It is worth noting that the cubic-ideal coupled mode shapes do not exhibit orthogonality concerning the original mass and stiffness matrices. Nevertheless, the subsequent matrices can be defined as below.

$$\mathbf{K}^* = \mathbf{X}_S^T \mathbf{K} \mathbf{X}_S; \mathbf{M}^* = \mathbf{X}_S^T \mathbf{M} \mathbf{X}_S \quad (25)$$

$$\mathbf{H}^* = \mathbf{X}_F^T \mathbf{H} \mathbf{X}_F; \mathbf{G}^* = \mathbf{X}_F^T \mathbf{G} \mathbf{X}_F; \quad (26)$$

$$\mathbf{L}^* = \mathbf{X}_F^T \mathbf{L} \mathbf{X}_F$$

Inserting Eq. (24) into Eq. (2) and performing some simple mathematical operations lead to the next result (Aftabi Sani and Lotfi, 2010).

$$\begin{bmatrix} -\omega^2 \mathbf{M}^* + \mathbf{K}^*(1 + 2\beta_d i) & -\mathbf{X}_S^T \mathbf{B}^T \mathbf{X}_F \\ -\mathbf{X}_F^T \mathbf{B} \mathbf{X}_S & \omega^{-2}(-\omega^2 \mathbf{G}^* + i\omega \mathbf{L}^* + \mathbf{H}^*) \end{bmatrix} \begin{bmatrix} \mathbf{Y}_S \\ \mathbf{Y}_F \end{bmatrix} \\ = \begin{bmatrix} -\mathbf{X}_S^T \mathbf{M} \mathbf{J} \mathbf{a}_g \\ -\omega^{-2} \mathbf{X}_F^T \mathbf{B} \mathbf{J} \mathbf{a}_g \end{bmatrix} \quad (27)$$

It is obvious that the vector, which includes the modal participation factors, can be computed with the help of this relation. At each frequency, the response vector can be calculated by introducing the modal participation factor into Eq. (24) in the case of cubic ideal-coupled modal analysis for a dam-finite reservoir system.

4.1. Dam-Reservoir System

Up until this point, the formulation of the dam within a finite reservoir was presented. However, when considering a reservoir that extends infinitely, it becomes necessary to incorporate hyper-elements in conjunction with the fluid finite elements. By assembling the hyper-elements matrices, Eq. (2) is converted into the next form.

$$\begin{bmatrix} -\omega^2 \mathbf{M}^* + \mathbf{K}^*(1 + 2\beta_d i) & -\mathbf{X}_S^T \mathbf{B}^T \mathbf{X}_F \\ -\mathbf{X}_F^T \mathbf{B} \mathbf{X}_S & \omega^{-2}(-\omega^2 \mathbf{G}^* + i\omega \mathbf{L}^* + \mathbf{H}^* + \mathbf{X}_F^T \bar{\mathbf{H}}_h(\omega) \mathbf{X}_F) \end{bmatrix} \begin{bmatrix} \mathbf{Y}_S \\ \mathbf{Y}_F \end{bmatrix} \\ = \begin{bmatrix} -\mathbf{X}_S^T \mathbf{M} \mathbf{J} \mathbf{a}_g \\ \omega^{-2} \mathbf{X}_F^T (-\mathbf{B} \mathbf{J} \mathbf{a}_g + \bar{\mathbf{R}}_p(\omega) \mathbf{a}_g) \end{bmatrix} \quad (28)$$

$$\bar{\mathbf{H}}_h(\omega) = \begin{bmatrix} \mathbf{H}_h(\omega) & \mathbf{0} \\ \mathbf{0} & \mathbf{0} \end{bmatrix} \quad (29)$$

$$\bar{\mathbf{R}}_p(\omega) = \begin{bmatrix} \mathbf{R}_p(\omega) \\ \mathbf{0} \end{bmatrix} \quad (30)$$

$\bar{\mathbf{H}}_h(\omega)$ and $\bar{\mathbf{R}}_p(\omega)$ are obtained by expanding $\mathbf{H}_h(\omega)$ and $\mathbf{R}_p(\omega)$, respectively. These matrices include all pressure degrees of freedom. Note that; Eqs. (27-28) are utilized to determine the vector of participation factors in cases where the reservoir is finite and extends to infinity, respectively.

4.2. Linearized Forms for Solving the Cubic Eigenproblems

In the process of the numerical solution of the Standard Eigen Problem (SEP) and the generalized one (GEP), the matrices involved are generally reduced to some simpler forms, which reveal the Eigenvalues. For nonlinear Eigenproblems, these forms cannot be developed. Numerical approaches applied for finding the solution of the cubic Eigenproblems are divided into two categories. The first group directly solves the cubic Eigenproblem, and the second one works with the linearized forms (Afolabi, 1987; Tisseur and Meerbergen, 2001). Note that; most of the numerical tactics, which belong to the first category, are the variants of Newton's methods whose rate of convergence is highly related to the closeness of the starting guess to the actual solution (Higham and Kim, 2001; Long et al., 2008). These algorithms are able to calculate one Eigen-pair at a time. In practice, it is impossible to guarantee that the scheme converges to the desired Eigenvalue even for an appropriate initial guess.

In the techniques based on the linearized forms, a $n \times n$ cubic Eigenproblem is transformed into a $3n \times 3n$ linear Eigenvalue problem. In this way, common linear Eigen-solvers incorporated in commercial and non-commercial software packages can be employed. It should be highlighted that the Eigenvalues of a cubic Eigenproblem are similar to their linear form. Furthermore, the eigen vectors can be obtained from the corresponding linear

problem. Based on the characteristics of the coefficient matrices of a given Eigenvalue problem, various linear forms can be presented for a given cubic Eigenvalue problem. The most important drawback of linearization is that the linearized Eigenproblem's dimension is three times the original cubic one. Based on the linear forms presented in Mackey et al. (2006), suitable symmetric linear forms of the aforementioned cubic ideal-coupled Eigenvalue problems, i.e., Eqs. (16-21), are respectively introduced, as follows.

$$\begin{aligned} & \left(\begin{array}{ccc|c} \text{QGQ}^T - \text{QGH}^{-1}\text{GQ}^T & \text{M} + \text{M}_a - \text{QGH}^{-1}\text{GQ}^T & -\text{K} & \\ \text{M} + \text{M}_a - \text{QGH}^{-1}\text{GQ}^T & \text{M} + \text{M}_a - \text{QGQ}^T - \text{K} & -\text{K} & \\ -\text{K} & -\text{K} & -\text{K} & \\ \hline -\omega^2 \begin{array}{ccc|c} \text{QGH}^{-1}\text{GQ}^T & \text{QGH}^{-1}\text{GQ}^T & \text{QGH}^{-1}\text{GQ}^T & \\ \text{QGH}^{-1}\text{GQ}^T & \text{QGQ}^T + \text{QGH}^{-1}\text{GQ}^T - (\text{M} + \text{M}_a) & \text{QGQ}^T + \text{K} & \\ \text{QGH}^{-1}\text{GQ}^T & \text{QGQ}^T + \text{K} & \text{M} + \text{M}_a + \text{K} & \end{array} & \begin{array}{c} \bar{\mathbf{r}} \\ \bar{\mathbf{r}} \\ \bar{\mathbf{r}} \end{array} \end{array} \right) \begin{array}{c} \bar{\mathbf{r}} \\ \bar{\mathbf{r}} \\ \bar{\mathbf{r}} \end{array} \\ & = \begin{array}{c} \bar{\mathbf{0}} \\ \bar{\mathbf{0}} \\ \bar{\mathbf{0}} \end{array} \end{aligned} \quad (31)$$

$$\begin{aligned} & \left(\begin{array}{ccc|c} \text{SMS}^T - \text{SMK}^{-1}\text{MS}^T & \text{G} + \text{G}_a - \text{SMK}^{-1}\text{MS}^T & -\text{H} & \\ \text{G} + \text{G}_a - \text{SMK}^{-1}\text{MS}^T & \text{G} + \text{G}_a - \text{SMS}^T - \text{H} & -\text{H} & \\ -\text{H} & -\text{H} & -\text{H} & \\ \hline -\omega^2 \begin{array}{ccc|c} \text{SMK}^{-1}\text{MS}^T & \text{SMK}^{-1}\text{MS}^T & \text{SMK}^{-1}\text{MS}^T & \\ \text{SMK}^{-1}\text{MS}^T & \text{SMS}^T + \text{SMK}^{-1}\text{MS}^T - (\text{G} + \text{G}_a) & \text{SMS}^T + \text{H} & \\ \text{SMK}^{-1}\text{MS}^T & \text{SMS}^T + \text{H} & \text{G} + \text{G}_a + \text{H} & \end{array} & \begin{array}{c} \bar{\mathbf{p}} \\ \bar{\mathbf{p}} \\ \bar{\mathbf{p}} \end{array} \end{array} \right) \begin{array}{c} \bar{\mathbf{p}} \\ \bar{\mathbf{p}} \\ \bar{\mathbf{p}} \end{array} \\ & = \begin{array}{c} \bar{\mathbf{0}} \\ \bar{\mathbf{0}} \\ \bar{\mathbf{0}} \end{array} \end{aligned} \quad (32)$$

where $\bar{\mathbf{p}}$, $\bar{\mathbf{p}}$, $\bar{\mathbf{r}}$ and $\bar{\mathbf{r}}$: contain fictitious entries. It is worthwhile to remark that the dimensions of these problems are equal to three times the unknown nodal pressures and displacements, correspondingly. Obviously, the coefficient matrices are symmetric. As a consequence, these linear Eigenproblems can be easily solved by employing common linear symmetric Eigenvalue solution routines.

5. Generalized Subspace Method

Various algorithms have been proposed for estimating the mode shapes and natural frequencies of the linear symmetric Eigenproblems. One of the famous schemes extensively applied is entitled subspace iteration technique developed by Bathe (1996). This method is very popular in the finite element analysis of huge structures (Rezaiee-Pajand et al., 2019). With the help of this procedure, any arbitrary number of

structural Eigenvalues and eigen vectors can be approximately calculated. Herein, this well-known approach is generalized for solving the cubic ideal-coupled problems.

In each iteration of the generalized approach, a set of vectors is achieved. It should be added that the number of these vectors is less than the size of the initial cubic problem, and the original problem is projected into the corresponding vector space. As a result, a smaller cubic Eigenvalue problem is established. Afterward, it is linearized in an analog manner to the previous subsection. Then, the common linear symmetric Eigenvalue solution routines are utilized for finding the eigen pairs of this smaller problem. Recall that; the obtained responses are the approximations of the Eigenvalues and eigen vectors of the initial cubic eigenproblem. Eventually, the Eigenvalues and eigen vectors of the projected Eigenproblem converge to the eigen pairs of the initial cubic one. It is worth emphasizing that the decoupled mode shapes are applied for establishing the starting set of vectors, which forms the basis of the vector space in the first iteration.

In Figures 1 and 2, the steps of this algorithm are proposed for Eigenproblems (16) and (21), respectively. In these flowcharts, $MaxIter$ and ε : are the maximum allowable iteration and error, correspondingly.

6. Numerical Examples

In this study, the finite element method was employed as the initial approach to conduct the analysis. To accomplish this task, a computer program was created by implementing the theories elucidated in the preceding sections. As previously mentioned, solid finite elements were employed to model the dam. Furthermore, the near-field and far-field fluid domains were discretized using fluid finite elements and hyper-elements, respectively. The computer program provides various options for dynamic modal analysis of gravity

dams, including the true coupled, decoupled, ideal-coupled, and new cubic ideal-coupled techniques. To solve the Eigenvalue problems with these approaches, different Eigen-solvers are employed. In what follows, the Eigenvalue solution routine of each scheme is introduced.

The linear symmetric subspace iteration tactic (Bathe, 1996), which is denoted by SS in the coming sections, is deployed for solving the decoupled and ideal-coupled Eigenproblems. Recall that; the true coupled problem is not symmetric. Hence, its Eigenproblem is solved by the pseudo-symmetric subspace iteration strategy abbreviated by PS (Arjmandi and Lotfi, 2011). Moreover, two methods are utilized for the cubic Eigenvalue problems. The first one uses linearization and symmetric subspace iteration strategy (LS), and the second one takes advantage of the suggested Generalized Subspace iteration algorithm (GS).

In the subsequent sections, to prove the high accuracy of the proposed new method, it is utilized for conducting dynamic analysis of the ideal triangle and Pine Flat gravity dams in the frequency domain. In these examples, the dynamic responses of the dam crests are calculated in response to both upstream and vertical excitations. This analysis takes into account two different values of wave reflection coefficients (α), specifically 1 and 0.5. It should be reminded that $\alpha = 1$ represents the full reflection and $\alpha = 0.5$ allows for the partial reflection of waves, which influences the reservoir-foundation boundaries (Bougacha and Tassoulas, 1991; Jafari and Lotfi, 2018). In each case, the amplitude of the complex-valued accelerations for the dam crest point is plotted versus the dimensionless frequency ω/ω_1^s . It should be added that ω and ω_1^s denote the excitation frequency and the first frequency of the dam on the rigid foundation with no water in the reservoir, respectively. The results obtained from the analysis are then compared with the exact solutions, which are derived using a direct

method that incorporates all the true coupled mode shapes. Additionally, the same comparison is conducted for the decoupled and ideal-coupled approaches.

Moreover, the accuracy and consumed time of the above-cited Eigen-solution routines in finding the eigen pairs are compared. For this purpose, the next efficiency and error indices are introduced.

$$TI_i = 100 \times \frac{T_{min}}{T_i} \quad (33)$$

$$EI_i = 100 \times \left(\frac{1}{nm} \sum_{j=1}^{nm} \frac{|f_{exact}^j - f_i^j|}{f_{exact}^j} \right) \quad (34)$$

where the consumed time of the fastest Eigen-solution routine and the i -th one are demonstrated by T_{min} and T_i , correspondingly. Furthermore, f_i^j and f_{exact}^j : are the j^{th} natural frequency of the i^{th} tactic and the true coupled one, respectively. Besides, nm : denotes the number of computed natural frequencies.

6.1. Ideal Triangle Gravity Dam

In this subsection, the mentioned methods are utilized for the dynamic analysis of a famous gravity dam named the ideal triangle gravity dam in the frequency domain. In what follows, the finite element model and basic parameters of this system are introduced, and the obtained results are presented.

6.1.1. Model

At this stage, the focus is on the finite element model of the ideal triangle dam situated on a rigid foundation. To represent this dam, a discretization technique is employed, utilizing 20 isoparametric 8-node plane-solid finite elements. As it was previously mentioned, the water domain includes near-field and far-field regions. The former one continues up to a specific length (L), which is measured at the dam crest point in the upstream direction. Herein, it is assumed that $L = 0.2H$. It should be added that H is the dam height or maximum water depth in the reservoir.

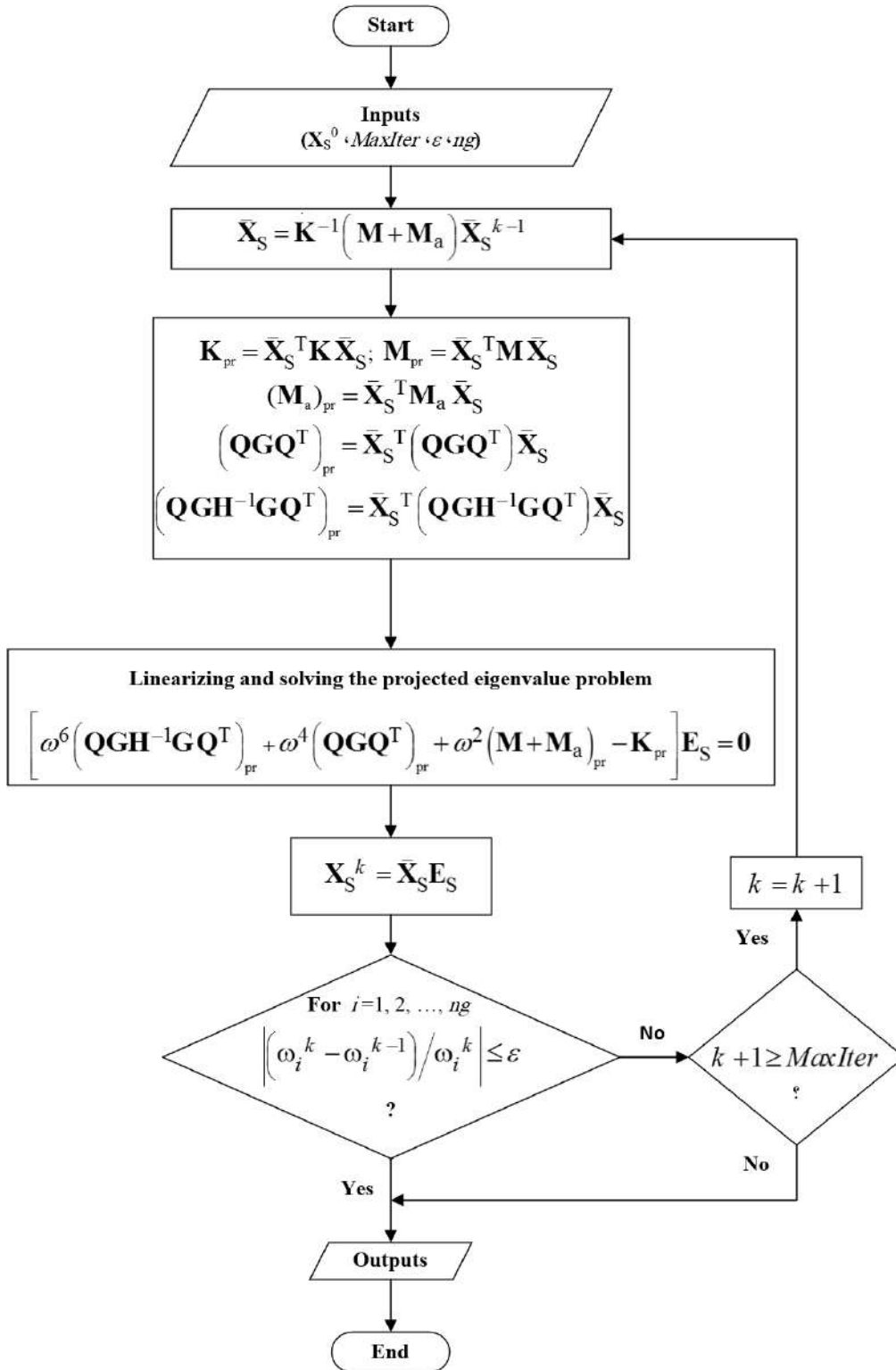


Fig. 1. Flowchart of generalized subspace method for Eigenproblem (16)

Following the near-field region, the far-field portion commences and stretches to infinity in the upstream direction. The near-field region is simulated using 5 isoparametric 8-node plane-fluid elements, while the far-field segment is modeled with a fluid hyper-element consisting of 5

isoparametric 3-node sub-elements. It is worthwhile to mention that the used mesh pattern has been previously applied by other researchers (Sotoudehnia et al., 2021; Ziaolhagh et al., 2016). Figure 3 depicts the finite element model of the ideal triangle dam and its reservoir.

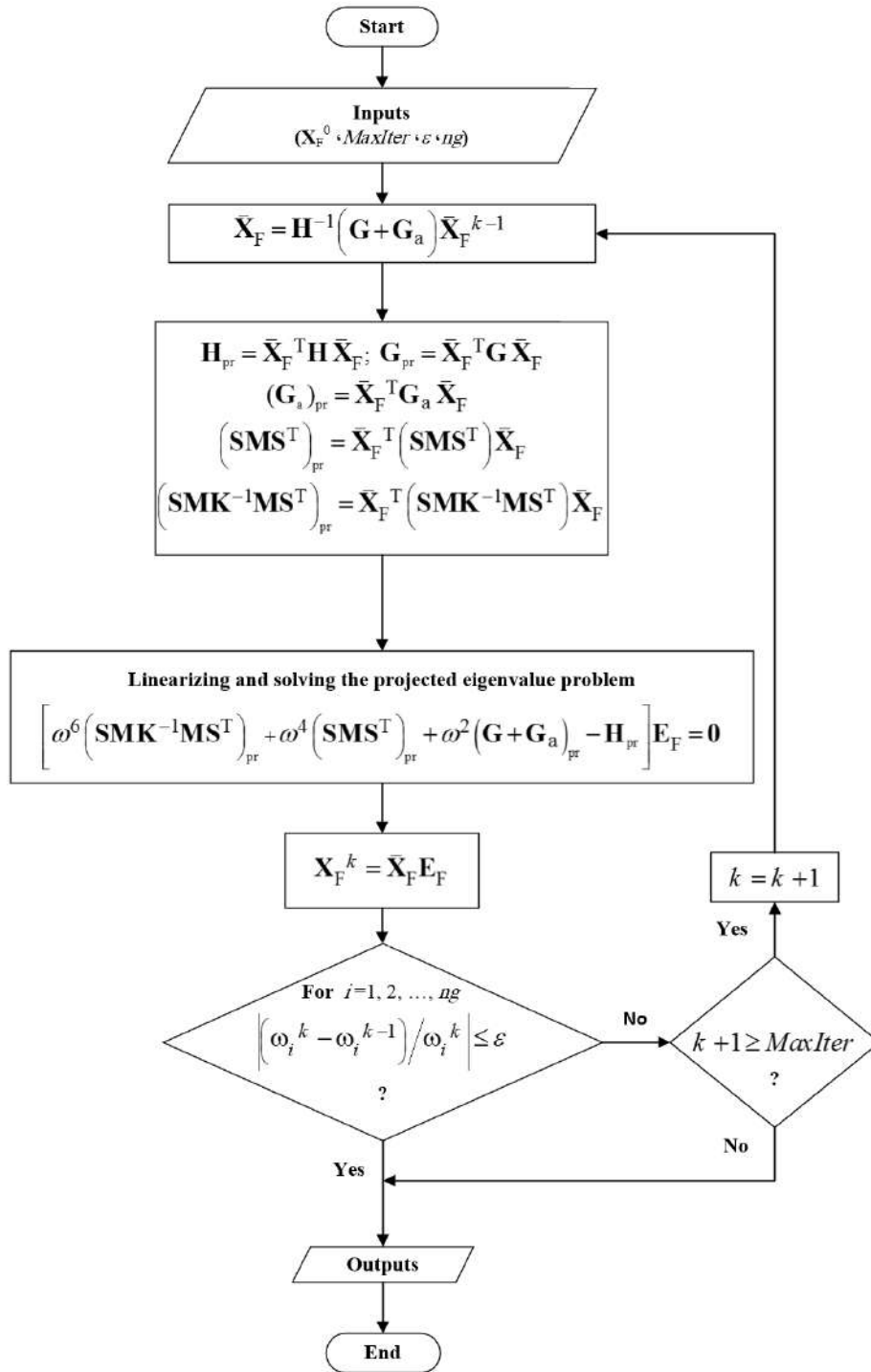


Fig. 2. Flowchart of generalized subspace method for Eigenproblem (21)

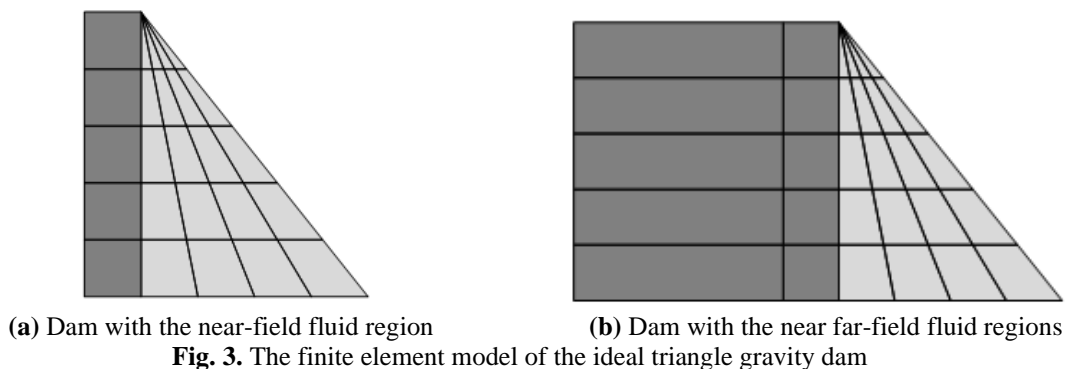


Fig. 3. The finite element model of the ideal triangle gravity dam

6.1.2. Basic Parameters

The concrete dam is presumed to be homogenous with isotropic linearly viscoelastic behavior. Its elastic modulus, unit weight, and Poisson's ratio are 27.5 Gpa, 24.8 kN/m³ and 0.2, respectively. Additionally, the hysteretic damping factor is 0.05. Furthermore, the impounded water is assumed to be irrotational, compressible, and inviscid, with a pressure wave velocity of 1440 m/s and a unit weight of 9.81 kN/m³.

6.1.3. Free Vibration Responses

It should be reminded that each aforementioned formulation includes two cases whose Eigenproblems are not similar. Consequently, each method has two sets of modes, except for the true coupled technique. It is worth emphasizing that the set of mode shapes associated with the nodal displacements can be computed by solving the first Eigenvalue problems, and the corresponding set of mode shapes related to the nodal pressures are calculated

by solving the second Eigenvalue problems. Accordingly, the frequencies of the first and second cases are listed in Tables 1 and 2, respectively.

The provided tables reveal that the natural frequencies of the true coupled problem generally appear to be lower than the two sets of natural frequencies computed in each instance of the decoupled, ideal-coupled, and cubic ideal-coupled approaches. For comparison, Figure 4 illustrates the error indices of the decoupled, ideal-coupled, cubic ideal-coupled, and true coupled approaches.

With the help of this figure, the accuracy of the aforesaid tactics can be compared. It is obvious that the natural frequencies of the cubic ideal-coupled approach are more accurate compared to the decoupled and ideal-coupled methods. In other words, the most accurate tactic is the authors' technique, and the error-index of the decoupled method is higher than those of others.

Table 1. The first five natural frequencies for the ideal triangle dam-reservoir system with $L = 0.2H$

| Mode number | Natural frequencies f_i (Hz) | | | |
|-------------|--|--|--|--------------|
| | Decoupled dam (Ziaolhagh et al., 2016) | Ideal-coupled First ideal case (Incompressible fluid assumption) | Cubic ideal-coupled First cubic ideal case | True coupled |
| 1 | 2.29 | 1.49 | 1.28 | 1.25 |
| 2 | 5.19 | 4.08 | 3.44 | 2.54 |
| 3 | 6.04 | 5.94 | 5.90 | 4.96 |
| 4 | 8.93 | 7.84 | 6.68 | 5.65 |
| 5 | 13.17 | 11.29 | 9.96 | 6.13 |

Table 2. The second five natural frequencies for the ideal triangle dam-reservoir system with $L = 0.2H$

| Mode Number | Natural frequencies f_i (Hz) | | | |
|-------------|--|---|---|--------------|
| | Decoupled Reservoir (Ziaolhagh et al., 2016) | Ideal-coupled Second ideal case (Incompressible fluid assumption) | Cubic ideal-coupled Second cubic ideal case | True coupled |
| 1 | 1.80 | 1.35 | 1.26 | 1.25 |
| 2 | 5.40 | 3.61 | 2.92 | 2.54 |
| 3 | 9.03 | 7.09 | 5.89 | 4.96 |
| 4 | 12.76 | 10.45 | 9.59 | 5.65 |
| 5 | 16.66 | 12.68 | 10.05 | 6.13 |

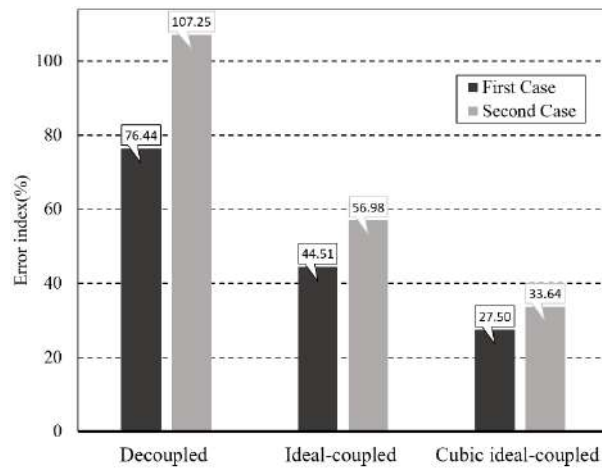


Fig. 4. Error index

In this example, the efficiency indices of the decoupled approach with SS, the ideal-coupled approach with SS, and the cubic ideal-coupled approach with GS and LS are equal to 100, 100, 100, and 4.49, respectively. For the truly coupled algorithm with PS, the efficiency index is 22.70. Clearly, the efficiency indices of the first three ones are the same, and the cubic ideal coupled with LS is the slowest one. Note that; the ratio of the efficiency index to the error-index is a key parameter for comparing the performance of numerical techniques. In other words, the performance of a numerical method is dependent on both its efficiency and accuracy. Accordingly, the cubic ideal-coupled technique with GS performs more successfully in comparison to the other schemes in this numerical example.

6.1.4. Forced Vibration Responses

At this stage, the magnitudes of the complex acceleration values for the dam crest point are plotted versus the dimensionless frequency ω/ω_1^s . To achieve this goal, the aforementioned strategies are used. It is important to note that the number of modes to perform the dynamic analysis in each case is the same. Recall that; other researchers previously presented the responses by using the true coupled tactic (Hojati and Lotfi, 2011; Samii and Lotfi, 2011). For $\alpha = 1$, the outcomes are illustrated in Figures 5 and 6 for the upstream and vertical excitations, respectively.

For all two types of excitations considered, it can be observed that the cubic ideal-coupled approach performance is mainly better than the decoupled and ideal-coupled strategies. Now, the results for $\alpha = 0.5$ are illustrated in Figures 7 and 8 for the upstream and vertical excitations, respectively.

Obviously, for these cases, the cubic ideal-coupled scheme's responses are also closer to the exact response (i.e., the direct method with the true coupled mode shapes) in comparison to the decoupled and ideal-coupled techniques' results.

6.2. Pine Flat Gravity Dam

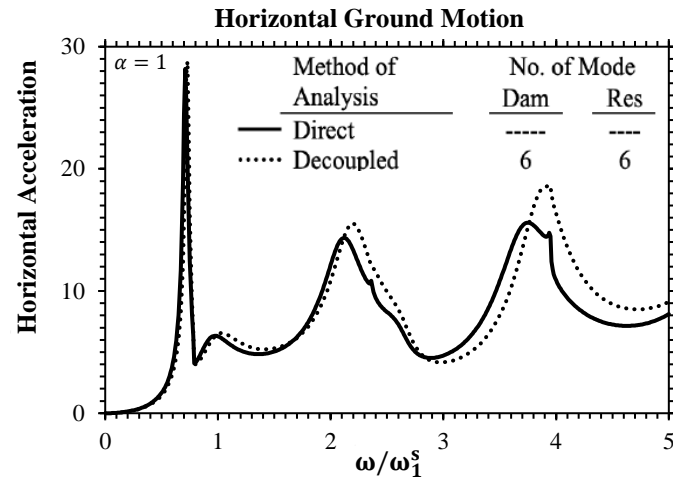
Herein, the mentioned strategies are applied for conducting a dynamic analysis of the Pine Flat gravity dam in the frequency domain. Subsequent sections will provide information about the finite element model, the essential parameters of this system, and the obtained results.

6.2.1. Model

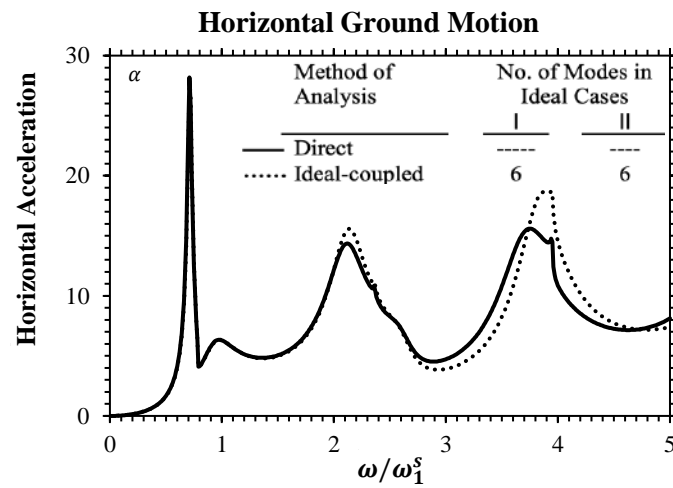
The finite element model of the Pine Flat dam on a rigid foundation has been examined. The dam is discretized using 40 isoparametric 8-node plane-solid finite elements. It is important to note that the water domain includes near-field and far-field regions. In this example, $L = 200$ m. The far-field portion initiates after the near-field region and extends infinitely in the upstream direction. For modeling the near-field region, 90 isoparametric 8-node plane-

fluid elements are utilized, while the far-field section is represented by a fluid hyper-element consisting of 9 isoparametric 3-node sub-elements. It is worth mentioning that the mesh pattern used here has been previously employed by other researchers

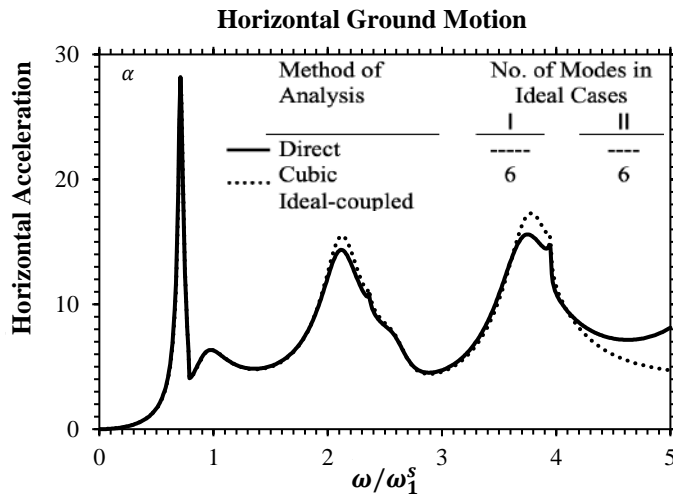
(Ganji and Lotfi, 2021; Omidi and Lotfi, 2017). Figures 9 and 10 provide a visualization of the finite element model of the Pine Flat dam and its corresponding reservoir.



(a) Decoupled method

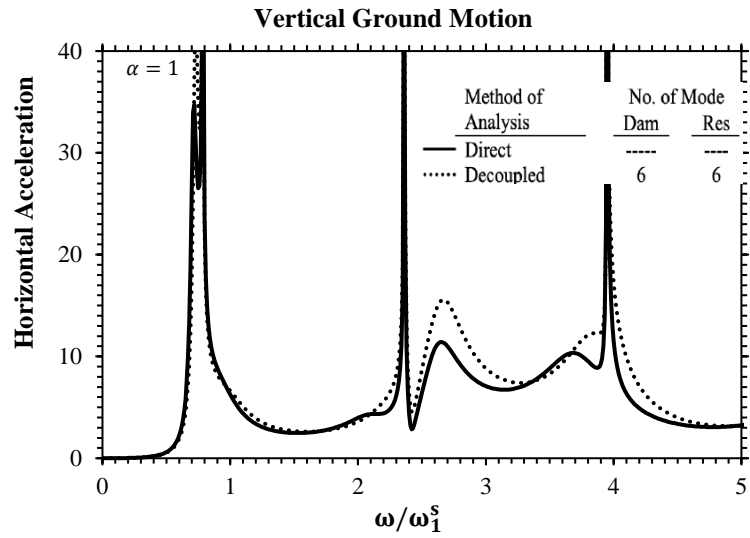


(b) Ideal-coupled method

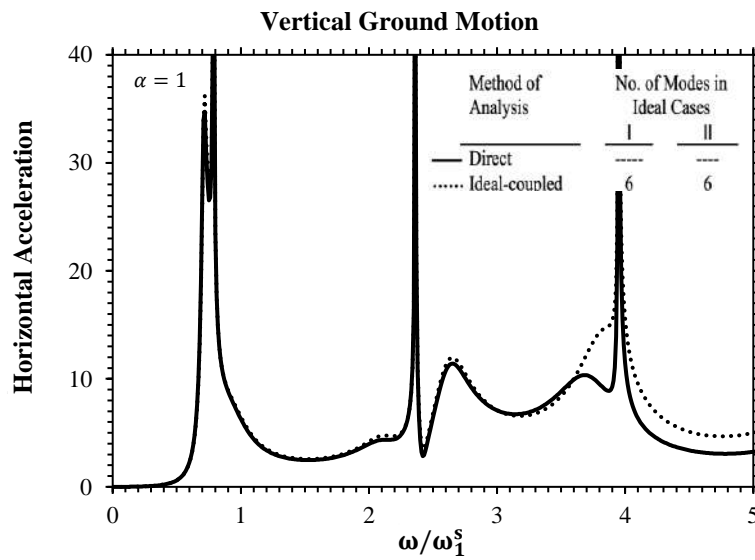


(c) Cubic ideal-coupled method

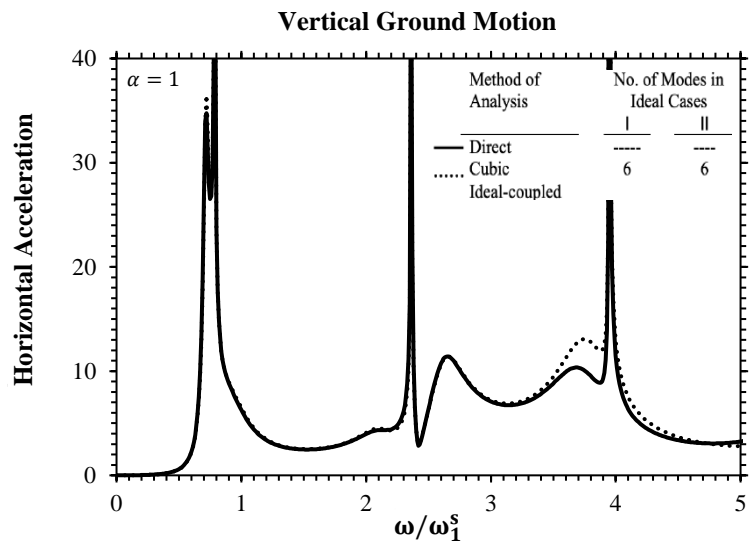
Fig. 5. Frequency response function at the dam crest resulting from horizontal excitation with $\alpha = 1$



(a) Decoupled method

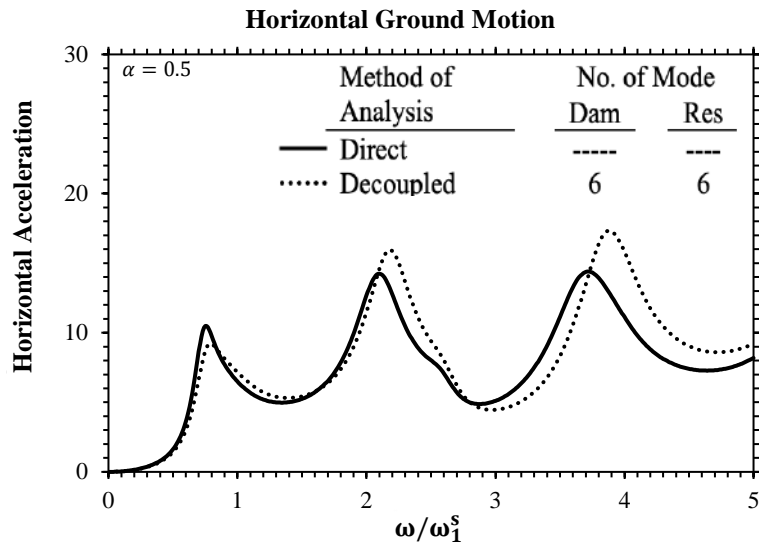


(b) Ideal-coupled method

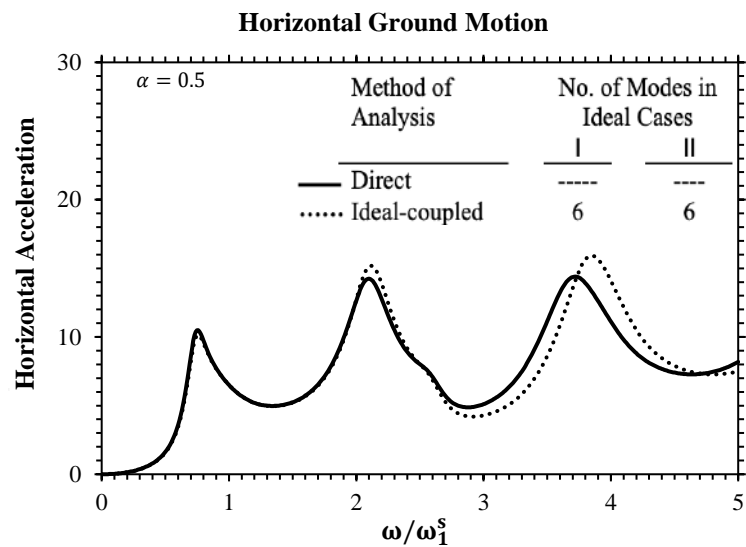


(c) Cubic ideal-coupled method

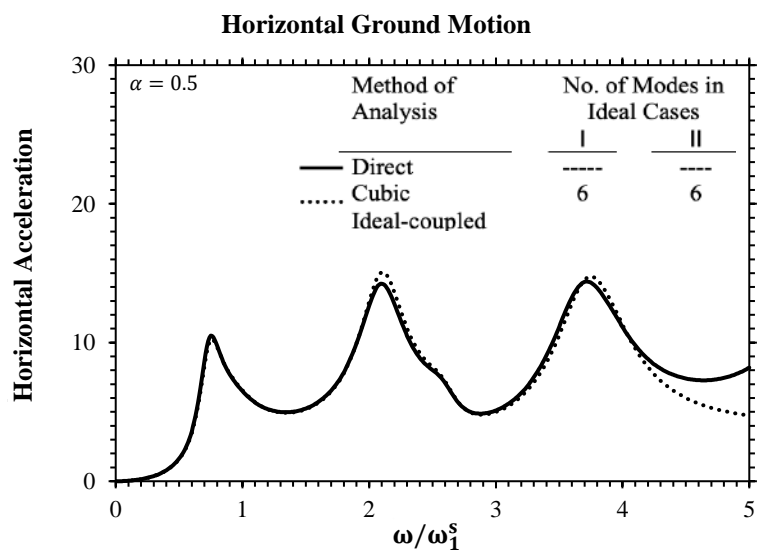
Fig. 6. Frequency response function at the dam crest resulting from vertical excitation with $\alpha = 1$



(a) Decoupled method



(b) Ideal-coupled method



(c) Cubic ideal-coupled method

Fig. 7. Frequency response function at the dam crest due to horizontal excitation with $\alpha = 0.5$

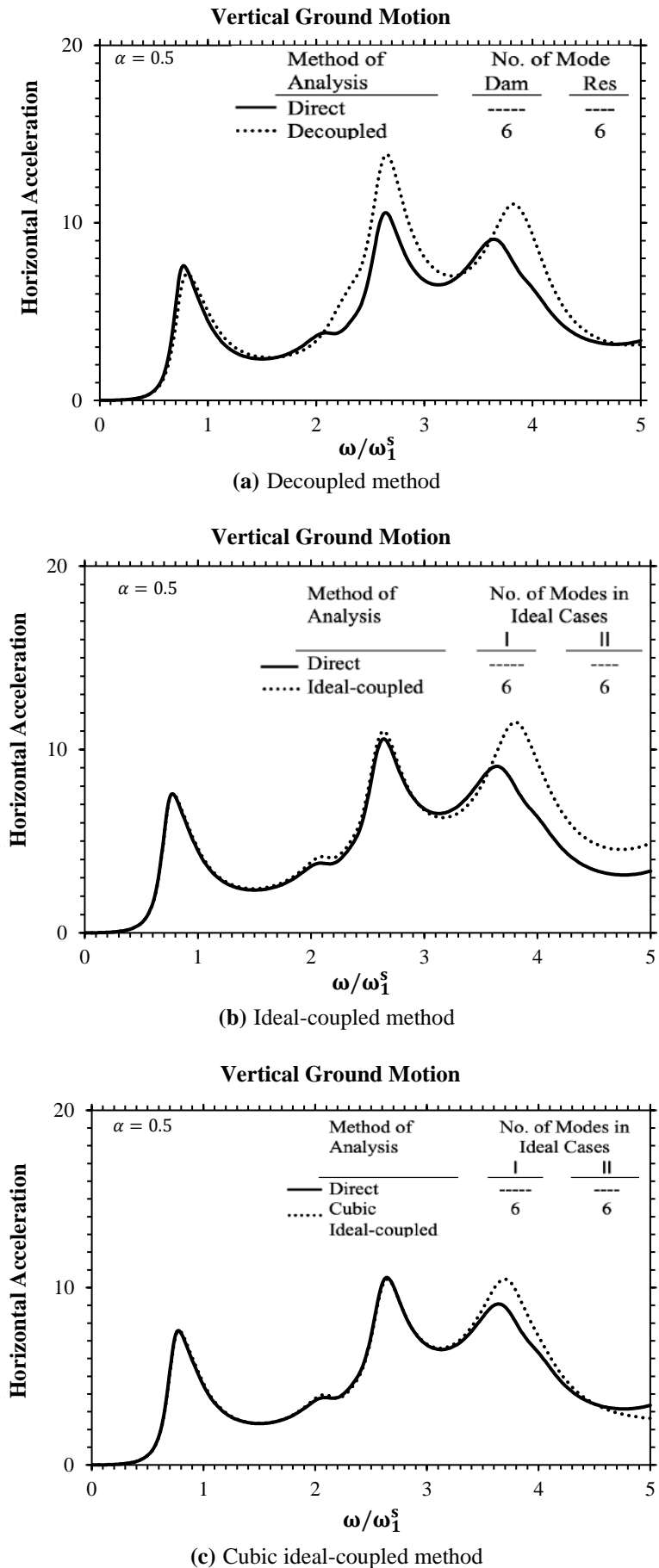


Fig. 8. Frequency response function at the dam crest resulting from vertical excitation with $\alpha = 0.5$

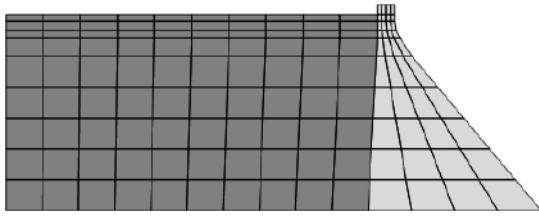


Fig. 9. Dam body with the near-field fluid region

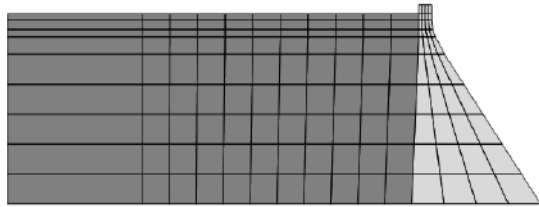


Fig. 10. Dam body with the near-field and far-field fluid regions

It is important to note that the Pine Flat dam features a sloped upstream face. To enhance accuracy, the hyper-elements need to be connected to the vertical sides of the finite elements. Consequently, within the finite element region, this slope should gradually decrease before establishing connections between the hyper-elements and the finite elements.

6.2.2. Basic Parameters

The dam body is constructed from homogeneous concrete with isotropic linearly viscoelastic behavior, possessing

an elasticity modulus of 22.75 Gpa, unit weight of 24.8 kN/m³, and a Poisson's ratio of 0.2. Moreover, a hysteretic damping factor of 0.05 is considered for the material. In addition, the impounded water is treated as irrotational, compressible, and inviscid, having a unit weight of 9.81 kN/m³ and a pressure wave velocity of 1440 m/s.

6.2.3. Free Vibration Responses

At first, the frequencies of the first and second Eigenproblems of this dam-reservoir system are proposed in Tables 3 and 4, respectively.

Clearly, the natural frequencies of the true coupled problem are generally lower than the corresponding sets of natural frequencies obtained using the decoupled, ideal-coupled, and cubic ideal-coupled approaches in each case. Furthermore, the natural frequencies of the cubic strategy are closer to those of the true coupled one in comparison to the other approaches.

At this stage, the first and second pressure mode shapes are demonstrated in Figures 11 and 12, respectively. Recall that; the true coupled mode shapes were previously proposed in other works (Samii and Lotfi, 2007).

Table 3. The first five natural frequencies for the Pine Flat dam-reservoir system with $L = 200$ m

| Mode number | Natural frequencies f_i (Hz) | | | |
|-------------|-----------------------------------|--|------------------------|--------------------------------------|
| | Decoupled (Samii and Lotfi, 2007) | Ideal-coupled | Cubic ideal-coupled | True coupled (Samii and Lotfi, 2007) |
| | Dam | First ideal case (Incompressible fluid assumption) | First cubic ideal case | |
| 1 | 3.15 | 2.67 | 2.58 | 2.53 |
| 2 | 6.48 | 5.77 | 4.95 | 3.27 |
| 3 | 8.74 | 8.66 | 8.45 | 4.67 |
| 4 | 11.25 | 10.35 | 9.27 | 6.22 |
| 5 | 16.99 | 15.98 | 13.51 | 7.92 |

Table 4. The second five natural frequencies for the Pine Flat dam-reservoir system with $L = 200$ m

| Mode number | Natural frequencies f_i (Hz) | | | |
|-------------|-----------------------------------|---|-------------------------|--------------------------------------|
| | Decoupled (Samii and Lotfi, 2007) | Ideal-coupled | Cubic ideal-coupled | True coupled (Samii and Lotfi, 2007) |
| | Reservoir | Second ideal case (Incompressible fluid assumption) | Second Cubic ideal case | |
| 1 | 3.12 | 2.94 | 2.68 | 2.53 |
| 2 | 4.75 | 4.24 | 3.52 | 3.27 |
| 3 | 7.80 | 6.05 | 5.01 | 4.67 |
| 4 | 9.30 | 7.92 | 7.28 | 6.22 |
| 5 | 9.96 | 9.46 | 8.89 | 7.92 |

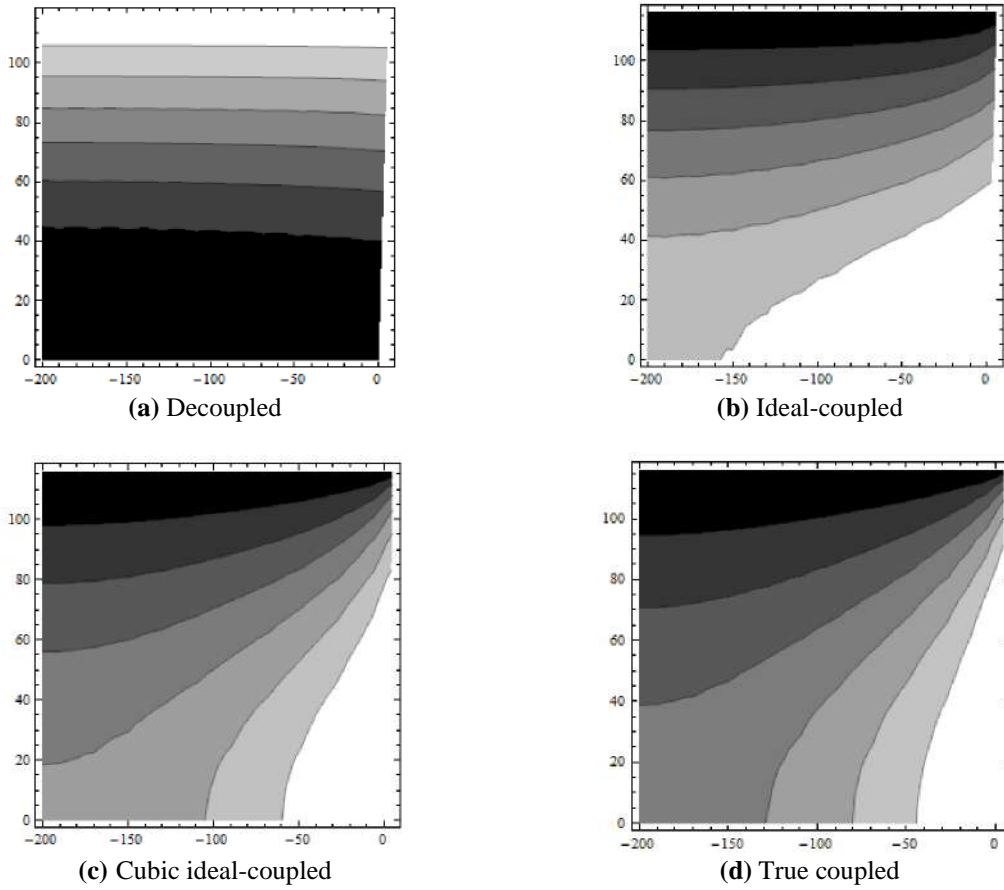


Fig. 11. First pressure mode shapes

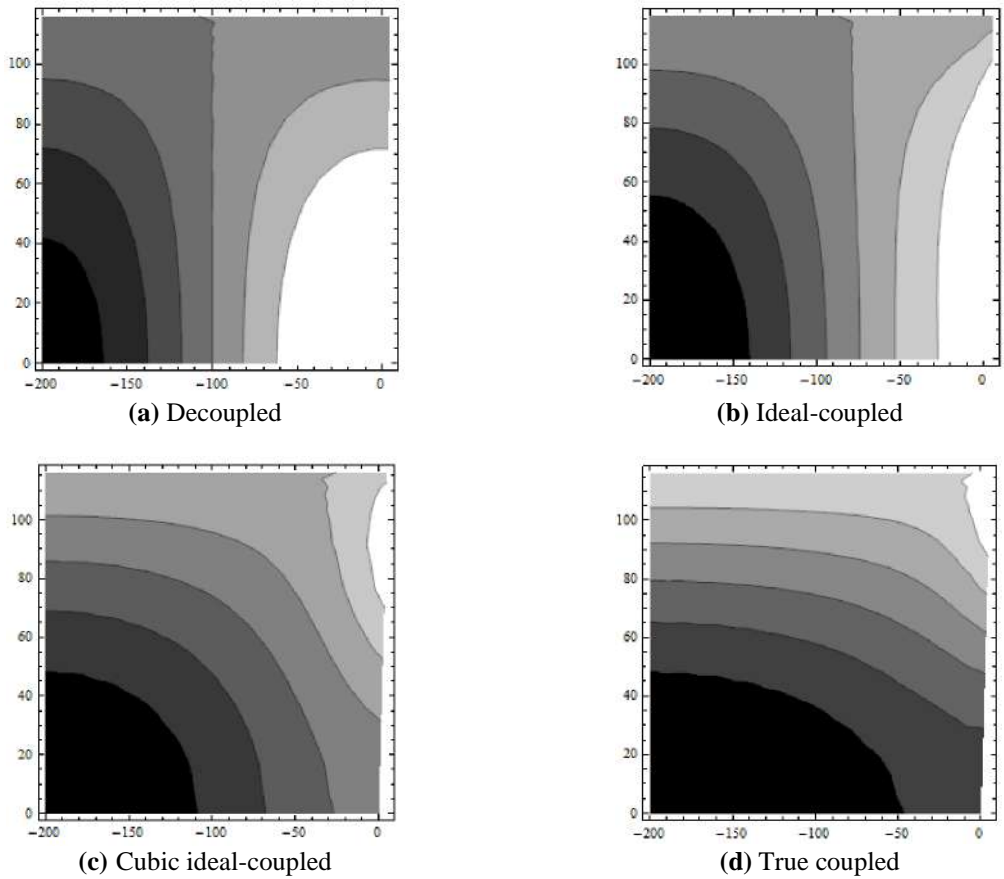


Fig. 12. Second pressure mode shapes

Obviously, the mode shapes of the cubic ideal-coupled are more similar to true coupled ones. For brevity, the dam mode shapes are not presented. However, the scheme of this paper is more successful in calculating these mode shapes than the other tactics.

For the aforesaid dam-reservoir system, Figures 13 and 14 show the error and efficiency indices of the decoupled, ideal-coupled, cubic ideal-coupled and true coupled strategies, correspondingly. With the help of these figures, the accuracy and analysis duration of the aforesaid schemes can be compared.

As it was previously mentioned, the ratio of the efficiency index to the error-index is a key parameter for comparing the performance of numerical techniques. Accordingly, the ideal-coupled scheme and

cubic ideal-coupled technique with GS perform more successfully in comparison to other algorithms. Obviously, the natural frequencies of the cubic ideal-coupled method are more closely aligned with the true coupled frequencies compared to the decoupled and ideal-coupled approaches. Consequently, if the same number of modes is employed, the cubic ideal-coupled approach is expected to offer improved accuracy in dynamic response compared to the decoupled and ideal-coupled techniques. Similarly, the decoupled and ideal-coupled tactics are faster than the other algorithms. The cubic ideal coupled with GS technique is ranked as second. Besides, the cubic ideal coupled with GS is much faster than the true coupled with PS, and the cubic ideal coupled with LS is the slowest one.

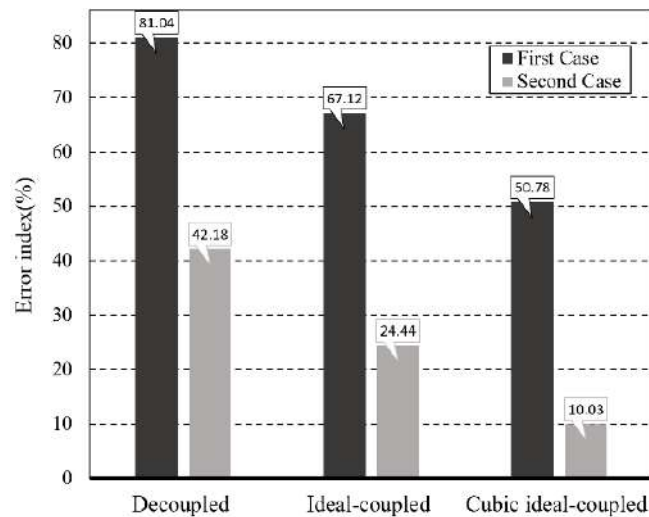


Fig. 13. Error index

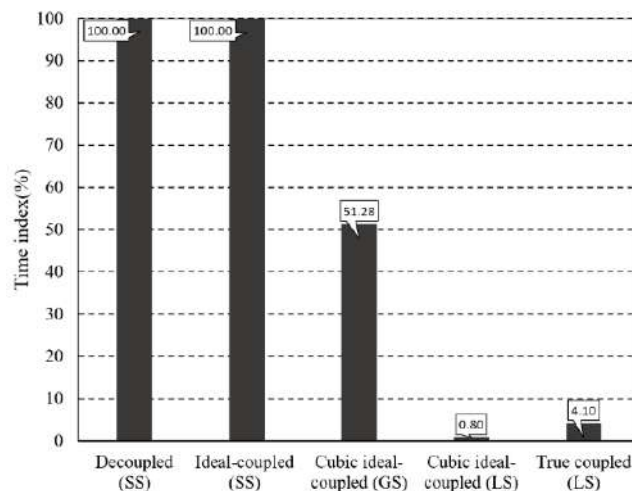
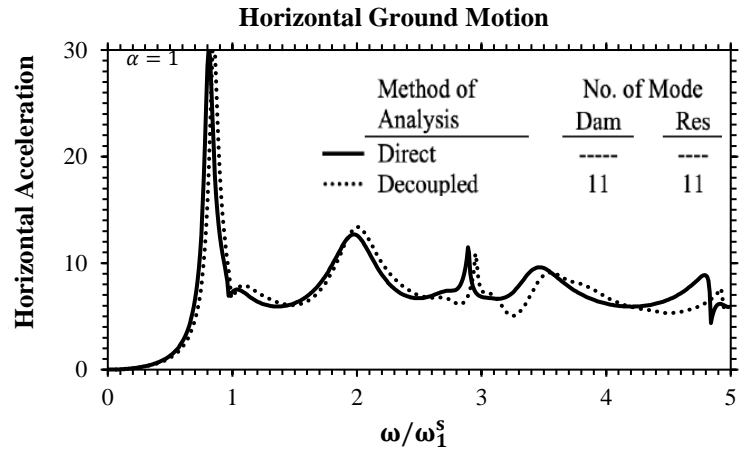


Fig. 14. Time index

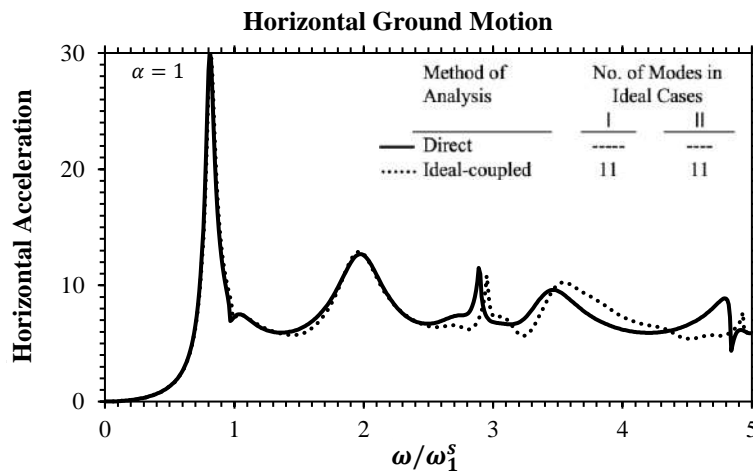
6.2.4. Forced Vibration Responses

In a similar manner to the previous example, the chart depicts the changes in the magnitudes of complex-valued accelerations at the crest of the dam in relation to the dimensionless frequency ω/ω_1^s . When considering $\alpha = 1$, the outcomes are illustrated in Figures 15 and

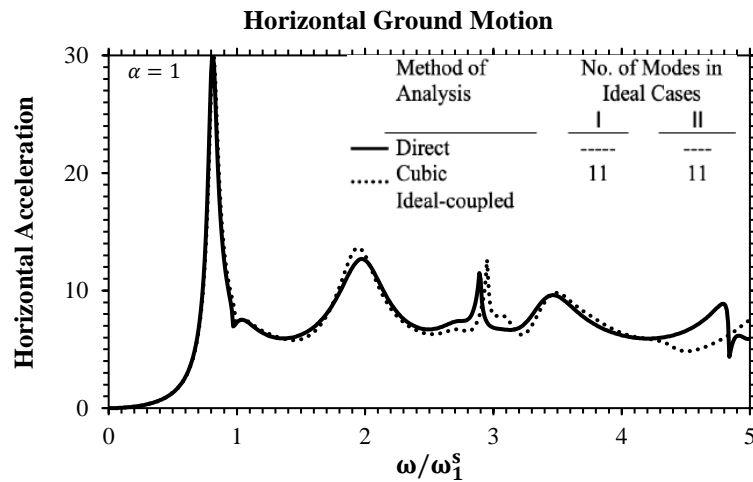
16 for the upstream and vertical excitations, respectively. Analogously, the aforesaid methods utilize the same number of modes to perform the dynamic analysis in each case. In previous research, true coupled responses were proposed (Chopra et al., 1980).



(a) Decoupled method

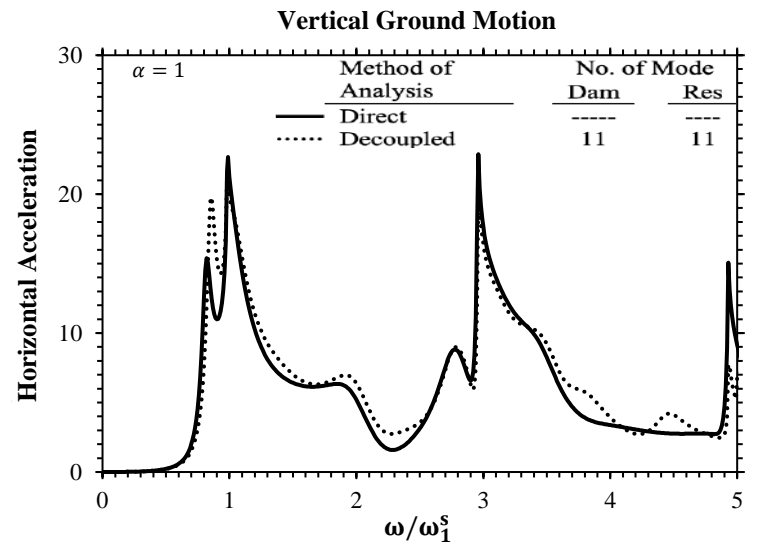


(b) Ideal-coupled method

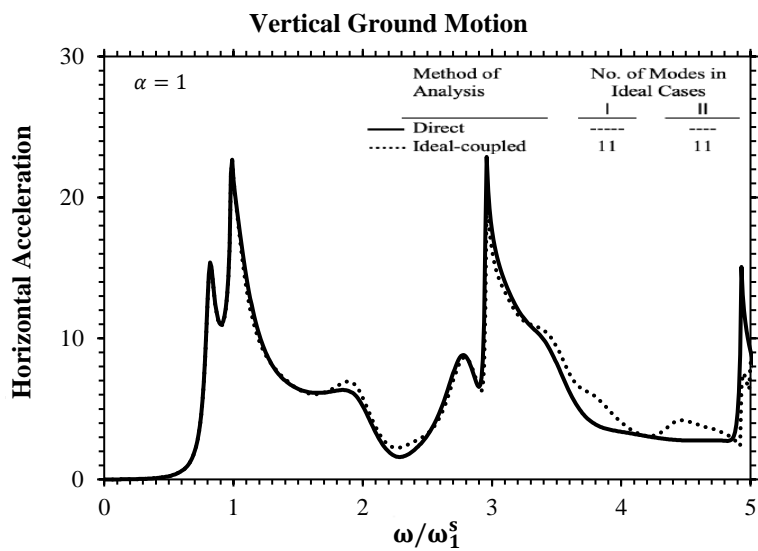


(c) Cubic ideal-coupled method

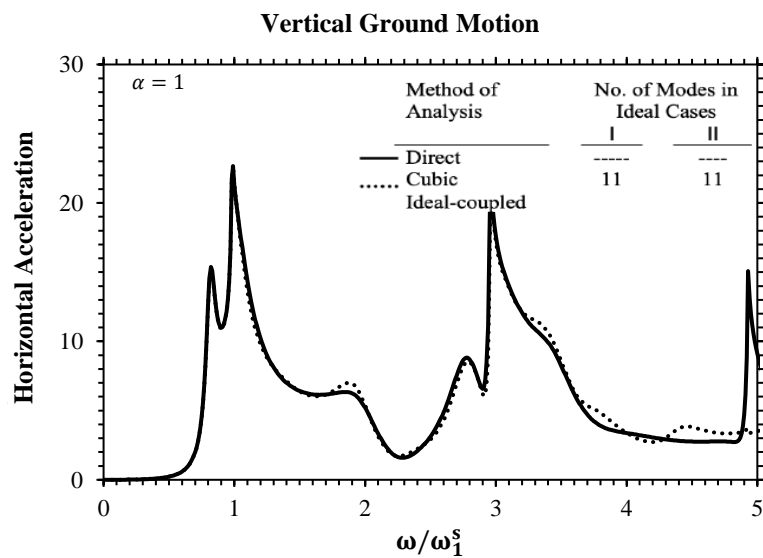
Fig. 15. Frequency response function at the dam crest resulting from horizontal excitation with $\alpha = 1$



(a) Decoupled method



(b) Ideal-coupled method



(c) Cubic ideal-coupled method

Fig. 16. Frequency response function at the dam crest resulting from vertical excitation with $\alpha = 1$

For all two types of excitations considered, the cubic ideal-coupled scheme performs more successfully than the decoupled and ideal-coupled approaches.

At this stage, the results for $\alpha = 0.5$ are depicted in Figures 17 and 18 for the upstream and vertical excitations, correspondingly.

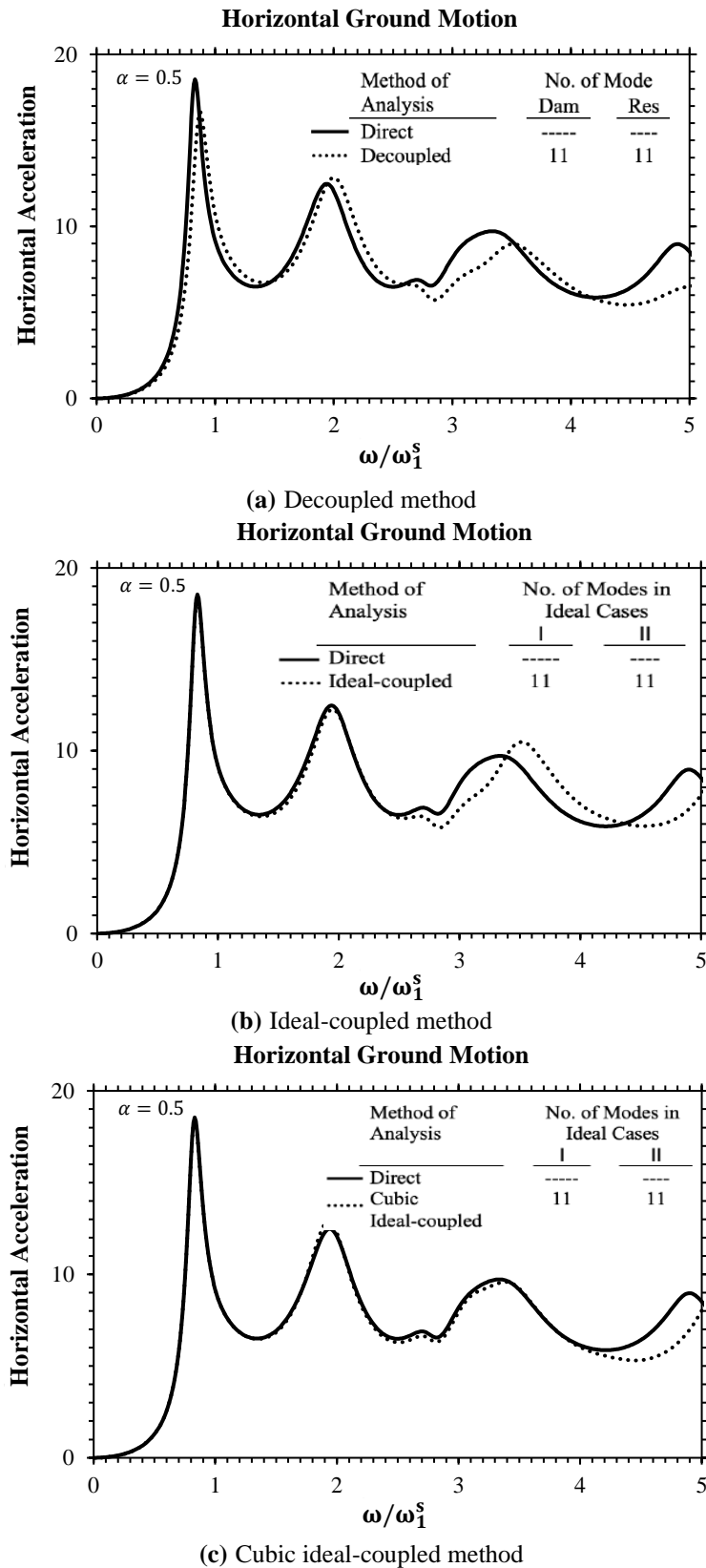
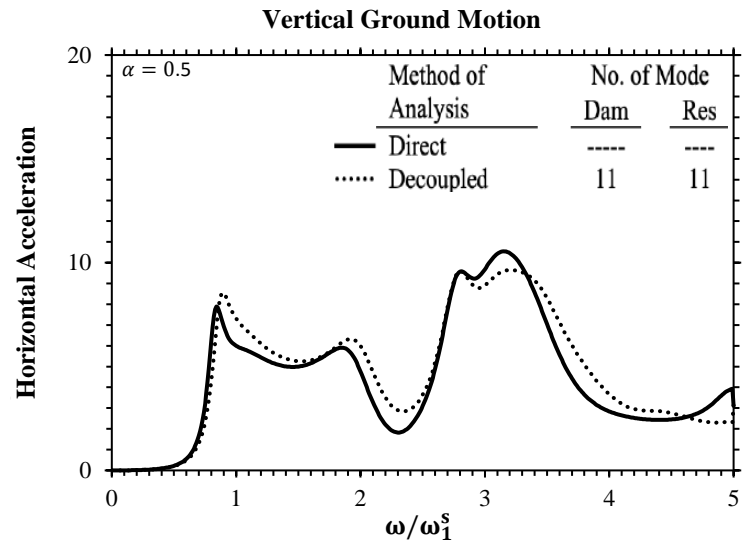
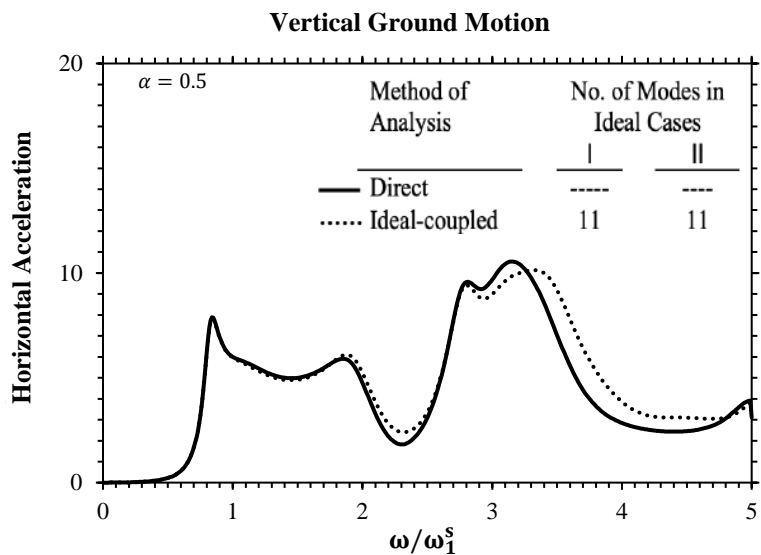


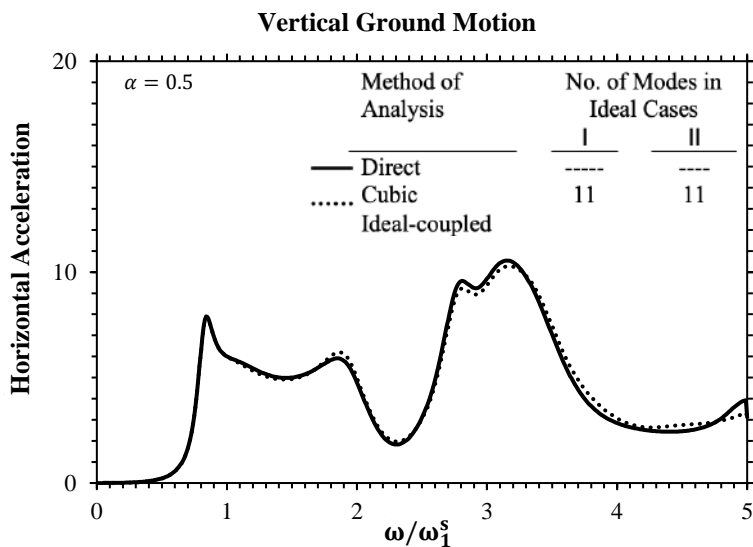
Fig. 17. Frequency response function at the dam crest resulting from horizontal excitation with $\alpha = 0.5$



(a) Decoupled method



(b) Ideal-coupled method



(c) Cubic ideal-coupled method

Fig. 18. Frequency response function at the dam crest resulting from vertical excitation with $\alpha = 0.5$

Obviously, for these cases, the responses obtained using the cubic ideal-coupled approach demonstrate a higher level of agreement with the exact responses obtained through the direct method when compared to the results obtained from the decoupled and ideal-coupled methods.

7. Discussion

One of the challenges which exists in the dynamic analysis of dam-reservoir systems is solving the corresponding non-symmetric Eigenproblem. Two well-known approaches, which are used for symmetrizing this problem, are decoupled and ideal-coupled methods. This paper has presented a novel method that is more accurate than both methods.

However, although it is faster than the true coupled approach, it is not as fast as the decoupled and ideal-coupled are. Hence, further research activities are suggested for developing more accurate and faster methods, in comparison to the decoupled and ideal-coupled tactics.

8. Summary and Conclusions

In this paper, a novel frequency-domain approach for performing modal analysis of concrete gravity dam-reservoir systems was presented. This method was developed based on two cubic Eigenvalue problems. To solve them, the well-known subspace algorithm was generalized. Moreover, their solution can be found with the combination of the classical subspace scheme with linearization. To achieve this goal, the linearized forms of the aforesaid Eigenproblems were proposed. This tactic was utilized for the dynamic analysis of two famous gravity dams, namely the ideal triangle dam and the Pine Flat Dam. It is worth noting that the far-boundary condition of the reservoir was considered by employing the hyper-elements. Furthermore, the dynamic responses of the dam crests were calculated in response to both upstream and vertical excitations,

considering two different values of wave reflection coefficients. The obtained results were compared with those of the decoupled and ideal-coupled strategies. By thoroughly investigating the findings, it is concluded that:

- The novel approach can find more accurately the forced and free vibration responses of the gravity dams in comparison to the decoupled and ideal-coupled approaches. This is because its eigen pairs are closer to those of the true coupled ones. In other words, this paper suggested a modal dynamic analysis strategy that is more accurate than the other aforementioned available ones.
- Moreover, it is observed that the cubic ideal-coupled scheme with the suggested Eigen-solver algorithm is faster than the true coupled one with the pseudo-symmetric method while it requires more time in comparison to the decoupled and ideal-coupled techniques, which are less accurate than authors' tactic.

9. References

- Afolabi, D. (1987). "Linearization of the quadratic Eigenvalue problem", *Computers and Structures*, 26(6), 1039-1040, [https://doi.org/10.1016/0045-7949\(87\)90120-9](https://doi.org/10.1016/0045-7949(87)90120-9).
- Aftabi Sani, A., and Lotfi, V. (2010). "Dynamic analysis of concrete arch dams by ideal-coupled modal approach", *Engineering Structures*, 32(5), 1377-1383, <https://doi.org/10.1016/j.engstruct.2010.01.016>.
- Ansari, M.D.I., and Agarwal, P. (2017). "Damage index evaluation of concrete gravity dam based on hysteresis behavior and stiffness degradation under cyclic loading", *International Journal of Structural Stability and Dynamics*, 17(01), 1750009, <https://doi.org/10.1142/S0219455417500092>.
- Arjmandi, S.A., and Lotfi, V. (2011). "Computing mode shapes of fluid-structure systems using subspace iteration methods", *Scientia Iranica A*, 18(6), 1159-1169, <https://doi.org/10.1016/j.scient.2011.09.011>.
- Bakhtiari-Nejad, F., Rahai, A. and Esfandiari, A. (2005). "A structural damage detection method using static noisy data", *Engineering Structures*, 27(12), 1784-1793, <https://doi.org/10.1016/j.engstruct.2005.04.019>.
- Bathe, K.J. (1996). *Finite Element procedure*, 2nd

- Edition, Prentice-Hall, INC.
- Bougacha, S. and Tassoulas, J.L. (1991). "Seismic response of concrete gravity dams, II: Effects of sediments", *Journal of Engineering Mechanics Division, ASCE*, 117(8), 1839-1850, [https://doi.org/10.1061/\(ASCE\)0733-9399\(1991\)117:8\(1839\)](https://doi.org/10.1061/(ASCE)0733-9399(1991)117:8(1839)).
- Casas, W.J.P. and Pavanello, R. (2017). "Optimization of fluid-structure systems by Eigenvalues gap separation with sensitivity analysis", *Applied Mathematical Modelling*, 42, 269-289, <https://doi.org/10.1016/j.apm.2016.10.031>.
- Chandravanshi, M.L. and Mukhopadhyay, A.K. (2017). "Modal analysis of a vertically tapered frame", *International Journal of Structural Stability and Dynamics*, 17(03), 1771001, <https://doi.org/10.1142/S0219455417710018>.
- Chen, H.Q., Li, D.-Y. and Guo, S.-S. (2014). "Damage-rupture process of concrete dams under strong earthquakes", *International Journal of Structural Stability and Dynamics*, 14(07), 1450021, <https://doi.org/10.1142/S0219455414500217>.
- Chopra, A.K., Chakrabarti, P. and Gupta, A.S. (1980). *Earthquake response of concrete gravity dams including hydrodynamic and foundation interaction effects*, University of California, California.
- Everstine, G.C. (1981). "A symmetric potential formulation for fluid structure interaction", *Journal of Sound and Vibration*, 79(1), 157-160, [https://doi.org/10.1016/0022-460X\(81\)90335-7](https://doi.org/10.1016/0022-460X(81)90335-7).
- Felippa, C.A. (1985). "Symmetrization of the contained compressible-fluid vibration Eigenproblem", *Communications in Applied Numerical Methods*, 1, 241-247, <https://doi.org/10.1002/cnm.1630010509>.
- Ganji, H.T., and Lotfi, V. (2021). "Transient analysis of concrete gravity dams by Wavenumber-TD method for general excitation", *Proceedings of the Institution of Civil Engineers-Structures and Buildings*, 174(4), 259-275, <https://doi.org/10.1680/jstbu.19.00041>.
- Gu, Q., Yu, C., Lin, P., Ling, X., Tang, L. and Huang, S. (2014). "Performance assessment of a concrete gravity dam at Shenwo reservoir of China using deterministic and probabilistic methods", *International Journal of Structural Stability and Dynamics*, 14(05), 1440002, <https://doi.org/10.1142/S0219455414400021>.
- Guo, S., Liang, H., Li, D., Chen, H. and Liao, J. (2019). "A comparative study of cantilever-and integral-type dead loads on the seismic responses of high arch dams", *International Journal of Structural Stability and Dynamics*, 19(03), 1950021, <https://doi.org/10.1142/S0219455419500214>.
- Hariri-Ardebili, M.A., and Mirzabozorg, H. (2013). "A comparative study of seismic stability of coupled arch dam-foundation-reservoir systems using infinite elements and viscous boundary models", *International Journal of Structural Stability and Dynamics*, 13(6), 1350032, <https://doi.org/10.1142/S0219455413500326>.
- Higham, N.J. and Kim, H.M. (2001). "Solving a quadratic matrix equation by Newton's method with exact line searches", *SIAM Journal on Matrix Analysis and Applications*, 23(2), 303-316, <https://doi.org/10.1137/S0895479899350976>.
- Hojati, M. and Lotfi, V. (2011). "Dynamic analysis of concrete gravity dams utilizing two-dimensional modified efficient fluid hyper-element", *Advances in Structural Engineering*, 14(6), 1093-1106, <https://doi.org/10.1260/1369-4332.14.6.1093>.
- Jafari, M. and Lotfi, V. (2018). "Dynamic analysis of concrete gravity dam-reservoir systems by a wavenumber approach for the general reservoir base condition", *Scientia Iranica*, 25(6), 3054-3065, <https://doi.org/10.24200/SCI.2017.4227>.
- Liang, H., Guo, S., Tu, J. and Li, D. (2019). "Seismic stability sensitivity and uncertainty analysis of a high arch dam-foundation system", *International Journal of Structural Stability and Dynamics*, 19(07), 1950066, <https://doi.org/10.1142/S0219455419500664>.
- Lokke, A. and Chopra, A.K. (2015). "Response spectrum analysis of concrete gravity dams including dam-water-foundation interaction", *Journal of Structural Engineering, ASCE*, 141(8), 1-9, [https://doi.org/10.1061/\(ASCE\)ST.1943-541X.0001172](https://doi.org/10.1061/(ASCE)ST.1943-541X.0001172).
- Long, J.H., Hu, X.Y. and Zhang, L. (2008). "Improved Newton's method with exact line searches to solve quadratic matrix equation", *Journal of Computational and Applied Mathematics*, 222, 645-654, <https://doi.org/10.1016/j.cam.2007.12.018>.
- Lotfi, V. (2005). "Significance of rigorous fluid-foundation interaction in dynamic analysis of concrete gravity dams", *Structural Engineering and Mechanics*, 21(2), 137-150.
- Lotfi, V. and Samii, A. (2012). "Frequency domain analysis of concrete gravity dam-reservoir systems by wavenumber approach", In: *The 15th World Conference on Earthquake Engineering*, Lisbon.
- Mackey, D.S., Mackey, N., Mehl, C. and Mehrmann, V. (2006). "Vector space of linearizations for matrix polynomials", *SIAM Journal on Matrix Analysis and Applications*, 28(4), 971-1004, <https://doi.org/10.1137/050628350>.
- Mandal, K.K., and Maity, D. (2016). "Transient response of concrete gravity dam considering dam-reservoir-foundation interaction", *Journal of Earthquake Engineering*, 22(2), 211-233,

- <https://doi.org/10.1080/13632469.2016.1217804>.
- Nariman, N.A., Lahmer, T. and Karampour, P. (2019). "Uncertainty quantification of stability and damage detection parameters of coupled hydrodynamic-ground motion in concrete gravity dams", *Frontiers of Structural and Civil Engineering*, 13(2), 303-323, <https://doi.org/10.1007/s11709-018-0462-x>.
- Olson, L.G. and Vandini, T. (1989). "Eigenproblems from finite element analysis of fluid-structure interactions", *Computers and Structures*, 33(3), 679-687, [https://doi.org/10.1016/0045-7949\(89\)90242-3](https://doi.org/10.1016/0045-7949(89)90242-3).
- Omidi, O. and Lotfi, V. (2017). "A symmetric implementation of pressure-based fluid-structure interaction for nonlinear dynamic analysis of arch dams", *Journal of Fluids and Structures*, 69, 34-55, <https://doi.org/10.1016/j.jfluidstructs.2016.12.003>.
- Rezaiee-Pajand, M., Aftabi Sani, A. and Kazemiyani, M.S. (2019). "An efficient Eigen-solver and some of its applications", *International Journal for Computational Methods in Engineering Science and Mechanics*, 20(2), 130-152, <https://doi.org/10.1080/15502287.2018.1534150>.
- Rezaiee-Pajand, M., Esfehiani, S. and Ehsanmanesh, H. (2022). "An explicit and highly accurate Runge-Kutta family", *Civil Engineering Infrastructures Journal*, 56(1), 51-78, <https://doi.org/10.22059/CEIJ.2022.330788.1792>.
- Rezaiee-Pajand, M., Kazemiyani, M.S., and Aftabi Sani, A. (2021). "A literature review on dynamic analysis of concrete gravity and arch dams", *Archives of Computational Methods in Engineering*, vol?? Issue?? 1-16, <https://doi.org/10.1007/s11831-021-09564-z>.
- Rezaiee-Pajand, M., Mirjalili, Z., and Kazemiyani, M.S. (2023). "Analytical 2D model for the liquid storage rectangular tank", *Engineering Structures*, 289, 116215, <https://doi.org/10.1016/j.engstruct.2023.116215>.
- Samii, A. and Lotfi, V. (2007). "Comparison of coupled and decoupled modal approaches in seismic analysis of concrete gravity dams in time domain", *Finite Elements in Analysis and Design*, 43, 1003-1012, <https://doi.org/10.1016/j.finel.2007.06.015>.
- Samii, A. and Lotfi, V. (2011). "High-order adjustable boundary condition for absorbing evanescent modes of waveguides and its application in coupled fluid-structure analysis", *Wave Motion*, 49(2), 238-257, <https://doi.org/10.1016/j.wavemoti.2011.10.001>.
- Sotoudeh, P., Ghaemian, M. and Mohammadnezhad, H. (2019). "Seismic analysis of reservoir-gravity dam-massed layered foundation system due to vertically propagating earthquake", *Soil Dynamics and Earthquake Engineering*, 116, 174-184, <https://doi.org/10.1016/j.soildyn.2018.09.041>.
- Sotoudehnia, E., Shahabian, F. and Sani, A.A. (2021). "A dynamic order reduction method for fluid-structure systems", *Applied Mathematical Modelling*, 89, 136-153, <https://doi.org/10.1016/j.apm.2020.06.071>.
- Tisseur, F. and Meerbergen, K. (2001). "The quadratic Eigenvalue problem", *SIAM Review*, 43(2), 235-286, <https://doi.org/10.1137/S0036144500381988>.
- Ziaolhagh, S.H., Goudarzi, M. and Aftabi Sani, A. (2016). "Free vibration analysis of gravity dam-reservoir system utilizing 21 node-33 Gauss points triangular elements", *Coupled Systems Mechanics*, 5(1), 59-86, <https://doi.org/10.12989/csm.2016.5.1.059>.



This article is an open-access article distributed under the terms and conditions of the Creative Commons Attribution (CC-BY) license.



Comparison of the Mechanical Performance of Concrete Reinforced with Recycled Steel Fibers from Waste Tires and Hooked-End Steel Fibers at Ambient and High Temperatures

Modarres, Y.¹  and Ghalehnovi, M.^{2*} 

¹ Ph.D. Candidate, Department of Civil Engineering, Ferdowsi University of Mashhad, Mashhad, Iran.

² Professor, Department of Civil Engineering, Ferdowsi University of Mashhad, Mashhad, Iran.

© University of Tehran 2023

Received: 11 Oct. 2022;

Revised: 15 Apr. 2023;

Accepted: 12 Jun. 2023

ABSTRACT: In this experimental study, a mechanical and economic analysis has been done to investigate the performance of recycled steel fibers (RSF) from waste tires. Two types of recycled fibers, including Recycled Steel Fibers with Impurities (with a high amount of rubber and textiles) (RSFI) and Clean Recycled Steel Fibers (CRSF), have been investigated. Recycled fiber's performance has been compared to Industrial Steel Fibers (ISF); these fibers have hook ends. The mechanical properties of normal concrete and concrete reinforced with steel fibers, including compressive strength, splitting tensile strength, and flexural strength, were investigated at ambient temperature and temperatures of 200 °C and 600 °C. The results showed that at ambient temperature and 200 °C, RSFI decreases the compressive strength of concrete due to the high amount of rubber and textiles, while CRSF has shown results comparable to ISF at all temperatures. The positive effect of RSFI has been observed at 600 °C by melting rubber and burning textiles. The specimens reinforced with steel fibers, regardless of their type, improved the tensile strength and modulus of rupture compared to the control specimen at all temperatures. RSFI has shown poorer performance compared to ISF and CRSF. The mechanical and economic analysis showed that CRSF could be a suitable alternative to ISF to strengthen concrete mixtures.

Keywords: Concrete, High Temperature, Industrial Steel Fibers, Recycled Steel Fibers, Waste Tires.

1. Introduction

Concrete is one of the common elements used in the construction industry. Every construction material has characteristics in which it has advantages or disadvantages (Mohajerani et al., 2019). For instance, the main feature of concrete is its high

compressive strength while having low tensile strength (Behfarnia and Behravan, 2014). Concrete always has internal micro-cracks due to temperature and relative humidity changes, which leads to poor tensile strength and consequent brittle failure (Shannag, 2011). One of the most effective ways to strengthen the brittle

* Corresponding author E-mail: ghalehnovi@um.ac.ir

matrix and prevent cracking is to add natural or synthetic fibers to the concrete mix (Jamshaid and Mishra, 2016; Karimipour et al., 2021). Fibers can be selected based on their properties and added to construction materials to improve the properties of the base material (Mohajerani et al., 2019; Roesler et al., 2006). The use of Industrial Steel Fibers (ISF), which is very common today and requires high raw materials and energy, leads to the adverse environmental effects of CO₂ emissions during production (Frazão, 2019). Therefore, finding fibers with the same function as ISF is essential.

One of the most popular fibers today is recycled fibers from waste materials. Increasing the volume of waste with limited landfills is a known problem due to population growth (Mohajerani et al., 2019). By using waste materials and fiber recycling, the volume of waste can be significantly reduced, and the energy required for the combustion process of landfills can be saved (Mohajerani et al., 2019). Vehicle waste tires are dumped or disposed of worldwide, posing a severe environmental threat. Most waste tires are used as fuel by some industries, but this type of waste use has a dangerous effect due to the production of greenhouse gases (Frazão, 2019). In recent years, extensive studies have been conducted on using these waste tires in the construction sector (Liew and Akbar, 2020; Awolusi et al., 2021; Modarres and Ghalehnovi, 2022). Products extracted from tires include nylon fibers, nylon pellets, steel fibers, crumb rubber, and rubber powder (Bulei et al., 2018).

The results of studies have shown that Recycled Steel Fibers (RSF) can be slightly helpful for the compressive strength of concrete (Liew and Akbar, 2020; Awolusi et al., 2021). Still, if a large volume of fibers is used, excess water to overcome workability problems can decrease the compressive strength of concrete due to increased porosity (Liew and Akbar, 2020; Awolusi et al., 2021). Dehghanpour et al. (2018) also showed that for fibers with a

fixed length of 25 mm, increasing the fiber content from 0% to 2% increased the compressive strength of concrete. Increasing the content by more than 2% decreased the compressive strength. The amount of rubber bonded to the RSF, the surface morphology, and the fiber form significantly impact concrete's compressive strength (Rossli and Ibrahim, 2012). Some studies have shown that rubber attached to the surface of steel fibers impairs concrete's compressive and tensile strength (Rossli and Ibrahim, 2012; Barros et al., 2017). Rubber particles' hydrophobicity and weak bonding with the surrounding cement matrix negatively impact the concrete performance (Awolusi et al., 2021; Rossli and Ibrahim, 2012). The mixture's fiber content and the type and quality of the fibers used influence fiber-reinforced concrete's post-peak behavior (Awolusi et al., 2021). RSF provides the ability to bridge cracks and stop cracking to improve post-cracking behavior (Wang and Li, 2000). RSF can have comparable results to ISF in energy absorption capacity and residual strength after cracking due to bending load (Aiello et al., 2009). Bedewi (2009) investigated the effect of fiber length and volumetric content on the flexural strength of reinforced concrete with RSF. The results indicated that the maximum fiber length (60 mm) had the highest flexural strength for each desired volume of fibers. Tlemat et al. (2006) studied reinforced concrete's stress-strain properties, compressive strength, and flexural strength with industrial and recycled steel fibers. This study showed that increasing the fiber content reduced the measurement workability. No significant differences were observed for compressive strength, and the flexural behavior of the prisms was improved by increasing the fiber volume.

Engineering structures may be subject to severe loads such as impact, fire, explosion, and combined effects (Ramezani and Esfahani, 2018; Alsaif et al., 2018). The properties of concrete may be significantly affected by high temperatures, which

reduces its compressive strength and cracking and spalling (Hager, 2014). In addition, at high temperatures, the bond between the cement paste and the aggregates decreases. The silicate gel, which provides the main strength of the concrete, decomposes, ultimately reducing the concrete's bearing capacity (Bezerra et al., 2019; Handoo and Agarwal, 2002). Insulation boards, coated panels, or sprays are used today to limit spalling in fire or high temperatures (Bezerra et al., 2019). However, fibers are the most effective method to reduce this damage. Fiber improves high-temperature resistance, prevents spalling, limits dimensional variations, and keeps concrete cohesive (Bezerra et al., 2019). Various studies have examined the performance of fiber-reinforced concrete at high temperatures.

The effect of steel fibers on the residual mechanical properties of concrete after exposure to high temperatures and the effect of explosive spalling of concrete during a fire or at high temperatures has been a common topic in recent years. In addition, many types of research have been conducted to investigate the residual properties and behavior of explosive spalling (Wu and Zhou, 2020). When concrete is exposed to fire or high temperatures, steel fibers can reduce the water vapor pressure in the concrete pores and prevent them from growing and spreading by bridging the cracks (Wu and Zhou, 2020; Hossain et al., 2013). Numerous investigations have been conducted on the impact of ISF on the characteristics of concrete subjected to high temperatures (Wu and Zhou, 2020). However, the effect of RSF from waste tires has not been studied much. Yang et al. (2019) investigated ultra-high-performance concrete's mechanical properties and explosive spalling behavior, including different steel fibers. The specimens were heated in a furnace at room temperature up to 800 °C to test for explosive spalling. The results showed that RSF significantly reduced the temperature range and the

duration of explosive spalling.

Based on the literature, more research is necessary to determine how recycled fibers affect concrete's mechanical performance, particularly at high temperatures. Therefore, this study investigated the compressive strength, splitting tensile strength, and flexural performance of reinforced concrete with RSF from waste tires at ambient and high temperatures. This study also considers reinforced concrete with ISF (hooked-end steel fibers) for better comparison. In addition, an economic analysis has been done to select the appropriate mixture.

2. Experimental Program

2.1. Materials and Mix Designs

The recycled fibers used in this study were obtained from the Mashhad waste tire recycling factory. Steel fibers are obtained with the help of the shredding method. In such a way, the bead wire of rubber tires is stretched or cut by the machines, and then the tires without bead wire are directed to the shredder in several different stages. Finally, two types of recycled fibers can be obtained. As shown in Figure 1a, the first type is recycled steel fibers with impurity (RSFI), which are prepared in the early stages of separation. These fibers have a high amount of rubber attached to the surface and textiles. The second type is the fibers obtained in the final stages. They have higher purity and are Clean Recycled Steel Fibers (CRSF) with fewer rubber and textile particles (Figure 1b).

Figure 1 shows that these fibers have irregular shapes and different dimensions. For this reason, 200 fibers were randomly selected as representatives for geometric analysis for both types of fibers. Figure 2 shows the fiber types' length, diameter, and aspect ratio. The fiber's average of both end diameters was measured with a micrometer. Since the fibers have an irregular and distorted shape, the length of the fibers is also considered as the distance between their two outer ends.

The measured diameter was the same for both types of fibers. The average fiber diameter was 0.24 mm, with 0.1 mm and 0.46 mm as the lower and upper limits (Figure 2a). 30.87% of the fibers are in the diameter range of 0.19-0.22 mm. RSFI has longer lengths. As shown in Figure 2b, the average fiber length was 28.17 mm, with 3 mm and 67 mm as the lower and upper limits. According to the results, the aspect

ratio of these fibers varies in the range of 9.57-300, with an average value of 111.24 (Figure 2c). The average length of CRSF was 21.87 mm, with 2 mm and 47 mm as lower and upper limits (Figure 2d). The aspect ratio of these fibers also varies in the range of 9.66-372, with an average value of 102.66 (Figure 2e). The tensile strength of fibers is also 2488 MPa.

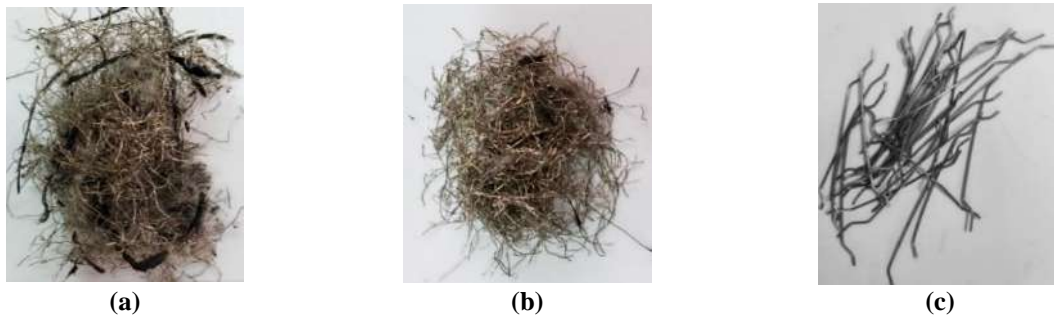
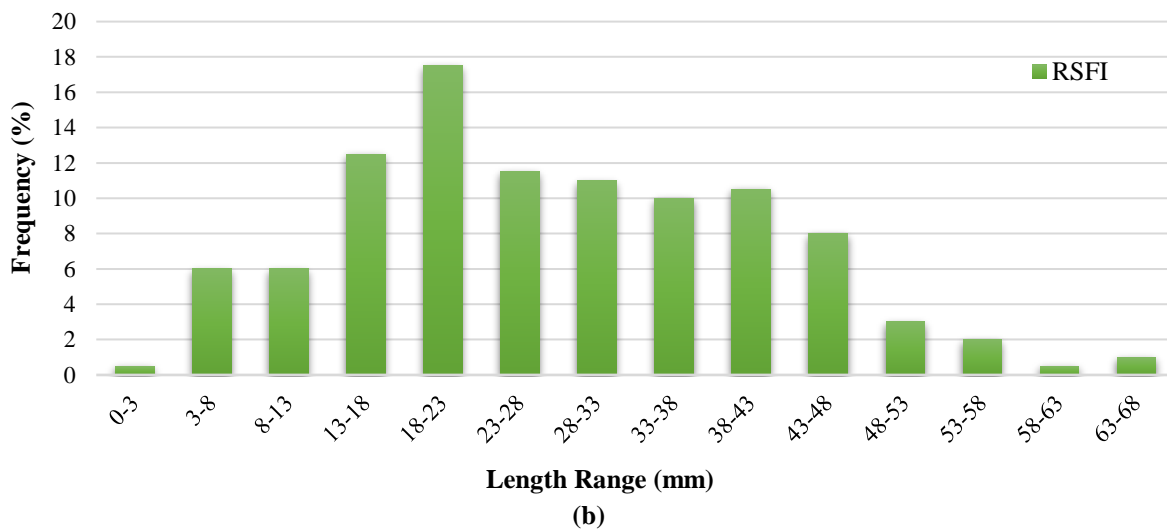
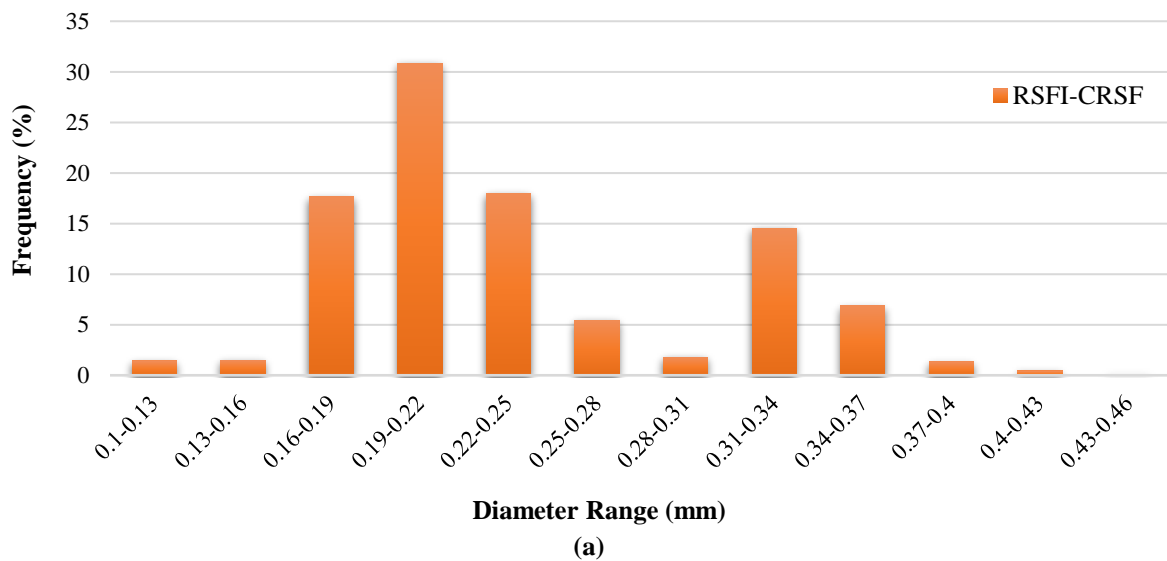
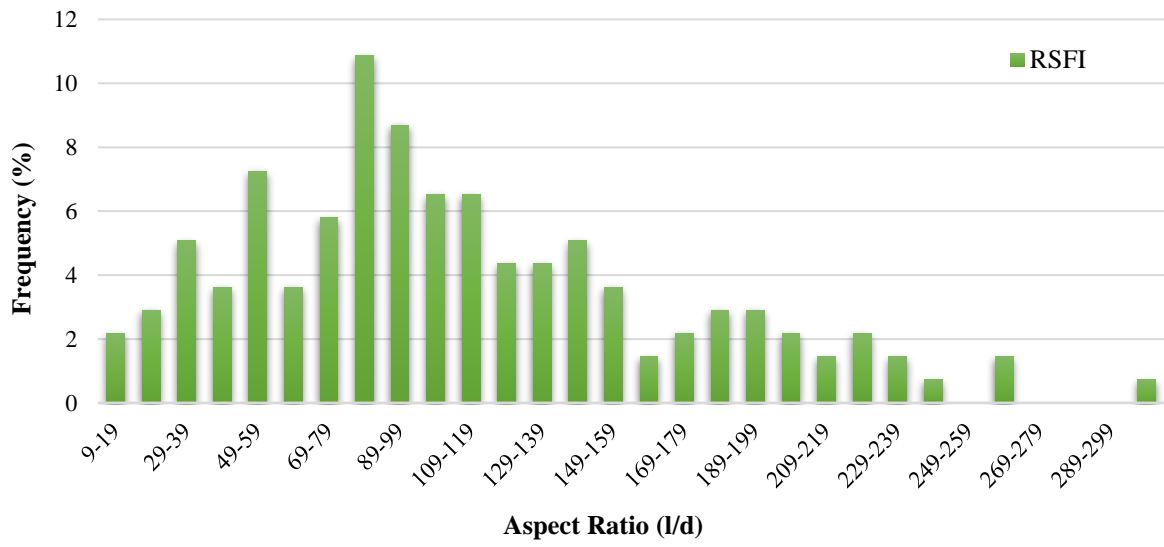
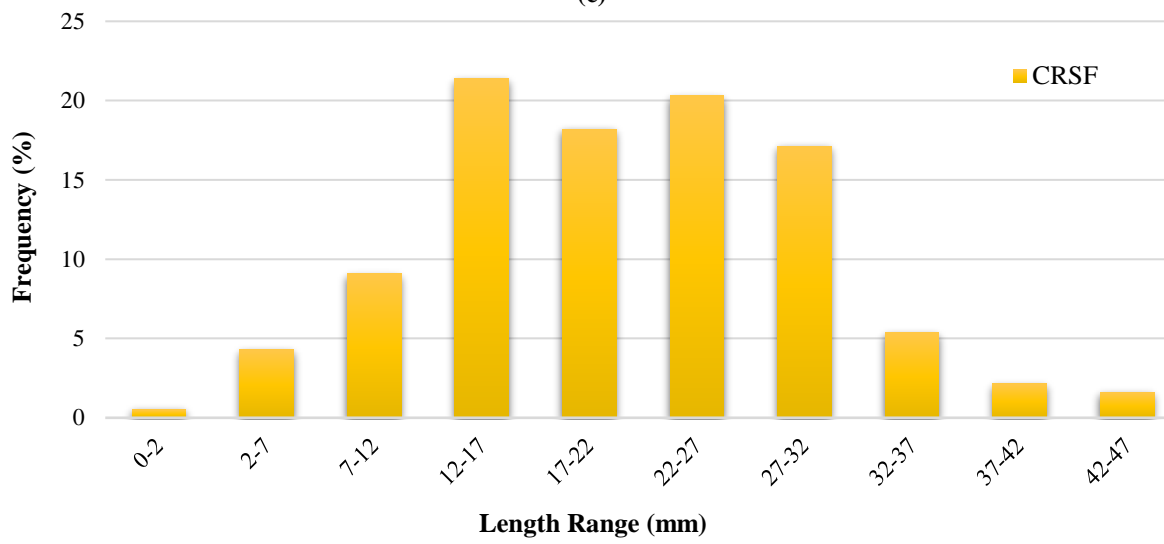


Fig. 1. Steel fibers used: a) RSFI; b) CRSF; and c) ISF

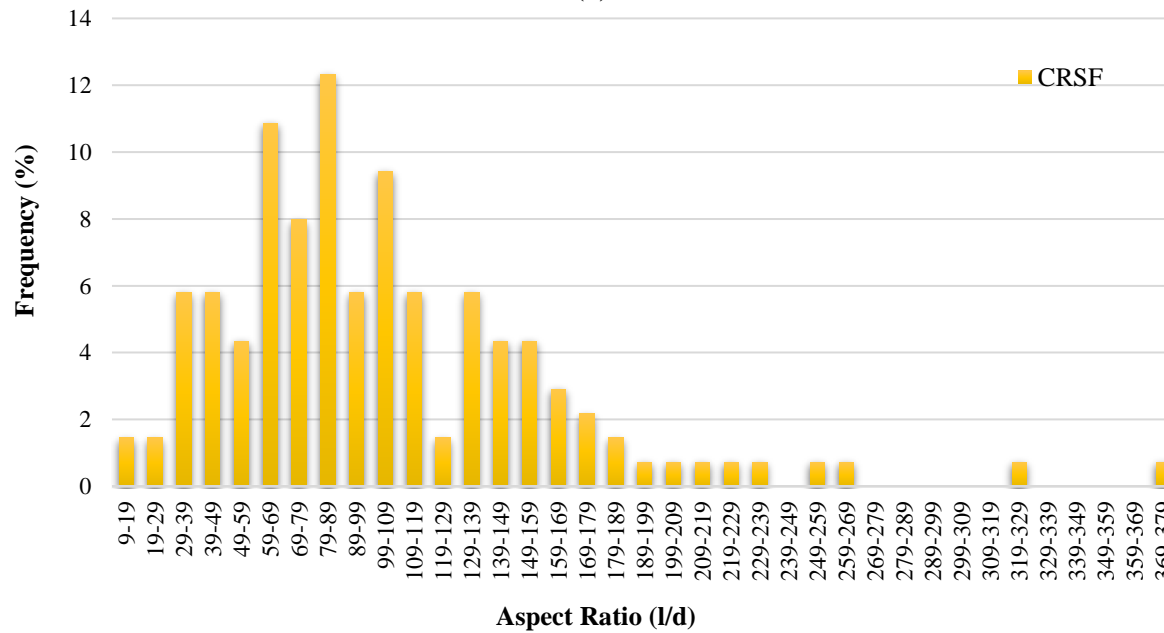




(c)



(d)



(e)

Fig. 2. Geometric analysis of recycled steel fibers: a) diameter of RSFI and CRSF; b) Length of RSFI; c) Aspect ratio of RSFI; d) Length of CRSF; and e) Aspect ratio of CRSF

In this study, ISF has also been used to better investigate the effect of recycled fibers. As shown in Figure 1c, these fibers have hooked ends. The supplied company provides the specifications of the industrial fibers. The average diameter of the fibers is 0.8 mm, the length of the fibers is 50 mm, and the aspect ratio is 62.5. The tensile strength of fibers is 1200 MPa.

The mixture ingredients used in this study are Portland cement type II, aggregates, water, and superplasticizer. Recycled and industrial fibers with a volume percentage of 0.5% were used to strengthen the mixtures. In the tests, Zaveh type II cement was used. The coarse aggregates used are broken and obtained from the stone materials suppliers in Mashhad's suburbs. The maximum nominal size of coarse aggregates used was 19 mm. The fine aggregates used were twice washed Sarakhs sand with minimum and maximum sizes of 0.2 and 4.75 mm. In order to maintain the workability of concrete, a superplasticizer based on modified polycarboxylates has been used according to the ASTM C494 standard (2015). The mix design used for this study based on ACI 211 (1996) is given in Table 1. Where NC stands for Normal Concrete, control specimen (without fibers); RSFI stands for Recycled Steel Fibers with Impurities (with rubber attached to the surface and textiles), CRSF stands for Clean Recycled Steel Fibers, and ISF stands for Industrial Steel Fibers. The numbers written in front of them indicate the volume of the fibers. For example, RSFI-0.5% represents the specimen reinforced with

0.5% recycled steel fibers with impurities.

2.2. Preparation of Specimens and Heat Treatment

First, the coarse aggregates, fine aggregates, and cement were added to the mixer and mixed for 1 min. After adding water and superplasticizer, the mixture was mixed for 3 to 5 min. The recycled fibers were separated by hand and gradually added to the mix to prevent the fibers from balling inside the mix and ensure their uniform and proper distribution in the concrete matrix. After adding all the fibers, the concrete was mixed for 5 min until it was completely homogeneous, and then the mixer was turned off. From each mixture, three cylinders with dimensions of 100 mm × 200 mm were prepared for the compression and tensile test, and three prisms with dimensions of 100 mm × 100 mm × 400 mm were prepared for the flexural test. After 24 hours, specimens were molded, then cured with water at room temperature for 28 days. The specimens were dried in an oven for 24 hours at 60 °C.

Before determining the mechanical behavior of concrete, the specimens were exposed to 200 °C and 600 °C inside an electric heating furnace (Figure 3). To obtain the desired temperature, a heating rate of 1-4 °C/min was applied for all specimens. Then, they were kept at a constant target temperature for 1 hour and a half to ensure uniform temperature distribution in the specimen volume. The specimens were heated, cooled in a furnace to room temperature, and tested the next day.

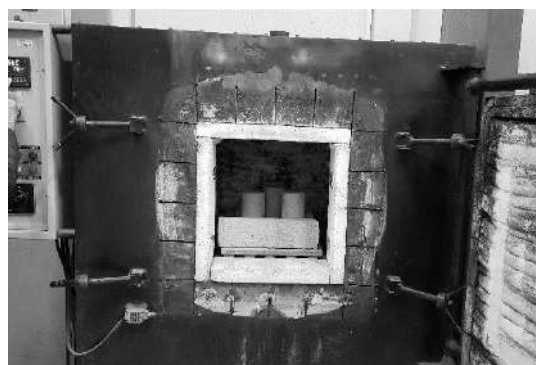


Fig. 3. Electric heating furnace

Table 1. The proportions of mix composition (kg/m³)

| Concrete type | W/C | Water | Cement | Sand 0 - 4 mm | Gravel 4 - 19 mm | Steel fiber (%) | Superplasticizer (%) |
|---------------|------|-------|--------|---------------|------------------|-----------------|----------------------|
| NC | 0.47 | 180 | 380 | 795 | 1002 | 0 | - |
| RSFI-0.5% | 0.47 | 180 | 380 | 795 | 1002 | 0.5 | 1.9 |
| ISF-0.5% | 0.47 | 180 | 380 | 795 | 1002 | 0.5 | 1.52 |
| CRSF-0.5% | 0.47 | 180 | 380 | 795 | 1002 | 0.5 | 1.9 |

2.3. Tests Methods

To investigate the compressive strength, according to the ASTM C39 standard (2018), a uniaxial compressive test was performed on cylindrical specimens with dimensions of 100 mm × 200 mm. A hydraulic compression machine with a capacity of 3000 kN with a constant loading rate of 0.3 MPa/s was used for compression tests. Three cylinders were tested for each mixture design to obtain mean values and standard deviation. The splitting tensile test was performed according to the ASTM C496 standard (2004) on cylindrical specimens with dimensions of 100 mm × 200 mm. A constant loading rate of 0.1 MPa/s was applied to all specimens in the test, and the maximum force was recorded. Figure 4a and b exhibit the setup for the compressive and tensile tests. The tensile strength is calculated based on the maximum applied force according to Eq. (1).

$$f_t = \frac{2P_t}{\pi L_c d_c} \quad (1)$$

where P_t : is the maximum tensile force, L_c : is the length of the cylinder (200 mm), and

d_c : is the diameter of the cylinder (100 mm).

Figure 4c represents the setup for the flexural tests. Four-point bending tests were performed on prisms with 100 mm × 100 mm × 400 mm dimensions. The bending load was recorded using a load cell with a capacity of 20 tons. The load was applied uniformly at a 0.2 mm/min rate to obtain the load-deflection curve. The distance between the two upper supports was 100 mm, and the two lower supports were 300 mm. Linear Variable Differential Transducers (LVDT) were installed on both sides of the specimen to measure the mid-span deflection. Three prisms were tested for each mixture design to obtain mean values and standard deviation. Ultimate flexural strength (f_p) or Modulus Of Rupture (MOR) is the flexural stress at peak load, which the following equation can calculate (ASTM C1609, 2012).

$$f_p = \frac{PL}{bd^2} \quad (2)$$

where P : is the peak load, L : is the clear span length (300 mm), b : is the width of the specimen (100 mm), and d : is the depth of the specimen (100 mm).

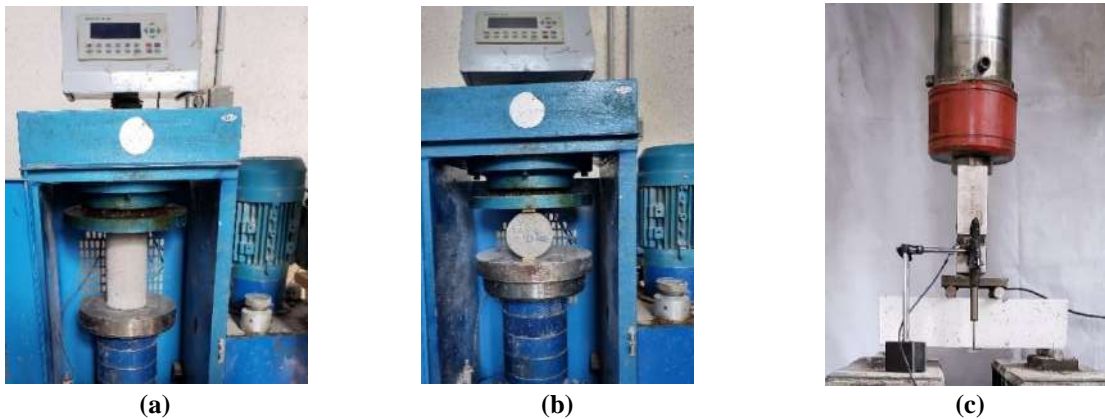


Fig. 4. Setup for: a) Compressive; b) Tensile; and c) Flexural test

According to ASTM C1018 (1997), the toughness indices I_5 , I_{10} , and I_{20} can be obtained based on the load-deflection curve as follows.

$$I_5 = \frac{A_{3\delta}}{A_\delta} \quad (3)$$

$$I_{10} = \frac{A_{5.5\delta}}{A_\delta} \quad (4)$$

$$I_{20} = \frac{A_{10.5\delta}}{A_\delta} \quad (5)$$

where δ : is the deflection of the first crack, A_δ , $A_{3\delta}$, $A_{5.5\delta}$, and $A_{10.5\delta}$: are the area under the load-deflection curve up to δ , 3δ , 5.5δ , and 10.5δ , respectively. Residual strength factors can be obtained from toughness indices (ASTM, 1997). These factors represent the resistance retained after the first crack with the help of the average post-crack load in a specific deflection interval. Residual strength factors $R_{5,10}$ and $R_{10,20}$ can be calculated from the value of $20(I_{10} - I_5)$ and $10(I_{20} - I_{10})$, respectively.

3. Discussion and Results

3.1. Appearance of Specimens and Cracking at High Temperatures

In order to investigate the influence of fibers on cracking and spalling behavior, the specimens were heated in an electric heating furnace at a rate of 4 °C/min to a temperature of 800 °C. Then the specimens' color, cracking, and spalling were checked at different temperatures. As shown in

Figure 5, the specimens were gray at the temperature of 200 °C, and no significant color change occurred. Cracking and spalling did not occur in the control and fiber-reinforced specimens. At the temperature of 400 °C, the color of the specimens was gray-brown. Micro-cracks were visible on the surface of the specimens. The specimens reinforced with ISF had less cracking than those reinforced with recycled fibers. At 600 °C, the color of the specimens was light gray. At this temperature, micro-cracks joined together and formed macro-cracks. Spalling and loss of corners had occurred in some control and reinforced with recycled fibers specimens.

At 800 °C, no explosive spalling occurred for the specimens. The morphology of all specimens after exposure to 800 °C is shown in Figure 6. The results show that using RSF can reduce the intensity of cracking and spalling of the surface of the specimens. Textiles and rubbers attached to the surface of the fibers melt completely at 800 °C. They can create open pores inside the concrete, which leads to easier evaporation of water vapor and helps reduce internal pore pressure. Deep cavities, macro-cracks, and spalling are visible on the surface of the specimens. The depth of the control specimens' cavities is more significant than those reinforced with recycled fibers. The specimens reinforced with CRSF and ISF showed similar and close performance.

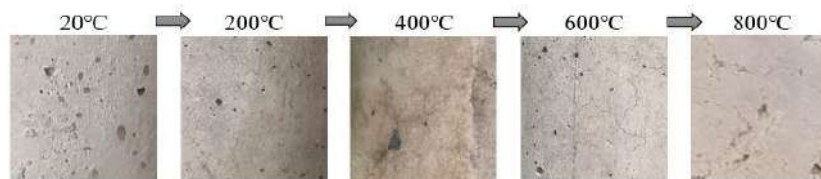


Fig. 5. Color change of specimens at different temperatures

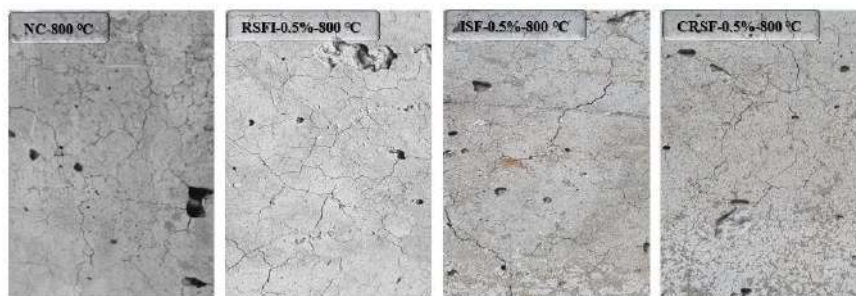


Fig. 6. Morphology of specimens after subjected to a temperature of 800 °C

3.2. Mass Loss of Specimens

In this study, the mass loss rate of cylindrical specimens has been evaluated as the ratio of the mass loss at high temperatures to the initial mass of the specimen at ambient temperature. Six specimens were weighed before and after exposure to high temperatures for each mixture. Figure 7 shows the mass loss of the specimens at different temperatures. At a temperature of 200 °C, the mass loss of the specimens is low. The decrease in mass at this temperature is related to the evaporation of free water in the pores and aggregates (Mastali et al., 2018a; Memon et al., 2019). The average mass loss percentage of the control specimen at a temperature of 200 °C is about 1.72%, but the mass loss is more for specimens reinforced with fibers. Fibers inside the concrete create pores and empty spaces due to difficult compaction (Mastali et al., 2018a).

On the other hand, the compaction of concrete with recycled fibers is more difficult due to the presence of rubber and textiles. The average mass loss percentage for specimens containing recycled fibers was 3.59%, and for industrial fibers was 3.49%. Recycled fibers have textiles and rubber attached to the surface. Some textiles, which are close to the surface, burn at this temperature and can cause mass loss.

At the temperature of 600 °C, the highest mass loss is related to RSFI-0.5%, with a value of 8.80%. At this temperature, all

rubbers and textiles burn entirely, which leads to porosity and, as a result, a significant mass loss. At 600 °C, the chemical bond of water is destroyed, and calcium hydroxide is dehydrated and decomposed (Memon et al., 2019). The dehydration of silicate gel is also progressive, completely dehydrated, and decomposed at approximately 600-700 °C (Memon et al., 2019). In addition, concrete loses all its capillary water at temperatures above 400 °C (Memon et al., 2019). The mass loss rate of NC and CRSF-0.5% specimens are close and 7.47% and 7.34%, respectively.

3.3. Compressive Strength at Ambient and High Temperatures

The results of the compressive failure mode for the control and fiber-reinforced specimens at different temperatures are shown in Figure 8. The results show that the specimens reinforced with ISF and CRSF have higher compressive strength than NC and RSFI at all temperatures. The failure mode of the control specimen was brittle and unexpected at all temperatures, and parts of the specimens were separated and scattered around. While specimens are reinforced with fibers, regardless of the type of steel fibers, the brittle failure mode becomes ductile because steel fibers prevent the propagation and joining of cracks and maintain the integrity of the specimens.

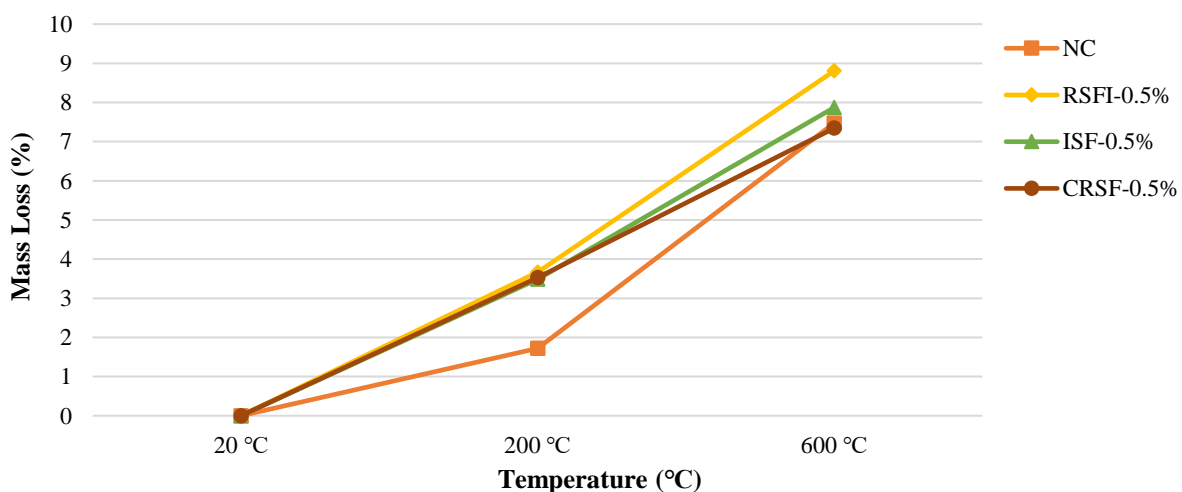


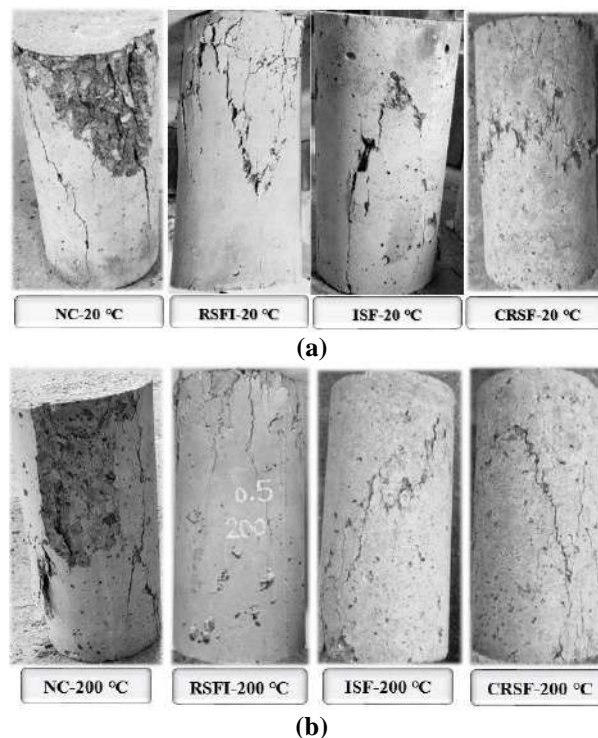
Fig. 7. Mass loss of specimens at different temperatures

In general, the results show that at ambient and high temperatures, CRSF has shown a performance close to ISF in improving the compressive strength of concrete. As shown in Figure 9, at ambient temperature, ISF-0.5% and CRSF-0.5% compressive strength is 27.73% and 29.53% higher than NC, respectively. Meanwhile, at ambient temperature and 200 °C, the compressive strength of RSFI-0.5% is 6.18% and 19.17% lower than NC, respectively. This decrease in compressive strength can be related to the high amount of rubber attached to the surface of fibers and textiles. Rubber forms a weak bond with the surrounding cement matrix, which leads to an increase in porosity and, as a result, a decrease in strength (Zhang et al., 2020; Fu et al., 2019).

At ambient temperature, the compressive strength of specimens reinforced with CRSF and ISF is close. However, at a temperature of 200 °C, the compressive strength of CRSF-0.5% is 7.44% lower than ISF-0.5%. Compared to RSFI, CRSF is cleaner fibers but still contains less rubber and textiles. Textiles close to the surface of the specimen burn at 200 °C and can lead to micro-cracks and porosity and, as a result, decrease in strength compared to ISF-0.5%

specimens.

At a temperature of 600 °C, a sharp drop in strength can be seen for all specimens. The lowest value of residual compressive strength is related to NC, with a value of 12.87 MPa, the highest value is CRSF-0.5%, with a value of 19.67 MPa. The residual compressive strength of RSFI-0.5% is 6.53% higher than NC at this temperature. The positive role of the presence of rubber and textiles with fibers can be seen at high temperatures. Rubber and textiles melt at a temperature of 600 °C and create a network of open pores inside the concrete, which helps escape the formed water vapor more efficiently and can reduce cracking and spalling caused by pore pressure (Wu and Zhou, 2020; Hossain et al., 2013). Of course, it is essential to mention that the complete melting of the rubber attached to the surface of the fibers reduces the bond between the cement paste and the fibers. Therefore, this issue can also justify the reduction of the compressive strength of specimens reinforced with RSFI compared to CRSF and ISF. The results of the average compressive strength of the specimens at different temperatures are presented in Table 2.



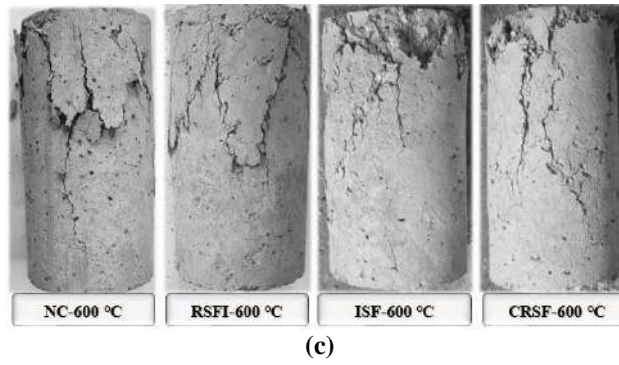


Fig. 8. Compressive failure mode of specimens: a) Ambient temperature; b) 200 °C; and c) 600 °C

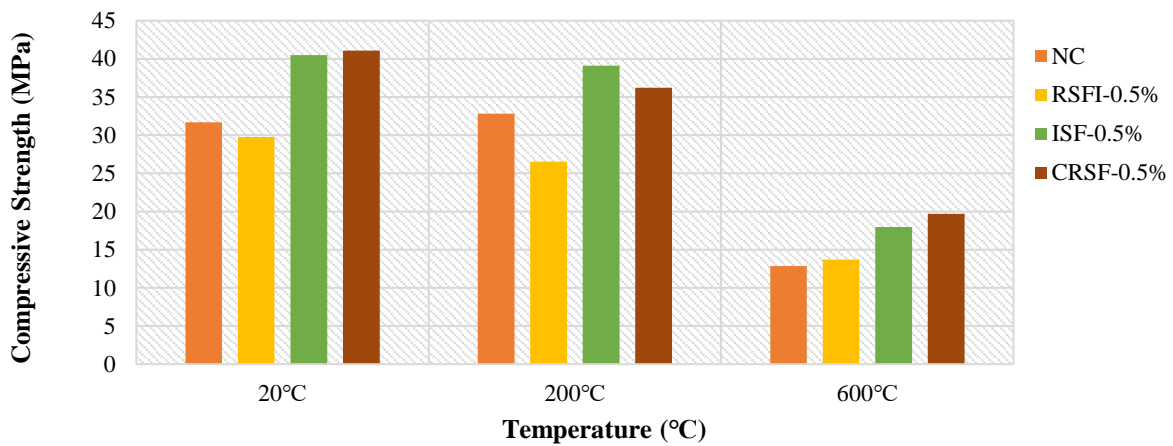


Fig. 9. Compressive strengths of specimens at different temperatures

Table 2. Average mechanical properties of concrete at different temperatures (MPa)

| Concrete mixes | Compressive strength (MPa) | | | | | Splitting tensile strength (MPa) | | | | |
|----------------|----------------------------|--------|--------|---------------------|--------|----------------------------------|--------|--------|---------------------|--------|
| | Temperatures | | | Reduction rate (%)* | | Temperatures | | | Reduction rate (%)* | |
| | 20 °C | 200 °C | 600 °C | 200 °C | 600 °C | 20 °C | 200 °C | 600 °C | 200 °C | 600 °C |
| NC | 31.70 | 32.81 | 12.87 | 3.50 | -59.40 | 4.59 | 3.59 | 1.04 | -21.79 | -77.34 |
| RSFI-0.5% | 29.74 | 26.52 | 13.71 | -10.83 | -53.90 | 4.67 | 3.61 | 1.46 | -22.70 | -68.74 |
| ISF-0.5% | 40.49 | 39.12 | 17.98 | -3.38 | -55.59 | 4.77 | 4.18 | 1.72 | -12.37 | -63.94 |
| CRSF-0.5% | 41.06 | 36.21 | 19.67 | -11.81 | -52.09 | 4.68 | 3.62 | 1.64 | -22.65 | -64.95 |

*The rate of resistance reduction compared to the ambient temperature

3.3.1. Stress-Strain Curve and Secant Modulus of Elasticity

The stress-strain diagrams related to the force-displacement values obtained during the compressive test are drawn in Figure 10. The modulus of elasticity of concrete is determined with the help of compressive tests of cylindrical specimens. The secant modulus is the slope of the line that connects from the origin to the point of the curve, such as 40% of the ultimate rupture stress. The results have shown that the compressive strength and modulus of elasticity decrease with increasing temperature while the strain related to the

maximum compressive stress increases. For all specimens at 200 °C, the strain corresponding to the maximum compressive stress is close to the ambient temperature strain, and only a tiny amount has increased. For example, the strain increase for RSFI-0.5% at 200°C is 0.45% compared to ambient temperature. Nevertheless, at a temperature of 600 °C, the increase in strain related to the maximum compressive stress is significant. At this temperature, the average strain increase (for all specimens) compared to the ambient temperature is 390.17%.

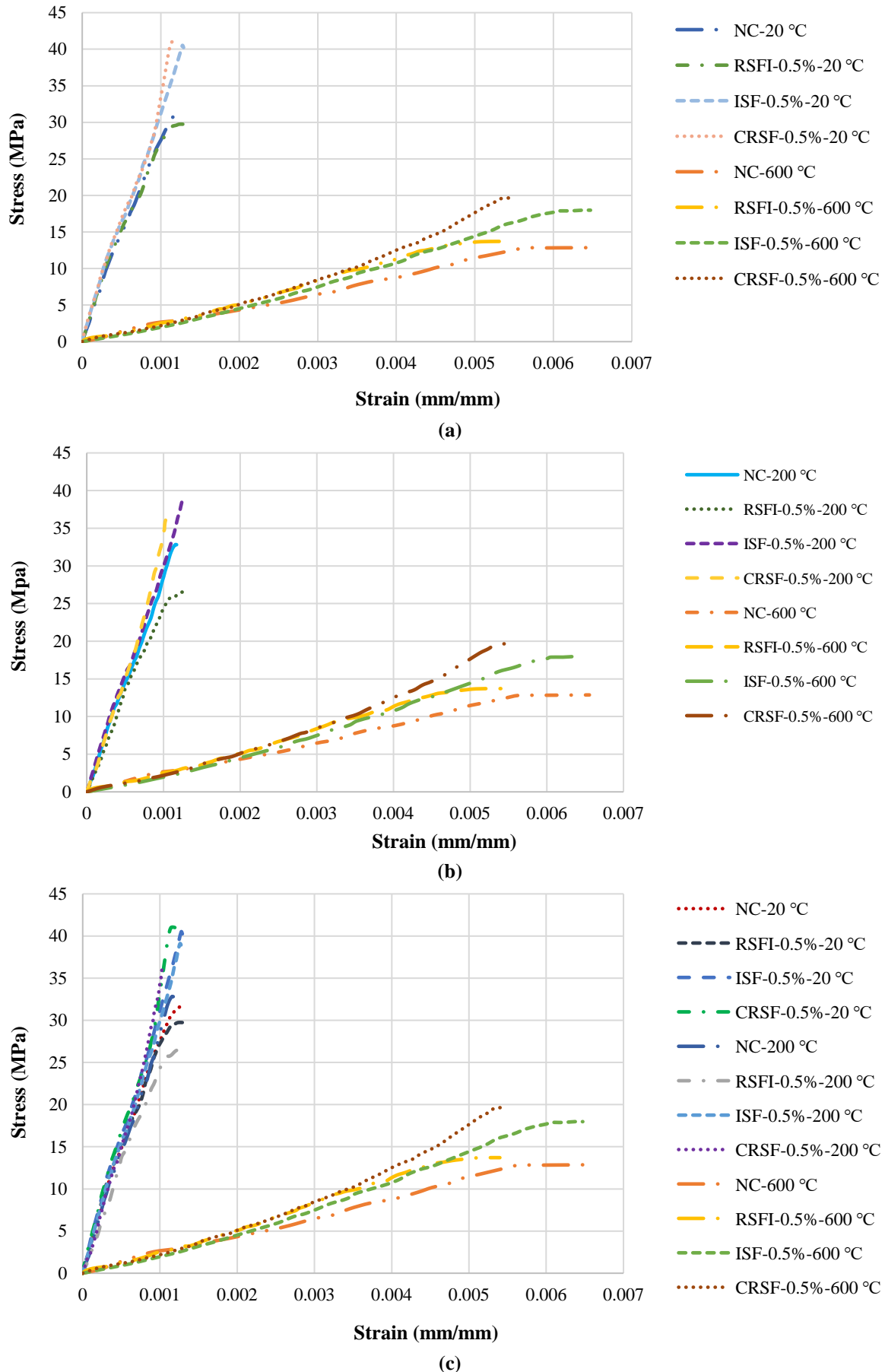


Fig. 10. Comparison of stress-strain curves of specimens at different temperatures: a) 20 °C vs 600 °C; b) 200 °C vs 600 °C; and c) All temperatures

At high temperatures, the modulus of elasticity decreases due to the formation of micro-cracks and the thermal degradation of concrete components (Zhang et al., 2020). At temperatures below 400 °C, the vapor pressure caused by the evaporation of free water in the concrete is the main factor in reducing the compressive strength and modulus of elasticity (Ma et al., 2015). At a temperature higher than 400 °C, cracks in the Interfacial Transition Zone (ITZ) caused by thermal reactions between the aggregate and the cement matrix and the fibers and the cement matrix lead to a decrease in compressive strength and elastic modulus. Figure 11 shows the modulus of elasticity for specimens at different temperatures.

The reduction of the modulus of elasticity at 200 °C is small. The lowest decrease in modulus of elasticity is related to NC, and the highest amount is related to RSFI-0.5%. At a temperature of 600 °C, a sharp decrease in the modulus of elasticity

is observed. Using fibers at high temperatures has improved the modulus of elasticity compared to the control specimen. The elastic modulus of RSFI-0.5%, ISF-0.5%, and CRSF-0.5% is 21.29%, 15.21%, and 26.72% higher than NC at this temperature, respectively. At a temperature of 600 °C, the value of the drop of the modulus of elasticity for specimens reinforced with fibers can be considered the same.

3.4. Splitting Tensile Strength at Ambient and High Temperatures

Figure 12 shows how tensile cracks are formed in specimens at different temperatures. All cracks occurred in the middle of the section, close to the diameter. In NC and RSFI-0.5% at 600 °C, the cracks were deeper, and near the cross-section wall, the cracks have spread in the form of branches. Steel fibers (regardless of their type) have partially prevented the branching growth of cracks at high temperatures.

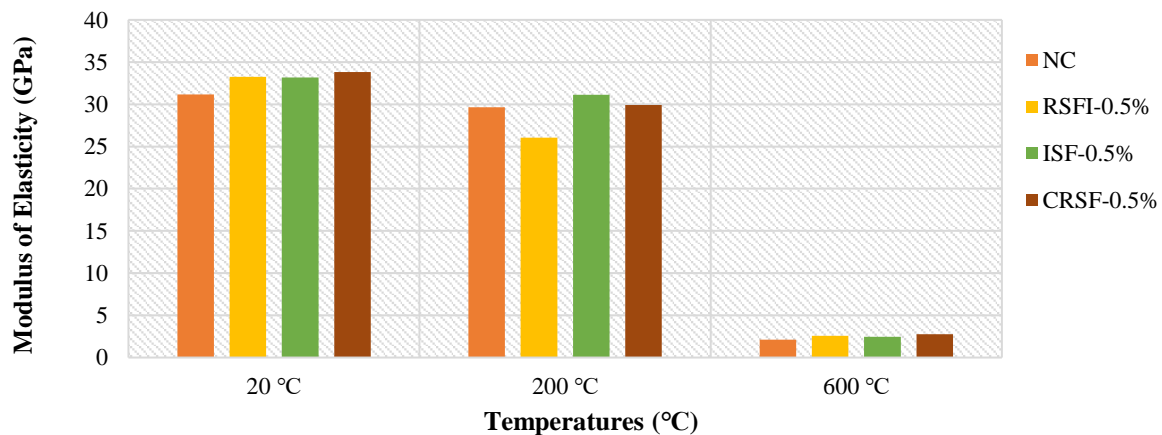


Fig. 11. The secant modulus of elasticity of the specimens at different temperatures

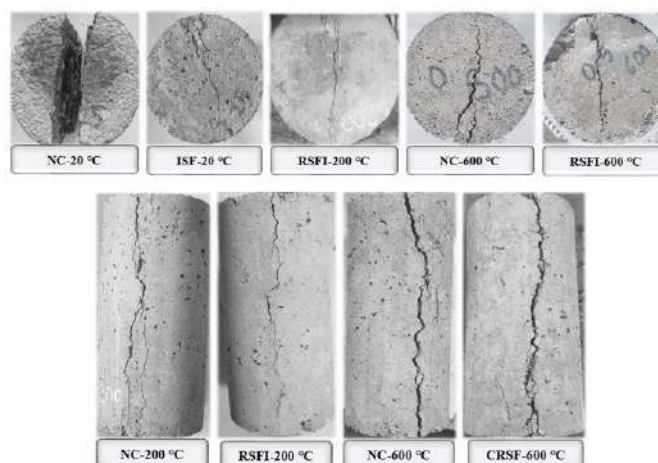


Fig. 12. Tensile failure mode of specimens at different temperatures

The results have shown that adding steel fibers (regardless of their type) has improved tensile strength at all temperatures. Figure 13 illustrates the tensile strength results of the control and fiber-reinforced specimens at different temperatures. At ambient temperature, the tensile strength of all specimens is close to each other. The highest tensile strength is related to ISF-0.5%, with a value of 4.77 MPa, and the lowest is related to NC, with a value of 4.59 MPa. As the temperature increases, the tensile strength of the specimens decreases, but the amount of this decrease is lower for the fiber-reinforced specimens than for the control specimens. At ambient temperature and 200 °C, the performance of CRSF-0.5% is only slightly higher than RSFI-0.5%, and generally, they have shown similar performance. However, both fibers have improved tensile strength compared to NC.

At a temperature of 200 °C, the residual tensile strength of ISF-0.5% has decreased to 12.37%. This is while the average strength reduction of specimens reinforced with recycled fibers reaches 22.67%. The recycled fibers' short length and small diameter and the presence of rubber and textiles can be the reason for the more significant decrease in residual tensile strength at this temperature compared to industrial fibers.

At a temperature of 600 °C, a significant drop in residual tensile strength is observed for all specimens. CRSF-0.5% has provided close and comparable performance at this temperature with ISF-0.5%. The residual tensile strength of RSFI-0.5%, ISF-0.5%, and CRSF-0.5% is 40.38%, 65.38%, and 57.69% more than the NC at this temperature. Overall, the results illustrate that the presence of rubber and textiles did not harm the tensile performance compared to the control specimen. However, the performance of these fibers was slightly weaker compared to industrial fibers. Table 2 displays the findings of the average tensile strength of the specimens at various temperatures.

3.5. Flexural Strength at Ambient and High Temperatures

As shown in Figure 14a, the control specimen showed brittle behavior at all temperatures and failed suddenly after reaching the maximum load. Specimens reinforced with fibers have shown semi-brittle behavior at all temperatures; Figures 14b and 14c show how cracks grow at 200 °C for specimens reinforced with recycled fibers. By bridging the cracks, steel fibers prevent their unstable growth and thus improve the ductility and flexural strength of the prism beams. Figure 14d shows how the fibers bridge the cracks.

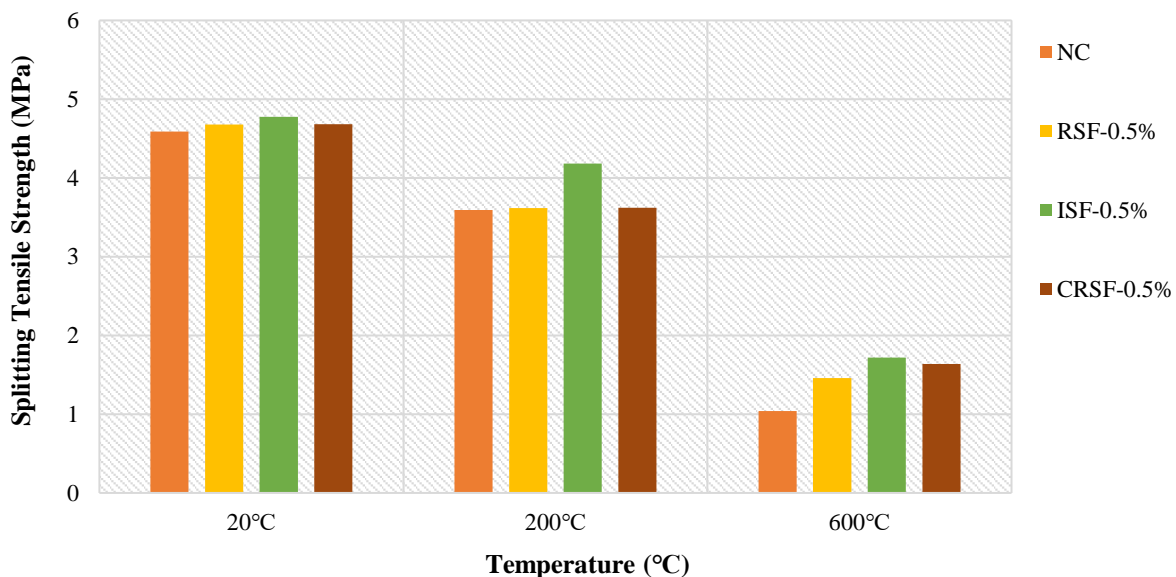


Fig. 13. Splitting tensile strength of specimens at different temperatures

The load-deflection curve obtained from the four-point bending test for prismatic specimens at different temperatures is shown in Figure 15. The results show that adding steel fibers increases the peak load compared to the control specimen. All temperatures' highest peak load value corresponds to CRSF-0.5%, followed by ISF-0.5%. Since NC specimens undergo sudden failure, they have a slight ultimate deflection compared to fiber-reinforced specimens. The ultimate deflection of NC specimens at ambient temperature, 200 °C, and 600 °C is 0.32, 0.55, and 2.34 mm, respectively. In comparison, the ultimate deflection of fiber-reinforced specimens is more than 6 mm at ambient temperature and 200 °C and more than 3 mm at 600 °C.

According to the load-deflection diagrams, the slope of the tangent to the curve is defined as flexural stiffness. In general, the results show that the flexural stiffness of all specimens decreases with increasing temperature. This behavior can be related to the decomposition of calcium hydroxide in cement paste and the release of chemical bonding water at higher temperatures (Memon et al., 2019). The most significant decrease in flexural stiffness is related to NC. In contrast, the

reduction in flexural stiffness of specimens reinforced with fibers is less. According to Figure 15a, the highest flexural stiffness at ambient temperature corresponds to CRSF-0.5%. At a temperature of 200 °C, the flexural stiffness of the specimens reinforced with fibers is close to the same (Figure 15b). At the temperature of 600 °C, the flexural stiffness of RSFI-0.5% and ISF-0.5% specimens is close to the same (Figure 15c).

Using Eq. (2), MOR was calculated for specimens at different temperatures. The results show that steel fibers (regardless of their type) have significantly increased the MOR compared to the control specimen at all temperatures. As shown in Figure 16, at ambient temperature, the highest MOR corresponds to CRSF-0.5% with a value of 5.99 MPa, and the lowest MOR corresponds to NC with a value of 3.05 MPa. RSFI-0.5% also significantly improved MOR with the presence of rubber and textiles and increased MOR at ambient temperature by 44.59% compared to NC. However, it still performs less than ISF-0.5% and CRSF-0.5%. ISF-0.5% at ambient temperature has increased MOR by 51.47% compared to NC.

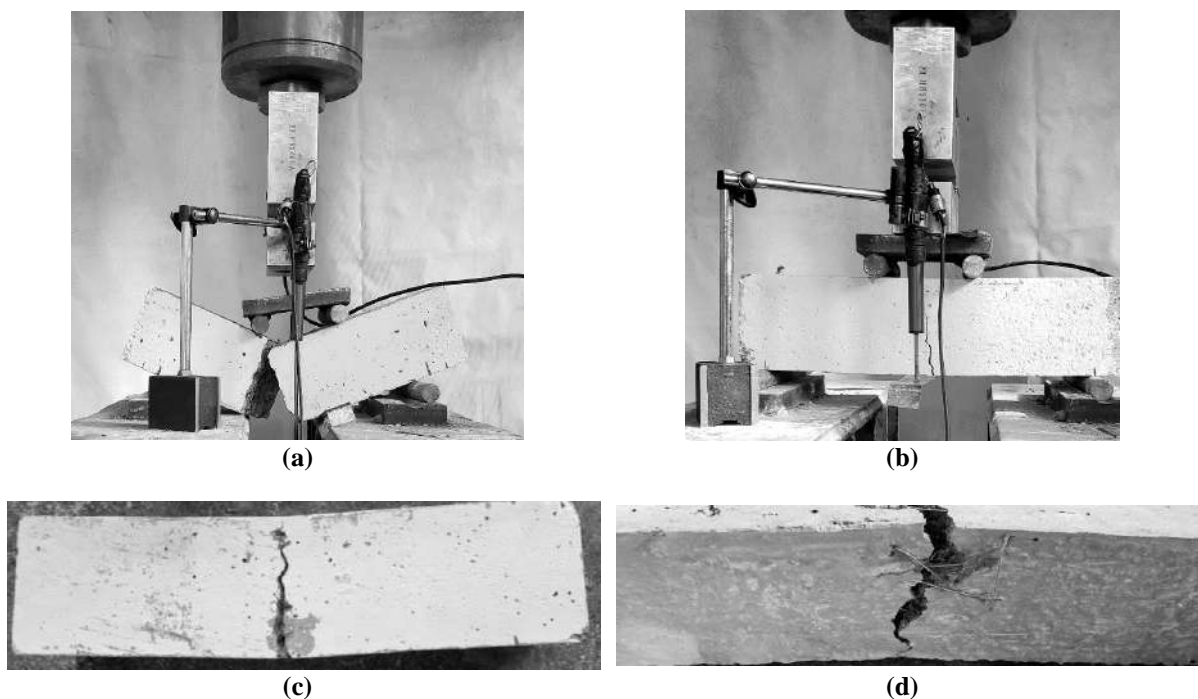


Fig. 14. Cracking of prism beams at 200 °C: a) NC; b) RSFI-0.5%; c) CRSF-0.5%; and d) ISF-0.5%

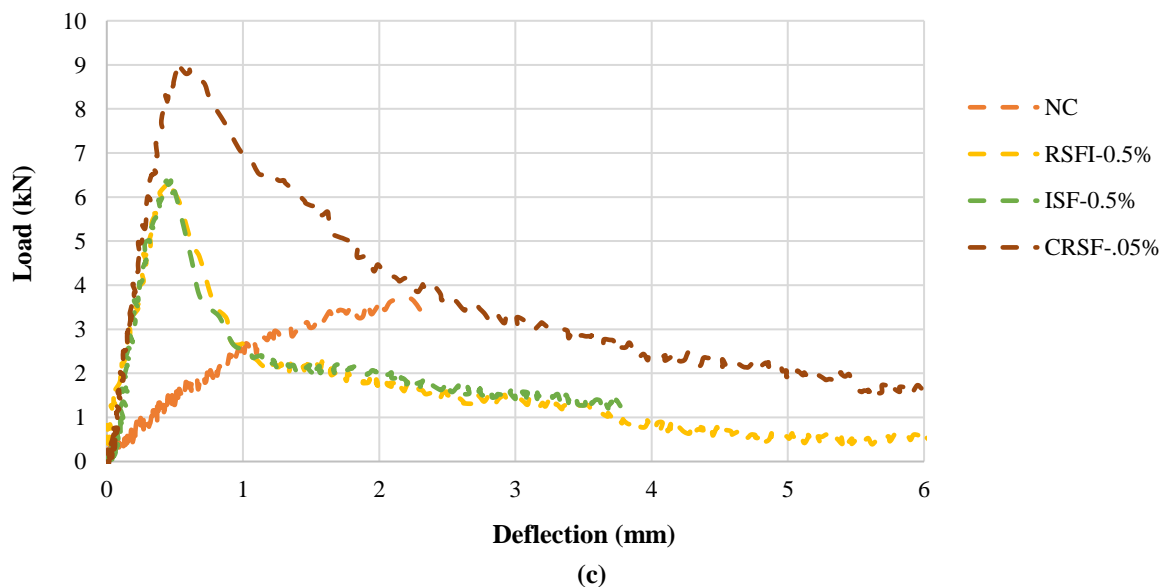
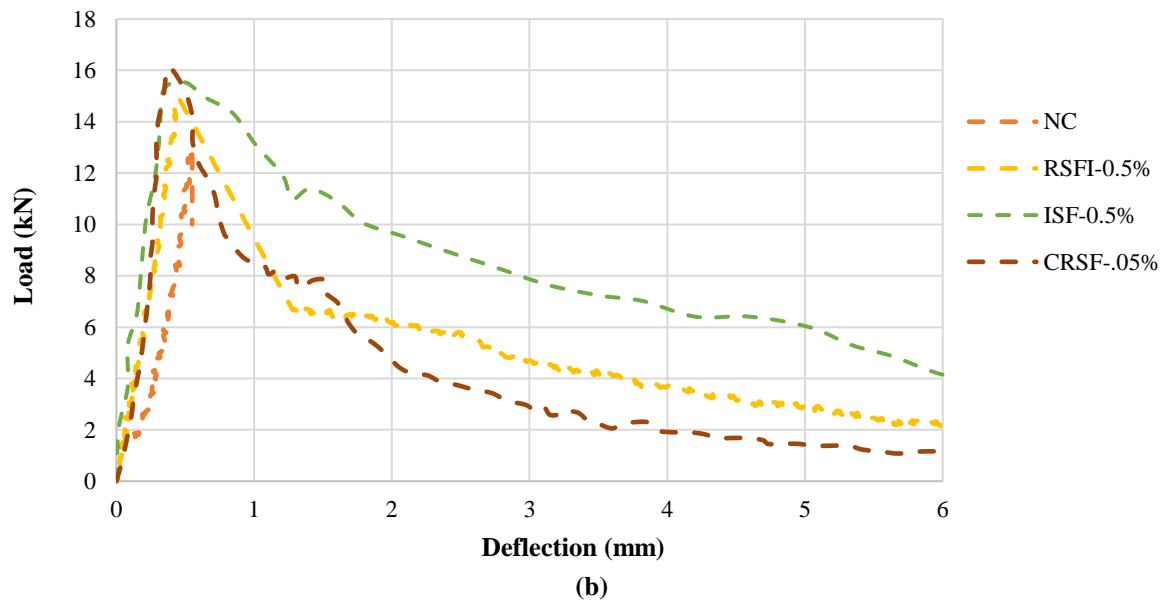
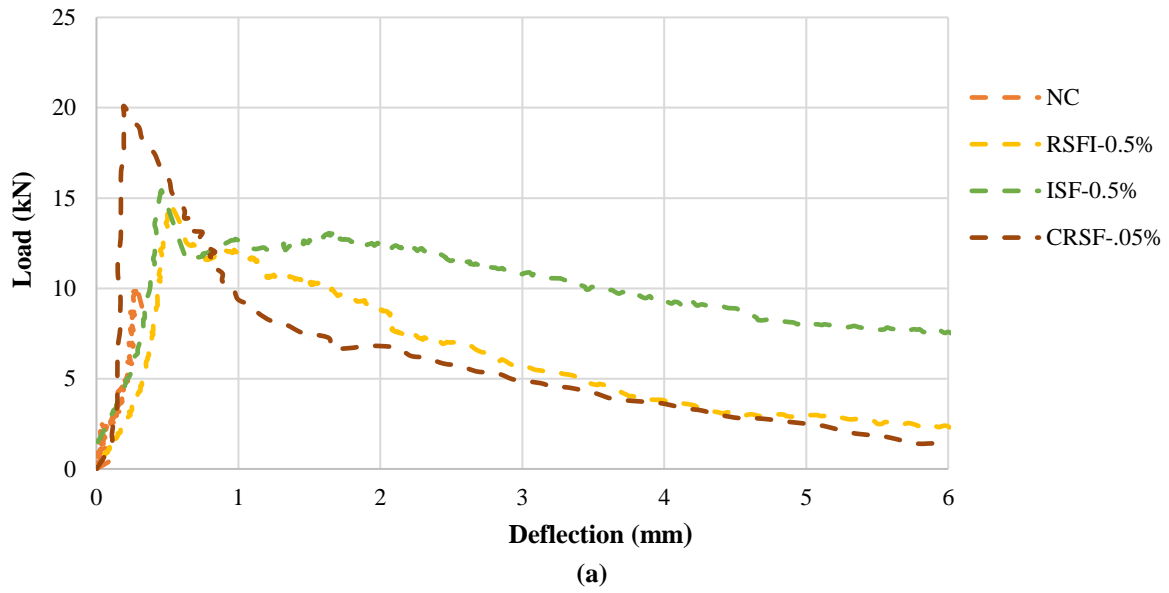


Fig. 15. Load-deflection curve of specimens at different temperatures: a) 20 °C; b) 200 °C; and c) 600 °C

At the temperature of 200 °C, MOR has increased slightly for all specimens except CRSF-0.5%. The results of other studies have also shown that at a temperature of 200 °C, the strength of specimens reinforced with steel fibers has increased compared to the ambient temperature (Fu et al., 2019). Fiber-reinforced specimens have shown similar performance at this temperature and have increased MOR by 19.40% on average compared to NC. At 600 °C, a severe drop in MOR has been observed for all specimens. The reduction of MOR for NC, RSFI-0.5%, ISF-0.5%, and CRSF-0.5% compared to ambient temperature is 63.61%, 56.92%, 44.80%, and 40.23%, respectively. Table 3 shows the specimens' average peak load and MOR at different temperatures.

3.5.1. Toughness Indices and Residual Resistance Factors

The ductility of the specimens was evaluated based on ASTM C1018 (1997). The toughness indices I_5 , I_{10} , and I_{20} for fiber-reinforced specimens are shown in Figure 17. The control specimens fail suddenly, and their deflection is slight; Hence, their toughness indices values are ignored. The results show that increasing

the temperature reduces the toughness indices. But the toughness indices value for RSFI-0.5% at 600 °C is more than 200 °C. At a temperature above 200 °C, the melting of rubber on the surface of the fibers leads to the strengthening of their bond with the cement matrix, which can also help to improve its flexural performance (Fu et al., 2019; Zhang et al., 2020). ISF-0.5% toughness indices are higher than RSFI-0.5% at all temperatures, while the toughness indices of CRSF-0.5% is higher than ISF-0.5% at all temperatures. The average decrease in toughness indices for RSFI-0.5% at 200 °C compared to ambient temperature is 75.07%, and for CRSF-0.5% is 54.13%.

The residual resistance factors $R_{5,10}$ and $R_{10,20}$ show the average resistance level maintained after the first crack as a percentage of the resistance of the first crack. 100 values represent entirely plastic behavior (ASTM, 1997). Low performance is indicated by lower values (ASTM, 1997). The control specimen has a zero residual resistance factor (ASTM, 1997). Table 4 shows the values of the residual resistance factors $R_{5,10}$ and $R_{10,20}$. At ambient temperature, CRSF-0.5% showed plastic behavior.

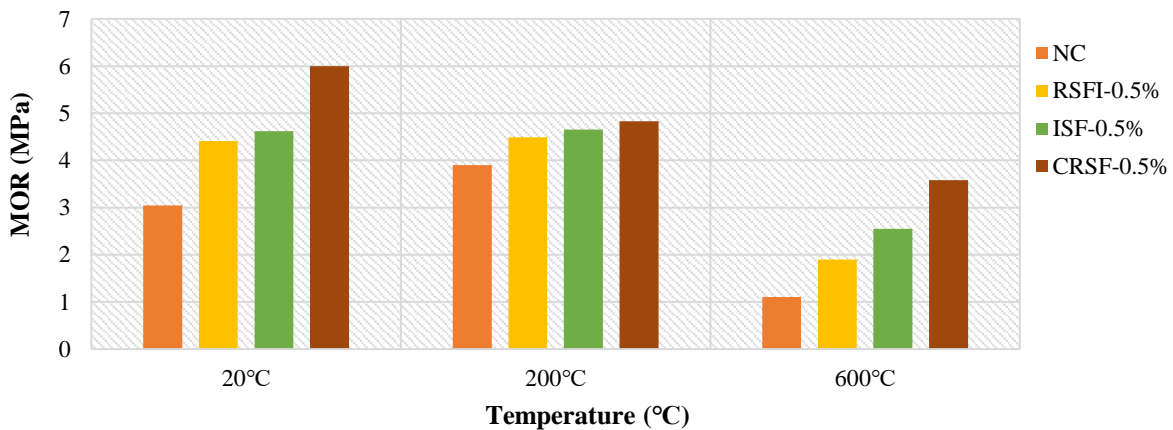


Fig. 16. MOR of specimens at different temperatures

Table 3. Average MOR of specimens at different temperatures (MPa)

| Concrete mixes | Peak load (kN) | | | MOR (MPa) | | |
|----------------|----------------|--------|--------|-----------|--------|-------|
| | 20 °C | 200 °C | 600 °C | 20°C | 200 °C | 600°C |
| NC | 10.16 | 13.01 | 3.69 | 3.05 | 3.90 | 1.11 |
| RSFI-0.5% | 14.69 | 14.96 | 6.32 | 4.41 | 4.49 | 1.90 |
| ISF-0.5% | 15.41 | 15.51 | 6.37 | 4.62 | 4.65 | 2.55 |
| CRSF-0.5% | 19.99 | 16.11 | 8.96 | 5.99 | 4.83 | 3.58 |

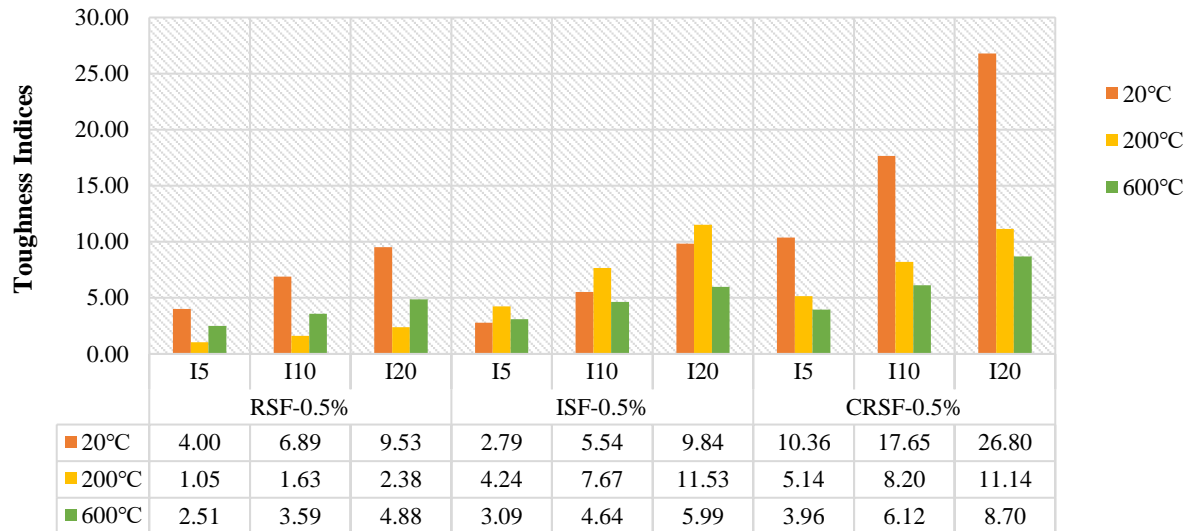


Fig. 17. Toughness indices at different temperatures

Table 4. Residual resistance factors at different temperatures

| Concrete mixes | Maximum heating temperatures (°C) | | | | | |
|----------------|-----------------------------------|--------------------|-------------------|--------------------|-------------------|--------------------|
| | 20 °C | | 200 °C | | 600 °C | |
| | R _{5,10} | R _{10,20} | R _{5,10} | R _{10,20} | R _{5,10} | R _{10,20} |
| RSF-0.5% | 57.77 | 26.36 | 11.54 | 7.53 | 21.58 | 12.89 |
| ISF-0.5% | 54.98 | 43.02 | 68.68 | 38.56 | 31.07 | 13.43 |
| CRSF-0.5% | 145.69 | 91.53 | 61.18 | 29.43 | 43.04 | 25.86 |

3.6. Microstructure of Concrete at Ambient and High Temperatures

With the help of scanning electron microscopy (SEM), the microstructure of the control and fiber-reinforced specimens at a temperature of 600 °C have been examined. Calcium hydroxide decomposes into CaO and water at 350-550 °C (Xing et al., 2015). Silicate gel, which forms the main strength of concrete, decomposes in the temperature range of 400-600 °C. Figure 18a shows the presence of calcium hydroxide at a temperature of 600 °C in the microstructure of the control specimen. The reason for observing calcium hydroxide can be related to the rehydration of CaO with ambient humidity inside the specimen, which occurred after the specimens were taken out of the furnace and exposed to ambient temperature. This issue is also mentioned in the results found in the Xing et al. study (2015).

In the control specimen, cracking can be seen in ITZ between aggregate and cement paste and inside the aggregate. In specimens reinforced with fibers, ITZ between

aggregate and cement paste and between fibers and cement paste is essential. At a temperature of 600 °C, significant changes are observed in the bonding of fibers and cement matrix. As can be seen in Figure 18b, cracking in ITZ between RSFI and cement matrix is more than in the specimens reinforced with ISF and CRSF. The rubber attached to the RSFI surface melts at temperatures above 200 °C. In this case, the bond between fibers and cement matrix is improved. Nevertheless, these rubbers burn completely at 400 °C and above, creating porosity and pores between the fibers and the cement matrix. As a result, it causes weaker bonding and more cracks in ITZ than ISF (Figure 18c) and CRSF (Figure 18d). In general, the microstructure analysis shows that the cracking of the control specimen is much higher than that of the specimens reinforced with fibers. Steel fibers maintain their properties at high temperatures and prevent cracks' growth and expansion by bridging them.

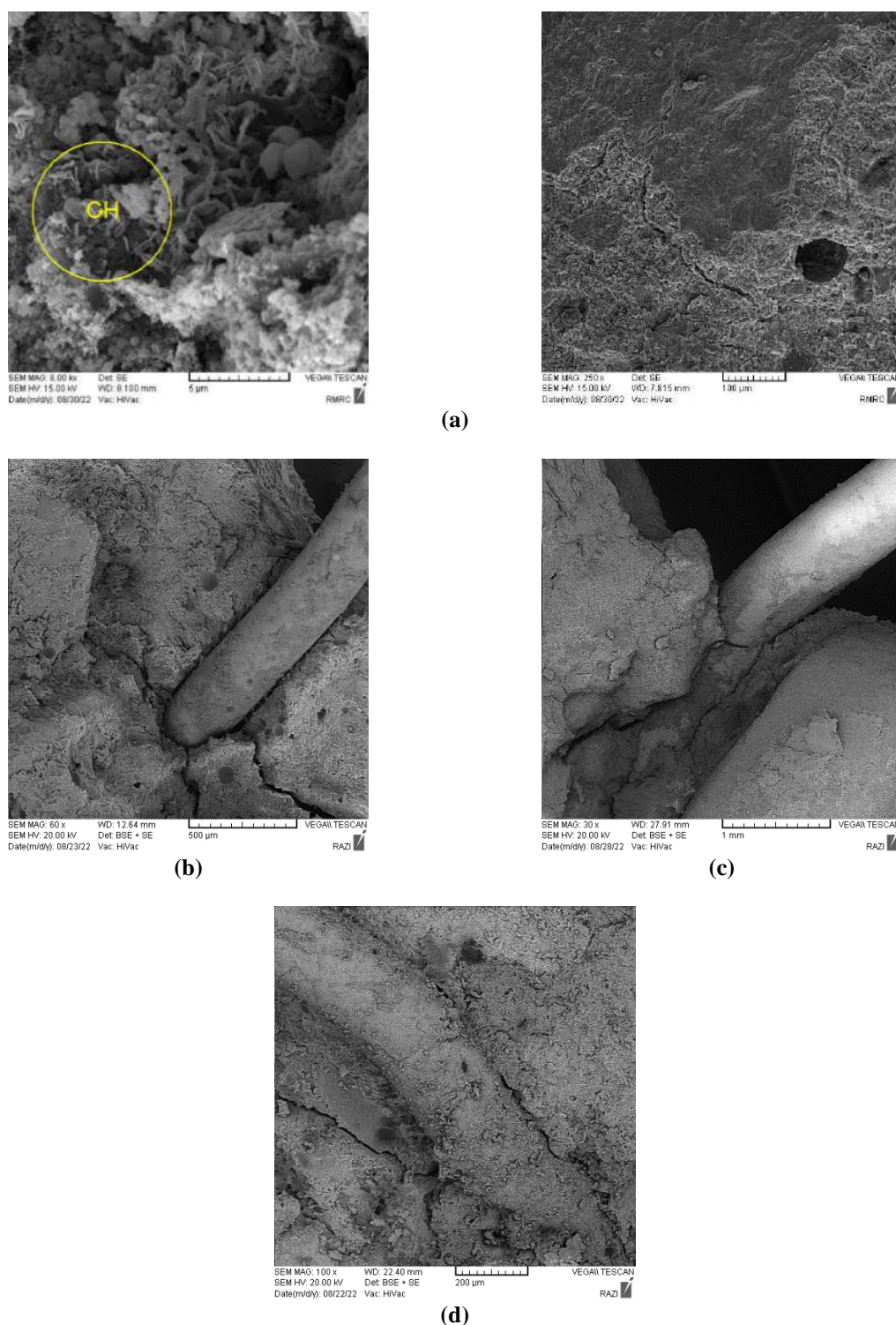


Fig. 18. SEM observations for specimens at 600 °C: a) NC; b) RSFI; C) ISF; and d) CRSF

3.7. Economic Analysis

When introducing and using new materials to strengthen and make concrete, in addition to examining their effect on the mechanical properties of concrete, it is also essential to investigate the impact on the cost of mixtures and global warming potential. In order to find an economical and

affordable mixture, the cost of the mixture was calculated considering the cost of the materials used. Since the same mixture design is considered for all mixtures, the most influential parameter in the economic analysis is the unit price of fibers and superplasticizer. The cost of mixtures can be calculated by multiplying the fiber

content by the unit price of fibers. The supplier company and the tire recycling factory provide information about the price of industrial and recycled steel fibers. To calculate the cost of mixtures, the cost of each mixture is normalized based on the maximum cost of materials (i.e., superplasticizer). Table 5 shows the normalized unit price. The highest mixture cost is related to ISF-0.5%, and the lowest belongs to RSFI-0.5%. Adding ISF increases the manufacturing cost significantly. Replacing industrial fibers with recycled fibers reduces the cost of mixtures.

Furthermore, mechanical properties and the cost of selecting the appropriate mixture should be considered. For this purpose, the

compressive strength gain and MOR gain (compared to the control specimen) per cost unit were calculated and compared for all mixtures at different temperatures. As mentioned in Section 3.3, RSFI leads to a decrease in compressive strength; Therefore, as shown in Figure 19a, the compressive strength gain is negative. Therefore, the ratio of compressive strength gain per unit cost is negative. MOR gain is less for RSFI compared to ISF and CRSF. However, due to its lower cost than ISF, it has a higher ratio of MOR gain to unit cost than ISF (Figure 19b). The results show that using RSFI for flexural members in structures at ambient temperature and after exposure to high temperatures can benefit resistance and economy.

Table 5. Normalized cost of mixtures

| Mixtures | RSFI-0.5% | ISF-0.5% | CRSF-0.5% |
|-----------------|-----------|----------|-----------|
| Normalized cost | 7.58 | 40.65 | 9.55 |

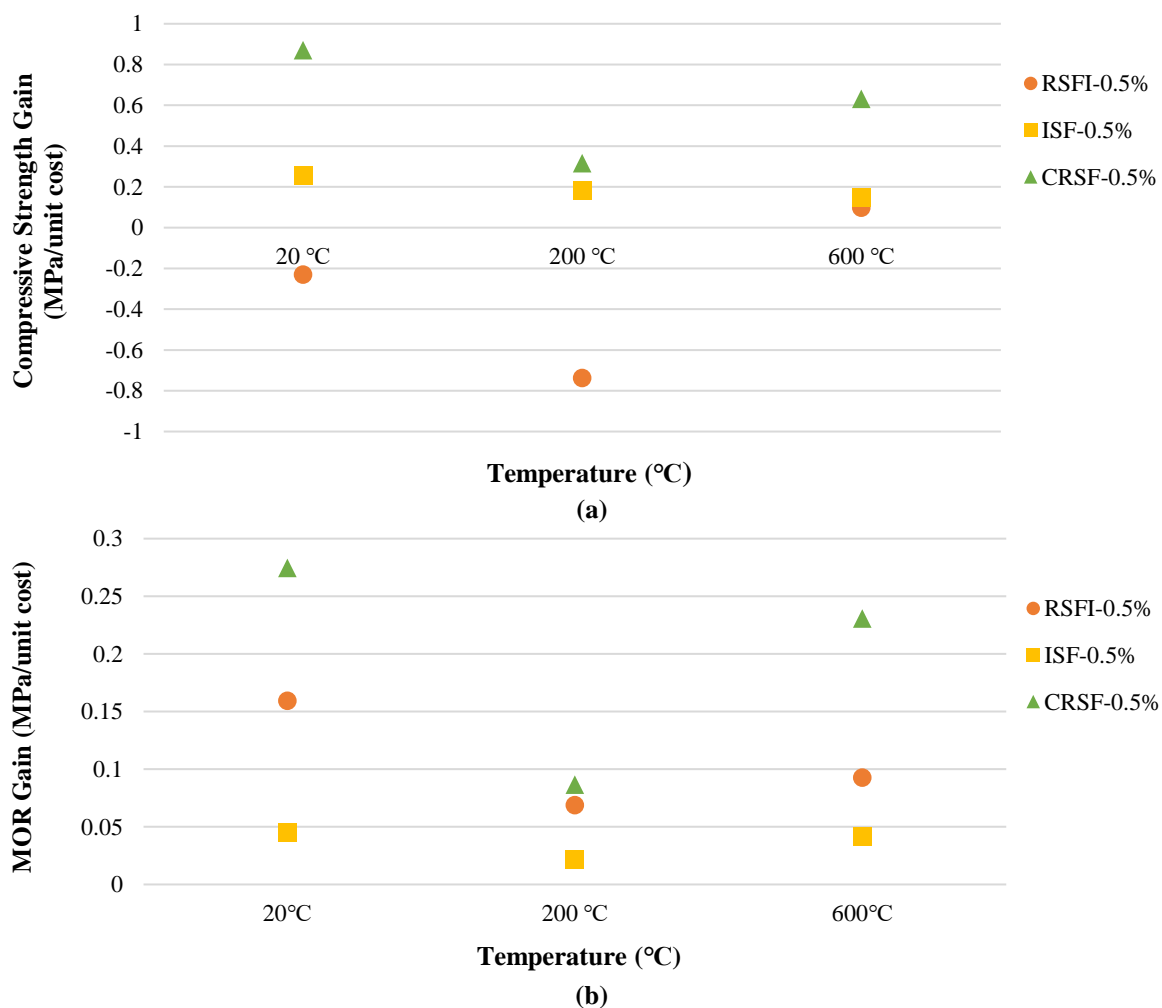


Fig. 19. a) Compressive strength; and b) MOR gain per cost unit for mixtures at different temperatures

To maximize mechanical properties while lowering cost, CRSF can be used. ISF performs best in terms of mechanical properties, but these fibers have high costs. RSFI containing textiles and rubber showed the opposite trend; They were weaker in terms of mechanical performance but had less cost and a negative environmental impact. Among the concrete mix components, cement contributes the most to CO₂ emissions (Mastali et al., 2018a; Mastali et al., 2018b). The addition of fibers also leads to an increase in CO₂ emissions (Mastali et al., 2018a). However, industrial fibers' contribution to CO₂ emissions is higher than recycled fibers. According to the mechanical and economic analysis, CRSF can be a suitable alternative to ISF to strengthen concrete.

4. Conclusions

Considering the environmental and economic issues and the mechanical performance of concrete, this study has investigated the effect of RSF from waste tires at ambient and after exposure to high temperatures. The results obtained in summary are as follows:

- RSFI-0.5% specimens at ambient temperature and 200 °C did not improve compressive strength and had lower compressive strength than NC. The presence of rubber attached to the surface of fibers and textiles makes concrete compaction difficult, increases porosity, and thus decreases concrete strength. However, at 600 °C, it showed more residual strength than NC. This was while CRSF-0.5% caused a significant increase in compressive strength at all temperatures and presented similar behavior with ISF-0.5% at all temperatures.
- Fiber-reinforced concrete showed improved tensile strength and MOR at all temperatures. Bridging the cracks' fibers prevents the cracks' connection and propagation. At ambient temperature, RSFI-0.5% and CRSF-

0.5% specimens slightly improved the tensile strength. The effect of recycled fibers is more significant at high temperatures. CRSF-0.5% specimens significantly improved the MOR at ambient and high temperatures, so their performance was better than ISF-0.5%.

- According to the mechanical and economic analysis, CRSF has shown results comparable to ISF at all temperatures; ISF is more expensive than CRSF. Therefore CRSF can be a suitable alternative to ISF to strengthen concrete.

5. References

- ACI Committee 2011. (1996). *Standard practice for selecting proportions for normal, heavyweight, and mass concrete*, American Concrete Institute, 1-38.
- Aiello, M.A., Leuzzi, F., Centonze, G. and Maffezzoli, A. (2009). "Use of steel fibres recovered from waste tyres as reinforcement in concrete: Pull-out behaviour, compressive and flexural strength", *Waste Management*, 29(6), 1960-1970, <https://doi.org/10.1016/j.wasman.2008.12.002>.
- Alsaif, A., Bernal, S.A., Guadagnini, M. and Pilakoutas, K. (2018). "Durability of steel fibre reinforced rubberised concrete exposed to chlorides", *Construction and Building Materials*, 188, 130-142.
- ASTM-C-1018-97. (1997). *Standard test method for flexural toughness and first-crack strength of fiber-reinforced concrete (Using beam with third-point loading)*, American Society for Testing and Materials, West Conshohocken, PA: ASTM International.
- ASTM-C-1609. (2012). *Standard test method for flexural performance of fiber-reinforced concrete (Using beam with third-point loading)*, American Society for Testing and Materials, West Conshohocken, PA: ASTM International.
- ASTM-C-39. (2018). *Standard test method for compressive strength of cylindrical concrete specimens*, American Society for Testing and Materials, West Conshohocken, PA: ASTM International.
- ASTM-C494-13. (2015). *Standard specification for chemical admixtures for concrete*, American Society for Testing and Materials, West Conshohocken, PA: ASTM International.
- ASTM-C496-C496M-11. (2004). *Standard test method for splitting tensile strength of cylindrical concrete specimens*, American Society for Testing and Materials, West

- Conshohocken, PA: ASTM International.
- Awolusi, T.F., Oke, O.L., Atoyebi, O.D., Akinkulore, O.O. and Sojobi, A.O. (2021). "Waste tires steel fiber in concrete: A review", *Innovative Infrastructure Solutions*, 6(1), 1-12, <https://doi.org/10.1007/s41062-020-00393-w>.
- Barros, J.A., Frazão, C., Caggiano, A., Folino, P., Martinelli, E., Xargay, H., Zamanzadeh, Z. and Lourenço, L. (2017). "Cementitious composites reinforced with recycled fibres", *Recent Advances on Green Concrete for Structural Purposes: The Contribution of the EU-FP7 Project EnCoRe*, 141-195, https://doi.org/10.1007/978-3-319-56797-6_8.
- Bedewi, N. (2009). "Steel fiber reinforced concrete made with fibers extracted from used tyres", M.Sc. Thesis in Civil Engineering, Addis Ababa University, Addis Ababa, Ethiopia.
- Behfarnia, K. and Behravan, A. (2014). "Application of high performance polypropylene fibers in concrete lining of water tunnels", *Materials and Design*, 55, 274-279, <https://doi.org/10.1016/j.matdes.2013.09.075>.
- Bezerra, A.C., Maciel, P.S., Corrêa, E.C., Soares Junior, P.R., Aguilar, M.T. and Cetlin, P. R. (2019). "Effect of high temperature on the mechanical properties of steel fiber-reinforced concrete", *Fibers*, 7(12), 100, <https://doi.org/10.3390/fib7120100>.
- Bulei, C., Todor, M.P., Heput, T. and Kiss, I. (2018). "Directions for material recovery of used tires and their use in the production of new products intended for the industry of civil construction and pavements", In: *IOP Conference Series: Materials Science and Engineering*, 294, 012064, <https://doi.org/10.1088/1757-899X/294/1/012064>.
- Dehghanpour, H. and Yılmaz, K. (2018). "Mechanical and impact behavior on recycled steel fiber reinforced cementitious mortars", *Scientific Herald of the Voronezh State University of Architecture and Civil Engineering*, 39(3), 67-84.
- Frazão, C.M.V. (2019). "Recycled steel fiber reinforced concrete for Structural elements subjected to chloride attack: Mechanical and durability performance", PhD Thesis, University of Minho, Braga/Guimarães, Portugal.
- Fu, C., Ye, H., Wang, K., Zhu, K. and He, C. (2019). "Evolution of mechanical properties of steel fiber-reinforced rubberized concrete (FR-RC)", *Composites Part B: Engineering*, 160, 158-166, <https://doi.org/10.1016/j.compositesb.2018.10.045>.
- Hager, I. (2014). "Colour change in heated concrete", *Fire Technology*, 50(4), 945-958, <https://doi.org/10.1007/s10694-012-0320-7>.
- Handoo, S.K., Agarwal, S. and Agarwal, S.K. (2002). "Physicochemical, mineralogical, and morphological characteristics of concrete exposed to elevated temperatures", *Cement and Concrete Research*, 32(7), 1009-1018, [https://doi.org/10.1016/S0008-8846\(01\)00736-0](https://doi.org/10.1016/S0008-8846(01)00736-0).
- Hossain, K.M.A., Lachemi, M., Sasmour, M. and Sonebi, M. (2013). "Strength and fracture energy characteristics of self-consolidating concrete incorporating polyvinyl alcohol, steel and hybrid fibres", *Construction and Building Materials*, 45, 20-29, <https://doi.org/10.1016/j.conbuildmat.2013.03.054>.
- Jamshaid, H. and Mishra, R. (2016). "A green material from rock: basalt fiber, A review", *The Journal of The Textile Institute*, 107(7), 923-937, <https://doi.org/10.1080/00405000.2015.1071940>.
- Karimipour, A., Ghalehnovi, M., Edalati, M. and De Brito, J. (2021). "Properties of fibre-reinforced high-strength concrete with nano-silica and silica fume", *Applied Sciences*, 11(20), 9696, <https://doi.org/10.3390/app11209696>.
- Liew, K.M. and Akbar, A. (2020). "The recent progress of recycled steel fiber reinforced concrete", *Construction and Building Materials*, 232, 117232, <https://doi.org/10.1016/j.conbuildmat.2019.117232>.
- Ma, Q., Guo, R., Zhao, Z., Lin, Z. and He, K. (2015). "Mechanical properties of concrete at high temperature, A review", *Construction and Building Materials*, 93, 371-383, <https://doi.org/10.1016/j.conbuildmat.2015.05.131>.
- Mastali, M., Dalvand, A., Sattarifard, A.R. and Illikainen, M. (2018a). "Development of eco-efficient and cost-effective reinforced self-consolidation concretes with hybrid industrial/recycled steel fibers", *Construction and Building Materials*, 166, 214-226, <https://doi.org/10.1016/j.conbuildmat.2018.01.147>.
- Mastali, M., Dalvand, A., Sattarifard, A.R., Abdollahnejad, Z. and Illikainen, M.J.C.P.B.E. (2018b). "Characterization and optimization of hardened properties of self-consolidating concrete incorporating recycled steel, industrial steel, polypropylene and hybrid fibers", *Composites Part B: Engineering*, 151, 186-200, <https://doi.org/10.1016/j.compositesb.2018.06.021>.
- Memon, S.A., Shah, S. F. A., Khushnood, R. A., and Baloch, W. L. (2019). "Durability of sustainable concrete subjected to elevated temperature—A review", *Construction and Building Materials*, 199, 435-455, <https://doi.org/10.1016/j.conbuildmat.2018.12.0>

40.
Modarres, Y., Ghalehnavi, M., (2022). "The effect of recycled steel fibers from waste tires on concrete properties", *Civil Engineering Infrastructures Journal*, 56(1), 1-18, <https://doi.org/10.22059/cej.2022.339592.1820>.
- Mohajerani, A., Hui, S.Q., Mirzababaei, M., Arulrajah, A., Horpibulsuk, S., Abdul Kadir, A., Rahman, M.T. and Maghool, F. (2019). "Amazing types, properties, and applications of fibres in construction materials", *Materials*, 12(16), 2513, <https://doi.org/10.3390/ma12162513>.
- Ramezani, A., Esfahani, M. (2018). "Evaluation of hybrid fiber reinforced concrete exposed to severe environmental conditions", *Civil Engineering Infrastructures Journal*, 51(1), 119-130, <https://doi.org/10.7508/cej.2018.01.007>.
- Roesler, J.R., Altoubat, S.A., Lange, D.A., Rieder, K. A. and Ulreich, G.R. (2006). "Effect of synthetic fibers on structural behavior of concrete slabs-on-ground", *ACI Materials Journal*, 103(1), 3.
- Rosli, S. and Ibrahim, I. (2012). "Mechanical properties of recycled steel tire fibres in concrete", Technical Report, Faculty of Civil Engineering, University Technology Malaysia.
- Shannag, M.J. (2011). "Characteristics of lightweight concrete containing mineral admixtures", *Construction and Building Materials*, 25(2), 658-662, <https://doi.org/10.1016/j.conbuildmat.2010.07.025>.
- Tlemat, H., Pilakoutas, K. and Neocleous, K. (2006). "Stress-strain characteristic of SFRC using recycled fibres", *Materials and structures*, 39(3), 365-377, <https://doi.org/10.1007/s11527-005-9009-4>.
- Wang, Y., Wu, H.C. and Li, V.C. (2000). "Concrete reinforcement with recycled fibers", *Journal of Materials in Civil Engineering*, 12(4), 314-319.
- Wu, H., Lin, X. and Zhou, A. (2020). "A review of mechanical properties of fibre reinforced concrete at elevated temperatures", *Cement and Concrete Research*, 135, 106117, <https://doi.org/10.1016/j.cemconres.2020.106117>.
- Xing, Z., Beaucour, A.L., Hebert, R., Noumowe, A. and Ledesert, B. (2015). "Aggregate's influence on thermophysical concrete properties at elevated temperature", *Construction and Building Materials*, 95, 18-28, <https://doi.org/10.1016/j.conbuildmat.2015.07.060>.
- Yang, J., Peng, G.F., Shui, G.S. and Zhang, G. (2019). "Mechanical properties and anti-spalling behavior of ultra-high performance concrete with recycled and industrial steel fibers", *Materials*, 12(5), 783, <https://doi.org/10.3390/ma12050783>.
- Zhang, P., Kang, L., Wang, J., Guo, J., Hu, S. and

Ling, Y. (2020). "Mechanical properties and explosive spalling behavior of steel-fiber-reinforced concrete exposed to high temperature, A review", *Applied Sciences*, 10(7), 2324, <https://doi.org/10.3390/app10072324>.



This article is an open-access article distributed under the terms and conditions of the Creative Commons Attribution (CC-BY) license.



Predicting the Fluctuation of Travel Time Reliability as a Result of Congestion Variations by Bagging-Based Regressors

Afandizadeh Zargari, Sh.¹, Amoei Khorshidi, N.², Mirzahosseini, H.^{3*} and Shakoori, S.²

¹ Professor, School of Civil Engineering, Iran University of Science and Technology, Tehran, Iran.

² M.Sc., School of Civil Engineering, Iran University of Science and Technology, Tehran, Iran.

³ Associate Professor, Department of Civil – Transportation Planning, Imam Khomeini International University, Qazvin, Iran.

© University of Tehran 2023

Received: 13 Oct. 2022;

Revised: 05 Apr. 2023;

Accepted: 01 May 2023

ABSTRACT: Travel time reliability affects the behavior of passengers in private or public transportation and can be seen as an important factor in the context of freight transportation. The main cause of travel time oscillation, known as travel time reliability, is congestion. Congestion is classified into two categories: recurring and nonrecurring. Recurring congestion, which is the topic of this study, is formed when supply surpasses capacity. Peak periods are good examples of recurring congestion. In this paper, by utilizing different bagging regressor methods, the effect of speed flow reduction, compared to Free Flow Speed (FFS) in terms of congestion was studied on the Planning Time Index (PTI) on a section of Interstate 64 in the United States (US). Then, by analyzing PTI changes based on congestion variation, it was revealed that when speed reduction surpasses 10%, travel time leaves its reliability. Also, when the congestion is somewhere around 0.7 to 0.75, the unreliability becomes severe. These findings were directly extracted from scatter plots drawn by bagging and bootstrapping samples which were used to improve the accuracy of PTI prediction.

Keywords: Bagging Regressor, Congestion, Machine Learning, Peak Period, Planning Time Index (PTI), Travel Time Reliability.

1. Introduction

The term Travel Time Reliability (TTR) refers to the travel time fluctuations for the same trip from day to day. The same trip is implied on a trip that is done for the same purpose, the same origin, and destination, within the same time of day, and by the same mode and route. Large variability

implies that travel time is unreliable, and this unpredictability causes travelers and shippers to have a challenge with planning their travel. The main cause of unreliability in travel time is congestion. With the occurrence of congestion, it could be expected that travel times become more variable, hence less reliable (National Academies of Sciences and Medicine,

* Corresponding author E-mail: mirzahosseini@eng.ikiu.ac.ir

2013).

Congestion can be studied in two categories: recurring and non-recurring. Recurring congestion is predictable and occurs when supply surpasses capacity, whereas the latter refers to conditions where an unexpected event occurs, such as crashes, inclement weather, work zones, and so on (Mahmassani et al., 2014).

Studies have revealed that the average congestion level is continuing to grow in cities and regarding the points mentioned earlier, TTR is a key part of the congestion problem. Travelers try to lessen the negative effect of their tardiness by assigning additional time beyond typical travel time to ensure they arrive on time. Unfortunately, this extra time is associated with extra costs, which has not been considered in previous transportation analyses (Zegeer et al., 2014).

Due to its importance, reliability has been the subject of many studies. Different researchers have attempted to depict the context of reliability by utilizing different methods, including linear regression, simulation, Machine Learning (ML) methods, and so on. This study is an attempt to provide further insight into the effect of recurring congestion (morning and evening peak periods) on TTR measurement, that is Planning Time Index (PTI). What has made this study unique, is utilizing bagging regressors. The advantage of these regressors will be described in detail in the methodology section. The body of the paper is organized as follows: the rest of this section analyzes conducted studies in the field of TTR from initial points, dating back to 1968, to the present studies. In the second section, the material and methods will be described and further information on dataset will be represented. Section three discusses modeling procedure and by utilizing scatter plots, depicts how congestion can affect PTI. Finally, the conclusion in Section 4 is represented.

The initial step of research in the field of congestion and travel time reliability started with Gaver Jr (1968)'s study which looked

at the policy choices that occur when both tardiness and an undesirable early departure are penalized. Connectivity reliability and travel time reliability were then introduced by Iida (1999) to address core ideas, unsolved challenges, and future prospects of road network reliability analysis. The fact that reducing travel time uncertainty is as important as saving time, was pointed out by Chen et al. (2002).

Later on, researchers attempted to calculate and assess travel time reliability and its effect on different aspects of transportation systems' behavior. The importance of travel time reliability as a decisive factor affecting travelers' route choice decisions was studied by Liu et al. (2004). Emam and Al-Deek (2006) created a novel approach for calculating travel time reliability using real-world traffic data from Florida's I-4 corridor. Lyman and Bertini (2008) predicted the reliability of travel time on a specific corridor by using the archived Intelligent Transportation System (ITS) data and investigating use of the measured travel time reliability indices for enhancing real-time transportation. To examine travel time reliability in New York City, three travel time reliability metrics were used by Yazici et al. (2012) to assess the influence of New York City's urban grid network on travel time. Wang et al. (2017) established a system for estimating highway vehicle travel time reliability for transportation planning utilizing probe GPS data. Also, Zheng et al. (2018) concluded that travelers' route and departure time decisions are influenced by the expected travel time and its reliability. In addition to the study of Liu et al. (2004), Li et al. (2019) investigated travel time reliability as a critical element influencing passenger behaviors. They used the Lempel-Ziv algorithm to make their study unique. Moghaddam et al. (2019) looked at how travelers perceive and respond to travel time information and its reliability in terms of route choice behavior, as measured by a driving simulator and a stated preference (SP) survey.

As another wave of modeling in the field of travel time reliability, researchers focused on congestion and factors that could cause it. Hojati et al. (2016) defined the Extra Buffer Time Index (EBTI) to quantify traffic incidents' effects on motorways TTR. The type of incident and the time it takes for travelers to arrive at their destination were factors that might also impact EBTI. Samal and Das (2020) intended to investigate and assess the possibility of modeling congestion metrics under diverse traffic scenarios in the Patia region. Gu et al. (2020) performed a review of studies on transportation network performance under perturbations to address reliability, vulnerability, and resilience in networks. They determined that although these notions differ in terms of focus, measurement, and application, their outcomes are not different. Zhang and Chen (2019) developed an integrated data mining framework based on decision tree and quantile regression approaches to identify periods with varying traffic characteristics and evaluate the impact of rain and snow events on both congestion and system reliability.

As the importance of TTR became more and more, many studies attempted to utilize novel approaches to address previous concerns and problems. Relying on the Cornish-Fisher expansion, Zang et al. (2018) used the travel time percentile function and provided a closed-form, adaptable, and high-quality technique that was sufficiently adaptive to predict the percentile function of various Travel Time Distributions (TTDs). Ghader et al. (2019) utilized Cumulative Prospect Theory (CPT) to study how travel mode choice is affected by travel time reliability. Their main focus was on mode choice, but their model could be extended to other choice dimensions. Chen and Fan (2019) provided a systematic framework for assessing TTR on highway segments in Charlotte, North Carolina. The numerical findings clearly demonstrated that TTR patterns in each case were unique, as well as on various days of the week and

weather conditions. The principal focus of Saedi et al. (2020) was to enhance the estimation of network travel time reliability by utilizing network partitioning. The results of Chen and Fan (2020) are noteworthy because they provided a systematic framework to evaluate TTR on various types of highway segments throughout a corridor. They realized that the Burr distribution could give the highest acceptance rate when different Times Of Day (TOD) and Days Of Week (DOW) were considered. Zhu et al. (2021) provided numerous categories of perceived information based on a generalized Bayesian traffic model to simulate travelers' daily route choice behavior in terms of travel time reliability. Zhang, et al. (2021) investigated statistical approaches for clustering Cumulative Distribution Functions (CDFs) of travel times at the segment level into an optimum number of homogenous clusters that could include all essential information about distributions. Hoseinzadeh et al. (2021) combined crowdsourced data from Waze to develop an algorithm for the hourly measurement of Level Of Service (LOS). Afandizadeh Zargari et al. (2023) evaluated the effect of recurrent congestion on travel time reliability on a 1.467-mile section of the I-64 highway in Virginia. They proposed Grey Models (GM) and Random Forest Regression (RFR) as evaluation tools. Chen et al. (2022) developed a Collaborative Intelligent Transportation System (CITS) to estimate present and future travel times. The findings indicated that the K-Nearest Neighbor (KNN) model could deliver the most accurate short-term forecasts. Also, Udayanga et al. (2022) recommended using crowdsourced travel time data from Google distance matrix Application Programming Interface (API) as a feasible approach to combine traffic congestion monitoring in their study. Meng et al. (2022) investigated the performance of the Support Vector Machine (SVM) in predicting short-term travel times.

Delving deep into the chronological

trajectory of the literature review reveals that travel time reliability was just a simple notion in the beginning, but as time went on, researchers concluded that TTR affects various parts of the transportation system. The tools for addressing these concerns were basic but became more complicated later.

2. Materials and Methods

To talk about bagging regressors, first, a background about ensemble methods is needed, then different branches of ensemble methods will be briefly discussed. Afterwards, bagging methods will be illustrated and finally, supplementary explanations about bagging regressor will be represented.

Ensemble methods aim to increase generalizability/robustness over a single estimator by combining the predictions of numerous base estimators created using a specific learning methodology. Typically, two groups of ensemble approaches are distinguished: averaging and boosting methods. The core argument behind averaging approaches is to create numerous independent estimators, then average their estimations. Because its variance is decreased, the composite estimator is generally better than the individual single-base estimators. Unlike the first method, the latter produces sequential base estimators, and the composite estimator's bias is reduced. This method merges numerous weak models into a powerful ensemble. Examples of averaging methods are bagging methods and forest of randomized trees. Also, AdaBoost and gradient tree boosting are examples of boosting methods. The interested reader is referred to the cited references for a detailed description of the methods (Zhou, 2012)

Bagging methods are a class of algorithms in which numerous samples of black-box estimators are built on random subsets of the original training set, and then their individual estimations are aggregated to generate a final prediction. These

techniques are used to lessen the variation of a base estimator by including randomization into its development mechanism and then constructing an ensemble from it. Under many circumstances, bagging methods are a fairly straightforward approach to improve compared to a single model without changing the underlying base algorithm. Bagging approaches perform best with strong and complicated models because they reduce overfitting. Please refer to Kadiyala and Kumar (2018) for further information.

As an ensemble estimator, a bagging regressor fits base regressors of the main database and then aggregates their individual forecasts (through voting or averaging) to generate a final prediction. A meta-estimator of this type is often used to minimize the variance of a black-box estimator by incorporating randomization into its building mechanism and then constructing an ensemble from it (Pedregosa et al., 2011). The parameters of the bagging regressor are as follows: base estimator (the base estimator that fits on subsets of the dataset which are created randomly), number of estimators (number of base estimators in the ensemble), maximum samples (number of samples which are drawn to train base estimators), maximum features (number of features to train base estimator), bootstrap (how samples are drawn, with or without replacement), bootstrap features (if features are extracted with replacement), out-of-bag score (determines whether out-of-bag samples are utilized for estimating the generalization error), warm start, number of jobs, random state, and verbose. The utilized methods in this study are Bagging regressor with:

- Stochastic Gradient Descent (SGD) base estimator (Mazloumi et al., 2022)
- Passive Aggressive base estimator (Mastelini et al., 2022)
- Ridge base estimator (Abdulhafedh, 2022)
- Linear base estimator (Shabbir et al.,

- 2022)
- Support Vector Regression (SVR) (Kernel = Radial Basis Function (RBF)) base estimator (Ara et al., 2020)
 - Support Vector Regression (SVR), (Kernel = Polynomial (Poly)) base estimator (Ara et al., 2020)
 - RANdom SAMple Consensus (RANSAC) base estimator (Almejr et al., 2022)
 - Decision Tree (DT) base estimator (Abdulhafedh, 2022)
 - Theil-Sen base estimator (Szafranski and Duan, 2022)
 - Gradient Boosting (GB) base estimator (Khan et al., 2022)
 - Random Forest (RF) base estimator (Zhan et al., 2021)
 - Polynomial (Poly) base estimator (Adhistian and Wibowo, 2022)
 - Support Vector Regression (SVR), (Kernel = linear) base estimator (Sarang, 2023)
 - Bayesian ridge base estimator (Gacto et al., 2019)
 - Quantile base estimator (Kang and Hansen, 2021)

For more information, you can also refer to “sklearn ensemble module” in Python. In SVR models, the type of kernel function has been written in parentheses.

The dataset of this paper is composed of two elements, namely the Travel Time Reliability (TTR) metric and congestion indices. As the dependent variable, congestion is defined as the ratio of traffic speed over a one-hour period to the free flow speed. This definition for congestion was directly extracted from INRIX. INRIX was also used to obtain the TTR and congestion statistics.

Every day, billions of data points are used by INRIX to gather anonymized data on traffic congestion, traffic incidents, and weather-related road conditions. The data has multiple sources, including connected cars and mobile devices, cameras and sensors on the road, major events that are expected to impact traffic, and other sources. This analysis is conducted by the

company to comprehend mobility trends. To put it another way, INRIX offers cutting-edge solutions for real-time traffic. The interested reader can refer to INRIX’s website for further information.

To calculate congestion, INRIX uses a multi-step process. First, the Space Mean Speed (SMS) is calculated for the desired segment. In fact, SMS is the mean speed of all cars crossing a specific segment of road over a given period. Then, this speed is divided by free flow speed to calculate the congestion of that segment for the specific period.

Also, the Planning Time Index (PTI), defined as the ratio of the 95th percentile of travel time to the free-flow travel time, is the independent variable (Lyman and Bertini, 2008). To extract PTI, INRIX builds a statistical distribution by the travel time data of vehicles passing a specific segment. Then, the 95th percentile of this distribution will be divided to travel time of free flow, which can be easily calculated, and PTI will be extracted.

The data collection period ranges from February 1, 2018, to October 31, 2018, for 273 days, and only considers workdays. Every day is split into 24 equal sections. Analyzing the trend of mean congestion values using the two-tailed comparing mean has proven that there are two peak periods in a day, namely morning peak and evening peak. The morning peak is from 7 a.m. until 9 a.m. and the evening peak starts at 15 and ends at 18. Each observation represents the average amount of congestion (the ratio of flow speed in one hour to free flow speed) and PTI of vehicles that have passed through the 1.467-mile segment during one hour. Also, it should be pointed out that all passing vehicles, regardless of their type (the information is gathered anonymously from cars, trucks, and many other types of vehicles) were considered. Furthermore, the number of observations (samples) that have been analyzed in this research for various days are as follows (The numbers in the parenthesis represent morning and evening peaks, respectively): Monday (78,117),

Tuesday (74,111), Wednesday (76,114), Thursday (78,117), Friday (76,114). Table 1 summarizes the statistical features of morning and evening peaks. As a case study, in this paper, a road segment along the I-64 freeway in Chesapeake, Virginia was analyzed, which is the same as Afandizadeh Zargari et al. (2023) dataset in their research. This segment contains 3 sections whose lengths are 1.467, 0.036, and 0.777 miles, respectively. The focus is on the first segment, which is shown in Figure 1.

3. Results and Discussion

To better explain the advantages of using bagging regressors, the results of modeling, including coefficient of determination, Mean Squared Error (MSE), and the

stability ratio, are represented in Tables 2 to 6. Coefficient of determination, R^2 , explains the variability of factors that would be caused by its relationship to another factor, and MSE assesses the average squared difference between the observed and predicted values. Coefficient of determination and MSE (consequently RMSE) are among well-known measures for quantifying the quality of an estimator and numerous studies have taken the advantage of such measures, e.g. Nohekhan et al. (2022). Stability ratio, or simply, ratio, is the ratio of train set coefficient of determination to test set coefficient of determination and is a numerical criterion to show whether the model has overfitting or underfitting.

Table 1. Summary of PTI and congestion statistics

| Metrics | Peaks | Time periods | Statistics | | | | | |
|------------------|---------|--------------|------------|------|--------|------|-------|---------|
| | | | Min | Q1 | Median | Q3 | Max | Average |
| PTI | Morning | 7:00-8:00 | 1.0 | 1.1 | 2.1 | 3.4 | 20.3 | 2.9 |
| | | 8:00-9:00 | 1.0 | 1 | 1.4 | 2.8 | 20.3 | 2.4 |
| | Evening | 15:00-16:00 | 1.0 | 1.4 | 2.3 | 2.7 | 8.7 | 2.2 |
| | | 16:00-17:00 | 1.0 | 2.2 | 2.8 | 3.4 | 12.2 | 3.0 |
| | | 17:00-18:00 | 1.0 | 1.3 | 2.4 | 3.2 | 20.3 | 2.6 |
| Congestion × 100 | Morning | 7:00-8:00 | 10.1 | 44.1 | 76 | 98.4 | 100.0 | 69.8 |
| | | 8:00-9:00 | 9.0 | 61.1 | 92.9 | 100 | 100.0 | 79.0 |
| | Evening | 15:00-16:00 | 16.3 | 55.2 | 71.7 | 95 | 100.0 | 72.2 |
| | | 16:00-17:00 | 16.2 | 39.1 | 46.9 | 69.3 | 100.0 | 54.6 |
| | | 17:00-18:00 | 7.1 | 43.5 | 60.6 | 95.3 | 100.0 | 65.5 |

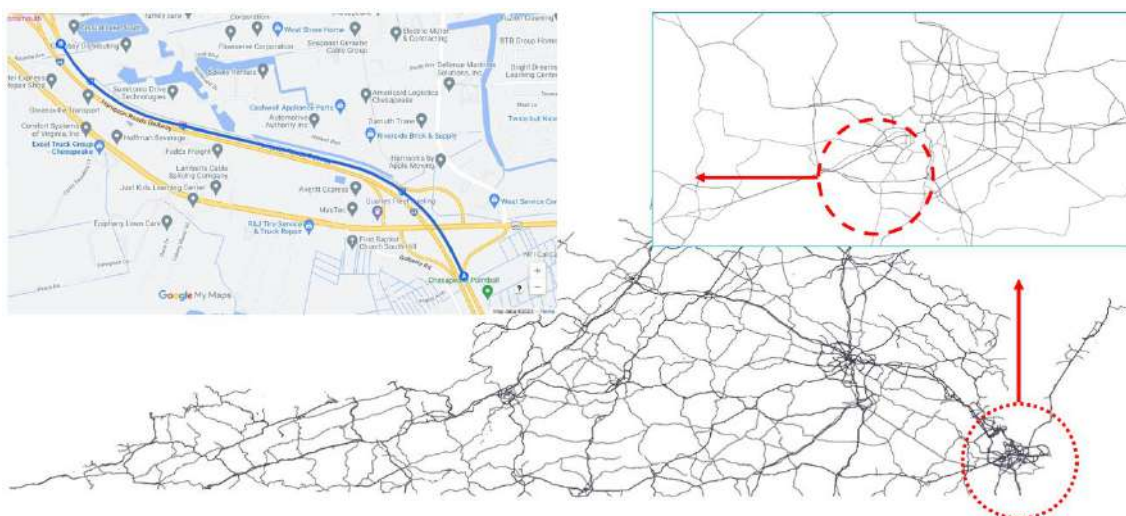


Fig. 1. Location of the sample segment (Source: Google Maps and Virginia shape files)

The ideal value for this ratio is one. When the ratio equals one, it means that the performance of the train set and test set is the same, in terms of coefficient of determination. When overfitting occurs, this ratio becomes bigger than one, and in the case of underfitting, this ratio is less than one. An in-depth review of the mentioned metrics can be found in Arias-Castro (2022).

To opt for the prior model, three metrics will be used: coefficient of determination, MSE, and ratio. The closer the coefficient of determination is to one, the better the model is (in both training set and test set). Also, the prior model has less error, so models with less MSE should be considered. Furthermore, overfitting and underfitting, which are common issues in machine learning models, are monitored through the stability ratio. Akaike Information Criterion (AIC), and Bayesian Information Criterion (BIC) are two statistical metrics that could be utilized to estimate the quality of each model, relative to each of the other models. AIC is simply used as a metric to compare the performance of models. The model with the lowest AIC offers the best fit. The absolute value of the AIC value is not important. For further information about these two metrics, please see Hastie et al. (2009).

As explicitly stated by Chakrabarti and Ghosh (2011), “The Bayesian Information Criterion (BIC) is more useful in selecting a correct model while the AIC is more appropriate in finding the best model for predicting future observations” since the purpose of this study is to predict fluctuations of PTI as congestion changes, AIC will be used for selecting prior model.

For Mondays, as the results of Tables 2a and 2b reveal, AIC suggests that the

bagging regressor with the gradient boosting as the base estimator is the prior model in both morning and evening peaks. The results of modeling for Tuesdays are shown in Tables 3a and 3b. As it can be seen, in both morning and evening peaks, gradient boosting regressor has the best set of metrics and is opted for the modeling process. The same story goes true for morning and evening peaks of Wednesdays. Gradient boosting has shown the most satisfying performance metrics for both peaks and was chosen as the prior model of this day.

For Thursdays, as the results of Tables 5a and 5b reveal, gradient boosting is the prior choice for both peaks and will be included in the sensitivity analysis stage. Finally, the gradient boosting regressor is the prior model of both peaks for Fridays. Surprisingly, the results show that gradient boosting is the top model of all days in both peaks.

As the main method of this study (the prior model) is an ML method, sensitivity plots are very useful tools to visualize how congestion influences PTI. Scatter plots are simple and have made interpretation and usability easy for everyone. After choosing the prior models of different days and peaks, this section is assigned to depict the sensitivity analysis plot. This step will depict how speed reduction (hence congestion reduction) will affect PTI. The intensity of increase is somehow different. This paper uses bagging and bootstrapping to improve the model results and more accurately predict the PTI. To do so, by using different training sets, hundreds of models were randomly produced by bootstrapping from the original dataset to produce these plots.

Table 2. Modeling results for Mondays-morning peak

| Models | Training | | | Validation | | | Stability |
|-------------------------|----------------|------|--------|----------------|------|--------|-----------|
| | R ² | MSE | AIC | R ² | MSE | AIC | |
| SVR (Kernel = RBF) | 0.55 | 2.46 | -100.2 | 0.72 | 0.81 | -27.09 | 0.76 |
| SVR (Kernel = linear) | 0.53 | 2.54 | -100.2 | 0.69 | 0.91 | -27.09 | 0.77 |
| RANSAC regressor | 0.6 | 2.19 | -104.2 | 0.77 | 0.69 | -31.09 | 0.78 |
| Decision tree regressor | 0.59 | 2.21 | -100.2 | 0.76 | 0.71 | -27.09 | 0.78 |
| TheilSen regressor | 0.62 | 2.07 | -110.2 | 0.78 | 0.64 | -37.09 | 0.79 |

| | | | | | | | |
|---------------------------------------|------|------|---------|------|------|--------|------|
| Passive aggressive regressor | 0.64 | 1.96 | -94.2 | 0.8 | 0.6 | -21.09 | 0.8 |
| SGD regressor | 0.58 | 2.28 | -84.2 | 0.71 | 0.84 | -11.09 | 0.81 |
| Ridge | 0.62 | 2.06 | -104.2 | 0.76 | 0.7 | -31.09 | 0.82 |
| Linear regression | 0.68 | 1.73 | -94.2 | 0.83 | 0.49 | -21.09 | 0.82 |
| Quantile regressor | 0.66 | 1.87 | -96.2 | 0.8 | 0.6 | -23.09 | 0.82 |
| Bayesian ridge | 0.65 | 1.88 | -112.2 | 0.79 | 0.61 | -39.09 | 0.83 |
| SVR (kernel = poly, degree = 2) | 0.79 | 1.12 | -88.2 | 0.86 | 0.41 | -15.09 | 0.92 |
| Polynomial regression | 0.88 | 0.64 | -100.2 | 0.87 | 0.39 | -27.09 | 1.02 |
| Gradient boosting regressor | 0.87 | 0.73 | -112.2 | 0.84 | 0.48 | -39.09 | 1.03 |
| Random forest regressor | 0.92 | 0.42 | -80.2 | 0.87 | 0.4 | -7.09 | 1.07 |
| Quantile regressor | 0.7 | 0.42 | -187.77 | 0.76 | 0.28 | -62.91 | 0.91 |
| Passive aggressive regressor ridge | 0.69 | 0.44 | -185.77 | 0.74 | 0.3 | -60.91 | 0.93 |
| Bayesian ridge | 0.67 | 0.45 | -195.77 | 0.72 | 0.33 | -70.91 | 0.94 |
| TheilSen regressor | 0.69 | 0.43 | -203.77 | 0.74 | 0.3 | -78.91 | 0.94 |
| RANSAC regressor | 0.66 | 0.47 | -201.77 | 0.68 | 0.37 | -76.91 | 0.98 |
| RANSAC regressor | 0.66 | 0.47 | -195.77 | 0.67 | 0.37 | -70.91 | 0.98 |
| Decision tree regressor | 0.66 | 0.48 | -191.77 | 0.66 | 0.39 | -66.91 | 0.99 |
| SVR (Kernel = linear) | 0.59 | 0.56 | -191.77 | 0.58 | 0.48 | -66.91 | 1.02 |
| SVR (Kernel = RBF) | 0.63 | 0.52 | -191.77 | 0.62 | 0.44 | -66.91 | 1.02 |
| Linear regression | 0.75 | 0.35 | -185.77 | 0.72 | 0.32 | -60.91 | 1.04 |
| Gradient boosting regressor | 0.88 | 0.17 | -203.77 | 0.82 | 0.21 | -78.91 | 1.08 |
| SGD regressor | 0.44 | 0.77 | -175.77 | 0.4 | 0.69 | -50.91 | 1.11 |
| SVR (Kernel = poly, degree = 2) | 0.89 | 0.15 | -179.77 | 0.79 | 0.24 | -54.91 | 1.12 |
| Random forest regressor | 0.95 | 0.07 | -171.77 | 0.79 | 0.24 | -46.91 | 1.2 |
| Polynomial regression | 0.96 | 0.05 | -191.77 | 0.75 | 0.29 | -66.91 | 1.28 |

Table 3. Modeling results for Tuesdays-morning peak

| Models | Training | | | Validation | | | Stability |
|---------------------------------|----------------|------|---------|----------------|------|--------|-----------|
| | R ² | MSE | AIC | R ² | MSE | AIC | |
| SVR (Kernel = linear) | 0.52 | 2.62 | -95.5 | 0.66 | 1.45 | -19.46 | 0.8 |
| SGD regressor | 0.62 | 2.11 | -79.5 | 0.71 | 1.21 | -3.46 | 0.86 |
| SVR (Kernel = RBF) | 0.55 | 2.46 | -95.5 | 0.64 | 1.53 | -19.46 | 0.87 |
| ridge | 0.66 | 1.87 | -99.5 | 0.76 | 1.01 | -23.46 | 0.87 |
| Passive aggressive regressor | 0.66 | 1.85 | -89.5 | 0.76 | 1 | -13.46 | 0.87 |
| TheilSen regressor | 0.64 | 1.98 | -105.5 | 0.74 | 1.11 | -29.46 | 0.87 |
| RANSAC regressor | 0.62 | 2.08 | -99.5 | 0.72 | 1.2 | -23.46 | 0.87 |
| Quantile regressor | 0.69 | 1.73 | -91.5 | 0.78 | 0.93 | -15.46 | 0.88 |
| Bayesian ridge | 0.68 | 1.77 | -107.5 | 0.76 | 1 | -31.46 | 0.89 |
| Decision tree regressor | 0.71 | 1.58 | -95.5 | 0.78 | 0.92 | -19.46 | 0.91 |
| Linear regression | 0.84 | 0.91 | -89.5 | 0.82 | 0.76 | -13.46 | 1.02 |
| Gradient boosting regressor | 0.97 | 0.18 | -107.5 | 0.79 | 0.88 | -31.46 | 1.22 |
| SVR (Kernel = poly, degree = 2) | 0.96 | 0.21 | -83.5 | 0.78 | 0.91 | -7.46 | 1.23 |
| Random forest regressor | 0.99 | 0.06 | -75.5 | 0.77 | 0.97 | 0.54 | 1.29 |
| Polynomial regression | 0.98 | 0.1 | -95.5 | 0.76 | 1 | -19.46 | 1.29 |
| Bayesian ridge | 0.66 | 0.64 | -203.04 | 0.53 | 1.23 | -71.54 | 1.25 |
| Quantile regressor | 0.66 | 0.63 | -187.04 | 0.52 | 1.24 | -55.54 | 1.26 |
| Random forest regressor | 0.97 | 0.05 | -171.04 | 0.77 | 0.6 | -39.54 | 1.27 |
| ridge | 0.64 | 0.68 | -195.04 | 0.5 | 1.32 | -63.54 | 1.28 |
| Linear regression | 0.78 | 0.41 | -185.04 | 0.6 | 1.05 | -53.54 | 1.31 |
| SVR (Kernel = linear) | 0.49 | 0.96 | -191.04 | 0.37 | 1.64 | -59.54 | 1.32 |
| Gradient boosting regressor | 0.96 | 0.08 | -203.04 | 0.72 | 0.73 | -71.54 | 1.32 |
| SVR (Kernel = poly, degree = 2) | 0.96 | 0.07 | -179.04 | 0.72 | 0.73 | -47.54 | 1.34 |
| TheilSen regressor | 0.6 | 0.76 | -201.04 | 0.44 | 1.45 | -69.54 | 1.34 |
| RANSAC regressor | 0.6 | 0.76 | -195.04 | 0.44 | 1.46 | -63.54 | 1.35 |
| SGD regressor | 0.5 | 0.94 | -175.04 | 0.37 | 1.65 | -43.54 | 1.35 |
| SVR (kernel = RBF) | 0.57 | 0.81 | -191.04 | 0.42 | 1.53 | -59.54 | 1.37 |
| Decision tree regressor | 0.82 | 0.34 | -191.04 | 0.59 | 1.06 | -59.54 | 1.38 |
| Polynomial regression | 0.97 | 0.05 | -191.04 | 0.7 | 0.79 | -59.54 | 1.4 |
| Passive aggressive regressor | 0.5 | 0.95 | -185.04 | 0.34 | 1.72 | -53.54 | 1.45 |

Table 4. Modeling results for Wednesdays-morning peak

| Models | Training | | | Validation | | | Stability |
|---------------------------------|----------------|------|---------|----------------|------|--------|-----------|
| | R ² | MSE | AIC | R ² | MSE | AIC | |
| SVR (Kernel = linear) | 0.35 | 6.2 | -93.94 | 0.74 | 0.6 | -20.46 | 0.48 |
| SVR (Kernel = RBF) | 0.41 | 5.68 | -93.94 | 0.79 | 0.48 | -20.46 | 0.51 |
| RANSAC regressor | 0.45 | 5.24 | -97.94 | 0.83 | 0.39 | -24.46 | 0.55 |
| Decision tree regressor | 0.49 | 4.88 | -93.94 | 0.86 | 0.32 | -20.46 | 0.57 |
| TheilSen regressor | 0.49 | 4.94 | -103.94 | 0.84 | 0.37 | -30.46 | 0.58 |
| Passive aggressive regressor | 0.52 | 4.63 | -87.94 | 0.76 | 0.55 | -14.46 | 0.68 |
| SGD regressor | 0.55 | 4.32 | -77.94 | 0.74 | 0.59 | -4.46 | 0.74 |
| ridge | 0.58 | 4 | -97.94 | 0.55 | 1.03 | -24.46 | 1.06 |
| Quantile regressor | 0.59 | 3.95 | -89.94 | 0.54 | 1.05 | -16.46 | 1.09 |
| Random forest regressor | 0.92 | 0.75 | -73.94 | 0.82 | 0.41 | -0.46 | 1.12 |
| Gradient boosting regressor | 0.93 | 0.66 | -105.94 | 0.81 | 0.43 | -32.46 | 1.15 |
| Polynomial regression | 0.96 | 0.35 | -93.94 | 0.81 | 0.43 | -20.46 | 1.19 |
| SVR (Kernel = poly, degree = 2) | 0.88 | 1.12 | -81.94 | 0.72 | 0.64 | -8.46 | 1.23 |
| Bayesian ridge | 0.59 | 3.95 | -105.94 | 0.47 | 1.2 | -32.46 | 1.24 |
| Linear regression | 0.81 | 1.87 | -87.94 | 0.77 | 0.31 | -31.46 | 1.02 |
| SVR (Kernel = linear) | 0.55 | 0.73 | -184.96 | 0.67 | 0.44 | -55.99 | 0.83 |
| SGD regressor | 0.5 | 0.82 | -168.96 | 0.59 | 0.54 | -39.99 | 0.84 |
| ridge | 0.64 | 0.58 | -188.96 | 0.76 | 0.32 | -59.99 | 0.85 |
| SVR (Kernel = RBF) | 0.59 | 0.67 | -184.96 | 0.69 | 0.41 | -55.99 | 0.85 |
| TheilSen regressor | 0.63 | 0.61 | -194.96 | 0.74 | 0.35 | -65.99 | 0.85 |
| RANSAC regressor | 0.62 | 0.62 | -188.96 | 0.73 | 0.36 | -59.99 | 0.85 |
| Passive aggressive regressor | 0.61 | 0.64 | -178.96 | 0.71 | 0.39 | -49.99 | 0.86 |
| Quantile regressor | 0.68 | 0.53 | -180.96 | 0.78 | 0.29 | -51.99 | 0.87 |
| Bayesian ridge | 0.68 | 0.53 | -196.96 | 0.78 | 0.29 | -67.99 | 0.87 |
| Decision tree regressor | 0.72 | 0.46 | -184.96 | 0.82 | 0.24 | -55.99 | 0.88 |
| Linear regression | 0.78 | 0.35 | -178.96 | 0.74 | 0.34 | -49.99 | 1.05 |
| SVR (Kernel = poly, degree = 2) | 0.95 | 0.09 | -172.96 | 0.74 | 0.35 | -43.99 | 1.28 |
| Random forest regressor | 0.97 | 0.05 | -164.96 | 0.74 | 0.35 | -35.99 | 1.32 |
| Gradient boosting regressor | 0.95 | 0.07 | -196.96 | 0.71 | 0.38 | -67.99 | 1.34 |
| Polynomial regression | 0.96 | 0.06 | -184.96 | 0.68 | 0.42 | -55.99 | 1.41 |

Table 5. Modeling results for Thursdays-morning peak

| Models | Training | | | Validation | | | Stability |
|---------------------------------|----------------|------|---------|----------------|------|--------|-----------|
| | R ² | MSE | AIC | R ² | MSE | AIC | |
| SVR (Kernel = linear) | 0.33 | 7.02 | -96.45 | 0.47 | 3.04 | -17.14 | 0.7 |
| TheilSen regressor | 0.45 | 5.78 | -106.45 | 0.55 | 2.57 | -27.14 | 0.82 |
| RANSAC regressor | 0.43 | 5.97 | -100.45 | 0.52 | 2.71 | -21.14 | 0.82 |
| SVR (Kernel = RBF) | 0.39 | 6.37 | -96.45 | 0.47 | 2.99 | -17.14 | 0.82 |
| Passive aggressive regressor | 0.51 | 5.12 | -90.45 | 0.61 | 2.24 | -11.14 | 0.84 |
| SGD regressor | 0.54 | 4.79 | -80.45 | 0.64 | 2.06 | -1.14 | 0.85 |
| ridge | 0.57 | 4.49 | -100.45 | 0.63 | 2.08 | -21.14 | 0.9 |
| Decision tree regressor | 0.65 | 3.66 | -96.45 | 0.69 | 1.75 | -17.14 | 0.94 |
| Bayesian ridge | 0.6 | 4.22 | -108.45 | 0.59 | 2.32 | -29.14 | 1.01 |
| SVR (Kernel = poly, degree = 2) | 0.9 | 1.03 | -84.45 | 0.79 | 1.18 | -5.14 | 1.14 |
| Random forest regressor | 0.97 | 0.34 | -76.45 | 0.83 | 0.98 | 2.86 | 1.17 |
| Quantile regressor | 0.6 | 4.18 | -92.45 | 0.51 | 2.77 | -13.14 | 1.17 |
| Gradient boosting regressor | 0.98 | 0.22 | -108.45 | 0.8 | 1.13 | -29.14 | 1.22 |
| Polynomial regression | 0.96 | 0.41 | -96.45 | 0.77 | 1.32 | -17.14 | 1.25 |
| Linear regression | 0.8 | 2.07 | -90.45 | 0.63 | 2.11 | -11.14 | 1.28 |
| SVR (Kernel = linear) | 0.2 | 5.11 | -193.05 | 0.39 | 1.82 | -62.21 | 0.53 |
| SVR (Kernel = RBF) | 0.28 | 4.62 | -193.05 | 0.47 | 1.56 | -62.21 | 0.59 |
| TheilSen regressor | 0.33 | 4.28 | -203.05 | 0.55 | 1.32 | -72.21 | 0.6 |
| SGD regressor | 0.36 | 4.08 | -177.05 | 0.6 | 1.19 | -46.21 | 0.61 |
| RANSAC regressor | 0.34 | 4.23 | -197.05 | 0.56 | 1.31 | -66.21 | 0.61 |
| Passive aggressive regressor | 0.39 | 3.89 | -187.05 | 0.63 | 1.08 | -56.21 | 0.62 |
| ridge | 0.41 | 3.76 | -197.05 | 0.65 | 1.03 | -66.21 | 0.64 |
| Decision tree regressor | 0.56 | 2.8 | -193.05 | 0.88 | 0.36 | -62.21 | 0.64 |

| | | | | | | | |
|---------------------------------|------|------|---------|------|------|--------|------|
| Quantile regressor | 0.44 | 3.6 | -189.05 | 0.65 | 1.04 | -58.21 | 0.68 |
| Bayesian ridge | 0.44 | 3.57 | -205.05 | 0.64 | 1.08 | -74.21 | 0.7 |
| SVR (Kernel = poly, degree = 2) | 0.89 | 0.71 | -181.05 | 0.93 | 0.21 | -50.21 | 0.96 |
| Gradient boosting regressor | 0.96 | 0.27 | -205.05 | 0.91 | 0.25 | -74.21 | 1.05 |
| Random forest regressor | 0.97 | 0.18 | -173.05 | 0.92 | 0.24 | -42.21 | 1.06 |
| Polynomial regression | 0.99 | 0.08 | -193.05 | 0.9 | 0.29 | -62.21 | 1.09 |
| Linear regression | 0.72 | 1.8 | -187.05 | 0.57 | 1.29 | -56.21 | 1.27 |

Table 6. Modeling results for Fridays-morning peak

| Models | Training | | | Validation | | | Stability |
|---------------------------------|----------------|------|---------|----------------|------|--------|-----------|
| | R ² | MSE | AIC | R ² | MSE | AIC | |
| SVR (Kernel = linear) | 0.27 | 7.63 | -119.87 | 0.91 | 0.04 | -58.81 | 0.3 |
| RANSAC regressor | 0.22 | 8.15 | -123.87 | 0.65 | 0.14 | -62.81 | 0.34 |
| SVR (Kernel = RBF) | 0.31 | 7.3 | -119.87 | 0.82 | 0.07 | -58.81 | 0.37 |
| Passive aggressive regressor | 0.43 | 6.03 | -113.87 | 0.95 | 0.02 | -52.81 | 0.45 |
| Decision tree regressor | 0.42 | 6.15 | -119.87 | 0.87 | 0.05 | -58.81 | 0.48 |
| ridge | 0.59 | 4.31 | -123.87 | 0.77 | 0.09 | -62.81 | 0.77 |
| SGD regressor | 0.61 | 4.09 | -103.87 | 0.64 | 0.14 | -42.81 | 0.96 |
| SVR (kernel = poly, degree = 2) | 0.92 | 0.89 | -107.87 | 0.93 | 0.03 | -46.81 | 0.98 |
| Gradient boosting regressor | 0.97 | 0.31 | -131.87 | 0.93 | 0.03 | -70.81 | 1.05 |
| Random forest regressor | 0.99 | 0.13 | -99.87 | 0.94 | 0.02 | -38.81 | 1.05 |
| Polynomial regression | 0.99 | 0.15 | -119.87 | 0.93 | 0.03 | -58.81 | 1.06 |
| Linear regression | 0.94 | 0.68 | -113.87 | 0.44 | 0.22 | -52.81 | 2.15 |
| TheilSen regressor | 0.67 | 3.44 | -129.87 | 0.19 | 0.32 | -68.81 | 3.47 |
| Quantile regressor | 0.65 | 3.66 | -115.87 | 0.82 | 0.29 | -52.81 | 0.89 |
| Bayesian ridge | 0.69 | 3.22 | -131.87 | 0.8 | 0.33 | -52.81 | 0.92 |
| SVR (Kernel = linear) | 0.59 | 0.9 | -167.91 | 0.73 | 0.44 | -46.48 | 0.8 |
| SVR (Kernel = RBF) | 0.65 | 0.76 | -167.91 | 0.78 | 0.36 | -46.48 | 0.84 |
| SGD regressor | 0.61 | 0.84 | -151.91 | 0.73 | 0.44 | -30.48 | 0.84 |
| RANSAC regressor | 0.67 | 0.72 | -171.91 | 0.8 | 0.33 | -50.48 | 0.84 |
| TheilSen regressor | 0.69 | 0.66 | -177.91 | 0.82 | 0.3 | -56.48 | 0.85 |
| Passive aggressive regressor | 0.67 | 0.73 | -161.91 | 0.78 | 0.36 | -40.48 | 0.85 |
| ridge | 0.71 | 0.62 | -171.91 | 0.82 | 0.29 | -50.48 | 0.87 |
| Quantile regressor | 0.73 | 0.59 | -163.91 | 0.82 | 0.29 | -42.48 | 0.89 |
| Bayesian ridge | 0.73 | 0.58 | -179.91 | 0.81 | 0.3 | -58.48 | 0.9 |
| Linear regression | 0.82 | 0.39 | -161.91 | 0.85 | 0.24 | -40.48 | 0.96 |
| Decision tree Regressor | 0.87 | 0.29 | -167.91 | 0.9 | 0.16 | -46.48 | 0.97 |
| Gradient boosting regressor | 0.96 | 0.09 | -179.91 | 0.9 | 0.17 | -58.48 | 1.07 |
| SVR (Kernel = poly, degree = 2) | 0.95 | 0.1 | -155.91 | 0.89 | 0.18 | -34.48 | 1.08 |
| Random forest regressor | 0.97 | 0.06 | -147.91 | 0.85 | 0.24 | -26.48 | 1.14 |
| Polynomial regression | 0.97 | 0.08 | -167.91 | 0.84 | 0.26 | -46.48 | 1.15 |

Figures 2 to 6, in two peaks: a) for the morning peak, and b) for the evening peak, represent the fluctuations in a scatter plot. According to Chen and Fan (2019), it is reliable when PTI is below 1.5. When it surpasses 1.5 but does not reach 2.5, it is labeled as moderately to heavily unreliable, and for the values of PTI bigger than 2.5, it is said to be extremely unreliable. Eqs. (1-3) show this classification numerically.

$$PTI < 1.5: \text{Reliable} \quad (1)$$

$$1.5 \leq PTI \leq 2.5: \text{Moderate to heavy} \quad (2)$$

$$PTI > 2.5: \text{Extremely unreliable} \quad (3)$$

As Figures 2 to 6 suggest, in both peaks, regardless of the day, when congestion is reduced to 0.9, PTI reaches 1.5. It means that a 10% reduction in speed (compared to free-flow speed), causes a 50% increase in travel time compared to free-flow travel time. In other words, when congestion is in the range of 1 to 0.9, PTI is reliable in both peaks. Somewhere between 0.7 and 0.75 is a point where the PTI reaches 2.5, meaning that PTI is leaving the moderate or heavy unreliable part, and enters an extremely unreliable phase. It is worth noting that, the intensity of PTI increase is slight until congestion is 0.5, then as congestion

decreases, the PTI increase will be more severe. This study's findings are compatible with the results of utilizing Random Forest (RF) regression, which was the main focus by Afandizadeh Zargari et al. (2023).

As the main aim of this study is to analyze on planning level, sub-temporal variations including possible variability

between the months were excluded. Undoubtedly, such variations are interesting to study, but could be the subject of later studies, and is out of the scope of this manuscript. Also, the type of road, road geometry, and the type of traffic (modal split) can influence the results but requires more detailed data.

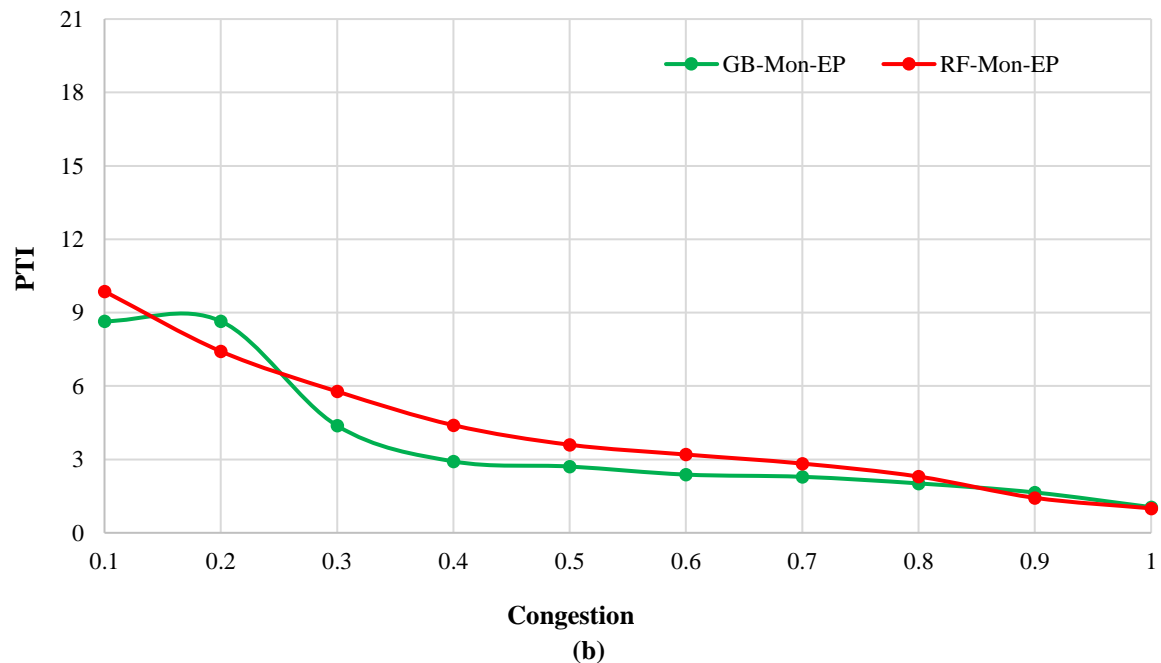
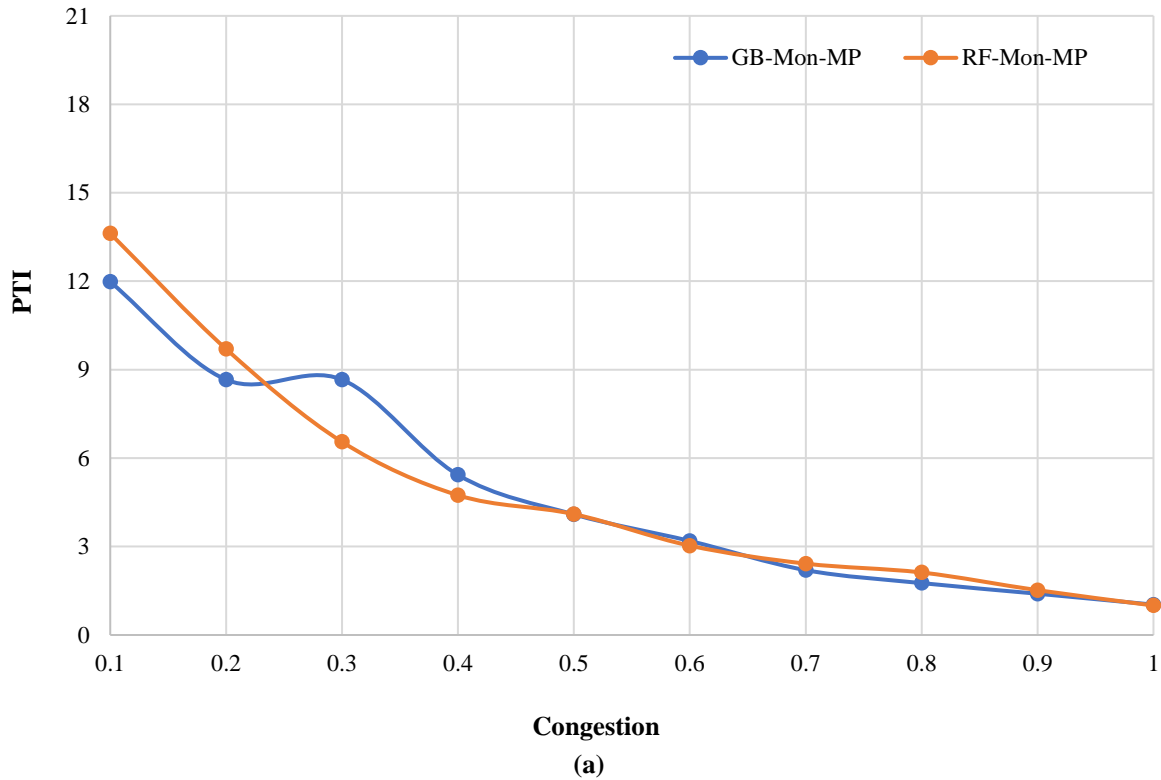


Fig. 2. a) Comparison between GB and RF modeling results- Monday morning peak; and b) Comparison between GB and RF modeling results- Monday evening peak

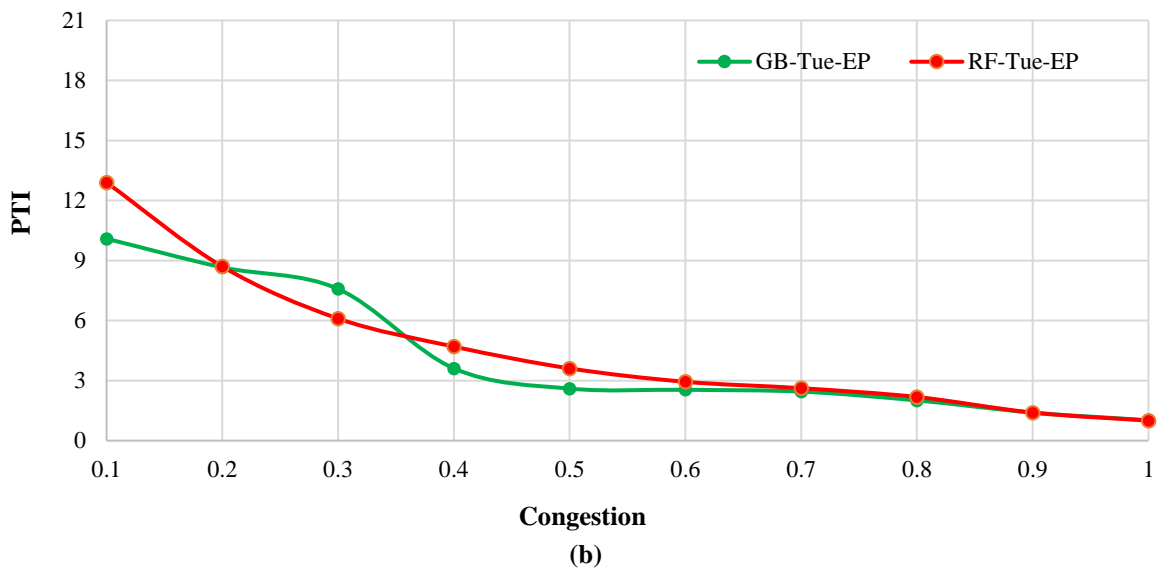
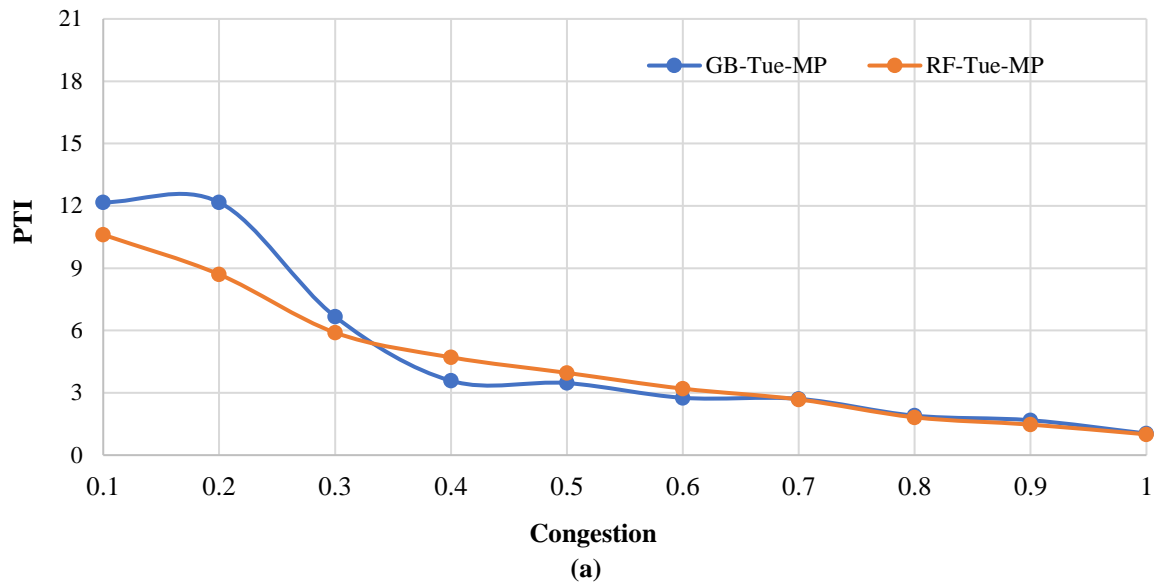
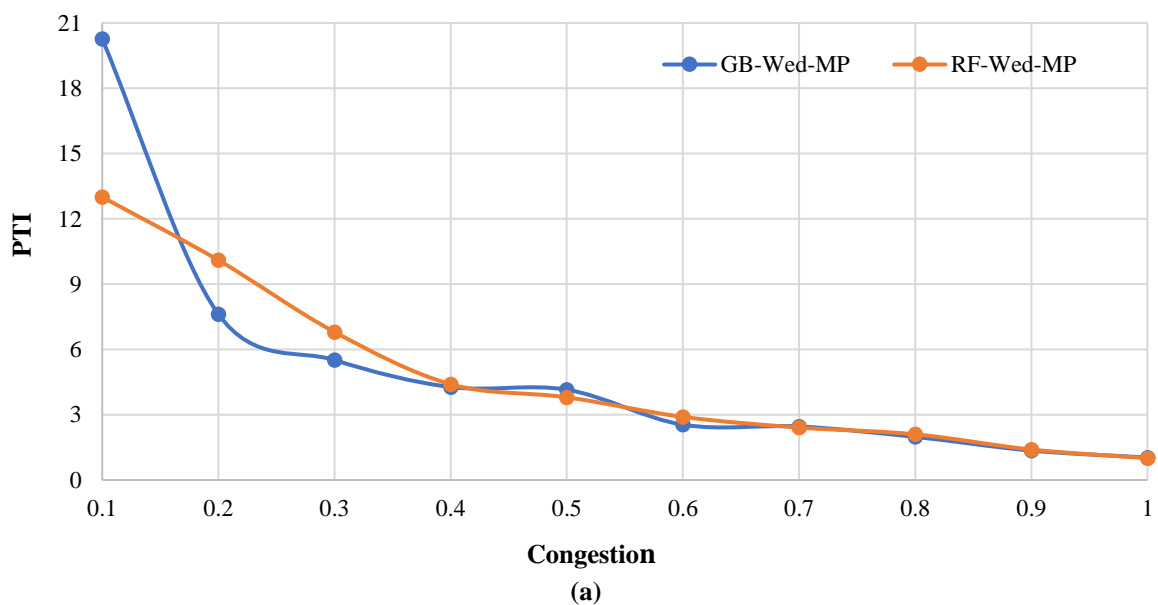


Fig. 3. a) Comparison between GB and RF modeling results- Tuesday morning peak; and b) Comparison between GB and RF modeling results- Tuesday evening peak



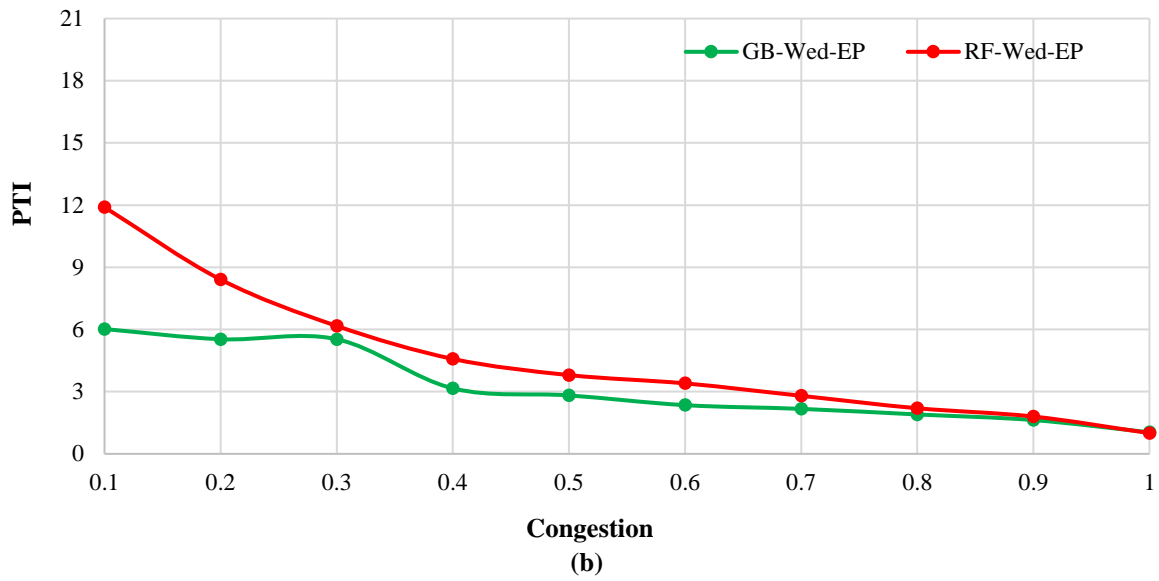


Fig. 4. a) Comparison between GB and RF modeling results- Wednesday morning peak; and b) Comparison between GB and RF modeling results- Wednesday evening peak

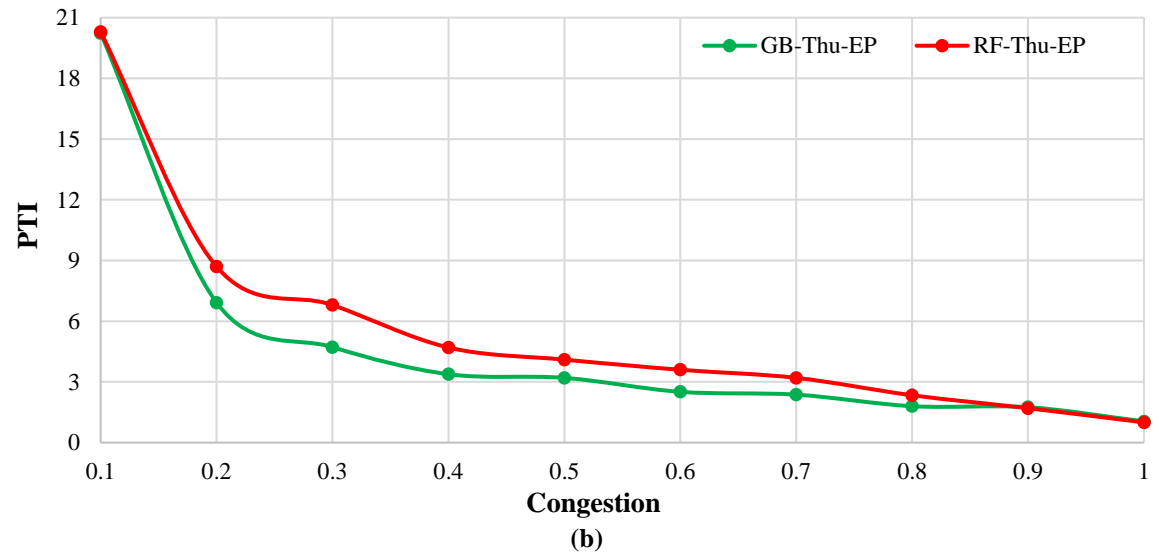
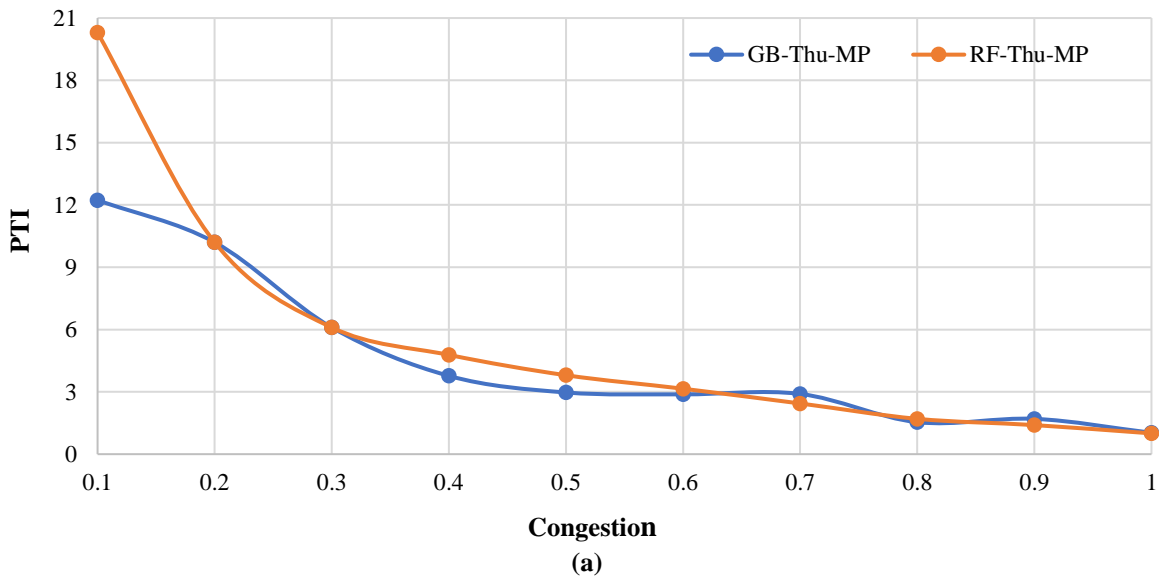


Fig. 5. a) Comparison between GB and RF modeling results- Thursday morning peak; and b) Comparison between GB and RF modeling results- Thursday evening peak

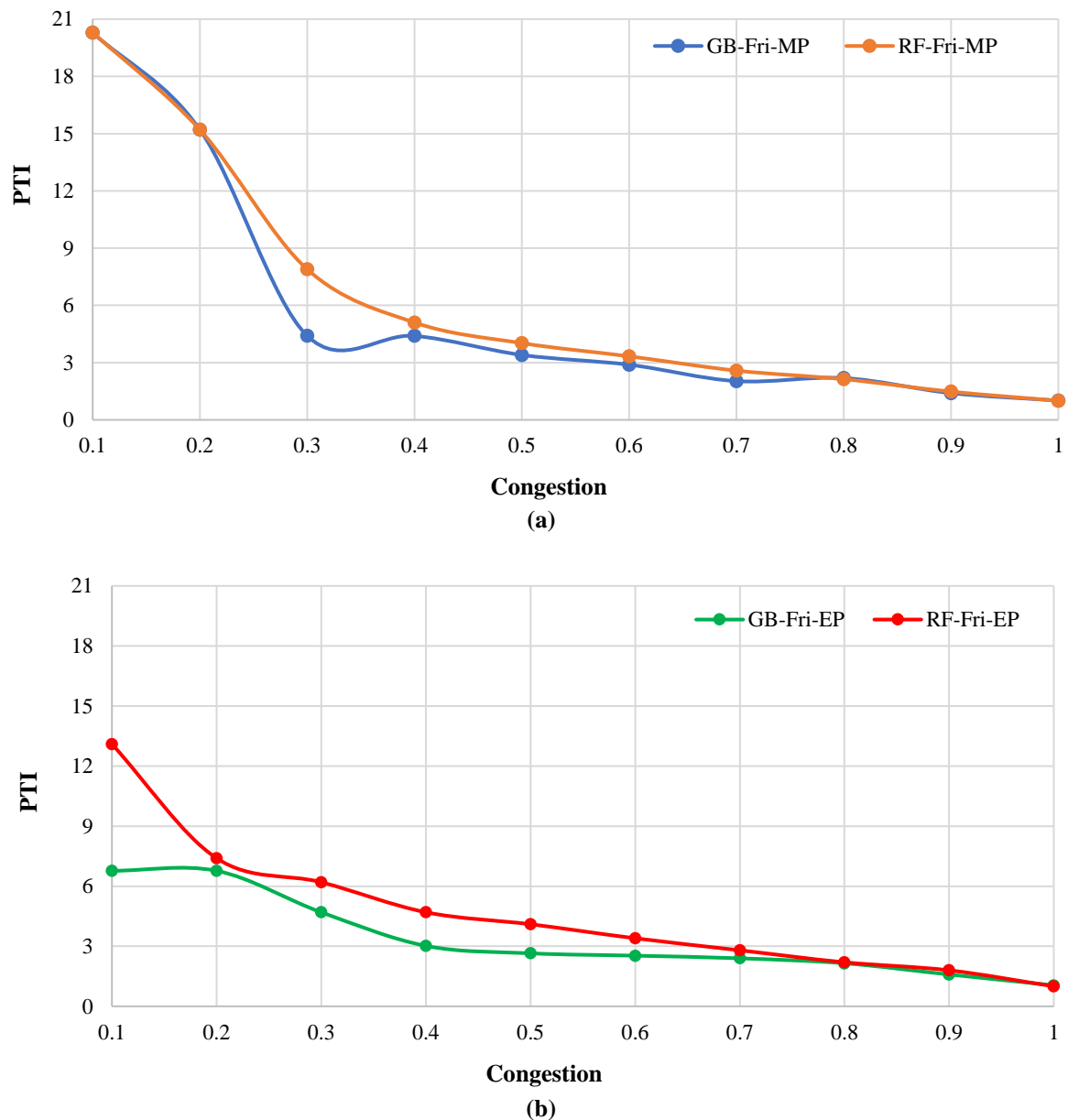


Fig. 6. a) Comparison between GB and RF modeling results- Friday morning peak; and b) Comparison between GB and RF modeling results- Friday evening peak

4. Conclusions

To predict how speed reduction (in terms of congestion) can lead to an increase in planning time index (PTI), the authors used 15 bagging-based regressor methods on a 1.467-mile section of I-64 in Virginia, US. The data of congestion, as the independent variable, and PTI as the dependent variable were considered for modeling. The performance of these methods was then assessed by Mean Squared Error (MSE), goodness of fit (R^2), stability ratio, and Akaike Information Criterion (AIC).

Surprisingly, the Gradient Boosting (GB) regressor could eliminate competitive methods (in terms of minimum AIC and stability ratio). After the model selection process, the results were separately depicted in a scatter plot for morning and evening peaks. The results revealed that when congestion reaches 0.9, PTI goes beyond the reliable area in both peaks. The corresponding congestion for entering the extremely unreliable area is between 0.7 and 0.75 for both peaks. Finally, somewhere between 0.5 and 0.4, the plots have shown an intense increase, meaning

that for congestion values less than these values, the increase in PTI is severe. TTR is a crucial component of congested traffic regimes that has not been taken into account traditionally by the Congestion Management Process (CMP). The emphasis on travel time reliability is driven by elements like restrictions on roadway expansion. This research points out potential areas where the CMP could incorporate TTR. A comprehensive knowledge of the regional transportation systems and a toolbox of techniques are produced by incorporating TTR into CMP. A CMP that incorporates reliability will usually intend to take advantage of operational strategies like Advanced Traveler Information Systems (ATIS) rather than capacity improvements, so the utilized methodology in this study will depict a framework that explains the value of TTR incorporation into the CMP.

Understanding the relationship between congestion and travel time reliability can improve the transportation system's performance in various ways. It can help in developing congestion mitigation strategies, identifying operation strategies, quantifying the benefits of traffic management, improving safety, and maximizing the use of existing capacity. Focusing on improving travel time reliability can lead to strategies that reduce the impact of congestion on travelers, improve safety, support economic growth, and make better use of existing infrastructure. Transportation agencies can use tools such as the Organizing for Reliability Tools from the Strategic Highway Research Program 2 (SHRP2) to systematically improve their capabilities in transportation systems management and operations.

5. References

Abdulhafedh, A. (2022). "Comparison between common statistical modeling techniques used in research, including: Discriminant analysis vs logistic regression, ridge regression vs LASSO, and decision tree vs random forest", *Open Access*

Library Journal, 9(2), 1-19, <https://doi.org/10.4236/oalib.1108414>.

Adhastian, P. and Wibowo, P. (2022). "Prediction of subscriber VoLTE using Machine Learning and Deep Learning", *International Seminar on Intelligent Technology and Its Applications (ISITIA)*, Surabaya, Indonesia, <https://doi.org/10.1109/ISITIA56226.2022.9855362>.

Afandizadeh Zargari, Sh., Khorshidi, N.A., Mirzahosseini, H. and Heidari, H. (2023). "Analyzing the effects of congestion on planning time index-grey models Vs random forest regression", *International Journal of Transportation Science and Technology*, 12(2), 578-593, <https://doi.org/10.1016/j.ijst.2022.05.008>.

Almejr, R.M., Sallabi, O.M. and Mohamed, A.A. (2022). "Applying C atboost regression model for prediction of house prices", *International Conference on Engineering & MIS (ICEMIS)*, Istanbul, Turkey, <https://doi.org/10.1109/ICEMIS56295.2022.9914345>.

Ara, A., Maia, M., Macêdo, S. and Louzada, F. (2020). "Random machines regression approach: An ensemble support vector regression model with free kernel choice", *arXiv preprint arXiv*, 2003, 12643, <https://doi.org/10.48550/arXiv.2003.12643>.

Arias-Castro, E. (2022). *Principles of statistical analysis: Learning from randomized experiments*, Cambridge University Press, England.

Chakrabarti, A. and Ghosh, J.K. (2011). "AIC, BIC and recent advances in model selection", In: P.S. Bandyopadhyay, and M.R. Forster (Eds.), *Philosophy of Statistics*, (pp. 583-605), Netherlands: Elsevier, <https://doi.org/10.1016/B978-0-444-51862-0.50018-6>.

Chen, A., Ji, Z. and Recker, W. (2002). "Travel time reliability with risk-sensitive travelers", *Transportation Research Record*, 1783(1), 27-33, <https://doi.org/10.3141/1783-04>.

Chen, M.-Y., Chiang, H.-S., and Yang, K.-J. (2022). "Constructing cooperative intelligent transport systems for travel time prediction with deep learning approaches", *IEEE Transactions on Intelligent Transportation Systems*, 23(9), 16590-16599, <https://doi.org/10.1109/TITS.2022.3148269>.

Chen, Z. and Fan, W. (2019). "Data analytics approach for travel time reliability pattern analysis and prediction", *Journal of Modern Transportation*, 27(4), 250-265, <https://doi.org/10.1007/s40534-019-00195-6>.

Chen, Z. and Fan, W.D. (2020). "Analyzing travel time distribution based on different travel time reliability patterns using probe vehicle data",

- International Journal of Transportation Science and Technology*, 9(1), 64-75, <https://doi.org/10.1016/j.ijst.2019.10.001>.
- Emam, E.B. and Al-Deek, H. (2006). "Using real-life dual-loop detector data to develop new methodology for estimating freeway travel time reliability", *Transportation Research Record*, 1959(1), 140-150, <https://doi.org/10.1177/0361198106195900116>.
- Gacto, M.J., Soto-Hidalgo, J.M., Alcalá-Fdez, J. and Alcalá, R. (2019). "Experimental study on 164 algorithms available in software tools for solving standard non-linear regression problems", *IEEE Access*, 7, 108916-108939, <https://doi.org/10.1109/ACCESS.2019.2933261>.
- Gaver Jr, D.P. (1968). "Headstart strategies for combating congestion", *Transportation Science*, 2(2), 172-181, <https://doi.org/10.1287/trsc.2.2.172>.
- Ghader, S., Darzi, A. and Zhang, L. (2019). "Modeling effects of travel time reliability on mode choice using cumulative prospect theory", *Transportation Research Part C: Emerging Technologies*, 108, 245-254, <https://doi.org/10.1016/j.trc.2019.09.014>.
- Gu, Y., Fu, X., Liu, Z., Xu, X. and Chen, A. (2020). "Performance of transportation network under perturbations: Reliability, vulnerability, and resilience", *Transportation Research Part E: Logistics and Transportation Review*, 133, 101809, <https://doi.org/10.1016/j.tre.2019.11.003>.
- Hastie, T., Tibshirani, R., Friedman, J.H. and Friedman, J.H. (2009). *The elements of statistical learning: data mining, inference, and prediction*, Springer, New York.
- Hojati, A.T., Ferreira, L., Washington, S., Charles, P. and Shobeirinejad, A. (2016). "Reprint of: Modelling the impact of traffic incidents on travel time reliability", *Transportation research part C: emerging technologies*, 70, 86-97, <https://doi.org/10.1016/j.trc.2015.11.017>.
- Hoseinzadeh, N., Gu, Y., Han, L.D., Brakewood, C. and Freeze, P.B. (2021). "Estimating freeway level-of-service using crowdsourced data", *Informatics*, 8(1), 17, <https://doi.org/10.3390/informatics8010017>.
- Iida, Y. (1999). "Basic concepts and future directions of road network reliability analysis", *Journal of advanced transportation*, 33(2), 125-134, <https://doi.org/10.1002/atr.5670330203>.
- INRIX website: <https://inrix.com/>
- Kadiyala, A. and Kumar, A. (2018). "Applications of python to evaluate the performance of bagging methods", *Environmental Progress & Sustainable Energy*, 37(5), 1555-1559, <https://doi.org/10.1002/ep.13018>.
- Kang, L. and Hansen, M. (2021). "Quantile regression-based estimation of dynamic statistical contingency fuel", *Transportation Science*, 55(1), 257-273, <https://doi.org/10.1287/trsc.2020.0997>.
- Khan, P.W., Park, S.-J., Lee, S.-J. and Byun, Y.-C. (2022). "Electric kickboard demand prediction in spatiotemporal dimension using clustering-aided bagging regressor", *Journal of Advanced Transportation*, 2022, 8062932, <https://doi.org/10.1155/2022/8062932>.
- Li, H., He, F., Lin, X., Wang, Y. and Li, M. (2019). "Travel time reliability measure based on predictability using the Lempel-Ziv algorithm", *Transportation Research Part C: Emerging Technologies*, 101, 161-180, <https://doi.org/10.1016/j.trc.2019.02.014>.
- Liu, H.X., Recker, W. and Chen, A. (2004). "Uncovering the contribution of travel time reliability to dynamic route choice using real-time loop data", *Transportation Research Part A: Policy and Practice*, 38(6), 435-453, <https://doi.org/10.1016/j.tra.2004.03.003>.
- Lyman, K. and Bertini, R.L. (2008). "Using travel time reliability measures to improve regional transportation planning and operations", *Transportation Research Record*, 2046(1), 1-10, <https://doi.org/10.3141/2046-01>.
- Mahmassani, H.S., Kim, J., Chen, Y., Stogios, Y., Brijmohan, A. and Vovsha, P. (2014). *Incorporating reliability performance measures into operations and planning modeling tools*, Transportation Research Board, Washington, DC.
- Mastelini, S.M., Nakano, F.K., Vens, C. and de Leon Ferreira, A.C.P. (2022). "Online extra trees regressor", *IEEE Transactions on Neural Networks and Learning Systems*, 34(10), 6755-6767, <https://doi.org/10.1109/TNNLS.2022.3212859>.
- Mazloumi, R., Abazari, S.R., Nafarieh, F., Aghsami, A. and Jolai, F. (2022). "Statistical analysis of blood characteristics of COVID-19 patients and their survival or death prediction using machine learning algorithms", *Neural Computing and Applications*, 34(17), 14729-14743, <https://doi.org/10.1007/s00521-022-07325-y>.
- Meng, M., Toan, T.D., Wong, Y.D. and Lam, S.H. (2022). "Short-term travel-time prediction using Support Vector Machine and Nearest Neighbor method", *Transportation Research Record*, 2676(6), 353-365, <https://doi.org/10.1177/03611981221074371>.
- Moghaddam, Z.R., Jeihani, M., Peeta, S. and Banerjee, S. (2019). "Comprehending the roles of traveler perception of travel time reliability on route choice behavior", *Travel Behaviour and Society*, 16, 13-22, <https://doi.org/10.1016/j.tbs.2019.03.002>.
- National Academies of Sciences, Engineering, and Medicine. (2013). *Evaluating alternative operations strategies to improve travel time reliability*, The National Academies Press,

- Washington, DC.
- Nohekhan, A., Samimi, A. and Zahedian, S. (2022). "Spatial transferability of a daily activity type and duration MDCEV model", *Civil Engineering Infrastructures Journal*, 55(1), 161-181, <https://doi.org/10.22059/CEIJ.2021.313889.1721>.
- Pedregosa, F., Varoquaux, G., Gramfort, A., Michel, V., Thirion, B., Grisel, O., Blondel, M., Prettenhofer, P., Weiss, R., Dubourg, V. and Vanderplas, J. (2011). "Scikit-learn: Machine learning in Python", *Journal of Machine Learning Research*, 12, 2825-2830.
- Saedi, R., Saeedmanesh, M., Zockaie, A., Saberi, M., Geroliminis, N. and Mahmassani, H.S. (2020). "Estimating network travel time reliability with network partitioning", *Transportation Research Part C: Emerging Technologies*, 112, 46-61, <https://doi.org/10.1016/j.trc.2020.01.013>.
- Samal, S.R. and Das, A.K. (2020). "Evaluation of traffic congestion parameters under heterogeneous traffic condition: A case study on Bhubaneswar City", In: *Transportation Research: Proceedings of CTRG 2017*, (pp. 675-684), Springer Singapore, https://doi.org/10.1007/978-981-32-9042-6_53
- Sarang, P. (2023). "Ensemble: Bagging and boosting: Improving decision tree performance by ensemble methods", In: *Thinking Data Science: A Data Science Practitioner's Guide*, (pp. 97-129), New York: Springer.
- Shabbir, M., Chand, S. and Iqbal, F. (2022). "Bagging-based ridge estimators for a linear regression model with non-normal and heteroscedastic errors", *Communications in Statistics-Simulation and Computation*. 1-15, <https://doi.org/10.1080/03610918.2022.2109675>.
- Szafrański, D. and Duan, B. (2022). "A workflow to integrate numerical simulation, machine learning regression and Bayesian inversion for induced seismicity study: Principles and a case study", *Pure and Applied Geophysics*, 179(10), 3543-3568, <https://doi.org/10.1007/s00024-022-03140-7>.
- Udayanga, S., Kato, T., Kojima, A. and Kubota, H. (2022). "Incorporating crowdsourced travel time data in congestion monitoring", *Journal of the Eastern Asia Society for Transportation Studies*, 14, 246-263, <https://doi.org/10.11175/easts.14.246>.
- Wang, Z., Goodchild, A. and McCormack, E. (2017). "A methodology for forecasting freeway travel time reliability using GPS data", *Transportation Research Procedia*, 25, 842-852, <https://doi.org/10.1016/j.trpro.2017.05.461>.
- Yazici, M.A., Kamga, C. and Mouskos, K.C. (2012). "Analysis of travel time reliability in New York city based on day-of-week and time-of-day periods", *Transportation Research Record*, 2308(1), 83-95, <https://doi.org/10.3141/2308-09>.
- Zang, Z., Xu, X., Yang, C., and Chen, A. (2018). "A closed-form estimation of the travel time percentile function for characterizing travel time reliability", *Transportation Research Part B: Methodological*, 118, 228-247, <https://doi.org/10.1016/j.trb.2018.10.012>.
- Zegeer, J.D., Nevers, B. and Kittelson, W. (2014). *A framework for improving travel time reliability*, Transportation Research Board, Washington, DC.
- Zhan, C., Zheng, Y., Zhang, H. and Wen, Q. (2021). Random-forest-bagging broad learning system with applications for covid-19 pandemic", *IEEE Internet of Things Journal*, 8(21), 15906-15918, <https://doi.org/10.1109/JIOT.2021.3066575>.
- Zhang, X. and Chen, M. (2019). "Quantifying the impact of weather events on travel time and reliability", *Journal of Advanced Transportation*, 2019, 8203081, <https://doi.org/10.1155/2019/8203081>.
- Zhang, X., Zhao, M., Appiah, J. and Fontaine, M.D. (2021). "Improving interstate freeway travel time reliability analysis by clustering travel time distributions", *Transportation Research Record*, 2675(10), 566-577, <https://doi.org/10.1177/03611981211012002>.
- Zheng, F., Li, J., Van Zuylen, H., Liu, X. and Yang, H. (2018). "Urban travel time reliability at different traffic conditions", *Journal of Intelligent Transportation Systems*, 22(2), 106-120, <https://doi.org/10.1080/15472450.2017.1412829>.
- Zhou, Z.-H. (2012). *Ensemble methods: Foundations and algorithms*, CRC press, Florida.
- Zhu, Z., Mardan, A., Zhu, S. and Yang, H. (2021). "Capturing the interaction between travel time reliability and route choice behavior based on the generalized Bayesian traffic model", *Transportation Research Part B: Methodological*, 143, 48-64, <https://doi.org/10.1016/j.trb.2020.11.005>.



This article is an open-access article distributed under the terms and conditions of the Creative Commons Attribution (CC-BY) license.



Effective Location of Shear Walls in High-Rise RCC Buildings Subjected to Lateral Loads

Shukla, K.¹ and Nallasivam, K.^{2*}

¹ P.G. Student, Department of Civil Engineering, National Institute of Technology (NIT) Hamirpur, Himachal Pradesh, India.

² Assistant Professor, Department of Civil Engineering, National Institute of Technology (NIT) Hamirpur, Himachal Pradesh, India.

© University of Tehran 2023

Received: 17 Oct. 2022;

Revised: 17 Mar. 2023;

Accepted: 17 Jul. 2023

ABSTRACT: The main objective of this research is to identify buildings with and without shear walls that adequately resist lateral load by utilizing finite element-based ETABS software that can minimize the displacement and drift of buildings induced by the earthquake and wind load. The equivalent static approach based on the IS Code was used to compute seismic loads. The results of storey displacements and drifts were obtained using four load combinations from the IS Code. It has been observed that shear walls located in the center, in the shape of a core, perform well against lateral loads. The displacement at the top of such a building is around 2.5 times less than the displacement at the top of a building without a shear wall. Shear walls near corners have the lowest effectiveness.

Keywords: Equivalent Static Method, ETABS Models, High-Rise Building, Seismic and Wind Load, Shear Wall.

1. Introduction

The attraction of mankind towards high-rise structures has started since ancient times. However, it becomes necessary as the urban population increases rapidly. Globally, more people live in urban areas than in rural areas (U.N. Organization, 2018). This fact leads us to the wide scope available for research and development in the field of high-rise buildings. From a structural engineer's perspective, a high-rise building is defined as a building that is affected by lateral loads due to wind or earthquake actions to such an extent that they play an

important role in the structural design (Bryan and Alex, 1991). Lateral load effects on buildings increase rapidly with an increase in height. In such a situation, the provision of lateral stiffness becomes the most important building component (Bungale, 1988).

Between two primary types of vertical load-resisting elements, columns, and shear walls, the latter provides more stiffness. A vertical plate like a reinforced concrete wall starting from the foundation level and extending up to the full height of the building to form a vertical cantilever is called a shear wall (Agarwal and

* Corresponding author E-mail: nallasivam_iit_nit@yahoo.co.in

Shrikhande, 2006). It is subjected to in-plane shear forces due to lateral loads. Due to higher in-plane stiffness, shear walls are suitable to use in buildings up to 35 stories (Bryan and Alex, 1991). For effective load resistance, the location and arrangement of shear walls are important factors. Although lateral loads due to earthquakes and wind are dynamic, codes permit the use of quasi-static analysis methods because of difficulties associated with dynamic analysis (Menon, 2008). The objective of the quasi-static analysis is to find an equivalent static load that results in maximum response. This study deals with multi-storey rectangular buildings with different arrangements of shear walls, modeled using ETABS software. The equivalent static method according to (IS Code 1893, Part-1, 2016) has been adopted to find out earthquake loads, and wind loads have been applied according to (IS Code 875, Part 3, 2015).

Akhil and Pradeep (2020) studied the effects of the location of shear walls in a twenty-storey residential building by adopting response spectrum analysis. Three models were made using ETABS, one without a shear wall, one with a shear wall at two corners on the same side of the building, and the last with shear walls at all four corners of the building. It was concluded that buildings with shear walls on all four corners perform better than others as they show lower displacement, drift, and base shear.

Lingeshwaran et al. (2021) examined the usage of shear walls in building with floating columns. Building without a floating column, building with a floating column, and building with a floating column and shear wall- such three G+9 storey models were made in ETABS software and analyzed using response spectrum and time history method. It was proven that using the shear wall in a building with a floating column provides much better stiffness.

Dodiya et al. (2018) studied the positioning of shear walls in 20-storey

buildings considering these three models: shear walls at corners, shear walls at opposite directions and shape shear walls. It was seen from the results that when shear walls are located in opposite directions show minimum displacement. Meena and Ramana (2021) designed G+3 R.C.C. framed Structure with a shear wall perpendicular and parallel to the blast load, and a shear wall at all the faces in ETABS. It was concluded that building with a shear wall perpendicular to the blast load and shear wall at all the faces performs almost with similar efficiency and is more effective than building with walls parallel to the load.

Sylviya and Eswaramoorthi (2018) proposed that the most effective building for resisting earthquake load is a building with shear walls located at the edges. To arrive at this conclusion, four models were made and results for storey drift, displacement, and storey shear were shown in all the zones i.e., Zone II, III, IV. Khadri et al. (2021) explained about the effectiveness of shear wall in resisting seismic load when the building is situated on sloping ground. Various models with different shear wall arrangements were prepared with the building located both on a plane and sloped ground for their study.

Al Agha and Umamaheshwari (2020) presented the study of irregular RCC buildings with only shear walls, and dual framed-shear wall systems subjected to seismic loads calculated using both equivalent static method and response spectrum method. Wang et al. (2001) studied the effect of shear wall height on the earthquake response of frame-shear wall structures. It was derived that the influence of the height of shear walls on the effective stiffness of the buildings is marginal for some buildings.

Tuppad and Fernandas (2015) studied about optimum positioning of shear walls in G+10 storey buildings when the seismic load is applied. A total of six models, one without a shear wall and the other five with a shear wall at different locations were prepared using ETABS and seismic loads

applied using an equivalent static method. A genetic algorithm was also used for optimization and it was concluded that the shear wall at the center gives better results. Titiksh and Bhatt (2017) prepared four different buildings in ETABS to give an idea about the effectiveness of shear wall positioning against lateral loads.

Sherkhane and Manjunath (2020) replaced all the columns in the G+20 storey building with shear walls. Four buildings were made providing shear walls as the only lateral load-resisting element and analyzed using an equivalent static method. Abd-el-Rahim and Farghaly (2010) studied the effect of edge shear walls in slender buildings resting on a raft foundation. Various models were prepared for this study considering different subgrade moduli and analyzed after applying seismic load using the time history method in SAP2000 software.

Bongilwar et al. (2018) checked the vulnerability of irregular G+8 storey building models using two models, one with shear walls and one without shear walls. The fundamental objective of the research was to identify buildings with various arrangements of shear walls and without shear walls that effectively resist lateral load by using finite element-based ETABS software and could minimize to a minimum the displacement and drift of buildings caused by the earthquake and wind load.

Tavakoli et al. (2022) performed a study to examine the influence of outrigger-braced system location optimization on the seismic response of a 50-storey structure. The seismic responses were investigated using IDA curves. The energy balance in the structures was evaluated, and the strain energy parameter was chosen as EDP, from which the damage level was computed. The plastic strain energy was used to examine the outcomes of plotting fragility curves. The results revealed that optimizing the location of an outrigger-braced system improves all structural characteristics while decreasing the likelihood of collapse.

Mesr Habiby and Behnamfar (2023)

investigated the maximum practical values of the eccentricity of torsionally-coupled structures, followed by an evaluation of the safety margin against the seismic collapse of such buildings. Different levels of mass eccentricity in a stiffness-eccentric plan were explored in nonlinear analysis. The eccentricity ratio, building height, and soil type all influenced the collapse safety margin and median spectral acceleration.

2. Materials and Methods

To establish identical circumstances throughout all nine models, the following assumptions are established before the commencement of the modeling procedure:

- ✓ Just the main block of the building is taken into account. The staircases are not considered in the design process.
- ✓ The building is employed for residential purposes, but no walls is built since the research will simply look at the reaction of the Frame configuration.
- ✓ No slabs are placed on the bottom floor.
- ✓ The beams are resting centrally on the columns to prevent eccentric circumstances. In ETABS, this is done automatically.
- ✓ The footings are designed. Fixed supports are used to assign supports.
- ✓ Seismic loads are only examined in the horizontal direction (X and Y), with vertical loads (Z) presumed to be minor.

A total of nine G+30-storey buildings are modeled using finite element-based ETABS software. Details about the arrangement of shear walls in all the models are listed below as Model-1 to Model-9:

Model-1: Rectangular building without any shear wall

Model-2: Buildings with shear walls located at all four corners-1

Model-3: Buildings with shear walls located at all four corners-2

Model-4: Buildings with shear walls located at only two opposite corners

Model-5: Buildings with shear walls located at all four edges

Model-6: Buildings with shear wall located

at the center as core
 Model-7: Buildings with shear walls located at two opposite edges and center
 Model-8: Buildings with shear wall located at the center in E-shape
 Model-9: Building with a shear wall located

at the center in I-shape
 The Floor plan and 3D view of the above models are shown in Figures 1 to 9, respectively. The fixed supports have been provided at the base of each building making it a vertical cantilever.

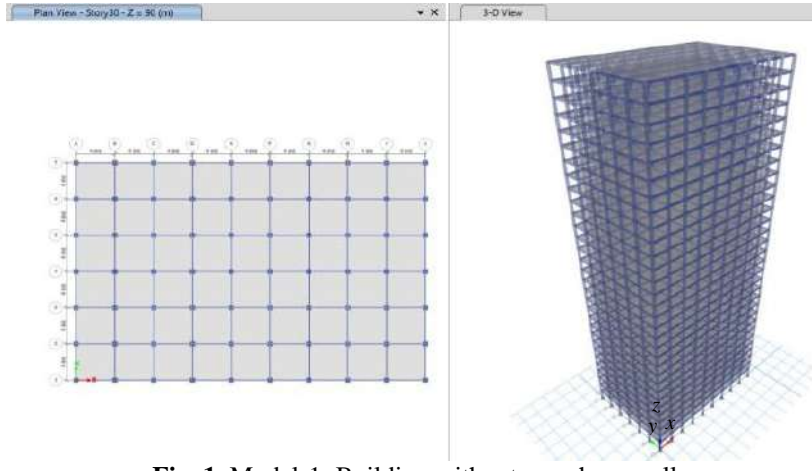


Fig. 1. Model-1: Building without any shear wall

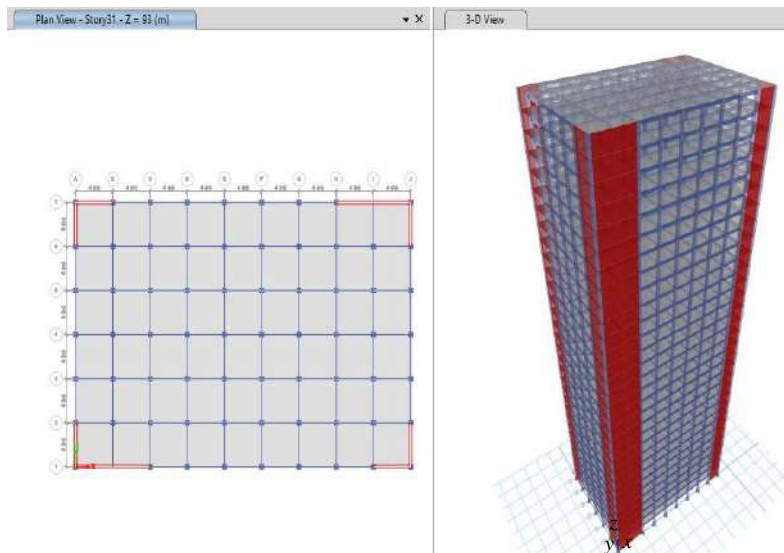


Fig. 2. Model-2: Buildings with shear walls located at all four corners-1

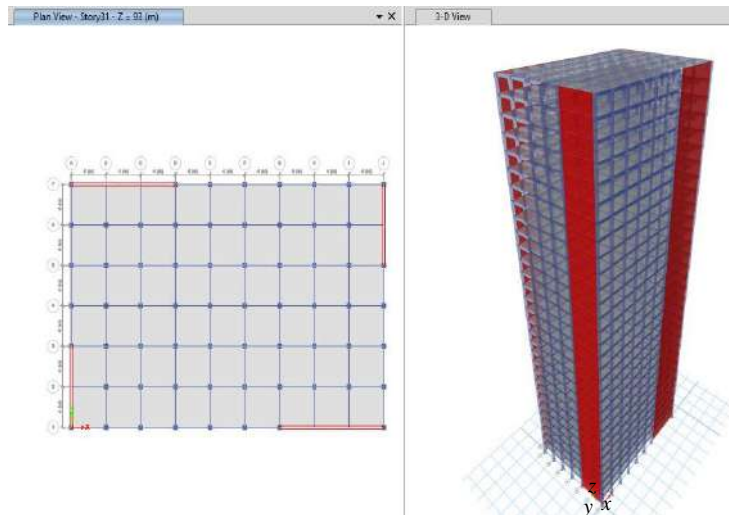


Fig. 3. Model-3: Buildings with shear walls located at all four corners-2

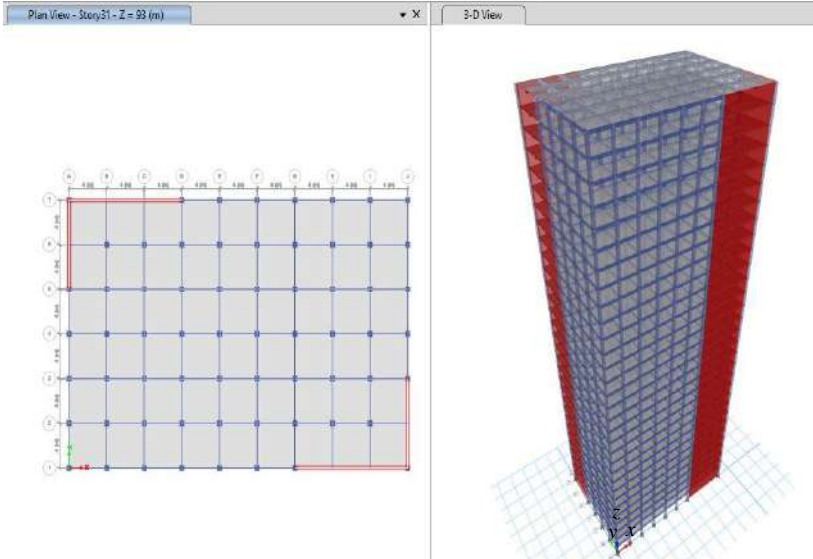


Fig. 4. Model-4: Buildings with shear walls located at only two opposite corners

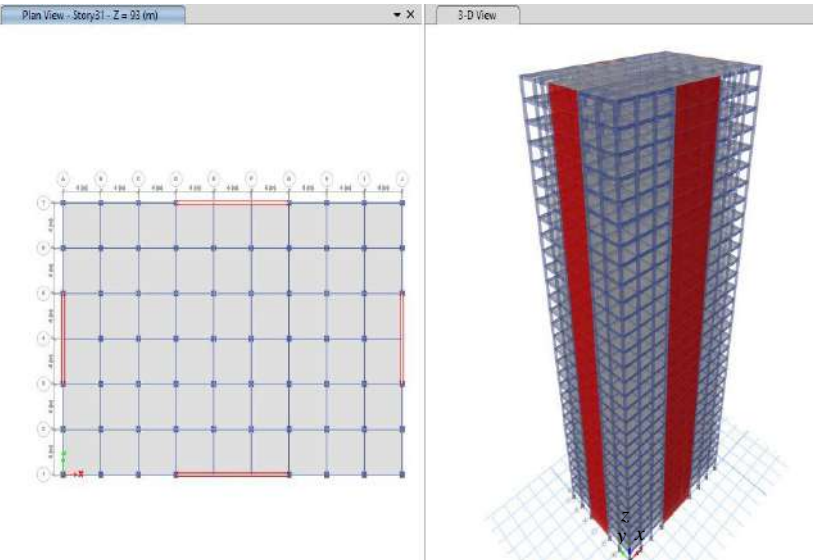


Fig. 5. Model-5: Buildings with shear wall located at all four edges

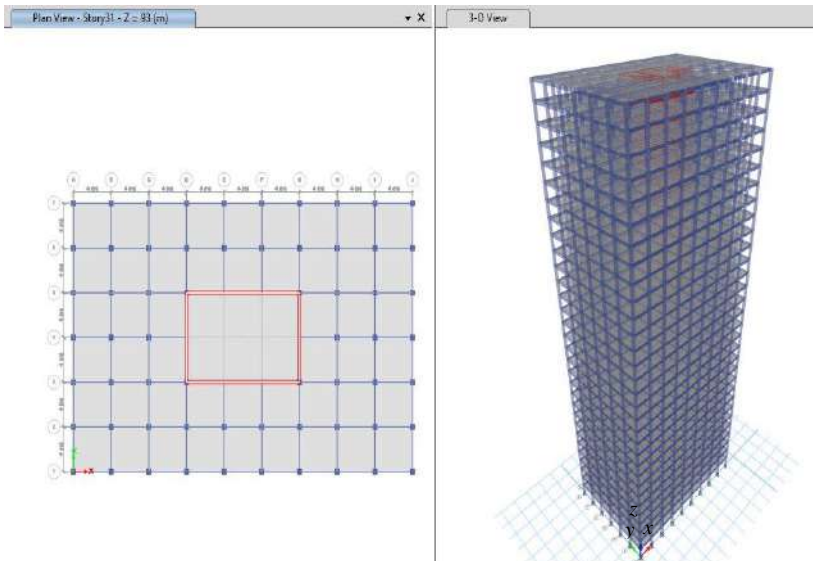


Fig. 6. Model-6: Buildings with shear wall located at the center as core

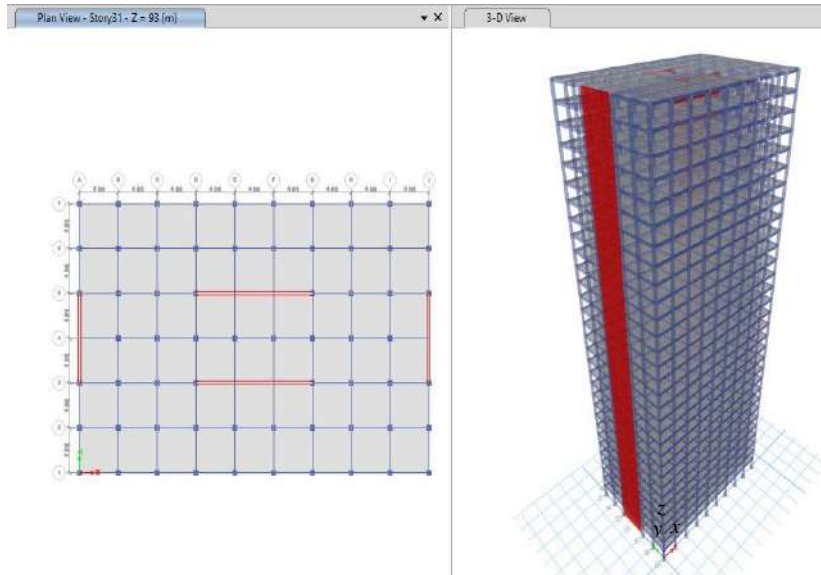


Fig. 7. Model-7: Buildings with shear wall located at two opposite edges and center

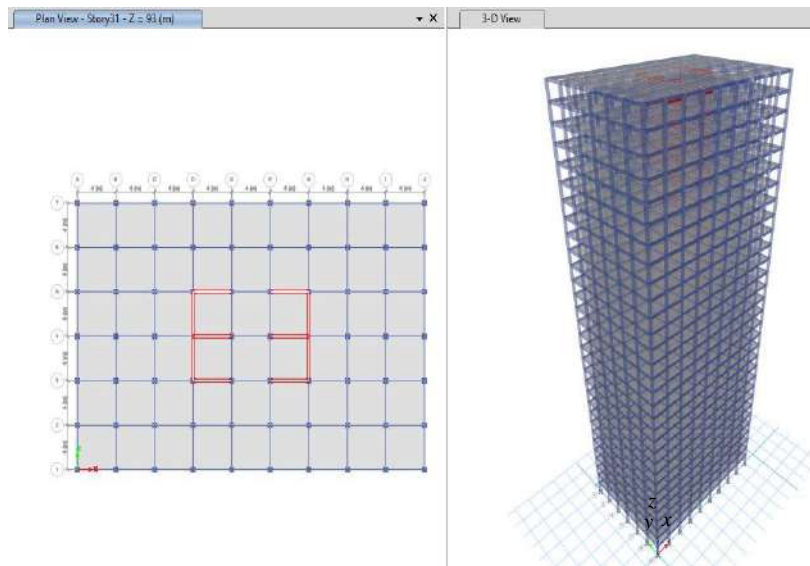


Fig. 8. Model-8: Buildings with shear wall located at the center in E-shape

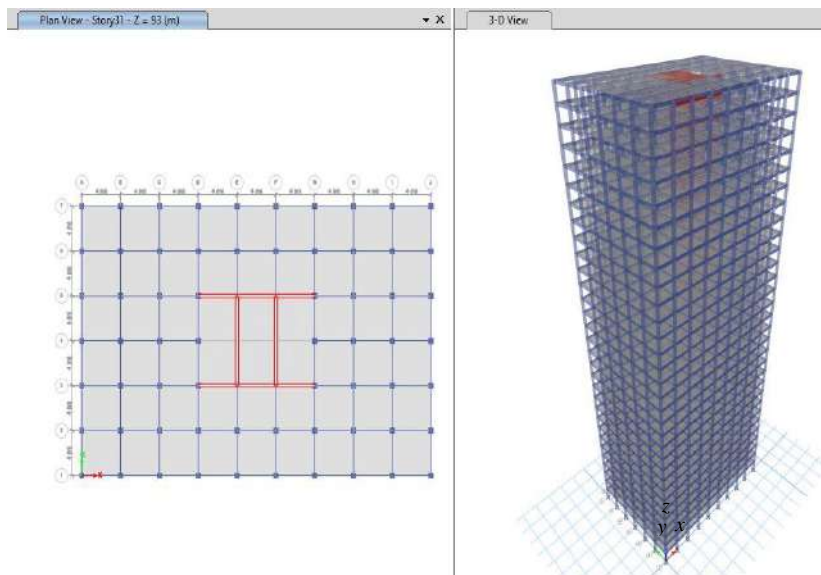


Fig. 9. Model-9: Building with shear wall located at the center in I-shape

2.1. Dimensional Configurations

The plane grid is defined with ten gridlines parallel to the Y-direction and seven gridlines parallel to the X-direction. Beams and columns are defined as 1D frame elements, and slabs and shear walls have been defined as 2D thin shell elements. Beam elements are modeled for the 'Bending moment design only' option. On the other hand, columns are modeled for the 'axial force with bi-axial bending moment' option, and a similar number of reinforcements in both directions is given because the column has the same dimensions in both directions. The design requirement of a section is not checked or mentioned as the design lies outside the scope of the study. Further, these dimensions and modeling configurations are similar in all the models as the objective of the study is to compare the effectiveness of shear walls. Dimensional data for the size of each element is shown in Table 1.

2.2. Material Properties

The properties of the two materials used in RCC building modeling are given in Table 2.

2.3. Material Properties

Dead loads are automatically calculated in the software. The floor finish load on

each floor, as well as the roof, is taken as 1 kN/m². Live loads on floors and roofs are taken as IS Code 875, Part 2 (1987), which are 2 kN/m² and 1.5 kN/m², respectively. Wall loads on floors and roofs are 11.26 kN/m and 6.28 kN/m respectively, which are applied on the four outer edges of the buildings. Earthquake load data are taken from IS Code 1893, Part 1 (2016) and shown in Table 3. Wind load data shown in Table 4 are according to IS Code 875, Part-3 (2015).

The following four load combinations are considered as per IS Code 456 (2000).

L.C.1: $1.2(DL+LL+EQX)$

L.C.2: $1.2(DL+LL+EQY)$

L.C.3: $1.2(DL+LL+WX)$

L.C.4: $1.2(DL+LL+WY)$

3. Results and Discussion

3.1. Validation of the Method

Two models were created for this validation. The following are the descriptions:

Model-1: Conventional frame (Building without shearwall) (Figure 10)

Model-2: Building with box-type shear wall at the center of the geometry (building with shear wall inform of core) (Figure 11)

Table 1. Dimension configurations

| Items | Values |
|--------------------------------------|-----------|
| No. of bays along the X-direction | 9 |
| No. of bays along the Y-direction | 6 |
| Length of each bay (m) | 4 |
| Height of each floor (m) | 3 |
| Total height of buildings (m) | 93 |
| Size of the beam (mm × mm) | 300 × 450 |
| Size of column (mm × mm) | 500 × 500 |
| The thickness of the slab (mm) | 150 |
| The thickness of the shear wall (mm) | 300 |

Table 2. Material properties

| Material | Concrete | Steel |
|--|---------------------|---------------------|
| Grade | M30 | Fe415 |
| Specific weight, γ (kN/m ³) | 25 | 76.97 |
| Density, ρ (kg/m ³) | 2549.29 | 7849.05 |
| Modulus of Elasticity, E (MPa) | 27386.13 | 200000 |
| Poisson's ratio, μ | 0.2 | ----- |
| Coefficient of Thermal Expansion (1/°C) | 10×10^{-6} | 12×10^{-6} |
| Shear Modulus, G (MPa) | 11410.89 | ----- |

Table 3. Earthquake load data

| Items | Values |
|-------------------------------|-----------------|
| Zone factor (Z) | 0.16 |
| Importance factor (I) | 1 |
| Response reduction factor (R) | 5 |
| Site type | 2 (Medium soil) |
| Time period (T) | 2.25 seconds |
| Damping ratio (ξ) | 5% |

Table 4. Wind load data

| Items | Values |
|-------------------------------|--------|
| Basic wind speed (v_b) | 39 m/s |
| Terrain category | 3 |
| Risk coefficient (k_1) | 1 |
| Topography factor (k_3) | 1 |
| Importance factor (k_4) | 1 |
| Windward coefficient (X-dir.) | 1.2 |
| Leeward coefficient (X-dir.) | 0.9 |
| Windward coefficient (Y-dir.) | 1.3 |
| Leeward coefficient (Y-dir.) | 0.6 |

Table 5 summarizes the model descriptions, material properties, and the load applied and load combinations. The structures with different framing systems

have been modeled using ETABS with the above-mentioned load conditions and combinations.

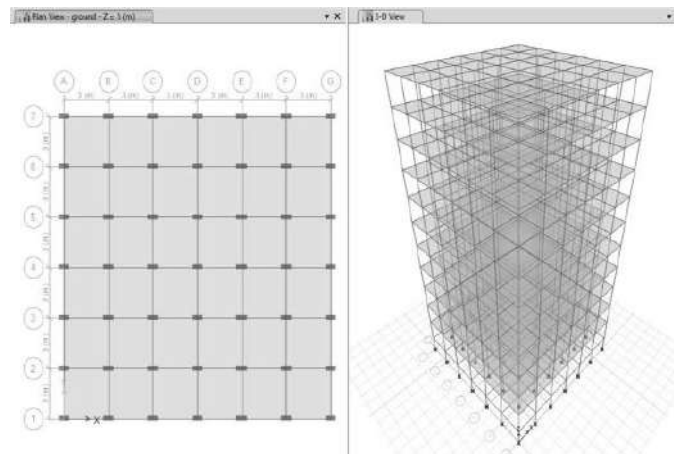


Fig. 10. Model-1: Conventional frame (Building without shear wall)

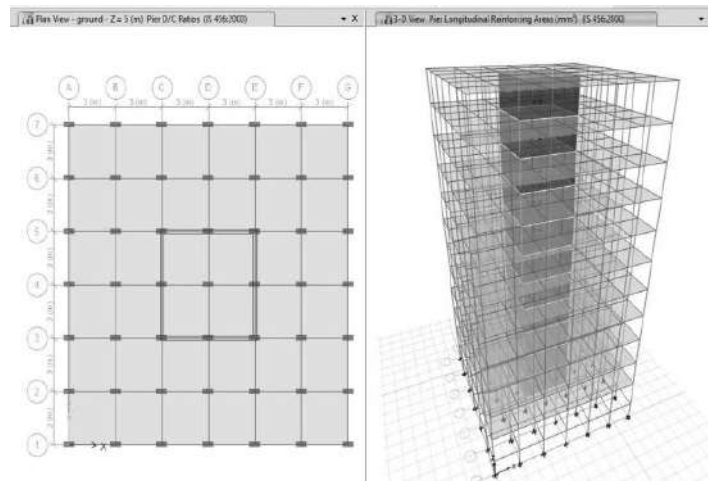


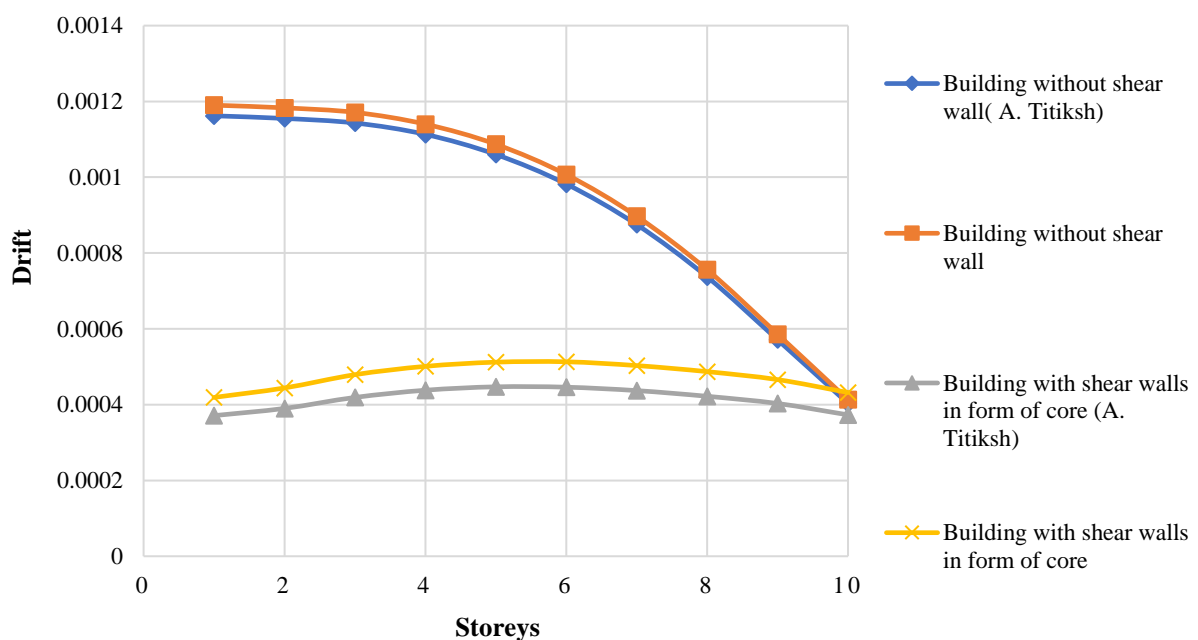
Fig. 11. Model-2: Building with box-type shear wall at the centre of the geometry (Building with shear wall inform of core)

Table 5. Model descriptions

| SN | Specifications | Size | |
|----|---------------------------------|--------------------------------|--------------------------------|
| 1 | Plan dimensions | 18 m × 18 m (X×Y) | |
| 2 | Length in X- direction | 18 m (6 Bays) | |
| 3 | Length in Z- direction | 18 m (6 Bays) | |
| 4 | Floor-to-floor height | 3.0 m | |
| 5 | Plinth level | 2 m | |
| 6 | Total height of building (G+10) | 35 m | |
| 7 | Slab thickness | 200 mm | |
| 8 | Type of structure | OMRF has shear walls | |
| 9 | Soil Type (as per IS:1893-2002) | Medium | |
| 10 | Response reduction factor | 5 | |
| 11 | Importance factor | 1 | |
| 12 | Seismic zone factor | 0.36 (Zone V) | |
| 13 | Time factor | 0.963 | |
| 14 | Grade of concrete | M25 | |
| 15 | Grade of steel | Fe 415 | |
| 16 | Plinth beam size | 0.23 m × 0.23 m | |
| 17 | Floor beam size | 0.23 m × 0.48 m | |
| 18 | Column size | 0.30 m × 0.70 m | |
| 19 | Loads Applied | DL Dead load | Calculated as per self-weight |
| | | LL Floor finish | 1 kN/m ² |
| | | LL Live load | 2.5 kN/m ² |
| | | EQX Seismic load (X direction) | Calculated as per IS:1893-2002 |
| 20 | Load combination | 1.2 DL + 1.2 LL + 1.2 EQX | |

The results of parameters like maximum storey drifts are carried out using the ETABS software. The results of storey drift are validated with the work of Titiksh and Bhatt (2017) for two models: A building without shear walls and a building with shear walls at the center in the form of a core. It is compared in Figure 12, in which current results show good agreement with

the results of the previous paper. The data presented in Figure 12 for Model-1 and Model-2 confirms the accuracy and applicability of the finite element method. Thus, the current modelling is correct and can be used to fulfil the objective of the study.

**Fig. 12.** Max. storey drift of the first 10th storey compared with the results of Titiksh and Bhatt (2017)

3.2. Present Study

The results of parameters like maximum storey displacements and maximum storey drifts are carried out using the ETABS software. For each parameter, comparison charts are developed to get an idea about how the height of a building has affected the variation in parameters for each model. The top displacement of Model-2 to Model-9 is compared with the top displacement of Model-1. The results are discussed in the following four sections, categorized according to the load combination mentioned before.

3.2.1. Earthquake load considering load combination 1.2 ($DL+LL+EQX$)

Maximum storey displacements are shown in Figure 13. The displacement increases non-linearly with the height of the building. When a shear wall is introduced in the building, it increases the rigidity of the building and displacements are less. Shear walls also decrease the rate of increment of displacement. Among the models with various arrangements of shear walls, Models 8 and 6 show maximum and minimum displacement at the top. Compared to Model-1, the top-storey displacement of other models is less by: 2.63 times for Model-6, 2.12 times for Model-7, 2.06 for Model-9, 1.97 for Model-5, 1.76 for Model-4, 1.6 for Model-3, 1.54 for Model-2, and 1.49 for Model-8. Storey drift is the relative displacement of one-storey relative to another storey. The introduction of shear walls also decreases

drift in buildings because of an increment in stiffness (Figure 14).

There is an increment in drift up to the 10th-15th storey depending upon the arrangement of walls, followed by a decrement at a much slower rate for models with shear walls than Model-1. So, Model-1 has experienced less drift at the top storey. In addition, in all models with the shear wall, there is less difference between the drifts of two adjacent stories. Model-6 shows the minimum drift value compared to others. When compared to other models with shear walls, Model-8 drifts more at lower stories.

3.2.2. Earthquake load considering load combination 1.2 ($DL+LL+EQY$)

When earthquake forces were applied in the Y-direction, Models-6, and Model-3 experienced minimum and maximum displacement (1.98 and 1.27 times less than Model-1), respectively (Figure 15). Among the other models, Model-2 was displaced 1.29 times, Model-4 by 1.32 times, Model-7 by 1.38 times, Model-5 by 1.48 times, Model-8 by 1.83 times, and Model-9 by 1.91 times less than Model-1 at the top storey. Buildings were drifted in the Y-direction in the same way that they were drifted in the X-direction (Figure 16). Here, Models 6 and 9 show almost similar drift values, which are the minimum among all models. At lower levels, Model-2 and Model-3 have greater drift values; however, Model-4 has the most drift on the top floor.

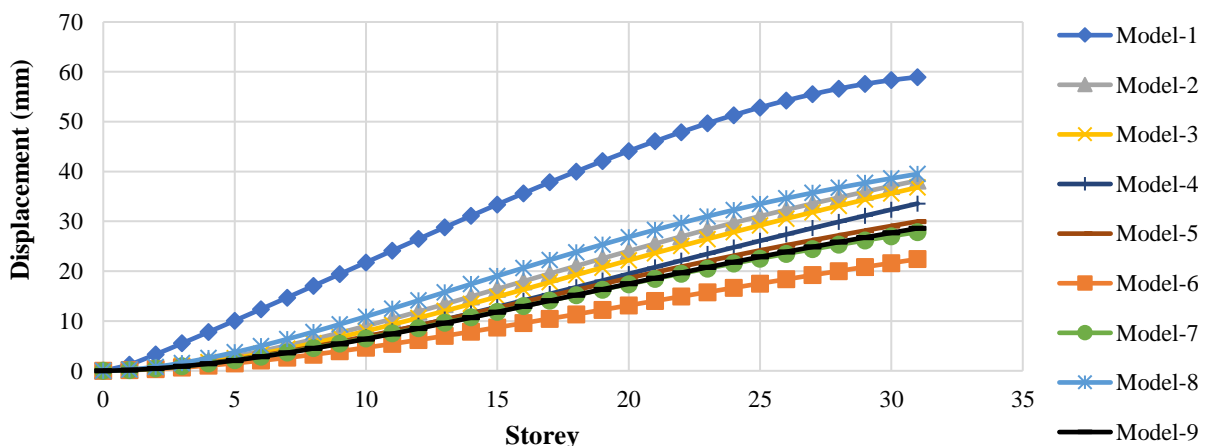


Fig. 13. Storey displacement in X-direction due to L.C.1

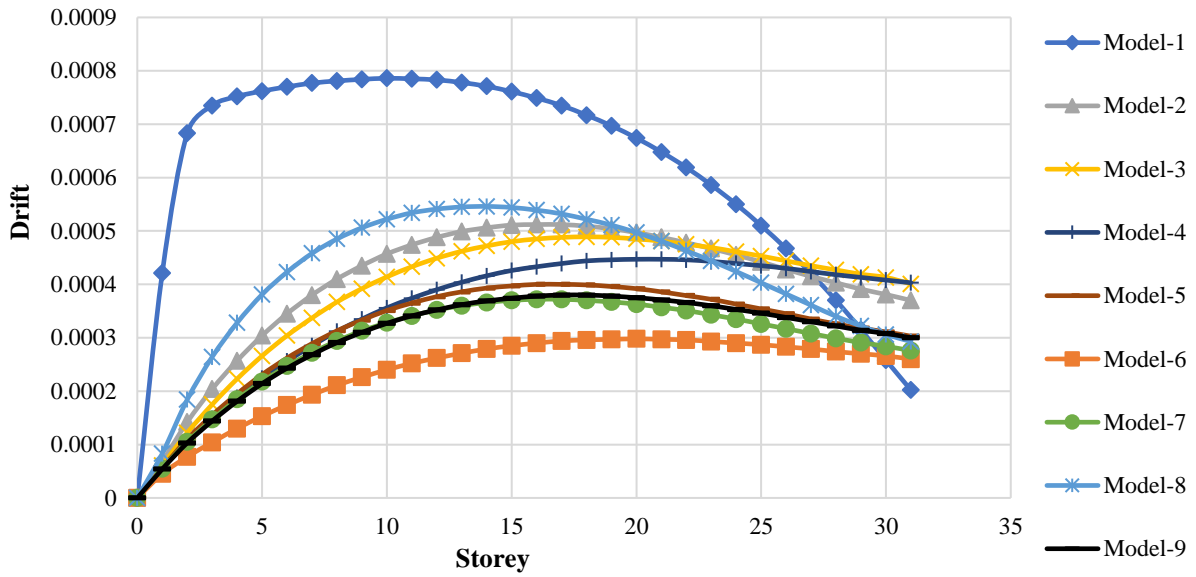


Fig. 14. Storey drift in X-direction due to L.C.1

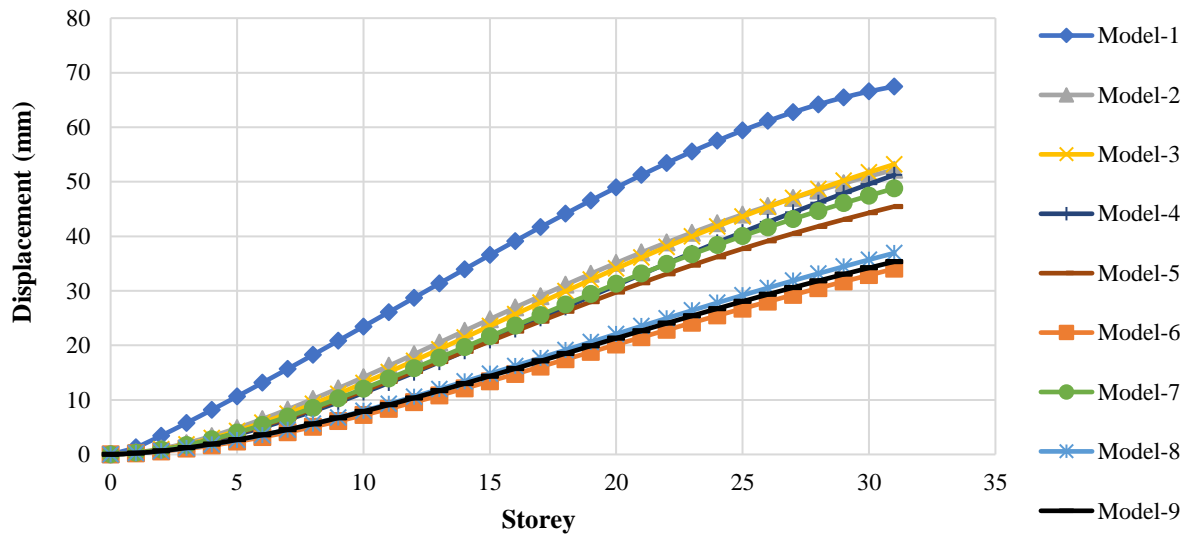


Fig. 15. Storey displacement in Y-direction due to L.C.2

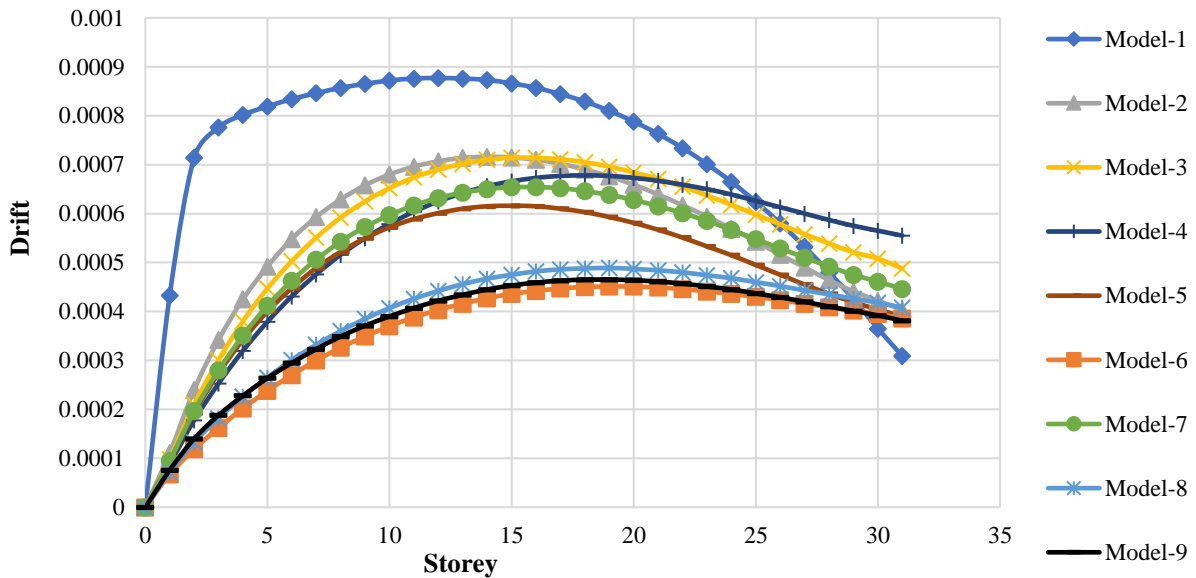


Fig. 16. Storey drift in Y-direction due to L.C.2

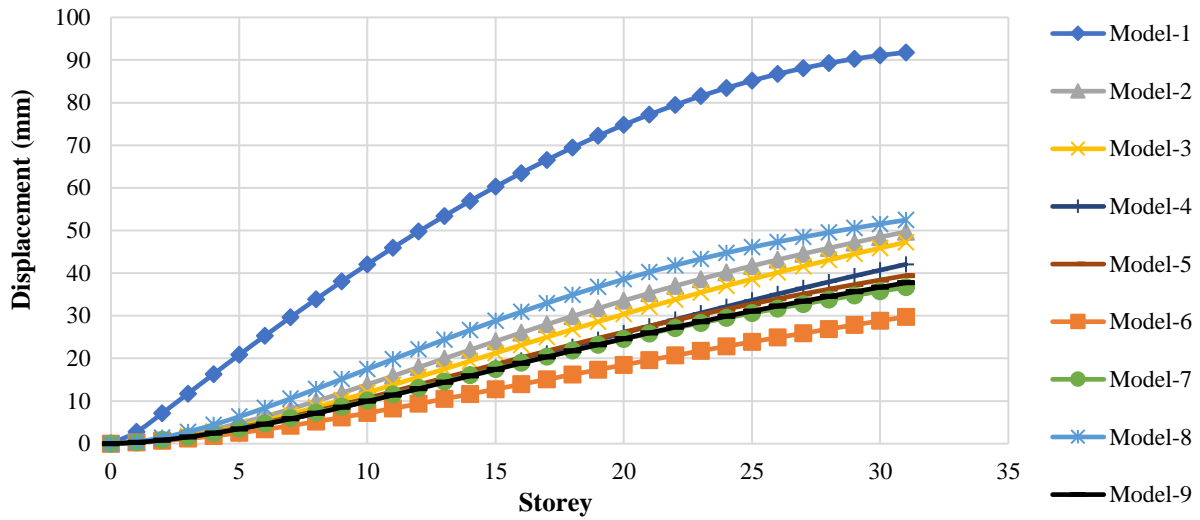


Fig. 17. Storey displacement in X-direction due to L.C.3

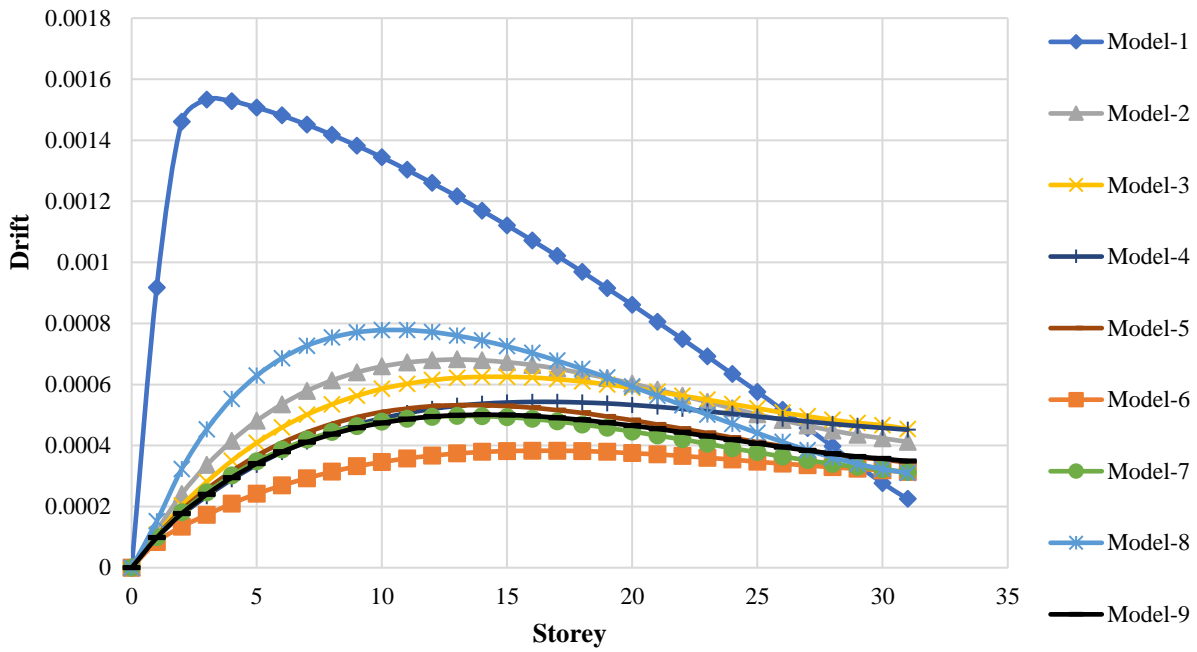


Fig. 18. Storey drift in X-direction due to L.C.3

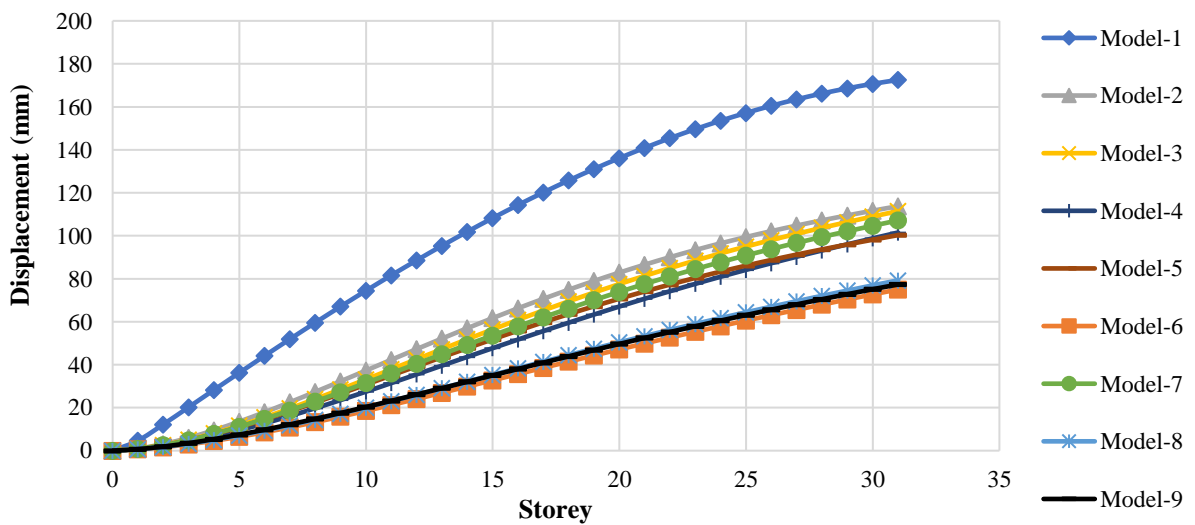


Fig. 19. Storey displacement in Y-direction due to L.C.4

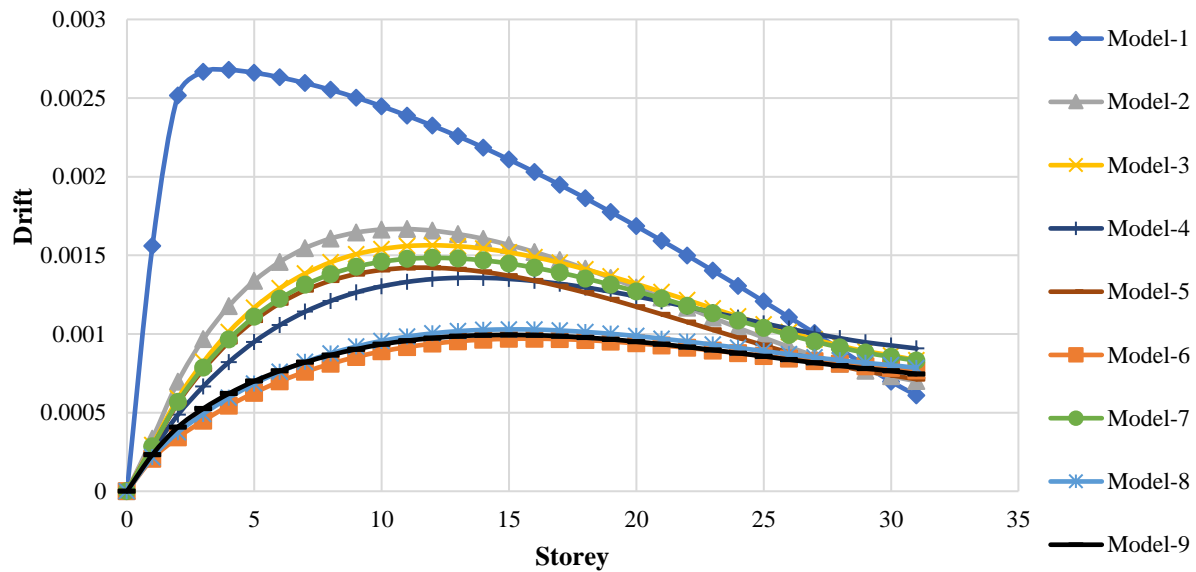


Fig. 20. Storey displacement in Y-direction due to L.C.4

3.2.3. Wind load considering load combination 1.2 ($DL+LL+WX$)

The maximum storey displacement chart for a given load combination is shown in Figure 17. Model-8 has a maximum displacement of the displaced top storey, which is 1.75 times less than Model-1. Model-6 has experienced a minimum displacement at the top (3 times less than Model-1). The top displacements of other models compared to Model-1 are 1.85, 1.94, 2.18, 2.33, and 2.5 times less for Model-2, Model-3, Model-4, Model-5, Model-9, and Model-7, respectively. The placement of shear walls serves to minimize the amount of drift that buildings experience when they are exposed to wind forces in the X-direction (Figure 18). The drift has increased up to 7th-12th stories depending upon the arrangement of walls, followed by decrement at a much slower rate than Model-1. So, Model-1 has less drift at the top storey. Similar to earthquake loads in the X-direction, Model-6 drifts less than other buildings with shear walls, and Model-8 drifts more at lower stories.

3.2.4. Wind load considering load combination 1.2 ($DL+LL+WY$)

When wind forces were applied to models in the Y-direction, Model-2 displaced its maximum, but its top displacement is still 1.52 times less than

Model-1 (Figure 19). Model-6 has experienced a minimum displacement at the top (2.3 times less than Model-1). The top displacements of other models compared to Model-1 are 1.55, 1.61, 1.70, 1.72, 2.18, and 2.23 times less for Model-3, Model-7, Model-4, Model-5, Model-8, and Model-9, respectively. The drift of the buildings on the application of Y-direction wind forces is shown to have a similar pattern to that of what was got on the application of X-direction wind forces (Figure 20).

4. Conclusions

This study presented the responses of various models subjected to seismic and wind loads. The findings of the study are concisely concluded here:

- Model-6, in which shear walls were arranged at the center in the form of a core, was performed most effectively against lateral loads in both directions.
- It cannot be stated from the study that walls at the center location always perform better, as Model-8 was shown comparatively poor performance against lateral loads in the X-direction, leading to the conclusion that the direction in which walls were arranged also plays an important role.
- It was seen that buildings with walls located at the corners were more

vulnerable to both earthquake and wind load compared to buildings with properly arranged walls at the center and buildings with shear walls located at the edges.

- Buildings with walls located at the edges and center were more effective than buildings with walls located only at the edge.
- Because the T-shape building lacks symmetry in the y-direction, it was not very good at withstanding lateral loads that come from the y-direction. While x-directional symmetry makes it effective at withstanding earthquakes that come from the x-direction.
- When compared to other shapes, regular shapes like rectangles and squares were done better than others when it comes to efficiently resisting the pressure of the wind.
- As a result of its form, the C-shape has a greater degree of stiffness in the y-direction than it does in the x-direction.

As the research limitations, it can be said that this study focused only on symmetrical building shapes, and lateral loads were calculated using the equivalent static method. Besides, this investigation may be improved in the following ways:

- Model analysis and forced vibration analysis of multi-storey buildings subject to seismic or wind forces may be emphasized in the study.
- The research may emphasize asymmetric building shapes, with the results applicable to real-world circumstances

5. Acknowledgment

The authors gratefully acknowledge the National Institute of Technology (NIT) Hamirpur, Himachal Pradesh, India for providing computational facility.

6. References

- Abd-el-Rahim, H.H.A. and Farghaly, A.A.E.R. (2010). "Role of shear walls in high rise buildings", *Journal of Engineering Sciences*, 38(2), 403-420,
- <https://doi.org/10.21608/jesaun.2010.124373>.
- Agarwal, P. and Shrikhande, M. (2006). *Earthquake resistant design of structures*, PHI Learning Private Limited.
- Akhil Ahamad, S. and Pratap, K.V. (2020). "Dynamic analysis of G+20 multi-storied building by using shear walls in various locations for different seismic zones by using Etabs", *Materials Today Proceedings*, 43, 1043-1048, Elsevier, <https://doi.org/10.1016/j.matpr.2020.08.014>.
- Al-Agha, W. and Umamaheswari, N. (2020). "Analytical study of an irregular reinforced concrete building with shear wall and dual Framed-Shear wall system by using Equivalent Static and Response Spectrum Method", *Materials Today Proceedings*, 43, 2232-2241, <https://doi.org/10.1016/j.matpr.2020.12.525>.
- Bongilwar, R., Harne, V.R. and Chopade, A. (2018). "Significance of shear wall in multi-storey structure with seismic analysis", *IOP Conference Series: Material Science and Engineering*, 330(1), 012131, <https://doi.org/10.1088/1757-899X/330/1/012131>.
- Bryan, S. and Alex, C. (1991). *Tall building structures: Analysis and design*, John Wiley & Sons, Inc.
- Bungale, S.T. (1988). *Structural analysis and design of tall buildings*, McGraw-Hill.
- Dodiya, J., Devani, M., Dobariya, A., Bhuva, M. and Padhiar, K. (2018). "Analysis of multistory building with shear wall using ETABS software", *International Research Journal of Engineering and Technology*, 5(2), 1543-1546.
- IS 1893, Part-1. (2016). "Criteria for earthquake resistant design of structures, Part 1: General provisions and buildings", 6th Revision, Bureau of Indian Standard, New Delhi.
- IS 875, Part-3. (2015). "Indian standard design loads (other than earthquake) for buildings and structures-code of practice: Wind load", 3rd Revision, Bureau of Indian Standard, New Delhi.
- IS 875, Part-2. (1987). "Code of practice for design loads (other than earthquake) for buildings and structures: Imposed loads", 2nd Revision, Bureau of Indian Standards, New Dehli.
- IS 456. (2000). "Plain and reinforced concrete-code of practice", 4th Revision, Bureau of Indian Standards, New Dehli.
- Khadri, S.N, Chaitanya, B.K., Rama Krishna, C.B. and Sai Nitesh, K.J.N. (2021). "Analysis of structure on slopes infill shear wall at different locations", *Materials Today Proceedings*, Elsevier, 47, 5451-5456, <https://doi.org/10.1016/j.matpr.2020.12.1146>.
- Lingeshwaran, N., Kranthinadimpalli, S., Kollasailaja, Sameer Uddin, S., Kumar, Y.H. and Madavarapu, S.B. (2021). "A study on

- seismic analysis of high-rise building with and without floating columns and shear wall", *Materials Today Proceedings*, 47, 5451-5456, <https://doi.org/10.1016/j.matpr.2021.07.120>.
- Meena, A. and Ramana, P.V. (2021). "Assessment of structural wall stiffness impact due to blast load", *Materials Today Proceedings*, 45(3),40-52, <https://doi.org/10.1016/j.matpr.2021.03.093>.
- Menon, D. (2008). *Structural analysis*, Narosa Publication House.
- Mesr Habiby, Y. and Behnamfar, F. (2023). "Seismic fragility analysis of torsionally-coupled steel moment frames against collapse", *Civil Engineering Infrastructures Journal*, 56(2), 415-438, <https://doi.org/10.22059/CEIJ.2023.347246.1862>.
- Sherkhane, V.B. and Manjunath, G.S. (2020). "Parametric analysis of multistory RC buildings with columns replaced by shear walls using ETABS", *International Research Journal of Engineering and Technology*, 7, 7471-7475.
- Sylviya, B. and Eswaramoorthi, P. (2018). "Analysis of RCC building with shear walls at various locations and in different seismic zones", *Internation Journal of Innovative Technology and Exploring Engineering*, 8(2), 336-339.
- Tavakoli, H.R., Moradi, M., Goodarzi, M.J. and Najafi, H. (2022). "Outrigger braced system placement effect on seismic collapse probability of tall buildings", *Civil Engineering Infrastructures Journal*, 55(2), 259-276, <https://doi.org/10.22059/CEIJ.2022.319629.1744>.
- Tuppad, S. and Fernandes, R.J. (2015). "Optimum location of shear wall in a multi-storey building subjected to seismic behavior using Genetic Algorithm", *International Research Journal of Engineering and Technology*, 2(04), 236-240.
- Titiksh, A. and Bhatt, G. (2017). "Optimum positioning of shear walls for minimizing the effects of lateral forces in multistorey-buildings", *Archives of Civil Engineering*, 63(1), 151-162, <https://doi.org/10.1515/ace-2017-0010>.
- U.N. Organization. (2018). *World urbanization prospects*, <https://population.un.org/wup/Publications/Files/WUP2018-Report>.
- Wang, Q., Wang, L. and Liu, Q. (2001). "Effect of shear wall height on earthquake response", *Engineering Structures*, 23(4), 376-384, [https://doi.org/10.1016/S0141-0296\(00\)00044-4](https://doi.org/10.1016/S0141-0296(00)00044-4).



This article is an open-access article distributed under the terms and conditions of the Creative Commons Attribution (CC-BY) license.



Three-Dimensional Numerical Investigation of Tunnel Behavior Based on Different Constitutive Models and Associated Parametric Analysis in Rock Medium

Chalajour, S.¹ and Hataf, N.^{2*}

¹ Ph.D. Candidate, Department of Civil and Environmental Engineering, Shiraz University, Shiraz, Iran.

² Professor, Department of Civil and Environmental Engineering, Shiraz University, Shiraz, Iran.

© University of Tehran 2023

Received: 17 Nov. 2022;

Revised: 08 Feb. 2023;

Accepted: 07 Mar. 2023

ABSTRACT: With the advancement of numerical modeling, predicting tunnels' behavior before construction has become possible for designers. Accurate prediction of tunnels' behavior in diverse environments requires the compatibility of numerical simulations with ground conditions. Although several constitutive models have been proposed for simulating ground characteristics, their appropriate utilization is crucial. In this study, the convergence of a tunnel is modeled, and the results are verified using actual convergence monitoring data. Then, a series of finite element simulations are conducted on a hypothetical TBM tunnel to demonstrate the difference in deformations, ground surface settlements, and stresses in the lining resulting from tunnel excavation under seven constitutive models in rock media. The models are categorized into four groups: rock-specified, soil-established, and general. Additionally, parametric studies are performed on specific gravity, Poisson's ratio, and dilation angle. The findings revealed that different constitutive models significantly influence numerical analysis results. Rock-specified models were found to be more sensitive to parameter variation in rock media than soil-established and general models. Moreover, changes in specific gravity and Poisson's ratio had a significant impact on the magnitude of surface settlements. Overall, the study highlights the importance of appropriately selecting constitutive models and accurately defining material parameters in numerical simulations to ensure reliable predictions of tunnel behavior.

Keywords: Constitutive Model, Finite-Element Simulation, Ground Surface Settlement, Parametric Study, Tunnel In Rock Mass.

1. Introduction

The rapid growth of urban areas in recent decades has resulted in the construction of numerous structures and infrastructures, including tunnels. Tunnels are critical

underground structures used for various purposes such as transportation, access roads, powerhouse caverns, and water transition ducts (Audi et al., 2020). Consequently, it is crucial to accurately predict their behavior during the design

* Corresponding author E-mail: nhataf@shirazu.ac.ir

phase. The behavior of tunnels can be evaluated by analyzing the crown settlement, ground surface settlement, and the stresses that develop on the lining system. Reliable predictions of tunnel behavior are necessary to ensure the safety and durability of the structure, as well as to avoid potential damages and costs associated with unforeseen events. Therefore, it is essential to utilize advanced numerical modeling techniques and appropriate constitutive models to accurately simulate the behavior of tunnels in different environments.

Excavation of a tunnel at any depth in the ground causes a redistribution of stresses, which affects the support system of the tunnel and causes displacement in the surrounding area. Accurate prediction of tunnel behavior is essential to optimize the design of the support system (Hajiazizi et al., 2021). In addition, ground surface settlement resulting from deformations can cause damage to structures located at the ground level. Several studies have been conducted to evaluate the displacement and stress distribution in the tunnel environment and the tunnel support system. These studies can be classified into three categories: empirical, analytical, and numerical methods. Empirical methods typically express the deformations and stresses developed in tunnel structures using empirical equations. These equations are a mathematical language that describes the behavior of the tunnel in terms of a series of variables and logical and quantitative relationships between these variables. Empirical equations are typically developed based on field measurements and observations, and they often incorporate simplifying assumptions to make them more practical and easier to apply. While empirical methods can be useful for quickly estimating the behavior of tunnels, they are often less accurate than analytical or numerical methods, which can take into account a wider range of factors and provide more detailed results. Analytical methods involve using mathematical models to

predict the behavior of the tunnel based on simplified assumptions. These methods simplify complex tunnel problems by making certain assumptions, which then allow for the derivation of theoretical equations to calculate stresses and deformations. These assumptions can include the homogeneity and isotropy of the tunnel lining, or that stresses and deformations are only a function of the radial distance from the tunnel center. While analytical methods can provide useful insights into tunnel behavior, they may not be as accurate as numerical methods which can consider a wider range of factors and provide more detailed results. Kirsch's solution to determine the stresses surrounding a tunnel in an elastic environment is this kind (Goodman, 1989).

Pinto (1991) developed an analytical solution to describe the curvature shape of surface settlement. Bobet (2001) studied 28 tunnels and suggested an analytical approach based on ignoring the time-dependent material behavior to calculate the ground deformations induced by tunnel excavation in saturated shallow depths. Bakker (2003) proposed several equations to compute axial forces, flexural moments, and radial displacements of a tunnel. Park (2004) presented an analytical method to calculate tunnels' elliptical deformations in clays by modifying the Bobet equations and elastic theory. Numerical methods, such as finite element analysis, use complex mathematical models to simulate the behavior of the tunnel and surrounding ground in great detail. From studies that have investigated the influence of constitutive models on tunnel's response, Oettl et al. (1998), Hejazi et al. (2008) and Rukhaiyar and Samadhiya (2016) can be named. Chen and Lee (2020) researched tunnel deformation by three-dimensional (3D) Finite Element (FE) analysis in horseshoe-shaped tunnels under various geological conditions by Mohr-Coulomb and Hoek-Brown constitutive models. They showed that the predicted deformations by the two models are close. Chalajour and

Hataf (2022) investigated the most appropriate constitutive model for each rock category based on the strength parameters based on the actual behavior of two tunnels.

The problem associated with design and analysis is the lack of knowledge in the nonlinear behavior of structure and soil interaction, affecting the magnitude of stresses (Shid Moosavi and Rahai, 2018). Zhao et al. (2017) and Beyabanaki and Gall (2017) performed a series of parametric studies on different characteristics of soil and the tunnel itself to investigate the effect of modulus of elasticity, construction steps, horizontal to vertical stress ratio, tunnel angle and tunnel diameter on tunnel behavior. Yoo (2016) conducted a series of 3D FE parametric studies on several tunnel cases and indicated that displacements at the tunnel crown and sidewalls could be related to the weak zone's spatial characteristic and the initial stress state. Ding and Liu (2018) investigated the effect of tunnel burial depth, tunnel diameter and lateral pressure coefficient on the stress and deformation of tunnel surrounding rock under sandstones.

Jallow et al. (2019), by 3D analyzing a TBM tunnel, investigated the effect of different soil constitutive models, the agreement of surface settlement calculations and monitoring, and parametric analysis of the impact of various parameters on long-term settlements. Zheng et al. (2017) investigated the unloading effect due to the tunnel excavations by considering the small strain characteristics of soil and showed it could cause adjacent tunnels' deformation. Wang et al. (2019) studied the effect of constructing a large diameter shallow buried twin tunnel in soft soil on the ground surface settlement. They showed the range of the longitudinal surface settlement affected by the tunnel excavation face for different soft soils.

Anato et al. (2021) investigated the effect of the shield-driven speed, modulus of elasticity of grout, and the stiffness of the tunnel lining on ground surface settlement.

They demonstrated that the ground surface settlement is considerably influenced by the tail void grouting properties and stiffness of tunnel lining. Various studies also for the assessment of the deformations due to tunnel excavation by comparing with data monitoring, have also been reported in the literature (Aksoy and Uyar, 2017; Su et al., 2019; Xing et al., 2018; Jin et al., 2020; Sun et al., 2020; Li et al., 2020; Ranjbarnia Su et al., 2020; Xue et al., 2021; Yang and Xu, 2021).

Numerous studies have examined ground surface settlements resulting from tunnelling and the associated stresses on the lining and deformations, however, most of these studies have focused solely on the soil medium. Consequently, a gap exists in the literature regarding the evaluation of tunnel behavior under different constitutive models in rock mediums. Additionally, parametric studies have been overlooked in some previous investigations.

This paper aims to address these shortcomings by utilizing three-dimensional numerical modelling based on the Rock Mass Rating (RMR) classification system proposed by Bieniawski (1973), with seven distinct constitutive models in four rock categories (very weak, weak, medium, and strong) typically utilized in tunnel analysis. By doing so, this study provides an understanding of the significant impact of selected behavior models and associated parametric studies on accurate results. By providing a better understanding of predicting and assessing tunnel behavior before construction, this study offers insight for engineers and can help improve tunnel design and construction.

2. Constitutive Models

Constitutive models provide a mathematical framework for describing the behavior of materials under different loading conditions. By using a single set of model constants, constitutive models enable predictions of how materials, such as soil and rock, will respond to stress paths of

varying complexity. These models maintain constant parameters, irrespective of the stress path, and allow for state parameters to be adjusted during the analysis process. Thus, constitutive models provide a means of defining the relationship between stress and strain, enabling the calculation of incremental strains resulting from changes in stress. The Finite Element (FE) method incorporates material properties through the use of a defined constitutive model. This study explores the impact of seven different constitutive models, which include Linear Elastic (LE) and Von Mises (VM) as general models, Mohr-Coulomb (MC), Drucker-Prager (DP), and Strain Softening (SS) as classical soil models, and Generalized Hoek-Brown (GHB) and Generalized Hoek-Brown with Residual (GHBR) as special rock models for analysis. The following section briefly describes the selected models, but additional information on their behavior can be found in the references.

2.1. Linear Elastic model

The elastic behavior of a material can be linear or nonlinear. In linear elasticity, the elastic material properties are constants, but in nonlinear elastic models, they change based on some assumptions. In the LE model, the stress is linearly correlated with the strain, and the elastic properties are constants, represented as Hooke's Law, Eq. (1).

$$\sigma = E\varepsilon \quad (1)$$

where E : is Young's modulus of the material, and σ and ε : are the stress and strain, respectively. The model's constants are Young's modulus and Poisson's ratio. This model does not define a failure criterion.

2.2. Von Mises Model

In the VM model, the yield occurs when the second invariant of the deviatoric stress tensor (q) reaching a critical value. This model is mostly used to simulate the ductile

behavior of the material. When the VM model is applied to a soil material, the effect of hydrostatic pressure is not considered, and the yield surface is the same for both tension and compression (Davis and Selvadurai, 2005). It can be assumed that the material response is nonlinear elastic, viscoelastic or linear elastic prior to yielding. VM yield formulation is expressed as Eq. (2).

$$q = k \quad (2)$$

where q : is the deviatoric stress and k : is the material's yield stress in pure shear respectively. VM criterion is formulated in terms of the von Mises stress or equivalent tensile stress. The first term predicts the yielding of materials under complex loading from the results of uniaxial tensile tests. On the other hand, the Von Mises stress satisfies the property where two stress states with equal distortion energy have an equal von Mises stress.

2.3. Mohr-Coulomb Model

The introduction of the MC model specification and associated yield criterion to rock mechanics was brought forward by Jaeger et al. (1979), which postulated a linear relationship between shear strength on a plane and the normal acting stress on the p-q plane. This elastic-perfectly plastic model is one of the most commonly used and well-suited for evaluating geotechnical problems describing the conditions for which an isotropic material will fail, with any effect from the intermediate principal stress σ_{II} being neglected. Mechanical behavior of the model includes features such as isotropic shear strength for the peak and residual, tensile strength, dilatancy and the shear strength dependency on Lode's angle. MC model is also being implemented to evaluate load-displacement magnitudes in the simulations, including geomaterials such as gravels, sands and rocks (Davis and Selvadurai, 2005).

This model possesses five parameters to express behavior. Two parameters are

adopted from Hooke's law (i.e., modulus of elasticity, E , and Poisson's ratio, ν), two parameters to express the failure criterion (angle of internal friction, ϕ , and cohesion, c), in addition to another parameter (dilation angle, ψ) that should be less than or equal to the (residual) friction angle which makes the flow rule non-associated or associated respectively, for determining the plastic volume change due to shear stress (Ng et al., 2015). MC criterion is written as Eq. (3).

$$\tau = c + \sigma \tan \phi \quad (3)$$

where τ and σ : are the shearing and normal stress (positive tension) on the physical plane through which material failure occurs, respectively. ϕ : is also the angle of internal friction and c : represents the cohesion value in this model.

2.4. Drucker–Prager Model

DP is a modification of VM model by introducing a dependence on the mean stress p according to Eq. (4). Constant parameters ξ and k could be selected such that the model agrees with the Coulomb surface. This model is intended to simulate cohesive geological materials exhibiting pressure-dependent yield, including soils and rocks.

$$q - \xi p = k \quad (4)$$

where q and k : are the material properties representing peak and residual strength values. P : is also defined as hydrostatic confinement. Similar to the MC criterion, this model simulates the elastic-perfectly plastic behavior; however, unlike the MC, which has the hexagonal yield surface on the deviatoric stress plane, the yield surface of the DP model in two and three-dimensional stress space is a line and a conical shape respectively (Davis and Selvadurai, 2005).

2.5. Strain Softening Model

Several studies have shown that the peak and residual strengths of rocks increase with

an increase in confining pressure. Conversely, at lower confining pressures, the loss of the cohesive strength component around peak load leads to strain localization, resulting in significant stress drop - this is commonly referred to as strain-softening behavior (Rummel and Fairhurst, 1970). Cohesion parameters in the Strain Softening (SS) model vary with plastic strain rate, allowing for a piecewise linear definition of the stress-strain relationship. The yield criterion, potential function, plastic flow rule, and stress correction in the SS model are similar to the Mohr-Coulomb (MC) criteria. The SS model is implemented in the numerical modeling process after material yielding. The units of new shear strength parameters are calculated based on the plastic strain at each iteration step, and the parameters are updated using a nonlinear equation between the shear strength parameter and plastic strain, before being used in the next iteration step. Through this cycle, the Strain-Softening (SS) behavior of rocks can be reflected (Li et al., 2019). SS refers to the deterioration of material strength as the strain increases. This model includes a linear component until the peak shear strength value is reached, after which failure occurs, and shear strength reduces to the residual shear strength. Softening behavior occurs when the stresses in the rock mass around the tunnel exceed the compressive stresses and gradually reduce to the residual strength with an increase in strain. The SS model features three nonlinear parameters that define its strain-softening behavior: Peak Cohesion (C_p), Residual Cohesion (C_r), and Softening Rate (R) (MIDAS Information Technology Co., 2018).

2.6. Generalized Hoek-Brown Model

Hoek-Brown criterion is an elastic-brittle-plastic material model utilized to evaluate the failure criteria based on strength and deformations for rock masses. This model was introduced based on an attempt to provide input data for the

analyses required for the design of underground excavations in hard rock, derived from the results of studies of the brittle failure of intact rock by Hoek (1968) and on model studies of jointed rock mass behavior by Brown (1970). This criteria idea commences from the features of intact rock, and then applying reduction factors based on the characteristics of joints in a rock mass is modified to suit the rock mass behavior. Mechanical behavior of the model is similar to the mechanical behavior of the MC criteria. Three different rock mass characteristics should be defined as input parameters of this model. The Uniaxial compressive strength of intact rock, σ_{ci} , Hoek-Brown constant value for rock mass, m_i , and Geological Strength Index, GSI, for rock mass. The modified Hoek-Brown equation is defined by Eqs. (5-7).

$$\sigma_1 = \sigma_3 + \sigma_{ci} \left(m_b \frac{\sigma_3}{\sigma_{ci}} + s \right)^a \quad (5)$$

$$m_b = m_i \exp \left(\frac{GSI - 100}{28 - 14D} \right) \quad (6)$$

$$a = 0.5 + \frac{1}{6} \left(e^{-GSI/15} - e^{-20/3} \right) \quad (7)$$

where σ_1 and σ_3 : are maximum and minimum principal stresses, respectively. m_b : is the Hoek-Brown constant parameter for rock mass, and a and s : are dimensionless parameters which are dependent on the rock mass Geological Strength Index (GSI). GSI system represents the rock structure and block surface conditions. The GSI was introduced by Hoek et al. (1992l, 1995) in order to evaluate the mass rock strength from the intact rock properties. D : is also the disturbance factor as a result of blast or stress relaxation. This parameter ranged from 0.0 for undisturbed in-situ rock mass to 1.0 for very disturbed rock mass. Hoek-Brown parameters can be connected to the MC criteria parameters through some proposed correlations (Yasitli, 2016; Hoek and Brown, 2019).

2.7. Generalized Hoek-Brown with Residual Model

The residual behavior is calculated from substituting the GSI_{Peak} instead of $GSI_{Residual}$ in the Hoek-Brown model (Russo et al., 1998). This model behaves similarly to the SS model and calculates smaller residual values than the peak values according to the plastic softening of rocks. In the design of underground excavations, the post-peak behavior of rocks shows essential effect on the excavation stability (Cai et al., 2007). Concerning the recommended behavior range based on GSI, rock masses with $GSI > 75$ show brittle behavior, $25 < GSI < 75$ have softening behavior, and $GSI < 25$ exhibits complete plastic behavior (Lazemi and Soleiman Dehkordi, 2019; Hoek and Brown, 1997). The determination of residual parameters based on Hoek-Brown criteria was discussed by He et al. (2020). For this study, the residual value of the GSI calculated from the empirical equation Eq. (8) proposed by Russo et al. (1998).

$$GSI_{residual} = GSI \cdot e^{-0.134GSI} \quad (8)$$

3. Verification of Numerical Modeling

3.1. Numerical Modeling

To evaluate the influence of constitutive models and associated parametric studies in predicting tunnel behavior, a three-dimensional (3D) modeling approach is employed for numerical simulations. The MIDAS GTS NX 2018, a Finite Element (FE) simulation program specifically designed for geotechnical analysis, is used for the computational resource in this research. This software is capable of modeling porous media, including rock and soil.

3.2. Case Study - Isfahan-Shiraz Railway Tunnel

The selected case study to verify the accuracy of the result obtained from the software, Isfahan-Shiraz railway tunnel monitoring data and field characteristics

report were adopted. The tunnel has a horseshoe-shaped cross-section, with an approximate length, height and width of 820 m, 5.75 m, and 8.2 m, respectively. On December 19th, 2006, the B1-1 monitoring convergence station was situated at 269 + 047.5 km, located at a distance of about 717.5 m from the tunnel entrance. The tunnel overburden at this station is 29 m, and the material types are mostly shale and sandstone. The tunnel's temporary support system consists of two layers of wire mesh, 25 cm thick shotcrete, and a steel frame (Sarikhani Khorami, 2012).

In the numerical simulation, the support system modeled as an equivalent shotcrete thickness and the tunnel excavation and base shotcrete application were simultaneously performed in a single stage. Elastic modulus, cohesion, internal friction angle, and lateral pressure coefficient of the tunnel medium are shown in Table 1. Parameters were calculated through the back analysis based on MC criteria by considering a constant value for Poisson's ratio and specific gravity. The calculated parameters represent the ground condition of the tunnel's environment. The adapted method to back analysis was performed by constant consideration of parameters in the reasonable range for the existing ground. Then other parameters were changed in a range to obtain the best match quality with

the recorded monitoring data.

Based on the method proposed by Singh and Goel (1999), 98% of the total tunnel displacements occur up to two times the tunnel diameter from the tunnel's face as a result of the tunnel face's advancing. In this zone, the rock mass's time-dependent behavior does not significantly impact the convergence of the tunnel face (Asadollahpour et al., 2014). Figure 1 shows the comparison of the tunnel walls' convergence monitoring data and the outcome of the performed FEM analysis at the B1-1 station. Numerical modeling results had a good agreement with the reported convergence value of the tunnel.

4. Numerical Modeling

In numerical modeling, the tunnel was modelled with a radius of 4.25 m, a depth of 36 m and a lining thickness of 25 cm. The dimensions of the model are 99 m × 85.5 m × 108 m, which was considered greater than five times the tunnel diameter at the sides (Vitali et al 2018), and 12 times greater than the tunnel diameter in the longitudinal direction (Carranza-Torres et al., 2013). The tunnel face is also located at a distance of 6 times the diameter (54 m) from the tunnel's beginning. Figure 2 shows the geometry and mesh elements of the simulated model.

Table 1. Ground parameters for Isfahan-Shiraz railway tunnel

| Modulus of elasticity (MPa) | Cohesion (kPa) | Angle of internal friction (deg.) | Lateral pressure coefficient | Poisson's ratio | Unit weight (kg/m ³) |
|-----------------------------|----------------|-----------------------------------|------------------------------|-----------------|----------------------------------|
| 321 | 112 | 16.15 | 2.48 | 0.25 | 2400 |

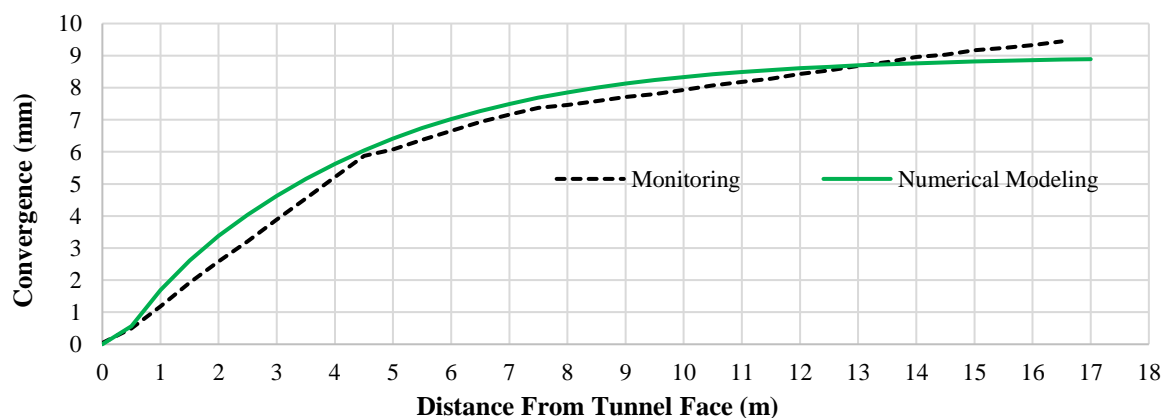


Fig. 1. Comparison of the results of Isfahan-Shiraz railway tunnel numerical modeling and monitoring

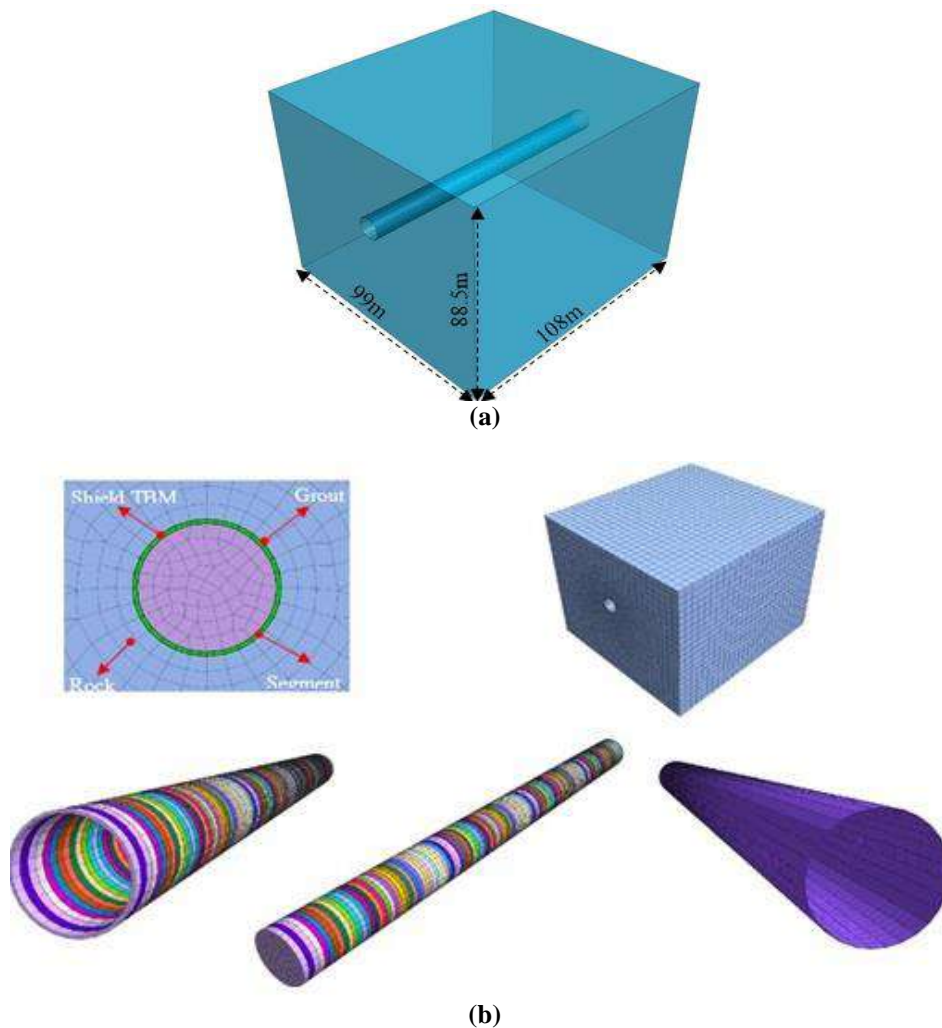


Fig. 2. a) Geometry; and b) the FE mesh

To accurately simulate the behavior of a typical TBM tunnel during construction, the numerical modeling considered the actual procedure and sequences involved in the construction process, such as drilling, installing steel shields, installing segments, grouting, and applying jack and face pressures. Solid elements were used to model the rock medium and concrete segments of the tunnel, while shell elements were employed to simulate the steel shield and grout. The concrete segments, steel shields, and grout were defined as elastic materials. The rock mass behavior was investigated using seven constitutive models: LE, VM, MC, DP, SS, GHB, and GHBR. The boundary condition of the model involved restraining the model in the horizontal directions as a roller on all sides, and the bottom part of the mesh was pinned and restrained in the horizontal and vertical

directions. Table 2 summarizes the characteristics of the tunnel support system in numerical modeling. The numerical modeling steps were also conducted as the following steps:

- Defining the geometry of the model.
- Defining the material constitutive model and support system material parameters.
- Incorporating the excavation and support system in the geometry of the model.
- Defining the boundary conditions and generating the mesh.
- Defining the analysis sequence in the mesh of the model, including the stage construction sequence of applying the in-situ condition, ground excavation, and application and activation of the tunnel support systems.
- Performing the analysis.
- Assessing the results

Table 2. Characteristics of the tunnel support system in numerical modeling

| Name | Shield | Grout | Segment |
|---------------------------------------|-------------------|-----------------|-------------------|
| Model type | Elastic | Elastic | Elastic |
| Thickness (Cm) | 5 | 5 | 25 |
| Elastic modulus (kPa) | 2.1×10^8 | 1×10^7 | 2.2×10^7 |
| Poisson's ratio | 0.2 | 0.3 | 0.3 |
| Specific gravity (kN/m ³) | 78 | 22.5 | 24 |

To investigate the behavior of the tunnel under different constitutive models, the rock mass has been classified from very weak to strong groups based on strength and the suggested groups by Singh and Goel (1999). Table 3 indicates the adopted categories and selected parameters for the rock samples as a representative of each category based on the RMR classification. RMR system represents an engineering classification of rock mass utilized to evaluate the quality of the rock with considering six parameters named Uniaxial Compressive Strength (UCS), Rock Quality Designation (RQD), spacing of discontinuity, condition of discontinuity, conditions of groundwater, and orientation of discontinuity. The method is also used to estimate the tunnel stand-up time. Representative values were determined for a median sample of each category. Each rock mass group's parameters were calculated by RocLab software. The software inputs are the uniaxial compressive strength of intact rock, Geological Strength Index (GSI), rock disturbance factor, and constant value of rock mass (*mi*). The outputs are elastic modulus of the rock mass, shear strength parameters, and uniaxial compressive strength of rock mass. The calculated

parameters for each rock group in numerical modeling are shown in Table 4.

5. Results and Discussions

5.1. The Vertical Settlements of the Tunnel Crown and the Invert Heave

Numerical analysis was used to obtain the tunnel crown settlements and invert heave along the longitudinal axis under various constitutive models for different types of rocks. Figure 3 displays the vertical displacement contours for very weak rocks, while Figure 4 compares the vertical displacement for each rock category.

For very weak rocks, the VM model predicts the highest crown settlement and invert heave at 24.5 mm and 22.5 mm, respectively, compared to other constitutive models. The MC, DP, and LE models have lower predictions with crown settlement values of 14.8, 10.8, and 8.7 mm and invert heave values of 17.6, 15.8, and 15.2 mm, respectively. In this rock group, the difference between the MC and DP models is significant, with MC predicting a higher value than DP, and the LE model predicting the lowest value. However, the FE equations of GHB, GHBR, and SS constitutive models did not converge in this rock group.

Table 3. Suggested parameters range for rock categories

| Rock type | Sample | σ_{ci} (MPa) | RMR | GSI | Mi |
|-----------|---------------|---------------------|-------|-------|-------|
| Strong | Conglomerates | 50-100 | 61-80 | 56-75 | 16-22 |
| Medium | Sandstone | 25-50 | 41-60 | 36-55 | 11-15 |
| Poor | Marl | 5-25 | 21-40 | 16-35 | 6-10 |
| Very poor | Shale | 1-5 | < 20 | 0-15 | 0-5 |

Table 4. Calculated parameters of each representative group of rocks for numerical modeling

| Rock type | Em (MPa) | σ_{cm} (kPa) | Φ (deg.) | C (kPa) | Ψ (deg.) | GSI residual | C residual (kPa) |
|-----------|----------|---------------------|---------------|---------|---------------|--------------|------------------|
| Strong | 15400 | 21382 | 38.60 | 3860 | 6.75 | 26.85 | 2288 |
| Medium | 3326 | 5352 | 29.09 | 1180 | 2.18 | 23.40 | 852 |
| Poor | 1060 | 1700 | 21.35 | 435 | 0 | 17.88 | 354 |
| Very poor | 300 | 228 | 14.95 | 65.65 | 0 | 12.27 | 58 |

For weak, moderate, and strong rocks, the VM, DP, and MC models predict almost the same values for crown settlements and invert heaves, while the SS model provides higher values than other models. The SS model's predictions for medium rocks are slightly different from other models, while for strong rocks, it is similar to other models' predictions.

Except for very weak rocks, both GHB and GHBR models predict higher values for crown settlements along the tunnel axis than other constitutive models. Furthermore, as the rock strength increases from weak to strong, the predicted values become closer to those of other constitutive models. The GHB model provides the highest value in the tunnel's invert heave for weak rocks, while GHBR has the lowest value. However, in moderate and strong rocks, GHBR has the highest, and the LE model has the lowest values in predicting the tunnel's invert heave.

5.2. Ground Surface Settlement Induced by Tunnel Excavation

Figures 5 and 6 present the surface settlement longitudinal profile and cross-section for different constitutive models in the studied rocks. The measurements were taken at a cross-section located 18 m from the tunnel face, which is twice the tunnel diameter, or 36 m from the beginning of the model. The Panet equation (Sulem et al., 1987) was used to calculate the results. This location was selected because 98% of the total tunnel displacements are due to the advancing of the tunnel face at this distance, without the interference of the creep and time-dependent behavior of rocks (Asadollahpour et al., 2014).

Observations reveal that the ground surface settlement has a parabolic shape, and its vertex aligns with the tunnel's center. In Figure 7, the maximum values of ground surface settlements are compared at a distance twice the tunnel's face diameter. Notably, as the rocks grow stronger, the differences in ground surface settlement values decrease. The GHBR constitutive

model consistently predicts higher levels of ground surface settlement than other models.

Figure 7a depicts that, for very weak rocks, the VM model predicts the highest maximum value of ground surface settlement, while the LE model predicts the lowest. Comparatively, the Mohr-Coulomb model produces higher values than the DP model. Moreover, as per Figure 5a, the LE, DP, and MC models suggest a slight heave on the ground surface when moving away from the cross-section's center for very weak rocks. The VM model shows a 1387% higher surface settlement than the LE model, while the MC model shows 508%, and the DP model shows 219% higher surface settlements.

In the weak rock category, as shown in Figure 5b, the settlement value reaches zero by moving away from the center of the cross-section. The GHBR model has predicted the maximum value of the ground surface settlement, followed by the GHB and then the SS constitutive models showing the second and third highest values. According to Figure 5b, the difference between SS and GHB constitutive models is in their ground surface settlement curves' vertex values. The two curves will coincide by moving away from the center of the cross-section to the sides. Figure 7b indicates that the VM, DP, and MC models offer the same results, and the LE model has a slightly lower value. The difference is only 1.45%, which is inconsiderable. However, the maximum values of the ground surface settlement in SS, GHB, and GHBR are 275, 323, and 942%, respectively, more than the LE model.

Regarding the results shown in Figure 7c, for medium rocks, the differences between the predicted values of ground surface settlement by each constitutive model have been reduced. It is evident that in this category of rocks, the predicted values of GHBR are greater than other constitutive models. By comparing the maximum ground surface settlement of

each constitutive model with the LE model, it was observed that VM, DP, and MC, indicate 3% greater value, SS and GHB models show a 6.1% greater value, and

GHBR shows a value that is 18.2% greater than the maximum surface settlement predicted by LE model.

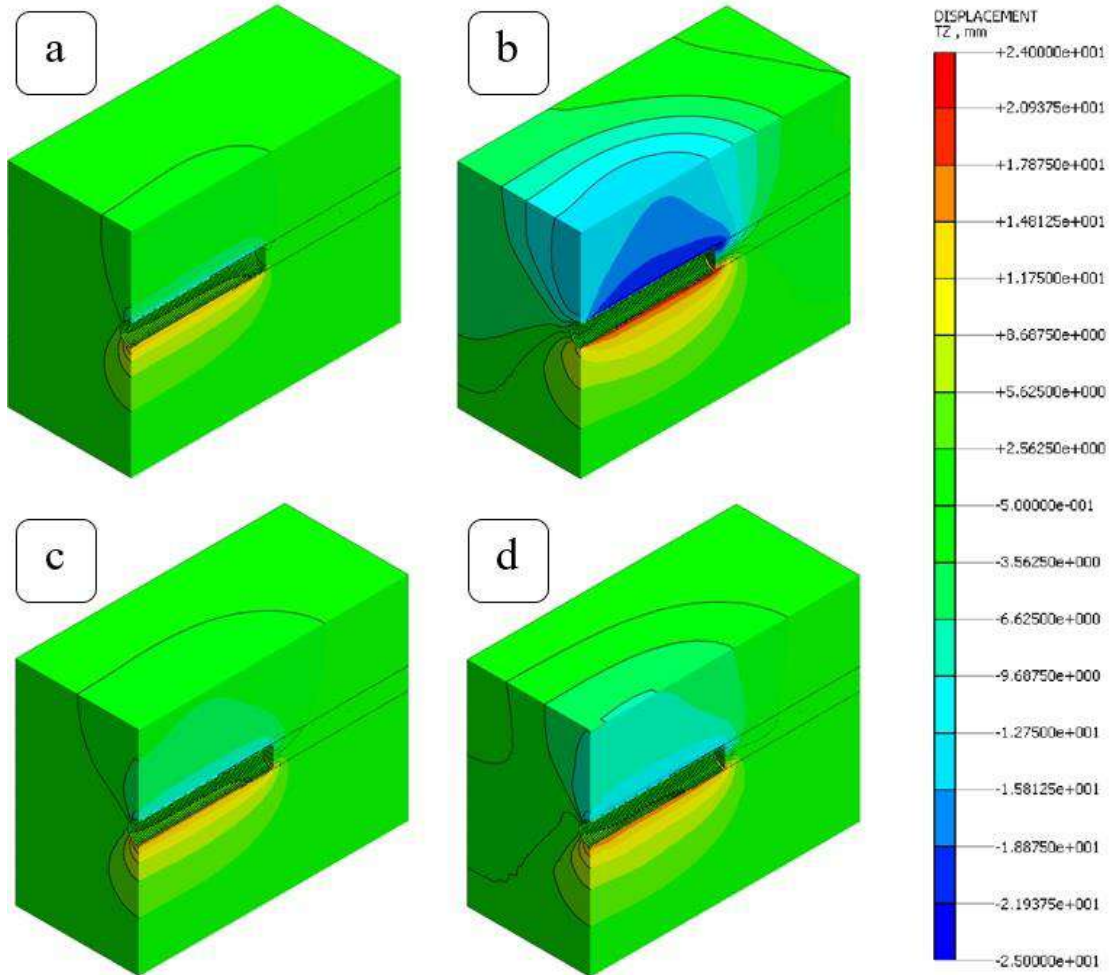
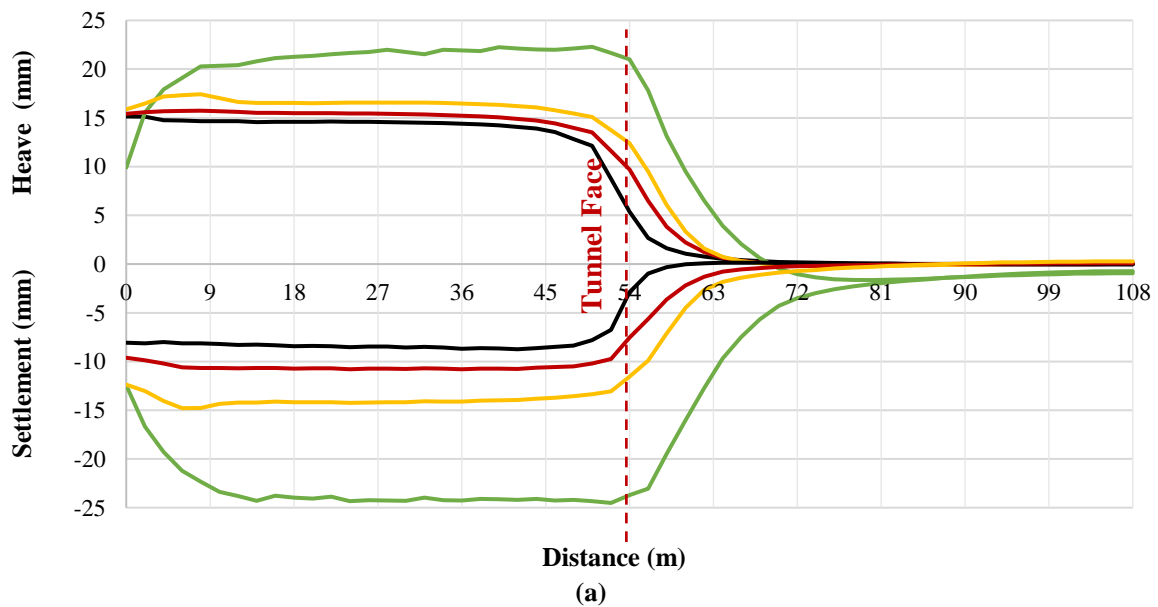


Fig. 3. Vertical displacement contours for: a) LE; b) VM; c) DP; and d) MC models in very weak rock



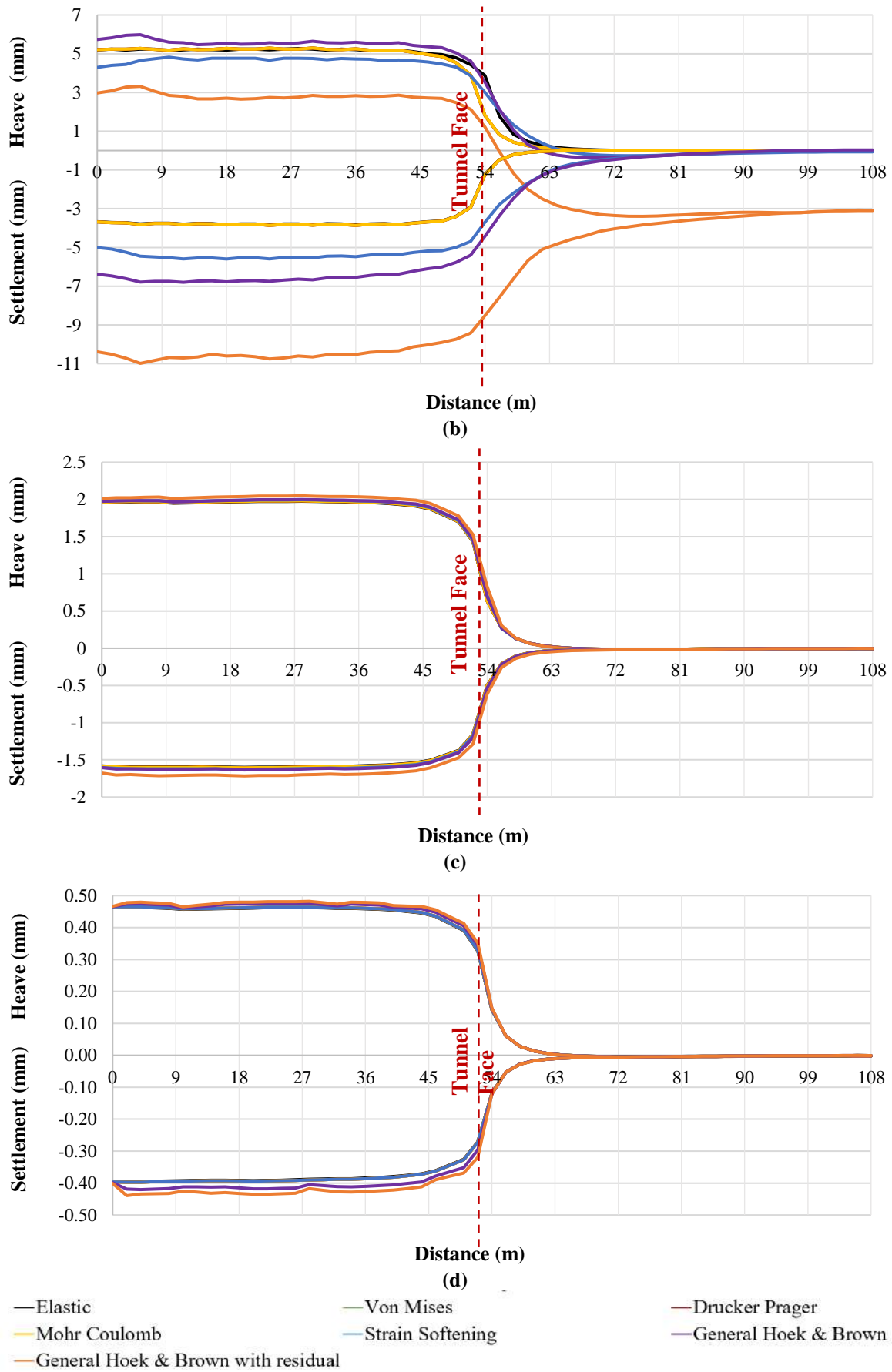
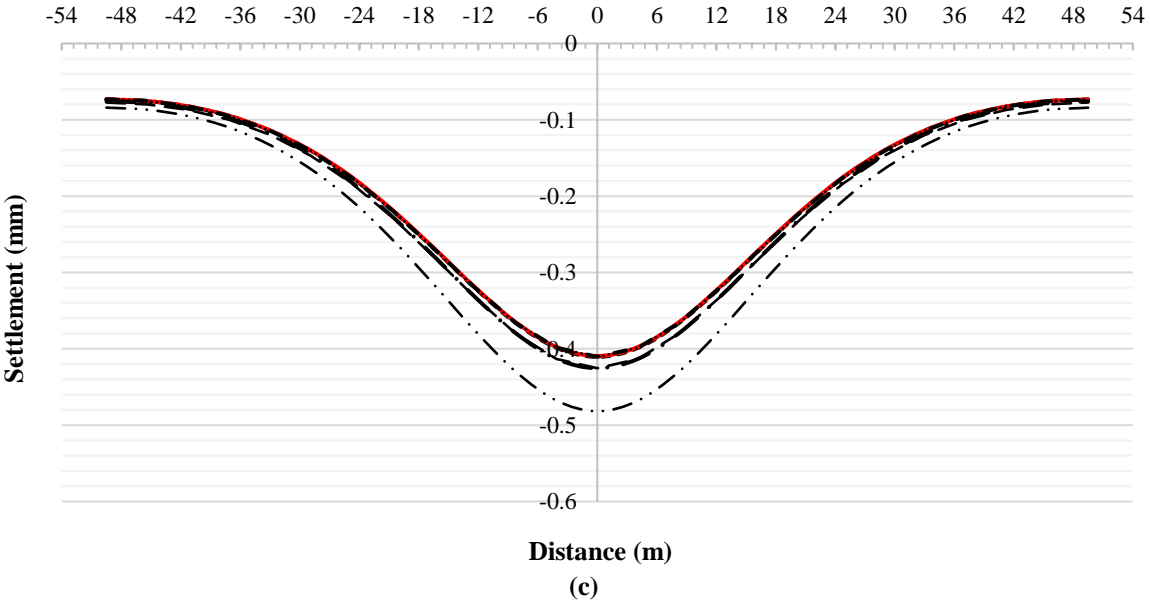
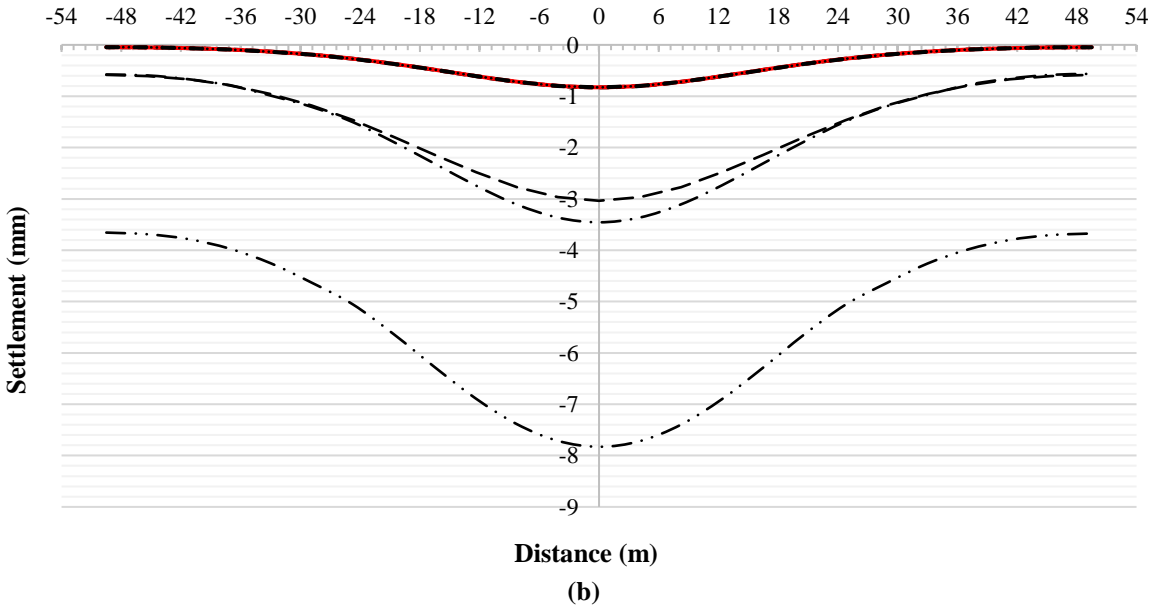
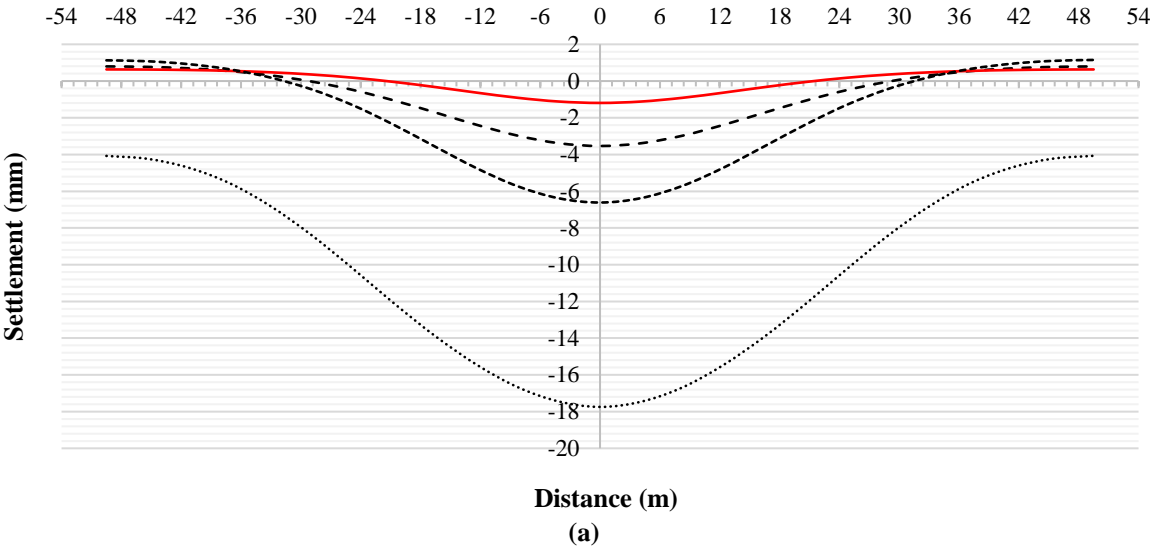


Fig. 4. Vertical settlements of the tunnel crown and the invert heave along the longitudinal axis of the tunnel for: a) Very weak; b) Weak; c) Moderate; and d) Strong rocks



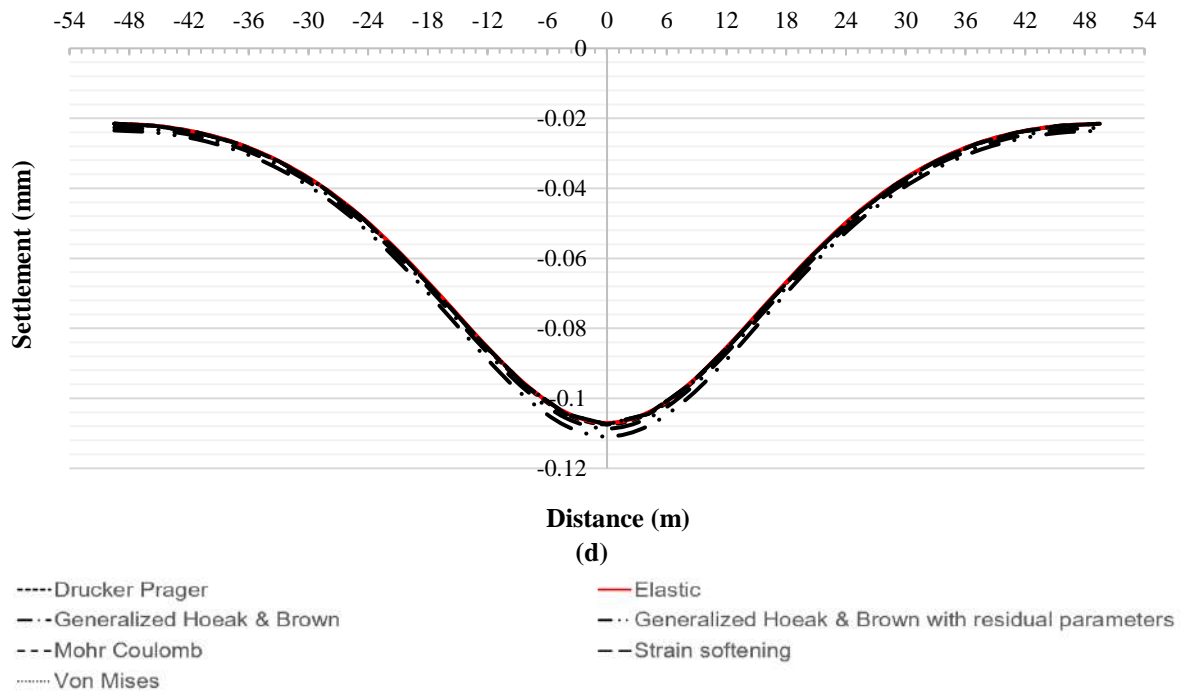
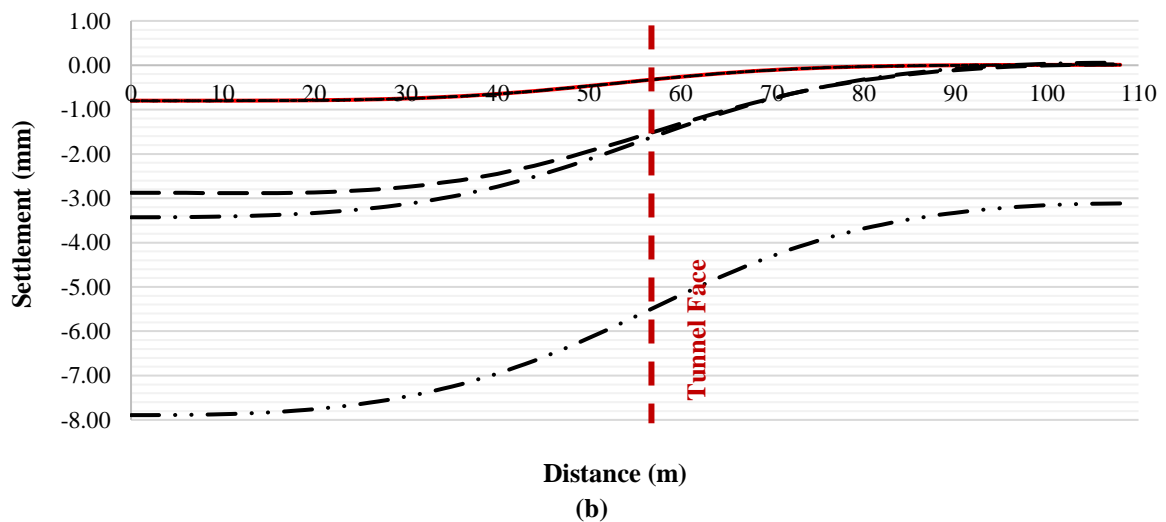
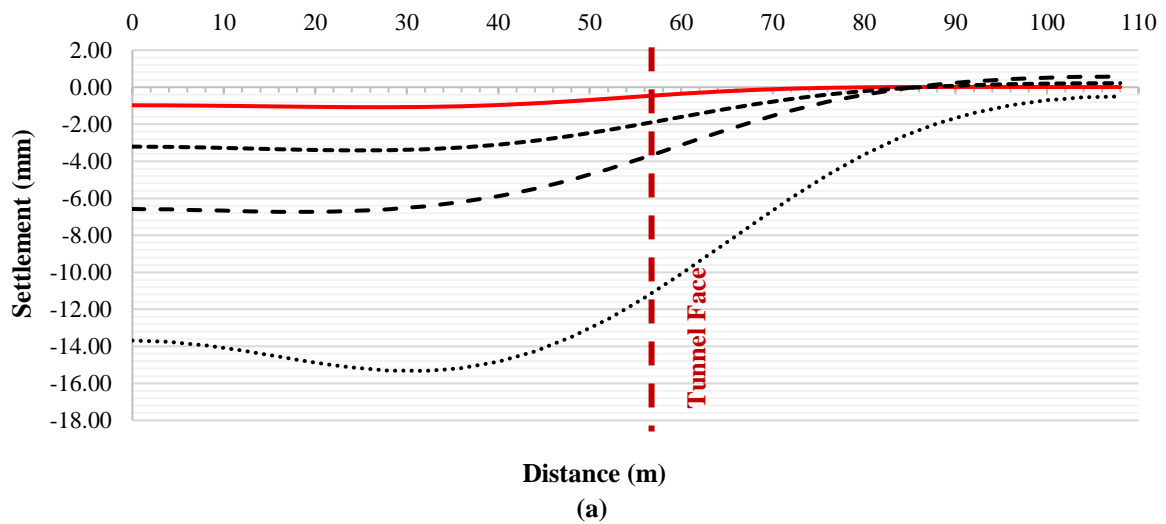
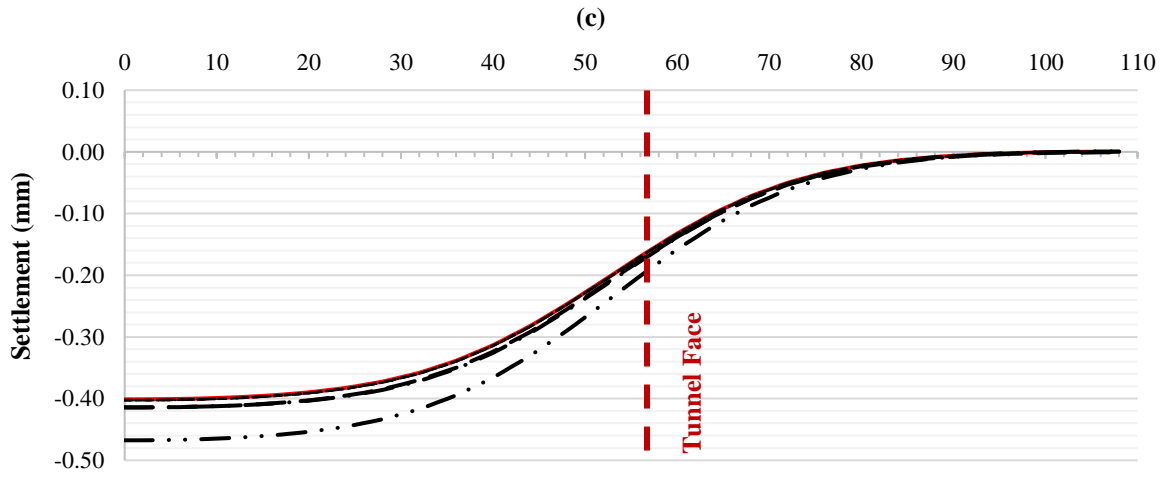
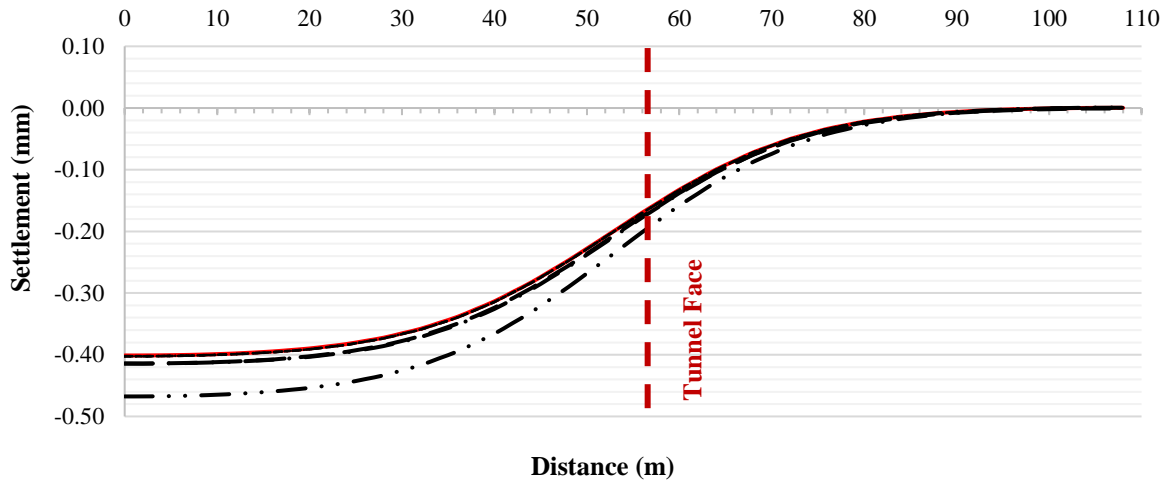


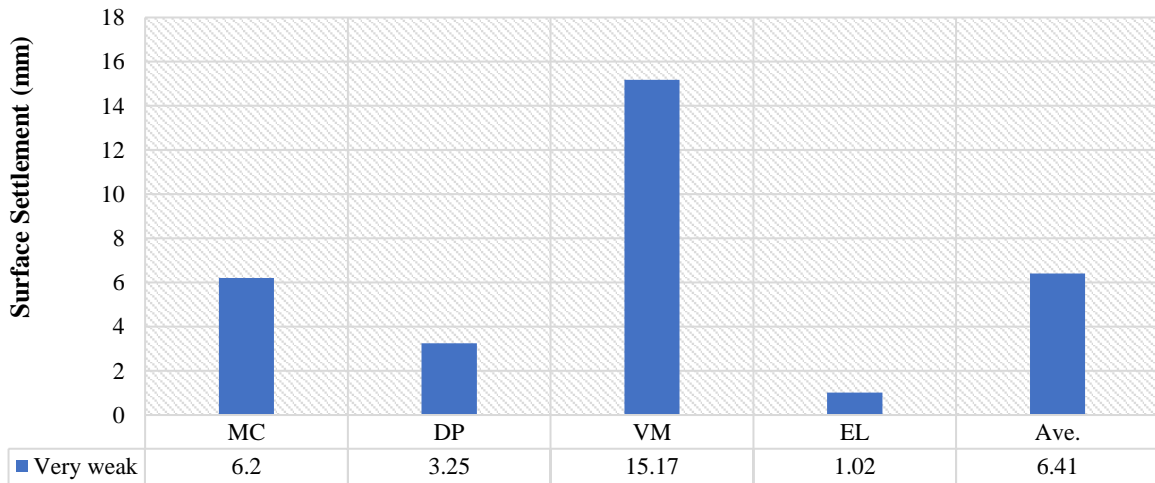
Fig. 5. Surface settlement cross-section for: a) Very weak; b) Weak, c) Moderate; and d) Strong rocks





- Elastic
- Drucker Prager
- Strain softening
- · - Generalized Hoek & Brown with residual parameter
- Von Mises
- Mohr Coulomb
- · - Generalized Hoek & Brown

Fig. 6. Longitudinal profile of surface settlement for: a) Very weak; b) Weak; c) Moderate; and d) Strong rocks



(a)

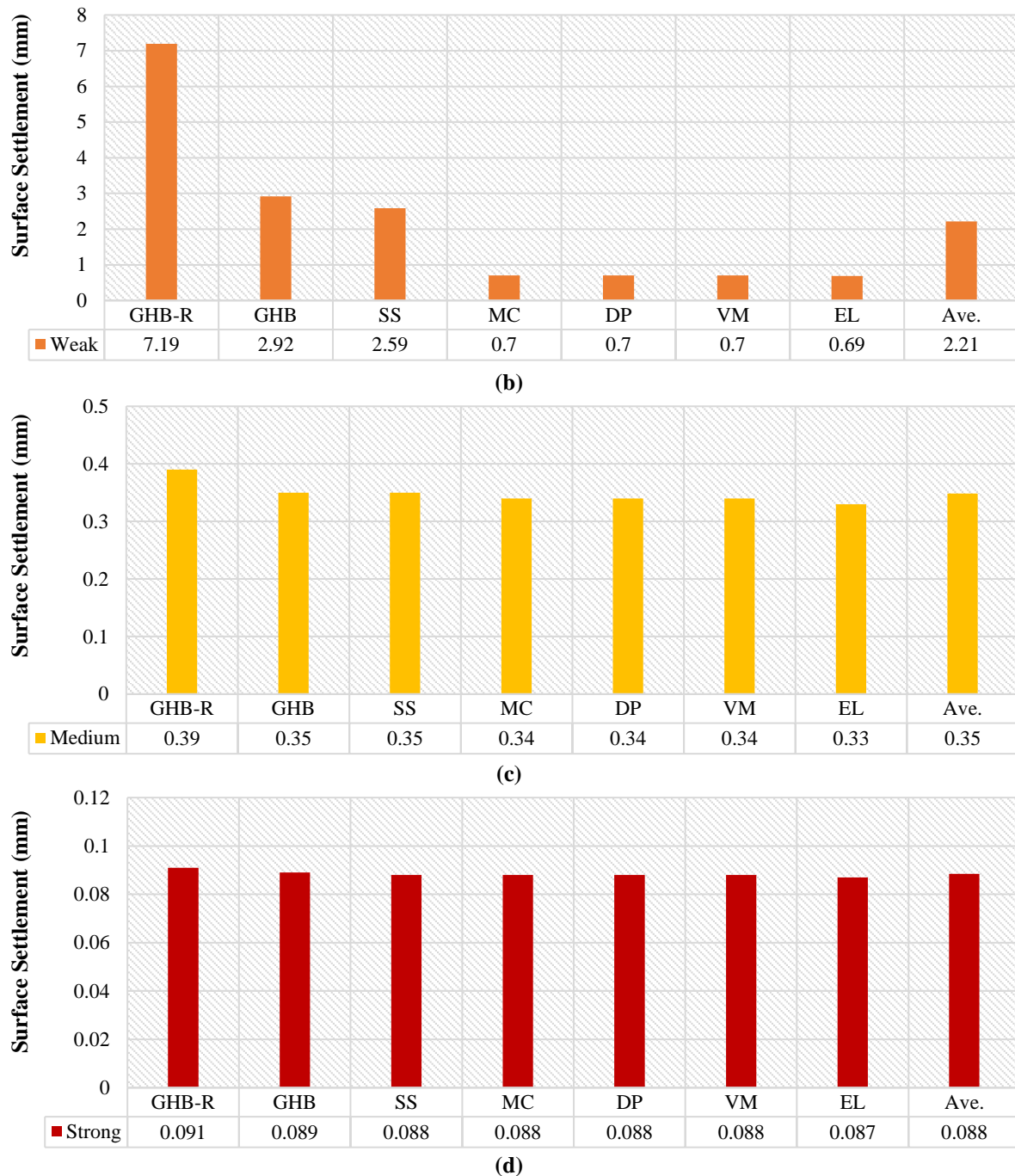


Fig. 7. Maximum surface settlements of the cross-section for: a) Very weak; b) Weak; c) Moderate; and d) Strong rocks

In the strong rocks, according to the results shown in Figure 7d, compared to the LE constitutive model, VM, DP, MC, and SS models show a value of 1.15%, GHB shows a value that is 2.3%. GHBR offers a value that is 4.6% greater than the ground surface settlement of the LE model. The minor differences between the results obtained from all the constitutive models for moderate and strong rocks compared to the LE model's values indicate that all these

models can reasonably predict the elastic behavior of these rock categories.

5.3. Stresses Applied to the Support System

Figure 8 shows the Z-Z vertical stress contours for very weak rocks, in the concrete segment, at a distance of twice the diameter of the tunnel face. In Figures 9a and 9b, the Z-Z and Z-X's maximum vertical and shear stresses are shown,

respectively. In general, in all the constitutive models, when the rocks get stronger, the maximum stress values applied to the support system have decreased as well as the difference in the calculated stresses by each constitutive model.

The LE constitutive model shows the highest value in the Z-Z direction for the very weak rock category. Afterward, MC

and DP have the same results, and then the VM model has the lowest value.

In the weak rocks, according to Figure 9a, among the studied constitutive models, the maximum vertical stress is predicted by SS model, then GHB and GHBR models, and then, the three constitutive models of MC, DP, and VM, and eventually the LE model.

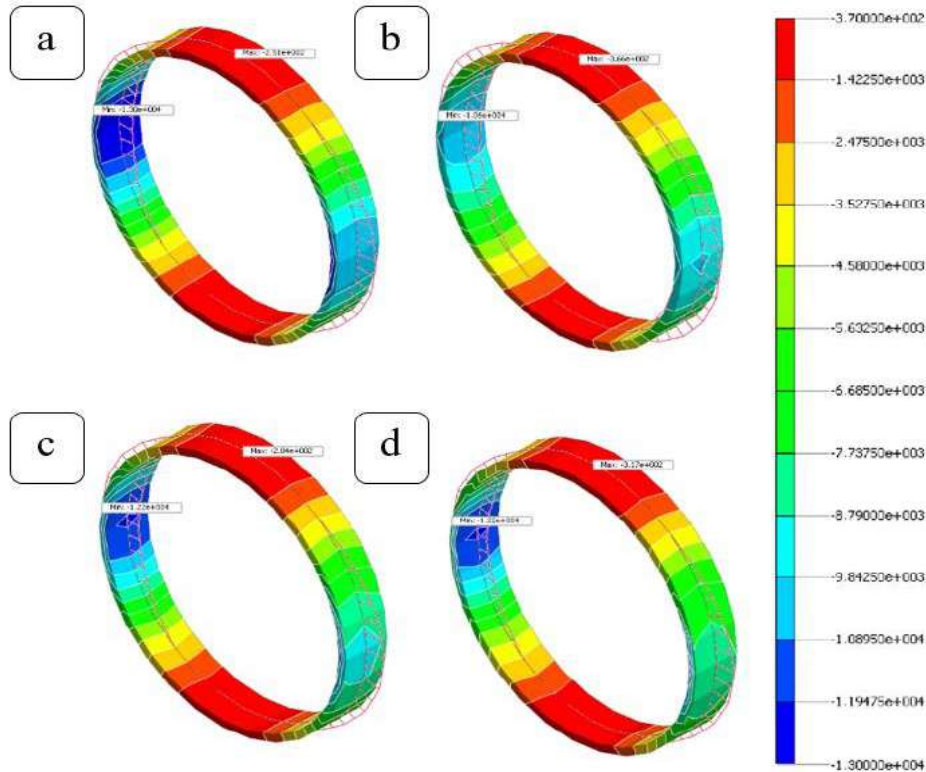
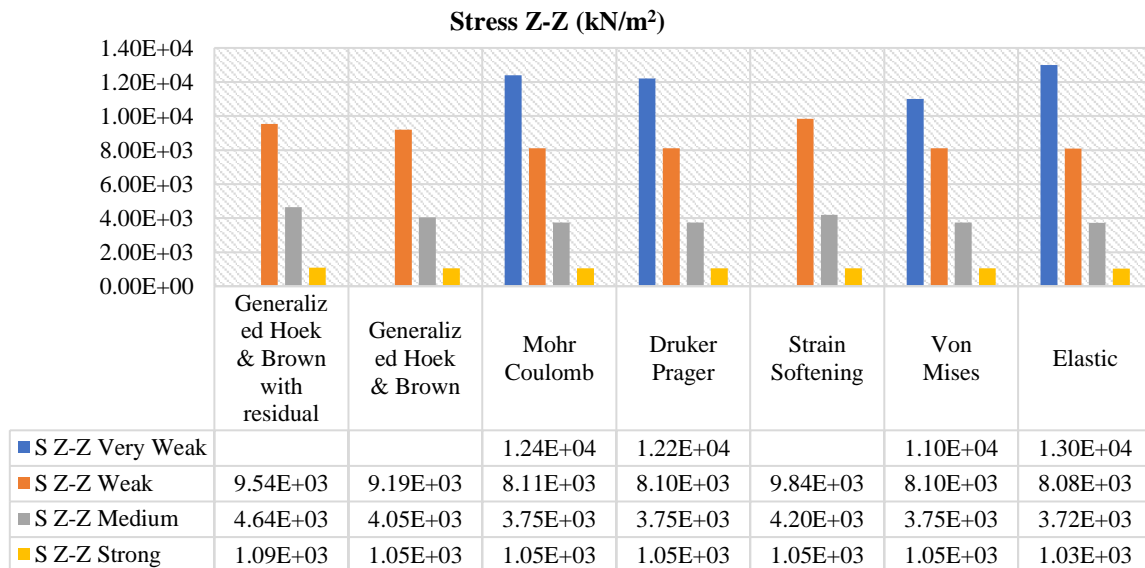
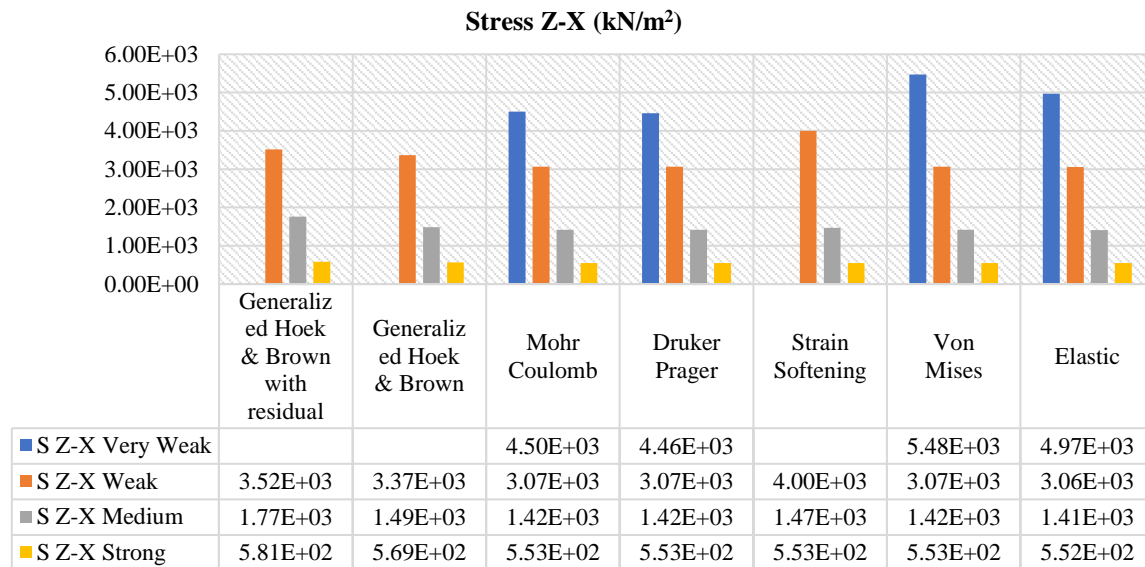


Fig. 8. Vertical stress contours for: a) LE; b) VM; c) DP; and d) MC models in very weak rock



(a)



(b)

Fig. 9. Absolute Maximum stresses in: a) Z-Z; and b) Z-X direction

The GHBR model has the highest stress in the Z-Z direction in the medium rocks. This is followed by the SS model and GHB, having the exact predictions, then the three constitutive models of MC, DP, and VM, and the lowest value of stress belongs to the LE model.

In the strong rock category, the result of Z-Z stress from highest to lowest is attributed to GHBR, having the highest stress value prediction, then, the four constitutive models of SS, MC, DP, and VM with the same values, then, the GHB, and finally the LE model.

Since the linear elastic constitutive model does not have a failure limit, it cannot predict the failure phenomenon. Therefore, in the range of very weak rocks, the LE model, in the assumed conditions for the tunnel, shows the stress values in the Z-Z direction more than other constitutive models, because in the other models, when reaching the yield status, the yielded FEs will no longer stand additional stress. In weak to strong rocks, due to characteristics of the examined tunnel, owing to the resistance of the rock, the failure did not occur, and therefore the elastic model does not have the highest stress value.

According to the results of Figure 9b, the VM constitutive model shows the maximum stress value in the Z-X direction

for the very weak rocks. After that, the LE and MC models have a lower value than the VM model, and finally, the lowest value belongs to DP.

The GHBR and SS have similar results in the weak rock category, with the maximum shear stress value in the Z-X direction. Afterwards, the three constitutive MC, DP, and VM models provide the same results. The minimum value is predicted using the LE model.

In the medium rocks, the highest value of shear stress in the Z-X direction is attributed to GHBR. Subsequently, the GHB and SS models have the same value, lower than the GHB value. The next are the three constitutive models of MC, DP, and VM. Finally, similar to the behavior of weak rocks, the LE model predicts the minimum value.

In the strong rock category, the maximum stress in the Z-X direction is shown by the GHBR and then the GHB, and after these two models, SS, MC, DP, and VM models have the same results. The lowest value belongs to simulations with the LE model.

6. Parametric Analysis

The following section presents parametric studies based on the LE, MC, and GHB

models for three sensitive parameters in numerical modeling: specific gravity, Poisson's ratio, and dilation angle. Weak rock category was adopted as a representative to perform the parametric analysis.

6.1. Specific Gravity

As shown in Figure 10, specific gravity is changed in the range of 21-27 kN/m³. The ground surface settlement cross-section has been drawn for the LE, MC, and GHB models.

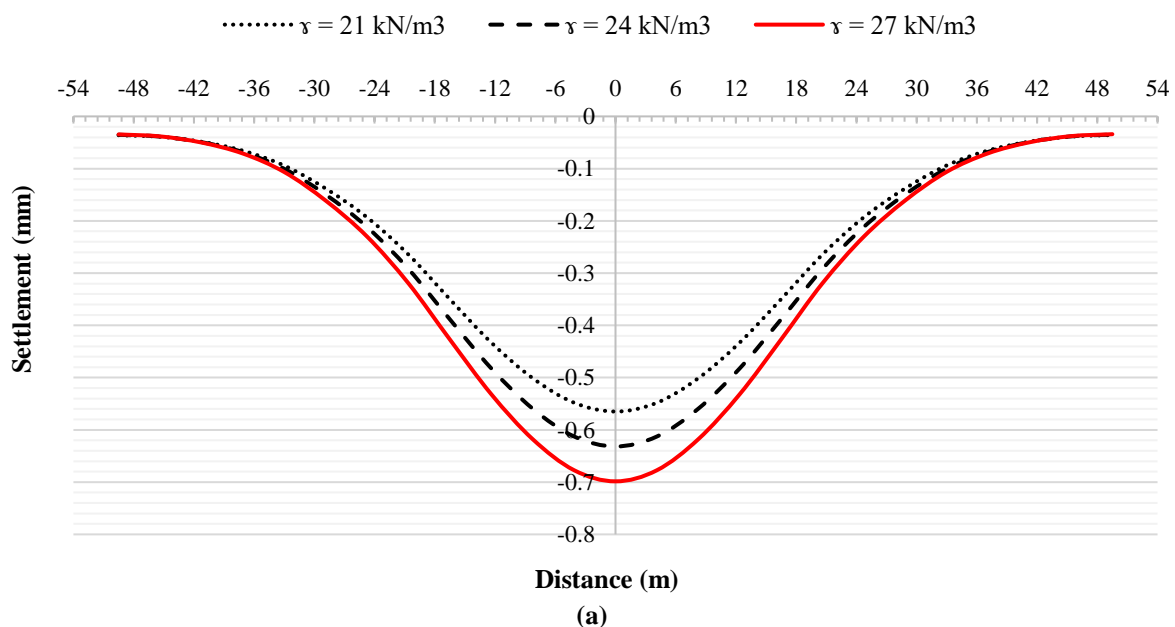
It is evident that decreasing the specific gravity in all models results in a reduction of the maximum ground surface settlement. The greatest decrease is observed in the GHB model, while the lowest is seen in the LE model. Additionally, the changes in the broader area of cross-section are more widespread in the GHB model. Specifically, a reduction of three kN/m³ in specific gravity, from 27 to 24 kN/m³, results in a 29% drop in maximum settlement for the GHB model, as well as 10.6% for MC and 10.58% for the LE model. Similarly, a reduction of specific gravity from 24 to 21 kN/m³ leads to a 38%, 11.85%, and 11.83% decrease in maximum settlement for the

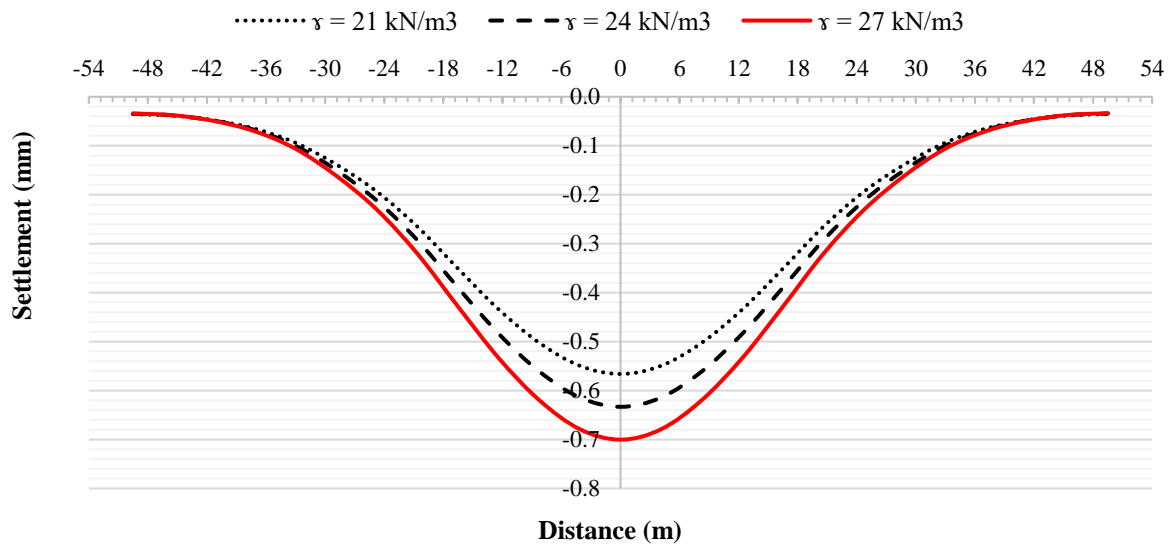
GHB, MC, and LE models, respectively.

6.2. Poisson's Ratio

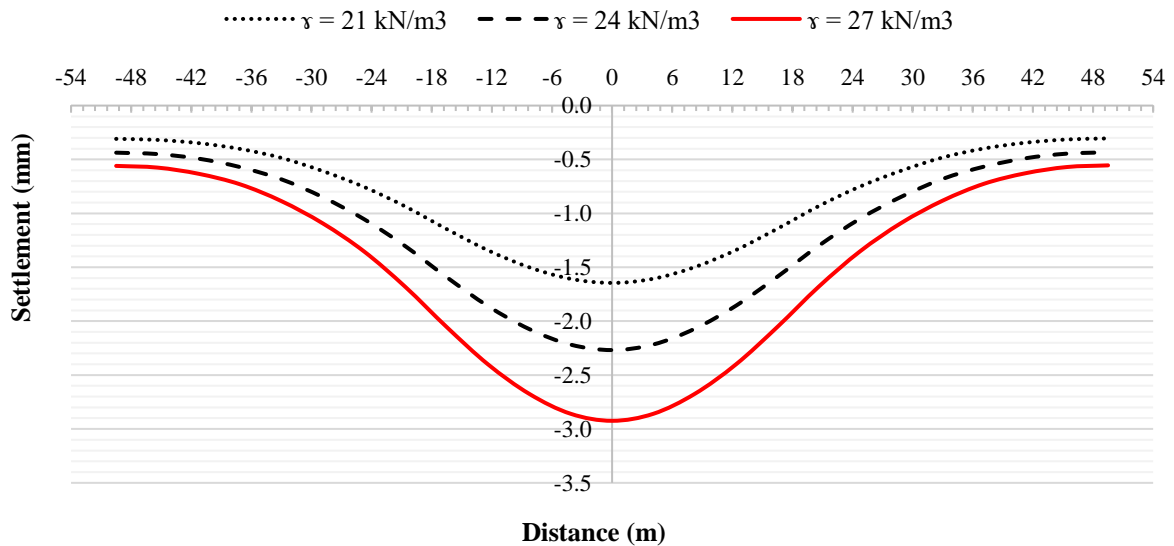
In Figure 11, Poisson's ratio of the rock is changed in the range of 0.2-0.4, and the ground surface settlement cross-section has been shown for the LE, MC, and GHB constitutive models.

As demonstrated by all the models, increasing the Poisson's ratio results in a decrease in the maximum ground surface settlement. The GHB model exhibits the highest magnitude of decrease, while the LE model displays the lowest. Additionally, in the MC and LE models, decreasing the Poisson's ratio results in a tighter parabola for the cross-section of ground surface settlements, with settlements decreasing away from the center of the parabola. When the Poisson's ratio equals 0.2, ground surface heave can be observed. Increasing the Poisson's ratio from 0.2 to 0.3 leads to a 58.6% drop in maximum settlement for GHB, 18% for MC, and 17.85% for the LE model. Similarly, increasing the Poisson's ratio from 0.3 to 0.4 results in a 210%, 16.3%, and 16.12% decrease in maximum settlement for GHB, MC, and LE, respectively.



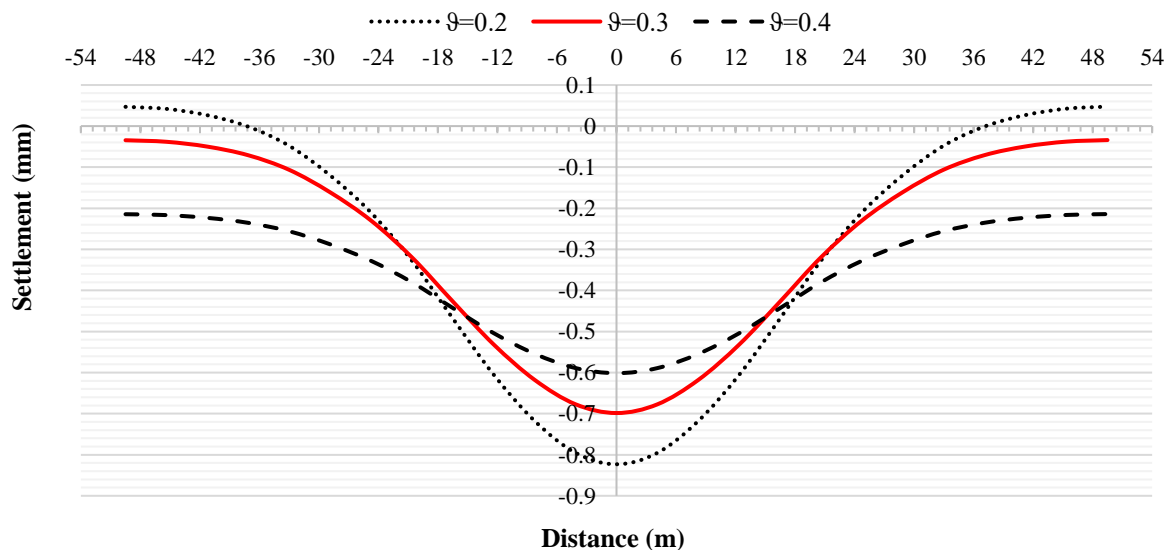


(b)

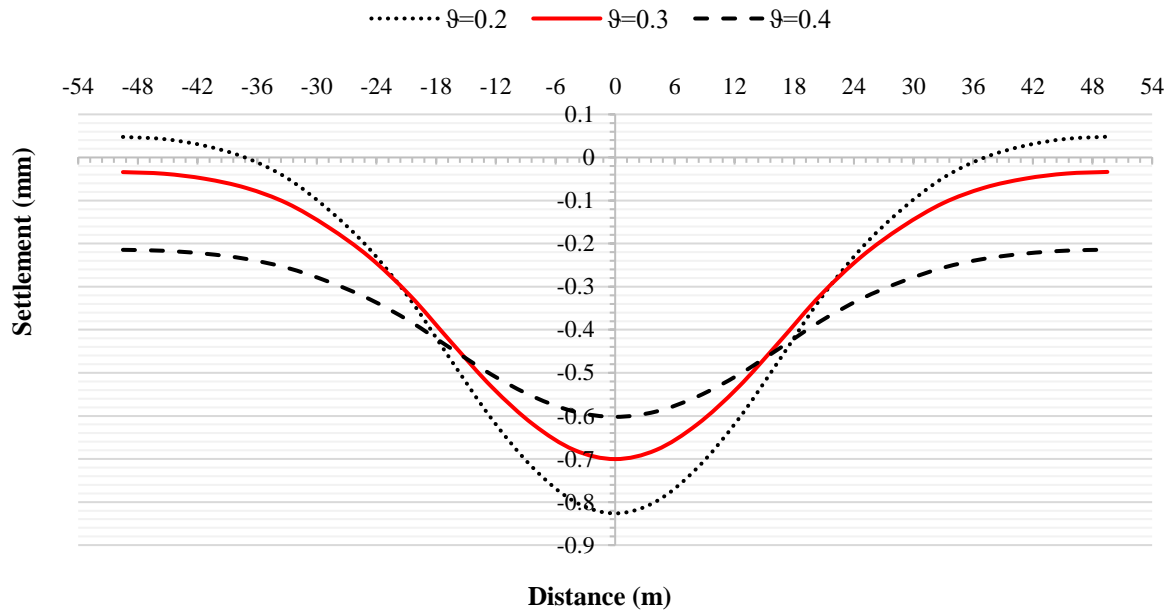


(c)

Fig. 10. Ground surface settlements in parametric analysis on specific gravity for: a) LE; b) MC; and c) GHB models



(a)



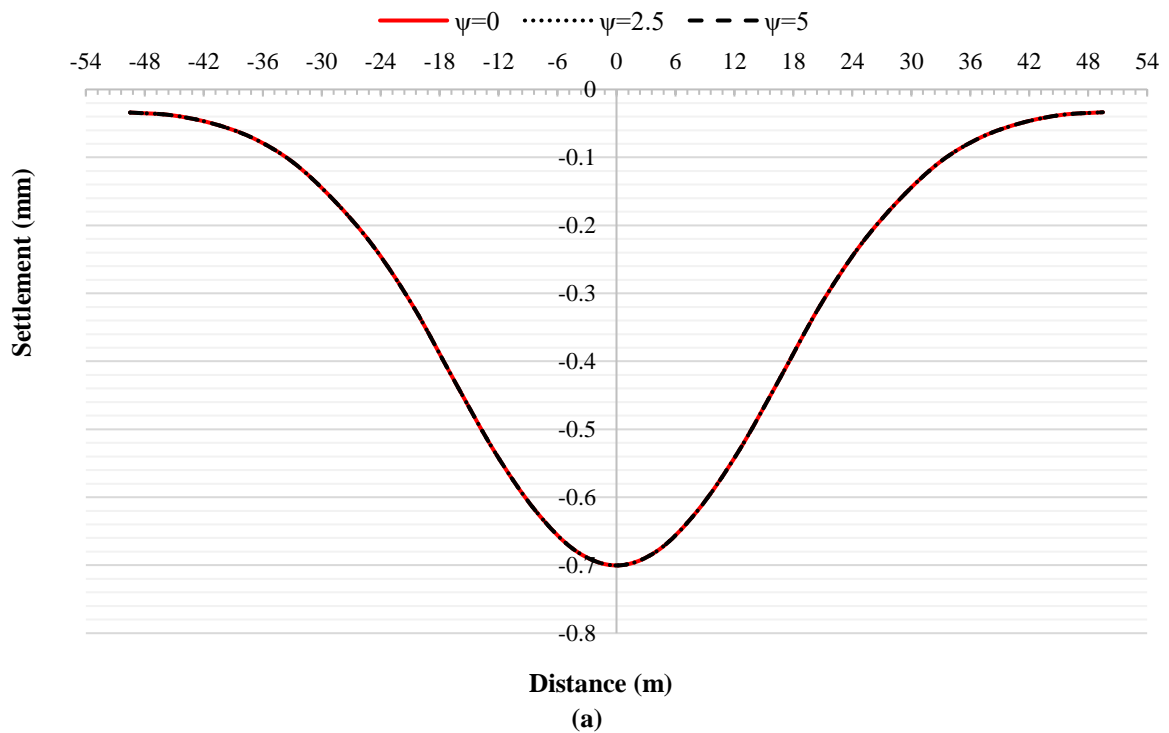
(b)
Fig. 11. Ground surface settlements in parametric analysis on Poisson's ratio for: a) LE; b) MC; and c) GHB models

6.3. Dilation Angle

As illustrated in Figure 12, the rock's dilation angle has been varied between 0 and 5 degrees, and the ground surface settlement cross-section has been plotted for the MC and GHB constitutive models. It is worth noting that the LE model does not account for the dilation angle.

As depicted in the figure, an increase in

the GHB model's dilation angle results in a decrease in the maximum settlement of the ground surface. Specifically, each 2.5-degree increase in the dilation angle leads to a 7% reduction in the maximum cross-section settlement. Conversely, changing the dilation angle does not have an impact on the ground surface settlement results for the MC model.



(a)

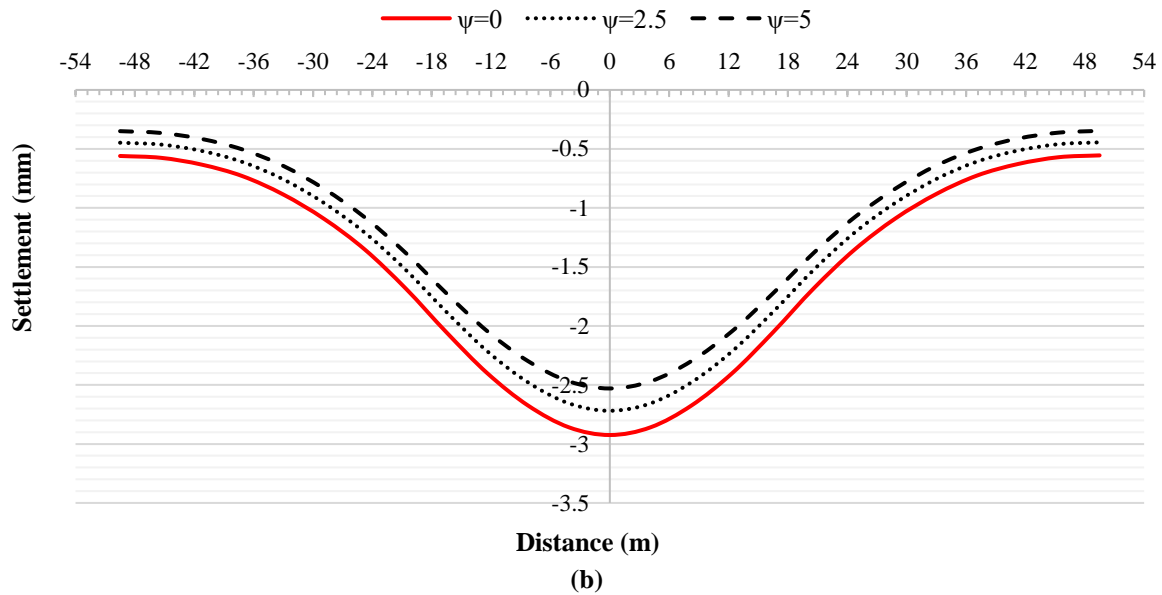


Fig. 12. Ground surface settlements in parametric analysis on dilation angle for: a) MC; and b) GHB models

7. Conclusions

In this study, numerical modeling was employed to evaluate the behavior of tunnels under different constitutive model. A series of 3D FE simulations were conducted to investigate the impact of various constitutive models and associated parametric analyses on tunnel behavior during typical rock medium construction with varying strengths. The simulations focused on analyzing displacements, ground surface settlements, and support system stresses across seven models. Furthermore, parametric analyses were performed on specific gravity, Poisson's ratio, and the rock's dilation angle for the LE, MC, and GHB constitutive models. Based on the analyses conducted, the following results can be presented for the prediction of rock tunnel behavior using the aforementioned models under the assumed conditions of this study:

- Constitutive models play a crucial role in numerical modeling as they represent material behavior and significantly impact analysis results. Therefore, selecting an appropriate model based on accurate data is essential to predict results accurately.
- It is important to note that the LE constitutive model lacks a failure

criterion, making it unsuitable for situations where element failure is likely. This model tends to underestimate deformations and overestimate stresses in very weak rocks. However, it can be used for a first estimation of deformations in strong rocks since it requires less modeling time than other models.

- Some constitutive models more accurately predict displacements and induced lining stresses in the specific strength rock category. Therefore, the appropriate model should be selected by considering the existing mechanical parameters and the rock's strength range.
- Rock-specific constitutive models such as GHB and GHBR are more sensitive to parameter variations than soil-established models like MC and DP. General models like LE and VM are less sensitive.
- In the parametric analysis of specific gravity, increasing this parameter increases ground surface settlements and stresses on the tunnel support system. Therefore, determining the rock's specific gravity accurately is recommended for design purposes.
- A small increase in Poisson's ratio can significantly reduce tunnel and ground surface settlements. Thus, accurately

testing rock samples and considering the correct Poisson's ratio for the material can be very effective in the design.

- For the GHB constitutive model, increasing the medium's dilation angle in the range of weak rocks will decrease tunnel and ground surface settlements. However, this parameter's increase in strong rocks will not significantly affect the results. The MC constitutive model results are not affected by changes in the dilation angle within the range of assumptions made.

8. References

- Aksoy, C.O. and Uyar, G.G. (2017). "Non-deformable support system in swelling and squeezing rocks", *Rock Mechanics and Engineering*, 4, 179-203.
- Anato, N.J., Chen, J., Tang, A. and Assogba, O.C. (2021). "Numerical investigation of ground settlements induced by the construction of Nanjing WeiSanLu tunnel and parametric analysis", *Arabian Journal for Science and Engineering*, 46(11), 11223-11239, <https://doi.org/10.1007/s13369-021-05642-3>
- Asadollahpour, E., Rahmannedjad, R., Asghari, A. and Abdollahipour, A. (2014). "Back analysis of closure parameters of Panet equation and Burger's model of Babolak water tunnel conveyance", *International Journal of Rock Mechanics and Mining Sciences*, 68, 159-166, <https://doi.org/10.1016/j.ijrmms.2014.02.017>.
- Audi, Y., Jullien, A., Dauvergne, M., Feraille, A. and Schwartzentruber, L.D.A. (2020). "Methodology and application for the environmental assessment of underground multimodal tunnels", *Transportation Geotechnics*, 24, 100389, <https://doi.org/10.1016/j.trgeo.2020.100389>.
- Bakker, K.J. (2003). "Structural design of linings for bored tunnels in soft ground", *Heron*, 48(1), 33-64.
- Beyabanaki, A.R. and Gall, V. (2017). "3D numerical parametric study of the influence of open-pit mining sequence on existing tunnels", *International Journal of Mining Science and Technology*, 27(3), 459-466, <https://doi.org/10.1016/j.ijmst.2017.03.018>.
- Bobet, A. (2001). "Analytical solutions for shallow tunnels in saturated ground", *Journal of Engineering Mechanics*, 127(12), 1258-1266, [https://doi.org/10.1061/\(ASCE\)0733-9399\(2001\)127:12\(1258\)](https://doi.org/10.1061/(ASCE)0733-9399(2001)127:12(1258)).
- Cai, M., Kaiser, P.K., Tasaka, Y. and Minami, M. (2007). "Determination of residual strength parameters of jointed rock masses using the GSI system", *International Journal of Rock Mechanics and Mining Sciences*, 44(2), 247-265, <https://doi.org/10.1016/j.ijrmms.2006.07.005>.
- Carranza-Torres, C., Rysdahl, B. and Kasim, M. (2013). "On the elastic analysis of a circular lined tunnel considering the delayed installation of the support", *International Journal of Rock Mechanics and Mining Sciences*, 61, 57-85, <https://doi.org/10.1016/j.ijrmms.2013.01.010>.
- Chalajour, S. and Hataf, N. (2022). "The comparison of tunnel convergence from numerical analysis with monitoring data based on different constitutive models in rock medium", *Civil Engineering Infrastructures Journal*, 56(2), 301-319, <https://doi.org/10.22059/CEIJ.2022.343391.1843>.
- Chen, S.L. and Lee, S.C. (2020). "An investigation on tunnel deformation behavior of expressway tunnels", *Geomechanics and Engineering*, 21(2), 215-226, <https://doi.org/10.12989/gae.2020.21.2.215>.
- Davis, R.O. and Selvadurai, A.P. (2005). *Plasticity and geomechanics*, Cambridge University Press.
- Ding, L. and Liu, Y. (2018). "Study on deformation law of surrounding rock of super long and deep buried sandstone tunnel", *Geomechanics and Engineering*, 16(1), 97-104, <https://doi.org/10.12989/gae.2018.16.1.097>.
- Goodman, R.E. (1989). *Introduction to rock mechanics*, 2nd Edition, Wiley & Sons Ltd., New York.
- He, M., Zhang, Z., Zheng, J., Chen, F. and Li, N. (2020). "A new perspective on the constant mi of the Hoek-Brown failure criterion and a new model for determining the residual strength of rock", *Rock Mechanics and Rock Engineering*, 53, 3953-3967, <https://doi.org/10.1007/s00603-020-02164-6>.
- Hejazi, Y., Dias, D. and Kastner, R. (2008). "Impact of constitutive models on the numerical analysis of underground constructions", *Acta Geotechnica*, 3, 251-258, <https://doi.org/10.1007/s11440-008-0056-1>.
- Hoek, E. and Brown, E.T. (1997). "Practical estimates of rock mass strength", *International Journal of Rock Mechanics and Mining Sciences*, 34(8), 1165-1186, [https://doi.org/10.1016/S1365-1609\(97\)80069-X](https://doi.org/10.1016/S1365-1609(97)80069-X).
- Hoek, E. and Brown, E.T. (2019). "The Hoek-Brown failure criterion and GSI-2018 edition", *Journal of Rock Mechanics and Geotechnical Engineering*, 11(3), 445-463, <https://doi.org/10.1016/j.jrmge.2018.08.001>.
- Hoek, E., Wood, D. and Shah, S. (1992). "A modified Hoek-Brown failure criterion for jointed rock masses" In: *Rock Characterization: ISRM Symposium, Eurock'92*, Chester, UK, (pp. 209-214), Thomas Telford Publishing.

- Hoek, E., Kaiser, P.K. and Bawden, W.F. (1995). *Support of underground excavation in hard rock*, Rotterdam: AA Balkema.
- Jallow, A., Ou, C.Y. and Lim, A. (2019). "Three-dimensional numerical study of long-term settlement induced in shield tunneling", *Tunneling and Underground Space Technology*, 88, 221-236, <https://doi.org/10.1016/j.tust.2019.02.021>.
- Jin, Y.F., Zhu, B.Q., Yin, Z.Y. and Zhang, D.M. (2019). "Three-dimensional numerical analysis of the interaction of two crossing tunnels in soft clay", *Underground Space*, 4(4), 310-327, <https://doi.org/10.1016/j.undsp.2019.04.002>.
- Lazemi, H.A. and Soleiman Dehkordi, M. (2019). "Estimation of the TBM penetration rate using the post-failure behavior of a rock mass and the equivalent thrust per cutter, A case study: The Amirkabir water transferring tunnel of Iran", *Bulletin of Engineering Geology and the Environment*, 78(3), 1735-1746, <https://doi.org/10.1007/s10064-017-1205-2>.
- Li, C., Hou, S., Liu, Y., Qin, P., Jin, F. and Yang, Q. (2020). "Analysis on the crown convergence deformation of surrounding rock for double-shield TBM tunnel based on advance borehole monitoring and inversion analysis", *Tunnelling and Underground Space Technology*, 103, 103513, <https://doi.org/10.1016/j.tust.2020.103513>.
- Li, G., Ma, F., Liu, G., Zhao, H. and Guo, J. (2019). "A strain-softening constitutive model of heterogeneous rock mass considering statistical damage and its application in numerical modeling of deep roadways", *Sustainability*, 11(8), 2399, <https://doi.org/10.3390/su11082399>.
- MIDAS Information Technology Co. (2018) *Chapter 4: Mesh*, In: Midas GTS NX User Manual, (pp. 145-146), Midas, South Korea.
- Ng, C.W.W., Sun, H.S., Lei, G.H., Shi, J.W. and Mašín, D. (2015). "Ability of three different soil constitutive models to predict a tunnel's response to basement excavation", *Canadian Geotechnical Journal*, 52(11), 1685-1698, <https://doi.org/10.1139/cgj-2014-0361>.
- Oettl, G., Stark, R.F. and Hofstetter, G. (1998). "A comparison of elastic-plastic soil models for 2D FE analyses of tunneling", *Computers and Geotechnics*, 23(1-2), 19-38, [https://doi.org/10.1016/S0266-352X\(98\)00015-9](https://doi.org/10.1016/S0266-352X(98)00015-9).
- Park, K.H. (2004). "Elastic solution for tunneling-induced ground movements in clays", *International Journal of Geomechanics*, 4(4), 310-318, [https://doi.org/10.1061/\(ASCE\)1532-3641\(2004\)4:4\(310\)](https://doi.org/10.1061/(ASCE)1532-3641(2004)4:4(310)).
- Pinto, F. (1999). "Analytical methods to interpret ground deformations due to soft ground tunneling", Doctoral Dissertation, Massachusetts Institute of Technology, USA.
- Ranjbarnia, M., Zaheri, M. and Dias, D. (2020). "Three-dimensional finite difference analysis of shallow sprayed concrete tunnels crossing a reverse fault or a normal fault: A parametric study", *Frontiers of Structural and Civil Engineering*, 14, 998-1011, <https://doi.org/10.1007/s11709-020-0621-8>.
- Rocscience, RocLab Version 1.031. (2007). *Rock mass strength analysis using the Hoek-Brown failure criterion*, Rocscience, Toronto.
- Rukhaiyar, S. and Samadhiya, N.K. (2016). "Analysis of tunnel considering Modified Mohr-Coulomb criteria", In: *Recent Advances in Rock Engineering (RARE 2016)*, (pp. 318-326), Atlantis Press, <https://dx.doi.org/10.2991/rare-16.2016.51>.
- Rummel, F. and Fairhurst, C. (1970). "Determination of the post-failure behavior of brittle rock using a servo-controlled testing machine", *Rock Mechanics*, 2, 189-204, <https://doi.org/10.1007/BF01245574>.
- Russo, G., Kalamaras, G.S. and Grasso, P. (1998). "A discussion on the concepts of geomechanical classes behavior categories and technical classes for an underground project", *Gallerie e Grandi Opere Sotterranee*, 54, 40-51.
- Sarikhani Khorami, M. (2012). "Analysis of geomechanical parameters and in situ stress of rock mass in Isfahan-Shiraz railway tunnel using back analysis based on displacement monitoring", M.Sc. Thesis, Isfahan University of Technology, Isfahan, Iran.
- Shid Moosavi, S.S. and Rahai, A.R. (2018). "The performance of integral and semi-integral pre-tensioned concrete bridges under seismic loads in comparison with conventional bridges", *AUT Journal of Civil Engineering*, 2(2), 219-226, [10.22060/ajce.2018.14338.5473](https://doi.org/10.22060/ajce.2018.14338.5473).
- Singh, B. and Goel, R.K. (1999). *Rock mass classification: A practical approach in civil engineering*, Elsevier, 267 p.
- Sulem, J., Panet, M. and Guenot, A. (1987). "An analytical solution for time-dependent displacements in a circular tunnel", *International Journal of Rock Mechanics and Mining Sciences and Geomechanics Abstracts*, 24(3), 155-164, [https://doi.org/10.1016/0148-9062\(87\)90522-5](https://doi.org/10.1016/0148-9062(87)90522-5).
- Sun, H., Liu, S., Zhong, R. and Du, L. (2020). "Cross-section deformation analysis and visualization of shield tunnel based on mobile tunnel monitoring system", *Sensors*, 20(4), 1006.
- Vitali, O.P., Celestino, T.B. and Bobet, A. (2018). "3D finite element modelling optimization for deep tunnels with material nonlinearity", *Underground Space*, 3(2), 125-139, <https://doi.org/10.1016/j.undsp.2017.11.002>.
- Wang, Z., Yao, W., Cai, Y., Xu, B., Fu, Y. and Wei, G. (2019). "Analysis of ground surface settlement induced by the construction of a large-

- diameter shallow-buried twin-tunnel in soft ground”, *Tunnelling and Underground Space Technology*, 83, 520-532, <https://doi.org/10.1016/j.tust.2018.09.021>.
- Xing, Y., Kulatilake, P.H.S.W. and Sandbak, L.A. (2018). “Investigation of rock mass stability around the tunnels in an underground mine in USA using three-dimensional numerical modeling”, *Rock Mechanics and Rock Engineering*, 51, 579-597, <https://doi.org/10.1007/s00603-017-1336-6>.
- Xue, Y., Zhou, B., Li, S., Qiu, D., Zhang, K. and Gong, H. (2021). “Deformation rule and mechanical characteristic analysis of subsea tunnel crossing weathered trough”, *Tunnelling and Underground Space Technology*, 114, 103989, <https://doi.org/10.1016/j.tust.2021.103989>.
- Yang, H. and Xu, X. (2021). “Structure monitoring and deformation analysis of tunnel structure”, *Composite Structures*, 276, 114565, <https://doi.org/10.1016/j.compstruct.2021.114565>.
- Yasitli, N.E. (2016). “Comparison of input parameters regarding rock mass in analytical solution and numerical modelling”, *Journal of African Earth Sciences*, 124, 497-504, <https://doi.org/10.1016/j.jafrearsci.2016.08.010>.
- Yoo, C. (2016). “Effect of spatial characteristics of a weak zone on tunnel deformation behavior”, *Geomechanics and Engineering*, 11(1), 41-58, <https://doi.org/10.12989/gae.2016.11.1.041>.
- Zhao, C., Lavasan, A.A., Barciaga, T., Kämper, C., Mark, P. and Schanz, T. (2017). “Prediction of tunnel lining forces and deformations using analytical and numerical solutions”, *Tunnelling and Underground Space Technology*, 64, 164-176, <https://doi.org/10.1016/j.tust.2017.01.015>.
- Zheng, G., Du, Y., Cheng, X., Diao, Y., Deng, X. and Wang, F. (2017). “Characteristics and prediction methods for tunnel deformations induced by excavations”, *Geomechanics and Engineering*, 12(3), 361-397, <https://doi.org/10.12989/gae.2017.12.3.361>.



This article is an open-access article distributed under the terms and conditions of the Creative Commons Attribution (CC-BY) license.



Optimization of Dynamic Compaction Procedure for Sandy Soils

Bayat, M.¹, Saadat, M.^{1*} and Hojati, A.³

¹ Associate Professor, Department of Civil Engineering, Najafabad Branch, Islamic Azad University, Najafabad, Iran.

² M.Sc., Department of Civil Engineering, Najafabad Branch, Islamic Azad University, Najafabad, Iran.

© University of Tehran 2023

Received: 18 Nov. 2022;

Revised: 18 Jun. 2023;

Accepted: 03 Jul 2023

ABSTRACT: Dynamic Compaction (DC) is employed as a simple and economical method to improve weak soils in the last few decades. DC is usually applied for granular soils by falling a heavyweight (up to 40 tons) from a height (up to 40 m) at regularly spaced intervals. Significant issues in DC are the weight and height of the tamper, compaction pattern and the distance between tamping locations. Incorporated innovation in this paper is to introduce an analytical approach to optimize the compaction pattern and DC variables regarding regular constraints. The required energy for compaction is evaluated for square and diamond patterns. DC optimization is a non-linear and non-convex problem due to nonlinear equations in soil compaction behavior. Thus, a metaheuristic approach (Genetic Algorithm) is employed to find global optimum. The optimum answer presents the minimum compaction energy in each pattern. Results indicated that the maximum allowed values of tamper mass and the number of tamper drops were required to minimize compaction energy. The ratio of compaction energy at diamond pattern to square one was also found to be about 0.75 to 0.90 for the same compaction conditions.

Keywords: Dynamic Compaction, Ground Improvement, Optimization, Sandy Soils.

1. Introduction

Soil improvement techniques improve the engineering properties of soil, like strength, stiffness, and permeability (Anand and Sarkar, 2021; Ghanbari and Bayat, 2022; Sahlabadi et al., 2021; Haghbin and Ghazavi, 2016; Salehi et al., 2021). Soil compaction is widely used in geotechnical projects to reduce the foundation and construction and/or any unexpected risks. During civil projects, geometrical compaction is essential in reducing the

inter-granular porosity to reach a high relative density (Ghassemi and Shahebrahimi, 2020; Mehdipour and Hamidi, 2017; Paranthaman and Azam, 2022; Raja and Thyagaraj, 2020; Silveira and Rodrigues, 2020). Dynamic Compaction (DC) is a relatively traditional and old-fashioned method introduced by Menard and Broise (1975) and was applied to improve the granular soils only. The DC technique is a type of ground improvement method that involves the repeated high-energy impacts to the soil surface using a

* Corresponding author E-mail: mohsen.saadat@pci.iaun.ac.ir

heavyweight (up to 40 tons) with drop heights from 10 m to 40 m. Previous studies revealed that DC technique could be widely used to stabilize loose granular materials and waste landfills to its ease of implementation, economically competitive and environmentally safe (Gu and Lee, 2002). Obtaining soil improvement in quantitative engineering units during the DC has been a challenge with various techniques used in previous studies (Adam et al., 2007).

Feng et al. (2000) used a conical-based pounder to improve the efficiency of DC. The results of laboratory DC tests showed that the efficiency of the used DC method depends on both the grain size distribution and the volumetric response of the sand. The same results have been reported for a conical pounder by Arslan et al. (2009). Hu et al. (2001) studied the effect of DC on the shear strength characteristics of loess. The experimental results revealed that the shear strength of loess increased with the number of drops and after a peak value, the shear strength decreased. Shen et al. (2018) studied the influence of DC on liquefaction potential of silty sand. The effect of DC on liquefaction potential was evaluated using CPTs before and after DC. There is nowadays a renewed interest in DC due to its advantages over other types of soil improvement techniques (Feng et al., 2010, 2015; Ghassemi et al., 2010; Li et al., 2011; Wang et al., 2013; Zhang et al., 2019).

Feng et al. (2017) presented a method of modeling preloading consolidation with drains and dynamic compaction in a centrifuge using a 3D printing technique. This method performed well in predicting the surface settlement, excess pore pressure and effective pressure, number of drops, and improvement depth by DC. So far, several models have been introduced for DC technique in the previous studies which were developed primarily based on several in situ experiences and physical modeling tests (An et al., 2020; Chen et al., 2019). However, previous studies mainly focused on the research of single-location tamping

but the influence of adjacent tamping locations and the multi-location tamping has not been widely considered (Feng et al., 2010, 2013; Ménard and Broise, 1975; Wang et al., 2013). Experimental studies of multi-location tamping consider the interaction between the adjacent tamping locations, which helps understand the soil behavior in response to the impact of tampers during DC procedure.

The effective depth of DC or the depth of improvement as the affected depth during compaction is a key parameter for designing the DC procedure. The improvement depth was usually predicted using empirical correlations in the practical design procedure (Scott et al., 2021). Ménard and Broise (1975) proposed Eq. (1) to estimate the improvement depth based on the energy per drop.

$$Z = n\sqrt{MH} \quad (1)$$

where n : is an influential factor in the sense of depth of improvement. Also, M , H and Z : are tamper mass, drop height and improvement depth of soil. This equation was modified later by other researchers.

Over the last several years, there have been quite extensive studies to identify appropriate values of n , ranging from 0.3 to 1 depending soil types (Mostafa and Liang, 2011). Zou et al. (2008) proposed an equation to estimate Z depending on the tamper mass and area, the falling height, the number of tamper drops, the dry unit weight and water content of soil. Oshima and Takada (1999) conducted a series of centrifuge tests to analyze Z values. Based on the results of centrifuge tests, Z was considered as the depth at which the relative density (D_r) of the soil increases by more than 5%. Oshima and Takada (1999) carried out a series of geotechnical centrifuge tests to evaluate the compacted areas of multi-location tamping. Based on the test results, the soil-improvement zone with depth Z and radius R was defined according to Figure 1.

The depth and radius of the soil-improvement zone were described by Eqs. (2) and (3) proposed by Oshima and Takada

(1999).

$$\begin{aligned} Z &= a_z + b_z \log(M \times \sqrt{2gH} \times N) \\ &= a_z \\ &\quad + 0.434b_z \ln(M \\ &\quad \times \sqrt{2gH} \times N) \end{aligned} \quad (2)$$

$$\begin{aligned} R &= a_R + b_R \log(M \times \sqrt{2gH} \times N) \\ &= a_R \\ &\quad + 0.434b_R \ln(M \\ &\quad \times \sqrt{2gH} \times N) \end{aligned} \quad (3)$$

where N and g : are the number of tamper drops and earth gravitational acceleration. Also, a_z , b_z , a_R and b_R : are the empirical constants.

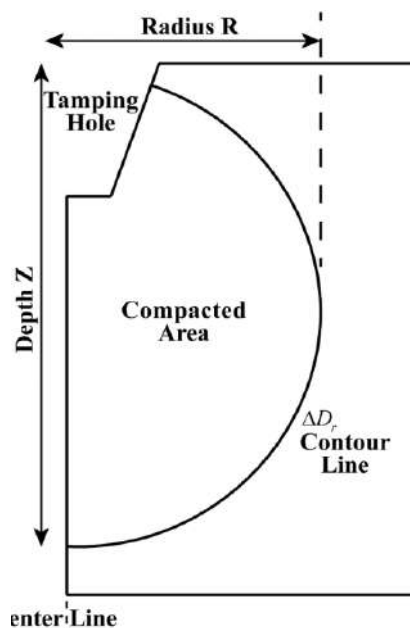


Fig. 1. Dimensions of the soil-improvement zone (Oshima and Takada, 1999)

Earlier studies mainly focused on the test results such as shear wave velocity measurement (V_s), Standard Penetration Test (SPT), and Cone Penetration Test (CPT) before and after DC which were applied widely in the site investigation (Du et al., 2019; Feng et al., 2010; Ménard and Broise, 1975). For example, Chow et al. (1992) studied the effect of print spacing (distance between tamper locations) on the degree of improvement in DC. Based on the results, an approach to estimate the improvement radius of the soil-improvement zone was presented based on assessing the degree of improvement by the increase in friction angle of granular soils.

The estimation of the friction angle was derived from indirect empirical correlation with CPT measurement.

Optimization techniques in Civil Engineering for reducing the time and cost of projects have attracted the interest of many researchers worldwide (Bağrıaçık et al., 2020; Biabani et al., 2022; Fazli, 2022; Hosseini et al., 2022; Kalantary and Kahani, 2019; Kaveh and Zaerreza, 2022). In recent years, many studies have been conducted on optimizing dynamic compaction design using various methods such as fuzzy logic and artificial intelligence (Pasdarpour et al., 2009). In the field of optimization approaches, the Genetic Algorithm (GA) is a well-known optimization method initiated by Holland (1992) and developed by Goldberg (1989). As a member of the family of metaheuristic algorithms, GA is constructed based on the Darwinian evolution theory. It is appropriate especially for non-convex and non-linear optimization problems, where traditional gradient-based algorithms do not have a satisfactory performance to find global optimum. Details of GA procedure may be found in many literature (Holland, 1992). Pasdarpour et al. (2009) presented a fuzzy-GA methodology for the optimal design of soil dynamic compaction. The results indicated that the GA produced the optimal design of soil dynamic compaction. An et al. (2020) studied the optimization of DC design to minimize the remaining compaction time using a Compaction Process-Dynamic Optimization Method (CPDOM) based on the GA. The results proved that CPDOM may be employed for civil engineering projects. Wang and Yin (2020) presented a model to predict the soil compaction parameters using Multi-Expression Programming (MEP). The validity analyses of the model indicated that the proposed model could be used for various soil types with high accuracy.

Wang et al. (2013) based on the experimental results indicated that DC frequency was an important parameter in soil densification. Wu et al. (2020) carried

out a large-scale field test to study vibration velocities from dynamic compaction of granular soil. The results indicated that the soil-improvement zone was roughly cylindrical with the same diameter as the tamper, located immediately beneath the tamper.

As mentioned, DC has been studied a lot during the past decades. However, this study aims to introduce an innovative approach to optimize the pattern and design variables incorporated in DC. Required relations for the simulation of DC were employed based on the proposition of Oshima and Takada (1999) according to Eqs. (2) and (3). The optimization problem consists of minimizing the required energy for DC by properly selecting patterns and related variables since certain practical constraints must be satisfied.

2. Materials and Methods

Proper simulation of soil compaction is essential to optimize the pattern and related variables of DC. The proposed equations by Oshima and Takada (1999) were employed in this study. The equations were presented to determine both of the depth and radius of the compacted zone. The compacted bubbles inside the soil were estimated for any combination of tamper mass, drop height and the number of drops. Proper choosing of the pattern and distances between tamping locations is needed for efficient and economical DC operation.

The intersection of adjacent compaction bubbles is presented in Figure 2 to consider the compacted zone between two adjacent tamping locations. This study assumes that the compaction characteristics at all tamping locations are the same. The intersection of two bubbles is taken place in the depths equal to Z' and Z'' according to Figure 2, where the common zone between bubbles has enough compaction. As shown by Figure 2, Z' and Z'' are the distance of the ground surface from the intersection point of the two bubbles at the bottom and upside of the bubbles, respectively. Evidently, the depths of Z' and Z'' depend on the horizontal

distance between tamping locations (KR). These depths may be determined in terms of KR , where K is a coefficient between 1 and 2 theoretically and R is introduced in the previous section. The values below about 1.2 for K is not economical while “ $K = 2$ ” means two adjacent compaction bubbles are tangent to each other.

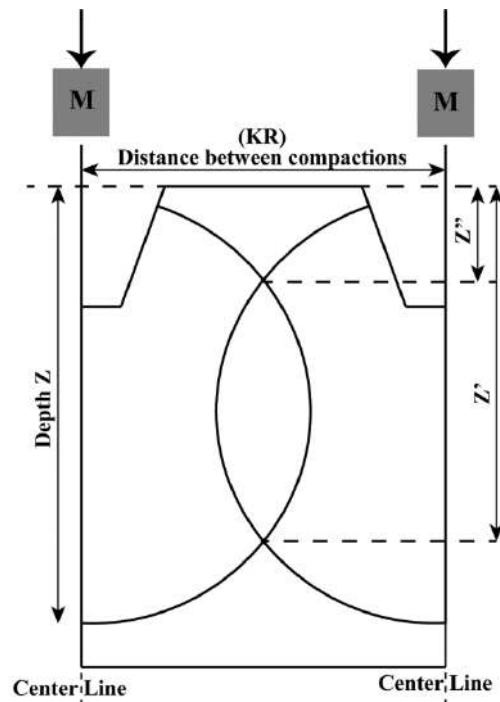


Fig. 2. Intersection of adjacent compaction bubbles with distance KR

Intersection points on the boundary of bubbles were employed to estimate the values of Z' and Z'' in terms of KR . For this purpose, 15 different values were chosen for K between 1.2 and 2 and the adjacent bubbles were drawn for each case. The values of Z' and Z'' were measured for each value of K and, as a result, 15 pairs of (K, Z') and (K, Z'') were obtained. After eliminating R in relations among KR , Z' and Z'' , the equations are estimated by fitting a quadratic function on the results. Finally, the relation of K' and K'' versus of K were calculated by Eqs. (4) and (5), respectively. These equations are required during the optimization procedure.

$$K' = -1.47K^2 + 4.14K - 1.35 \quad (4)$$

$$Z' = K' \times R$$

$$K'' = 1.54K^2 - 4.33K + 3.55 \quad (5)$$

$$Z'' = K'' \times R$$

Another issue during DC is the compaction pattern. Generally, two patterns of square and diamond were employed in this study according to Figures 3 and 4.

The distances between tamping locations in Figures 3 and 4 were selected so that the maximum distance between adjacent tamping locations was KR and, as a result, required compaction was met for any point of the land along of the X or Y direction. For each square or diamond pattern case, all distances between tamping locations were depicted. The number of tamping locations inside the land was also calculated according to Eqs. (6) and (7) for the square and diamond patterns, respectively. These numbers were required to compute the total compaction energy in each pattern. It is obvious that “NC” is a nonlinear function in terms of “R” and “K” in both cases of

square or diamond patterns. Eqs. (6) and (7) were obtained employing Figures 3 and 4 by multiplying the number of rows and columns of tamping locations. The number of rows and columns is calculated by dividing the total length of land in any direction by distances between tamping locations. In square pattern, a distance equal to $0.5KR$ exists between tamping locations and the boundary of land. The distance value on each side should be subtracted from the total amounts of X or Y before division. In the diamond pattern, the available distance is different for hollow and solid circle signs and is indicated precisely in Figure 4. It is essential to remember that solid and hollow circle signs are the same regarding compaction properties and the distinction is just for facilitating their enumeration.

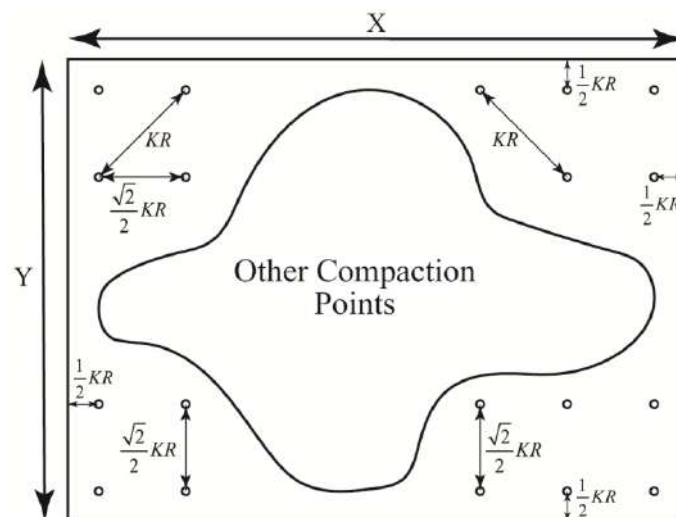


Fig. 3. Square compaction pattern and the distances between tamping locations

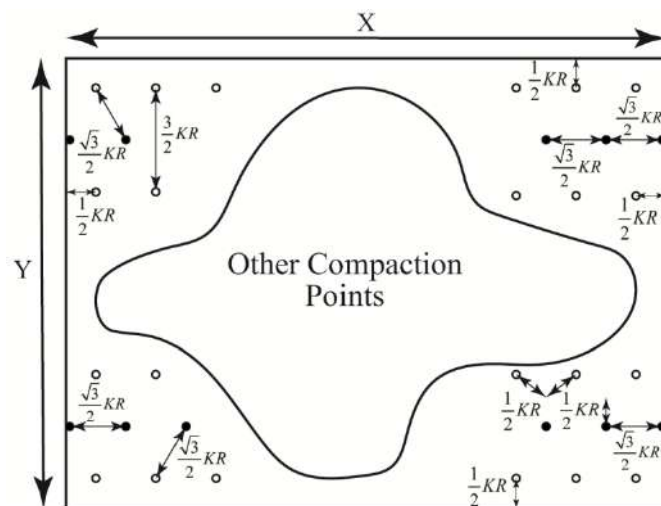


Fig. 4. Diamond compaction pattern and the distances between tamping locations

$$\begin{aligned}
NC_{Square} &= n_1 \times n_2 \\
&= \left(\frac{Y - KR}{\frac{\sqrt{2}}{2}(KR)} + 1 \right) \times \left(\frac{X - KR}{\frac{\sqrt{2}}{2}(KR)} + 1 \right) \quad (6)
\end{aligned}$$

$$\begin{aligned}
NC_{Diamond} &= n_1' \times n_2' + n_1'' \times n_2'' \\
&= \left(\frac{Y - KR}{\frac{3}{2}KR} + 1 \right) \times \left(\frac{X - KR}{\frac{\sqrt{3}}{2}(KR)} + 1 \right) \\
&\quad + \left(\frac{Y - 2\left(\frac{5}{4}KR\right)}{\frac{3}{2}KR} + 1 \right) \times \left(\frac{X}{\frac{\sqrt{3}}{2}(KR)} + 1 \right) \quad (7)
\end{aligned}$$

In this paper, the objective function is assumed to required energy (or cost, equivalently) of DC according to Eq. (8). The decision variables in the optimization problem are tamper mass (M), drop height (H), the number of drops in each point (N) and the number of tamping locations in the whole land (NC).

$$\text{Minimize}(F = NC \times N \times M \times g \times H) \quad (8)$$

where H , M and N are forced to be integer numbers in this study according to practical applications. Value of N is restricted to 120 to facilitate the optimization procedure; however, there is no limitation in practical applications.

Regular constraints incorporated in optimization problems are according to Eqs. (9) to (15).

$$Z'' \leq Z' \leq Z \quad (9)$$

$$\text{Reuired Depth for Compaction} \leq Z' \quad (10)$$

$$0.5m \leq Z'' \leq \text{Foundation Depth} \quad (11)$$

$$5\text{tons} \leq M \leq 40\text{ tons} \quad (12)$$

$$10m \leq H \leq 40\text{ m} \quad (13)$$

$$N \leq 120 \quad (14)$$

$$1.2 \leq K \leq 2 \quad (15)$$

where *Foundation Depth*: is the depth that the foundation is constructed and the *Required Depth for Compaction*: is the

depth that a specified amount of compaction (ΔD_r) is required and is undoubtedly more than the foundation depth. The study driven by Oshima and Takada (1999) is one the few ones that considered the influence of “ M ”, “ N ” and “ H ” on the dimension and degree of compaction in sandy soils. The dimensions of compacted bubbles and the degree of compaction in terms of different values of “ R ” and “ Z ” are investigated. This study was performed experimentally and the results were assumed valid for our study.

Solving the optimization problem within Eqs. (8) to (15) requires efficient algorithms to conquer the non-convex and non-linear nature of the problem. As a well-known metaheuristic optimization method, GA is one of the best choices. This research used Solver Add-in in Microsoft Excel package to implement GA where required parameters were adjusted before starting the solution. Objective function and constraints were defined in solver, while the population size in each generation and other GA parameters were regulated. Population size and mutation rate were equal to 200 and 0.075, respectively.

The main advantage of the GA is moving toward the global extremum in a non-convex problem. However, there is no guarantee to achieve the global extremum, exactly. As a result, a gradient-based algorithm is required to get the GA answer as an initial guess and continue the search process. In the current study, Generalized Reduced Gradient (GRG) method available again in Solver Add-in was employed to improve the GA results. GRG gets the near-optimum answers obtained by GA and converges to exact value of global extremum. Initial GA cooperation is essential because GRG needs help finding global extremum. Generally, gradient-based algorithms like GRG may be trapped in local extremum without support of metaheuristic algorithms. This paper’s main objectives are to examine the proposed method’s effectiveness and compare the square and diamond compaction patterns.

For this purpose, four square lands with dimensions of 30 m, 50 m, 100 m and 200 m were assumed, and the total required compaction energy was calculated.

Sensitivity analysis was also performed according to Eqs. (16) and (17) to show the influence of different parameters on the depth and radius of the compaction zone. Differentiating of Z and R in terms of M , N and H is performed by applying Eqs. (2) and (3).

$$dZ = \frac{\partial Z}{\partial M} dM + \frac{\partial Z}{\partial N} dN + \frac{\partial Z}{\partial H} dH$$

$$= 0.434b_z \left(\frac{dM}{M} + \frac{dN}{N} + \frac{dH}{2H} \right) \quad (16)$$

$$dR = \frac{\partial R}{\partial M} dM + \frac{\partial R}{\partial N} dN + \frac{\partial R}{\partial H} dH$$

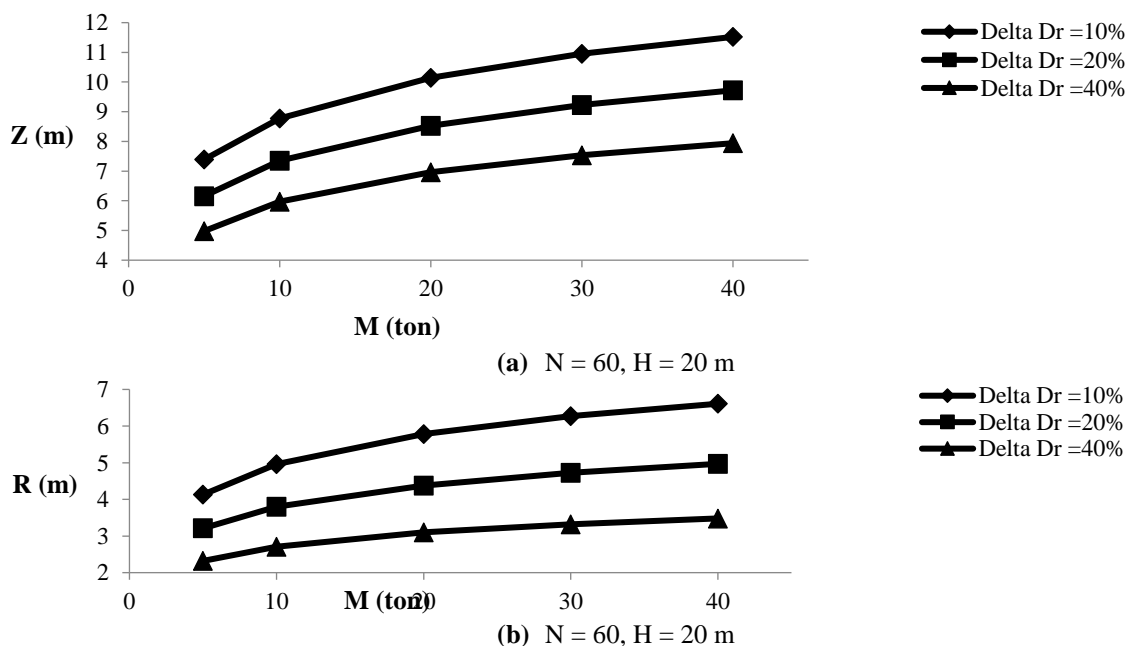
$$= 0.434b_r \left(\frac{dM}{M} + \frac{dN}{N} + \frac{dH}{2H} \right) \quad (17)$$

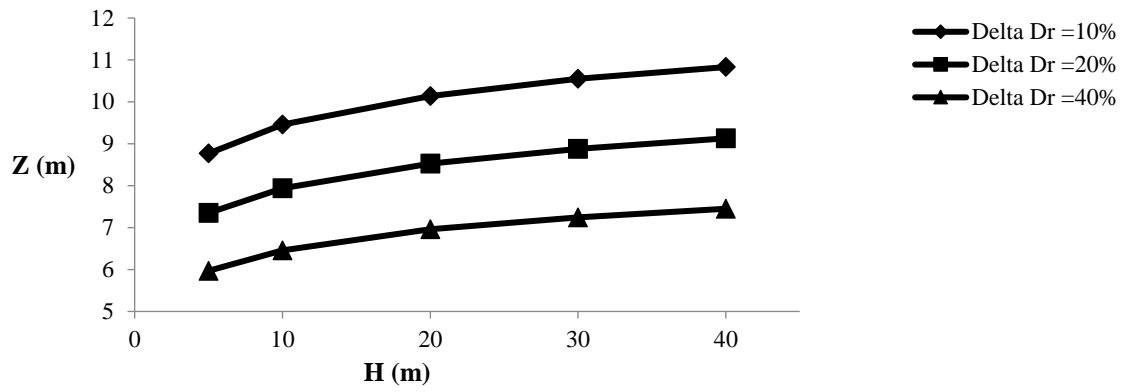
3. Results and Discussion

Before considering the optimization results, it is appropriate to analyze the variation of Z and R in terms of three influential variables of M , H and N . This analysis specifies each variable's impact on the compacted zone's depth and radius. Figure 5 is drawn according to Eqs. (2) and (3) for

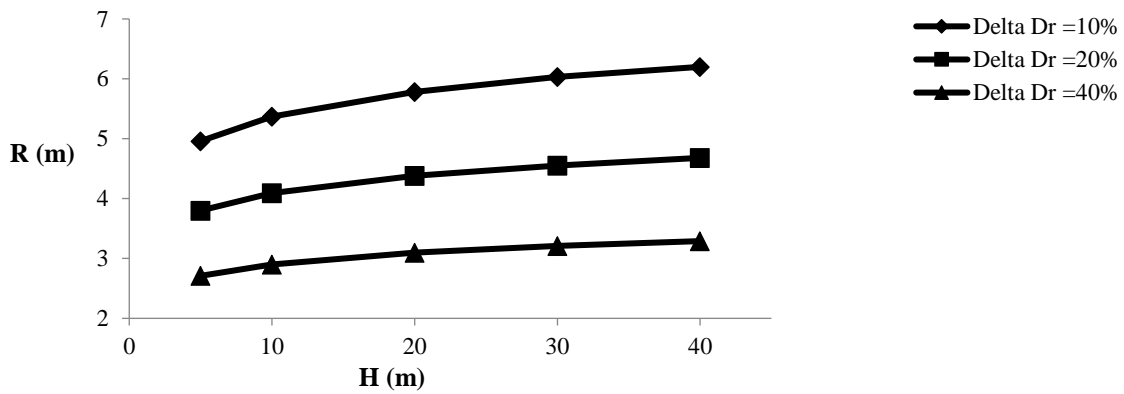
cases ΔD_r equal to 10%, 20% or 40%. The values of a_z, b_z, a_r, b_r are based on the proposed values by Oshima and Takada (1999). As expected, the least required compaction ($\Delta D_r = 10\%$) results in the largest amounts of Z and R and vice versa.

Figure 5 indicates that H has a minor influence on the depth and radius of the compaction zone when compared to other variables. This is induced regarding the relatively horizontal curves for variation of Z and R versus H in Figures 5c and 5d which also is concluded from the results of sensitivity analysis obtained by Eqs. (16) and (17). The reason is the small value for the coefficient of dH in Eqs. (16) and (17) because of the presence of "2" in the denominator of the coefficient. On the other hand, variables M and N are more effective than H to increase the depth and radius of compaction zone. The steep curves of Z and R versus M and N indicate the influential nature of these variables in improving the compaction zone. Considering Eqs. (16) and (17), it is concluded that M is even more effective than N . The reason is that usually, dM has a larger coefficient than dN . In other words, the values of N are normally more than M (in terms of tons) and thus $(1/M > 1/N)$. However, the tamper mass M may have some limitations to implement in practical applications.

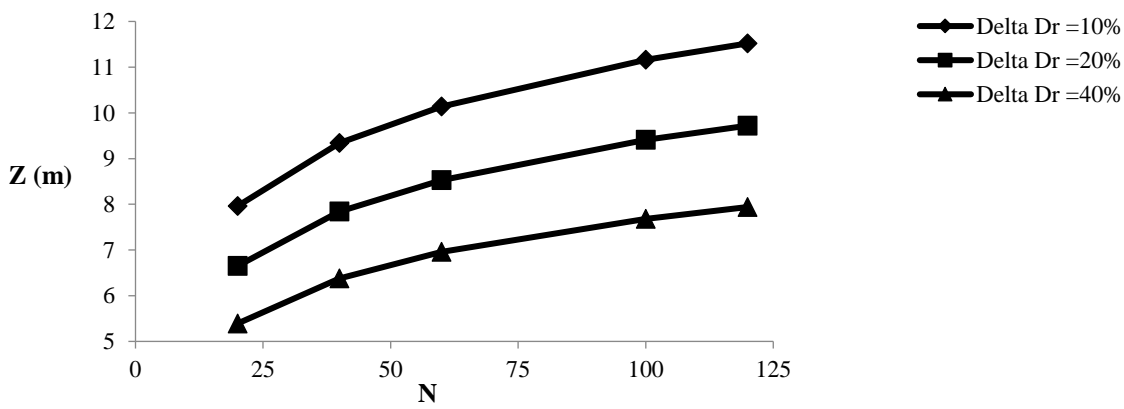




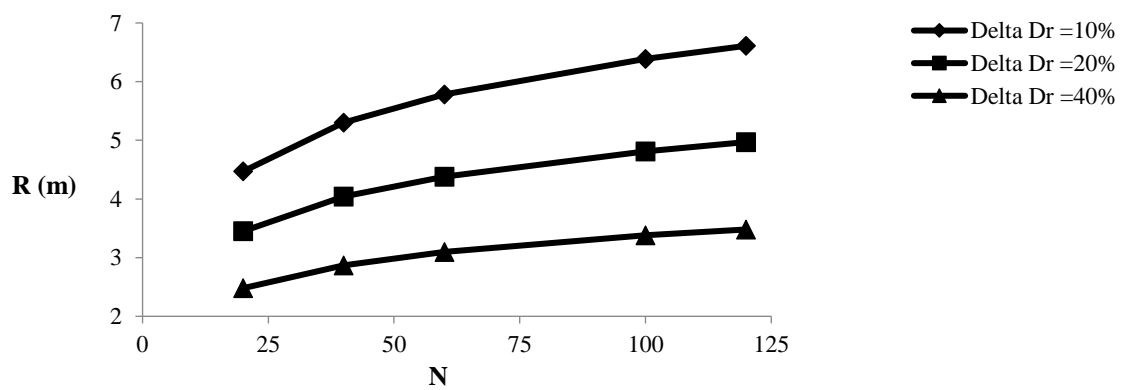
(c) $N = 60, M = 20$ t



(d) $N = 60, M = 20$ t



(e) $M = 20, H = 20$ m



(f) $M = 20$ t, $H = 20$ m

Fig. 5. Variation of depth and radius of compacted zone in terms of the effective DC variables: a) Z vs. M ; b) R vs. M ; c) Z vs. H ; d) R vs. H ; e) Z vs. N ; and f) R vs. N

Calculating the minimum required energy for compaction in each square and diamond pattern case and comparing them is another objective of this study. It is apparent that compaction energy is dependent on parameters like Z' , Z'' and ΔD_r , where more values for parameters Z' or ΔD_r cause more required energy. Small value of Z'' on the other hand needs more tamping locations and thus more energy. However, a minimal value of Z'' may cause an infeasible situation in the solution procedure. Generally, infinite combinations of Z' , Z'' and ΔD_r may occur. As a typical example, Table 1 indicates the obtained values of DC optimization for $Z' = 6$, $Z'' = 2$ and $\Delta D_r = 40\%$. The results show that the preferred value for M is the maximum practical (40 tons here). The optimum value for N is also the maximum assumed value in the problem. However, in some cases, the value for N has a slight deviation from the maximum. It seems it is taking place because only integer values for M , N and H are allowed. The optimum values of M and N are the maximum allowed ones because of the larger coefficients of dM and dN to improve dZ and dR in Eqs. (16) and (17).

Another important point regarding Table 1 is the efficiency of the diamond pattern compared with square one. Results indicate that ratio of the required energy of diamond to the square pattern is between 0.75 and 0.9; however, no regular trend is observed in terms of land dimension. It seems that the diamond pattern is more effective than the square one due to better interlock of compaction bubbles in each other.

The proposed approach in this study is

quite analytical and is performed based on the empirical equations obtained by Oshima and Takada (1999). As a result, the verification phase has no sense here, and optimization results are valid for all cases.

4. Conclusions

This paper presented an innovative method to implement dynamic compaction so that minimum compaction energy is consumed while required constraints are satisfied. For this purpose, the DC problem was formulated regarding all physical and practical constraints. The depth and radius of the compacted zone were estimated for a single tamper. Then, extra equations were developed to determine the intersection points of compaction bubbles. Afterwards, the best values for horizontal distances between tamping locations were determined to satisfy compaction requirements specified by the operator. Obtaining the best horizontal distances needs to solve a non-linear and non-convex optimization problem. Generally, finding the global optimum in a non-convex problem is a challenge. To overcome this challenge, a combination of metaheuristic (GA) and gradient-based (GRG) algorithms was employed. All calculations were performed for two compaction patterns of square and diamond. A sensitivity analysis was also performed to identify the impacts of influential variables on the DC procedure. The impacts of variables were compared and some discussion about the range of each one was presented. Finally, the main obtained points are as follows.

Table 1. Obtained DC variables for various land dimensions for $Z' = 6$, $Z'' = 2$ and $\Delta D_r = 40\%$

| Land dimension (m × m) | | 30×30 | 50×50 | 100×100 | 200×200 |
|------------------------|-----------|-------|--------|---------|---------|
| Square pattern for DC | K | 1.483 | 1.476 | 1.448 | 1.455 |
| | N | 120 | 119 | 120 | 117 |
| | H (m) | 19 | 19 | 18 | 19 |
| | M (ton) | 40 | 40 | 40 | 40 |
| | F (MJ) | 32197 | 107316 | 488042 | 2093690 |
| Diamond pattern for DC | K | 1.469 | 1.429 | 1.487 | 1.467 |
| | N | 118 | 119 | 120 | 118 |
| | H (m) | 19 | 18 | 19 | 19 |
| | M (ton) | 40 | 40 | 40 | 40 |
| | F (MJ) | 25504 | 96627 | 374740 | 1602377 |

Tamper mass (M), drop height (H) and the number of drops in each tamping location (N) affect the radius and depth of the compacted zone. The compaction energy is enhanced by increasing each of these variables. However, the tamper mass and the number of drops in each tamping location are the most effective variables for increasing the radius and depth of compacted zone while the drop height is the least effective one. It is required to note that tamper mass and drop height have some practical limitations, while the number of drops has no such limitation. The required energy (or equivalently cost) for DC in a diamond pattern is about 75% to 90% of the energy of a square pattern, for the same conditions of compaction. Applying the following results may benefit operators economically during DC, especially in large projects.

- The optimum value for K is between 1.4 and 1.5 in all cases.
- The optimum value for M is the largest practical value in all cases.
- The optimum value for N is the largest allowable value. However, in some cases the maximum values of N are not obtained due to the integer variables incorporated in the problem.
- The optimum value for H is about 18 m to 19 m for DC operations with dimensions near to the values of this study. This value is almost half of the maximum allowed value for H . It seems the reason is the presence of number "2" in the denominator of the coefficient of dH within sensitivity analysis equations.

5. References

- Adam, D., Brandl, H., Kopf, F. and Paulmichl, I. (2007). "Heavy tamping integrated dynamic compaction control", *Ground Improvement*, 11(4), 237-243, <https://doi.org/10.1680/grim.2007.11.4.237>.
- An, Z., Liu, T., Zhang, Z., Zhang, Q., Huangfu, Z., and Li, Q. (2020). "Dynamic optimization of compaction process for rockfill materials", *Automation in Construction*, 110(2020), <https://doi.org/10.1016/j.autcon.2019.103038>.
- Anand, A. and Sarkar, R. (2021). "A comprehensive study on bearing behavior of cement-fly ash composites through experimental and probabilistic investigations", *Innovative Infrastructure Solutions*, 6(1), 39, <https://doi.org/10.1007/s41062-020-00404-w>.
- Arslan, H., Baykal, G. and Ertas, O. (2009). "Discussion: Influence of tamper weight shape on dynamic compaction", *Proceedings of the Institution of Civil Engineers: Ground Improvement*, 162(3), 153-154, <https://doi.org/10.1680/grim.2009.162.3.153>.
- Bağrıaçık, B., Yıldırım, Z.B., Güner, E.D. and Beycioğlu, A. (2020). "Assessment of pipe powder in soil improvement applications: An optimization by response surface methodology", *Arabian Journal of Geosciences*, 13(19), 1-11, <https://doi.org/10.1007/s12517-020-05962-y>.
- Biabani, F., Razzazi, A., Shojae, S. and Hamzehei-Javaran, S. (2022). "Design and application of a hybrid meta-heuristic optimization algorithm based on the combination of PSO, GSA, GWO and Cellular Automaton", *Iran University of Science & Technology*, 12(3), 279-312, <http://ijoce.iust.ac.ir/article-1-520-en.html>.
- Chen, L., Qiao, L. and Li, Q. (2019). "Study on dynamic compaction characteristics of gravelly soils with crushing effect", *Soil Dynamics and Earthquake Engineering*, 120(January 2017), 158-169, <https://doi.org/10.1016/j.soildyn.2019.01.034>.
- Chow, Y.K., Yong, D.M., Yong, K.Y. and Lee, S.L. (1992). "Dynamic compaction analysis", *Journal of Geotechnical Engineering*, 118(8), 1141-1157, [https://doi.org/10.1061/\(ASCE\)0733-9410\(1992\)118:8\(1141\)](https://doi.org/10.1061/(ASCE)0733-9410(1992)118:8(1141)).
- Du, J., Wu, S., Hou, S. and Wei, Y. (2019). "Deformation analysis of granular soils under dynamic compaction based on stochastic medium theory", *Mathematical Problems in Engineering*, 2019(1), 6076013, <https://doi.org/10.1155/2019/6076013>.
- Fazli, H. (2022). "An efficient method for optimum performance-based seismic design of fused building structures", *Iran University of Science & Technology*, 12(4), 501-516, <http://ijoce.iust.ac.ir/article-1-531-en.html>.
- Feng, S.J., Du, F.L., Chen, H.X. and Mao, J.Z. (2017). "Centrifuge modeling of preloading consolidation and dynamic compaction in treating dredged soil", *Engineering Geology*, 226, 161-171, <https://doi.org/10.1016/j.enggeo.2017.06.005>.
- Feng, S.J., Du, F.L., Shi, Z.M., Shui, W.H. and Tan, K. (2015). "Field study on the reinforcement of collapsible loess using dynamic compaction", *Engineering Geology*, 185, 105-115, <https://doi.org/10.1016/j.enggeo.2014.12.006>.
- Feng, S.J., Shui, W.H., Gao, L.Y., He, L.J. and Tan, K. (2010). "Field studies of the effectiveness of dynamic compaction in coastal reclamation

- areas", *Bulletin of Engineering Geology and the Environment*, 69(1), 129-136, <https://doi.org/10.1007/s10064-009-0242-x>.
- Feng, S.J., Tan, K., Shui, W.H. and Zhang, Y. (2013). "Densification of desert sands by high energy dynamic compaction", *Engineering Geology*, 157, 48-54, <https://doi.org/10.1016/j.enggeo.2013.01.017>.
- Feng, T.W., Chen, K.H., Su, Y.T. and Shi, Y.C. (2000). "Laboratory investigation of efficiency of conical-based pounders for dynamic compaction", *Geotechnique*, 50(6), 667-674, <https://doi.org/10.1680/geot.2000.50.6.667>.
- Ghanbari, M. and Bayat, M. (2022). "Effectiveness of reusing steel slag powder and polypropylene fiber on the enhanced mechanical characteristics of cement-stabilized sand", *Civil Engineering Infrastructures Journal*, 55(2), 47-63, <https://doi.org/10.22059/CEIJ.2021.319310.1742>.
- Ghassemi, A., Pak, A. and Shahir, H. (2010). "Numerical study of the coupled hydro-mechanical effects in dynamic compaction of saturated granular soils", *Computers and Geotechnics*, 37(1-2), 10-24, <https://doi.org/10.1016/j.compgeo.2009.06.009>.
- Ghassemi, A. and Shahebrahimi, S.S. (2020). "Discrete element modeling of dynamic compaction with different tamping condition", *Civil Engineering Infrastructures Journal*, 53(1), 173-188, <https://doi.org/10.22059/cej.2020.282153.1587>.
- Goldberg, D.E. (1989). *Genetic algorithms in search, optimization, and machine learning*, Addison-Wesley Professional, United States.
- Gu, Q. and Lee, F.H. (2002). "Ground response to dynamic compaction of dry sand", *Geotechnique*, 52(7), 481-493, <https://doi.org/10.1680/geot.2002.52.7.481>.
- Haghighin, M. and Ghazavi, M. (2016). "Seismic bearing capacity of strip footings on pile-stabilized slopes", *Civil Engineering Infrastructures Journal*, 49(1), 111-126, <https://doi.org/10.7508/cej.2016.01.008>.
- Holland, J.H. (1992). *Adaptation in Natural and Artificial Systems*, MIT Press, United States.
- Hosseini, P., Kaveh, A. and Hoseini Vaez, S.R. (2022). "Robust design optimization of space truss structures", *Iran University of Science & Technology*, 12(4), 595-608, <http://ijoce.iust.ac.ir/article-1-536-en.html>.
- Hu, R.L., Yeung, M.R., Lee, C.F. and Wang, S.J. (2001). "Mechanical behavior and microstructural variation of loess under dynamic compaction", *Engineering Geology*, 59(3-4), 203-217, [https://doi.org/10.1016/S0013-7952\(00\)00074-0](https://doi.org/10.1016/S0013-7952(00)00074-0).
- Kalantary, F. and Kahani, M. (2019). "Optimization of the biological soil improvement procedure", *International Journal of Environmental Science and Technology*, 16(8), 4231-4240, <https://doi.org/10.1007/s13762-018-1821-9>.
- Kaveh, A. and Zaerreza, A. (2022). "Optimum design of the braced dome with frequency constraint using the improved shuffled based Jaya Algorithm", *Iran University of Science & Technology*, 12(4), 609-625, <http://ijoce.iust.ac.ir/article-1-537-en.html>.
- Li, W., Gu, Q., Su, L. and Yang, B. (2011). "Finite element analysis of dynamic compaction in soft foundation", *Procedia Engineering*, 12, 224-228, <https://doi.org/10.1016/j.proeng.2011.05.035>.
- Mehdipour, S. and Hamidi, A. (2017). "Impact of tamper shape on the efficiency and vibrations induced during dynamic compaction of dry sands by 3D Finite Element modeling", *Civil Engineering Infrastructures Journal*, 50(1), 151-163, <https://doi.org/10.7508/cej.2017.01.009>.
- Ménard, L. and Broise, Y. (1975). "Theoretical and practical aspect of dynamic consolidation", *Geotechnique*, 25(1), 3-18, <https://doi.org/10.1680/geot.1975.25.1.3>.
- Mostafa, K.F. and Liang, R.Y. (2011). "Numerical Modeling of Dynamic Compaction in Cohesive Soils", In: *Geo-Frontiers 2011: Advances in Geotechnical Engineering*, (pp. 738-747). [https://doi.org/10.1061/41165\(397\)76](https://doi.org/10.1061/41165(397)76).
- Oshima, A. and Takada, N. (1999). "Evaluation compacted area of heavy damping by cone point resistance", In: *Proceedings of the Centrifuge, Tokyo*, 1641-1644.
- Paranthaman, R. and Azam, S. (2022). "Effect of compaction on desiccation and consolidation behavior of clay tills", *Innovative Infrastructure Solutions*, 7(1), 1-8, <https://doi.org/10.1007/s41062-021-00644-4>.
- Pasdarpour, M., Ghazavi, M., Teshnehlab, M. and Sadrnejad, S.A. (2009). "Optimal design of soil dynamic compaction using genetic algorithm and fuzzy system", *Soil Dynamics and Earthquake Engineering*, 29(7), 1103-1112, <https://doi.org/10.1016/j.soildyn.2008.09.003>.
- Raja, P.S.K. and Thyagaraj, T. (2020). "Effect of compaction time delay on compaction and strength behavior of lime-treated expansive soil contacted with sulfate", *Innovative Infrastructure Solutions*, 5(1), 1-15, <https://doi.org/10.1007/s41062-020-0268-2>.
- Sahlabadi, S.H., Bayat, M., Mousivand, M. and Saadat, M. (2021). "Freeze-thaw durability of cement-stabilized soil reinforced with polypropylene/basalt fibers", *Journal of Materials in Civil Engineering*, 33(9), 04021232, [https://doi.org/10.1061/\(asce\)mt.1943-5533.0003905](https://doi.org/10.1061/(asce)mt.1943-5533.0003905).
- Salehi, M., Bayat, M., Saadat, M. and Nasri, M. (2021). "Experimental study on mechanical properties of cement-stabilized soil blended with crushed stone waste", *KSCE Journal of Civil Engineering*, 25(6), 1974-1984,

- <https://doi.org/10.1007/s12205-021-0953-5>.
- Scott, B., Jaksa, M. and Mitchell, P. (2021). "Depth of influence of rolling dynamic compaction", *Proceedings of the Institution of Civil Engineers: Ground Improvement*, 174(2), 85-94, <https://doi.org/10.1680/jgrim.18.00117>.
- Shen, M., Martin, J.R., Ku, C.S. and Lu, Y.C. (2018). "A case study of the effect of dynamic compaction on liquefaction of reclaimed ground", *Engineering Geology*, 240, 48-61, <https://doi.org/10.1016/j.enggeo.2018.04.003>.
- Silveira, I.A. and Rodrigues, R.A. (2020). "Collapsible behavior of lateritic soil due to compacting conditions", *International Journal of Civil Engineering*, 18(10), 1157-1166, <https://doi.org/10.1007/s40999-020-00523-6>.
- Wang, H.L. and Yin, Z.Y. (2020). "High performance prediction of soil compaction parameters using multi expression programming", *Engineering Geology*, 276, 105758, <https://doi.org/10.1016/j.enggeo.2020.105758>.
- Wang, S.Y., Chan, D.H., Lam, K.C. and Au, S.K.A. (2013). "A new laboratory apparatus for studying dynamic compaction grouting into granular soils", *Soils and Foundations*, 53(3), 462-468, <https://doi.org/10.1016/j.sandf.2013.04.007>.
- Wang, Y., Li, X.B. and Jiang, W.D. (2003). "Application of fuzzy model of multi-objective system to optimization of parameters of dynamic compaction", *Rock and Soil Mechanics-Wuhan*, 24(3), 410-412.
- Wu, S., Wei, Y., Zhang, Y., Cai, H., Du, J., Wang, D., Yan, J. and Xiao, J. (2020). "Dynamic compaction of a thick soil-stone fill: Dynamic response and strengthening mechanisms", *Soil Dynamics and Earthquake Engineering*, 129(November 2019), 105944, <https://doi.org/10.1016/j.soildyn.2019.105944>.
- Zhang, R., Sun, Y. and Song, E. (2019). "Simulation of dynamic compaction and analysis of its efficiency with the material point method", *Computers and Geotechnics*, 116(August), 103218, <https://doi.org/10.1016/j.compgeo.2019.103218>.
- Zou, J.F., Luo, H. and Yang, X.L. (2008). "Effective depth of dynamic compaction in embankment built with soils and rocks", *Journal of Central South University of Technology (English Edition)*, 15(SUPPL. 2), 34-37, <https://doi.org/10.1007/s11771-008-0432-x>.



This article is an open-access article distributed under the terms and conditions of the Creative Commons Attribution (CC-BY) license.



Pushover Analysis of Reinforced Concrete Moment-Resisting Frames to Account for the Variations of Axial Forces on the Moment Curvature Properties

Samadi, N.¹, Aghayari, R.² and Izadpanah, M.^{3*}

¹ M.Sc., Department of Civil Engineering, Razi University, Kermanshah, Iran.

² Associate Professor, Department of Civil Engineering, Razi University, Kermanshah, Iran.

³ Assistant Professor, Department of Civil Engineering, Kermanshah University of Technology, Kermanshah, Iran.

© University of Tehran 2023

Received: 26 Dec. 2022;

Revised: 09 May 2023;

Accepted: 10 May 2023

ABSTRACT: Nonlinear static (pushover) analysis is widely used for analyzing structures, especially in the performance-based design method. Increasing the lateral load in pushover analysis causes changing the axial forces of beam-column members during the analysis. Whereas the axial load of beam-column elements can significantly affect the moment-curvature properties of these elements, in most pushover analyses, the moment-curvature curve of these elements is generally achieved based on the gravity axial loads and remain constant throughout the analysis. Furthermore, the confining action depends on the axial load of beam-column elements. In this study, a novel pushover analysis is developed to update the moment-curvature properties of beam-column elements based on the axial forces of these elements throughout the analysis. The confining effect is considered on the moment-curvature properties of beam-column elements as well. Furthermore, the influence of updating the moment-curvature properties is shown by comparing the responses of the updated and traditional pushover analyses. The method is applied to three reinforced concrete frames from the previous studies to assess the influence of the variation of moment-curvature properties on the capacity curve of these frames. Outcomes show that the variation of axial loads significantly affects the moment-curvature of beam-column elements especially for edge columns located in the lower stories of frames. Furthermore, considering the progressive changes of moment-curvature properties of beam-column elements during the pushover analysis accounting for the variations of axial forces leads to reducing the lateral load-carrying capacity e.g, ductility, secant stiffness ultimate strength, etc.

Keywords: Axial Force, Beam-Column, Confining Action, Moment-Curvature, Nonlinear Static Analysis.

1. Introduction

The nonlinear dynamic analysis is known as

a robust method for predicting the seismic responses of structures. Inherent complexity and uncertainties are some

* Corresponding author E-mail: m.izadpanah@kut.ac.ir

difficulties that make civil engineers do not interest in using this method in practice. The nonlinear static analysis method is found as a substitute approach for nonlinear dynamic analysis due to less computational endeavors coupled with providing helpful information dealing with the lateral load capacity, potential failure mechanisms, and the sequence formation of plastic hinges of building structures. In pushover analysis, lateral load distribution is monotonically imposed on the structure until a predefined target displacement at the control node (usually considered the roof displacement) is reached. The axial load of beam-column elements depends on the imposed lateral load and varies during the pushover analysis. On the whole, the moment-curvature characteristics of each beam-column element are calculated at the first step of analysis considering simply the gravity axial loads and remaining constant throughout the analysis while neglecting the influence of the variation of its axial load.

Studies of Gulkan and Sozen (1974) and Fajfar and Fischinger (1988) are known as the first investigations of pushover analysis. More complete pushover analyses have been introduced in various code provisions e.g., FEMA273, ATC-40, and Eurocode 8. Pushover analysis has some limitations and shortcomings that have motivated researchers to develop some boost pushover methods to mitigate these deficiencies. In the conventional pushover procedure, a constant lateral load distribution is used along the height of the building and increased until the target displacement reaches. This constant lateral load pattern raised the question that how much this force distribution can reflect the inertial loads imposed on the structures subjected to seismic excitations. Hence, numerous studies have focused on obtaining an appropriate lateral load pattern to improve the responses of pushover analysis (e.g., Chopra and Goel, 2002; Antoniou and Pinho, 2004; Rahmani et al., 2018; Amini and Poursha, 2018; Habibi et al., 2019; Bakalis and Makarios, 2021; Worku and

Hsiao, 2022; Lherminier et al., 2023). Evaluation of the responses of pushover analysis has been addressed in many studies (Fajfar and Gašperšič, 1996; Gupta and Krawinkler, 2000; Mwafy and Elnashai, 2001; Olivito and Porzio, 2019; Hassan and Reyes, 2020; Cao et al., 2021). Regarding the works of Fajfar and Gašperšič (1996) and Gupta and Krawinkler (2000), it was found that distributing lateral loads along the height of buildings proportional to the main vibration mode leads to an appropriate estimation of the seismic responses in low-rise buildings. However, some studies e.g., Krawinkler and Seneviratna (1998) and Mwafy and Elnashai (2001) evaluated the validity of the lateral load pattern proportional to the first mode for high-rise or irregular structures. They concluded that pushover analysis does not present reasonable responses for these categories of buildings since the influence of higher modes on the responses is significant.

As per the previous investigations, the conventional pushover analysis cannot reflect the higher mode effects and the progressive variations of the dynamic characteristics (Lawson et al., 1994; Elnashai, 2001; Antoniou and Pinho, 2004). A multi-run method with an invariant lateral load distribution matching each desired mode was developed by Chopra and Goel (2002). In this method, the achieved responses were combined applying a combination way such as SRSS or CQC. Chopra and Goel (2004) improved the previous method and used it for predicting asymmetric-plan buildings' responses. Kalkan and Kunnath (2006) put forward a novel pushover analysis method using adaptive multimodal displacement distribution for estimating the seismic response of structures. The proposed method was used for two existing steel moment frames. They demonstrated that the procedure gives reasonable results in comparison with nonlinear dynamic analysis.

Reyes and Chopra (2011) extended the model pushover analysis for predicting the

seismic responses of buildings simultaneously under two horizontal components of an earthquake. This procedure (named practical modal pushover analysis) was applied to calculating the seismic responses of two tall buildings (48- and 62-story) and the outcomes were compared with those of modal pushover analysis and nonlinear response history analysis. Habibi (2011) conducted a nonlinear sensitivity analysis of reinforced concrete frames taking both axial and flexural effects into account. He derived sensitivity equations on the base of the pushover procedure as a powerful tool for the nonlinear analysis of buildings in performance base design.

The observations of Nazri and Alexander (2014) showed that lateral load distribution should be decreased instead of increasing along the height of the structure. Nazri and Alexander (2015) demonstrated that the inverse parabolic lateral load pattern presents a proper prediction of the capacity of structures. Rahmani et al. (2018) developed a new nonlinear static analysis to evaluate the seismic performance of tall buildings. This model was capable of considering the higher modes effects coupled with the progressive changes in structural characteristics during the nonlinear response. Comparing the responses of different types of pushover analyses with nonlinear time history analysis showed that the proposed procedure presented more reasonable outcomes than other pushover methods (e.g., upper-bound pushover, improved upper-bound, modal pushover analysis, displacement-based adaptive pushover methods).

A multi-mode adaptive displacement-based pushover procedure for predicting the seismic responses of Reinforced Concrete (RC) moment-resisting frames was developed by Jalilkhani et al. (2020). In this procedure, the seismic responses of structures were predicted utilizing several multi-stage modal pushover analyses. The seismic structural demands of four RC

moment resisting frames with various stories were calculated using the developed method, the modal pushover, as well as consecutive modal pushover methods. Results verified the efficiency of the proposed method in comparison with nonlinear dynamic analysis (considered as a benchmark).

Daei and Poursha (2021) evaluated the performance of different pushover methods. The structural demands of three RC frames subjected to pulse-like and non-pulse-like ground motions were achieved using various pushover analyses. Results showed that some procedures present reasonable responses for pulse-like excitations, some for non-pulse-like ground motions, and some for both of them. A multi-direction pushover method was developed for the evaluation of the seismic performance of RC buildings with torsional irregularity by Ghayoumian and Emami (2020). Pushover analysis was used in a plethora of studies (e.g., Costa et al., 2017; Ozgenoglu and Arıcı, 2017; Tian and Qiu, 2018; Izadpanah and Habibi, 2018a; Moradi and Tavakoli, 2020; Kheirollahi et al., 2021; Dehghani and Soltani Mohajer, 2022; Wang et al., 2023; Zhou et al., 2023; etc.).

Lu and Li (2023) studied the efficacy of the energy-based modal pushover analysis and the direct vectorial addition based pushover method in estimating the curvature ductility demands of tall single-column piers. They compared the responses of the piers acquired from pushover analyses with those calculated using incremental dynamic analysis. It was found that the curvature ductility demands can be predicted effectively using the direct vectorial addition based pushover method.

Faruk et al. (2023) conducted a comparative study on the performance of buckling restrained bracing and fluid viscous damper (as two types of energy dissipators) used in reinforced concrete buildings. Taking advantages of pushover analysis, the responses of four buildings equipped by these dissipators were acquired and compared. Lawson et al. (1994) and

Krawinkler and Seneviratna (1998) evaluated the advantages and deficiencies of pushover analysis.

The literature proves that despite of the plethora research for improving pushover analysis, the progressive changes of the moment-curvature characteristics of beam-column elements due to the variation of their axial forces were disregarded. Furthermore, considering the confinement effects and its changes as a result of changing the axial forces of beam-column elements is relatively rare. In addition, comparing the responses of updated and traditional pushover analyses, it is illustrated how much considering the progressive changes of the moment-curvature characteristics throughout pushover analysis can affect the responses.

This study focuses on a new pushover analysis to update the moment-curvature properties of beam-column elements based on the axial force of these members during the analysis. To do so, pushover analysis is conducted on three RC moment resisting frames with 3-, 7-, and 10-story. The base shear-roof displacement curves of these frames are achieved once with a moment-curvature curve for each beam-column element that remains constant throughout the analysis and again with updating the moment-curvature properties of the beam-columns during the analysis. It is worth emphasizing that the tri-linear moment-curvature relations are used for the calculation of the moment-curvature properties; therefore, the assumptions were made in these relations to best fit with test results are presented in the current study. Confining action is considered using the developed method by Mander et al. (1988). Using of the linear flexibility model developed by Kunnath and Reinhorn (1989) as a reputable macro plasticity model, the nonlinear behavior of beam-column elements is modeled. Moreover, the comparison of responses in this study is limited to three RC moment resisting frames, so future works are required to be done for expanding knowledge concerning

different lateral load systems, different connection systems, and so on.

2. Nonlinear Analysis

2.1. Moment-Curvature Relation

Regarding the nonlinear behavior of RC sections, the tri-linear moment-curvature relation is used (Figure 1) (Reinhorn et al. 2009). Three distinctive portions consisting of elastic, cracked, and yield states are shown in Figure 1. The moment-curvature properties are affected by the elasticity modulus of concrete and steel, the modulus of the rupture, and the compressive strength of concrete, the yield strength of steel, the ultimate strain of concrete, the yield strain of steel, dimensions, and the moment of inertia of section, etc. The following relations are used to define the moment-curvature properties.

a) Cracking state:

$$M_{cr} = \frac{f_r I}{(h-y)} + \frac{N d}{6} \quad (1)$$

$$\varphi_{cr} = \frac{f_r}{E_c (h-y)} \quad (2)$$

b) Yielding state:

$$M_y = 0.5 f_c b_t d^2 (h-c)^2 [(1+\beta - \eta)n_0 + (2-\eta)\rho + (\eta - 2\beta)\alpha\rho'] \quad (3)$$

$$\varphi_y = \frac{c \varepsilon_y}{(1-k)d} \quad (4)$$

c) Ultimate state:

$$M_u = (1.24 - 0.15p - 0.5n_0)M_y \quad (5)$$

$$\frac{\varphi_u}{\varphi_y} = \frac{\beta_1 \varepsilon_u E_s}{f_y} \frac{(1-k)}{(R^2 + S \frac{c}{d}) - \frac{R}{(h-c)}} \quad (6)$$

where

$$R = \frac{(\rho' \varepsilon_u E_s - \rho f_y)(h-c)}{(1.7 f_c)} \quad (7)$$

$$S = \frac{\rho' \varepsilon_u E_s \beta_1 c (h-c)}{(0.85 f_c)} \quad (8)$$

Full details dealing with other parameters were presented in Habibi (2011).

The flexural stiffness of elastic, cracked,

and yield branches (Figure 1) can be calculated for the ends of the member as follows.

$$EI_{p1} = \frac{M_{crp}}{\varphi_{crp}} \quad M \leq M_{cr} \quad (9)$$

$$EI_{p2} = \frac{M_{yp} - M_{crp}}{\varphi_{yp} - \varphi_{crp}} \quad M_{cr} < M \leq M_y \quad (10)$$

$$EI_{p3} = \frac{M_{up} - M_{yp}}{\varphi_{up} - \varphi_{yp}} \quad M_y < M \leq M_u \quad (11)$$

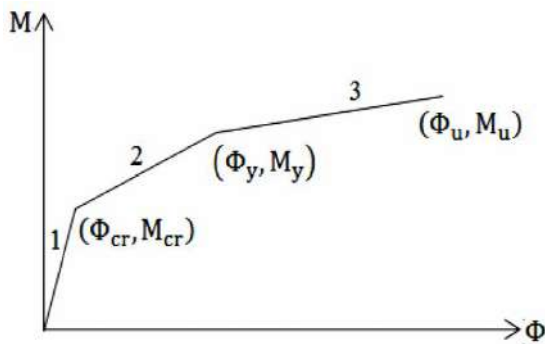


Fig. 1. Tri-linear moment curvature curve

The vertex-oriented hysteric model (Reinhorn et al., 2009) is applied in this study. Lateral pressure significantly affects the stress-strain relationship of compressed concrete. In contrast with unconfined

concrete, confining concrete provides a higher resistance to internal cracking, ultimate strain, and axial strength. The concrete core of columns should be confined to retain flexural strength as high curvatures in the plastic hinges. In other words, to achieve ductile performance, the higher axial compressive load requires a higher amount of confining reinforcement (Mander et al., 1988). The confinement of concrete boosts the strength coupled with the ductility of compressed concrete.

The enhanced strength along with the slope of the descending branch of the concrete stress-strain curve improves the flexural strength and ductility of RC columns. When the compressive strength reaches, in contrast to the core concrete keeping bearing stress at a high level of strains, the cover concrete will not be efficient because of an unconfined situation. Confining the compressed concrete, preventing the buckling of the longitudinal bars and a shear failure are some advantages of the transverse reinforcements. In the current study, the stress-strain model of Mander et al. (1988) is applied to take the confining action into consideration (Figure 2).

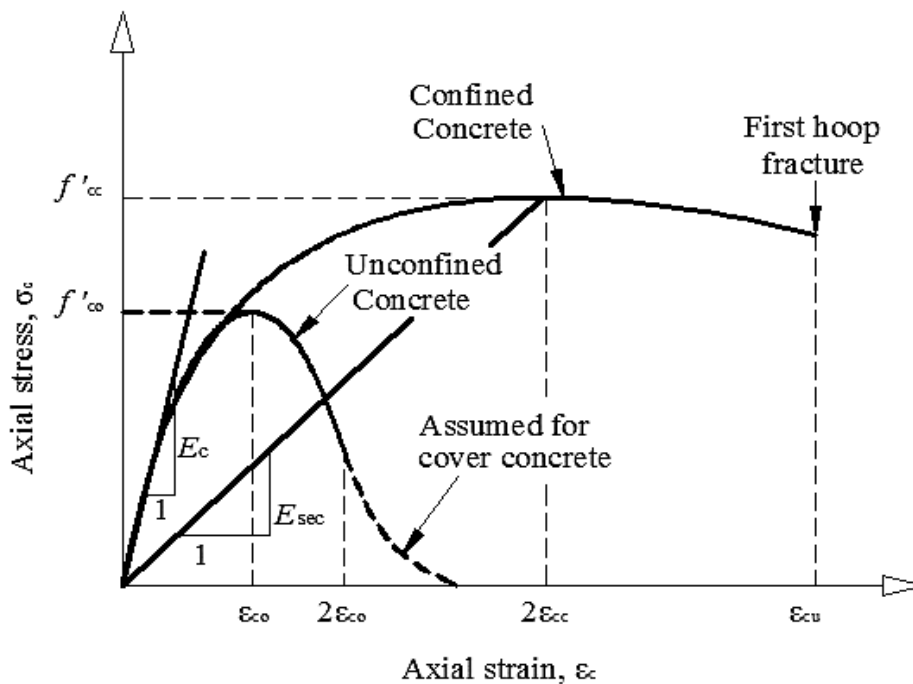


Fig. 2. Stress-strain model (Mander et al., 1988)

2.2. Stiffness Matrix

The linear plasticity model developed in Kunnath and Reinhorn (1989) is used to simulate the nonlinear behavior of beam-column members. The macro plasticity models are categorized into two classes, a) lumped and b) distributed plasticity models. In the lumped plasticity models, the plasticity is concentrated in the two ends of beam-column elements. The member between these ends stays elastic. In RC

members, inelastic deformations are spread throughout the member, hence the concentrated plasticity models do not comply with the inelastic behavior of these elements. In spread plasticity models, a predefined distribution for flexural flexibility along the elements' length is assumed. In the linear plasticity model (Figure 3), the inelastic zones encounter variations in flexibility and the rest of the member stays elastic.

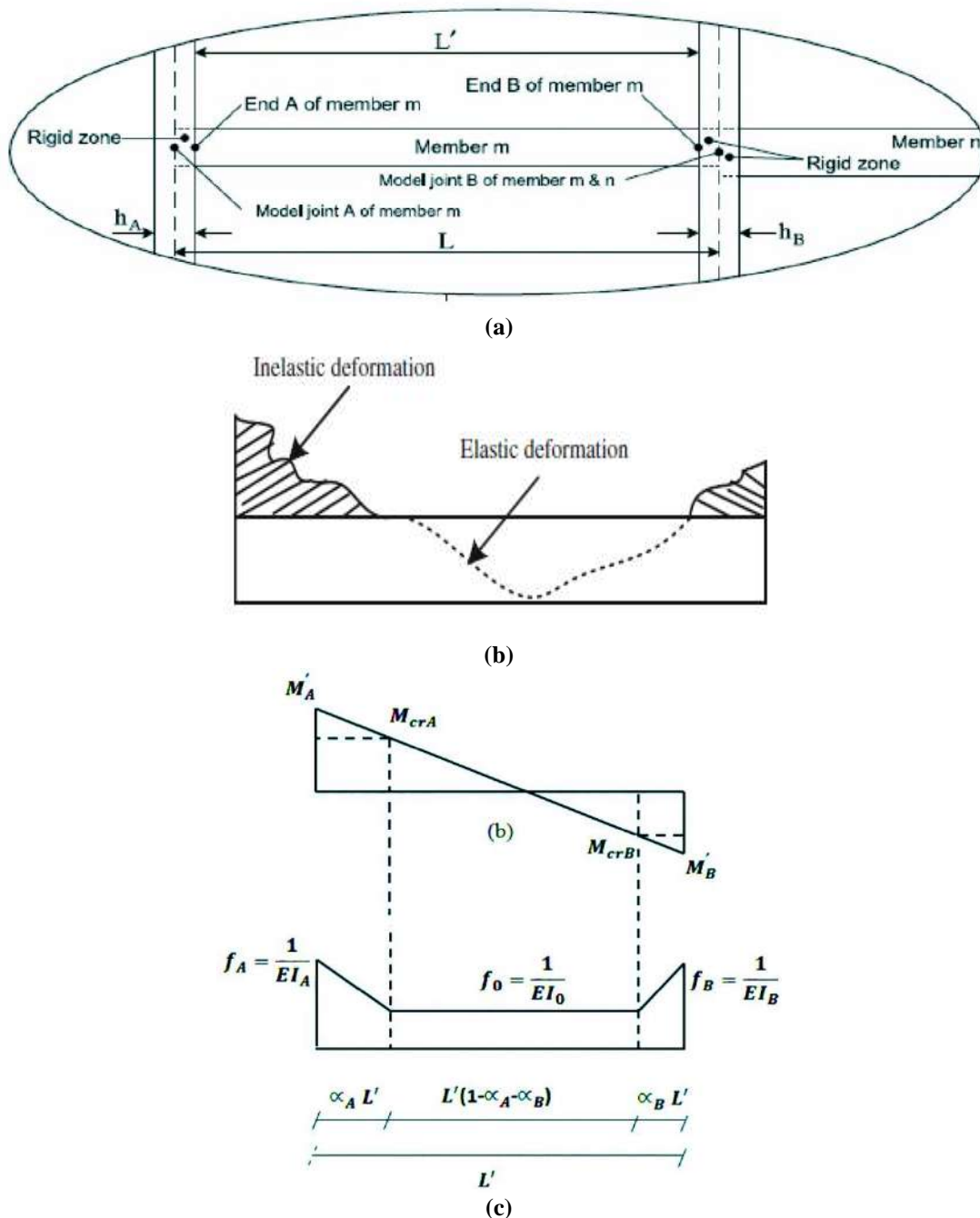


Fig. 3. a) Rigid zone and ends definitions of a RC element; b) Moment distribution; and C) Linear flexibility distribution (Reinhorn et al., 2009)

The cracked parts of the element at the ends are defined via the yield penetration coefficients (α_A and α_B) (Reinhorn et al., 2009). The element stiffness matrix relating the rotations and moments at the member ends is defined as follows.

$$\begin{bmatrix} M'_A \\ M'_B \end{bmatrix} = \begin{bmatrix} K_{AA} & K_{AB} \\ K_{BA} & K_{BB} \end{bmatrix} \begin{bmatrix} \theta'_A \\ \theta'_B \end{bmatrix} = [K'] \begin{bmatrix} \theta'_A \\ \theta'_B \end{bmatrix} \quad (12)$$

The components of the stiffness matrix are calculated as follows.

$$K_{AA} = \frac{12EI_0EI_AEI_B}{L'D_{et}} (L'^2GA_zf'_{BB} + 12EI_0EI_AEI_B) \quad (13)$$

$$K_{BB} = \frac{12EI_0EI_AEI_B}{L'D_{et}} (L'^2GA_zf'_{AA} + 12EI_0EI_AEI_B) \quad (14)$$

$$K_{AB} = K_{BA} = \frac{-12EI_0EI_AEI_B}{L'D_{et}} (L'^2GA_zf'_{AB} + 12EI_0EI_AEI_B) \quad (15)$$

$$D_{et} = L'^2GA_z(f'_{AA}f'_{BB} - f'_{AB}{}^2) + 12EI_0EI_AEI_B(f'_{AA} + f'_{BB} - 2f'_{AB}) \quad (16)$$

$$f'_{AA} = 4EI_AEI_B + 4EI_B(EI_0 - EI_A)(3\alpha_A - 3\alpha_A^2 + \alpha_A^3) + 4EI_A(EI_0 - EI_B)\alpha_B^3 \quad (17)$$

$$f'_{AB} = 2EI_AEI_B + EI_B(EI_0 - EI_A)(2\alpha_A^2 - \alpha_A^3) + EI_A(EI_0 - EI_B)(2\alpha_B^2 - \alpha_B^3) \quad (18)$$

$$f'_{BB} = 4EI_AEI_B + EI_B(EI_0 - EI_A)(\alpha_A^3) + EI_A(EI_0 - EI_B)(6\alpha_B - 4\alpha_B^2 + \alpha_B^3) \quad (19)$$

where GA_0 : is the shear stiffness of an element. To consider the rigid zone effects and shear components are calculated as Habibi (2011).

Bending moments and axial forces are presumed uncoupled.

$$\begin{bmatrix} Y_a \\ Y_b \end{bmatrix} = \frac{EA}{L} \begin{bmatrix} 1 & -1 \\ -1 & 1 \end{bmatrix} \begin{bmatrix} v_a \\ v_b \end{bmatrix} = [K_a] \begin{bmatrix} v_a \\ v_b \end{bmatrix} \quad (20)$$

Assembling the above-mentioned stiffness matrices, the tangential stiffness matrix is obtained.

To consider $P - \Delta$ effect, a geometric stiffness matrix is added to the tangential stiffness matrix (Eq. (21)).

$$K_g = N/L \begin{bmatrix} 0 & & & & & \\ 0 & 6/5 & & & & \\ 0 & L/10 & 2L^2/15 & & & \\ 0 & 0 & 0 & 0 & & \\ 0 & -6/5 & -L/10 & 0 & 6/5 & \\ 0 & L/10 & -L^2/30 & 0 & -L/10 & 2L^2/15 \end{bmatrix} \quad (21)$$

The geometric matrix depends on the axial load and the length of the element (N and L). The modified Newton-Raphson procedure is used for nonlinear analysis and to achieve the internal forces.

2.3. Pushover Analysis

A structure can behave between entirely elastic and collapse states. A nonlinear analysis is necessary to expand knowledge about the actual demands of structures (especially those subjected to severe ground motions). Pushover analysis is a nonlinear procedure that is widely used as the main tool for the inelastic analysis of structures. In pushover analysis, firstly, the gravity loads are exerted on the building frame. After that, the lateral loads are monotonically increased while the structure gravity loads remain constant. The lateral loads are distributed along the height of the structure based on a predefined pattern. In this study, the lateral load pattern recommended by FEMA273 is used.

$$\Delta F_i = \frac{w_i h_i^k}{\sum_{i=0}^N w_i h_i^k} \Delta V_b \quad (22)$$

$$k = \begin{cases} 1 & T < 0.5 \\ 0.5T + 0.75 & 0.5 \leq T \leq 2.5 \\ 2 & T > 2.5 \end{cases}$$

3. Numerical Study

The applicability and the efficiency of the developed procedure are assessed through three numerical case studies. The roof displacement-base shear curves of these frames are calculated once with a constant moment-curvature remaining constant throughout the analysis and again regarding the progressive changes of the moment-

curvature relations based on the axial forces updated during the analysis (henceforth named convenient and updated pushover analysis, respectively).

3.1. Case Study 1

The first example is an asymmetric 3-story, 3-bay moment-resisting reinforced concrete frame (Izadpanah and Habibi, 2018a) (Figure 4) in which the width and height of all beams and columns are 300 mm. All beams possess the reinforcement of 763 mm^2 at the bottom and top. The reinforcement of all columns on each face is 763 mm^2 . The concrete has a cylinder strength of 20 MPa. The concrete presents a strain of 0.002 regarding the maximum strength. The ultimate strain of concrete is

0.003. The concrete has a modulus of rupture of 2.82 MPa and a modulus of elasticity of 22360 MPa. The yield strength and modulus of elasticity of steel are 300 MPa and 200000 MPa, respectively. A uniformly-distributed gravity load exerted on the beams of each story is 20 kN/m. A cover to the reinforcement centroid of 50 mm is assumed.

The convenient and updated pushover analysis of this frame is conducted inclusion/exclusion of the confinement effect (CE). The roof displacement-base shear curves are compared in Figure 5. In Figure 6, the roof displacement-base shear curves of this frame from Izadpanah and Habibi (2018a) are depicted.

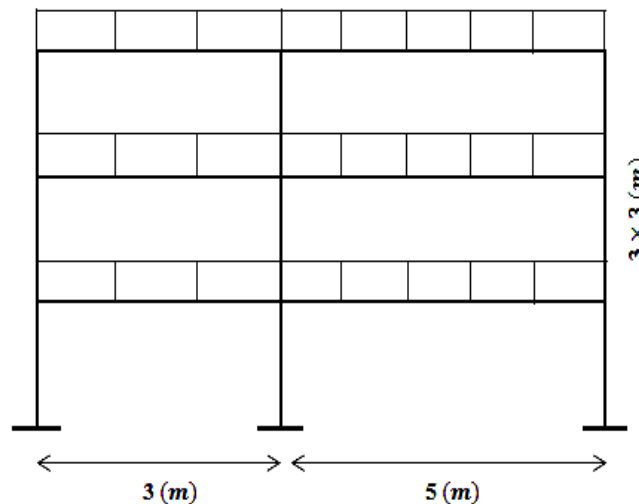


Fig. 4. Tri-linear moment curvature curve

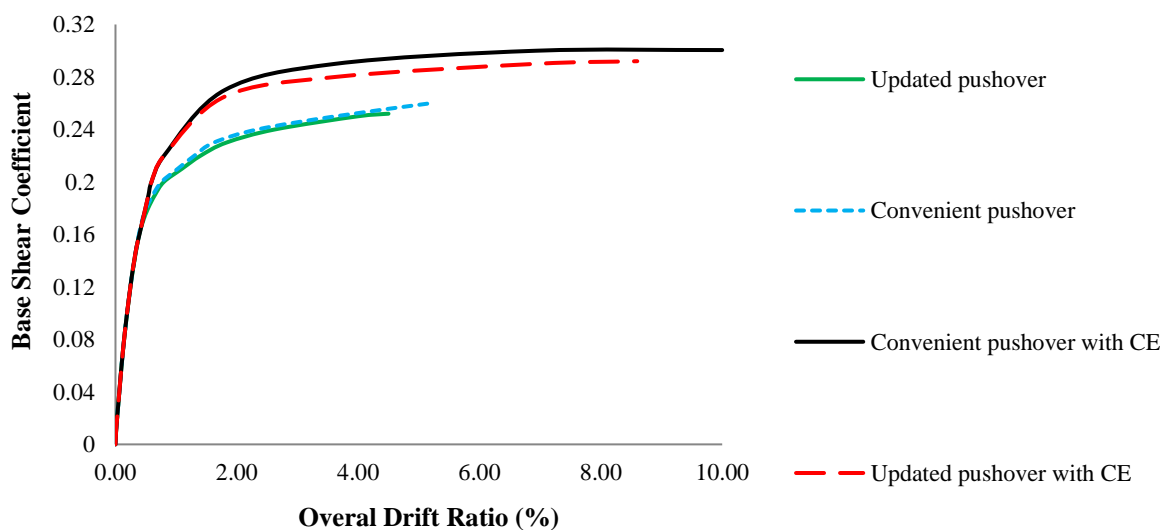


Fig. 5. The roof displacement-base shear curves of 3-story frame

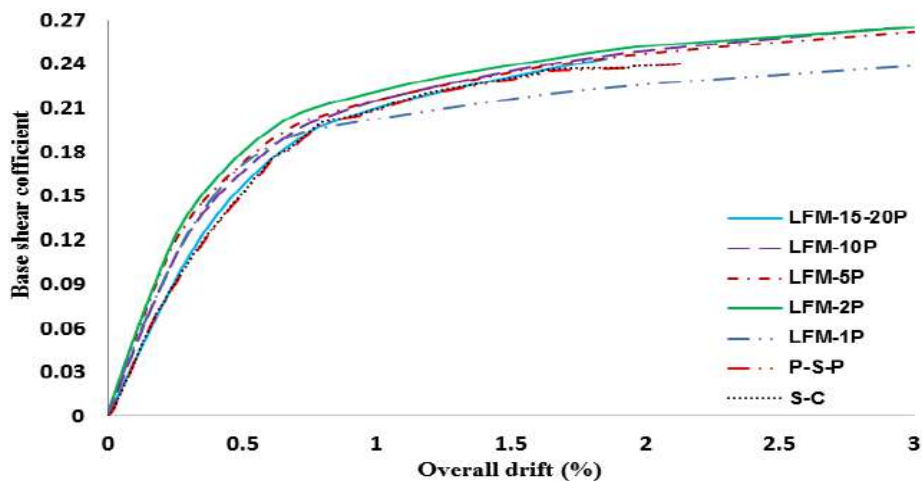


Fig. 6. The roof displacement-base shear curves of 3-story frame (Izadpanah and Habibi, 2018a)

As shown in Figure 5, considering the confinement effect leads to an enhancement in the lateral load-resisting characteristics of the frame. In comparison with the unconfined state, the secant stiffness, energy dissipation capacity, ductility, and ultimate strength of the confined frame are boosted. For convenient pushover analysis, the ductility and ultimate base shear coefficient of the confined frame are around 9 and 0.3 whereas those of the unconfined frame are 6.5 and 0.26. For the updated pushover analysis, the values of the ductility, and ultimate base shear coefficient of the confined frame are 7.75 and 0.29, and those of the unconfined frame are 5.6 and 0.25. The second stiffness of the confined frame is around 1.2 times of the unconfined frame in the overall drift ratio of 2% and 4%.

Comparing the curves of updated and convenient pushover analyses indicates that updating moment-curvature properties of the beam-column elements results in decreasing the ductility of the frame. For the confined frame, the ultimate strength of a convenient pushover is higher than the updated one. On the contrary, for the unconfined frame, the difference is negligible. Comparing the convenient pushover curve in Figure 5 and LFM-1P curve in Figure 6 confirms the accuracy of the procedure applied in this study.

3.2. Case Study 2

A 7-story, 3-bay planner reinforced

concrete frame as the second example is evaluated (Figure 7) (Izadpanah and Habibi, 2018b). The cross-section properties of this frame are listed in Table 1. Concrete has a cylinder strength of 38 Mpa and a strain of 0.002 regarding the maximum strength. The ultimate strain of concrete is assumed as 0.006. Steel possesses the yield strength and modulus of elasticity of 300 MPa and 200000 MPa, respectively. On all beams, a uniform gravity load of 30 kN/m is exerted. Each story has a height of 3.2 m and the length of each bay is 5 m.

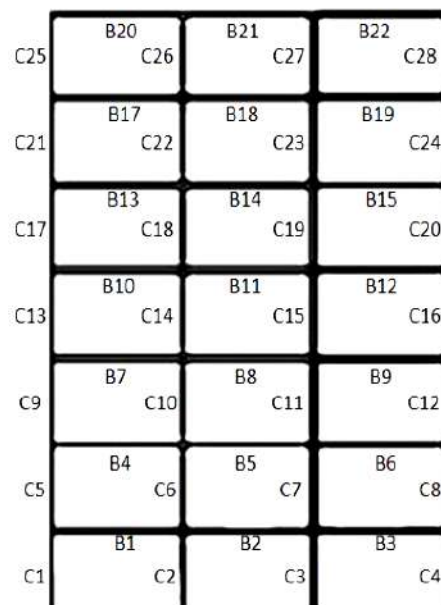
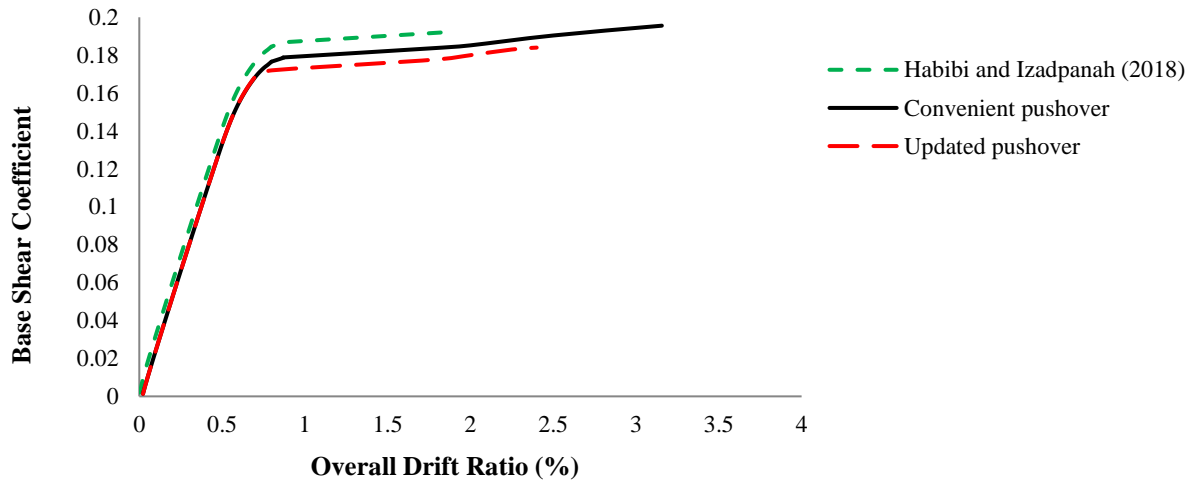


Fig. 7. Geometry of seven-story RC frame

The convenient and updated pushover analyses of this frame are performed and the roof displacement-base shear curves are compared in Figure 8.

Table 1. The cross section properties of seven-story RC frame

| Element type | Dimension (mm) | | Reinforcement | |
|---|----------------|--------|----------------------------|------|
| | Width | Height | Bottom | Top |
| Beam | | | | |
| 1 st to 5 th story | 300 | 450 | 3Ø20 | 7Ø20 |
| 6 th and 7 th story | 350 | 400 | 3Ø20 | 4Ø20 |
| Column | Dimension (mm) | | Reinforcement on each face | |
| | Width | Height | | |
| 1 st story | 500 | 500 | 7Ø20 | |
| 2 nd and 3 rd story | 500 | 500 | 6Ø20 | |
| 4 th and 5 th story | 450 | 450 | 5Ø20 | |
| 6 th and 7 th story | 350 | 350 | 5Ø20 | |

**Fig. 8.** The roof displacement-base shear curves of 7-story frame

As shown in Figure 8, for updated pushover procedure, the lateral load-carrying capacity of the frame is weakened in comparison with the convenient pushover method. In other words, considering the progressive changes of moment-curvature properties of columns leads to reducing the ductility coupled with the ultimate strength of the frame (around 30% and 6%). The convenient pushover curve complies with that of Izadpanah and Habibi (2018b). The gap between the convenient pushover curve and Izadpanah and Habibi (2018b) is due to the different plasticity models considered in these studies. Izadpanah and Habibi (2018b) used an improved linear plasticity model to consider the gravity load effects. They proved that when a member is subdivided into several elements, the responses of the linear plasticity model converge to the improved linear plasticity model that used one element for each member. In Figure 9, the changes in axial force of columns C_1 , C_2 , C_9 , C_{10} , C_{17} , C_{18} , C_{25} , and C_{26}

throughout the pushover analysis are indicated. In Figure 10, the moment-curvature curves of column C_1 at the first and the last steps of pushover analysis are demonstrated.

As indicated in Figure 9, the axial force of edge columns significantly varies throughout the pushover analysis and these changes for lower story columns are higher e.g. the axial load of C_1 reaches 9.88 kN in overall drift of 2.4% from 54 kN in the first step of analysis that means around 80 percent reduction. The axial load changes reduce for higher story columns e.g. the axial load of C_{25} reduces to 4 kN in overall drift 2.4% from 7 kN in the first step of analysis which means around 40 percent reduction. For middle columns, the variation of axial forces is negligible. Comparing the moment-curvature curves of C_1 in Figure 10 shows how axial load can affect the moment-curvature properties of columns. As it is clear, the flexural properties of C_1 including cracking, yielding, ultimate moments, and also

stiffness of all branches decrease along the analysis. Since during the pushover analysis on one side of frames, the axial forces of edge columns decrease and on another side, the axial forces increase; therefore, the gap between capacity curves of convenient and

updated pushover analysis is not significant. However, the changes in moment-curvature properties of columns especially edge columns in the lower levels affect the behavior and demands of columns.

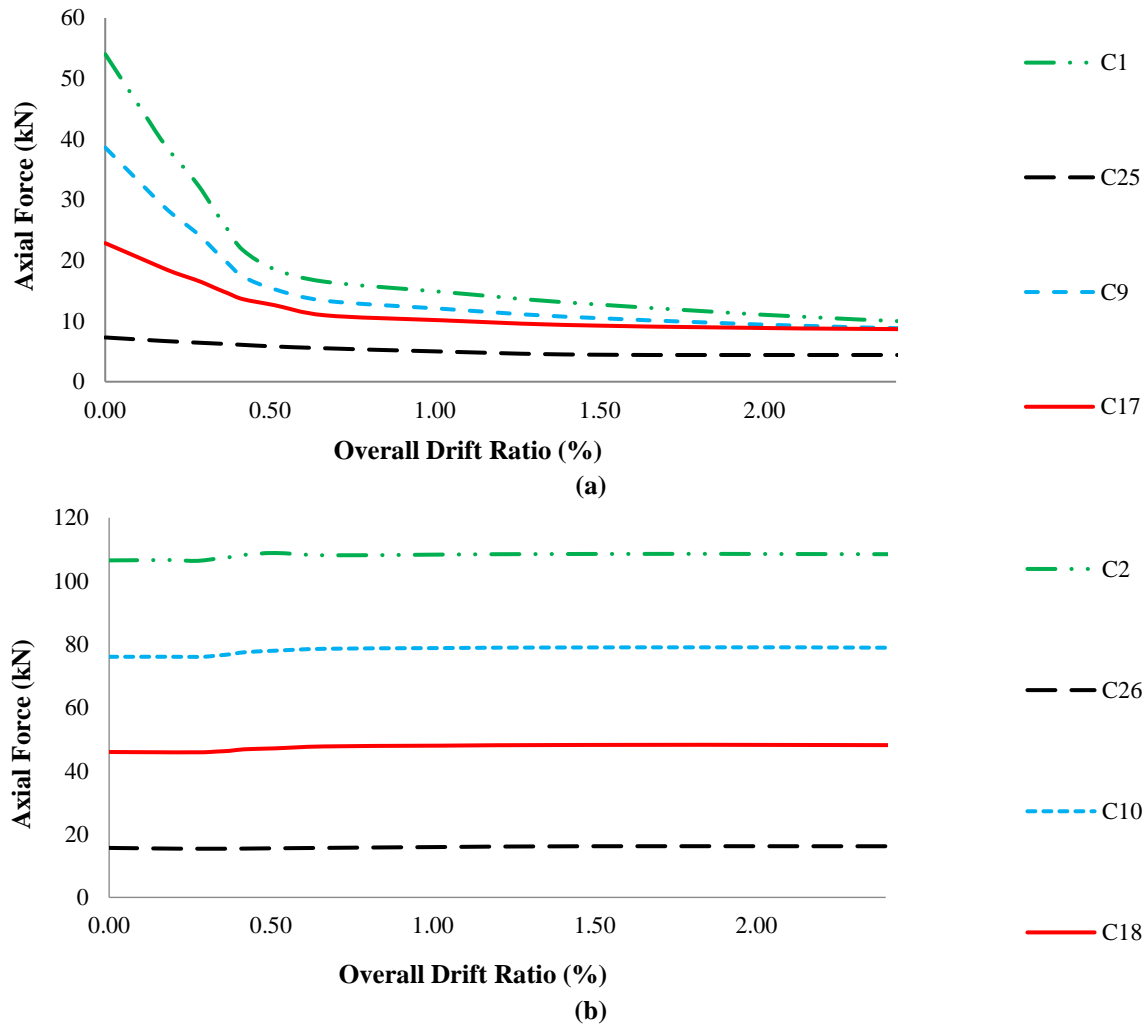


Fig. 9. The changes in axial forces of the columns: a) Edge columns; and b) Middle columns

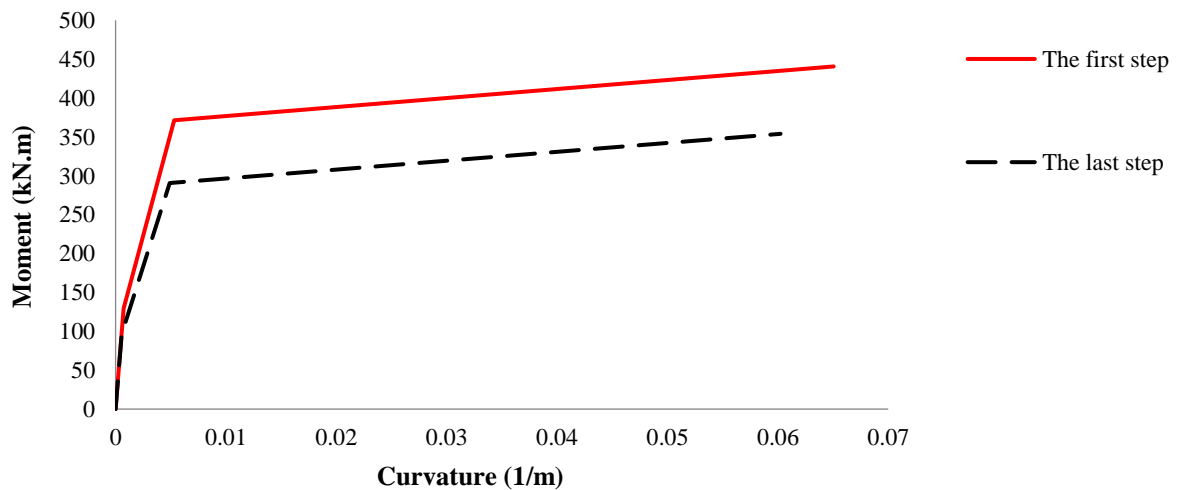


Fig. 10. The moment-curvature curve of column C₁ at the first and the last steps of pushover analysis

3.3. Case Study 3

The third example is a 10-story, 2-bay planner reinforced concrete moment-resistant frame indicated in Figure 11 (Izadpanah and Habibi, 2018a). A cylinder strength of 30 MPa and a modulus of rupture of 3.45 MPa are assumed for concrete. Concrete has a modulus of elasticity of 27,400 MPa and an ultimate strain of 0.004. A strain of 0.002 regarding

the maximum strength is considered for concrete. The steel is assumed to possess a yield strength of 300 MPa and a modulus of elasticity of 200,000 MPa. The distributed gravity load of 35 KN/m is assumed to impose on the beams. In Figure 12, the roof displacement-base shear curves of the convenient- and updated pushover analysis of this frame are shown.

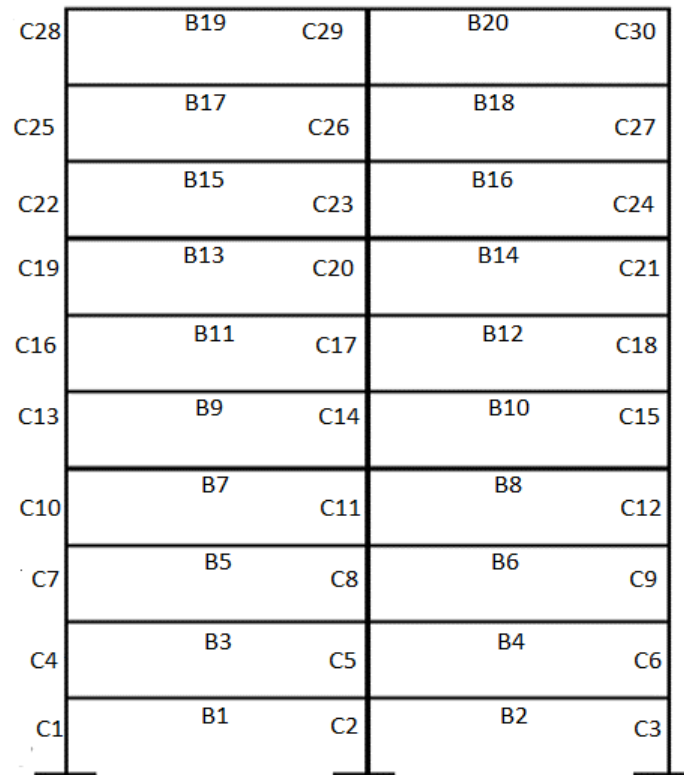


Fig. 11. Ten-story RC frame

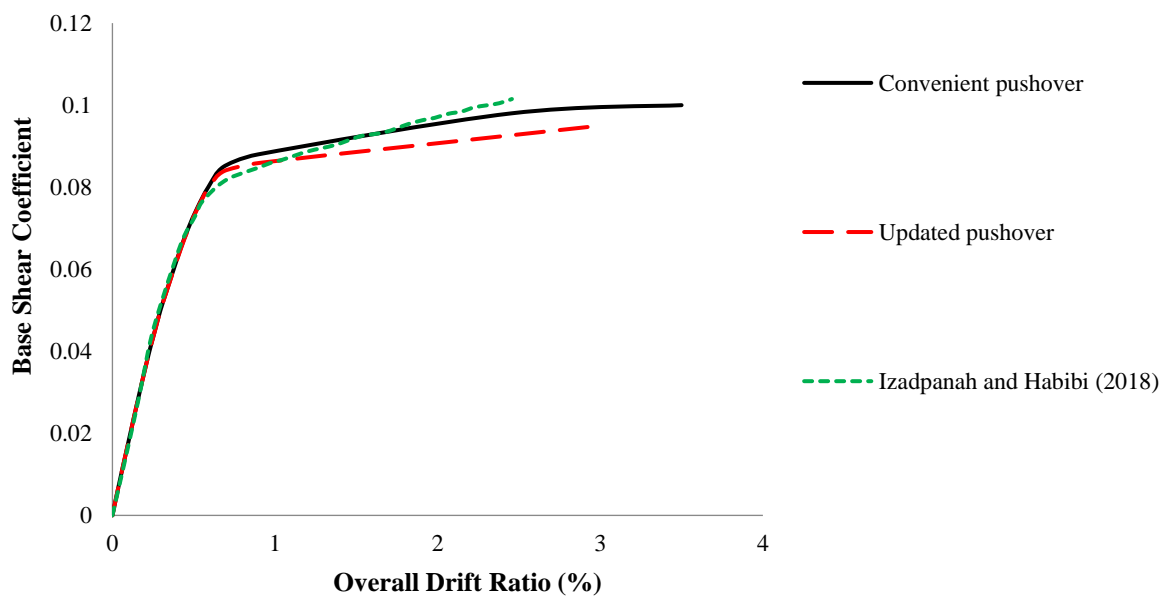


Fig. 12. The roof displacement-base shear curves of 10-story frame

As shown in Figure 12, the roof displacement-base shear curve acquired in this study is in good agreement with that of Izadpanah and Habibi (2018a). Considering the influence of the changes of the axial load on the moment-curvature of beam-column elements results in a reduction in the lateral load resistance of the frame. The secant stiffness, energy dissipation capacity, ductility, and ultimate strength of the updated pushover are lower than the convenient one. In Figure 13, the variation of axial force of column C_1 during the pushover analysis and the moment-curvature curve of this column at the first and the last steps of pushover analysis calculated using Opensees (fiber-based analysis) are demonstrated.

As indicated in Figure 13, the axial force of edge columns at the last step of the pushover analysis is around 3% of that of the first step of the analysis. The yielding and ultimate moments at the last step are significantly lower than the first step of the analysis. On the contrary, the ductility of the column in the last step is higher than in the first step.

4. Conclusions

The moment-curvature properties of the beam-column elements depend on the axial load of these elements. The pushover analysis as a way capable of providing valuable information about the behavior of structures from elastic to collapse has become a popular procedure of engineers. In the pushover analysis, in common, the moment-curvature properties of beam-column elements are achieved based on the axial forces achieved at the first step of analysis (regarding the gravity loads) and remain constant throughout the analysis. This study focused on developing a new pushover analysis to account for updating the moment-curvature properties of beam-column elements during the analysis. The updated pushover analysis was applied on three reinforced concrete frames and the roof displacement-base shear curves were compared with those of convenient pushover analysis. As per the outcomes, the following can be summarized.

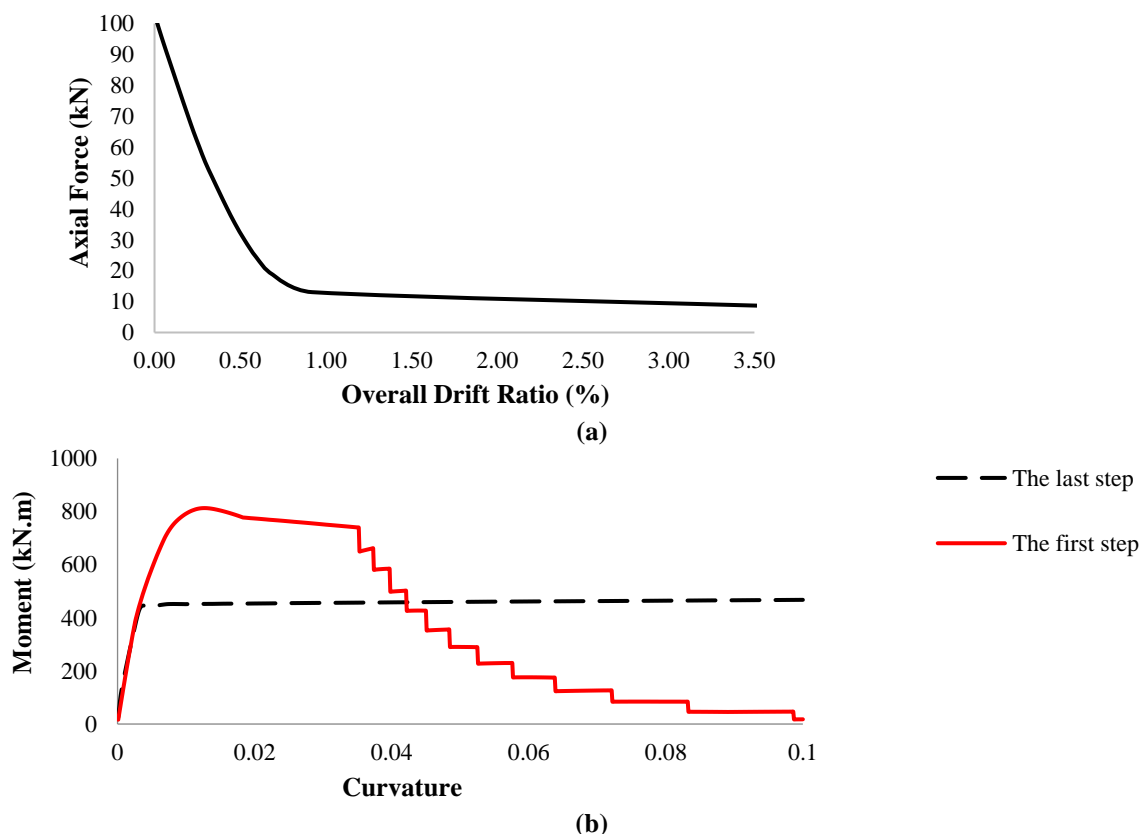


Fig. 13. The beam-column C_1 : a) The changes of axial forces; and b) The moment-curvature curves

- Updating the moment-curvature properties leads to reducing the lateral load-carrying capacity of the frames e.g. ductility, ultimate strength, second stiffness, and so on. This reduction for higher frames is more significant than for lower ones.
- In comparison with the unconfined condition, when the confinement effect is considered, the gap between updated- and convenient-pushover analysis increases.
- The changes in axial loads during the pushover analysis for the edge columns located in the lower stories are higher than those placed in higher levels or middle columns. Therefore, the moment-curvature properties of the edge columns in the lower stories e.g., cracking, yielding, and ultimate moments are higher than others.
- The moment-curvature properties of

beam-column elements significantly depend on the axial forces. In pushover analysis, the axial force of one side of the frame increases and another side decreases; therefore, the gap between the roof displacement-base shear curves of updated- and convenient-pushover analysis is not significant. Despite the low differences between the roof displacement-base shear curves of updated- and convenient-pushover analysis, the changes in axial force of beam-column members can significantly affect the responses of these members.

Further research could determine the influence of changing the moment-curvature properties of beam-column elements and confining action on the responses of reinforced concrete frames with various geometry and material properties, different lateral load systems, different connection systems, and so on.

5. Symbols

| | | | |
|-----------------|--|----------------|---|
| E_c | Modulus of elasticity of concrete | M_{crB} | Cracking moment at the end 'B' |
| E_s | Modulus of elasticity of concrete | α_A | Cracked part at the end 'A' |
| f_r | Concrete modulus of rupture | α_B | Cracked part at the end 'B' |
| f_c | Cylinder strength of concrete | M'_A | Moment at the member' end 'A' |
| f_y | Yield strength of steel | M'_B | Moment at the member' end 'B' |
| ε_y | Yield strain of steel | θ'_A | Rotation at the member' end 'A' |
| ε_u | Ultimate strain of concrete | θ'_B | Rotation at the member' end 'B' |
| β_l | Depends on the strength of concrete | GA_0 | Shear stiffness |
| N | Axial force | Y_a | Axial force |
| h | Height of section | Y_b | Axial force |
| c | Cover-to-steel centroid | v_a | Axial displacement |
| b_t | Top width of section | v_b | Axial displacement |
| y | Distance from the section neutral axis to the extreme fiber in tension | $\frac{EA}{L}$ | Axial stiffness of element |
| I | Moment of inertia of the section | L | Length of the element |
| $1/EI_A$ | Sections' flexural flexibility regarding the end 'A' | h_i | Distance from base to i^{th} story level |
| $1/EI_B$ | Sections' flexural flexibility regarding the end 'B' | W_i | Seismic weight at i^{th} story level |
| $1/EI_0$ | Flexibility in the elastic part of the member | T | Main vibration period of the building |
| M_{crA} | Cracking moment at the end 'A' | | |

6. References

- Amini, M.A. and Poursha, M. (2018). "Adaptive force-based multimode pushover analysis for seismic evaluation of midrise buildings", *Journal of Structural Engineering*, 144(8), 04018093, [https://doi.org/10.1061/\(ASCE\)ST.1943-541X.0002070](https://doi.org/10.1061/(ASCE)ST.1943-541X.0002070).
- Antoniou, S. and Pinho, R. (2004). "Development and verification of a displacement-based adaptive pushover procedure", *Journal of earthquake engineering*, 8(05), 643-661, <https://doi.org/10.1142/S136324690400150X>.
- ATC-40, (1997), "Seismic evaluation and retrofit of concrete buildings", Applied Technology Council, California Seismic Safety Commission.
- Bakalis, A.P. and Makarios, T.K. (2021). "Seismic enforced-displacement pushover procedure on multistorey R/C buildings", *Engineering Structures*, 229, 111631, <https://doi.org/10.1016/j.engstruct.2020.111631>.
- Cao, X.Y., Feng, D.C. and Wu, G. (2021). "Pushover-based probabilistic seismic capacity assessment of RCFs retrofitted with PBSPC BRBF sub-structures", *Engineering Structures*, 234, 111919, <https://doi.org/10.1016/j.engstruct.2021.111919>.
- CEN. (2004), "Eurocode 8: Design of structures for earthquake resistance. Part 1: General rules, seismic actions and rules for buildings", EN 1998-1, CEN, Brussels, December.
- Chopra, A.K. and Goel, R.K. (2002). "A modal pushover analysis procedure for estimating seismic demands for buildings", *Earthquake Engineering & Structural dynamics*, 31(3), 561-582, <https://doi.org/10.1002/eqe.144>.
- Chopra, A.K. and Goel, R.K. (2004). "A modal pushover analysis procedure to estimate seismic demands for unsymmetric-plan buildings", *Earthquake Engineering & Structural Dynamics*, 33(8), 903-927, <https://doi.org/10.1002/eqe.380>.
- Costa, R., Providencia, P. and Ferreira, M. (2017). "Influence of joint modelling on the pushover analysis of a RC frame", *Structural Engineering and Mechanics: An International Journal*, 64(5), 641-652, <https://doi.org/10.12989/sem.2017.64.5.641>.
- Daei, A. and Poursha, M. (2021). "On the accuracy of enhanced pushover procedures for seismic performance evaluation of code-conforming RC moment-resisting frame buildings subjected to pulse-like and non-pulse-like excitations", *Structures*, 32, 929-945, <https://doi.org/10.1016/j.istruc.2021.03.035>.
- Dehghani, E. and Soltani Mohajer, M. (2022). "Development of the fragility curves for conventional reinforced concrete moment resistant frame structures in Qods Town, Qom City, Iran", *Civil Engineering Infrastructures Journal*, 55(1), 31-41, <https://doi.org/10.22059/CEIJ.2021.306156.1690>.
- Elnashai, A.S. (2001). "Advanced inelastic static (pushover) analysis for earthquake applications", *Structural Engineering and Mechanics*, 12(1), 51-70, <https://doi.org/10.12989/sem.2022.84.1.085>.
- Fajfar, P. and Fischinger, M. (1988). "N2-A method for non-linear seismic analysis of regular buildings", In: *Proceedings of the Ninth World Conference in Earthquake Engineering*, (Vol. 5, pp. 111-116).
- Fajfar, P. and Gašperšič, P. (1996). "The N2 method for the seismic damage analysis of RC buildings", *Earthquake Engineering & Structural Dynamics*, 25(1), 31-46, [https://doi.org/10.1002/\(SICI\)1096-9845\(199601\)25:1<31::AID-EQE534>3.0.CO;2-V](https://doi.org/10.1002/(SICI)1096-9845(199601)25:1<31::AID-EQE534>3.0.CO;2-V).
- Faruk, M.O., Singh, S.K. and Mondal, S. (2023). "Comparative study of buckling restrained braces and fluid viscous damper applied in an RCC structure following pushover analysis", *Materials Today: Proceedings*, <https://doi.org/10.1016/j.matpr.2023.03.471>.
- FEMA273, (1997), "NEHRP guideline for the seismic rehabilitation of buildings", Federal Emergency Management Agency, Washington, DC.
- Ghayoumian, G. and Emami, A.R. (2020). "A multi-direction pushover procedure for seismic response assessment of low-to-medium-rise modern reinforced concrete buildings with special dual system having torsional irregularity", *Structures*, 28, 1077-1107, <https://doi.org/10.1016/j.istruc.2020.09.031>.
- Gulkan, P. and Sozen, M.A. (1974). "Inelastic responses of reinforced concrete structure to earthquake motions", *Journal Proceedings*, 71(12), 604-610.
- Gupta, A. and Krawinkler, H. (2000). "Estimation of seismic drift demands for frame structures", *Earthquake Engineering & Structural Dynamics*, 29(9), 1287-1305, [https://doi.org/10.1002/1096-9845\(200009\)29:9%3C1287::AID-EQE971%3E3.0.CO;2-B](https://doi.org/10.1002/1096-9845(200009)29:9%3C1287::AID-EQE971%3E3.0.CO;2-B).
- Habibi, A.R. (2011). "Nonlinear sensitivity of analysis of RCMRF considering both axial and flexure effects", *IJE Transactions A: Basics*, 24(3), 223-238, <https://doi.org/10.5829/idosi.ije.2011.24.03a.02>.
- Habibi, A., Saffari, H. and Izadpanah, M. (2019). "Optimal lateral load pattern for pushover

- analysis of building structures”, *Steel and Composite Structures*, 32(1), 67-77, <https://doi.org/10.12989/scs.2019.32.1.067>.
- Hassan, W.M. and Reyes, J.C. (2020). “Assessment of modal pushover analysis for mid-rise concrete buildings with and without viscous dampers”, *Journal of Building Engineering*, 29, 101103, <https://doi.org/10.1016/j.jobe.2019.101103>.
- Izadpanah, M. and Habibi, A. (2018b). “Evaluating the accuracy of a new nonlinear reinforced concrete beam-column element comprising joint flexibility”, *Earthquakes and Structures*, 14(6), 525-535, <https://doi.org/10.12989/eas.2018.14.6.525>.
- Izadpanah, M. and Habibi, A. R. (2018a). “New spread plasticity model for reinforced concrete structural elements accounting for both gravity and lateral load effects”, *Journal of Structural Engineering*, 144(5), 04018028, [https://doi.org/10.1061/\(ASCE\)ST.1943-541X.0002016](https://doi.org/10.1061/(ASCE)ST.1943-541X.0002016).
- Jalilkhani, M., Ghasemi, S.H. and Danesh, M. (2020). “A multi-mode adaptive pushover analysis procedure for estimating the seismic demands of RC moment-resisting frames”, *Engineering Structures*, 213, 110528, <https://doi.org/10.1016/j.engstruct.2020.110528>.
- Kalkan, E. and Kunnath, S.K. (2006). “Adaptive modal combination procedure for nonlinear static analysis of building structures”, *Journal of Structural Engineering*, 132(11), 1721-1731, <https://doi.org/10.1016/j.engstruct.2020.110528>.
- Kheirollahi, M., Abedi, K. and Chenaghloou, M.R. (2021). “A new pushover procedure for estimating seismic demand of double-layer barrel vault roof with vertical double-layer walls”, *Structures*, 34, 1507-1524, <https://doi.org/10.1016/j.istruc.2021.08.090>.
- Krawinkler, H. and Seneviratna, G.D.P.K. (1998). “Pros and cons of a pushover analysis of seismic performance evaluation”, *Engineering Structures*, 20(4-6), 452-464, [https://doi.org/10.1016/S0141-0296\(97\)00092-8](https://doi.org/10.1016/S0141-0296(97)00092-8).
- Kunnath, S.K. and Reinhorn, A.M. (1989). “Inelastic three-dimensional response analysis of reinforced concrete building structures (IDARC-3D)”, National Center for Earthquake Engineering Research, Buffalo, NY.
- Lawson, R.S., Vance, V. and Krawinkler, H. (1994). “Nonlinear static pushover analysis, why, when and how”, In: *Proceedings of Fifth US National Conference on Earthquake Engineering*, (Vol. 1, p. 283), Chicago, IL.
- Lherminier, O., Erlicher, S., Huguet, M. and Barakat, M. (2023). “The E-DVA method for multi-modal pushover analysis and dominant modes”, *Procedia Structural Integrity*, 44, 528-535, <https://doi.org/10.1016/j.prostr.2023.01.069>.
- Lu, X. and Li, J. (2023). “The evaluation of the seismic performance of tall bridge piers with non-adaptive pushover methods”, *Structures*, 48, 839-851, <https://doi.org/10.1016/j.istruc.2023.01.021>.
- Mander, J.B., Priestley, M.J. and Park, R., (1988). “Theoretical stress-strain model for confined concrete”, *Journal of Structural Engineering*, 114(8), 1804-1826, [https://doi.org/10.1061/\(ASCE\)0733-9445\(1988\)114:8\(1804\)](https://doi.org/10.1061/(ASCE)0733-9445(1988)114:8(1804)).
- Moradi, M. and Tavakoli, H. (2020). “Proposal of an energy based assessment of robustness index of steel moment frames under the seismic progressive collapse”, *Civil Engineering Infrastructures Journal*, 53(2), 277-293, <https://doi.org/10.22059/CEIJ.2019.283574.1591>.
- Mwafy, A.M. and Elnashai, A.S. (2001). “Static pushover versus dynamic collapse analysis of RC buildings”, *Engineering Structures*, 23(5), 407-424, [https://doi.org/10.1016/S0141-0296\(00\)00068-7](https://doi.org/10.1016/S0141-0296(00)00068-7).
- Nazri, F.M. and Alexander, N.A. (2014). “Exploring the relationship between earthquake intensity and building damage using single and multi-degree of freedom models”, *Canadian Journal of Civil Engineering*, 41(4), 343-356, <https://doi.org/10.1139/cjce-2012-0477>.
- Nazri, F.M. and Alexander, N.A. (2015). “Predicting collapse loads for buildings subjected to seismic shock”, *Bulletin of Earthquake Engineering*, 13(7), 2073-2093, <https://doi.org/10.1007/s10518-014-9707-9>.
- Olivito, R.S. and Porzio, S. (2019). “A new multi-control-point pushover methodology for the seismic assessment of historic masonry buildings”, *Journal of Building Engineering*, 26, 100926, <https://doi.org/10.1016/j.jobe.2019.100926>.
- Ozgenoglu, M. and Arıcı, Y. (2017). “Comparison of ASCE/SEI Standard and modal pushover-based ground motion scaling procedures for pre-tensioned concrete bridges”, *Structure and Infrastructure Engineering*, 13(12), 1609-1623, <https://doi.org/10.1080/15732479.2017.1310258>.
- Rahmani, A.Y., Bourahla, N., Bento, R. and Badaoui, M. (2018). “An improved upper-bound pushover procedure for seismic assessment of high-rise moment resisting steel frames”, *Bulletin of Earthquake Engineering*, 16(1), 315-339, <https://doi.org/10.1007/s10518-017-0204-9>.
- Reinhorn, A.M., Roh, H., Sivaselvan, M.V., Kunnath, S.K., Valles, R.E., Madan, A., Li, C., Lobo, R. and Park, Y.J. (2009). “IDARC 2D

version 7.0: A program for the inelastic damage analysis of structures”, MCEER Technical Report, MCEER-09-0006, State University of New York, Buffalo, NY.

- Reyes, J.C. and Chopra, A.K. (2011). “Three-dimensional modal pushover analysis of buildings subjected to two components of ground motion, including its evaluation for tall buildings. *Earthquake Engineering and Structural Dynamics*, 40(7), 789-806, <https://doi.org/10.1002/eqe.1060>.
- Tian, L. and Qiu, C. (2018). “Modal pushover analysis of self-centering concentrically braced frames”, *Structural Engineering and Mechanics: An International Journal*, 65(3), 251-261, <https://doi.org/10.12989/sem.2018.65.3.251>.
- Wang, J., Wang, X., Ye, A. and Guan, Z. (2023). “Deformation-based pushover analysis method for transverse seismic assessment of inverted Y-shaped pylons in kilometer-span cable-stayed bridges: Formulation and application to a case study”, *Soil Dynamics and Earthquake Engineering*, 169, 107874, <https://doi.org/10.1016/j.soildyn.2023.107874>.
- Worku, A.M. and Hsiao, P.C. (2022). “An improved first-mode-based pushover analytical procedure for assessing seismic performance of special moment resisting frame building structures”, *Engineering Structures*, 252, 113587, [10.1016/j.engstruct.2021.113587](https://doi.org/10.1016/j.engstruct.2021.113587).
- Zhou, P., Xiong, Z., Chen, X. and Wang, J. (2023). “Seismic performance of RC frame structure across the earth fissure based on pushover analysis”, *Structures*, 52, 1035-1050, <https://doi.org/10.1016/j.istruc.2023.03.148>.



This article is an open-access article distributed under the terms and conditions of the Creative Commons Attribution (CC-BY) license.



Upper Bound Solution for the Stability of Surcharged Soil Slope Using Nonlinear Failure Criterion

Aminpour, M.M.¹  and Maleki, M.^{2*} 

¹ Ph.D., Civil Engineering Department, Bu-Ali Sina University, Hamedan, Iran.

² Associate Professor, Civil Engineering Department, Bu-Ali Sina University, Hamedan, Iran.

© University of Tehran 2023

Received: 05 Jan. 2023;

Revised: 05 Apr. 2023;

Accepted: 17 Apr. 2023

ABSTRACT: In this paper using the upper bound limit analysis method, the stability of soil slope, uniformly surcharged at the crest is investigated. According to the soil behavior at the failure state, a continuous failure criterion nonlinear function of confining stress, and soil initial density is considered. The stress field along the slip surface is entered into the limit analysis formulation according to the Airy stress function. The ultimate uniformly distributed load is obtained by optimizing the virtual work equation. The effects of different parameters such as slope angle, soil unit weight, and initial density are investigated. Considering the nonlinear effects of confining stresses leads to a reduction in the ultimate load. This reduction is more obvious in slopes with lower angles. According to the proposed formulation, with increasing soil density, the ultimate load of the slope stability is increased. The results for different slope angles are compared with those obtained from the limit equilibrium-based methods. The ultimate loads of the proposed method are in some cases lower and in some cases more than the results of different methods based on limit equilibrium.

Keywords: Airy Stress Function, Nonlinear Failure Criterion, Slope Stability, Upper Bound Limit Analysis Method.

1. Introduction

The construction of footing on the crest of a slope has a significant effect on its stability. In the technical literature, there are many studies dedicated to loading on the slopes, slope stability, and bearing capacity of footing near the slope. In general, the analytical approaches to this problem can be divided into three categories of limit equilibrium (Vo and Russell, 2017; Shukla and Jakka, 2018; Hajiazizi et al., 2018; Mirzazadeh and Hajiazizi, 2020; Hu et al.,

2022; Tozato et al., 2022), method of characteristics and limit analysis (Mofidi et al., 2014; Tang et al., 2015; Qin and Chain, 2018; Zhou et al., 2018; Froutan Kalourazi et al., 2019, Guanhua, 2023; Zhou and Qin, 2023). In addition, several experimental studies (e.g. Hajiazizi and Nasiri, 2019; Razali et al., 2023; Thomas et al., 2023) have been performed in this field.

The stability of surcharged slopes using the limit analysis technique was studied by several researchers (e.g. Mofidi Rouchi, 2014; Tang et al., 2015; Haghbin and

* Corresponding author E-mail: maleki@basu.ac.ir

Ghazavi, 2016; Vo and Russell, 2017; Qin and Chin, 2017, 2018; Aminpour et al., 2017, 2018; Aminpour and Maleki, 2022). Tang et al. (2015) presented some practical charts for assessing the slope stability in different loading conditions taking into account the effect of pore water pressure. Vo and Russell (2017) studied the slope stability of nonhomogeneous unsaturated slopes subjected to uniform loading using the limit equilibrium technique. Qin and Chain (2017, 2018) discretized the log-spiral failure wedge into vertical slices and calculated the ultimate load applied to the slope.

Using the limit analysis technique, Aminpour et al. (2017, 2018) investigated the effect of surcharge on the behavior of soil slopes under various seismic conditions and soil reinforcement. Aminpour and Maleki (2022) estimated the bearing capacity of strip footing on the slope by using finite element limit analysis technique considering nonlinear continuous failure criterion with a non-associated flow rule. Tran et al. (2019) investigated the stability of the slope with the foundation during rainfall using a finite difference program. Komasi and Beiranvand (2022) investigated the stability analysis of earth dam under drawdown conditions. In this study, the finite element method was used to study the seepage from the body of the earth dam.

The majority of the above-mentioned studies are based on Mohr-Coulomb (MC) failure criterion. In the limit analysis technique, upon using the MC criterion, the stress fields do not affect the rate of dissipated energy. In this case, the rate of internal work will only depend on cohesion and will be obtained by multiplying cohesion by the tangential component of the velocity vector (Chen, 1975).

A considerable number of studies show that almost all geomaterials obey nonlinear failure criteria. On this basis, different nonlinear failure surfaces have been proposed and applied for stability analysis in geotechnical problems (e.g. Maleki et al., 2000; Liu and Carter, 2003; Baker, 2004;

Sun and Song, 2016; Wu et al., 2017).

In the present research, using the upper bound limit analysis, the ultimate uniformly distributed load adjacent to a slope is investigated. Instead of the non-continuous MC criterion, the continuous criterion of CJS (Maleki et al., 2000) is used. In this criterion, the failure state is a nonlinear function of confining pressure and material density. The stress components along the slip surface are determined based on chosen Airy function. To find the critical condition, the virtual work is subjected to unconstrained nonlinear optimization in the MATLAB program. Finally, the results are compared with those of the slices methods.

2. The Log-Spiral Rotational Failure Mechanism

The slope undergoes a shear failure with a rotational log-spiral failure mechanism due to building loading (Figure 1). In this study, for simplicity and by ignoring the stiffness of the building, the load of the building is replaced by an infinite uniformly distributed load. The soil wedge will fail around point O with an angular velocity of $\dot{\Omega}$. The equation of log-spiral failure surface can be written as Eq. (1), in which, $R(\theta)$: is the radius of an arbitrary angle θ and $u(\theta)$: is the velocity that depends on $R(\theta)$ and can be obtained from Eq. (2).

$$R(\theta) = R_0 \exp(\theta - \theta_0) \quad (1)$$

$$u(\theta) = R\dot{\Omega} = R_0 \exp(\theta - \theta_0)\dot{\Omega} \quad (2)$$

3. Stress Field in the Soil Mass in Polar Coordinates

In the upper bound solution, the plastic deformation rate is related to the stress components through the flow rule ($\dot{\epsilon}_{ij}^p = \lambda \partial f / \partial \sigma_{ij}$). Therefore, the stress components in the slip log spiral bond of the failure mechanism must be known as a function of coordinate variables. By considering perfectly plastic behavior for material, stress components in the plastic state remain constant. The stress

components in this state can be considered as components obtained at the beginning of yielding. At this point, kinematic and equilibrium equations accompanied by isotropic linear elasticity constitutive equations, lead to a solution for determining the stress components.

In the theory of elasticity, the stresses applied to the soil mass can be expressed by Eq. (3) using the Airy stress function. In this equation, $\varphi(r, \theta)$ is the Airy stress function in polar coordinates. It is assumed that the body force is derivable from a scalar potential \hat{V} . In the polar coordinates, \hat{V} can be expressed by Eq. (4).

$$\begin{cases} \sigma_{rr} = \sigma_{rr}(r, \theta) = \frac{1}{r} \frac{\partial \varphi}{\partial r} + \frac{1}{r^2} \frac{\partial^2 \varphi}{\partial \theta^2} + V \\ \sigma_{\theta\theta} = \sigma_{\theta\theta}(r, \theta) = \frac{\partial^2 \varphi}{\partial r^2} + V \\ \sigma_{r\theta} = \tau_{r\theta} = \tau_{r\theta}(r, \theta) = -\frac{\partial}{\partial r} \left(\frac{1}{r} \frac{\partial \varphi}{\partial \theta} \right) \end{cases} \quad (3)$$

$$\hat{V} = \gamma r \sin \theta \quad (4)$$

The Airy stress function is written in polar

coordinated (Sadd, 2009) as follows.

$$\varphi(r, \theta) = r^2 (c_1 + c_2 \theta + c_3 \sin 2\theta + c_4 \cos 2\theta) \quad (5)$$

Substituting Eq. (5) into Eq. (3), the stress components in polar coordinates can be obtained as following expressions.

$$\begin{aligned} \sigma_{rr} &= 2c_1 + 2c_2\theta + 2c_3\sin 2\theta \\ &\quad + 2c_4\cos 2\theta \\ &\quad - 4c_3\sin 2\theta - 4c_4\cos 2\theta + \gamma r \sin \theta \\ \sigma_{\theta\theta} &= 2c_1 + 2c_2\theta + 2c_3\sin 2\theta \\ &\quad + 2c_4\cos 2\theta + \gamma r \sin \theta \\ \sigma_{r\theta} &= -c_2 - 2c_3\cos 2\theta + 2c_4\sin 2\theta \end{aligned} \quad (6)$$

Initially, the center of polar coordinates is considered at the edge of the slope. The geometry of the problem in polar coordinate, center of rotation, and slip surface are shown in Figure 2.

Boundary conditions on the ground surface and along the slope are expressed in Eq. (7) where L : is the length of failure wedge on the ground surface.

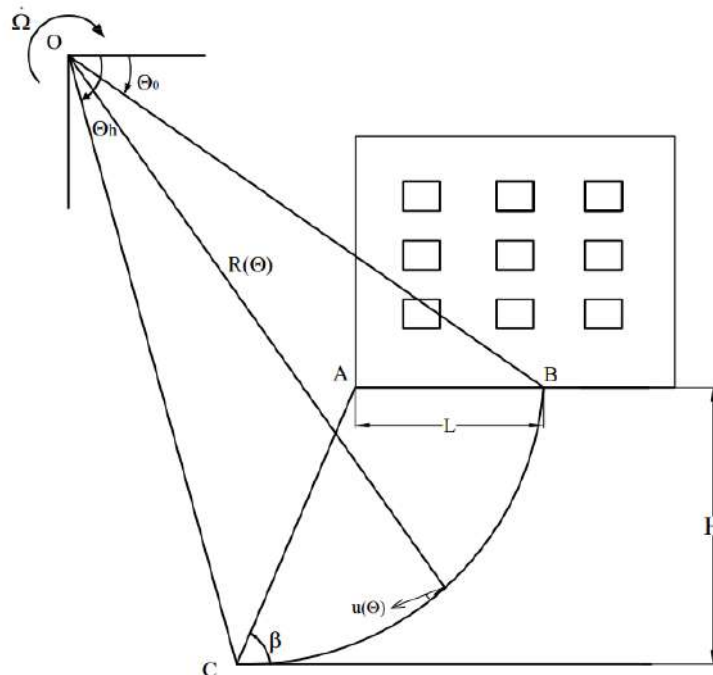


Fig. 1. The rotational failure mechanism with a surcharge due to uniform loading adjacent to the slope

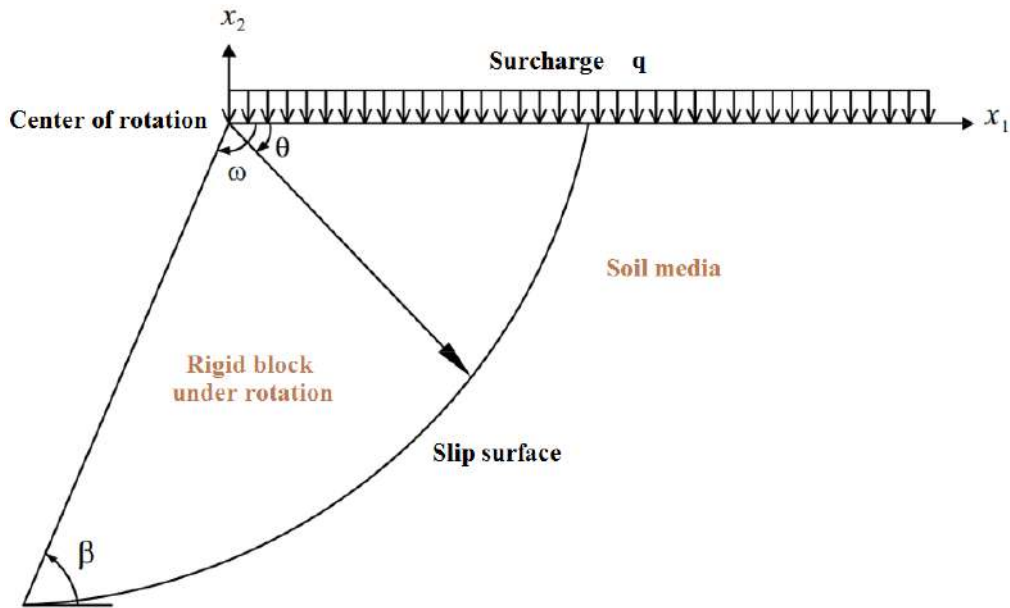


Fig. 2. Cartesian and polar coordinates considered in the present research

$$\begin{aligned}
 \theta = 0, \quad \sigma_{r\theta} = 0 &\Rightarrow -c_2 - 2c_3 = 0 \\
 \sigma_{\theta\theta} = q &\Rightarrow 2c_1 + 2c_4 = q \\
 \\
 \theta = \omega, \quad \sigma_{r\theta} = 0 &\Rightarrow -c_2 - 2c_3 \cos 2\omega \\
 &+ 2c_4 \sin 2\omega = 0 \\
 \sigma_{\theta\theta} = 0 &\Rightarrow 2c_1 + 2c_2 \omega + \\
 &2c_3 \sin 2\omega + 2c_4 \cos 2\omega + \gamma r \sin \omega \\
 &= 0 \\
 \omega = \pi - \beta, \quad r = r_0 \exp(\theta - \theta_0) &= \\
 L \exp(\theta) & \quad (7)
 \end{aligned}$$

Finally, solving the above equations, the constants of the Airy stress function are obtained as follows.

$$\begin{aligned}
 c_1 &= \frac{q}{2} - c_4, \quad c_2 = -2c_3 \\
 c_3 &= \\
 &= \frac{q + \gamma r \sin \omega}{2(1 + \cos 2\omega) - \frac{2 \sin 2\omega}{1 - \cos 2\omega} (2\omega - \sin 2\omega)} \\
 &\times \frac{\sin 2\omega}{1 - \cos 2\omega} \\
 c_4 &= \\
 &= \frac{q + \gamma r \sin \omega}{2(1 + \cos 2\omega) - \frac{2 \sin 2\omega}{1 - \cos 2\omega} (2\omega - \sin 2\omega)} \quad (8)
 \end{aligned}$$

4. Nonlinear Failure Criteria

The Mohr-Coulomb failure criterion has

been widely used in upper-bound solutions of geotechnical problems. Mohr-Coulomb criterion, for a given internal friction angle, considers a linear relationship between shear strength and normal stress. Besides, the effect of density has not been automatically provided so that, for a given problem, the internal friction angle must be identified based on medium density. However, based on experimental observation, the failure state in soils is a nonlinear function of confining pressure as well as soil density. Besides, lack of intermediate principal stress in Mohr-Coulomb led to discontinuity of the failure surface relative to the stress components.

In the present study, the failure surface equation of the CJS elastoplastic constitutive model is used as the failure criterion for identifying upper bound solution. This model has been originally proposed for predicting the stress-strain behavior of granular soils (Cambou et al., 1989). The failure surface of the CJS model was then extended based on experimental observations in order to improve its prediction (Maleki et al., 2000). The general form of CJS failure surface for granular materials is given by:

$$f(\sigma) = s_{II} h(\theta) - R_m I_1 = 0 \quad (9)$$

in which, $s_{II} = \sqrt{s_{ij}s_{ij}}$: represents the second invariant of the deviatoric stress tensor of s_{ij} with $s_{ij} = \sigma_{ij} - \frac{\sigma_{kk}}{3}\delta_{ij}$, $I_1 = \sigma_{kk}$: is the first invariant of the stress tensor, R_m : illustrates the mean radius of the failure surface and the function $h(\theta)$: controls the geometrical form of failure surface about hydrostatic axis in stresses space with the following expression.

$$h(\theta) = (1 - \gamma \cos 3\theta)^{1/6} = \left[1 - \sqrt{54}\gamma \frac{\det(s_{ij})}{s_{II}^3} \right]^{1/6} \quad (10)$$

where θ : is Lode's angle and γ : is a constant parameter of the model. The choice of γ depends on material behavior at the failure state.

As seen from Figure 3a, for $\gamma = 0$ a circular form of failure surface is achieved in the deviatoric stresses plane, however, choosing a value greater than zero for γ leads to an asymmetric form of failure surface about the hydrostatic axis. In the present study, by considering $\gamma = 0$, a simplified form of the failure surface of the CJS model with the following expression was used.

$$f(\sigma) = s_{II} - R_m I_1 = 0 \quad (11)$$

Based on the experimental observations, the shear strength of the granular soils at the

peak state depends on the confining stress and soil density. In the CJS failure surface, these issues have been well described in the framework of critical state soil mechanics. The mean radius of the failure surface R_m in Eq. (11), is a function of stress level and soil density and varies between a maximum initial value (R_{mi}) corresponding to peak resistance to a minimum value ($R_{critical}$) related to the critical state resistance.

$$R_m = R_{critical} + (R_{mi} - R_{critical}) \left(1 - \frac{I_1}{3p_c} \right)^\alpha \quad (12)$$

The critical state pressure p_c depends on the soil density through an exponential relationship (Maleki et al., 2000). According to the experimental observations concerning the stress-strain behavior of granular soils at peak and post-peak states α has been fixed equal to 1.5 (Bathayian and maleki, 2018). A typical soil stress-strain curve is shown in Figure 3b. The maximum and critical state mean radii (R_{mi} and $R_{critical}$) of the failure surface, are related to point A (peak state) and point B (critical state) respectively. The manner of determination of CJS criterion parameters has been given in Maleki et al. (2000). Intersecting CJS and Mohr-Coulomb criteria in axisymmetric triaxial conditions results in the direct relationships for R_{mi} and $R_{critical}$ in terms of internal friction angle at peak and critical states, respectively, which are presented in Appendix A.2 (Eqs. (A2-1 and A2-2)).

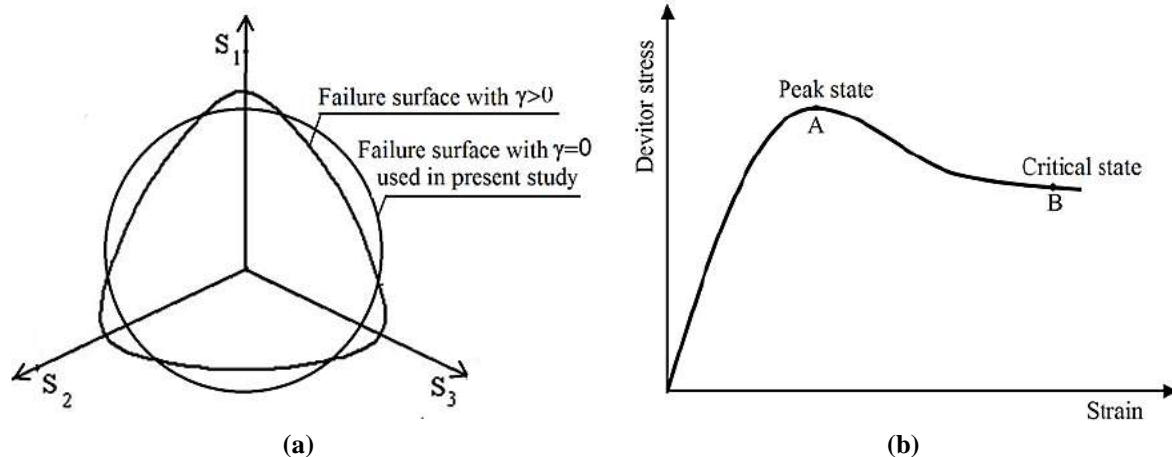


Fig. 3. a) CJS failure surface in deviatoric stress space; and b) Schematic deviator stress-strain behavior of soil

5. Internal Power Dissipation

Based on the upper bound limit analysis theorem and virtual work equation, by setting the rate of external work equal to the rate of internal Power dissipation, obtained loads in this field will not be smaller than the actual failure loads. The mathematical form of the virtual work equation can be written as follows.

$$\iint_{\bar{V}} \sigma_{ij} \dot{\epsilon}_{ij} dV = \iint_V b_i u_i dV + \iint_{S_t} T_i u_i dS_t \quad (13)$$

where σ_{ij} : is the state of stress and $\dot{\epsilon}_{ij}$: is the rate of plastic strain. The internal power dissipation is equal to the product of the stress tensor and plastic strain rate. T_i : is the unknown distributed load on the boundaries S_t and b_i : is the body force on the volume V and u_i : is the incipient velocity in the selected mechanism. The stress components are identified depending on the failure mechanism geometry and considered Airy function. The second invariant of the deviatoric stress tensor of the CJS failure criterion in plane strain conditions are defined as follows.

$$\begin{aligned} s_{II} &= \sqrt{S_{ij}S_{ij}} \\ &= \sqrt{s_{11}^2 + s_{22}^2 + s_{33}^2 + 2s_{12}^2} \\ &= \sqrt{s_{rr}^2 + s_{\theta\theta}^2 + s_{33}^2 + 2s_{r\theta}^2} \\ &= v(\sigma_{rr} + \sigma_{\theta\theta})I_1 = \sigma_{rr} + \sigma_{\theta\theta} + \sigma_3 \end{aligned} \quad (14)$$

The CJS failure surface in S_{II} - I_1 coordinates has a nonlinear form as illustrated in Figure 4. In this figure, the shear strain rate, $\dot{\epsilon}_{II}$, versus volumetric strain rate, $\dot{\epsilon}_V$, is also shown. Based on the normality rule, the dilation angle of ξ can be expressed in terms of stress state by differentiation of failure surface as follows.

$$\begin{aligned} \frac{ds_{II}}{dI_1} = \tan \xi &= (R_{mi} \\ &- R_{critical}) \left(1 - \frac{I_1}{3p_c} \right)^\alpha \left(\frac{\alpha}{3p_c} \left(1 - \frac{I_1}{3p_c} \right)^{\alpha-2} (I_1) - 1 \right) \\ &+ R_{critical} \end{aligned} \quad (15)$$

According to Figure 5, if t : is the thickness of the region including discontinuity of velocity, the shear strain can be obtained by dividing the tangential velocity by this thickness. Therefore, the increment of dissipated internal energy in the unit area of discontinuous surfaces is defined as Eq. (16).

$$d\dot{D} = (s_{II}\dot{\epsilon}_{II} - I_1\dot{\epsilon}_v)(t \times 1 \times 1) \quad (16)$$

Based on Figure 4 and the expression of the dilation angle, the increment of dissipated internal energy is defined as follows.

$$\begin{aligned} \dot{\epsilon}_v &= \tan \xi \dot{\epsilon}_{II} \\ d\dot{D} &= (s_{II} - I_1 \tan \xi) \dot{\epsilon}_{II} (t \times 1 \times 1) \\ &= (s_{II} - I_1 \tan \xi) (\delta u) \end{aligned} \quad (17)$$

The dissipated internal energy is adopted based on a center coordinate at the edge of the slope (local coordinates). In order to establish the virtual work equation, the dissipated energy has to be defined based on the center of the global coordinates at the rotational log-spiral outside of the slope. The local coordinates (x_1, x_2, r, θ) , as well as the global coordinates (X_1, X_2, R, Θ) are shown in Figure 6. The transformation matrix is expressed as the following form.

$$\begin{aligned} \begin{pmatrix} \cos(R, r) & \cos(R, \theta) \\ \cos(\theta, r) & \cos(\theta, \theta) \end{pmatrix} \\ = \begin{pmatrix} \cos \eta & \sin \eta \\ \sin \eta & -\cos \eta \end{pmatrix} \end{aligned} \quad (18)$$

As shown in Figure 6, the angle η : is defined as $\theta - \Theta$ by extending the radius, r . According to this figure, the relationship

between the polar angles of two coordinate systems can be obtained as shown in Eqs. (19) and (20), respectively. The r_0 is equal to the length of failed soil mass on the ground, L .

$$\begin{aligned}
 R \sin \theta &= R_0 \sin \theta_0 + r \sin \theta \\
 \rightarrow \exp(\theta - \theta_0) \sin \theta &= \\
 \sin \theta_0 + \frac{r_0}{R_0} \exp(\theta) \sin \theta & \\
 R_0 \cos \theta_0 - R \cos \theta + r \cos \theta &= L \quad (19) \\
 \rightarrow \exp(\theta - \theta_0) \cos \theta &= \\
 \cos \theta_0 + \frac{r_0}{R_0} \exp(\theta) \cos \theta - \frac{L}{R_0} &
 \end{aligned}$$

$$\begin{aligned}
 \theta &= \\
 \tan^{-1} \left(\frac{\sin \theta_0 + \frac{r_0}{R_0} \exp(\theta) \sin \theta}{\cos \theta_0 + \frac{r_0}{R_0} \exp(\theta) \cos \theta - \frac{L}{R_0}} \right) \eta & \\
 = \theta - \theta & \quad (20)
 \end{aligned}$$

By transforming the local coordinates to the global coordinates, the limit stresses in global coordinates are identified for establishing the virtual work equation.

$$\begin{pmatrix} \sigma_{RR} & \sigma_{R\theta} \\ \sigma_{R\theta} & \sigma_{\theta\theta} \end{pmatrix} = \begin{pmatrix} \cos \eta & \sin \eta \\ \sin \eta & -\cos \eta \end{pmatrix} \times \begin{pmatrix} \sigma_{rr} & \sigma_{r\theta} \\ \sigma_{r\theta} & \sigma_{\theta\theta} \end{pmatrix} \times \begin{pmatrix} \cos \eta & \sin \eta \\ \sin \eta & -\cos \eta \end{pmatrix}^T \quad (21)$$

or,

$$\begin{aligned}
 \sigma_{RR} &= \sigma_{rr} \cos^2 \eta + \sigma_{\theta\theta} \sin^2 \eta \\
 &+ \sigma_{r\theta} \sin 2\eta \\
 \sigma_{\theta\theta} &= \sigma_{rr} \sin^2 \eta + \sigma_{\theta\theta} \cos^2 \eta \\
 &- \sigma_{r\theta} \sin 2\eta \quad (22)
 \end{aligned}$$

$$\begin{aligned}
 \sigma_{R\theta} &= 0.5 \sigma_{rr} \sin 2\eta - 0.5 \sigma_{\theta\theta} \sin 2\eta \\
 &+ \sigma_{r\theta} (\sin^2 \eta - \cos^2 \eta)
 \end{aligned}$$

The stress invariants are also expressed as follows.

$$\begin{aligned}
 s_{II} &= \sqrt{s_{RR}^2 + s_{\theta\theta}^2 + s_{33}^2 + 2s_{R\theta}^2} \\
 I_1 &= \sigma_{RR} + \sigma_{\theta\theta} + \sigma_{33} \\
 \sigma_{33} &= \nu (\sigma_{RR} + \sigma_{\theta\theta}) \\
 s_{RR} &= \frac{2\sigma_{RR} - \sigma_{\theta\theta} - \sigma_{33}}{3} \\
 s_{\theta\theta} &= \frac{2\sigma_{\theta\theta} - \sigma_{RR} - \sigma_{33}}{3} \\
 s_{33} &= \frac{2\sigma_{33} - \sigma_{RR} - \sigma_{\theta\theta}}{3} \\
 s_{R\theta} &= \sigma_{R\theta} - \frac{\sigma_{RR} + \sigma_{\theta\theta} + \sigma_{33}}{3} \quad (23)
 \end{aligned}$$

The rate of total dissipated energy is obtained by integrating the increments of dissipated energy along the log-spiral slip surface.

$$\begin{aligned}
 \dot{D} &= \int_{\theta_0}^{\theta_h} (s_{II} - I_1 \tan \xi) (\delta u) R d\theta \\
 &= \int_{\theta_0}^{\theta_h} R_0^2 (s_{II} - I_1 \tan \xi) \\
 &\times \exp[2(\theta - \theta_0)] \dot{\Omega} d\theta \quad (24) \\
 &= \int_{\theta_0}^{\theta_h} R_0^2 (s_{II} - I_1 \tan \xi) \\
 &\times \exp[2(\theta - \theta_0)] \dot{\Omega} \frac{d\theta}{d\theta} d\theta
 \end{aligned}$$

where the shear velocity is based on the global coordinates. The stresses are also transformed from the local coordinates to the global coordinates.

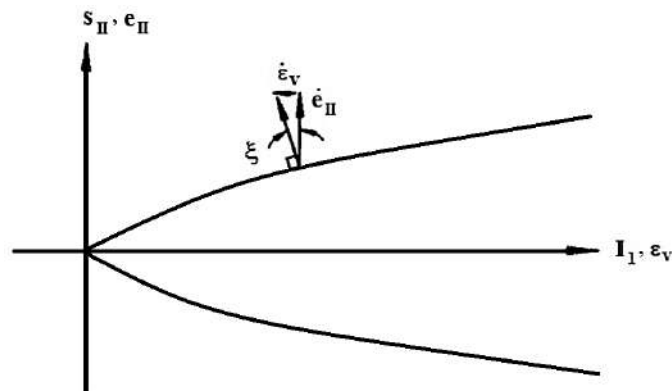


Fig. 4. CJS failure line in S_{II} - I_1 coordinates

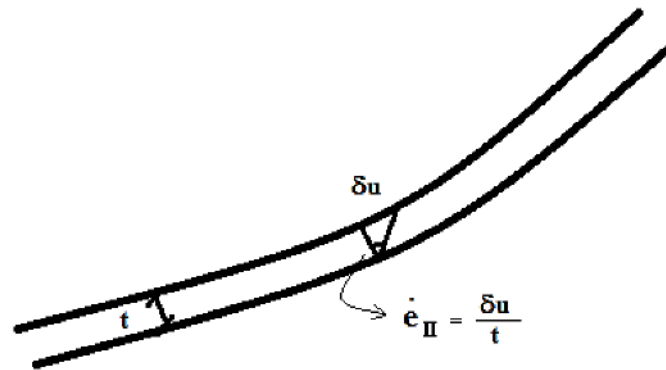


Fig. 5. Differential discontinuity in the slip surface

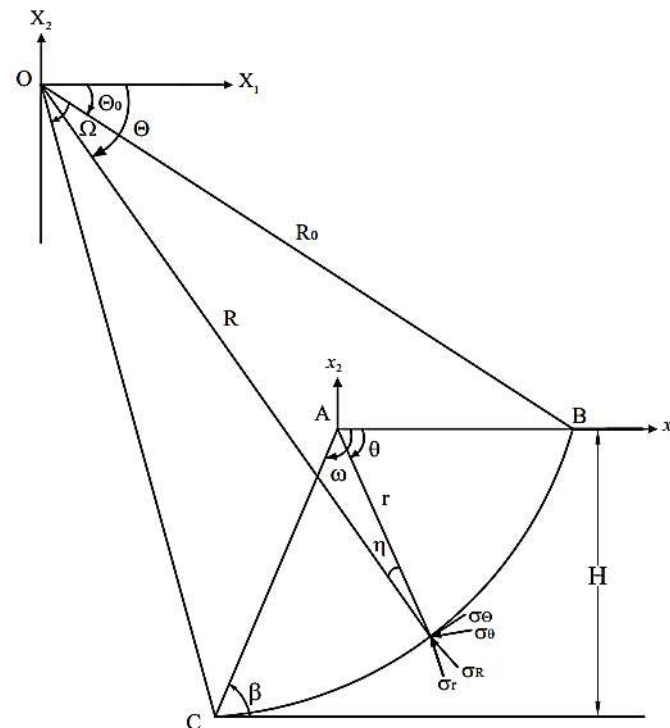


Fig. 6. Coordinate transformation and polar stress components applied at the failure state

6. The Ultimate Load

The rate of external work due to the weight of the failure wedge can be obtained from Eq. (25). In this equation, the functions f_1 , f_2 , and f_3 are defined in Appendix A.1 (Eqs. (A1-1 and A1-2)) (Chen, 1975). The rate of work done by the uniform surcharge adjacent to the slope is obtained from Eq. (26) by multiplying the moment of surcharge by the rotational velocity.

$$\dot{W} = \gamma R_0^3 \dot{\Omega} (f_1 - f_2 - f_3) \quad (25)$$

$$\dot{Q} = qL \left(R_0 \cos \theta_0 - \frac{L}{2} \right) \dot{\Omega} \quad (26)$$

At the onset of failure, the dissipated

internal energy is equal to the rate of external work. By minimizing the virtual work equation, the ultimate uniform load, q , is obtained. It has to be noted that the rate of external work done by surcharge and dissipated energy is obtained based on the unknown, q .

$$\min \dot{D} - \dot{W} - \dot{Q} \text{ on } (\theta_0, \theta_h, q) \quad (27)$$

The virtual work equation is subjected to unconstrained nonlinear optimization. For this purpose, numerical methods such as `fminsearch` or `fminunc` optimization in the MATLAB program or repetitive loops on the θ_0 , θ_h angle, and surcharge can be used. Therefore, by writing codes in MATLAB

programming language, the minimum ultimate uniform load can be obtained.

7. Results of the Proposed Formulation

In order to analyze the formulation and extract the uniform load, a 4 m slope with geotechnical properties listed in Table 1 was assumed. The values of R_{mi} and $R_{critical}$ were identified regarding internal friction angles at peak and critical states based on the relationships presented in the Appendix. It should be noted that, for simplicity in the optimization process, p_c was fixed as a constant parameter of p_{c0} .

In the presented formulation, an infinite uniform surcharge was considered. So, the length of the failure surface on the ground was not predefined. This length can be deduced as one result of optimization of Eq. (27). Table 2 shows different values of the length of failure surface, start and end angles around the center of rotation, and ultimate load on different slopes for nonlinear CJS method and variable R_m .

The nonlinear dependence of the failure state of soils on confining pressure has been well introduced in the formulation of the CJS failure criterion, so increasing confining pressure leads to a decrease in the rate of shear strength augmentation. Figure 7 shows the variations of the ultimate load in terms of slope angle for different maximum surface failure radii. In this analysis, the nonlinear CJS method has been used and, with the constant parameters in Table 1, the maximum failure radius has been changed. As can be observed in this figure, as the failure surface radius is increased, the ultimate load is also increased for all values of slope angles. Besides, for a given failure surface radius, while the slope angle is increased, the ultimate load is augmented. The rate of decrease in the ultimate load due to an increase in slope angle augments with an increase in the failure surface radius.

In order to study the effect of confining pressure on ultimate load, a constant mean radius of the failure surface equal to its

maximum value, R_{mi} , was assumed and the results were compared with the case in which the radius is variable. As can be observed in Figure 8, for the fixed radius, the ultimate load is always greater than when the variable radius is used. For the slope angle equal to 30 degrees, a smaller difference in results is observed. The analysis with constant R_m is related to the upper bound solution in which shear strength varies as a linear function of stress level. It should be noted that the majority of existing works concerning the upper bound solution of slope stability have used Mohr-Coulomb or Drocker-Prager criteria. The results of the analysis with constant R_m presented in Figure 8 are similar to the upper bound solution of surcharged slopes stability based on the Drocker-Prager criterion because parameter γ in the CJS criterion is assumed to be zero.

Figure 9 shows variations of the ultimate load versus the initial critical state stress for different slope angles. This parameter is related to the initial density of granular soil. The large values of initial critical state pressure correspond to the high values of relative density. By increasing the initial critical state stress, p_{c0} , the ultimate load has been increased. According to Figure 9, the maximum difference between the ultimate loads for the initial critical stresses of 200 and 2000 kPa is about 160 kPa on a slope of 30 degrees.

Variations of the ultimate load versus soil unit weight for different slope angles are shown in Figure 10. By increasing the soil unit weight, the ultimate load is increased. The rate of decrease in the ultimate load by increasing slope angle is maximum in the unit weight, $\gamma = 20 \text{ kN/m}^3$ compared to other conditions. By increasing the unit weight, the stresses and the effect of confining stress have increased.

In the following, the results of the proposed method are compared with the equilibrium method of GeoSlope software (2007). The GeoSlope software is a subset of the GeoStudio software and the slope stability analysis in this program is

performed by studying the equilibrium of the vertical slices of the soil mass. In this regard, various methods of slices including the Ordinary method of the slice, Bishop's method, Janbu's generalized method, and Morgenstern-Price method are used.

The factor of safety of a slope is defined as the ratio of the available shear strength of the soil to the minimum shear strength required to maintain stability. In the GeoSlope software, the shear strength of soils for effective stress analysis is governed by the Coulomb failure criterion. The proposed formulation is in the limit state and in this case, the factor of safety is equal to one.

In Figure 11, the performed model in the GeoSlope software is shown. The slope has, a height of 4 m and an angle of 30° . Besides, a specific weight of 18 kN/m^3 , internal friction angle of 37° , and zero cohesion was considered. The intensity of the surcharge in this figure is equivalent to the ultimate load extracted from the proposed formulation in Table 2. In this figure, the critical failure wedge and the center of its rotation are shown for the Morgenstern-

Price method. The factor of safety in the Morgenstern-Price method is 0.946.

Figure 12 shows the comparison between the factors of safety in various methods. The values obtained from the proposed method with the CJS failure criterion are among the values obtained from the various methods of slices based on the Mohr-Coulomb failure criterion. The results of different slices methods at a 30° slope are always less than the ultimate load value of the proposed method. However, with the decrease of the slope, the amount of ultimate load resulting from the different methods of slices has increased. At 20° slope angle, the results of the Ordinary method and Janbu's generalized method are lower than the proposed method and the results of Bishop's method and Morgenstern-Price method are more than the proposed method. At 10° slope angle, the results of slices methods are always more than the proposed method. The factor of safety at 10° slope angle in the Ordinary method is 1.005 which is very close to the results obtained from the proposed method.

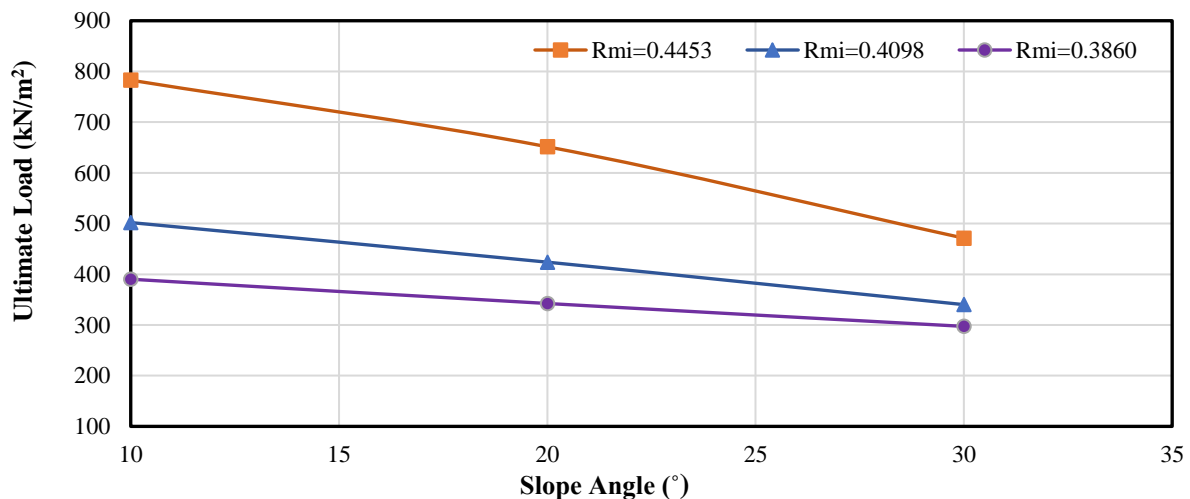


Fig. 7. Variations of the ultimate load versus angle of slope in different failure surface radii

Table 1. Geotechnical properties of slope material

| P_{c0} (kPa) | $R_{critical}$ | R_{mi} | $\phi_{critical}$ (°) | ϕ_{peak} (°) | ν | γ (kN/m ³) |
|----------------|----------------|----------|-----------------------|-------------------|-------|-------------------------------|
| 1000 | 0.3503 | 0.4098 | 32 | 37 | 0.35 | 18 |

Table 2. Optimization results obtained from the suggested method

| q_u (kPa) | L (m) | L/H | θ_h (°) | θ_0 (°) | H (m) | β (°) |
|-------------|-------|-------|----------------|----------------|-------|-------------|
| 501.93 | 1.05 | 0.262 | 155.6 | 77.6 | 4 | 10 |
| 423.88 | 1.51 | 0.433 | 145.5 | 74.3 | 4 | 20 |
| 340.08 | 2.43 | 0.607 | 138.8 | 71.9 | 4 | 30 |

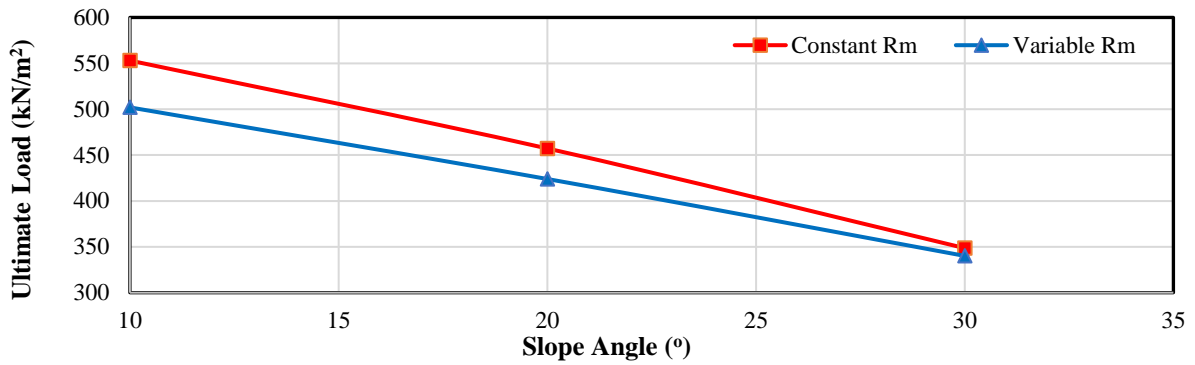


Fig. 8. Comparison between the ultimate load in fixed and variable failure surface radius

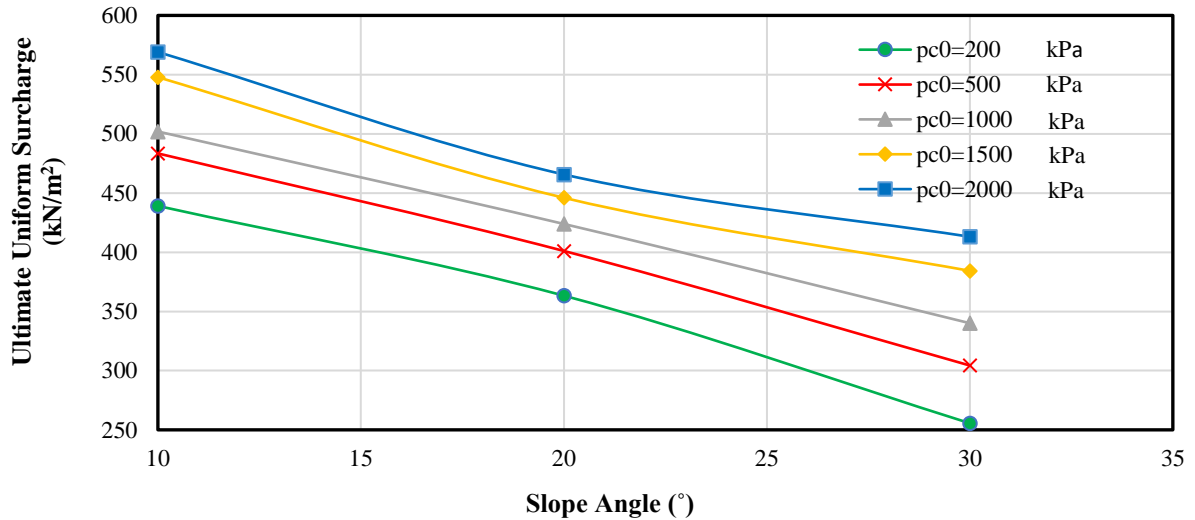


Fig. 9. Effect of initial critical state stress on the ultimate load in terms of slope angle

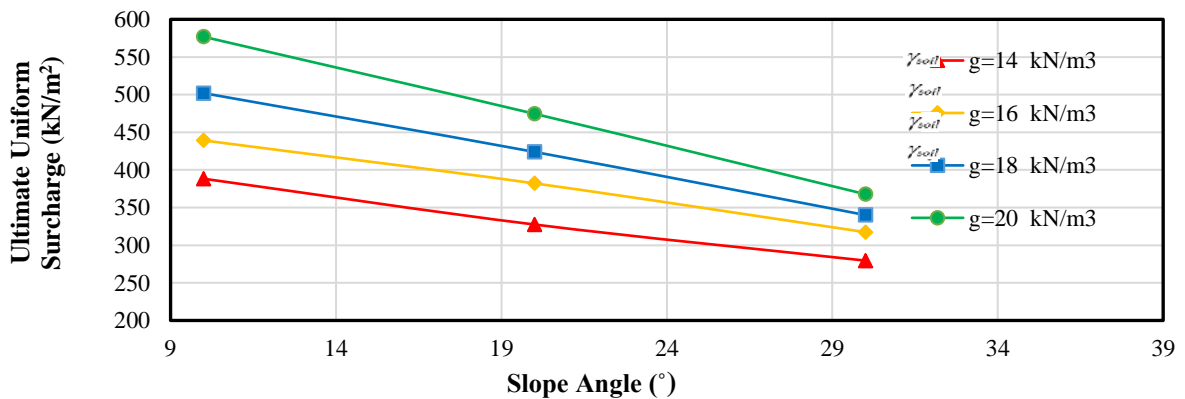


Fig. 10. Variations of the ultimate load versus angle of slope in different unit weights

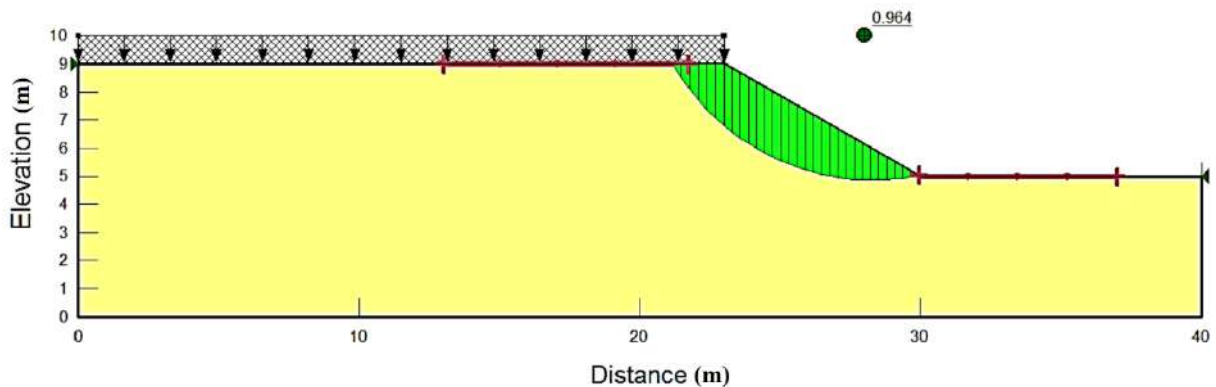


Fig. 11. Critical failure wedge and factor of safety in the GeoSlope software

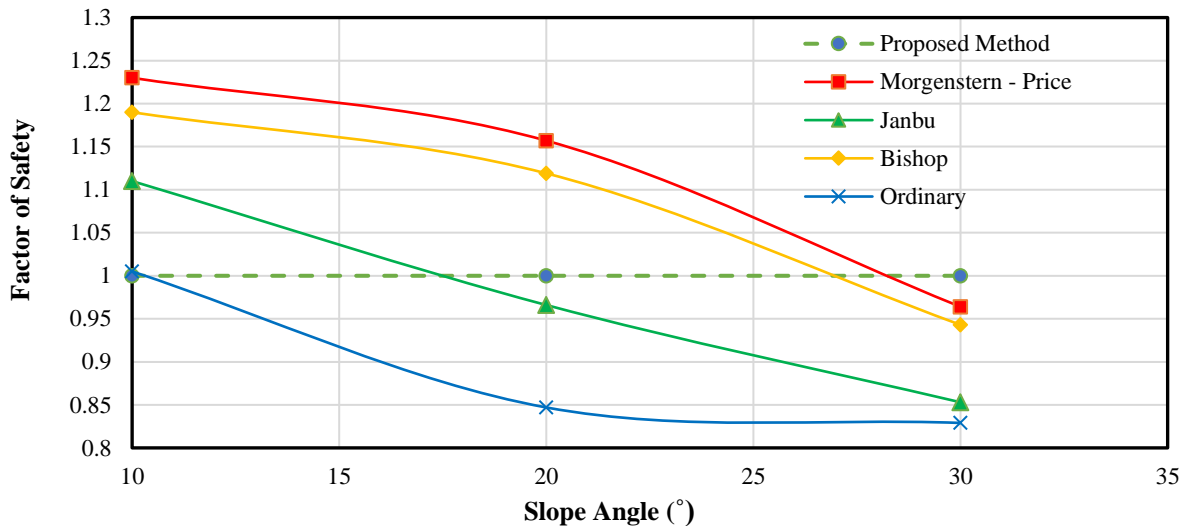


Fig. 12. Comparison between the results of the present study with those of the slices methods

8. Conclusions

In this paper using a continuous failure criterion as a nonlinear function of confining stress and soil density, formulation of the upper bound limit analysis method for estimating the ultimate uniform load adjacent to a slope was presented. In order to estimate the rate of dissipated internal energy, the stress field along the slip surface was determined in polar coordinates based on the Airy stress function.

Taking into account the nonlinear effect of confining pressure in the analyses, led to a decrease in the ultimate load. This reduction was more obvious in slopes with smaller angles. An increase in the radius of the soil failure criterion caused an increase in the ultimate load. This increase was more significant in slopes with lower angles.

With a set of failure state parameters, the ultimate load was affected by the change in soil initial density, so the increase of initial density led to a rise in the ultimate load. Using the presented failure criterion resulted in a more accurate estimation of the soil behavior.

The results of the proposed method were compared with different slices methods based on the Mohr-Coulomb failure criterion. The suggested limit analysis technique results in greater values for ultimate load at a 30° slope angle and

smaller values at a 10° slope angle compared to different methods of slices.

The analysis with a constant mean radius of the failure surface is related to the upper bound solution in which shear strength varies as a linear function of stress levels such as Mohr-Coulomb and Drockner-Prager criteria. A considerable difference was observed between the results of analyses with constant and variable mean radii of the failure surface.

9. References

- Aminpour, M.M., Maleki, M. and Ghanbari, A. (2017). "Investigation of the effect of surcharge on behavior of soil slopes", *Geomechanics and Engineering*, 13(4), 653-669, <https://doi.org/10.12989/gae.2017.13.4.653>.
- Aminpour, M.M., Maleki, M. and Ghanbari, A. (2018), "Predicting seismic permanent displacement of soil walls under surcharge based on limit analysis approach", *Earthquake Engineering and Engineering Vibration*, 17(4), 747-759, <https://doi.org/10.1007/s11803-018-0473-6>.
- Aminpour, M.M. and Maleki, M. (2022). "Finite Element limit analysis using nonlinear continuous failure criterion and non-associated flow rule and its application to estimating bearing capacity of strip footing on slope", *Geotechnical and Geological Engineering*, 40, 723-734.
- Baker, R. (2004). "Nonlinear Mohr envelopes based on triaxial data", *Journal Geotechnical and Geoenvironmental Engineering*, 130(5), 498-506, [https://doi.org/10.1061/\(ASCE\)1090-0241\(2004\)130:5\(498\)](https://doi.org/10.1061/(ASCE)1090-0241(2004)130:5(498)).

- Bathayian, M.H. and Maleki, M. (2018). "Adaptation of an existing constitutive model for describing mechanical behaviour of cemented granular soils", *Geomechanics and Geoengineering an International Journal*, 13(3), 184-197, <https://doi.org/10.1080/17486025.2018.1434243>.
- Cambou, B., Jafari, K. and Elamrani, K. (1989). "An elastoplastic model for granular material using three yielding mechanisms", Numerical Models in Geomechanics, NUMOG III, Proceedings of the 3rd International Symposium, Niagara Falls, Canada, (pp. 149-167).
- Chen, W.F. (1975). *Limit analysis and soil plasticity*, Elsevier Science, Amsterdam, Netherlands.
- Froutan Kalourazi, A., Izadi, A. and Jamshidi Chenari, R. (2019). "Seismic bearing capacity of shallow strip foundations in the vicinity of slopes using the lower bound finite element method", *Soils and Foundations*, 59(6), 1891-1905, <https://doi.org/10.1016/j.sandf.2019.08.014>.
- Guanhua, Q. (2023). "Stability analysis of nonhomogeneous and anisotropic stepped slopes under the influence of earthquakes", *Heliyon*, 9(4), e15057, <https://doi.org/10.1016/j.heliyon.2023.e15057>.
- Haghibin, M. and Ghazavi M. (2016). "Seismic bearing capacity of strip footings on pile-stabilized slopes", *Civil Engineering Infrastructure Journal*, 49(1), 111-126, [https://doi.org/10.1061/\(ASCE\)GM.1943-5622.0002530](https://doi.org/10.1061/(ASCE)GM.1943-5622.0002530).
- Hajiazizi, M., Kilanehei, P. and Kilanehei, F. (2018). "A new method for three-dimensional stability analysis of earth slopes", *Scientia Iranica*, 25(1), 129-139, <https://doi.org/10.24200/sci.2017.4173>.
- Hajiazizi, M., Mazaheri, A.R. and Orense, R.P. (2018). "An analytical approach to evaluate stability of pile-stabilized slope", *Scientia Iranica*, 25(5), 2525-2536, <https://doi.org/10.24200/sci.2017.4218>.
- Hajiazizi, M. and Nasiri, M. (2019). "Experimental and numerical investigation of reinforced sand slope using geogird encased stone column", *Civil Engineering Infrastructures Journal*, 52(1), 85-100, <https://doi.org/10.22059/cej.2019.253069.1468>.
- Hu, L., Takahashi, A. and Kasama, K. (2022). "Effect of spatial variability on stability and failure mechanisms of 3D slope using random limit equilibrium method", *Soils and Foundations*, 62(6), 101225, <https://doi.org/10.1016/j.sandf.2022.101225>.
- Komasi, M. and Beiranvand, B. (2021). "Seepage and stability analysis of the Eyvashan Earth Dam under drawdown conditions", *Civil Engineering Infrastructures Journal*, 54(2), 205-223, <https://doi.org/10.22059/cej.2020.293429.1634>.
- Liu, M.D. and Carter, J.P. (2003). "General strength criterion for geomaterials", *International Journal of Geomechanics*, 3(2), 253-259, [https://doi.org/10.1061/\(ASCE\)1532-3641\(2003\)3:2\(253\)](https://doi.org/10.1061/(ASCE)1532-3641(2003)3:2(253)).
- Maleki, M., Dubujet, Ph. and Cambou, B. (2000). "Modélisation Hierarchisée du comportement des sols", *Revue Francais de Genie Civil*, 4(7-8), 895-928, <https://doi.org/10.1080/12795119.2000.9692702>.
- Mirzazadeh, Z. and Hajiazizi, M. (2020). "Determination of creep-induced displacement of soil slopes based on LEM", *Civil Engineering Infrastructures Journal*, 53(2), 341-358, <https://doi.org/10.22059/cej.2020.285244.1598>.
- Mofidi Rochi, J., Farzaneh, O. and Askari, F. (2014). "Bearing capacity of strip footings near slopes using lower bound limit analysis", *Civil Engineering Infrastructures Journal*, 47(1), 89-109, <https://doi.org/10.7508/CEIJ.2014.01.007>.
- Qin, C. and Chian, S.C. (2017). "Kinematic stability of a two-stage slope in layered soils", *International Journal of Geomechanics*, 17(9), [https://doi.org/10.1061/\(ASCE\)GM.1943-5622.0000928](https://doi.org/10.1061/(ASCE)GM.1943-5622.0000928).
- Qin, C. and Chian, S.C. (2018). "Bearing capacity analysis of a saturated non-uniform soil slope with discretization-based kinematic analysis", *Computers and Geotechnics*, 96, 246-257, <https://doi.org/10.1016/j.compgeo.2017.11.003>.
- Razali, I.H., Taib, A.M., Rahman, N.A., Abang Hasbollah, D.Z., Mohd Firdaus Md Dan, M.F., Ramli, A.B. and Ibrahim, A. (2023). "Slope stability analysis of riverbank in Malaysia with the effects of vegetation", *Physics and Chemistry of the Earth, Parts A/B/C*, 129, 103334, <https://doi.org/10.1016/j.pce.2022.103334>.
- Sadd, M.H. (2009). *Elasticity: Theory, applications and numerics*, 2nd Edition, Elsevier, Academic Press, Burlington, MA, USA, Oxford, UK.
- Shukla, R.P. and Jakka R.S. (2018). "Critical setback distance for a footing resting on slopes under seismic loading", *Geomechanics and Engineering*, 15(6), 1193-1205, <https://doi.org/10.12989/gae.2018.15.6.1193>.
- Sun, Y. and Song, E. (2016). "Active earth pressure analysis based on normal stress distribution function along failure surface in soil obeying nonlinear failure criterion", *Acta Geotechnica*, 11(2), 255-268, <https://doi.org/10.1007/s11440-015-0390-z>.
- Tang, G., Zhao, L., Li, L. and Yang, F. (2015). "Stability charts of slopes under typical conditions developed by upper bound limit analysis", *Computers and Geotechnics*, 65, 233-240, <https://doi.org/10.1016/j.compgeo.2014.12.008>.
- Thomas, J., Gupta, M. and Prusty, G. (2023). "Assessing global parameters of slope stability

- model using Earth data observations for forecasting rainfall, Induced shallow landslides”, *Journal of Applied Geophysics*, 212, 104994, <https://doi.org/10.1016/j.jappgeo.2023.104994>.
- Tozato, K.J., Dolojan, N.L., Touge, Y., Kure, S., Moriguchi, S., Kawagoe, S., Kazama, S. and Terada, K. (2022). “Limit equilibrium method-based 3D slope stability analysis for wide area considering influence of rainfall”, *Engineering Geology*, 308, 106808, <https://doi.org/10.1016/j.enggeo.2022.106808>.
- Tran, A.T.P., Kim, A.R. and Cho, G.C. (2019). “Numerical modeling on the stability of slope with foundation during rainfall”, *Geomechanics and Engineering*, 17(1), 109-118, <https://doi.org/10.12989/gae.2019.17.1.109>.
- Vo, T. and Russell, A.R. (2017). “Stability charts for curvilinear slopes in unsaturated soils”, *Soils and Foundations*, 57(4), 543-556, <https://doi.org/10.1016/j.sandf.2017.06.005>.
- Wu, S., Zhang, S., Guo, C. and Xiong, L. (2017). “A generalized nonlinear failure criterion for frictional materials”, *Acta Geotechnica*, 12(6), 1353-1371, <https://doi.org/10.1007/s11440-017-0532-6>.
- Zhou, H., Zheng, G., Yin, X., Jia, R. and Yang, X. (2018). “The bearing capacity and failure mechanism of a vertically loaded strip footing placed on the top of slopes”, *Computers and Geotechnics*, 94, 12-21, <https://doi.org/10.1016/j.compgeo.2017.08.009>.
- Zhou, J. and Qin, C. (2023). “Influence of soft band on seismic slope stability by finite-element limit-analysis modelling”, *Computers and Geotechnics*, 158, 105396.

A. Appendix

A.1. Determination of Coefficients f_1 , f_2 and f_3

The coefficients f_1 , f_2 , and f_3 are the rate of external work done in log spiral OBC and two OAB and OAC triangles in Figure 6, respectively (Chen, 1975). These coefficients can be written as the following equations. Also, according to the geometry shown in Figure 6, the parameters L and R_0 can be expressed based on θ_h and θ_0 (Chen, 1975).

$$f_1(\theta_0, \theta_h) = \frac{1}{30} ((3 \cos \theta_h + \sin \theta_h) \times \exp[3(\theta_h - \theta_0)] - 3 \cos \theta_0 - \sin \theta_0)$$

$$f_2(\theta_0, \theta_h) = \frac{1}{6} \frac{L}{R_0} \left(2 \cos \theta_0 - \frac{L}{R_0} \right) \sin \theta_0$$

$$f_3 = \frac{1}{6} \exp(\theta_h - \theta_0) \quad (\text{A1-1})$$

$$\times \left(\sin(\theta_h - \theta_0) - \frac{L}{R_0} \sin \theta_h \right) \times \left(\cos \theta_0 - \frac{L}{R_0} + \cos \theta_h \exp(\theta_h - \theta_0) \right)$$

$$\frac{L}{R_0} = \frac{1}{\sin \theta_h} \left[\sin(\theta_h - \theta_0) - \frac{H \sin(\beta + \theta_h)}{R_0 \sin \beta} \right] \quad (\text{A1-2})$$

$$\frac{H}{R_0} = \sin \theta_h \exp(\theta_h - \theta_0) - \sin \theta_0$$

A.2. Relation between Failure Surface Radius and Soil Internal Friction Angle

By intersecting the two MC and CJS failure criteria, the following relationships exist between the maximum and critical state failure surfaces radii and the internal friction angle of the soil at peak and critical states (Maleki et al., 2000).

$$R_{mi} = 2 \sqrt{\frac{2}{3} \frac{\sin \varphi_{peak}}{3 - \sin \varphi_{peak}}} \quad (\text{A2-1})$$

$$R_{critical} = 2 \sqrt{\frac{2}{3} \frac{\sin \varphi_{critical}}{3 - \sin \varphi_{critical}}} \quad (\text{A2-2})$$



This article is an open-access article distributed under the terms and conditions of the Creative Commons Attribution (CC-BY) license.



Determination of DBTT of Functionally Graded Steels Using Artificial Intelligence

Anjali, K.^{1*}, Yesilyurt, S.N.², Samui, P.³, Dalkilic, H.Y.⁴ and Katipoglu, O.M.⁵

¹ Ph.D. Candidate, Research Scholar, School of Water Resources, Indian Institute of Technology, Kharagpur, India.

² Ph.D. Candidate, Graduate School of Natural and Applied Sciences, Department of Civil Engineering, Dokuz Eylul University, Izmir, Turkey.

³ Associate Professor, Department of Civil Engineering, National Institute of Technology, Patna, India.

⁴ Associate Professor, Department of Civil Engineering, Erzincan Binali Yildirim University, Erzincan, Turkey.

⁵ Professor, Department of Civil Engineering, Erzincan Binali Yildirim University, Erzincan, Turkey.

© University of Tehran 2023

Received: 08 Jan. 2023;

Revised: 22 Jun. 2023;

Accepted: 03 Jul. 2023

ABSTRACT: This study applied three Artificial Intelligence (AI) models to project the Ductile to the Brittle Transition Temperature (DBTT) of Functionally Graded Steels (FGS). These prediction models are Minimax Probability Machine Regression (MPMR) model, Genetic Programming (GP), and Emotional Neural Network (ENN) algorithms with strong prediction performance. The data of FGS type, crack tip configuration, the thickness of the graded ferritic zone, the thickness of the graded austenitic region, the distance of the notch from the Bainite or Martensite intermediate layer, and temperature were used as inputs in the establishment of the AI models. Charpy impact test (CVN) values obtained from experiments used as output. The datasets have been divided into two groups: one for training and another for testing. The performance of the established AI models was evaluated through 16 statistical indicators and graphically used regression error characteristics, an area over the curve, Taylor diagrams, and scatter plots. As a result, the GP model showed superior prediction performance to other models. The primary objective of this study was to decrease the parameter count while also facilitating model comparisons. In this way, in areas with complex studies such as civil engineering; it allows the work to be completed more practically.

Keywords: Artificial Intelligence, ENN, Genetic Programming, Minimax Probability Machine Regression, Taylor Diagram.

1. Introduction

Depending upon the composition and microstructure of steel, such as grain size,

phase fractions, etc., the mechanical properties' mechanisms are highly complex. Recent Studies throw light on establishing a data-driven technique-based mechanical

* Corresponding author E-mail: kanjali19feb@kgpian.iitkgp.ac.in

property prediction model (Kumar et al., 2022; Hoang and Tran, 2023). A mechanical property prediction model is advantageous to guide the procedure design of steel at least cost in a shorter production cycle. Insufficient understanding of the physical principles governing effective mechanical properties hinders the development of a first-principle-based physical model. Consequently, models propelled by data, such as Artificial Intelligence models, are more preferable (Dastorani et al., 2018; Ziggah et al., 2022; Al Adwan et al., 2023). This paper describes research aimed at devising a reliable prediction model for predicting the DBTT of FGS. Determining the DBTT of steel is essential in manufacturing engineering and structural applications (Bae et al., 2023). Researchers generally use the Charpy impact test, alternatively referred to as the Charpy V-Notch test (CVN), to predict the DBTT of steel (Dubey et al., 2023; Switzner et al., 2023). The experimental methods always give some limitations. Hence, The CVN does not provide a reliable result.

Therefore, alternative methods are required to determine the DBTT of steel. Nazari et al. (2011) applied Artificial Neural Network (ANN) to find out the DBTT of the steel. ANN gave encouraging and comparatively better performance. However, ANN has several drawbacks, such as low generalization capability, overtraining, a black-box approach, etc. (Park and Rilett, 1999; Kecman, 2001; Kovalev, 2021). This article employs the following three Artificial Intelligence (AI) techniques for determining the DBTT of steel. It adopts widely used AI techniques such as Minimax Probability Machine Regression (MPMR), Emotional Neural Network (ENN), and Genetic Programming (GP) to determine the DBTT of steel.

Thanks to the developing AI technology, experimental studies and predictions made in many engineering fields in recent years have been more accurate, and their reliability has increased. AI techniques are

closed-box models used for prediction and verification and have been used to solve many problems in the literature (Vouros, 2022; Alyousef et al., 2023). Methods such as MPMR, GA, and ENN, which are the subject of this study, have an essential place in the literature of their superior performance. MPMR model is constructed by Lanckriet et al. (2001) and it gives the bound over future prediction. There are many implementations of MPMR in literature (Deng et al., 2018; Bonakdari et al., 2019; Kar et al., 2023). Koza (1992) is credited with the development of GP, which is founded on the fundamental concept of Genetic Algorithms (GA) and functions by manipulating parse trees. GP model exhibited good performance for solving various problems (Koshiyama et al., 2015; Papa et al., 2017; Lin et al., 2018; Astarabadi and Ebadzadeh, 2019). The ENN model is built on top of the Emotional Back Propagation (EBP), which is an innovative training algorithm that incorporates emotional cues and weights to enhance individuals' learning processes and decision-making abilities (Kumar et al., 2021). Recently, there has been extensive research into the incorporation of emotions into machine learning (Babaie et al., 2008; Khashman, 2008, 2009; Biswas et al., 2019). AI models have been created based on the database compiled from the research conducted by Nazari et al. (2011) as shown in Table 1. The dataset comprises of 140 experimental results of the CVN.

This study aims to evaluate the prediction potential of experimentally obtained CVN values with GP, MPMR, and ENN algorithms. To achieve this objective, three AI algorithms are employed to analyze data encompassing FGS type, crack configuration, graded ferritic zone thickness, graded austenitic region thickness, notch-to-intermediate layer distance, and temperature parameters, ultimately yielding CVN values. Estimated and experimentally obtained CVN values are compared with 16 different statistical indicators, and Regression Error

Characteristic (REC), Area Over Curve (AOC), and Taylor diagrams, and the most successful model are decided.

2. Materials and Methods

This study estimates CVN values of FGS using various experimental parameters. Figure 1 illustrates the graphs employed to depict the interrelationships among the data sets. Key statistical measures were examined, such as mean, standard deviation, distortion and kurtosis to assess the central tendency, spread, and shape of the data to ensure a comprehensive understanding of its properties and distribution characteristics. In addition, the experimental data used in this work are shown in Table A1.

2.1. Comprehensive Overview of MPMR Model

The foundation of the MPMR model lies in the Minimax Probability Machine Classification algorithm (MPMC). It builds a regression function using the Mercer Kernel, establishing a direct boundary ($\pm\varepsilon$) on the minimum probability and maximizing it (Lanckriet et al., 2001). The

MPMR model does not rely on assumptions about the distribution of data, which can result in reduced validity and generality.

The prominent characteristic of the MPMR model is the regression function provides a low limit to the probability. An unspecified regression function $g : R^n \rightarrow R$ is employed to generate the training data from the data set $(u_i, v_i); i = 1, 2, \dots, n$. The interrelationship between u_i and v_i is outlined as Eq. (1).

$$v_i = g(u_i) + \delta_i \quad (1)$$

where δ_i : indicates the error such that $E[\delta] = 0, Var[\delta] = \sigma\delta^2$.

The primary objective of MPMR is to maximize the minimum probability under the error $\pm\varepsilon$ constraint.

The calculation of the bound on minimum probability (Ω) is given by Eqs. (2-3).

$$\hat{v} = \hat{g}(u) \quad (2)$$

$$\Omega = \inf P_r \{ |\hat{v} - v| \leq \varepsilon \} \quad (3)$$

Much like the kernel formulation for the MPMC, the MPMR formulation is depicted as Eq. (4).

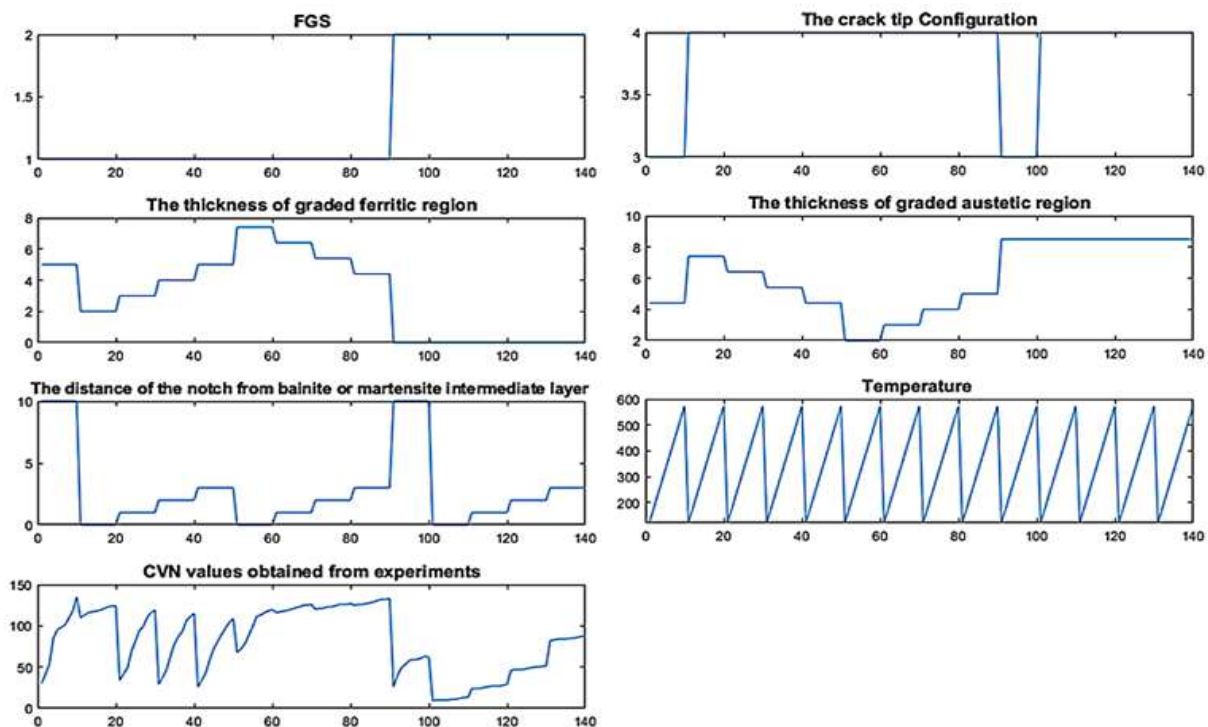


Fig. 1. Change graphs of the data used in the study

$$\hat{v} = \hat{g}(u) = \sum_{i=1}^N \beta_i K(u_i, u) + b \quad (4)$$

where $K(u_i, u) = \varphi(u_i) \cdot \varphi(u)$ is Mercer's Kernel, u_i : denotes the training data whereas $\beta_i, b \in \mathbb{R}$ indicated the result of the MPMR algorithm. W : is the weight and b : is the bias.

For the development of the MPMR model, the dataset was split into two segments: one for training and the other for testing. Thus, this eliminates the generalization and memorization problems of the model. Also, Radial basis function was employed as a kernel function for the development of the MPMR model. The training dataset is used to learn the MPMR model. This study employs 98 datasets as the training dataset. To evaluate the conduct of the MPMR model, the test data was normalized within the range of 0 to 1. Eq. (5) was used for normalization.

$$X_{norm} = \frac{X_{act} - X_{min}}{X_{max} - X_{min}} \quad (5)$$

where X_{norm} : is the normalized value, X_{act} : is the actual value, X_{min} : is the minimum value, and X_{max} : is the maximum value.

2.2. Comprehensive Overview of ENN Model

The ENN model is the neural network that has been developed based on emotions in order to enhance decision-making and learning capabilities. Although it is not anticipated that machines will feel emotions and respond emotionally, regulatory signals and informational signals do progress within the ENN model. Emotions may be imitated in machines analogous to machine intelligence. This enhances the model's ease of use, swift learning and immediate response. This model is based on EBP and takes into account things like self-esteem, stress levels, and anxiety, also emotional weights in the cerebral emotional neurons. The neural network contains a multitude of hormone-producing glands that release

virtual hormones, subsequently influencing the functioning of specific nodes within the neural system (Babaie et al., 2008).

An ENN is composed of three layers according to the course of information: the input layer, the hidden layer, and the output layer. The input, hidden, and output layers each consists i, j , and h neurons. Here, X_i and Y_i : denote input and output values of i neurons, respectively, in a way that $X_i = Y_i$. Input and output estimates of the hidden neurons are designated by X_h and Y_h , respectively, and are interconnected by Eq. (6). Input and output which estimates of output neurons are designated by X_j and Y_j , respectively, and are interconnected by Eq. (7).

$$Y_h = \frac{1}{1 - \exp(-X_h)} \quad (6)$$

$$Y_j = \frac{1}{1 + \exp(-X_j)} \quad (7)$$

The ENN model employs the same training data set, testing data set, input, output, and standardization approach as the MPMR model does.

2.3. Comprehensive Overview of GP Model

GP is an AI-based method used to formulate experimental studies with multivariate parameters for which analytical models are unavailable (Cevik and Sonebi, 2008). GP imitates the biological advancement of living creatures and creates a computer model of functions and terminals known as chromosomes (Kohestani et al., 2017)

There are 5 stages involved in GP model to lead to the solution as follows:

- Stage 1: A population of randomly generated programs is created.
- Stage 2: The programs with higher fitness/better accuracy concerning the output are chosen using any methods such as Roulette Wheel Selection, Tournament, Ranking, etc.
- Stage 3: Two selected winner programs are copied onto the next generation by

exchanging parts to generate cross overs and then randomly changing the winner programs. Only similar parts of the programs can be replaced.

- Stage 4: The programs that relatively lose/have higher error are replaced by the transformed winner programs obtained in Stage 3.
- Stage 5: Stages 2 to 4 are repeated until the consecutive error values do not have an appreciable reduction in them, i.e., many generations rise till the convergence of predicted value and the actual output leads to a satisfactory limit. The GP model utilizes identical training

and testing datasets, input features, output variables, and normalization techniques as those employed by the MPMR and ENN models.

2.4. Performance Indicators

This study utilized a vast array of statistical indicators to assess the efficacy of Artificial Intelligence models employed. The success of the model was made according to the most appropriate values of the estimation criteria obtained during the training and testing stages. Table 1 displays the equations of the parameters used in model selection.

Table 1. Statistical parameters

| Statistical parameter | Equation |
|--|---|
| Nash-Sutcliffe Efficiency (NS) | $NS = 1 - \frac{\sum_{i=1}^n (d_i - y_i)^2}{\sum_{i=1}^n (d_i - d_{mean})^2}; -\infty < NS \leq 1$ (8) |
| Variance Account Factor (VAF) | $VAF = \left(1 - \frac{\text{var}(d_i - y_i)}{\text{var}(d_i)}\right) \times 100$ (9) |
| Coefficient of Determination (R^2) | $R^2 = \frac{\sum_{i=1}^n (d_i - d_{mean})^2 - \sum_{i=1}^n (d_i - y_i)^2}{\sum_{i=1}^n (d_i - d_{mean})^2}$ (10) |
| Adjusted Determination Coefficient (Adj. R^2) | $AdjR^2 = 1 - \frac{(n-1)}{(n-p-1)}(1-R^2)$ (11) |
| Performance Index (PI) | $PI = adj \cdot R^2 + 0.01VAF - RMSE$ (12) |
| Bias Factor | $Bias\ Factor = \frac{1}{N} \sum_{i=1}^n \frac{y_i}{d_i}$ (13) |
| Normalized Mean Bias Error (NMBE) | $NMBE(\%) = \frac{\frac{1}{N} \sum_{i=1}^n (y_i - d_i)}{\frac{1}{N} \sum_{i=1}^n d_i} \times 100$ (14) |
| Mean Absolute Percentage Error (MAPE) | $MAPE = \frac{1}{N} \sum_{i=1}^n \left \frac{d_i - y_i}{d_i} \right $ (15) |
| Relative Percent Difference (RPD) | $RPD = \frac{SD}{RMSE}$ (16) |
| Willmott's Index of agreement (WI) | $WI = 1 - \left[\frac{SD}{\sum_{i=1}^N (y_i - d_{mean} + d_i - d_{mean})^2} \right]$ (17) |
| Mean Absolute Error (MAE) | $0 < WI \leq 1$ $MAE = \frac{1}{N} \sum_{i=1}^n y_i - d_i $ (18) |
| Mean Bias Error (MBE) | $MBE = \frac{1}{N} \sum_{i=1}^n (y_i - d_i)$ (19) |
| Legate and McCabe's Index (LMI) | $LMI = 1 - \left[\frac{\sum_{i=1}^N d_i - y_i }{\sum_{i=1}^N d_i - d_{mean} } \right], 0 < LMI \leq 1$ (20) |
| Expanded Uncertainty (U_{95}) | $U_{95} = 1.96(SD^2 + RMSE^2)^{1/2}$ (21) |
| t-statistic (t-stat) | $t\text{-stat} = \sqrt{\frac{(N-1)MBE^2}{RMSE^2 - MBE^2}}$ (22) |
| Global Performance Indicator (GPI) | $GPI = MBE \times RMSE \times U_{95} \times t_{stat} \times (1 - R^2)$ (23) |

In Table 1, d : is the observed value and y : is the predicted value, d_i and y_i are the the observed and predicted i^{th} value, d_{mean} : is the mean of observed, R^2 : is the coefficient of determination, n : is the number data samples and p : is the model input quantity which is equal to 3, $RMSE$: is the Root mean Square Error, VAF : is the Variance Account Factor. In determining the best model, especially the models with the lowest error and high R^2 and Willmott's Index of agreement (WI) values were taken into account. Comparing sixteen parameters and streamlining the parameter selection process is one of the primary objectives of this study. Thus, the absence of conflict between these parameters is essential and indicates that the two conflicting parameters cannot be substituted for one another. In essence, the study has concluded that parameters yielding comparable results to all sixteen parameters can be employed. This approach enables achieving similar outcomes in a more straightforward manner, avoiding the complexity associated with the original set of parameters.

2.5. Taylor Diagrams

Taylor Diagrams (Taylor, 2001) is a diagram of the interrelationship between predicted and observed values. It facilitates statistical comparison of different models by plotting the normal deviation of simulated values versus observed values; the correlation coefficient between observed values and simulated values; and the averaged mean square difference. Taylor diagram provides a systematic and mathematical way of demonstrating goodness of fit measures. Following Ee. (24) is the underlying mathematical relationship of Taylor diagram.

$$E = \sigma_o^2 + \sigma_s^2 - 2\sigma_o\sigma_s\rho \quad (24)$$

where E : is the averaged mean square difference, σ_o : is the normal deviation of observed values, σ_s : is the normal deviation of simulated values, and ρ : is the correlation coefficient.

2.6. Rank Analysis

When performing rank analysis, each performance parameter is assigned a rank. In models where multiple statistical indicators are combined, it is difficult to determine the best model. Therefore, rank values of statistical indicators were calculated separately in this work, and the most efficient model was marked based on the total rank value. In this study, rankings ranged from a maximum of three models to a minimum of one. The model with the greatest performance is given the third position, and the model with the worst functionality takes up the first position. The model ranked the highest in total score represents the best performance, whereas the model ranked lowest indicates the poorest performance (Zhang et al., 2020).

3. Results and Discussion

In present study, it is aimed to estimate experimental CVN values with GP, MPMR, ENN models and to compare model performances based on statistical parameters. For this purpose, many experimental results are presented to AI algorithms and an equation is proposed to determine CVN values.

The implementation of the MPMR model, GP and ENN algorithms for predicting the DBTT of FGS was accomplished using MATLAB, a powerful numerical computing software which offers a comprehensive environment for implementing and experimenting with various AI models. Depending on factors such as the specific requirements of the project, familiarity of the researchers, and availability of suitable libraries and tools, the choice of software was made. It provides extensive libraries and toolboxes for machine learning and optimization, enabling the implementation of MPMR, GP and ENN algorithms for DBTT prediction.

Figure 2 shows the correlation coefficients connecting inputs and outputs used in the setup of AI models. Accordingly, while there was a very high

positive correlation between CVN data and the thickness of graded ferritic region values, it was determined that there was a negative and very high relationship with FGS and the thickness of graded austenitic

region values.

Figure 3 shows the comprehensive evaluation of the algorithms with respect to various influence factors.

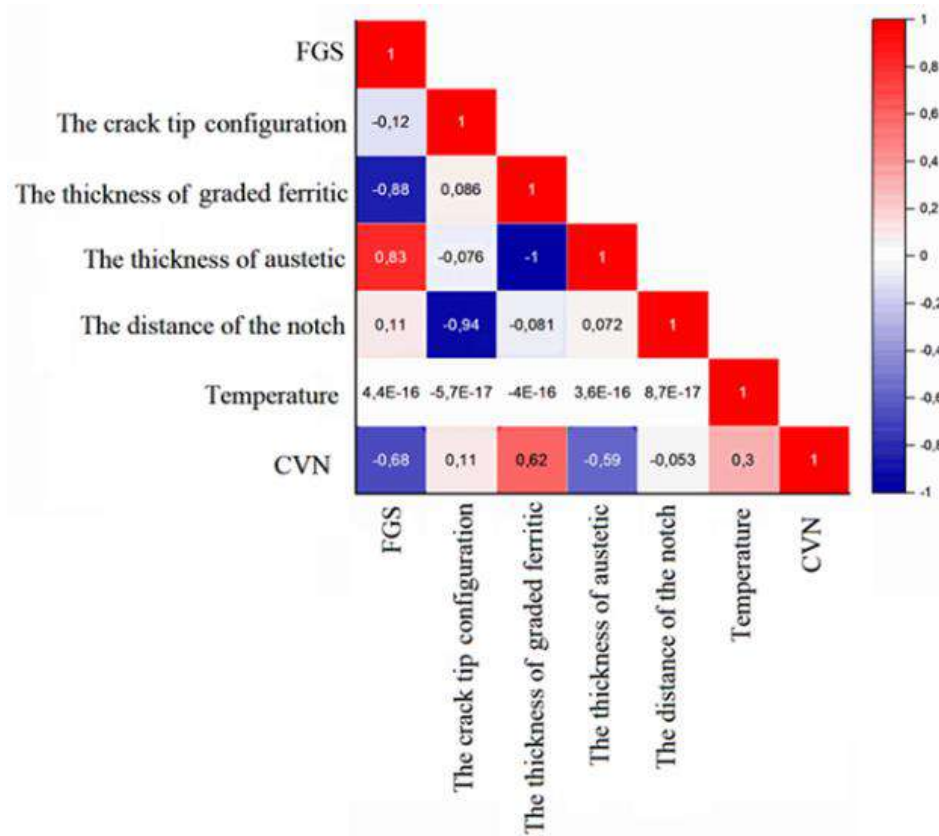


Fig. 2. Correlation matrix of the created models

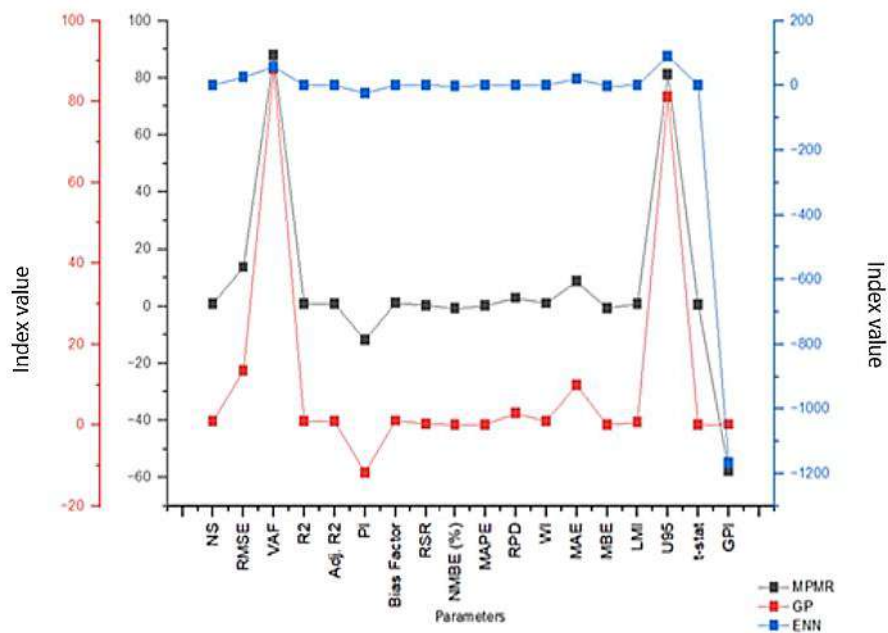


Fig. 3. Performance of different algorithm considering multiple influence factors

Figure 4 illustrates the effectuation of the training dataset. It has been clear from Figure 4 that the value of the correlation coefficient (R) is approximately one, and the predicted and actual values are scattered around the 45-degree linear line. Hence, the developed MPMR model gives good performance for the training dataset. The performance of the testing dataset has been depicted in Figure 5. The value of the R is approximately one and the predicted and actual values are scattered around the 45-degree linear line for the testing dataset also. Hence, the developed GP model has the ability to predict CVN value. In addition, Figures 4 and 5 illustrate the performance of ENN model as well. The R value is not near to one for training and testing dataset. Hence, the ENN model does not give a reliable result.

The developed GP model gives the best performance for the size of population = 800 and the size of generation = 400. The obtained results hold validity not only for the specific data set used in this study but also for data sets exhibiting similar characteristics. This suggests that the findings can be generalized to other datasets sharing comparable traits, enhancing the applicability and relevance of the study's conclusions. The performance of GP model has been shown in Figures 3 and 4. The value of R is close to one for training as well as testing dataset. Hence, the developed GP has successfully captured the relationship between inputs and output. The developed GP gives Eq. (25) for the prediction of CVN

value.

$$\begin{aligned}
 CVN = & 376.5 C^2 G^4 D^2 - 2.203(F \\
 & + 8.651)^2 \\
 & - 368.3 F^4 C^2 D^2 \\
 & - 639 A^4 G^4 \\
 & + 0.5171 \cos(CG) \quad (25) \\
 & + 0.5171 \sin(F + T) \\
 & + 39.7 A^2 G^2 \\
 & - 2.303 CA(A + D) \\
 & + 164.8
 \end{aligned}$$

where A : is the thickness of graded ferritic region, G : is the thickness of graded austenitic region, C : is the crack tip configuration, D is the distance of the notch from bainite or martensite intermediate layer and T : is temperature.

An attempt has been made for constructing REC of the developed models. Figure 6 displays the REC curves of the developed MPMR, GP and ENN models. Figure 7 shows the bar chart of AOC values of the developed MPMR, ENN and GP models. For a better model, the AOC value should be small. The value of AOC is almost same for MPMR and GP models. The performance of MPMR and GP is comparatively better than the ENN models.

Figures 8 and 9 shows the cumulative probability plot and probability density function plots of predicted/actual of the MPMR, GP and ENN models. It is clear from Figures 8 and 9 that the developed MPMR and GP give reasonable performance.

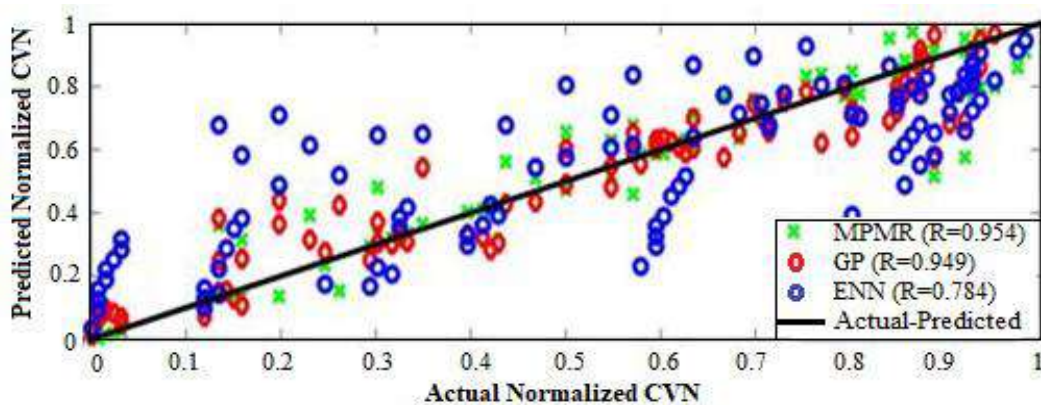


Fig. 4. Scatter plot of training dataset

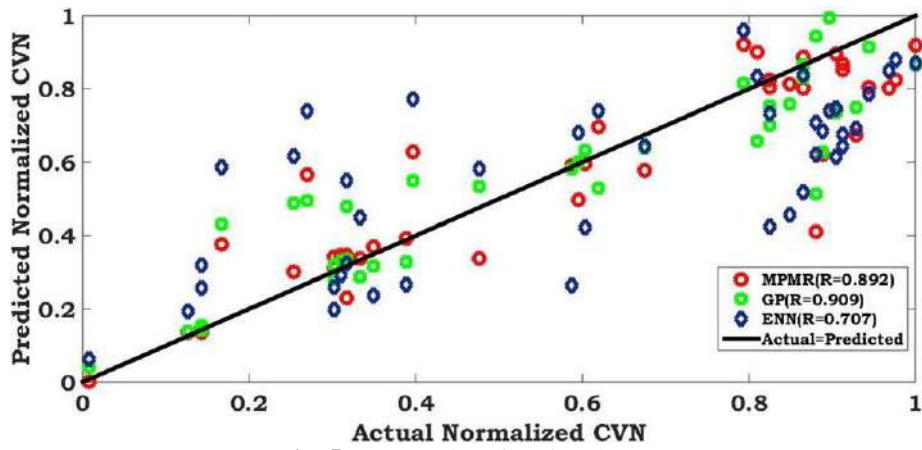


Fig. 5. Scatter plot of testing dataset

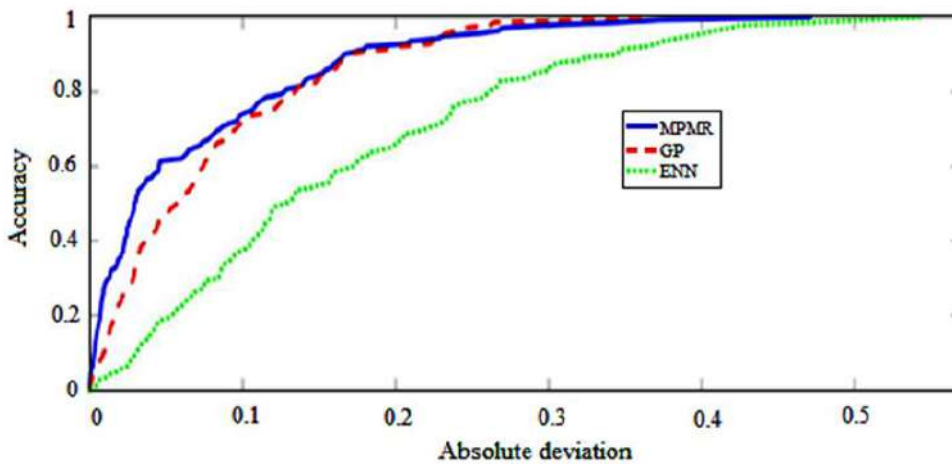


Fig. 6. REC curves of the developed MPMR, GP and ENN models

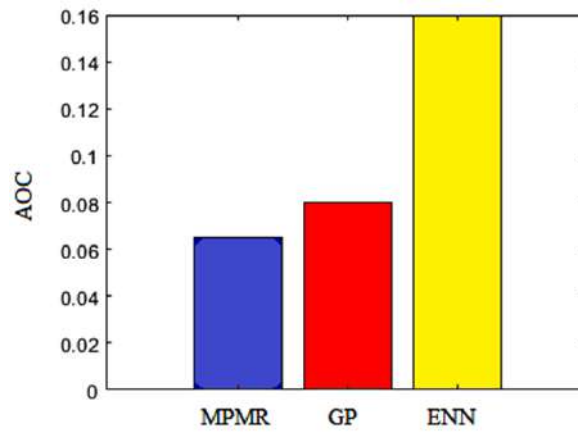


Fig. 7. Bar chart of AOC values of the different models

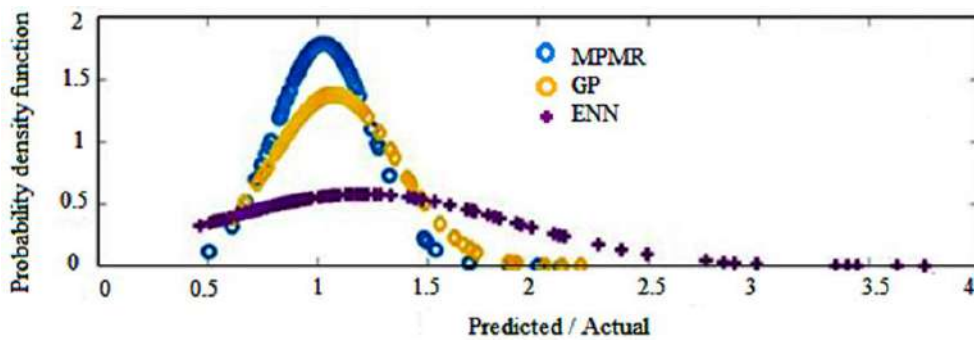


Fig. 8. Cumulative probability plots of predicted/actual of the MPMR, GP and ENN models

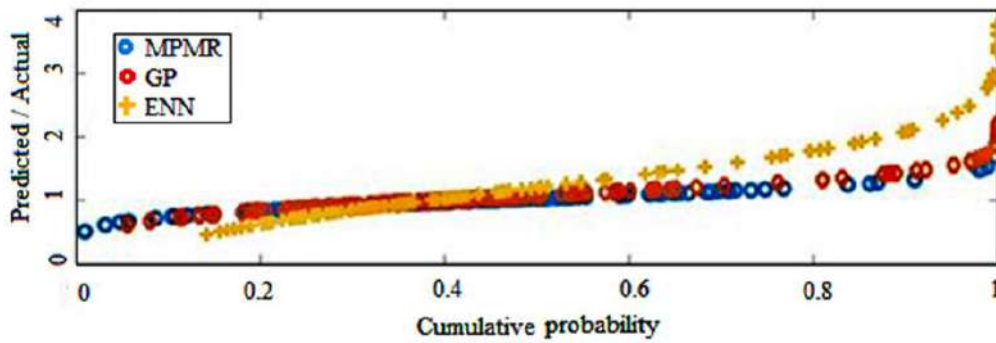


Fig. 9. Probability density function plots of predicted/actual of the MPMR, GP and ENN model

Figure 10 shows the Taylor diagrams of the MPMR, GP and ENN models. It can be seen from Figure 3 that the developed GP and MPMR models have lower RMSE, higher R^2 and closer to reference point than the ENN model. Therefore, GP and MPMR models outperform the ENN model. In addition, the almost overlapping performance points of the GP and MPMR models indicate that the success of the two models is very close. However, the fact that the GP model is slightly closer to the reference line indicates that the standard deviation of the model is closer to the actual data. This concludes that the GP model is slightly better than the MPMR.

In Table 2, the developed models were assessed according to different statistical indicators and the success order of these indicators. In addition, the ideal values of the statistical parameters used are expressed. It is clear from Table 2 that the developed GP and MPMR models predict CVN values quite well from the ENN

model. When the prediction performances of all my models were sorted according to rank analysis, it was found as $GP > MPMR > ENN$.

4. Conclusions

This article inspected the applicability of MPMR, GP and ENN models for the prediction of CVN values of functionally graded steels. The performance and accuracy of the developed models were tested according to statistical and graphical approaches such as different statistical criteria, rank analysis and scatter diagrams, REC analysis. The major findings of the study are listed as follows:

- The performance of MPMR and GP is almost same.
- Users can use the developed GP equation for practical purposes.
- The performance of ENN is not comparatively good.

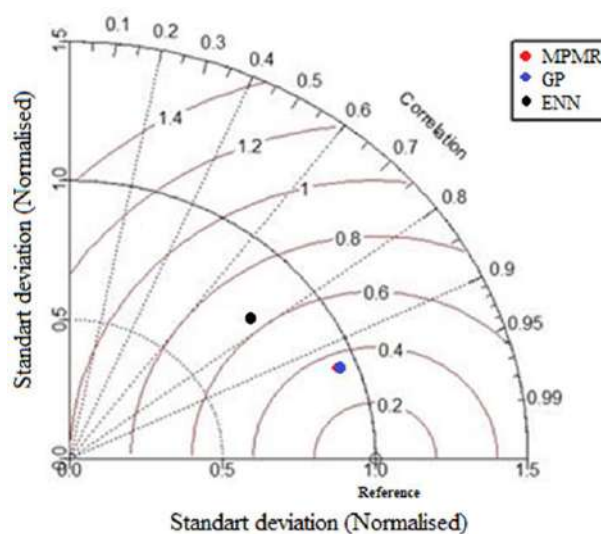


Fig. 10. Taylor diagrams of the developed GP, MPMR and ENN models

Table 2. Various parameters of the developed models

| Parameters | MPMR | GP | ENN | Ideal Values |
|---------------------|---------|---------|---------|---------------|
| NS | 0.8786 | 0.88147 | 0.57904 | 1 |
| (Rank) | -2 | -3 | -1 | |
| RMSE | 13.6594 | 13.4967 | 25.4352 | 0 |
| (Rank) | -3 | -2 | -1 | |
| VAF | 87.8917 | 88.1472 | 58.0706 | 100% |
| (Rank) | -2 | -3 | -1 | |
| R2 | 0.8786 | 0.88147 | 0.57904 | 1 |
| (Rank) | -2 | -3 | -1 | |
| Adj. R ² | 0.87682 | 0.87974 | 0.57289 | 1 |
| (Rank) | -2 | -3 | -1 | |
| PI | -11.904 | -11.736 | -24.282 | > 1.0 |
| Bias Factor | 1.02611 | 1.07368 | 1.20422 | 1 |
| (Rank) | -3 | -2 | -3 | |
| RSR | 0.34843 | 0.34428 | 0.64881 | 0 |
| (Rank) | -2 | -3 | -1 | |
| NMBE (%) | -0.8707 | 0.05263 | -1.9827 | 0 |
| (Rank) | -2 | -3 | -1 | |
| MAPE | 0.12394 | 0.17859 | 0.42507 | 0 |
| (Rank) | -3 | -2 | -1 | |
| RPD | 2.87001 | 2.90461 | 1.54127 | > 2.5 |
| WI | 0.9997 | 0.9997 | 0.99875 | 1 |
| (Rank) | -2 | -3 | -1 | |
| MAE | 8.63595 | 9.86508 | 20.49 | 0 |
| (Rank) | -3 | -2 | -1 | |
| MBE | -0.7027 | 0.04248 | -1.6002 | 0 |
| (Rank) | -2 | -3 | -1 | |
| LMI | 0.75127 | 0.71587 | 0.40986 | 1 |
| (Rank) | -3 | -2 | -1 | |
| U95 | 81.3679 | 81.2635 | 91.5931 | 0 |
| (Rank) | -2 | -3 | -1 | |
| t-stat | 0.60734 | 0.03711 | 0.7432 | Smaller value |
| (Rank) | -2 | -3 | -1 | |
| GPI | -57.589 | 0.2049 | -1166.3 | Higher value |
| (Rank) | -2 | -3 | -1 | |
| Total Rank | 37 | 43* | 18 | |

Note: * and red indicates the best model

- It has been concluded that the developed GP and MPMR models can provide high accuracy in the determination of CVN values of functionally graded steels. Thus, CVN values can be easily calculated when different the data of FGS type, crack type configuration, the thickness of the graded ferritic zone, the thickness of the graded austenitic region, the distance of the notch from the Bainite or Martensite intermediate layer and temperature parameters are used.
- The equations obtained from the study will contribute to the determination of CVN values with theoretical approaches by reducing the number of experiments and analyzes.
- The study is a reference for studies on data analysis and modeling in civil

engineering. This study proposes to make the operations more practical by using a small number of parameters instead of using all parameters.

5. Acknowledgements

The data used in the paper were obtained from the study of Nazari et al., (2012). The help of P. Samui and A. Kumari; is appreciated for providing data in this study. The statistical analysis part was performed by H.Y. Dalkılıç, S.N. Yesilyurt and O.M. Katipoglu.

6. References

- Al Adwan, J., Alzubi, Y., Alkhdour, A. and Alqawasmeh, H. (2023). "Predicting compressive strength of concrete using

- histogram-based gradient boosting approach for rapid design of mixtures”, *Civil Engineering Infrastructures Journal*, 56(1), 159-172, <https://doi.org/10.22059/CEIJ.2022.337777.1811>.
- Alyousef, R., Rehman, M.F., Khan, M., Fawad, M., Khan, A.U., Hassan, A.M. and Ghamry, N.A. (2023). “Machine learning-driven predictive models for compressive strength of steel fiber reinforced concrete subjected to high temperatures”, *Case Studies in Construction Materials*, 19, e02418, <https://doi.org/10.1016/j.cscm.2023.e02418>.
- Astarabadi, S.S.M. and Ebadzadeh, M.M. (2019). “Genetic programming performance prediction and its application for symbolic regression problems”, *Information Sciences*, 502, 418-433, <https://doi.org/10.1016/j.ins.2019.06.040>.
- Babaie, T., Karimizandi, R. and Lucas, C. (2008). “Learning based brain emotional intelligence as a new aspect for development of an alarm system”, *Soft Computing*, 12, 857-873, <https://doi.org/10.1007/s00500-007-0258-8>.
- Bae, K.O., Nguyen, T.T., Park, J., Park, J.S. and Baek, U.B. (2023). “Temperature dependency of hydrogen-related impact energy degradation of type 304 austenitic stainless steel”, *Journal of Mechanical Science and Technology*, 37(6), 2891-2901, <https://doi.org/10.1007/s12206-023-0515-5>.
- Biswas, R., Samui, P. and Rai, B. (2019). “Determination of compressive strength using relevance vector machine and ENN”, *Asian Journal of Civil Engineering*, 20(8), 1109-1118, <https://doi.org/10.1007/s42107-019-00171-9>.
- Bonakdari, H., Ebtehaj, I., Samui, P. and Gharabaghi, B. (2019). “Lake water-level fluctuations forecasting using minimax probability machine regression, relevance vector machine, Gaussian process regression, and extreme learning machine”, *Water Resources Management*, 33(11), 3965-3984, <https://doi.org/10.1007/s11269-019-02346-0>.
- Cevik, A. and Sonebi, M. (2008). “Modelling the performance of self-compacting SIFCON of cement slurries using genetic programming technique”, *Computers Concrete*, 5(5), 475-490, <https://doi.org/10.12989/cac.2008.5.5.475>.
- Dastorani, M.T., Mahjoobi, J., Talebi, A. and Fakhari, F. (2018). “Application of machine learning approaches in rainfall-runoff modeling (Case Study: Zayandeh Rood basin in Iran)”, *Civil Engineering Infrastructures Journal*, 51(2), 293-310, <https://doi.org/10.7508/CEIJ.2018.02.004>.
- Deng, Z., Chen, J., Zhang, T., Cao, L. and Wang, S. (2018). “Generalized hidden-mapping minimax probability machine for the training and reliability learning of several classical intelligent models”, *Information Sciences*, 436, 302-319, <https://doi.org/10.1016/j.ins.2018.01.034>.
- Dubey, Y., Sharma, P. and Singh, M.P. (2023). “Optimization using genetic algorithm of GMAW parameters for Charpy impact test of 080M40 steel”, *International Journal on Interactive Design and Manufacturing (IJIDeM)*, 1-11, <https://doi.org/10.1007/s12008-023-01371-z>.
- Hoang, N.D. and Tran, D.V. (2023). “Machine learning-based estimation of concrete compressive strength: a multi-model and multi-dataset study”, *Civil Engineering Infrastructures Journal*, <https://doi.org/10.1007/s12008-023-01371-z> (Online).
- Kar, S.S., Athawale, A.A., Bhushan, M. and Roy, L.B. (2023). “Dynamic soil-structure interaction of multi-story buildings using the finite element method and minimax probability machine regression”, *Engineering, Technology & Applied Science Research*, 13(4), 11170-11176, <https://doi.org/10.48084/etasr.5870>.
- Kecman, V. (2001). *Learning and soft computing: support vector machines, neural networks, and fuzzy logic models*, MIT press.
- Khashman, A. (2008). “A modified backpropagation learning algorithm with added emotional coefficients”, *IEEE Transactions on Neural Networks*, 19(11), 1896-1909, <https://doi.org/10.1109/TNN.2008.2002913>.
- Khashman, A. (2009). “Blood cell identification using emotional neural networks”, *Journal of Information Science & Engineering*, 25(6), 1737-1751.
- Kohestani, V.R., Vosoghi, M., Hassanlourad, M. and Fallahnia, M. (2017). “Bearing capacity of shallow foundations on cohesionless soils: A random forest based approach”, *Civil Engineering Infrastructures Journal*, 50(1), 35-49, <https://doi.org/10.7508/ceij.2017.01.003>.
- Koshiyama, A.S., Vellasco, M.M. and Tanscheit, R. (2015). “GPFIS-CLASS: A genetic fuzzy system based on Genetic Programming for classification problems”, *Applied Soft Computing*, 37, 561-571, <https://doi.org/10.1016/j.asoc.2015.08.055>.
- Kovalev, M. (2021). “Ontology-based representation of an Artificial Neural Networks”, *International Conference on Open Semantic Technologies for Intelligent Systems*, (pp. 132-151), Springer International Publishing, Cham, https://doi.org/10.1007/978-3-031-15882-7_8.
- Koza, J.R. (1994). “Genetic programming as a means for programming computers by natural selection”, *Statistics and Computing*, 4, 87-112, <https://doi.org/10.1007/BF00175355>.
- Kumar, C., Vardhan, H. and Murthy, C.S. (2022). “Artificial neural network for prediction of rock properties using acoustic frequencies recorded during rock drilling operations”, *Modeling Earth Systems and Environment*, 8(1), 141-161, <https://doi.org/10.1007/s40808-021-01103-w>.

- Kumar, M., Bardhan, A., Samui, P., Hu, J.W. and Kaloop, M.R. (2021). "Reliability analysis of pile foundation using soft computing techniques: A comparative study", *Processes*, 9(3), 486, <https://doi.org/10.3390/pr9030486>.
- Lanckriet, G., Ghaoui, L., Bhattacharyya, C. and Jordan, M. (2001). "Minimax probability machine", *Advances in Neural Information Processing Systems*, 14.
- Lin, C.C., He, R.X. and Liu, W.Y. (2018). "Considering multiple factors to forecast CO2 emissions: A hybrid multivariable grey forecasting and genetic programming approach", *Energies*, 11(12), 3432, <https://doi.org/10.3390/en11123432>.
- Nazari, A., Milani, A.A. and Zakeri, M. (2011). "Modeling ductile to brittle transition temperature of functionally graded steels by artificial neural networks", *Computational Materials Science*, 50(7), 2028-2037.
- Papa, J.P., Rosa, G.H. and Papa, L.P. (2017). "A binary-constrained geometric semantic GP for feature selection purposes", *Pattern Recognition Letters*, 100, 59-66, <https://doi.org/10.1016/j.patrec.2017.10.002>.
- Park, D. and Rilett, L.R. (1999). "Forecasting freeway link travel times with a multi-layer feed forward neural network", *Computer Aided Civil and Infrastructure Engineering*, 14, 358-367, <https://doi.org/10.1111/0885-9507.00154>.
- Switzner, N.T., Anderson, J., Ahmed, L.A., Rosenfeld, M. and Veloo, P. (2023). "Algorithms to estimate the ductile to brittle transition temperature, upper shelf energy, and their uncertainties for steel using Charpy V-Notch shear area and absorbed energy data", *Metals*, 13(5), 877, <https://doi.org/10.3390/met13050877>.
- Taylor, K.E. (2001). "Summarizing multiple aspects of model performance in a single diagram", *Journal of Geophysical Research: Atmospheres*, 106(D7), 7183-7192, <https://doi.org/10.1029/2000JD900719>.
- Vouros, G.A. (2022). "Explainable deep reinforcement learning: state of the art and challenges", *ACM Computing Surveys*, 55(5), 1-39, <https://doi.org/10.1145/3527448>.
- Zhang, H., Zhou, J., Jahed Armaghani, D., Tahir, M.M., Pham, B.T. and Huynh, V.V. (2020). "A combination of feature selection and random forest techniques to solve a problem related to blast-induced ground vibration", *Applied Sciences*, 10(3), 869, <https://doi.org/10.3390/app10030869>.
- Ziggah, Y.Y., Issaka, Y. and Laari, P.B. (2022). "Evaluation of different artificial intelligent methods for predicting dam piezometric water level", *Modeling Earth Systems and Environment*, 8(2), 2715-2731, <https://doi.org/10.1007/s40808-021-01263-9>.

Appendix

Table A1. Dataset used in this study

| FGS Type (F) | The crack tip configuration (C) | The thickness of graded ferritic region (A) | The thickness of graded austenitic region (G) | The distance of the notch from bainite or martensite intermediate layer (D) | Temperature (T) | CVN values obtained from experiments. |
|--------------|---------------------------------|---|---|---|-----------------|---------------------------------------|
| 1 | 3 | 5 | 4.4 | 10 | 123 | 30 |
| 1 | 3 | 5 | 4.4 | 10 | 173 | 41 |
| 1 | 3 | 5 | 4.4 | 10 | 223 | 53 |
| 1 | 3 | 5 | 4.4 | 10 | 273 | 84 |
| 1 | 3 | 5 | 4.4 | 10 | 323 | 95 |
| 1 | 3 | 5 | 4.4 | 10 | 373 | 98 |
| 1 | 3 | 5 | 4.4 | 10 | 423 | 101 |
| 1 | 3 | 5 | 4.4 | 10 | 473 | 109 |
| 1 | 3 | 5 | 4.4 | 10 | 523 | 118 |
| 1 | 3 | 5 | 4.4 | 10 | 573 | 135 |
| 1 | 4 | 2 | 7.4 | 0 | 123 | 110 |
| 1 | 4 | 2 | 7.4 | 0 | 173 | 113 |
| 1 | 4 | 2 | 7.4 | 0 | 223 | 116 |
| 1 | 4 | 2 | 7.4 | 0 | 273 | 117 |
| 1 | 4 | 2 | 7.4 | 0 | 323 | 118 |
| 1 | 4 | 2 | 7.4 | 0 | 373 | 119 |
| 1 | 4 | 2 | 7.4 | 0 | 423 | 121 |
| 1 | 4 | 2 | 7.4 | 0 | 473 | 123 |
| 1 | 4 | 2 | 7.4 | 0 | 523 | 124 |
| 1 | 4 | 2 | 7.4 | 0 | 573 | 124 |
| 1 | 4 | 3 | 6.4 | 1 | 123 | 34 |

| | | | | | | |
|---|---|-----|-----|---|-----|-----|
| 1 | 4 | 3 | 6.4 | 1 | 173 | 42 |
| 1 | 4 | 3 | 6.4 | 1 | 223 | 49 |
| 1 | 4 | 3 | 6.4 | 1 | 273 | 69 |
| 1 | 4 | 3 | 6.4 | 1 | 323 | 81 |
| 1 | 4 | 3 | 6.4 | 1 | 373 | 94 |
| 1 | 4 | 3 | 6.4 | 1 | 423 | 99 |
| 1 | 4 | 3 | 6.4 | 1 | 473 | 110 |
| 1 | 4 | 3 | 6.4 | 1 | 523 | 116 |
| 1 | 4 | 3 | 6.4 | 1 | 573 | 119 |
| 1 | 4 | 4 | 5.4 | 2 | 123 | 29 |
| 1 | 4 | 4 | 5.4 | 2 | 173 | 38 |
| 1 | 4 | 4 | 5.4 | 2 | 223 | 47 |
| 1 | 4 | 4 | 5.4 | 2 | 273 | 64 |
| 1 | 4 | 4 | 5.4 | 2 | 323 | 78 |
| 1 | 4 | 4 | 5.4 | 2 | 373 | 87 |
| 1 | 4 | 4 | 5.4 | 2 | 423 | 93 |
| 1 | 4 | 4 | 5.4 | 2 | 473 | 106 |
| 1 | 4 | 4 | 5.4 | 2 | 523 | 111 |
| 1 | 4 | 4 | 5.4 | 2 | 573 | 115 |
| 1 | 4 | 5 | 4.4 | 3 | 123 | 26 |
| 1 | 4 | 5 | 4.4 | 3 | 173 | 34 |
| 1 | 4 | 5 | 4.4 | 3 | 223 | 43 |
| 1 | 4 | 5 | 4.4 | 3 | 273 | 59 |
| 1 | 4 | 5 | 4.4 | 3 | 323 | 72 |
| 1 | 4 | 5 | 4.4 | 3 | 373 | 81 |
| 1 | 4 | 5 | 4.4 | 3 | 423 | 89 |
| 1 | 4 | 5 | 4.4 | 3 | 473 | 97 |
| 1 | 4 | 5 | 4.4 | 3 | 523 | 104 |
| 1 | 4 | 5 | 4.4 | 3 | 573 | 109 |
| 1 | 4 | 7.4 | 2 | 0 | 123 | 68 |
| 1 | 4 | 7.4 | 2 | 0 | 173 | 72 |
| 1 | 4 | 7.4 | 2 | 0 | 223 | 78 |
| 1 | 4 | 7.4 | 2 | 0 | 273 | 89 |
| 1 | 4 | 7.4 | 2 | 0 | 323 | 99 |
| 1 | 4 | 7.4 | 2 | 0 | 373 | 111 |
| 1 | 4 | 7.4 | 2 | 0 | 423 | 113 |
| 1 | 4 | 7.4 | 2 | 0 | 473 | 116 |
| 1 | 4 | 7.4 | 2 | 0 | 523 | 118 |
| 1 | 4 | 7.4 | 2 | 0 | 573 | 120 |
| 1 | 4 | 6.4 | 3 | 1 | 123 | 116 |
| 1 | 4 | 6.4 | 3 | 1 | 173 | 117 |
| 1 | 4 | 6.4 | 3 | 1 | 223 | 118 |
| 1 | 4 | 6.4 | 3 | 1 | 273 | 119 |
| 1 | 4 | 6.4 | 3 | 1 | 323 | 120 |
| 1 | 4 | 6.4 | 3 | 1 | 373 | 122 |
| 1 | 4 | 6.4 | 3 | 1 | 423 | 123 |
| 1 | 4 | 6.4 | 3 | 1 | 473 | 125 |
| 1 | 4 | 6.4 | 3 | 1 | 523 | 125 |
| 1 | 4 | 6.4 | 3 | 1 | 573 | 126 |
| 1 | 4 | 5.4 | 4 | 2 | 123 | 120 |
| 1 | 4 | 5.4 | 4 | 2 | 173 | 121 |
| 1 | 4 | 5.4 | 4 | 2 | 223 | 121 |
| 1 | 4 | 5.4 | 4 | 2 | 273 | 123 |
| 1 | 4 | 5.4 | 4 | 2 | 323 | 123 |
| 1 | 4 | 5.4 | 4 | 2 | 373 | 124 |
| 1 | 4 | 5.4 | 4 | 2 | 423 | 126 |
| 1 | 4 | 5.4 | 4 | 2 | 473 | 126 |
| 1 | 4 | 5.4 | 4 | 2 | 523 | 126 |
| 1 | 4 | 5.4 | 4 | 2 | 573 | 127 |
| 1 | 4 | 4.4 | 5 | 3 | 123 | 125 |
| 1 | 4 | 4.4 | 5 | 3 | 173 | 126 |
| 1 | 4 | 4.4 | 5 | 3 | 223 | 126 |
| 1 | 4 | 4.4 | 5 | 3 | 273 | 127 |
| 1 | 4 | 4.4 | 5 | 3 | 323 | 128 |

| | | | | | | |
|---|---|-----|-----|----|-----|-----|
| 1 | 4 | 4.4 | 5 | 3 | 373 | 129 |
| 1 | 4 | 4.4 | 5 | 3 | 423 | 131 |
| 1 | 4 | 4.4 | 5 | 3 | 473 | 132 |
| 1 | 4 | 4.4 | 5 | 3 | 523 | 132 |
| 1 | 4 | 4.4 | 5 | 3 | 573 | 133 |
| 2 | 3 | 0 | 8.5 | 10 | 123 | 26 |
| 2 | 3 | 0 | 8.5 | 10 | 173 | 40 |
| 2 | 3 | 0 | 8.5 | 10 | 223 | 49 |
| 2 | 3 | 0 | 8.5 | 10 | 273 | 53 |
| 2 | 3 | 0 | 8.5 | 10 | 323 | 58 |
| 2 | 3 | 0 | 8.5 | 10 | 373 | 59 |
| 2 | 3 | 0 | 8.5 | 10 | 423 | 59 |
| 2 | 3 | 0 | 8.5 | 10 | 473 | 61 |
| 2 | 3 | 0 | 8.5 | 10 | 523 | 63 |
| 2 | 3 | 0 | 8.5 | 10 | 573 | 62 |
| 2 | 4 | 0 | 8.5 | 0 | 123 | 9 |
| 2 | 4 | 0 | 8.5 | 0 | 173 | 10 |
| 2 | 4 | 0 | 8.5 | 0 | 223 | 10 |
| 2 | 4 | 0 | 8.5 | 0 | 273 | 10 |
| 2 | 4 | 0 | 8.5 | 0 | 323 | 10 |
| 2 | 4 | 0 | 8.5 | 0 | 373 | 11 |
| 2 | 4 | 0 | 8.5 | 0 | 423 | 11 |
| 2 | 4 | 0 | 8.5 | 0 | 473 | 12 |
| 2 | 4 | 0 | 8.5 | 0 | 523 | 13 |
| 2 | 4 | 0 | 8.5 | 0 | 573 | 13 |
| 2 | 4 | 0 | 8.5 | 1 | 123 | 24 |
| 2 | 4 | 0 | 8.5 | 1 | 173 | 24 |
| 2 | 4 | 0 | 8.5 | 1 | 223 | 24 |
| 2 | 4 | 0 | 8.5 | 1 | 273 | 25 |
| 2 | 4 | 0 | 8.5 | 1 | 323 | 26 |
| 2 | 4 | 0 | 8.5 | 1 | 373 | 27 |
| 2 | 4 | 0 | 8.5 | 1 | 423 | 27 |
| 2 | 4 | 0 | 8.5 | 1 | 473 | 27 |
| 2 | 4 | 0 | 8.5 | 1 | 523 | 28 |
| 2 | 4 | 0 | 8.5 | 1 | 573 | 29 |
| 2 | 4 | 0 | 8.5 | 2 | 123 | 46 |
| 2 | 4 | 0 | 8.5 | 2 | 173 | 47 |
| 2 | 4 | 0 | 8.5 | 2 | 223 | 47 |
| 2 | 4 | 0 | 8.5 | 2 | 273 | 47 |
| 2 | 4 | 0 | 8.5 | 2 | 323 | 48 |
| 2 | 4 | 0 | 8.5 | 2 | 373 | 49 |
| 2 | 4 | 0 | 8.5 | 2 | 423 | 50 |
| 2 | 4 | 0 | 8.5 | 2 | 473 | 50 |
| 2 | 4 | 0 | 8.5 | 2 | 523 | 51 |
| 2 | 4 | 0 | 8.5 | 2 | 573 | 51 |
| 2 | 4 | 0 | 8.5 | 3 | 123 | 82 |
| 2 | 4 | 0 | 8.5 | 3 | 173 | 83 |
| 2 | 4 | 0 | 8.5 | 3 | 223 | 84 |
| 2 | 4 | 0 | 8.5 | 3 | 273 | 84 |
| 2 | 4 | 0 | 8.5 | 3 | 323 | 84 |
| 2 | 4 | 0 | 8.5 | 3 | 373 | 85 |
| 2 | 4 | 0 | 8.5 | 3 | 423 | 85 |
| 2 | 4 | 0 | 8.5 | 3 | 473 | 86 |
| 2 | 4 | 0 | 8.5 | 3 | 523 | 87 |
| 2 | 4 | 0 | 8.5 | 3 | 573 | 88 |



This article is an open-access article distributed under the terms and conditions of the Creative Commons Attribution (CC-BY) license.



Comparative Study of the Effects of Key Factors on Concrete-to-Concrete Bond Strength

Mack, V.¹, Salehfard, R.² and Habibnejad Korayem, A.^{3*}

¹ M.Sc., School of Civil Engineering, Iran University of Science and Technology (IUST), Tehran, Iran.

² Post-Doctoral Researcher, School of Civil Engineering, Iran University of Science and Technology (IUST), Tehran, Iran.

³ Associate Professor, School of Civil Engineering, Iran University of Science and Technology (IUST), Tehran, Iran.

© University of Tehran 2023

Received: 09 Jan. 2023;

Revised: 19 Apr. 2023;

Accepted: 20 May 2023

ABSTRACT: This study aims to investigate the effects of key parameters on the interfacial bond strength between two concrete members. Different types of overlay in terms of strength (normal-strength concrete, high-strength concrete), surface roughness, and adhesive type are considered as variable factors influencing the bond behavior. First, the surface roughness of the old concrete and the compressive strength of the concrete overlay are evaluated separately. Then among the specimens, the composite with the highest bond strength is chosen as the optimum concrete composite. After finding the optimum composite, epoxy adhesive and cellulose mortar are applied to the optimum sample, and its corresponding interfacial strength is evaluated by bi-surface shear and splitting tensile strength tests. The results showed that, as the compressive strength of new concrete and concrete roughness increases, the bond strength increases. The highest bond strength achieved in composites containing high-strength concrete is 23.37% higher than that of samples with normal-strength concrete. Moreover, the interfacial bond strength of composite with the wire-brushed surface is the highest among other treatment methods, due to the interlocking action it provides. The bond strength of concrete composites containing epoxy adhesive is ~100-200% higher than that of samples without epoxy resin. However, the addition of cellulose mortar slightly reduces the adhesion resistance of the optimum sample. Therefore, it is anticipated that the use of high-strength concrete concomitant with wire-brushed surface treatment and epoxy resin adhesive shows substantial potential as an excellent method for repair of concrete structure.

Keywords: Adhesive Agent, Concrete Repair, High-Strength-Concrete, Interfacial Strength, Surface Preparation.

1. Introduction

Concrete structures can undergo intense forces during construction for a variety of

reasons. These forces can impose maximum stress on a concrete structure, causing cracks and finally, failure of that member (Zhou et al., 2008). The construction budget

* Corresponding author E-mail: ahkorayem@iust.ac.ir

used for maintenance and repair of structures in U.S. is estimated at \$18-21 billion per year (Du et al., 2019). Therefore, the safe and reliable design of repair materials is vital. It relies heavily on the availability of validated engineering materials and necessitates standardized quality improvement measures based on the constituents and mix design of the repair material.

Adding new concrete to old concrete or replacing new concrete with damaged concrete is one of the essential methods in repairing and strengthening concrete structures (EL Afandi et al., 2023; Behforouz et al., 2023). This procedure produces concrete-to-concrete interfaces with distinct properties. The interface plays a vital role in concrete-to-concrete bond strength. Therefore, the new concrete must have good adhesion to the old concrete substrate (Ezoddin et al., 2020; Jafarinejad et al., 2019; Al-Osta et al., 2022). However, consequence of insufficient bonding may cause a decrease in bond strength between composites (Austin et al., 1995). It has been represented that extreme interfacial roughness may further restrain the overlay shrinkage, causing higher tensile and shear stresses on the overlay and interface, which increases the probability of overlay cracking or interface detachment (Zhou et al., 2008).

In general, there are three different types of concrete-to-concrete interfaces. One includes when a new concrete overlay is placed against a concrete substrate (hardened concrete). This process is common in renovating damaged concrete structures such as concrete jacketing, precast connections, and ground support in tunnel operations. Placing hardened concrete against hardened concrete is another example of a concrete-to-concrete interface common in precast structures, such as bridge decks made of post-tension/pre-stressed concrete members. Eventually, adding concrete overlay on fresh concrete is widely used in additive manufacturing and digital fabrication, such

as 3D concrete printing (Babafemi et al., 2021).

Factors that affect the bond strength (Santos et al., 2012; Momayez et al., 2005; Julio et al., 2006; He et al., 2017; Julio et al., 2004; Daneshvar et al., 2022; Baharuddin et al., 2020) include the type and mechanical properties of both old and new concrete (compressive strength, young's modulus, age, and curing condition) (Julio et al., 2006; Huang et al., 2019), substrate roughness, and moisture condition (Santos et al., 2012; Piotrowski and Garbacz, 2014; Zhou et al., 2008; Beushausen et al., 2017), the environmental conditions (temperature, freeze-thaw cycles, etc.) (Çolak et al., 2009), the use of interface adhesion agents (type, thickness, casting and curing conditions) (Huang et al., 2019; Valikhani et al. 2020; Guo et al., 2018), and finally methods being used to measure the interfacial strength between new and old concrete (Feng et al., 2020; Farzad et al., 2019).

Many studies have focused on the interfacial bond strengths of concrete-concrete composites by considering overlays with different types and strength properties (Al-Madani et al., 2022; Prado et al., 2022; Feng et al., 2022). Julio et al. (2006) studied the influence of added concrete compressive strength on bond strength between concrete prisms. They used three different concrete mixtures with compressive strength of 30, 50, and 100 MPa for the added concrete. They noticed an increment of bond strength in shear with the increase of added concrete compressive strength.

Mangat and Flaherty (2000) investigated feasibility of using two materials for repairing highway bridges. One of the materials had low stiffness relative to the substrate and the other one had higher stiffness. Their results showed that using relatively stiff materials displayed efficient structural interaction with the substrate. Zhou et al. (2008) conducted an experiment to assess the impact of the elastic modulus of concrete overlay on bond strength. Their

findings indicated that repair materials with higher mechanical properties exhibit superior bond strength.

Carbonell Muñoz et al. (2014) and Valipour et al. (2020) evaluated the interfacial bond performance between Ultra-High Performance Concrete (UHPC) overlay and Normal-Strength Concrete (NSC). It was deduced that regardless of other involved parameters and applied loads, the bond strengths between two concretes were strong enough when UHPC was used. Tayeh et al. (2012) assessed the permeability characteristics of the UHPC-NSC interface using water, gas, and Rapid Chloride Permeability (RCP) tests. Prado et al. (2022) revealed that high-strength concrete (HSC)-UHPC interface represented a bond strength similar or superior to that of the monolithic HSC specimen.

In another study, the effects of bond properties of Light-Weight Concrete (LWC)-Normal Weight Concrete (NWC) were evaluated by considering different parameters (strength grade, interface roughness, use of steel fiber, etc.) (Huang et al., 2019). It was reported that the selection of interfacial agents (epoxy resin, cement paste, polymer binder, etc.) has a considerable effect on the bond strength between the new and old concretes (Shin and Lange, 2012). He et al. (2017) pointed out that different types of bonding agents have different efficiency and may lead to a different degree of increase in mechanical performance. Moreover, the use of bonding agents significantly affects failure types (Courard et al. 2014).

Nevertheless, the advantages of the use of bonding agents are not approved by all the researchers. Some researchers asserted that the application of a bonding agent leads to the formation of an extra plane contributing to the decrement of effective interlocking between substrate and overlay concrete (Julio et al., 2004). Valikhani et al. (2020) reported that the application of a bonding agent could be harmful to the strength of the bond between new and old

concrete.

Several surface preparation techniques have been utilized by researchers, namely wire-brushing, shot blasting, grinding, sand-water blasting, water jetting, chipping, pneumatic hammer, milling, and hydro-demolition (Diab et al., 2017; Gadri and Guettala, 2017). Santos et al. (2012) and Valikhani et al. (2020) demonstrated that the sand-blasting method could be used as the best interface preparation technique to get the highest bonding strength. Whilst, it is envisaged that some methods, such as pneumatic hammer, are harmful to the concrete interface since this method causes micro-cracks in the concrete substrate.

It is still under debate how interface bonding strength is affected by the roughness (Santos et al., 2012; Julio et al., 2004). HSC is designed to have better mechanical performances and greater resistance to aggressive chemicals than normal concrete (Tu et al., 2006). HSC possesses high strength and less inhomogeneity and micro-cracks at the Interfacial Transition Zone (ITZ). Therefore, it is being paid more attention to and can be used to repair and strengthen the damaged concrete owing to its excellent mechanical properties (Dybel and Wałach, 2017).

A quantitative definition of HSC is impossible for an engineer since it is relative and depends on time and location (Nawy, 2000). In North American and Canadian codes (Nawy, 2000; ACI 213R-87, 1987), concrete has a 28-day compressive strength of at least 41 MPa and is regarded as HSC. On the other hand, the FIP/CEB code (de la Precontrainte, 1983) describes HSC as concrete, having a minimum 28-day compressive strength of 60 MPa.

In light of the previous discussion, the purpose of this study is to evaluate the bonding strength behavior between NC or HSC as an overlay and NC as a substrate layer. Three different surface-preparation methods are used to elaborate the interfacial bond strength. The bond strength is

measured through bi-surface and tensile splitting tests. The highest bond strength obtained by considering the above parameters is selected as the optimum specimen. Afterwards, two types of adhesive agents, namely epoxy resin and hydroxyethyl methylcellulose (HEMC) powder, are also applied to the optimum concrete sample substrate, and the conclusions are made.

2. Experimental program

2.1. Materials

2.1.1. Concrete

The adopted concrete mixtures for NSC and HSC were set to achieve 28-day compressive strengths of 40 MPa and 70 MPa, respectively. The aggregates used in the mix design were fine sand, coarse sand, and coarse limestone. The maximum aggregate size in the mix design of normal and high-strength concrete was chosen as 19 mm. Aggregates used in the mix design were fine sand with most particles passing through a 4.75 mm sieve, and coarse limestone with mostly rounded shape. The Fineness modulus of aggregates was obtained at 5.46 according to the Fuller-Thompson curve (Xu and Hao, 2012).

The physical and chemical compositions of cement and silica fume used in NSC and HSC are shown in Table 1. A carboxylic-based superplasticizer was also concluded in the mix design of silica fume concrete to obtain a concrete with a workability and slump according to the normal-strength

concrete. The details can be found in Table 2. The optimum mixtures for both normal and high-strength concrete were designed and modified to meet the desired compressive strength and workability for both normal-strength and high-strength concrete. The concrete mix proportions are listed in Table 3. The amount of water for both concretes was chosen, 180 kg/m³. Silica-fume used in high-strength concrete was 10% per unit weight of cement.

2.1.2. Epoxy Resin

Epoxy-based resins are the most generally used adhesives in bonded concrete composites, which enhance the interfacial zone and alter the bond strength and failure modes of the produced composites (Baloch et al., 2021). The efficiency of epoxy resin is highly attributed to its curing conditions and thickness (Michels et al., 2016). In this study, an epoxy resin under the brand name Araldite 420 was used as the bonding agent between concrete materials, known as the most common commercial resin epoxies widely used in reinforcing civil structures. The epoxy is DGEBA (diglycidyl ether of Bisphenol A) based, supplied by Huntsman Company, Australia, and the hardener was Trioxatridecanediamine. This epoxy was chosen due to its higher strength, less viscosity, and less elongation at breakage. The chemical formula of epoxy adhesive is shown in Figure 1. The physical properties of resin, hardener, and the mixture can be found in Table 4.

Table 1. The constituents of cementitious materials

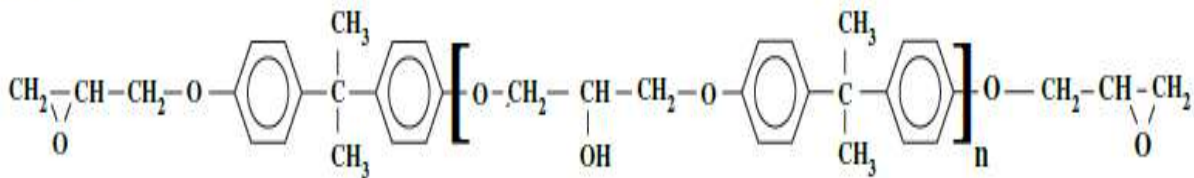
| Chemical composition (%) | | |
|---------------------------------------|-----------------|-------------|
| Chemical ingredient | Portland cement | Silica fume |
| CaO | 63.00 | 0.45 |
| SiO ₂ | 19.42 | 88.71 |
| Al ₂ O ₃ | 3.63 | 0.43 |
| Fe ₂ O ₃ | 3.23 | 1.52 |
| SO ₃ | 6.79 | 0.46 |
| MgO | 2.69 | 0.46 |
| Physical properties | | |
| Specific gravity | 3.12 | 2.30 |
| Specific surface (m ² /gr) | 0.35 | 17.13 |

Table 2. Properties of superplasticizer

| Color | pH | Specific weight (kg/L) | Chemical base |
|-------------|----|------------------------|-----------------------|
| Light brown | 7 | 1.03 | Poly-carboxylic ether |

Table 3. Concrete mixture design

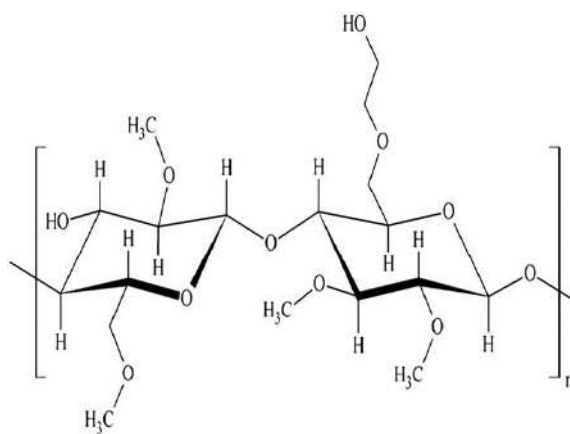
| Concrete | Cement (kg/m ³) | W/B | Gravel (kg/m ³) | Sand (kg/m ³) | Silica fume (kg/m ³) | SP (% unit weight of cement) |
|----------|-----------------------------|------|-----------------------------|---------------------------|----------------------------------|------------------------------|
| NSC | 360 | 0.5 | 1066 | 686 | - | - |
| HSC | 467 | 0.35 | 983 | 632 | 47 | 0.3 |

DGEBA**Fig. 1.** DGEBA epoxy resin chemical formulae (Delor-Jestin et al., 2006)**Table 4.** The physical properties of epoxy adhesive and its constituents

| Property | Araldite 420 A | Araldite 420 B | Mixed adhesive |
|---------------------------|----------------|----------------|----------------|
| Color | Yellow | blue | Dark green |
| Specific gravity | 1.2 | 1.0 | Approx. 1.1 |
| Viscosity at 25 °C (Pa.s) | 100-300 | 0.6-1.4 | 35-45 |
| Young's modulus (MPa) | - | - | 1495 |
| Tensile strength (MPa) | - | - | 29 |

The powder used in order to increase the adhesion between the concrete layers was cellulose-based, known as hydroxyethyl methylcellulose (HEMC). This powder is a multifunctional additive for construction materials, especially dry-mix products. It can improve the workability of both cement-based and gypsum-based materials by extending open time and enhancing adhesion, lubricity, shrink and crack

resistance. They are primarily used in tile adhesive, plasters, render finishes, and exterior insulation systems. Figure 2a shows the chemical formulae of the HEMC powder used in the mortar, and Figure 2b demonstrates the white HEMC powder as a dry product. The physical and chemical properties of HEMC powder are according to Table 5.



(a)



(b)

Fig. 2. a) Chemical formulae of powder adhesive (Bilichen et al. 2012); and b) the white HEMC powder adhesive**Table 5.** The physical and chemical properties of HEMC powder adhesive

| Appearance | Bulk density (g/cm ³) | Particle size | Moisture (%) | pH value | Brookfield viscosity (mPa. s) (2% solution 20-25 °C) |
|---------------------------------|-----------------------------------|---------------|--------------|----------|--|
| White to cream-colored powdered | 0.3-0.6 | 99% < 180 μm | 5.0 max | 5-8 | 40000-55000 |

2.2. Test Methods

2.2.1. Compressive Strength Test

Compressive strength tests were performed in order to classify the materials to ensure that the chosen concrete materials satisfied the strength criteria set out earlier. The tests were carried out on concrete cubes measuring 150 mm, following standard procedures in BS EN-12390 (EN, 2009). The specimens were tested when both NSC and HSC reached 28-days of age. Three compression tests were conducted on concrete composites. The cubic specimens were loaded according to BS EN-12390 (EN, 2009). Constant rate of loading within the range 0.4-0.8 MPa/s was applied and then increased continuously until no greater load can be sustained. The compressive strength was calculated using Eq. (1).

$$f_c = \frac{F}{A_c} \quad (1)$$

where f_c : is the compressive strength (MPa), F : is the maximum load at failure (N) and A_c : is the cross section of the specimen (mm^2).

2.2.2. Splitting Tensile and Bi-Surface Tests

The bond strength between the normal and high-strength concrete was examined using splitting tensile and bi-surface shear tests. A Universal Testing Machine (UTM) with a capacity of 2000 KN was used to apply the load to the test specimens in compression and tension. The interfacial tensile strength was evaluated by conducting the splitting tensile test on a 150 mm cubical specimen. The schematic diagram of the bi-surface shear and splitting tensile test is represented in Figures 3a-3b (Santos et al., 2012; BSI, 2000). In the proposed methods, the experimental bond strength can be calculated using the Eqs. (2) and (3).

$$F_{ct} = \frac{P}{2bd} \quad (2)$$

$$F_{ct} = \frac{2P}{\pi bd} \quad (3)$$

where F_{ct} : is the tensile splitting strength (MPa); F : is the maximum load applied to

the specimen until failure (N), L : is the length of the specimen, and d : is the depth of the specimen.

The required loading rate on the testing machine for splitting tensile test was chosen as per BS-EN 12390-6 (BSI, 2000). For the bi-surface shear test, constant loading rate of 0.3 MPa/s was applied until composite specimens failed. Cubic specimens with the dimensions of $15 \times 15 \times 15$ cm were used for both splitting tensile and bi-surface shear tests. These experimental tests have some advantages compared to other bond tests. For instance, the specimen geometry is similar to the standard cubic specimens, and the same molds can be used to make the concrete composites. Besides, all the specimens are tested in a universal testing machine similar to a compression test without the need for specific apparatus.

Loads are also applied symmetrically and produce uniform stress along with the interface. For the bi-surface shear test, the substrate concrete and the concrete overlay comprise two-thirds and one-third of the molds, respectively (Figure 4a). Contrary to the bi-surface shear specimens, for the splitting tensile test, the substrate concrete and the concrete overlay comprise half of the molds (Figure 4b). First, the concrete substrate was made in the laboratory by a 100-liter mixer capacity and was placed in lubricated plastic molds. Then, the specimens were kept in a water tank for 28 days to achieve their ultimate strength. After casting, the specimens were placed in plastic molds for the addition of concrete overlay. Where appropriate, the substrate surface was roughened, and epoxy adhesive and HEMC mortar were applied before placing the new concrete. Three composite specimens were cast based on each surface treatment method, compressive strength of the concrete overlay, and the application of binders between the specimens. After casting concrete overlay, the specimens were cured for additional 28 days before testing. In order to prevent moisture loss, the outside surface of the samples was covered by plastic sheets.

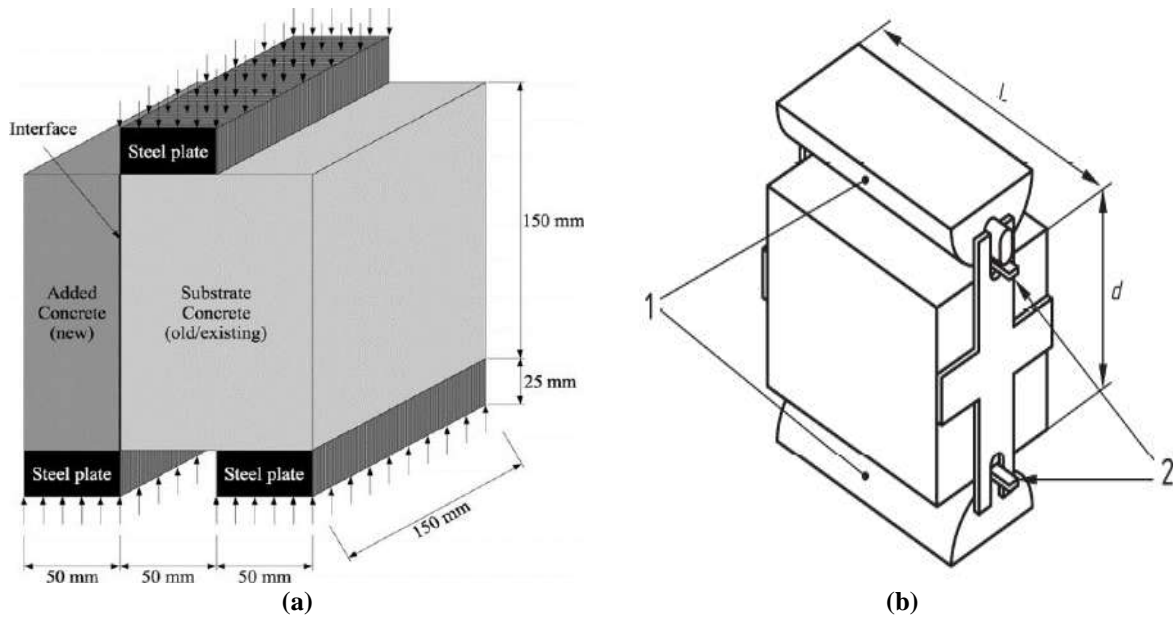


Fig. 3. a) Bi-surface shear test (Santos et al., 2012); and b) Splitting tensile test (BSI, 2000)

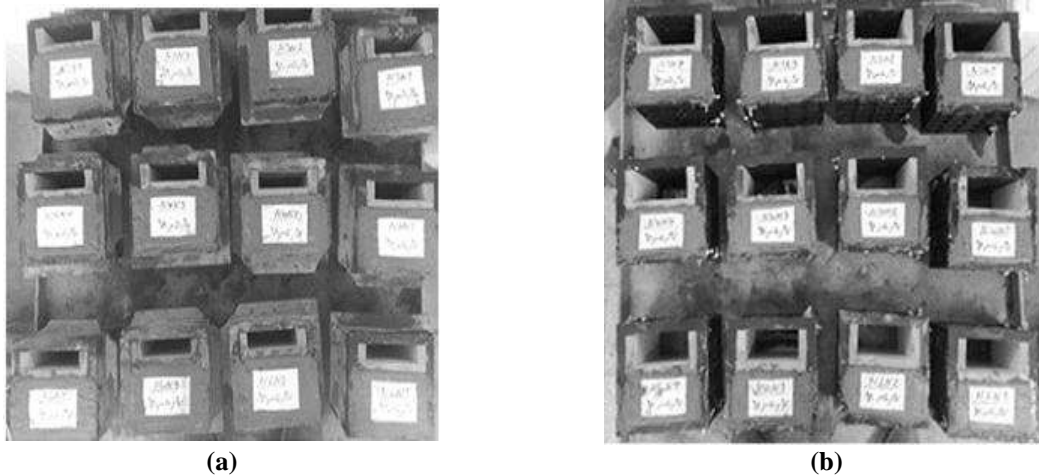


Fig. 4. a) Tensile splitting samples; and b) Bi-surface shear specimens

2.2.3. Concrete Interface Treatment

Three different surface roughness were considered in this study, including surface left as cast, surface wire-brushed, and surface partially chipped. The surface preparation methods used were practical and primarily implemented in the construction industry. The term surface left as cast (LAC) in Figure 5c implies that the concrete overlay was placed directly against the concrete substrate, and no increase in the surface texture of the substrate can be observed. Before placing the concrete overlay, the substrate surface was cleaned with compressed air and a brush to remove any possible dust from the surface. Wire-Brushed surface (WB) produces enhanced friction between concrete materials due to

revealing some of the substrate aggregates. After the preparation, the surface was once again cleaned with compressed air (Figure 5a). The third method used for increasing the roughness of the substrate concrete was scrabbling or chipping with a commercial chipping drill (Figure 5b). This method strikes the surface repeatedly with hardened points to produce momentary mechanical loads that exceed the strength of the concrete, causing it to fracture.

2.2.4. Application of Bonding Agent

After the concrete surface treatment, the epoxy adhesive and HEMC mortar were applied to concrete surfaces immediately before adding a concrete overlay. The specifications for mixing and preparation of

epoxy adhesive and mortar samples were described by the manufacturer. The water to cement ratio was chosen as 0.5, and HEMC powder with an amount of 0.7 %-unit weight of cement was used for HEMC mortar. The mixture design and mechanical properties of reference and HEMC mortars including compressive strength and tensile strength are shown in Table 6. The results showed that the compressive strength of HEMC mortar is lower than reference mortar which can be due to delayed hydration of cement in the mortar (Pourchez et al., 2006). On the other hand, the tensile strength was higher than that of reference mortar. Approximately 1-2 mm thickness was adopted for epoxy adhesive and was applied via cutter. The intended thickness for the mortar was considered as 2-3 mm. The adhesive was then applied to the surface of the hardened specimens by the spatula, and afterwards, new concreting was performed on the hardened concrete.

This spatula was also used to apply the mortar to the hardened concrete specimens. The thicknesses of epoxy bonding agent and HEMC mortar were measured by vernier caliper. The thickness was calculated by subtracting the total thickness (specimen and adhesive) from the specimen's length (150 mm). The uniformities were visually checked and precisely controlled by vernier caliper.

After applying the mortar to the surfaces, the mortar was smoothed with a trowel to produce a constant and steady thickness. Then, fresh concrete was prepared and added to the old concrete. The surface of the concrete substrate was moistened using a water sprinkler to remain in a saturated surface-dry condition (SSD) and prevent the absorption of water available in HEMC mortar by the substrate. To reach a proper saturated surface dry state, it is critical to

achieve a substrate surface showing no signs of water film. Finally, samples were cured at 100% humidity for seven days and then stored in a water tank for additional 21 days at 50% humidity and room temperature. The humidity inside the water tank was regulated by a hydrometer.

2.2.5. Interface Microscopy

The surface texture of the specimens was examined by optical microscopy (stereo optical microscope) with a magnitude of 20x and scanning electron microscopy (SEM) on the scale of nanometers. Two plates of 25 × 25 mm were cut per concrete surface profile for each microscope analysis. The specimens prepared for the SEM analysis have been thoroughly dried in the oven for 24 hr. The epoxy specimens were put in the vacuum machine to facilitate the hardening of epoxy and eliminate bubbles created while mixing the epoxy components.

The mesostructured wire-brushed and chipped surfaces obtained from the stereo microscope are shown in Figures 6a-6b. Using the results obtained from the observation of the microstructure with a scanning electron microscope (Figures 6c-6d), one can conclude that concrete surfaces significantly had different surface textures after various treatments. The aggregates are exposed using the wire-brush technique, which is dominant for bonding old concrete and repair material (Figure 6a). According to Figure 6c, the surface of the substrate has wave-like irregularities, which can increase the mechanical interlocking and, therefore, friction. Figures 6b and 6d depict the chipped surface on macroscopic and microscopic scales, respectively. These figures indicate that the chipping method causes micro-cracks on the concrete surface.

Table 6. The mixture design and mechanical properties of HEMC mortar

| Cement (gr) | Water to cement ratio | Aggregate to cement ratio | SP (% unit weight of cement) | HEMC (% unit weight of cement) |
|-------------|----------------------------|---------------------------|------------------------------|--------------------------------|
| 500 | 0.5 | 3 | 0.5 | 0.7 |
| | Compressive strength (MPa) | | Tensile strength (MPa) | |
| | Reference mortar | HEMC mortar | Reference mortar | HEMC mortar |
| | 31.5 | 23 | 1.41 | 1.94 |

2.2.6. Specimen Identification

All specimens were designated as NXYZ, where N: specifies the substrate concrete (N for the normal strength concrete). X: represents the surface texture of the substrate concrete (L for the left as cast, W for wire-brushed, and S for scrabbling (chipping)). Y: represents epoxy addition or HEMC mortar on the substrate (Y is ignored-when the specimen is considered adherend free). The letter Z: shows the overlay concrete (N for the NSC and H for HSC). Taking the NLH specimen as an example, the first N represents substrate material (NSC), the second H is overlay concrete (HSC), and the character L

symbolizes surface texture (left as cast), and no bonding agent was used between concrete materials. In order to compare concrete to concrete bond strength with the real bond strength (continuous concrete composed of the substrate concrete), it was also decided to conclude them in this research. The comparison aimed to see how much strength the composites need to act as a monolithic material, which indicates proficient bond strength. For continuous concrete (15 × 15 × 15 cm), the letters N-BR and N-BI have been used, in which BR stands for Brazilian (splitting) tensile test and BI stands for the bi-surface shear test.

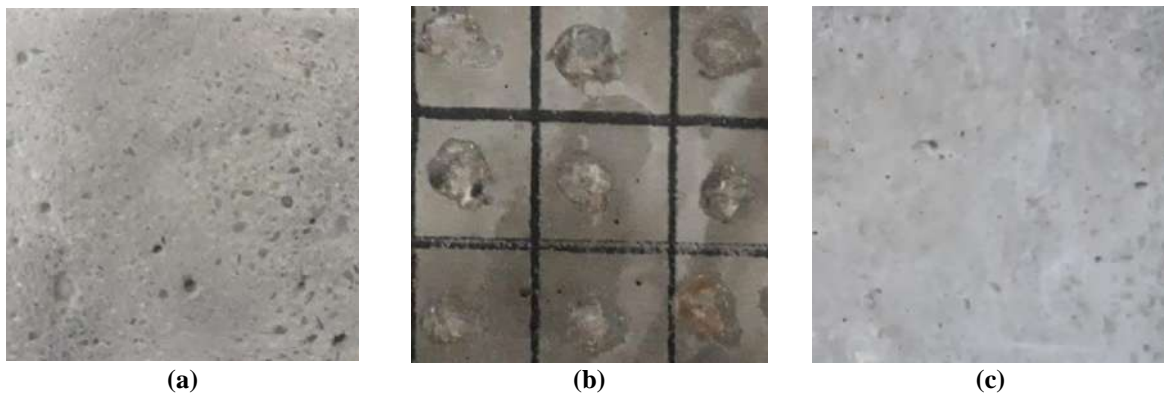


Fig. 5. Surface preparation methods: a) Surface wire brushed; b) Surface partially chipped; and c) Surface left as cast

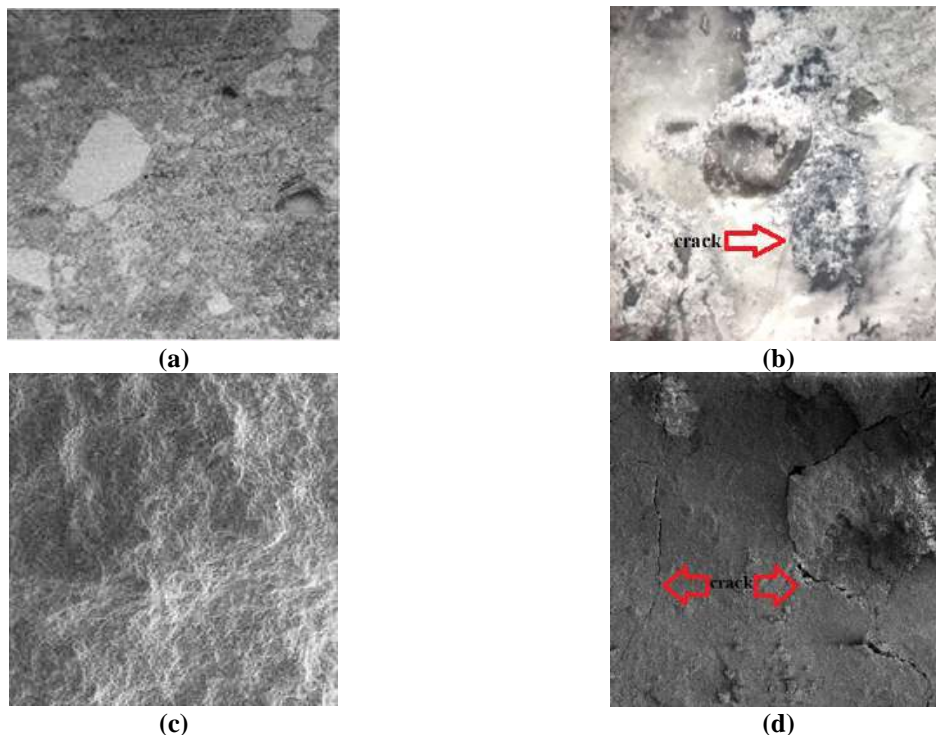


Fig. 6. The microstructure images of new-to-old concrete interface: a, c) Wire-brushed surface; and b, d) Chipped surface

3. Results and Discussion

3.1. Compressive Strength

The results of the compression test for NSC and HSC concrete are shown in Table 7. The average compressive strength for NSC concrete was 40.12 MPa, which was well matched with the desired compressive strength. The average compressive strength for HSC concrete was 67.75 MPa with a standard deviation of 1.7, which was close to the desired strength. The compressive failures of the specimens are shown in Figures 7a and 7b. As illustrated in Figure 7a, the failure of the normal-strength concrete was non-explosive, contrary to the high-strength concrete, which had an explosive failure (Figure 7b). The compressive stress-strain curves for both materials are shown in Figure 7c.

3.2. Evaluation of Interfacial Bonding Strength

3.2.1. The Effect of Surface Treatment

In Figure 8a, one can see that shear bond strength increases with the increase in the roughness of the concrete substrate. On the other hand, the highest increase in shear among different surface roughness was for the NWN sample.

The reason was the manifestation of aggregates outside the surface of the substrate, which increased the friction between the aggregates of the substrate and the cement paste of the fresh concrete. The wire-brushing method increased the friction of aggregates more than other methods of roughening techniques used in this experiment and, as a result, increased the adhesion.

Table 7. Compressive strength of cubic specimens for both normal strength and high strength concrete as an overlay material

| Concrete composite | Layer | Failure stress (MPa) | Average (MPa) | SD (MPa) | COV (%) |
|--------------------|--------------------|----------------------|---------------|----------|---------|
| NSC-NSC | Concrete substrate | 39.95 | 40.12 | 1.96 | 4.88 |
| | | 38.26 | | | |
| | | 42.17 | | | |
| NSC-NHC | Added concrete | 40.9 | 39.01 | 2.0 | 5.12 |
| | | 39.24 | | | |
| | | 36.9 | | | |
| NSC-NHC | Concrete substrate | 38.26 | 39.23 | 1.45 | 3.69 |
| | | 40.9 | | | |
| | | 38.5 | | | |
| NSC-NHC | Added concrete | 69.77 | 67.85 | 1.7 | 2.5 |
| | | 67.30 | | | |
| | | 66.50 | | | |

Note: SD: standard deviation, COV: coefficient of variance



(a)



(b)

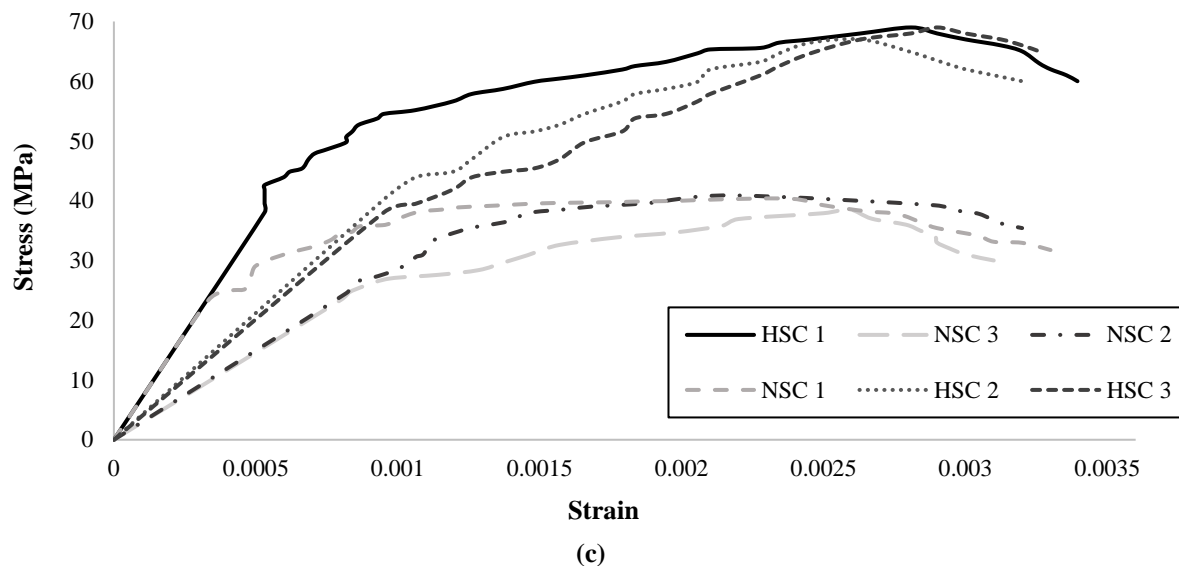


Fig. 7. a) Compressive failure of NSC; b) Compressive failure of HSC; and c) The stress-strain curves obtained from compressive strength tests for of NSC and HSC

As shown in Figure 8a, the shear resistance of NLN, NWN, and NSN were approximately 12%, 25%, and 16% of shear strength relative to monolithic concrete (continuous concrete). Lower adhesion resistance of the NSN (chipped sample) can be due to the presence of micro-cracks in old concrete caused by chipping drill, which reduced the adhesion resistance (Figure 6d). The highest bond strength obtained from the splitting tensile test was also due to the increased roughness associated with the wire-brushing method (Figure 8b). The increase in tensile strength of this sample was 1.18 and 1.04 greater than the tensile strength of the left as cast and chipped samples, respectively. As a result, one can conclude that increasing the roughness does not significantly affect the tensile strength. As shown in Figure 8b, the tensile strength of NLN, NWN, and NSN were approximately 16%, 19%, and 18% of the tensile strength of monolithic concrete.

3.2.2. Influence of Overlay Strength

The results of the bi-surface shear and splitting tensile tests for concrete composites containing high-strength concrete as an overlay material are shown in Figures 9a and 9b. Comparing Figure 9 with Figure 8, it can be concluded that among concrete samples, the sample

containing high-strength concrete as an overlay achieved the highest value in bond strength. The increased adhesion of concrete composites containing high-strength concrete can be attributed to the role of silica compound of silica fume which generates Calcium Silicate Hydrate (C-S-H) by reacting with calcium hydroxide (Mizan et al., 2020; Shibao et al., 2019), that corroborates the findings of Momayez et al. (2005).

As shown in Figure 9a, the shear strength of NLH, NWH, and NSH were approximately 15%, 28%, and 20% of the shear strength of monolithic concrete, respectively. The shear strength of NLH, NWH and NSH samples were 1.23, 1.12, and 1.23 times greater than NLN, NWN, and NSN samples, respectively, which indicated that as the roughness of the substrate increases, the influence of the compressive strength of fresh concrete was reduced. The highest tensile strength among different surface roughness also was belonged to the wire-brushed sample, which has a magnitude of 1.35 times greater than the concrete composite, without any surface roughness. The highest tensile strength was also due to the increased roughness associated with the NWH sample (wire-brushed surface profile and the use of high-strength concrete), which was similar to the

shear adhesion resistance.

As illustrated in Figure 9b, the tensile strength of NLH, NWH and NSH samples were approximately 19%, 26%, and 23% of the tensile strength of the monolithic concrete. Therefore, the specimen with the highest shear and tensile strength; that is NWH sample, can be considered as the optimum specimen. The epoxy adhesive and HEMC mortar were added, and further experiments were undertaken.

3.2.3. Effect of Bonding Agent

The bi-surface shear strength of the optimum specimen containing epoxy resin adhesive, as shown in Table 8, was 126% greater than the NWH sample, which indicated the good bonding performance of the adhesive. Comparing Table 8 with Figure 9a, one can conclude that the shear strength of the epoxy-contained sample was 86.4% of the shear strength of the monolithic concrete.

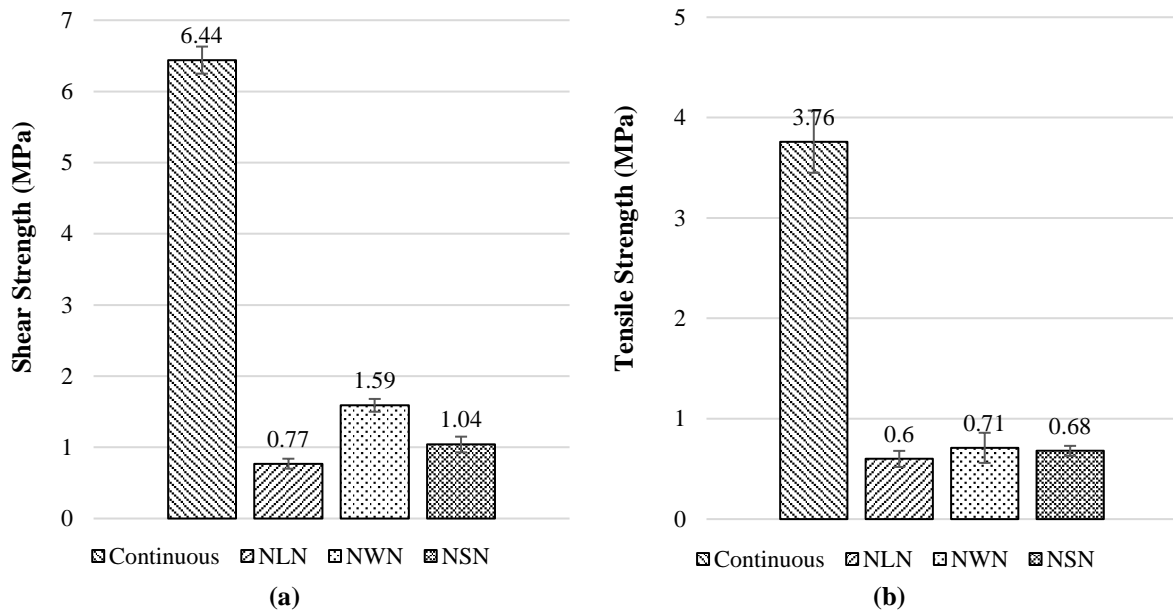


Fig. 8. The interfacial strength of composites with different surface preparations: a) Composites subjected to shear; and b) Composites subjected to tension

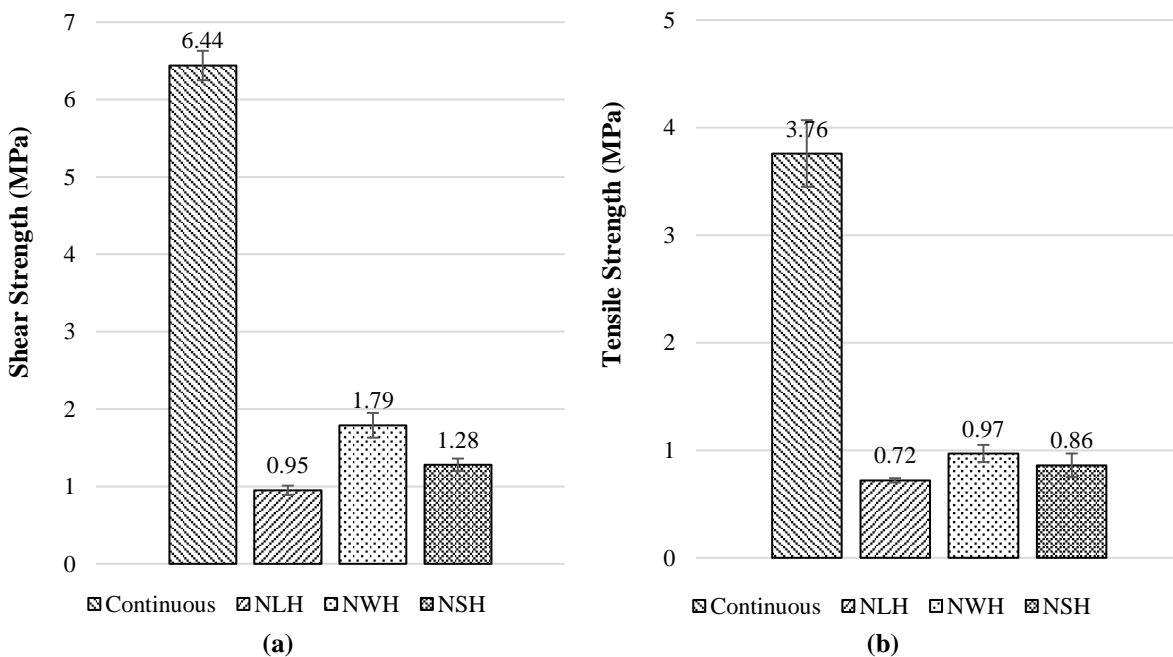


Fig. 9. The interfacial strength of composites containing high-strength concrete as an overlay: a) Composites subjected to shear; and b) composites subjected to tension

The tensile strength of the optimum specimen with epoxy resin binder showed an increase of 196% compared to the sample without adhesive. The shear and tensile strengths of the samples containing cellulose-based powder adhesive as an overlay are given in Table 9. The shear strength of the optimum specimen containing cellulose-based adhesive mortar (NWPH) was 10% lower than the specimen without cellulose adhesive, which can be attributed to the loss of significant effect of wire brush roughness on adhesion resistance. It can also be seen that the tensile strength of the NWPH was lower than the specimen without HEMC, although the reduction was not significant.

3.3. Failure Modes

The failure modes of concrete materials without adhesive are shown in Figure 10. Based on Figures 10a-10c, the location of the failure plane of the NLN, NWN, and NSN composite specimens observed in the bi-surface shear test, one can deduce that cracks initiated from the top of the bond line and then propagated through the bottom of the specimen. When the load exceeded a specific value, sudden slippage occurred between the two concrete materials. It can be concluded that modes of fracture for all the specimens were adhesive failure, indicating the complete separation of the overlay concrete from the substrate; the surfaces of the two materials remained smooth, and no further cracking was observed in both substrate and overlay.

Table 8. Average bond strength of composite specimens containing epoxy adhesive as a bonding agent

| Test type | Strength (MPa) | SD (MPa) | COV (%) |
|------------------------|----------------|----------|---------|
| Shear test | 4.05 | 0.34 | 8.4 |
| Splitting tensile test | 2.87 | 0.055 | 1.85 |

Note: SD: standard deviation, COV: coefficient of variance.

Table 9. Average bond strength of composite specimens containing HEMC mortar as a bonding agent

| Test type | Strength (MPa) | SD (MPa) | COV (%) |
|------------------------|----------------|----------|---------|
| Shear test | 1.61 | 0.071 | 4.40 |
| Splitting tensile test | 0.96 | 0.047 | 4.99 |



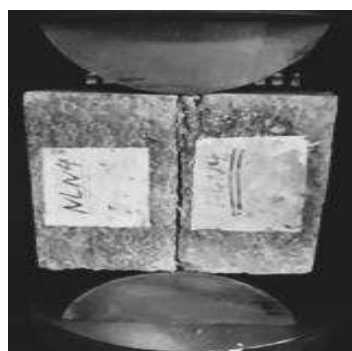
(a)



(b)



(c)



(d)



(e)



(f)

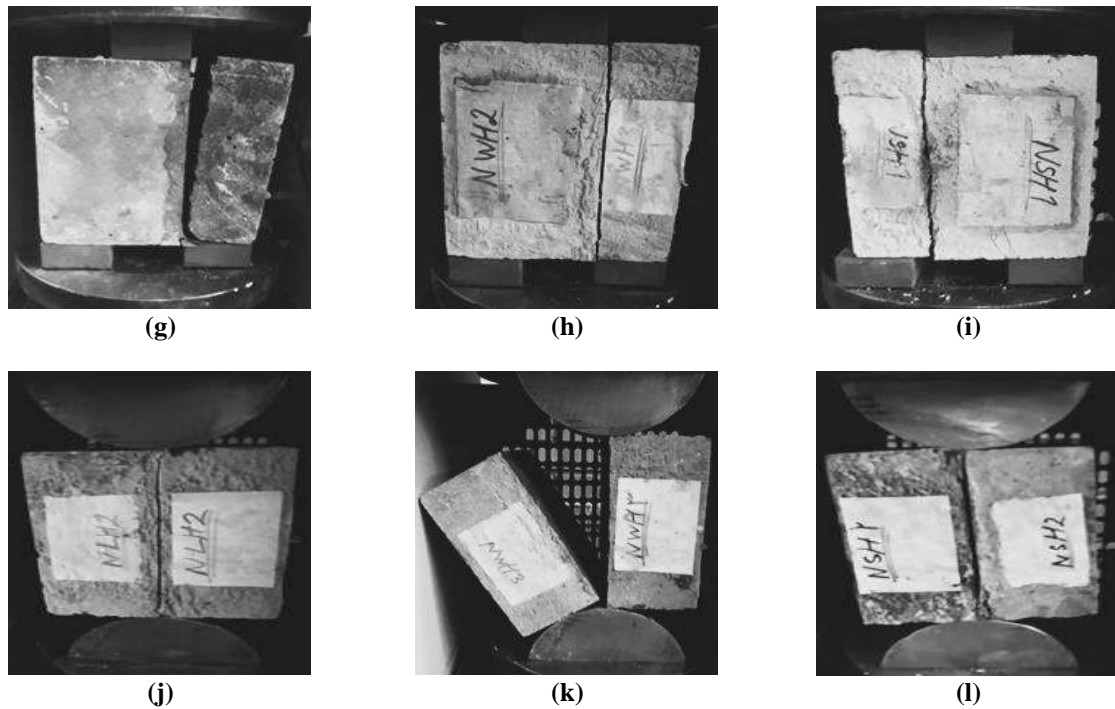
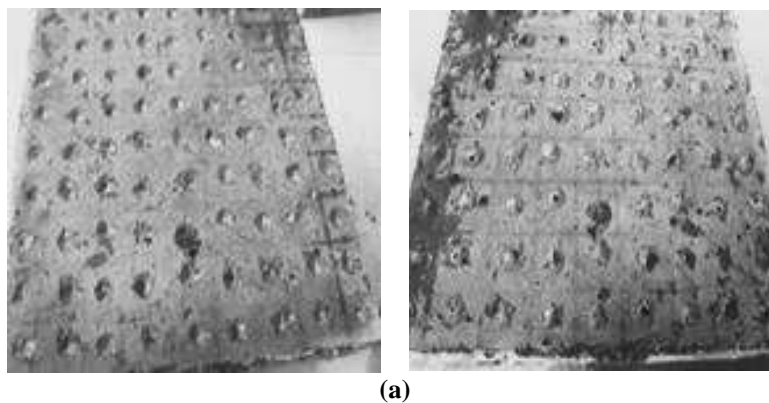


Fig. 10. The shear and tensile failure between two concrete materials: NSC-NSC and NSC-HSC

Figures 10d-10f demonstrate the tensile failure of the specimens containing NSC overlay. The failure in tension is similar to the failure in shear. In other words, the specimens had interface fractures, and no damage was observed either from the substrate or the overlay concrete. The crack in the specimens subjected to tension emerged from the middle of the interface and propagated on both sides until it reached the top and bottom of the specimen, and total failure of the specimens occurred. The failure modes of the specimens containing HSC as an overlay, evaluated by bi-surface shear and tensile splitting tests, were all interfacial failures (Figures 10g-10l). The interface failure indicates that the interfacial bond strength is weaker than the

concrete substrate.

The complete separation of concrete surfaces in both shear and tensile stresses in interface failure is represented in Figures 11a-11c. Figure 11a demonstrates NSN specimens subjected to the splitting tensile test, in which a small portion of concrete was penetrated the hollows created by the chipping process, but the surface of concrete remained intact, and no further damage was observed on the surfaces. Figure 11b shows the NWH specimen subjected to the bi-surface shear test. The interface failure mode occurred between the surfaces, similar to NSN samples. Figure 11c also depicts the complete separation of NLH surfaces without harming either the substrate or the overlay concrete.



(a)

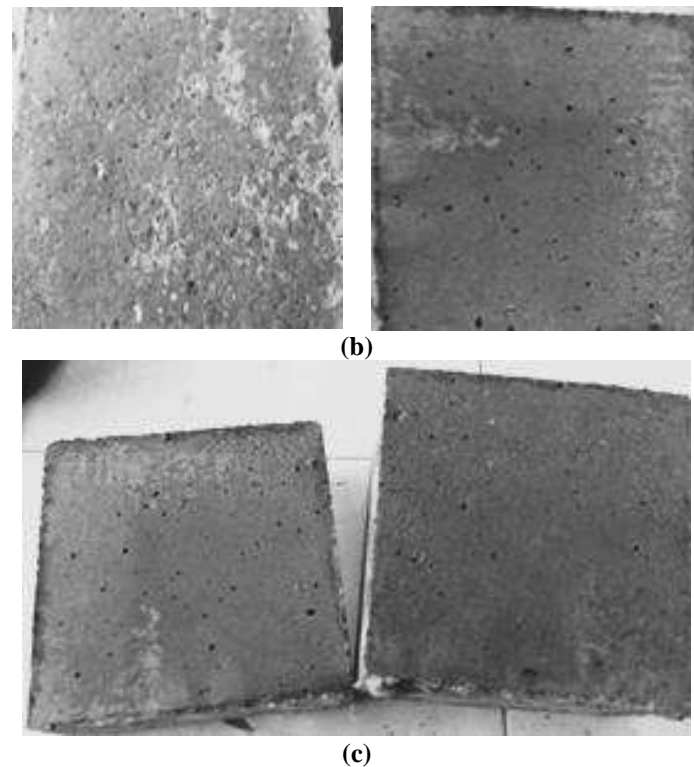


Fig. 11. The surfaces of the composites after failure in shear and tension (NSC-HSC): a) NSN specimen subjected to the splitting tensile test; b) NWH specimen subjected to the bi-surface shear test; and c) NLH specimen subjected to the splitting tensile test

Figure 12a demonstrates the failure mode of the specimen containing epoxy adhesive under shear stress, and Figure 12b demonstrates the failure mode of the specimen containing HEMC mortar at their interface that was subjected to tensile stress. Some specimens had mixed-mode failure, and some had interface failure. In other words, minor substrate failure and interface failure occurred in some specimens containing epoxy adhesive and HEMC as binding materials.

Almost the total failure plane in shear and tension, originated from the interaction between the concrete substrate and the

epoxy adhesive, not the epoxy adhesive itself (Figures 13a-13b). The same conclusion can be made for the HEMC specimens (Figures 13c-13d). In some of the specimens, the bond strength was distinctively stronger than that of the substrate because a failure occurred partially in the substrate without complete interfacial separation or debonding between the substrate and the overlay concrete. The failure from the concrete substrate highlights a good bond proficiency, indicating that the interfacial bond strength is more significant than the concrete substrate strength.

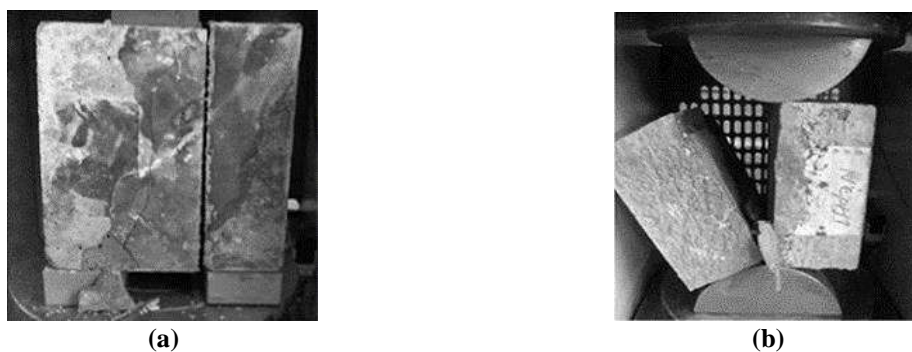


Fig. 12. The shear and tensile failure of the specimens: a) Epoxy-contained specimen; and b) HEMC-contained specimen

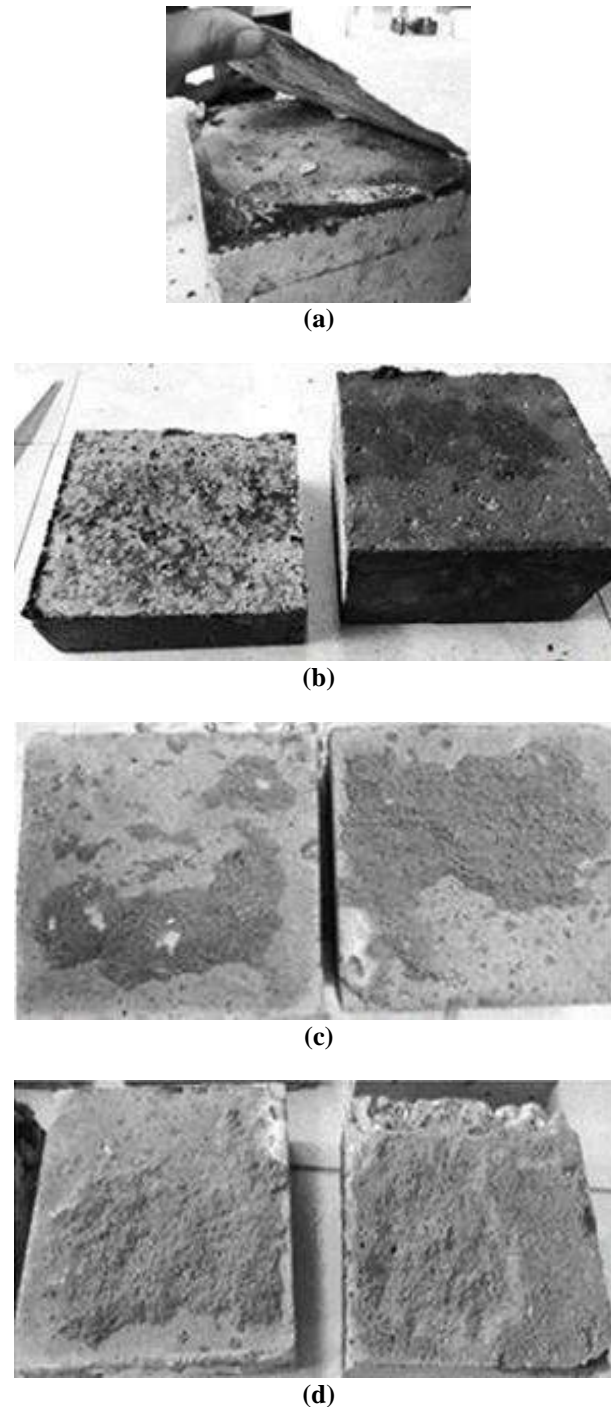


Fig. 13. The separation of concrete surfaces in shear and tension: a, b) Epoxy-contained specimen; and c, d) HEMC-contained specimen

4. Conclusions

The purpose of this study was to investigate the bonding strength behavior between two concrete materials by considering different parameters. To this end, the roughness parameters of the substrate concrete, including smooth surface, wire-brushed surface, and chipped surface, were

examined, and the compressive strength of new concrete with two strength classes of 40 MPa and 70 MPa was evaluated separately by bi-surface shear and tensile splitting tests. Then the sample with the highest shear and tensile strength was introduced as the optimum specimen. Finally, an epoxy-based bonding agent and cellulose-based mortar were applied to the

sample, and their failure mode and bond strength were compared to the optimum specimen. The following conclusions can be drawn:

- Surface treatment had a high impact on the shear and tensile strength of concrete composites. The shear and tensile strength of the concrete with the wire-brushed surface were the highest among other treatment methods. The reason was the mechanical interlocking between old concrete's exposed aggregates and overlay concrete's cement paste caused by wire-brushing. The shear and tensile strength of the composite specimens roughened by chipping was less than those roughened by the wire-brushed method. The reason behind this was the propagation of micro-cracks on the concrete substrate. Using high-strength concrete as an overlay material caused an increment in shear and tensile bond strength. The reason was due to the inclusion of micro silica in overlay concrete mix-proportion, which fills small voids at the interfacial zone and thus enhances adhesion and bonding strength.
- Shear and tensile strength of optimum design increased by adding epoxy adhesive between layers due to its strong adhesion and chemical forces between concrete and the epoxy itself.
- The shear and tensile strength of the optimum design with cellulose-based adhesive mortar was less than the optimum specimen without cellulose mortar due to having a large thickness and the loss of roughness effect and in the concrete substrate. Due to conflicting results obtained from compressive and tensile strength tests, it cannot be definitely concluded that the other reason is the low mechanical performance of HEMC mortar.

5. References

Al-Osta, M.A., Ahmad, S., Al-Madani, M.K., Khalid, H.R., Al-Huri, M. and Al-Fakih, A. (2022). "Performance of bond strength between

ultra-high-performance concrete and concrete substrates (concrete screed and self-compacted concrete): An experimental study", *Journal of Building Engineering*, 51(March), 104291, <https://doi.org/10.1016/j.jobe.2022.104291>.

- ACI Committee 213. (1987). *Guide for structural light-weight aggregate concrete (ACI 213R-87)*, American Concrete Institute, MI.
- Austin, S., Peter, R. and Youguang P. (1995). "Tensile bond testing of concrete repairs", *Materials and Structures*, 28, 249-259.
- Babafemi, A.J., Temitope K., Miah, Md.J., Paul, S.C. and Panda, B. (2021). "A concise review on interlayer bond strength in 3D concrete printing", *Sustainability*, 13, 7137, <https://doi.org/10.3390/su13137137>.
- Baharuddin, N.K., Fadzli M.N., Badorul Hisham, A.B., Salmia B. and A Tayeh, B. (2020). "Potential use of ultra high-performance fibre-reinforced concrete as a repair material for fire-damaged concrete in terms of bond strength", *International Journal of Integrated Engineering*, 12, 87-95, <https://doi.org/10.1016/j.cscm.2022.e01290>.
- Baloch, W.L., Siad, H., Lachemi, M. and Sahmaran, M. (2021). "A review on the durability of concrete-to-concrete bond in recent rehabilitated structures", *Journal of Building Engineering*, 44, 103315, <https://doi.org/10.1016/j.jobe.2021.103315>.
- Behforouz, B., Tavakoli, D., Gharghani, M. and Ashour, A. (2023). "Bond strength of the interface between concrete substrate and overlay concrete containing fly ash exposed to high temperature", *Structures*, 49(2023), 183-197, <https://doi.org/10.1016/j.istruc.2023.01.122>.
- Beushausen, H., Björn, H. and Marco T. (2017). "The influence of substrate moisture preparation on bond strength of concrete overlays and the microstructure of the OTZ", *Cement and Concrete Research*, 92, 84-91, <https://doi.org/10.1016/j.cemconres.2016.11.017>.
- BSI. (2000). *BS EN 12390-6: 2000: Testing hardened concrete—tensile splitting strength of test specimens*, BSI, London, UK.
- Bülchen, D., Kainz, J. and Plank, J. (2012). "Working mechanism of methyl hydroxyethyl cellulose (MHEC) as water retention agent", *Cement and Concrete Research*, 42, 953-959, <https://doi.org/10.1016/j.cemconres.2012.03.016>.
- Carbonell Muñoz, M.A., Harris, D.K., Ahlborn, T. M. and Froster, D.C. (2014). "Bond performance between ultrahigh-performance concrete and normal-strength concrete", *Journal of Materials in Civil Engineering*, 26, 04014031, [https://doi.org/10.1061/\(ASCE\)MT.1943-5533.0000890](https://doi.org/10.1061/(ASCE)MT.1943-5533.0000890).
- Çolak, A., Turgay, Ç. and E Bakırcı, A. (2009).

- “Effects of environmental factors on the adhesion and durability characteristics of epoxy-bonded concrete prisms”, *Construction and Building Materials*, 23, 758-767, <https://doi.org/10.1016/j.conbuildmat.2008.02.013>.
- Courard, L., Piotrowski, T. and Garbacz A. (2014). “Near-to-surface properties affecting bond strength in concrete repair”, *Cement and Concrete Composites*, 46, 73-80, <https://doi.org/10.1016/j.cemconcomp.2013.11.005>.
- Daneshvar, D., Behnood A. and Robisson, A. (2022). “Interfacial bond in concrete-to-concrete composites: A review”, *Construction and Building Materials*, 359, 129195, <https://doi.org/10.1016/j.conbuildmat.2022.129195>.
- de la Precontrainte, Federation Internationale. (1983). *FIP manual of lightweight aggregate concrete*, Surrey University Press.
- Delor-Jestin, F., Drouin, D., Cheval, P-Y. and Lacoste, J. (2006). “Thermal and photochemical ageing of epoxy resin–Influence of curing agents”, *Polymer Degradation and Stability*, 91, 1247-1255, <https://doi.org/10.1016/j.polymdegradstab.2005.09.009>.
- Diab, A.M., Elmoaty, M.A. and Tag Eldin, M.R. (2017). “Slant shear bond strength between self compacting concrete and old concrete”, *Construction and Building Materials*, 130, 73-82, <https://doi.org/10.1016/j.conbuildmat.2016.11.023>.
- Du, W., Yu, J., Gu, Y., Li, Y., Han, X. and Liu, Q. (2019). “Preparation and application of microcapsules containing toluene-di-isocyanate for self-healing of concrete”, *Construction and Building Materials*, 202, 762-769, <https://doi.org/10.1016/j.conbuildmat.2019.01.007>.
- Dybel, P. and Wałach, D. (2017). “Evaluation of the development of bond strength between two concrete layers”, In: *IOP Conference Series: Materials Science and Engineering*, (Vol. 245, No. 3, p. 032056), IOP Publishing, <https://doi.org/10.1088/1757-899X/245/3/032056>.
- EL Afandi, M., Yehia, S., Landolsi, T., Qaddoumi, N. and Elchalakani, M. (2023). “Concrete-to-concrete bond Strength: A review”, *Construction and Building Materials*, 363, 129820, <https://doi.org/10.1016/j.conbuildmat.2022.129820>.
- EN, British Standard. (2009). *Testing hardened concrete, Part 3: Compressive strength of test specimens*, British Standard Institution, London, UK.
- Ezoddin, A., Kheyroddin, A. and Gholhaki, M. (2020). “Investigation of the effects of link beam length on the RC frame retrofitted with the linked column frame system”, *Civil Engineering Infrastructures Journal*, 53(1), 137-159, <https://doi.org/10.22059/cej.2019.280596.1580>.
- Farzad, M., Shafieifar, M. and Azizinamini, A. (2019). “Experimental and numerical study on bond strength between conventional concrete and ultra high-performance concrete (UHPC)”, *Engineering Structures*, 186, 297-305, <https://doi.org/10.1016/j.engstruct.2019.02.030>.
- Feng, S., Xiao, H. and Li, H. (2020). “Comparative studies of the effect of ultrahigh-performance concrete and normal concrete as repair materials on interfacial bond properties and microstructure”, *Engineering Structures*, 222, 111122, <https://doi.org/10.1016/j.engstruct.2020.111122>.
- Feng, S., Xiao, H., Liu, R. and Liu, M. (2022). “The bond properties between ultra-high-performance concrete and normal strength concrete substrate: Bond macro-performance and overlay transition zone microstructure”, *Cement and Concrete Composites*, 128, 104436, <https://doi.org/10.1016/j.cemconcomp.2022.104436>.
- Gadri, K. and Guettala, A. (2017). “Evaluation of bond strength between sand concrete as new repair material and ordinary concrete substrate (The surface roughness effect)”, *Construction and Building Materials*, 157, 1133-1144, <https://doi.org/10.1016/j.conbuildmat.2017.09.183>.
- Guo, T., Xie, Y. and Weng, X. (2018). “Evaluation of the bond strength of a novel concrete for rapid patch repair of pavements”, *Construction and Building Materials*, 186, 790-800, <https://doi.org/10.1016/j.conbuildmat.2018.08.007>.
- He, Y., Zhang, X., Hooton, R.D. and Zhang, X. (2017). “Effects of interface roughness and interface adhesion on new-to-old concrete bonding”, *Construction and Building Materials*, 151, 582-590, <https://doi.org/10.1016/j.conbuildmat.2017.05.049>.
- Huang, H., Yuan, Y., Zhang, W. and Gao, Z. (2019). “Bond behavior between lightweight aggregate concrete and normal weight concrete based on splitting-tensile test”, *Construction and Building Materials*, 209, 306-314, <https://doi.org/10.1016/j.conbuildmat.2019.03.125>.
- Jafarinejad, S., Rabiee, A. and Shekarchi, M. (2019). “Experimental investigation on the bond strength between ultra high strength fiber reinforced cementitious mortar and conventional concrete”, *Construction and Building Materials*, 229(2019), 116814, <https://doi.org/10.1016/j.conbuildmat.2019.116814>.

814.
Julio, E.N., Branco, F.A. and Silva, V.D. (2004). "Concrete-to-concrete bond strength. Influence of the roughness of the substrate surface", *Construction and Building Materials*, 18, 675-681, <https://doi.org/10.1016/j.conbuildmat.2004.04.023>.
- Julio, E.N., Branco, F.A., Silva, V.D. and Lourenço, J.F. (2006). "Influence of added concrete compressive strength on adhesion to an existing concrete substrate", *Building and Environment*, 41, 1934-1939, <https://doi.org/10.1016/j.buildenv.2005.06.023>.
- Mangat, P.S. and O'Flaherty, F.J. (2000). "Influence of elastic modulus on stress redistribution and cracking in repair patches", *Cement and Concrete Research*, 30, 125-136, [https://doi.org/10.1016/S0008-8846\(99\)00217-3](https://doi.org/10.1016/S0008-8846(99)00217-3).
- Michels, J., Sena Cruz, J., Christen, R., Czaderski, C. and Motavalli, M. (2016). "Mechanical performance of cold-curing epoxy adhesives after different mixing and curing procedures", *Composites Part B: Engineering*, 98, 434-443, <https://doi.org/10.1016/j.compositesb.2016.05.054>.
- Mizan, M.Ha., Ueda, T. and Matsumoto, K. (2020). "Enhancement of the concrete-PCM interfacial bonding strength using silica fume", *Construction and Building Materials*, 259, 119774, <https://doi.org/10.1016/j.conbuildmat.2020.119774>.
- Momayez, A., Ehsani M.R., Ramezani pour A.A. and Rajaie, H. (2005). "Comparison of methods for evaluating bond strength between concrete substrate and repair materials", *Cement and Concrete Research*, 35, 748-57, <https://doi.org/10.1016/j.cemconres.2004.05.027>.
- Nawy, E.G. (2000). *Fundamentals of high-performance concrete*, John Wiley & Sons.
- Pourchez, J., Peschard, A., Grosseau, P., Guyonnet, R., Guilhot, B. and Vallée, F. (2006). "HPMC and HEMC influence on cement hydration", *Cement and Concrete Research*, 36, 288-294, <https://doi.org/10.1016/j.cemconres.2005.08.003>.
- Prado, L.P., Carrazedo, R. and El Debs, M.K. (2022). "Interface strength of high-strength concrete to ultra-high-performance concrete", *Engineering Structures*, 252, 113591, <https://doi.org/10.1016/j.engstruct.2021.113591>.
- Santos, D.S., Santos, P.M. and Dias-da-Costa, D. (2012). "Effect of surface preparation and bonding agent on the concrete-to-concrete interface strength", *Construction and Building Materials*, 37, 102-110, <https://doi.org/10.1016/j.conbuildmat.2012.07.028>.
- Shibao, H., Mizan, M.H., Ueda, T., Miyaguchi, K. and Takahashi, J. (2019). "A study on effect of silica fume and surface penetrant on bond-ing strength for overlaying", *Journal of Asian Concrete Federation*, 5, 1-14, <https://doi.org/10.18702/acf.2019.06.30.1>.
- Shin, A.H. and A Lange, D. (2012). "Effects of overlay thickness on surface cracking and debonding in bonded concrete overlays", *Canadian Journal of Civil Engineering*, 39, 304-312, <https://doi.org/10.1139/2012-007>.
- Tayeh, B.A., Bakar, B.A., Johari, M.M., and Voo, Y.L. (2012). "Mechanical and permeability properties of the interface between normal concrete substrate and ultra high performance fiber concrete overlay", *Construction and Building Materials*, 36, 538-548, <https://doi.org/10.1016/j.conbuildmat.2012.06.013>.
- Tu, T., Chen, Y. and Hwang, C. (2006). "Properties of HPC with recycled aggregates", *Cement and Concrete Research*, 36, 943-950, <https://doi.org/10.1016/j.cemconres.2005.11.022>.
- Valikhani, A., Jaber Jahromi, A., Mantawy I. and Azizinamini, A. (2020). "Experimental evaluation of concrete-to-UHPC bond strength with correlation to surface roughness for repair application", *Construction and Building Materials*, 238, 117753, <https://doi.org/10.1016/j.conbuildmat.2019.117753>.
- Valipour, M. and Khayat K.H. (2020). "Debonding test method to evaluate bond strength between UHPC and concrete substrate", *Materials and Structures*, 53, 1-10, <https://doi.org/10.1617/s11527-020-1446-6>.
- Xu, J. and Hao, P. (2012). "Study of aggregate gradations in foamed bitumen mixes", *Road Materials and Pavement Design*, 13, 660-677, <https://doi.org/10.1080/14680629.2012.742627>.
- Zhou, J., Ye, G., Schlangen, E. and Breugel, K. (2008). "Modelling of stresses and strains in bonded concrete overlays subjected to differential volume changes", *Theoretical and Applied Fracture Mechanics*, 49, 199-205, <https://doi.org/10.1016/j.tafmec.2007.11.006>.



This article is an open-access article distributed under the terms and conditions of the Creative Commons Attribution (CC-BY) license.

AIMS AND SCOPE

Since the College of Engineering (Former Faculty of Engineering, FOE) of the University of Tehran has renewed its policy toward scientific publication, the Civil Engineering transaction of the well- built 45 years old Persian journal of "*Nashrieh Daneshkadeh Fanni*" is to be published in English and as separate independent journal with the name of ***Civil Engineering Infrastructures Journal***.

Civil Engineering Infrastructures Journal is an international journal which publishes high quality scientific papers in all areas of engineering and management of civil infrastructures. The civil infrastructures include, but are not limited to: buildings, bridges, dams, transportation systems, geotechnical structures, underground constructions, water distribution systems, offshore platforms, pipelines, ocean structures, airports and power plants.

The scope of this journal encompasses, but is not restricted to the following aspects of engineering and management of infrastructures:

- Mathematical modeling
- Computational and experimental methods
- Environmental Impact assessment
- Passive defense and security issues
- Monitoring and assessment
- Construction and design for durability
- Deterioration modeling and aging
- Failure analysis
- Field testing
- Financial planning
- Inspection and diagnostics
- Life-cycle analysis and prediction

- Maintenance, rehabilitation, repair and replacement strategies
- Non-destructive testing
- Optimization of maintenance and management
- Specifications and codes
- Reliability and risk management
- Supervisory Control and Data Assimilation (SCADA)
- Automation and Robotics in Construction
- Smart civil infrastructure Systems
- Sustainable civil infrastructure systems
- Case studies

Audiences of *Civil Engineering Infrastructures Journal* are researchers and practitioners as well as people working in infrastructure design, construction, maintenance and operation. Papers considered for publication must contain a clear and well-defined engineering component and make a significant contribution to the engineering and management of civil infrastructures. All articles submitted to this journal will undergo a rigorous peer review by anonymous independent experts.

Additional information can be obtained from:

Civil Engineering Infrastructures Journal

College of Engineering,

University of Tehran

P.O. Box: 11155- 4563

Tehran, Iran

Tel/ Fax: +98-21-88956097

Web Site: www.ceij.ir

Email: ceij@ut.ac.ir



University of Tehran
College of Engineering

Copyright Transfer Agreement

In order to protect the author(s), from the consequences of unauthorized use, the publisher requests that all author(s) sign the appropriate statement below:

The author(s) undersigned hereby approves submission of this work and all subsequent revisions for publication and transfers, assigns, or otherwise conveys copyright ownership to the Civil Engineering Infrastructures Journal (CEIJ). I (we) acknowledge that i) the submitted material represents original material, ii) does not infringe upon the copyright of any third party, and iii) that no part of the work has been published or under consideration for publication elsewhere unless and until it is rejected by Civil Engineering Infrastructures Journal (CEIJ). I (we) agree to indemnify the publisher against any loss or damages arising out of a breach of this agreement. In the event that my (our) submission is not published, copyright ownership shall revert to the author (s).

Manuscript Title:

Corresponding Author

Author:

Date:

Signature;

Author:

Date:

Signature:

Author:

Date:

Signature:

Author:

Date:

Signature:

Please submit the signed agreement with the final manuscript to:

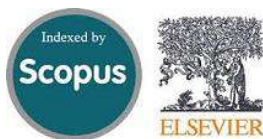
Civil Engineering Infrastructures Journal (CEIJ)
School of Civil Engineering,
College of Engineering, University of Tehran
Enghelab Ave., P.O. Box: 11155-4563, Tehran, Iran.
Tel: 88956097
Fax: 66498981
E-mail: ceij@ut.ac.ir
Website: www.ceij.ir

CIVIL ENGINEERING INFRASTRUCTURES JOURNAL (CEIJ)

is indexed and abstracted in the bibliographical databases including:



Web of Science (ESCI)
<http://science.thomsonreuters.com>



Scopus
<https://www.scopus.com>



Islamic World Science Citation
Center;
<http://www.isc.gov.ir>



Directory of Open Access Journals
(DOAJ)
<https://doaj.org>



Google Scholar
<https://scholar.google.com>



General Impact Factor (GIF)
<http://generalimpactfactor.com>



Scientific Indexing Services (SIS)
<http://www.sindex.org>



International Institute of
Organized Research (I2OR)
<http://www.i2or.com>



Information Matrix for the Analysis
of Journals (MAIR)
<http://miar.ub.edu>



ROAD: the Directory of Open
Access scholarly Resources
<http://road.issn.org>



Scientific World Index
<http://www.sciwindex.com>



International Innovative Journal
Impact Factor (IIJIF)
<http://www.ijif.com>



Science library index
<http://scinli.com>



Journal Factor
<http://www.journalfactor.org>



Open Academic Journals Index
(OAJI)
<http://oaji.net>



Electronic Journals Library (EZB)
<https://rzblx1.uni-regensburg.de>



Systematic Impact Factor
(SIF)
<http://www.sifactor.org>



COSMOS IMPACT FACTOR
<http://www.cosmosimpactfactor.com>

INDEX COPERNICUS
INTERNATIONAL
Polish Ministry of Science and
Higher Education (MSHE)
<https://journals.indexcopernicus.com>

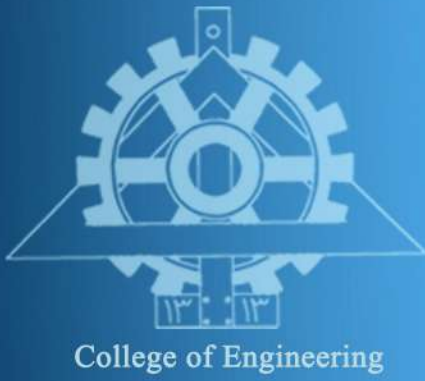


Magiran
<http://www.magiran.com>



Scientific Information Database
(SID); Iran;
<http://www.Sid.ir>

Ministry of Science, Research and Technology of Iran has granted the Science and Research (Elmi-Pajouheshi) credit to CEIJ according to the letter No. 3/252445 at 25 Feb. 2012.



Civil Engineering Infrastructures Journal

Volume 57, Number 1, June 2024

CONTENTS:

Research Papers

- Compressive Strength and Microstructural Properties of Sustainable Concrete 1**
Containing Nanosilica, Alccofine and Metakaolin
Bhat, A.H., Naqash, J.A., Habib, T. and Islam, S.U.
- Damage Detection of Truss Bridges Using Wavelet Transform of Rotation Signal 17**
Ghafouri, H.R., Khajehdezfuly, A. and Saadat Poor, O.
- A Novel Method for Modal Analysis of Dam-Reservoir Systems 33**
Rezaiee-Pajand, M., Kazemiyani, M.S. and Mirjalili, Z.
- Comparison of the Mechanical Performance of Concrete Reinforced with Recycled Steel Fibers 61**
from Waste Tires and Hooked-End Steel Fibers at Ambient and High Temperatures
Modarres, Y. and Ghalehnovi, M.
- Predicting the Fluctuation of Travel Time Reliability as a Result of Congestion 85**
Variations by Bagging-Based Regressors
Afandizadeh Zargari, Sh., Amoei Khorshidi, N., Mirzahosseini, H. and Shakoobi, S.
- Effective Location of Shear Walls in High-Rise RCC Buildings Subjected to Lateral Loads 103**
Shukla, K. and Nallasivam, K.
- Three-Dimensional Numerical Investigation of Tunnel Behavior Based on Different 119**
Constitutive Models and Associated Parametric Analysis in Rock Medium
Chalajour, S. and Hataf, N.
- Optimization of Dynamic Compaction Procedure for Sandy Soils 145**
Bayat, M., Saadat, M. and Hojati, A.
- Pushover Analysis of Reinforced Concrete Moment-Resisting Frames to Account for 157**
the Variations of Axial Forces on the Moment Curvature Properties
Samadi, N., Aghayari, R. and Izadpanah, M.
- Upper Bound Solution for the Stability of Surcharged Soil Slope Using 175**
Nonlinear Failure Criterion
Aminpour, M.M. and Maleki, M.
- Determination of DBTT of Functionally Graded Steels Using Artificial Intelligence 189**
Anjali, K., Yesilyurt, S.N., Samui, P., Dalkilic, H.Y. and Katipoglu, O.M.
- Comparative Study of the Effects of Key Factors on Concrete-to-Concrete Bond Strength 205**
Mack, V., Salehfard, R. and Habibnejad Korayem, A.